

AIAA Sydney Section Student Conference

Technical Paper Proceedings

Available for Viewing: 15 December 2020 – 15 January 2021

The technical papers enclosed were submitted and presented at the AIAA Sydney Section Student Conference, held virtually 25-26 November 2020 and hosted by the University of New South Wales AIAA Student Branch. This conference featured students from around AIAA Region VII who presented in three (3) categories: Undergraduate, Masters by Coursework, and Masters by Research. To submit, submitters must be AIAA Student Members and must be attending an accredited university in AIAA Region VII. The submission topic was Open Topic, which allowed students to submit on a variety of topics in the Aerospace field. Student presentations were evaluated by AIAA professional members from a variety of backgrounds. You will find papers enclosed - please note that all authors retain their copyright.

If you have any questions about AIAA Student Programs or the AIAA Student Conference Program, please contact us at studentprogram@aiaa.org.

Contents

All papers are organized by category and then alphabetically by paper title. Please use Adobe navigator to go directly to the pages you would like to view.

Undergraduate Category.....	2 - 148
Masters by Coursework Category	149 - 173
Masters by Research Category	174 - 275

Aeroacoustic Impact of Propeller Tip Geometry on Low Reynolds Number UAV Propellers

Marco Alberto * and Con Doolan †
University of New South Wales, Kensington, NSW, 2052

The popularity of unmanned aerial vehicles (UAVs) has taken off in the past decade and as a result, small-scale propeller noise has been thrust into the spotlight. This paper aims to investigate the noise production of small-scale propellers and reduce the noise produced by modifying propeller tip geometry, primarily using proplets. Through an experimental approach combined with a numerical model, two 11 x 6" propellers were designed, 3D printed, and then tested in an acoustic wind tunnel under dynamic flow conditions of 10 *m/s*. The results presented in this paper show that the proplets have an overall positive effect on the noise produced, with a sound pressure level difference of 1.63 dB(A) observed at 6850 RPM. The differences were primarily due to reductions in tone noise, while the proplets tended to have a lesser effect on broadband noise. These results show the viability of proplets as a method of reducing UAV propeller noise, while also prompting further investigation into thrust generation, efficiency, and the effect of proplet design parameters.

I. Nomenclature

c_n	=	Fourier coefficients
c_o	=	Speed of sound at an observer, <i>m/s</i>
f_D	=	Drag force, <i>N</i>
\bar{f}_i	=	Normalised frequency, <i>Hz</i>
f_L	=	Lift force, <i>N</i>
h	=	Blade thickness, <i>m</i>
k_x	=	Chord-wise wave number
l_w	=	Proplet length, <i>mm</i>
n	=	Blade passing frequency number
r	=	Radial position
r_e	=	Propagation distance, <i>m</i>
r_w	=	Proplet radius, <i>mm</i>
z	=	Vertical position, <i>m</i>
B	=	Number of propeller blades
F_i	=	Spectral function
L	=	Turbulent length, <i>m</i>
M	=	Mach number
R	=	Propeller tip radius, <i>m</i>
Re	=	Reynolds number
U_∞	=	Free stream flow velocity, <i>m/s</i>
V	=	Blade volume, <i>m</i> ³
V_j	=	Displaced volume, <i>m</i> ³
Ω	=	Rotational speed, <i>rev/min</i>
ω	=	Angular velocity, <i>rad/s</i>
ϕ_b	=	Blend angle, <i>deg</i>
ρ_o	=	Density at an observer, <i>kg/m</i> ³

*Undergraduate Student, School of Mechanical and Manufacturing Engineering, AIAA Student Member.

†Professor (Faculty Advisor), School of Mechanical and Manufacturing Engineering, AIAA Senior Member.

II. Introduction

The presence of unmanned aerial vehicles (UAVs), commonly referred to as drones, in use worldwide has dramatically increased since the turn of the century, particularly with the development of low cost, reliable on-board control systems. Software like Ardupilot combined with hardware like Pixhawk has allowed for many hobbyists and companies to develop UAVs which are capable of long-range autonomous missions. UAVs have been developed for aerial surveying, disaster and humanitarian relief, parcel delivery, and aerial surveillance, though most applications are still in military scenarios [1].

As this technology becomes more common, the number of commercial applications will increase dramatically, leading to a greater presence of small-scale UAVs in populated areas [2], posing a variety of new challenges. With modern commercial UAV systems generally taking the form of either multi-rotors, or multi-rotor-plane hybrids, as shown in Fig. 1, security and safety are the two biggest concerns. Following a study conducted by Chang et al. [3] looking into human perception of UAVs in urban environments, it was found that 80% of participants were concerned about recording without consent, and 75% were worried about the consequences of a potential crash or failure.

In addition to the safety of UAVs, Chang et al. [3] found all participants in the study commented negatively on the noise UAVs produce, noting a threatening and annoying presence. The perceived annoyance of UAVs versus other vehicles poses a large hurdle to the commercialisation of UAV systems. This creates an increasing distrust of the technology even when safe practices are undertaken, reducing the economic potential of UAVs [2]. A study conducted by Christian and Cabell [4] compared the perceived annoyance due to noise for four ground vehicles and three quad-copter UAVs, with UAVs found to be more annoying than ground vehicles when operating at equivalent noise levels.



Fig. 1 Two commercial options available for UAV parcel delivery systems, a multi-copter-plane hybrid (left) [5] and a multi-copter (right) design [6].

While safety and privacy issues can be primarily addressed through proper education and legislation, noise from UAVs must be addressed on a design level. In general, majority of this noise is from propellers or propulsion systems, with the fuselage, support structure, and payload noise negligible for most small UAVs. For this reason, the focus of this paper will be on propeller-generated noise and how the modification of propellers impacts on their aeroacoustic behaviour. There are two main methods for modifying propellers for noise and performance benefits, altering the propeller tip geometry and adding serrations to the trailing edge. The focus of this paper is primarily on the alteration of tip geometry, due to the extensive research base already available for trailing edge serrations on both large- and small-scale propellers.

The idea of altering the propeller tip geometry, like adding winglet structures to the ends of propellers (known as proplets) is not new. In a review of literature, Metzger [7] outlined a variety of practical noise reduction methods available to the general aviation industry. An analysis by Korkan et al. [8] on a subset of Cessna aircraft showed that the implementation of proplets on general aviation propellers resulted in a significant noise reduction. This reduction was attributed to the lower rotational speed, as the propellers with proplets produced more thrust at the same speed as propellers without proplets. It was also noted that propellers with lower tip loading showed more significant noise reduction when proplets were implemented.

In addition to the work of Korkan et al. [8], Irwin and Mutzman [9] described an experimental approach to testing propeller modification using a basic proplet design, which involved attaching an airfoil to the tip of an existing propeller. While there was a lack of experimental data, theoretical background supporting the use of proplets was presented, showing that proplets provided a 1% increase in efficiency. Using a basic proplet design was noted as a major drawback, with further analysis required on the effect of proplet angle, height and cross-sectional geometry; the efficiency gains of a well-designed proplet were theorised to be much higher than 1%.

Sullivan et al. [10] further analysed the effect of a variety of different proplets in presenting theoretical data which supported the work of Korkan et al. [8]. Sullivan proposed that proplets were an effective way of increasing efficiency

and decreasing noise generation of propellers. Using analytical methods, Sullivan showed that an increase in efficiency of 1-5% was possible by adding proplets to the ends of an existing propeller. The article also concluded that reducing the blade diameter with proplets added would decrease noise generation while keeping efficiency constant (relative to a propeller without proplets), even while there was no change in noise measured by adding proplets in the experiments conducted. While these experiments were conducted on general aviation aircraft, the analysis and operation of UAV propellers are very similar, showing their potential for use on a smaller scale.

In order to investigate the effects of proplets on UAV propellers, several experiments have been conducted, including by Intravartolo et al. [11] and Bessa [12]. Both experiments were conducted in open air environments for static flow cases, allowing for environmental noise to contribute to the overall noise measured. While the results determined by Intravartolo et al. [11] suggest that proplets did not reduce the overall noise of a propeller, it was also concluded that propeller balancing and structural instabilities may have contributed to this result. The experimental analysis conducted by Bessa [12] addressed some of these concerns with 3D printed custom propellers with proplets, as shown by the designs in Fig. 2.



Fig. 2 Three designs of proplets used by Bessa [12] in the analysis of noise, with a proplet height 7mm (top), 10mm (middle), and 15mm (bottom).

In contrast to Intravartolo et al. [11], noise reductions were observed in comparison to a baseline propeller, while Bessa [12] also conceded that the inability to conduct experiments in an acoustic wind tunnel likely contributed to some inaccuracy of measurements. The lack of acoustic simulations to guide the design process was also mentioned as a potential source of inefficiency in the design. From these recent experiments, the need for acoustic wind tunnel testing of custom-designed propellers with proplets is vital for determining their viability in UAV applications, along with a predictive method to aid in the design process.

This paper will focus on an experimental approach to modified propeller tip geometry, with the aim of analysing the noise signature of these propellers in a dynamic flow environment. In doing this, a secondary aim of developing a more robust numerical predictive model for small-scale UAV propellers was undertaken and is also outlined in this paper. This model was then validated using the experimental results gained for an unmodified propeller.

III. Numerical Model

The design phase for the modified propellers used an existing numerical model with several additions to predict the noise signature of propellers and was iterated to determine a set of suitable designs with increasing predicted noise reductions. A summary of the main equations and theory used for the numerical model is presented below.

The acoustic portion of the model was developed using a number of tone and broadband noise formulations for propeller noise. The major component of tone noise is steady loading noise, built upon the Lighthill wave equation and equations developed by Curle [13], Ffowcs-Williams and Hawkings [14]. These formulations showed tone noise depends primarily on the rotor flow conditions (density, viscosity, etc.) and propeller tip speed. These formulations can be represented in both the time and frequency domains. Time domain solutions are primarily used for propellers with high subsonic or supersonic speeds, generally on large-scale propeller-driven aircraft or helicopters.

Hanson [15] developed a solution in the frequency domain, finding that the calculated terms had an advantage in the design and modification of propellers. In particular, the effects of propeller geometry and operating conditions were found to be significantly easier to identify and design for compared with time domain methods. For these reasons, the frequency domain solution is more appropriate for small-scale, low Reynolds number propellers. An existing code developed by Doolan et al. [16] implemented this frequency domain solution, summarised by the major equations Eq. (1), (2), and (3) and was used as the basis for the numerical model in this paper.

$$p'(\mathbf{x}, t) = B \sum_{m=-\infty}^{\infty} c_{n=mB} e^{-imB\Omega t} \quad (1)$$

$$c_n(\mathbf{x}) = \frac{in\Omega e^{\frac{in\Omega|\mathbf{x}|}{c_o}}}{4\pi|\mathbf{x}|c_o} \sum_{m=-\infty}^{\infty} \int_{r_{hub}}^R Q_{m,n}(r, \mathbf{x}) J_m\left(\frac{n\Omega r \sin \theta_o}{c_o}\right) dr \quad (2)$$

$$Q_{m,n}(r, \mathbf{x}) = \int_{\phi_{TE}}^{\phi_{LE}} \left[f_L^{(n-m)}(r, \phi_1) \cos \theta_o \delta_{mn} + f_D^{(k)}(r, \phi_1) \sin \theta_o \frac{\delta_{n,m+k+1} - \delta_{n,m+k-1}}{2i} + im\Omega \rho_{\infty} c_o h(r, \phi_1) \delta_{mn} \right] e^{-im(\phi_1 - \phi_o + 0.5\pi)} r d\phi_1 \quad (3)$$

Blade element momentum (BEM) theory has been used in a variety of applications, equally useful for small and large-scale propellers and wings. Due to the aerodynamic force requirements (f_L and f_D) of Eq. (3), these forces must be resolved for each blade element. A BEM theory code implemented by Doolan et al. [16] was used to determine the aerodynamic forces on a propeller, and integrated into the acoustics model.

As an improvement to the existing code, XFOIL analyses were conducted for a NACA 4412 airfoil under non-stall conditions of the airfoil (between -20 and 10 degrees) at Reynolds numbers between 25,000 and 100,000 in 25,000 increments. Blade element Reynolds numbers or angles of attack in these regions were linearly interpolated to determine the aerodynamic coefficients.

To further increase the accuracy of the acoustic portion of the numerical model, several broadband noise sources were implemented into the existing tone noise prediction code. The first was trailing edge noise, a natural by-product of flow leaving the trailing edge of an airfoil, primarily caused by the pressure differential between the upper and lower surfaces creating turbulence in the region behind the airfoil. Many methods of analysing and calculating the trailing edge noise have been derived, with those from Ffowcs-Williams and Hall [17], Amiet [18], and Brooks et al. [19] being several of the most commonly used for propeller noise.

The method developed by Brooks et al. [19] is one of the most popular, due to the empirical nature of the formulas, while also agreeing with the analytical solutions proposed by Ffowcs-Williams and Hall [17] and Amiet [18]. The trailing edge noise can be calculated for a wide range of Reynolds numbers, boundary layer thicknesses (δ_i^*) and most importantly, angles of attack (α). This allows for a robust prediction of the trailing edge noise, as well as any noise generated from trailing edge vortex shedding, and vortices caused by a stalled airfoil. The major equation for this method is shown in Eq. (4) with the required empirical equations taken from Glegg and Devenport [20].

$$SPL_i(\mathbf{x}, \bar{f}_i; Re, \alpha, M) = 10 \log_{10} \left(\frac{2 \sin^2(\frac{1}{2}\theta_r) \sin^2(\phi_r)}{(1 + M \cos(\theta_r))(1 + (M - M_c) \cos(\theta_r))} \frac{b\delta_i^* M^5}{r_r^2} \right) + F_i(\bar{f}_i; Re, \alpha, M) \quad (4)$$

The other broadband noise source modelled was the inflow noise, which is generated around the leading edge due to turbulent flow. Amiet [21] derived a simple formula to calculate the sound pressure level for 1/3-octave bands. The generalised formula is shown in Eq. (5), with the one assumption made in this equation being the flow velocity variance (u^2), assumed to be $0.01 m^2/s^2$.

$$SPL_{1/3} = 10 \log_{10} \left[\frac{0.07cb}{2z^2} \frac{u^2}{U_{\infty}^2} M^5 \frac{(-k_x/k_e)^3}{(1 + (-k_x/k_e)^2)^{7/3}} \right] + 10 \log_{10} \left[\frac{0.231 \times 10^{10}}{2} \frac{4}{9\sqrt{\pi}} \frac{\Gamma(1/3)}{\Gamma(5/6)} \left(\frac{\rho_o}{\pi}\right)^2 c_o^4 \right] \quad (5)$$

The complete model was then used to generate predictions for the noise generated over the first five blade pass frequencies for all designs, as well as showing the contribution of each noise source to the overall noise signature. These predictions were also useful in modifying the design parameters for the proplet to ensure a small noise reduction.

IV. Experimental Method

The designed propellers were a simplified version of the Master Airscrew 11x6" propeller, using a NACA4412 airfoil along the whole blade at discrete radial locations. The geometry of the unmodified propeller (radius, chord, and angle of attack) was taken from the UIUC database for small-scale propellers developed by Brandt [22].

To test the effect of tip changes, modifications were limited to the last 10% of the radius (0.90R outwards). This method also had the best potential to retain the aerodynamic properties of the propeller despite the modifications. Design parameters were chosen based on the design of a simple proplet for the propellers, including proplet length, proplet radius, blend angle, chord at 0.95R, and chord at 1.00R (propeller tip). This simplified 2D geometry is shown in Fig. 3.

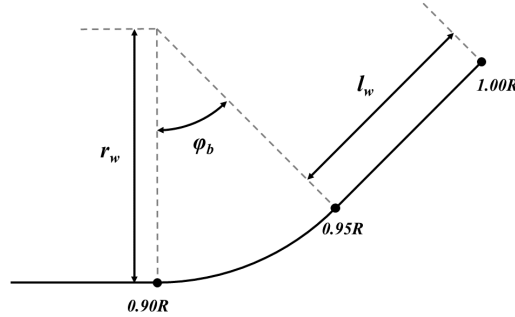


Fig. 3 Winglet design parameters.

The modified design (Design 1) used a proplet length of 5 mm, a proplet radius of 10 mm and a blend angle of 45 degrees. The baseline design (Design 0) was based on the geometry and airfoil simplifications, and also modelled in CATIA and manufactured to ensure results could be compared fairly. The baseline and modified propellers modelled in CATIA are shown in Fig. 4.

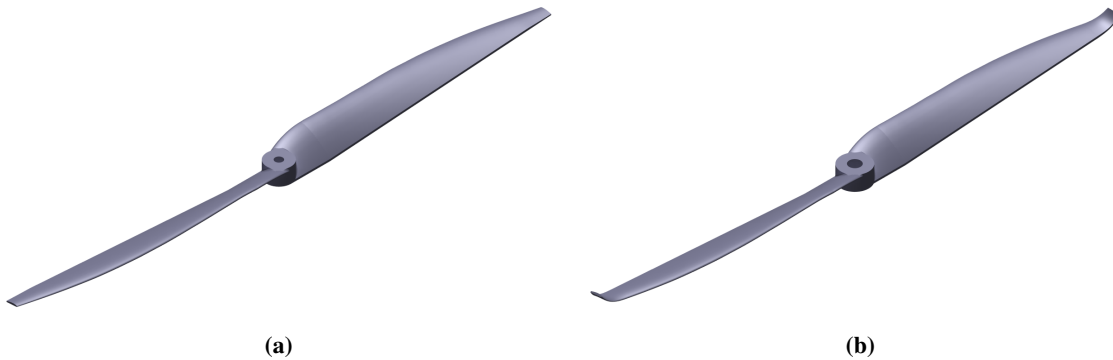


Fig. 4 Design 0, (a) and Design 1 (b) propeller CAD renders.

The designed propellers were then manufactured using the selective laser sintering (SLS) 3D printing method, with Nylon as the material. Using SLS allowed for thin sections (<1 mm) to be printed accurately, while also having the required strength to withstand the aerodynamic loading during the experiments.

The designed propellers were experimentally tested in the UNSW Acoustic Wind Tunnel (UAT), an open-jet wind tunnel with a test section measuring 0.455 m x 0.455 m in an anechoic chamber of 3 m x 3.2 m 2.15 m. Further details about the UAT can be found in experiments conducted by Yauwenas et al. [23]. The complete setup of the wind tunnel for the experiments is shown in Fig. 5a.

The acoustic measurements were taken using a microphone array, consisting of 64 G.R.A.S 40PH phase and magnitude matched microphones. The array was arranged in 7 concentric circles of 9 microphones each, in addition to a centre microphone, as shown in Fig. 5b. The array was placed perpendicular to the flow, with only microphone 44 (Mic 44) used due to being directly in line with the propeller blade. The positioning of Mic 44 was measured as

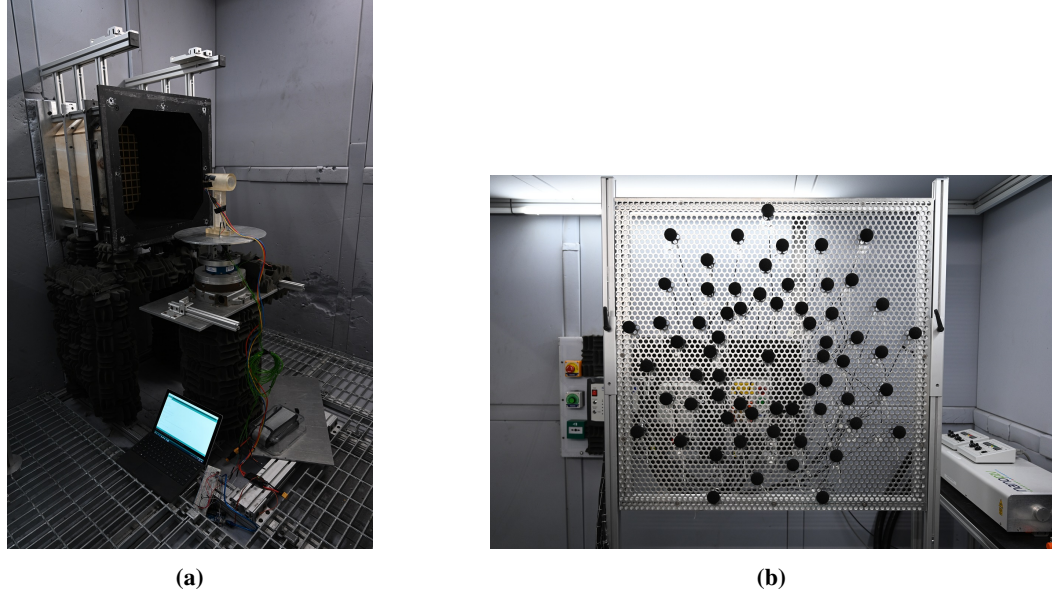


Fig. 5 Experimental setup in the wind tunnel, including laptop, Arduino, battery and propeller mount (a) and microphone array (b).

having a directional angle (θ) of 0 deg, elevation (ϕ) of 3.06 deg, and radial distance (r) of 1.312 m relative to the centre of the propeller. A PXIe-4499 24-bit National Instrument data acquisition system was used to record the data, for a collection time of 30 seconds at a sampling rate of 65536 Hz. This raw data was then converted into a Matlab data file in a two-step process using several conversion scripts.

An Arduino UNO microcontroller was used to control the motor speed and monitor motor RPM. The signal to the motor through the Arduino was controlled through TeamViewer to remotely access the computer inside the wind tunnel. A 5000 mAh 4S Lithium-polymer (LiPo) battery and 60 A electronic speed controller (ESC) were used to power and control the Turnigy Air Brushless 3730-1000KV motor.

A simple 3D printed mounting was used to hold the motor and attach to the supports in the UAT, as illustrated in Fig. 6. The motor was housed in a thick-walled cylinder and supported by a symmetric airfoil pylon to reduce the aerodynamic forces on the mounting.

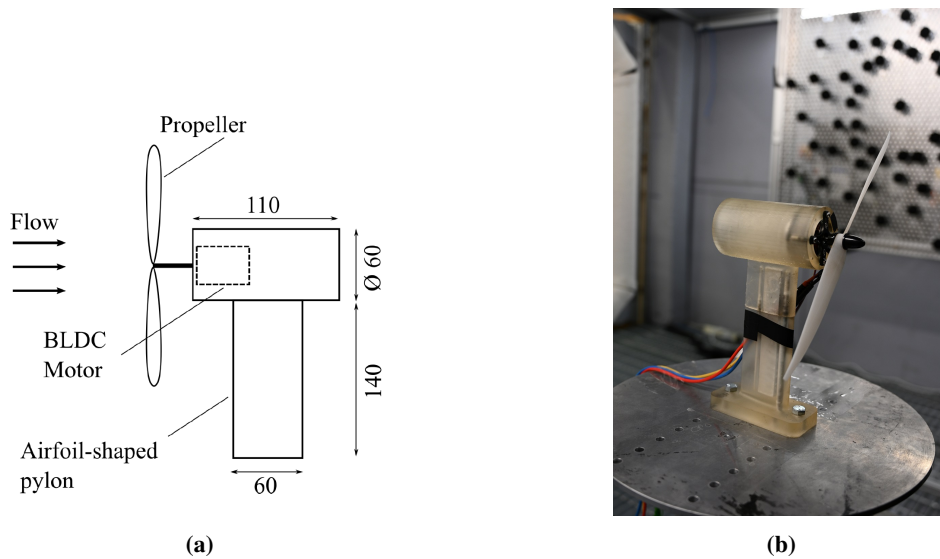


Fig. 6 General dimensions for motor mount (a), and propeller mounted on motor mount in wind tunnel (b).

The propellers were tested at a variety of motor speeds to ensure the integrity of the propellers and compare the effect of motor speed on noise. The five motor speed values tested were 3600, 4700, 5400, 6100, and 6850 RPM. Both propellers were tested at these speeds, using a flow velocity in the wind tunnel of 10 *m/s* for all tests.

The experimental data gained from the wind tunnel was analysed in two different ways, to determine both the total and the broadband noise at each blade passing frequency (BPF). For the total noise determination, a first order filter was used to correct the data for an apparent moving average in the data. Following this correction, a two-sided bandpass filter was applied around the blade passing frequencies of ± 40 Hz. The RMS of the pressure values filtered was then taken and converted into a sound pressure level (SPL) for each BPF.

For the broadband noise determination, a third order filter was firstly applied to correct the data for any moving average in the data, as with the tone noise determination. The mean revolution pressure over the first 15 seconds of data was then determined and subtracted from the initial time-domain pressure data. The second 15 seconds was omitted to reduce the potential error in the broadband noise extraction. Using Welch's averaged modified periodogram method, the power spectral densities (PSD) of the pressures were determined, filtered with a Hamming window, and has a frequency resolution of 5 Hz. A two-sided bandpass filter was again applied around the blade passing frequencies of ± 40 Hz. The RMS of the PSD values filtered was then taken and converted into an SPL for each BPF.

V. Results

A. Numerical Predictions

The predictions based on the numerical model were made for a motor speed of 6850 RPM only due to the breakdown of the model at slower motor speeds. This is likely due to the slow free stream velocity of the flow resulting in the propeller acting as a turbine (i.e. generating power) rather than a propeller. For this reason, results shown in this paper are for a motor speed of 6850 RPM and flow velocity of 10 *m/s* unless otherwise stated.

Figure 7 shows the components of tone noise produced by the Design 0 propeller over the first five blade passing frequencies, with predictions for both designs having a comparable shape and magnitude. The steady loading noise contributes mostly to the tone noise, while thickness noise was less due to the thin airfoil used for the propeller. The total tone noise can be shown to reduce linearly with each blade passing frequency, to the point of complete inaudibility by the fifth BPF.

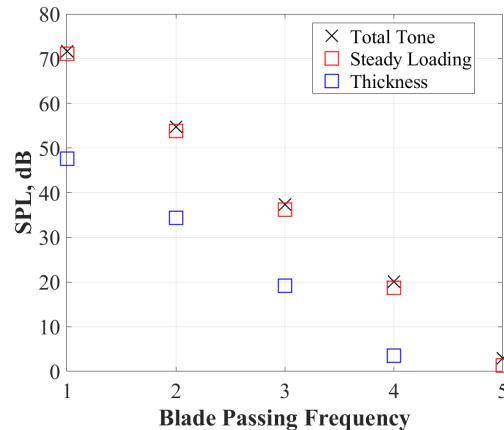


Fig. 7 Design 0 tone noise signature over the first five blade passing frequencies.

Figure 8 shows the components of broadband noise produced over the first five BPFs. The broadband noise shows a logarithmic trend with increasing BPF, with the inflow noise dominating the total over all the BPFs. The broadband noise reaches a near constant value of around 54 dB for both designs, having a different trend to the linearly decreasing tone noise.

Figure 9 combines the two tone and broadband components to propeller noise to predict the overall noise signature of the propeller at 6850 RPM in a 10 *m/s* free stream flow. The first two BPFs are dominated by the tone noise, however the broadband noise begins to dominate from the third BPFs onwards. The shape of the predicted noise matches

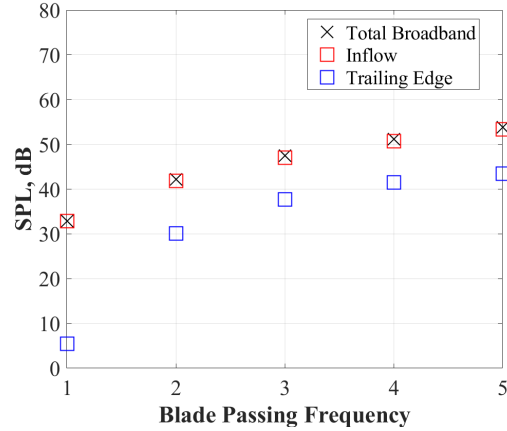


Fig. 8 Design 0 broadband noise signature over first five blade passing frequencies.

experimental results for a similarly sized propeller gathered by Doolan et al. [16], while both designs demonstrated comparable shapes and magnitudes.

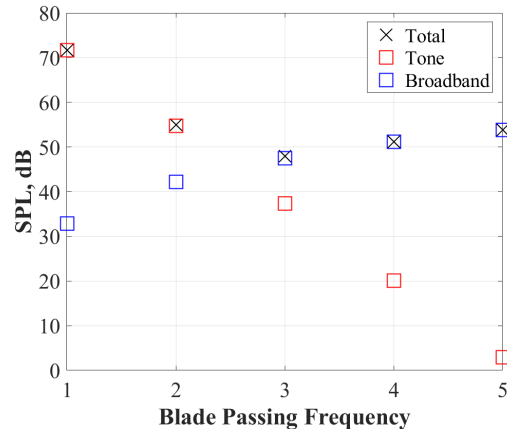


Fig. 9 Total predicted noise for the Design 0 propeller over the first five blade passing frequencies.

B. Experimental Results

Figure 10 shows the comparison between numerical and experimental results for both designs. The numerical predictions appear to under-predict in the tone noise-dominated BPFs (1-2), while marginally over-predicting in the broadband noise-dominated BPFs (3-5). This would suggest that the tone noise predictions are missing a small portion, potentially due to misalignments in the testing rig or other factors causing an unsteady loading of the propeller. Further, the over-prediction of broadband noise suggests slight inconsistencies in the assumptions for inflow noise, including the characteristic turbulent length scale and flow velocity variance. Both of these values could be measured for greater accuracy; however, the results were close enough to suggest any increases in accuracy would have minimal design benefit.

Figure 11 shows a direct comparison between the experimental results for both designs, with Design 1 showing clear differences over the first four BPFs (0.686, 4.65, 5.20, and 1.88 dB respectively). The greatest differences between the designs are found in the second and third BPFs, while the reduction in the first BPF also carries significant weight due to the magnitude of this BPF. From this comparison, it is clear that the proplet has a positive effect on the noise produced over the first five BPFs. These results also show that the proplets have a greater effect on tone noise than broadband noise, given the large differences in the first three BPFs where tone noise dominates.

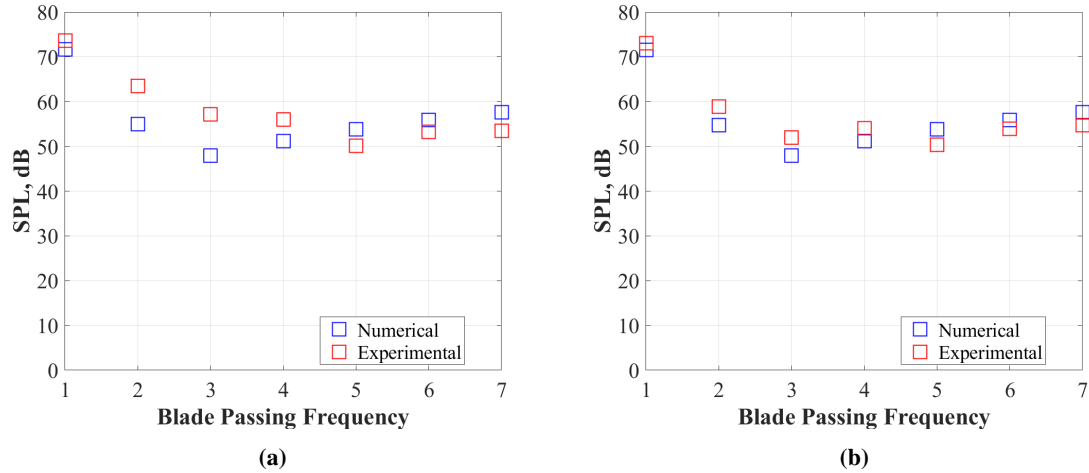


Fig. 10 Design 0 (a) and Design 1 (b) noise signature over the first 7 blade passing frequencies.

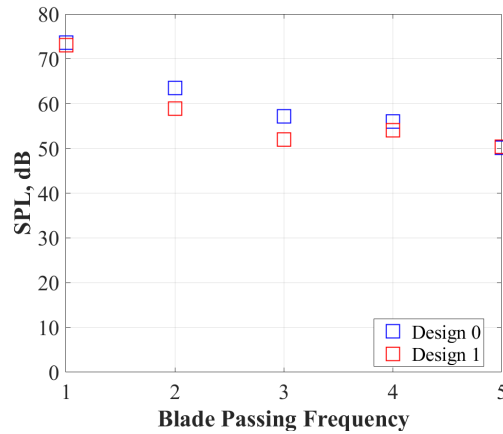


Fig. 11 Experimental result comparison between Design 0 and Design 1 over the first five blade passing frequencies.

Table 1 shows a summary of the numerical and experimental total SPL values for both Design 0 and Design 1, as well as the appropriately A-weighted values. For each blade passing frequency, the A-weighting was determined using linear interpolation between the two nearest weightings, and then applied to the unweighted values. Each BPF value was then added logarithmically for both numerical and experimental results. These summations show that the numerical model significantly under-predicts the expected noise reduction, while also under-predicting more for Design 0 more than Design 1. This is a direct result, and further confirmation, of the effect that proplets can have on tone noise, while the broadband noise is relatively unchanged between the designs, as shown in Fig. 10.

By A-weighting the results, the overall difference between the two designs increases to 1.63 dB(A), better representing the actual human-audible difference between the designs. The greater difference between the designs is primarily at the second and third blade passing frequencies (457 and 686 Hz respectively), where A-weighting has a lesser impact on the apparent SPL.

Figure 12 shows the comparison between the numerical prediction for broadband noise and the extracted broadband noise from the experimental data. The overall shape of the experimental data matches the prediction, with a slight over-prediction across all BPFs, matching the overall noise predictions for broadband dominated BPFs in Fig. 10. In both designs, the second BPF was significantly lower than expected, and this may be due to the numerical methods applied to the data to extract the broadband noise from a tone-dominated noise region. The Design 1 propeller showed a slight decrease in broadband noise, further demonstrating the impact that proplets have is primarily on tone noise.

Table 1 Numerical and experimental un-weighted and A-weighted sound pressure levels for both Design 0 and Design 1.

	Numerical Design 0	Experimental Design 0	Numerical Design 1	Experimental Design 1	Numerical Difference	Experimental Difference
Total SPL (dB)	71.90	74.24	71.79	73.26	0.109	0.982
Total SPL (dB(A))	63.36	66.34	63.27	64.71	0.092	1.63

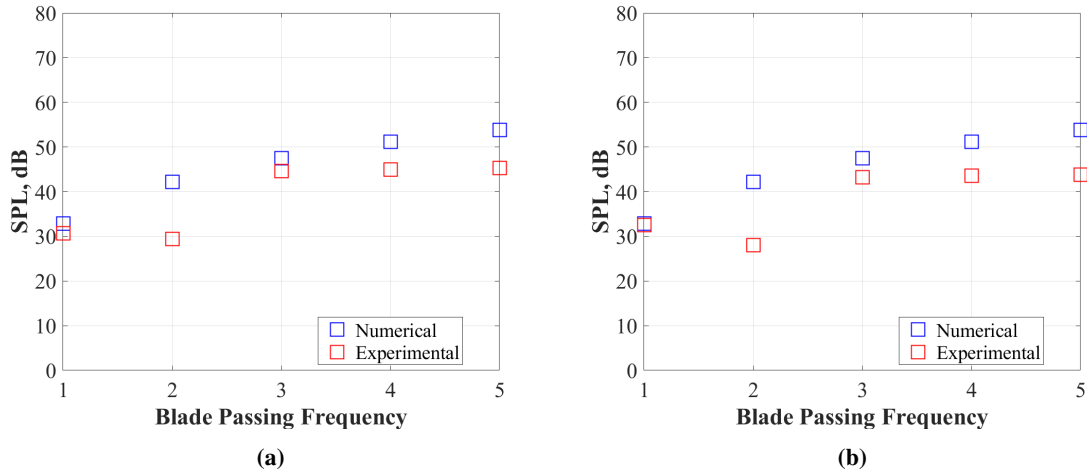


Fig. 12 Design 0 (a) and Design 1 (b) broadband noise signature over the first 5 blade pass frequencies.

VI. Conclusions

This paper presents an experimental approach to investigate the effect of proplets on tone and broadband noise generated by small-scale UAV propellers. The experimental results showed a positive effect of proplets on the noise generated over the first five blade passing frequencies. An A-weighted decrease of 1.63 dB(A) was observed for the propeller using proplets, primarily reducing the tone-generated noise over the first three BPFs. These results show that proplets can be viable as a noise reduction method and could allow for a much more widespread use of UAVs, particularly in commercial and future military applications.

A numerical model was also used and improved to provide more accurate predictions for propellers both with and without proplets. Even with these improvements, the numerical model tended to under-predict noise for tone-dominated regions and slightly over-predict in broadband-dominated regions. The under-predicted tone noise may have been due to the omission of unsteady loading effects, while over-predicted broadband noise may have been due to assumptions in the inflow noise prediction. Further development of the numerical model could be undertaken to help increase the accuracy of the predictions. Given the lack of available low-resource prediction methods, the numerical prediction model presented in this paper provides a fast and relatively accurate predictions during conceptual design of UAV propellers.

Several different aspects of proplets were identified during this paper which would require further investigation to fully understand the impact of each of these. The effect of proplet design parameters on the overall noise generated would be useful to develop a greater understanding of how proplets effect UAV propeller noise. Additional research on how proplets impact noise generated by propellers of different diameter and pitch could explore the scalability of the results shown in this paper. Finally, thrust and power measurements could be taken while taking noise measurements to understand the trade-off between noise reduction, propeller efficiency, and thrust loss.

Overall, this paper shows the viability of proplets in limited scenarios and the potential, through further investigation, to be implemented in a wider variety of civil and military applications.

References

- [1] Calvo, J., “Drones, Drones Everywhere! The Rise of Drone Technology,” March 2019. URL <https://e.globis.jp/tech-innovation/drones-drones-everywhere-the-rise-of-drone-technology/>, accessed on 16 March 2020.
- [2] Castellano, F., “Commercial Drones Are Revolutionizing Business Operations,” n.d. URL <https://www.toptal.com/finance/market-research-analysts/drone-market>, accessed on 16 March 2020.
- [3] Chang, V., Chundury, P., and Chetty, M., “Spiders in the Sky: User Perceptions of Drones, Privacy, and Security,” *CHI Conference on Human Factors in Computing Systems*, 2017, pp. 6765–6776.
- [4] Christian, A., and Cabell, R., “Initial Investigation into the Psychoacoustic Properties of Small Unmanned Aerial System Noise,” *17th AIAA Aviation Technology, Integration, and Operations Conference*, 2017.
- [5] Summers, N., “Alphabet’s Wing launches drone delivery service in Australia,” September 2019. URL <https://www.engadget.com/2019/04/09/alphabet-wing-drone-delivery-service-australia/>, accessed on 16 March 2020.
- [6] Unmanned Publications, “Drone delivery operations underway in 27 countries,” April 2019. URL <https://www.unmannedairspace.info/latest-news-and-information/drone-delivery-operations-underway-in-26-countries/>, accessed on 16 March 2020.
- [7] Metzger, F. B., “An Assessment of Propeller Aircraft Noise Reduction Technology,” *NASA Contractor Report 198237*, 1995.
- [8] Korkan, K. D., Gregorek, G. M., and Keiter, I., “An Acoustic Sensitivity Study of General Aviation Propellers,” *AIAA Aircraft Systems Meeting*, 1980.
- [9] Irwin, K., and Mutzman, R., “Propeller Proplet Optimisation Based Upon Analytical and Experimental Methods,” *AIAA/SAE/ASME 16th Joint Propulsion Conference*, 1980.
- [10] Sullivan, J. P., Chang, L. K., and Miller, C. J., “The Effect of Proplets and Bi-Blades on the Performance and Noise of Propellers,” *SAE Transactions Vol. 90*, 1981.
- [11] Intravartolo, N., Sorrells, T., Ashkharian, N., and Kim, R., “Attenuation of Vortex Noise Generated by UAV Propellers at Low Reynolds Numbers,” *AIAA Region VI Student Conference*, 2016.
- [12] Bessa, R. K., “Experimental Aeroacoustic Study of Noise Reduction Devices for UAVs,” Bachelors thesis, Federal University of Uberlandia, 2018.
- [13] Curle, N., “The Influence of Solid Boundaries upon Aerodynamic Sound,” *Proceedings of the Royal Society Series A. Mathematics and Physical Sciences Vol. 231 No. 1187*, 1955.
- [14] Ffowcs-Williams, J. E., and Hawkings, D. L., “Sound Generation by Turbulence and Surfaces in Arbitrary Motion,” *Philosophical Transactions of the Royal Society of London Series A. Mathematical and Physical Sciences Vol. 264 No. 1151*, 1969.
- [15] Hanson, D., “Helicoidal Surface Theory for Harmonic Noise of Propellers in the Far Field,” *AIAA Journal Vol. 18, No. 10*, 1980.
- [16] Doolan, C., Yauwenas, Y., and Moreau, D., “Drone Propeller Noise Under Static and Steady Inflow Conditions,” *UNSW*, 2019.
- [17] Ffowcs-Williams, J. E., and Hall, L. H., “Aerodynamic Sound Generation by Turbulent Flow in the Vicinity of a Scattering Half Plane,” *Journal of Fluid Mechanics Vol. 40*, 1970.
- [18] Amiet, R. K., “Noise due to Turbulent Flow past a Trailing Edge,” *Journal of Sound and Vibration Vol. 47*, 1976.
- [19] Brooks, T. F., Pope, D. S., and Marcolini, M. A., “Airfoil Self-Noise and Prediction,” *NASA Reference Publication 1218*, 1989.
- [20] Glegg, S., and Devenport, W., *Aeroacoustics of Low Mach Number Flows*, Elsevier, 2017.
- [21] Amiet, R. K., “Acoustic Radiation from an Airfoil in a Turbulent Stream,” *Journal of Sound and Vibration Vol. 41*, 1975.
- [22] Brandt, J. B., “Small-Scale Propeller Performance at Low Speeds,” 2005.
- [23] Yauwenas, Y., Fisher, J., Moreau, D., and Doolan, C., “The effect of inflow disturbance on drone propeller noise,” *25th AIAA/CEAS Aeroacoustics Conference*, 2019.

Aeroacoustics of Aerofoils Inspired by Insect Wing Geometry

Ashley Su Lynn Lim¹

The University of New South Wales (UNSW), Sydney, NSW 2031, Australia

This paper aimed to identify how two insect inspired passive trailing edge geometry modifications, namely hindwing tails and corrugation, affect both the aerodynamic and acoustic efficiency of a NACA0021 aerofoil. These two trailing edge modifications were compared against a flat plate trailing edge and a serrated trailing edge which is known to be an effective noise attenuator. Two experiments to examine the aeroacoustic and aerodynamic performance of these trailing edge modifications have been carried out in two different wind tunnels, which were a subsonic wind tunnel and an anechoic wind tunnel, at UNSW Sydney. In both experiments, tests were performed with the NACA0021 aerofoil at angles of attack between 0° and 12° in increments of 2° and at a Reynolds chord number (Re_c) range of between $4.55(10^4)$ and $1.37(10^5)$. The corrugated attachment experienced the highest maximum lift coefficient, C_L while the hindwing tail achieved lowest maximum C_L at all Reynolds numbers except $Re_c = 1.37(10^5)$, in which the serrated attachment achieved the lowest maximum C_L . The maximum C_D experienced by the hindwing tail was greatest at all Reynolds numbers, while the serrated attachment experienced the least drag overall. The glide ratio of the serrated attachment was highest while the hindwing tail attachment had the lowest glide ratio. The corrugated attachment experienced the second lowest glide ratio. At all Reynolds numbers, the serrated attachment experienced the lowest PSD compared to the flat base plate attachment, indicating that it is the best noise attenuator. At the lowest Reynolds number of $Re_c = 4.55(10^4)$, the hindwing tail attachment also experienced low PSD levels with the PSD recorded being close to the background noise level. At the highest Reynolds number, $Re_c = 1.37(10^5)$, a similar result was also recorded with the hindwing tail. Overall, while the corrugated trailing edge attachment was found to be aerodynamically superior to the hindwing tail attachment, it does not act as a noise attenuator. On the other hand, the hindwing tail attachment achieved poor gliding ratios but is a very effective trailing edge noise attenuator.

I. Nomenclature

α	=	angle of attack, in degrees (°)
C_D	=	drag coefficient
C_L	=	lift coefficient
Re_c	=	chord Reynolds number
PSD	=	power spectral density, in decibels (dB)

II. Introduction

Aeroacoustics, which involves both fluid mechanics in the aerodynamic field as well as sound propagation in the acoustic field has been an essential subject in the aviation industry amongst many others since its creation in the 1950s due to highly enforced rules regarding noise pollution of aircraft. Much of the research carried out in the scientific field of aeroacoustics involves investigating and modelling the mechanisms of sound generation due to flow over aerofoils and wings.

The study of aeroacoustics in regard to aircraft noise is concerned with far-field noise. The acoustic far field begins at a distance of two wavelengths away from the source of sound and extends until infinity, which can and will greatly impact human activity and the environment at sea level despite being a significant distance away from the aircraft itself. The human ear responds to frequencies between 20 Hz and 20 kHz [1], and thus aeroacoustic studies often target this range when modifying aerofoils and wings to decrease the sound levels generated by aircraft.

¹ AIAA student member, Undergraduate. Member Number: 1192751

An important source of aircraft and UAV noise is trailing edge noise generated at the trailing edge of wings, which is caused by turbulence in the boundary layer formed on the surface of the aerofoil interacting with the sharp trailing edge. The turbulence is scattered by the trailing edge, generating noise that is radiated into the far field.

Bio-inspired passive geometrical modifications such as those in insect wings have been used in previous studies to observe their effects on the aerodynamic and aeroacoustic efficiency on the modified wing. For example, it has been noted that some butterflies that employ gliding movement such as swallowtail butterflies have longer and narrower wings [2]. Swallowtail butterflies also have hindwing tails that improve flight stability by decreasing the aspect ratio of the wing which affects its aerodynamic efficiency as observed in a study carried out by Park et al [3]. Figure 1 shows the wings used in Park et al's study, which was a swallowtail butterfly with hindwing tails and the same wing without the hindwing tails attached. It was found in the study that the lift coefficient was consistently higher for the wing with hindwing tails compared to the wing without any hindwing tails. Park suggested that trailing edge vortices in the wake region behind the wing had pushed the wingtip vortex closer to the upper surface of the wing, leading to a larger pressure difference between upper and lower surfaces of the wings and thus providing a greater lift force.

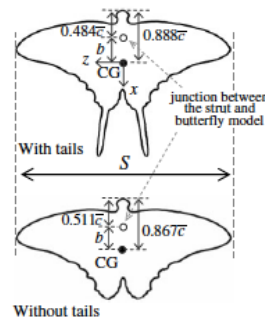


Figure 1. Models of swallowtail butterflies with and without hindwing tails. [3]

In another study carried out by Hu and Wang, two wings of different butterfly species, one with hindwing tails and one without, were compared at angles between -4° to 30° . [4] It was found that the wing with no hindwing tails experienced a larger glide ratio, or lift-to-drag ratio at angles below 20° , which contrasted with Park et al's study. Hu suggested that the strong wing tip vortex formed on the wing with hindwing tail created a larger induced drag which decreased the lift-to-drag ratio. However, at angles of attack greater than 20° , the wing with hindwing tail was preferred as the wing without hindwing tail stalled at 20° , which led to a decrease in C_L after the angle of attack exceeded 20° .

Another popular study carried out on the aerodynamic efficiency of insect wings is that of dragonfly wings. Dragonfly wing venation creates corrugate-like profiles of wings in which a flat plate is folded into continuous ridges. Despite the multiple experiments that have been carried out to determine the effect of corrugation on aerofoils, there is no single conclusion of how corrugation affects aerofoil aerodynamic performance. A study conducted by Kesel [5] compared corrugated wings against their filled profiles and a flat plate. The results indicated that the three corrugated wings studied produced higher lift and thus higher C_L compared to both the filled in profiles and the flat plate at $Re_c=10,000$. None of the profiles showed flow separation, and it was suggested that the corrugation behaved similarly to cambered aerofoils. Similarly, Vargas et al [6] carried out an experiment on Kesel's wing profiles at a Re_c range of 500 to 10,000. Vargas et al found that the flat plate achieved glide ratios 1.75 times greater than that of the filled in profile wings and 1.3 times greater than that of the corrugated wing at $Re_c < 5000$. At $Re_c > 5000$, the flat plate experienced a large leading-edge stall which caused a decline in glide ratio, while both corrugated and filled in wings continued to have an increase in C_L and C_D .

Aerofoil noise is generated by pressure changes on body surfaces converted into sound waves that radiate through air. One of the main foci of aerofoil acoustics is the far-field sound generated at the trailing edge of the aerofoil. According to Lighthill, trailing edge noise can be reduced by sweeping the trailing edge and increasing the distance between the source of turbulence and the trailing edge. Studies carried out by Moreau et al [7] and Jones and Sandberg [8] showed that modifying the trailing edge of aerofoils by adding sawtooth serrations reduced the trailing edge noise. Avallone et al [9] stated that elongated coherent flow structures in the empty space between serrations caused destructive interference between pressure waves which in turn caused a reduction in noise. While sawtooth serrations are a known noise attenuator, no other passive geometrical modifications have been studied for possible noise reduction. As insect wings have been studied for their aerodynamic efficiency, insect inspired geometrical

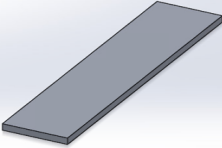
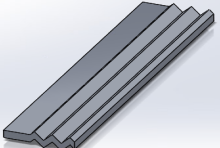
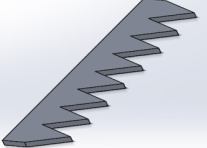
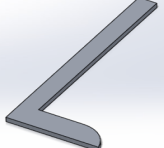
modifications can also be examined for their aeroacoustic efficiency and how these modifications can compare to serrations.

This paper investigates how insect inspired passive shape changes such as corrugations and hindwing tails in the trailing edge of wings can affect the aerodynamic and aeroacoustic performances of aerofoils. These two passive geometrical trailing edge changes were compared against a flat plate as well as a sawtooth serration trailing edge modification for aeroacoustic purposes.

III. Methodology

Two experiments, an aerodynamic experiment and an aeroacoustic experiment, were carried out to achieve the aims of this paper, which were to investigate how insect inspired passive shape changes such as corrugations and hindwing tails in the trailing edge of wings can affect the aerodynamic and aeroacoustic performances of aerofoils. A symmetrical NACA0021 aerofoil of span 72 mm and average chord 69 mm was designed with a trailing edge slot to insert four different trailing edge attachments. The trailing edge attachments consisted of a rectangular flat plate, extended hindwing tail, a corrugated plate, and a sawtooth serration plate, each 2mm thick. Both experiments were carried out at a Reynolds number range between $4.55(10^4)$ to $1.37(10^5)$ and at angles of attack from 0° to 12° in increments of 2° . Images and details of each trailing edge attachment are shown in Table 1.

Table 1. Trailing edge attachments and their key features.

	Flat plate attachment	Corrugated attachment	Serrated Attachment	Hindwing Tail
Diagram				
Key features	Flat plate 10 mm long with 5 mm insert	<ul style="list-style-type: none"> • Corrugation 10 mm long with 5 mm insert • Corrugated part 2 mm thick with wavelength 4 mm 	<ul style="list-style-type: none"> • Serration 10 mm long with 5 mm insert • Serrated wavelength of 9 mm 	Tail 25 mm long with 5 mm insert

In the aerodynamic experiment, each trailing edge attachment was affixed to the aerofoil through the slot. The edges of the slot were then covered with metal tape to avoid unintentional boundary layer tripping, as that would affect the lift and drag measurements taken. All measurements were taken using a two-component force balance attached to the AFF1125 Subsonic Wind Tunnel found in the aerodynamic laboratory of UNSW. The wind tunnel has a test section size of 125 mm x 125 mm x 350 mm and mounted the aerofoil using a rod of 6 mm diameter.

The two-component balance was mounted to the side of the wind tunnel test section at two different orientations to obtain both lift and drag force results. The wing was placed in the middle of the test section to ensure that it did not exceed 10% total blockage of the test section for reliable results. The lift and drag measurements were obtained directly from the two-component balance. To determine the velocity, and thus Reynolds number, of airflow for the lift and drag coefficient calculations, the upstream dynamic pressure was found from Pitot tubes fitted in the test section of the wind tunnel. These Pitot tubes were connected to a manometer with water as a working fluid.

In the aeroacoustic experiment, each far-field trailing edge acoustic dataset was measured using a microphone for 32 s at a sampling frequency of 65536 Hz, or 2^{16} Hz. The microphone was 1.043 m away from the trailing edge of the aerofoil, directly perpendicular to the chord. The UNSW Anechoic Wind Tunnel is a suction type open-jet wind tunnel facility with a 0.455 m x 0.455 m test section with an anechoic chamber treated with 0.25 m Melamine foam. The power spectral density (PSD) was estimated using Welch's method in MATLAB, in which the acoustic pressure data was divided into segments of 8192 points with 50% overlapping. Welch's method Fast Fourier Transformed the time series acoustic pressure to frequency domain and estimated the PSD to represent the sound pressure level (SPL).

IV. Experimental Results and Discussion

A. Aerodynamic Results & Discussion

The lift and drag measurements directly obtained from the two-component balance were converted into C_L and C_D and plotted against angle of attack for all trailing edge attachments for each Re_c . The noise floor for the instrumentation was also recorded and plotted on the graphs.

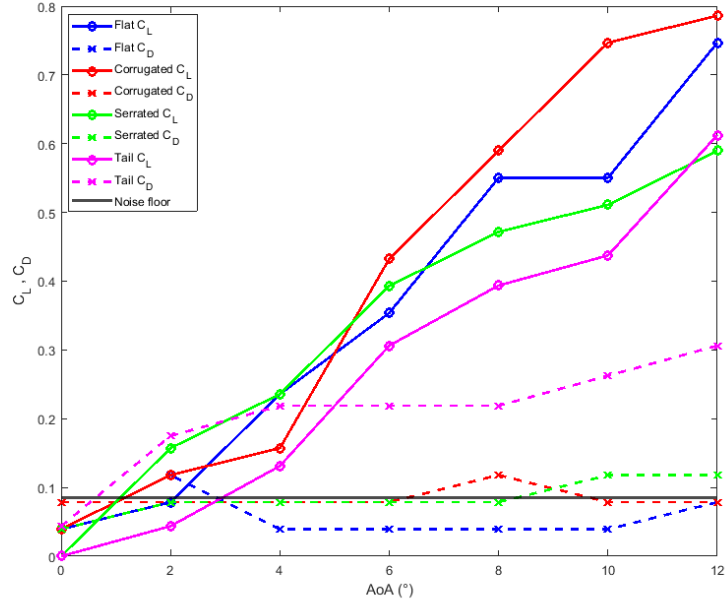


Figure 2. Graph of C_L and C_D against α for $Re_c = 4.55(10^4)$

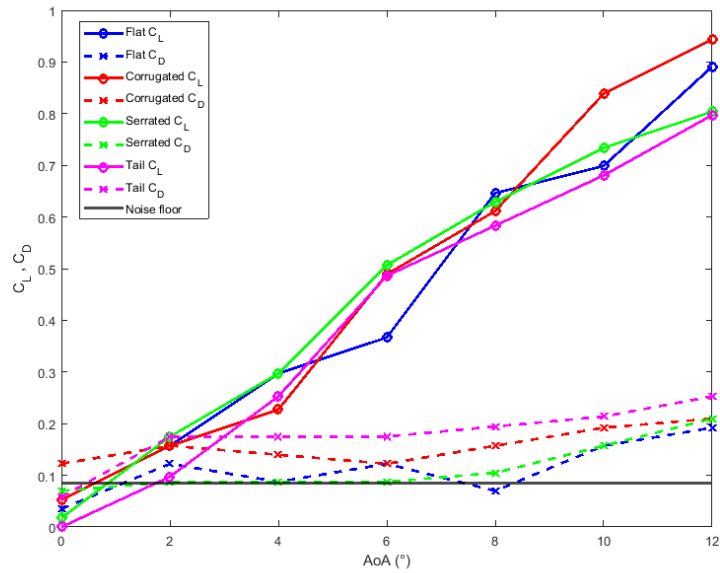


Figure 3. Graph of C_L and C_D against α for $Re_c = 6.83(10^4)$

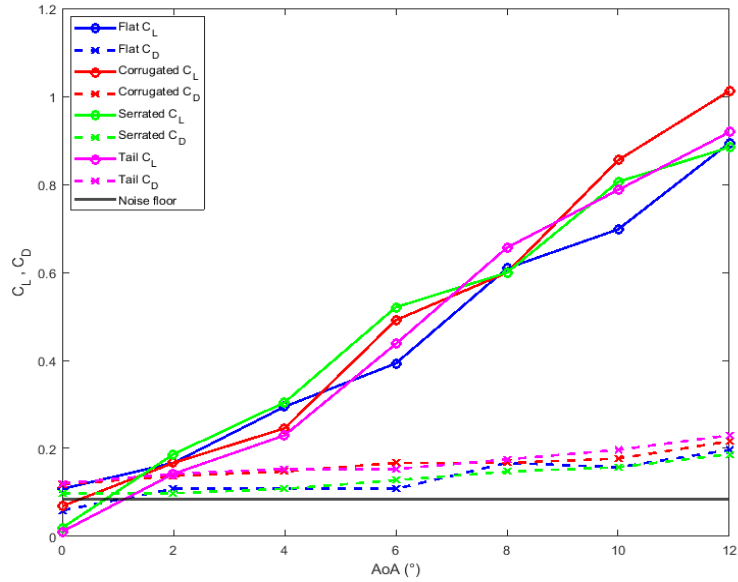


Figure 4. Graph of C_L and C_D against α for $Re_c = 9.10(10^4)$

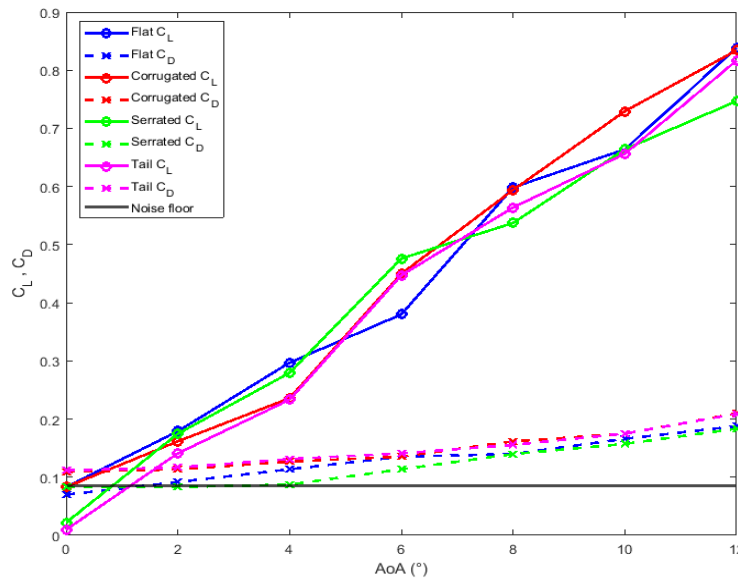


Figure 5. Graph of C_L and C_D against α for $Re_c = 1.37(10^5)$

From Figures 2-5, which show how C_L and C_D change over angles of attack at different Re_c , it can be observed that C_L increased with angle of attack for every trailing edge attachment. At angles between 0° to 4° for all Reynolds numbers, there were no significant differences between the C_L for all trailing edge attachments. From 6° onwards at $Re_c = 4.55(10^4)$ the corrugated attachment continuously achieved higher C_L compared to the other attachments until 12° in which the corrugated attachment had a lift coefficient of 0.786. The second highest C_L at the Reynolds number which was achieved by the flat plate attachment was 0.747, followed by the hindwing tail attachment and serrated attachment at 0.612 and 0.590 respectively. A similar pattern can be seen at the next Reynolds number, $Re_c = 6.83(10^4)$, where the corrugated attachment had the highest lift coefficient at 12° , followed by the flat plate attachment, and finally the serrated attachment and hindwing tail.

At $Re_c = 9.10(10^4)$ the corrugated attachment proved to have the highest lift coefficient among the four trailing edge attachments at 1.01 while the other three trailing edge attachments had similar C_L at 12° . However, at $Re = 1.37(10^5)$, the corrugated attachment, flat plate attachment, and hindwing tail attachment had similar C_L at 12° of 1.81 for the hindwing tail and 1.83 for both the flat plate and corrugated attachment. The serrated attachment experienced the lowest C_L at 0.747 . From these observations, it can be inferred that overall across the different Reynolds numbers the corrugated attachment achieved higher lift coefficients at 12° .

In terms of drag coefficient C_D it must first be noted that some of the measurements taken did not exceed the noise floor threshold recorded. The noise floor of the force balance is the lowest signal it can measure without any model mounted in the wind tunnel and was found to be approximately 0.022 N. When converted to a coefficient similar to that of C_L and C_D , the noise floor coefficient was calculated to be 0.085 . At $Re_c = 4.55(10^4)$, the majority of C_D results obtained for the flat plate attachment, serrated attachment, and corrugated attachment did not exceed the noise floor, and thus cannot be accepted as valid data in this experiment. Similarly, the results at $Re_c = 6.83(10^4)$ cannot be accepted as half the C_D recorded did not exceed the noise floor. Thus, the main C_D results studied were those taken at $Re_c = 9.10(10^4)$ and $Re_c = 1.37(10^5)$, in which all the C_D calculated for all attachments were above the noise floor and were considered valid data.

For all attachments at these two Reynolds numbers, the C_D increased with angle of attack with the hindwing tail experiencing the most drag and the serrated attachment experiencing the least drag overall.

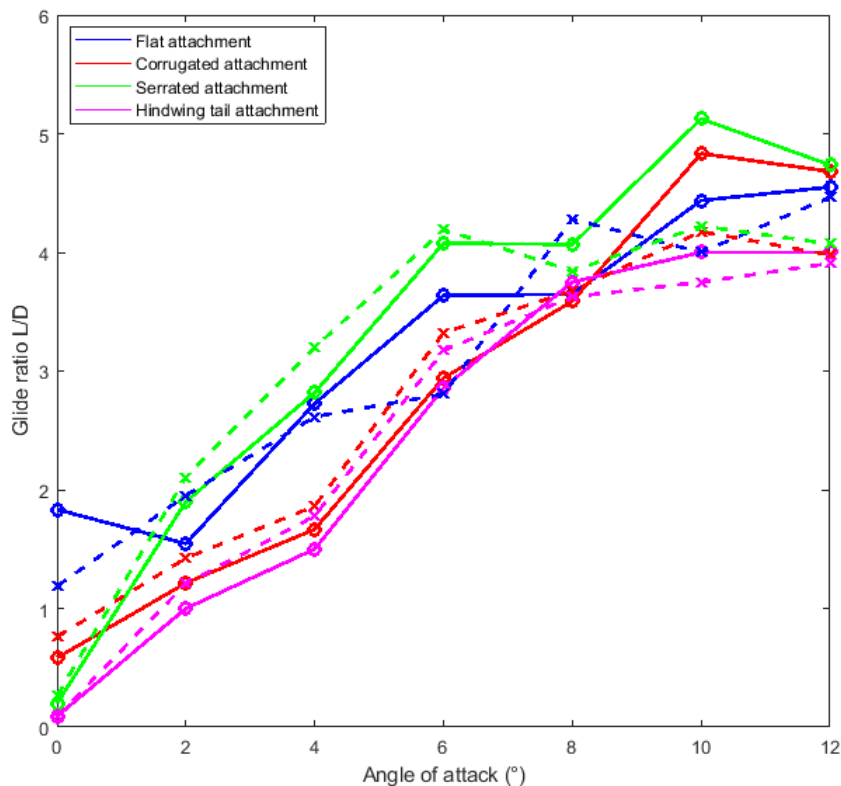


Figure 6. Glide ratio against angle of attack for each trailing edge attachment.
Solid lines: $Re_c = 9.10(10^4)$, dashed lines: $Re_c = 1.37(10^5)$

Figure 6 shows the glide ratio, or lift-over-drag ratio, of each attachment at $Re_c = 9.10(10^4)$ and $Re_c = 1.37(10^5)$. Firstly, as the angle of attack increases, the glide ratio of all attachments at both Reynolds numbers also generally increase. It can be observed that at $Re_c = 9.10(10^4)$, which lines are represented by solid lines with circle markers, that the serrated trailing edge attachment consistently achieves the largest glide ratio from 2° onwards. From 0° to 8° , the flat plate attachment had a higher glide ratio than the corrugated attachment; however, from 8° onwards, the corrugated attachment had a higher glide ratio with a final difference of 0.18 . At this Reynolds number, the hindwing tail attachment had the lowest glide ratio at all angles of attack.

At $Re_c = 1.37(10^5)$, the serrated attachment obtained the highest glide ratio from 2° to 6° . After 6° , the rate of increase in glide ratio for the serrated attachment plateaued, with the flat plate attachment achieving the highest glide ratio from 6° onwards. At 12° , the glide ratio for the flat plate attachment was 4.47, while the serrated attachment, corrugated attachment, and hindwing tail attachment attained glide ratios of 4.07, 3.98, and 3.91 respectively. Similar to the previous Reynolds number, the hindwing tail attachment at this Reynolds number also consistently experienced low glide ratios at all angles of attack.

The aerodynamic results obtained in this experiment were consistent with results from previous studies such as Vargas et al [6], where corrugated aerofoils at $Re_c > 10,000$ experienced greater C_L than the flat plate. The higher glide ratio achieved by the corrugated attachment was also consistent with Levy and Seifert's study [10] where polar comparisons for lift-drag performance indicated a superior lift-to-drag ratio for the corrugated aerofoil compared to the classical Eppler-E61 aerofoil. A possible explanation for this behaviour has been suggested by Levy and Seifert, where it was found that the long travelling waves created over the classical aerofoil, or the flat plate attachment, caused flow separation from the aerofoil, while the vortices produced between the peaks of the corrugated trailing edge attachment may allow intermittent flow reattachment to the aerofoil.

The hindwing tail attachment results from this experiment did not align with those from Park et al's [3] study as in this experiment the hindwing tail had the lowest glide ratio at both $Re_c = 9.10(10^4)$ and $Re_c = 1.37(10^5)$. However, the results were supported by that of Hu and Wang [4]. At angles below 20° , Hu and Wang found that the wing without hindwing tails experienced a larger lift-to-drag ratio than the wing with hindwing tails, which was supported by these experimental results. An explanation for this was suggested by Hu and Wang where the strong wing tip vortex formed on the wing with a hindwing tail created a larger induced drag which decreased the glide ratio, as the definition of glide ratio is lift over drag, or C_L/C_D .

In summary, the serrated attachment was the most aerodynamically superior model followed by the corrugated attachment at both Reynolds numbers past angles of attack of 8° . The flat plate was more aerodynamically efficient than the corrugated attachment at angles of attack lower than 8° . The hindwing tail attachment was the least aerodynamically efficient of all the attachments.

B. Aeroacoustics

The acoustic power spectral densities (PSD) in Hertz attained from the experiment at the different angles of attack and Reynolds numbers were plotted to identify which attachment was the best noise attenuator at different Reynolds numbers.

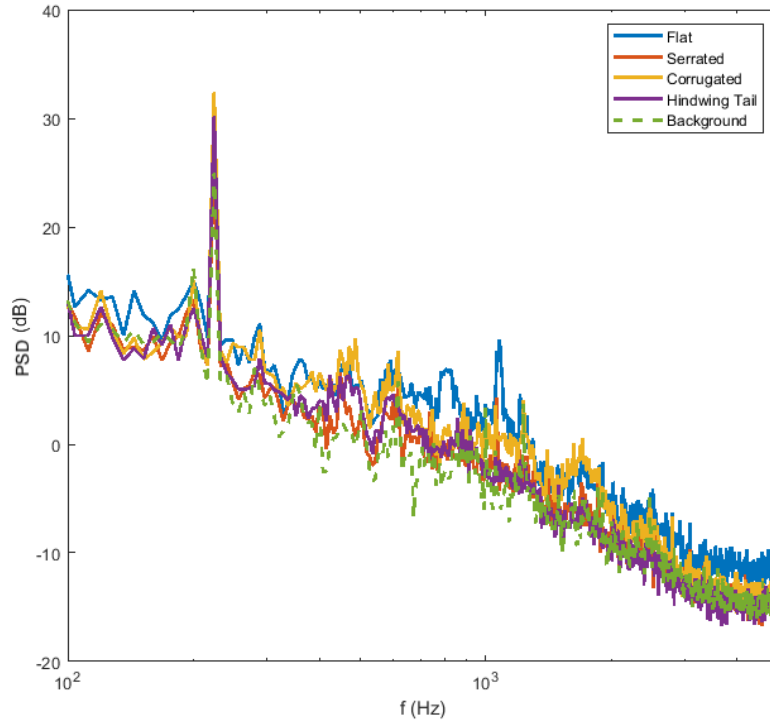


Figure 7. Graph of PSD against frequency for $Re_c = 4.55(10^4)$ at $\alpha = 0^\circ$.

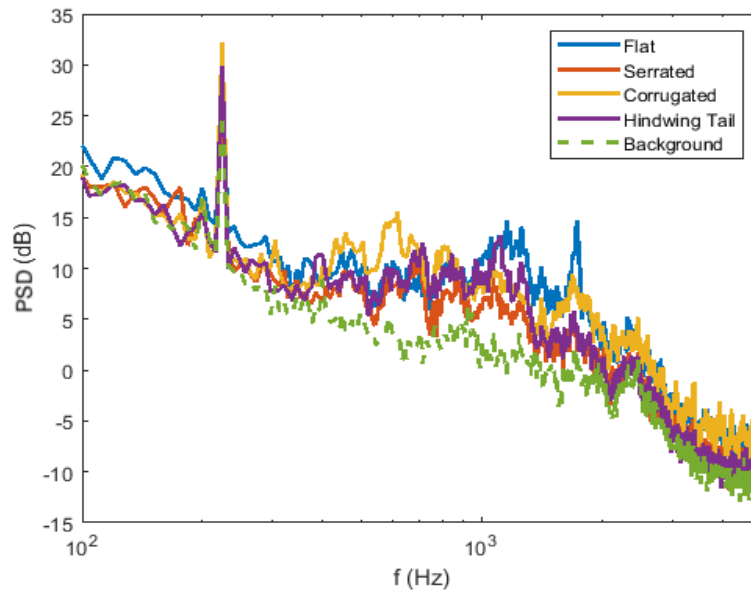


Figure 8. Graph of PSD against frequency for $Re_c = 6.83(10^4)$ at $\alpha = 0^\circ$.

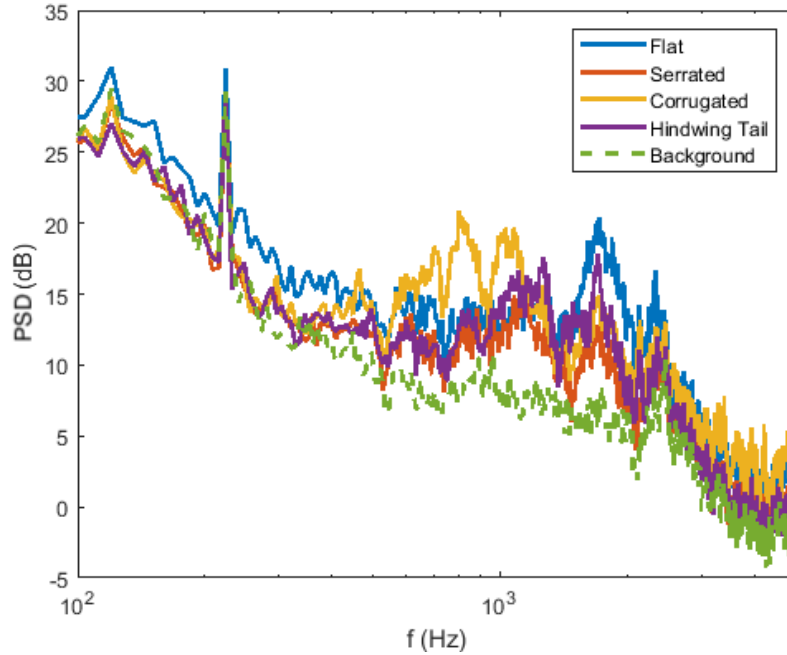


Figure 9. Graph of PSD against frequency for $Re_c = 9.10(10^4)$ at $\alpha = 0^\circ$.

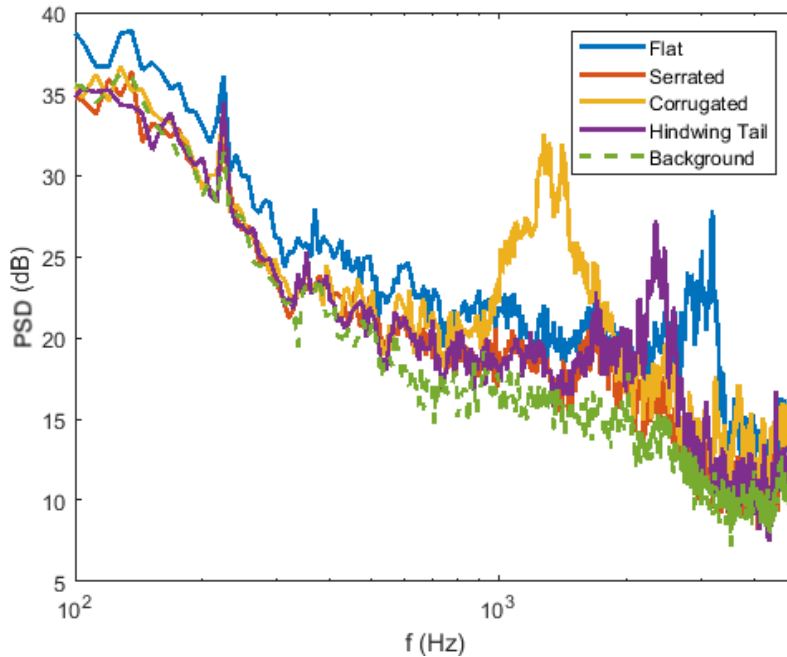


Figure 10. Graph of PSD against frequency for $Re_c = 1.37(10^5)$ at $\alpha = 0^\circ$.

Figures 7-10 show the power spectral density of all test cases at zero angle of attack and different Re_c . From these four figures it can be seen that at frequencies lower than 400 Hz at all Reynolds numbers, all the attachments except the flat plate attachment the same noise level as background noise. The flat plate indicated by the blue line has the highest PSD generated of all the trailing edge attachments across the entire frequency range shown. The corrugated trailing edge attachment has less noise attenuation compared to the flat plate at all Reynolds numbers except between frequencies of 700 Hz to 1000 Hz at $Re_c = 9.10(10^4)$ and frequencies of 900 Hz to 1100 Hz at $Re_c = 1.37(10^5)$, at which the corrugated attachment produced more noise than the flat plate. The hindwing tail attachment and serrated attachment both experience similar levels of noise attenuation as can be seen from the purple and orange lines often overlapping in Figure 4. Both have a minimum PSD difference of 2 dB and a maximum of 10 dB with the flat plate.

At $Re_c = 1.37(10^5)$, the corrugated attachment, hindwing tail attachment, and flat plate attachment introduce a high amplitude broad peak at frequencies past 1000 Hz, while the serrated attachment does not experience this high amplitude broad peak.

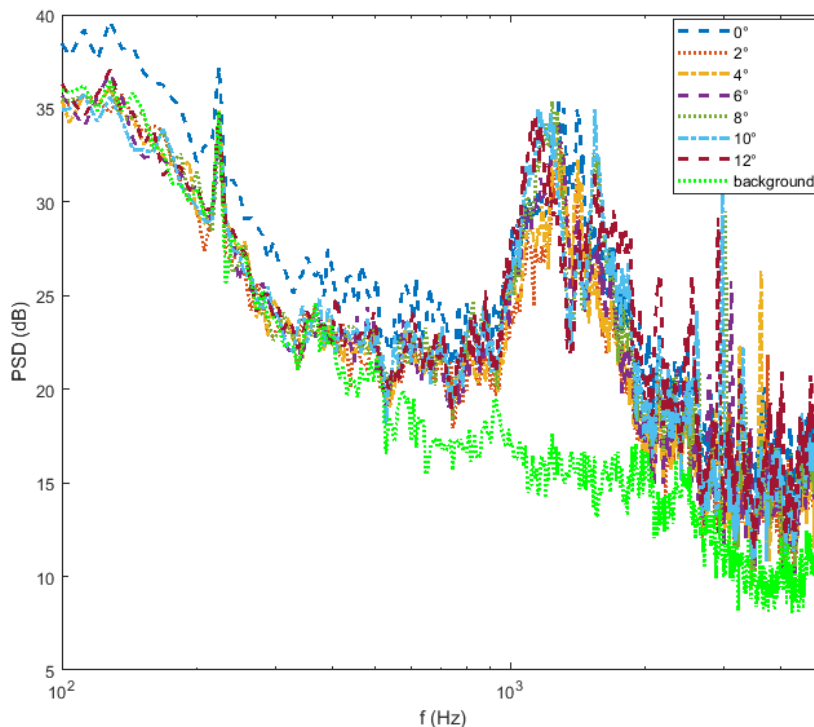


Figure 11. Graph of PSD against frequency at all α at $Re_c = 1.37(10^5)$

Another key result from the aeroacoustic experiment is the high amplitude broad peak recorded for the corrugated attachment between frequencies of 900 Hz to 1100 Hz. This is seen in Figure 11 where the PSD recorded in the frequency range for the corrugated attachment greatly exceeds that recorded by the other three trailing edge attachments. However, at frequencies below 400 Hz, the corrugated attachment PSD generally overlaps the background noise at angles above 0° .

At all Reynolds numbers and at all angles of attack, the serrated attachment was consistently the best noise attenuator, achieving a PSD difference up to 10 dB compared to the flat plate. The next best noise attenuator was the hindwing tail attachment followed by the corrugated attachment. The corrugated attachment only behaved as a noise attenuator at frequencies lower than 900 Hz for $Re_c = 1.37(10^5)$. At $Re_c = 6.83(10^4)$ the corrugated attachment generated more noise than the flat plate between frequencies of 300 Hz to 1000 Hz at $\alpha = 10^\circ$ to 12° . Thus, the corrugated attachment cannot be considered to be a consistent noise attenuator unlike the hindwing tail.

The behaviour of the serrated attachment as an efficient noise attenuator was supported by Jones and Sandberg's study [8], where the sound radiation recorded for the serrated trailing edge aerofoil was lower than that of the straight trailing edge with a noise reduction range of 6-10 dB. The decrease in sound radiation may have been caused by changes in the scattering process of turbulent structures in the wake region as suggested by Jones and Sandberg.

While the noise mechanisms of hindwing tails and corrugations are unknown, a plausible explanation for the PSD changes in the corrugated trailing edge attachment may be due to the pressure difference between the upper and lower surfaces. The formation of vortices in the ridges of the corrugated attachment, and the strength of these vortices, could affect the efficiency of noise reduction. This was inferred from León et al [11], where a trailing edge serrated flap was angled at different angles in relation to the chord line. An angle greater than 6° caused more noise to be generated, which may be a possible mechanism that contributed to the increase in PSD for the corrugated trailing edge attachment.

V. Conclusion

This paper investigated how passive shape changes such as corrugations and hindwing tails in the trailing edge of wings can affect the aerodynamic and aeroacoustic performances of aerofoils, as well as compare their aeroacoustic

performance against serrations which is a known noise attenuator. Four trailing edge attachments, which were a hindwing tail attachment, corrugated attachment, serrated attachment, and rectangular flat plate attachment, were designed to slot into a modified NACA0021 aerofoil. The parameters used for the two experiments, aerodynamic and aeroacoustic, were angles of attack from 0° to 12° in increments of 2° , and a range of Reynolds numbers from $Re_c = 4.55(10^4)$ to $Re_c = 1.37(10^5)$.

The aerodynamic experiment was carried out in the UNSW subsonic wind tunnel, in which lift and drag measurements of each attachment were taken using a two-component force balance. The lift and drag measurements were converted into lift and drag coefficients, C_L and C_D , and valid glide ratios for each attachment at each Reynolds number were calculated. It was found that the corrugated attachment experienced the highest maximum C_L while the hindwing tail achieved lowest maximum C_L at all Reynolds numbers except $Re_c = 1.37(10^5)$, in which the serrated attachment achieved the lowest maximum C_L . The maximum C_D experienced by the hindwing tail was greatest at all Reynolds numbers, while the serrated attachment experienced the least drag overall. The corrugated attachment was more aerodynamically efficient than the flat plate at angles above 8° , while the hindwing tail attachment was the least aerodynamically efficient as the glide ratio across all angles of attack at all Reynolds numbers were lower than that of the flat plate.

The aeroacoustic experiment was carried out in the UNSW anechoic wind tunnel to determine how the power spectral density PSD generated by the aerofoil with different trailing edge attachments varied across the stated parameter range. At all Reynolds numbers, the serrated attachment experienced the lowest PSD compared to the flat base plate attachment, indicating that it is the best noise attenuator, providing a maximum noise reduction of 10dB. The hindwing tail attachment also experienced similar PSD to that of the serrated attachment. The corrugated attachment was not as efficient at decreasing the levels of noise generated, and at $Re_c = 1.37(10^5)$ produced greater amounts of noise than the flat plate at frequencies between 900 Hz to 1100 Hz.

Therefore, while the corrugated attachment was aerodynamically superior to the hindwing tail, the hindwing tail was a better noise attenuator than the corrugated attachment.

References

- [1] S. Glegg and W. Devenport, *Aeroacoustics of Low Mach Number Flows*. Elsevier Science and Technology Books, Inc., 2017.
- [2] A. Cespedes, C. Penz and P. DeVries, "Cruising the rain forest floor: butterfly wing shape evolution and gliding in ground effect", *Journal of Animal Ecology*, vol. 84, no. 3, pp. 808-816, 2015. Available: 10.1111/1365-2656.12325.
- [3] H. Park, K. Bae, B. Lee, W. Jeon and H. Choi, "Aerodynamic Performance of a Gliding Swallowtail Butterfly Wing Model", *Experimental Mechanics*, vol. 50, no. 9, pp. 1313-1321, 2010. Available: 10.1007/s11340-009-9330-x.
- [4] Y. Hu and J. Wang, "Experimental Investigation on Aerodynamic Performance of Gliding Butterflies", *AIAA Journal*, vol. 48, no. 10, pp. 2454-2457, 2010. Available: 10.2514/1.45156.
- [5] A. Kesel, "Aerodynamic characteristics of dragonfly wing sections compared with technical airfoils", *The Journal of Experimental Biology*, vol. 203, 2000.
- [6] A. Vargas, R. Mittal and H. Dong, "A computational study of the aerodynamic performance of a dragonfly wing section in gliding flight", *Bioinspiration & Biomimetics*, 2008.
- [7] D. Moreau, L. Brooks and C. Doolan, "Flat plate self-noise reduction at low-to-moderate Reynolds number with trailing edge serrations", 2011.
- [8] L. Jones and R. Sandberg, "Acoustic and hydrodynamic analysis of the flow around an aerofoil with trailing edge serrations", *Journal of Fluid Mechanics*, vol. 706, pp. 295-322, 2012. Available: 10.1017/jfm.2012.254.
- [9] F. Avallone, W. van der Velden, D. Ragni and D. Casalino, "Noise reduction mechanisms of sawtooth and combed-sawtooth trailing-edge serrations", *Journal of Fluid Mechanics*, vol. 848, pp. 560-591, 2018. Available: 10.1017/jfm.2018.377.
- [10] D. Levy and A. Seifert, "Simplified dragonfly airfoil aerodynamics at Reynolds numbers below 8000", *Physics of Fluids*, vol. 21, no. 7, p. 071901, 2009. Available: 10.1063/1.3166867.
- [11] C. Arce León, D. Ragni, S. Prbsting, F. Scarano and J. Madsen, "Flow topology and acoustic emissions of trailing edge serrations at incidence", *Experiments in Fluids*, vol. 57, no. 5, 2016. Available: 10.1007/s00348-016-2181-1.

Aerodynamic Performance of Passive Noise Reducing Wingtip Devices

Michael Yanez*

UNSW School of Manufacturing and Mechanical Engineering, Sydney, NSW, 2052

This is an experimental study aimed to investigate the aerodynamic behaviour of wing tips with a flat side edge, rounded side edge, side edge porosity and side edge sinusoidal serrations. These wing tips were tested on both a NACA0012 and NACA6412 base wing section. Fully assembled, the models have a real chord length of 67 mm and a span of 140 mm. These models were tested in an open circuit wind tunnel at a Reynolds chord number of 142,000. For the NACA0012 airfoil, sinusoidal wingtips resulted in the largest increases in lift coefficient at 15%. However, drag increased at a maximum rate of 13% where when using the rounded tip, a lift coefficient increase of 8% occurred and the drag coefficient was reduced by 4.5%. Introducing porosity results in increases in the lift and drag coefficients. As porosity increases, the rate at which lift coefficients increase decreases while the drag coefficients are unaffected. When using the NACA6412 airfoil, lift and drag coefficients are negatively impacted, showing how the success of the wing tip device is dependent on the airfoil profile.

I. Nomenclature

N	=	Normal Force
A	=	Axial Force
L	=	Lift
D	=	Drag
α	=	Angle of attack
C_L	=	Lift coefficient
C_D	=	Drag coefficient
C_L/C_D	=	Lift to drag coefficient
C_x	=	force coefficient in the x direction
C_y	=	force coefficient in the y direction
c	=	chord
A	=	Amplitude
W	=	Number of Peaks
λ	=	Wavelength

II. Introduction

HISTORICALLY the aircraft engines were the main source of noise from commercial aircraft. However, as engines have evolved with increased by-pass ratios, the airframe has become the dominant source of noise generation[1]. Within the airframe, the wing tip is a major focal point of investigation. It is relatively simple to investigate and findings are applicable to other parts of aircraft such as flaps, stabilisers and rotor and propeller blades. Furthermore, these findings will benefit other mechanical systems that utilise airfoils such as submarines, fans, wind turbines and other control systems.

Past research has extensively investigated the vortex structure and noise mechanisms of a wing tip. Passive noise reduction techniques, such as modifying the wing tip geometry and introducing porosity, has proven to reduce noise levels [2, 3]. However, there is less understanding on the aerodynamic effects of these noise reduction techniques.

It is important to understand the flow structure over a simplified wing tip geometry. Within the near field region, as flow passes over the tip of a flat tipped finite airfoil, a multi-structured vortex forms which can dominate the airfoil's

*Student Member Undergraduate, School of Manufacturing and Mechanical Engineering, UNSW Sydney 2052, Student Member

wake and cause increased drag and reduced lift. A primary vortex (A) develops as the pressure surface high-pressure flow rolls up from under the wing tip towards the low-pressure suction side. A secondary vortex (B) develops as the suction side flow rolls up at the tip side edge. These vortices merge together at some point along the chord line and become one multi-structured vortex with a thick viscous core. As the vortex travels past the tip's trailing edge it interacts with another secondary vortex (C), which develops at the trailing edge tip as the pressure side flow rolls up towards the suction surface. As the vortex travels further downstream, it is highly dominated by tangential velocities and increases in its size. Figure 1 depicts this vortex formation on a NACA0012 airfoil.

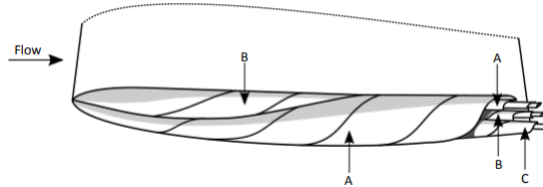


Fig. 1 Tip vortex formation on a NACA0012 airfoil

By altering wingtip geometry, the vortex formation and flow mechanisms are impacted. For a rounded tip, the primary vortex forms over the suction side of the wing tip in a more stable fashion than square tips [4]. Secondary vortices form close to the tip edge and merge steadily with the primary vortex. For a square tip, more secondary vortices forming unsteadily and adding to the instability of the vortex core. Guini et al. concluded that the vortex behaviour of a rounded tip reaches an axisymmetric flow condition earlier in the far field wake region than the square tip [4].

Sinusoidal serrations are believed to have beneficial impacts on reducing noise levels. Shown below in Figure 2, they form a saw like feature on an edge with heights and spacings corresponding to the amplitude (a) and wavelength (λ) of the serrations. Past studies have focused on using serrations on the leading and trailing edges only [5]. Using these serrations led to a 33% coefficient of lift reduction but the result from using side edge sinusoidal serrations will differ.

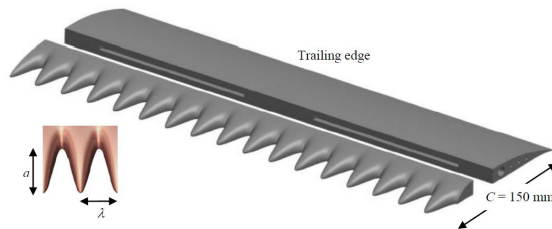


Fig. 2 Tip vortex formation on a NACA0012 airfoil

Another effective way of reducing noise levels generated at the wing tip is by using a porous edge. Wing porosity has been researched extensively throughout the years and has been accepted as a means to reduce noise levels. By introducing porosity to a wing tip, a steady leakage flow of air is able to pass through the porous wing tip. This results in drastically different vortex generation behaviour and can lead to beneficial flow and noise results [2]. However, no studies have compared lift and drag coefficient results. This is experimental study aims to investigate the aerodynamic behaviour of wing tips with a baseline flat side edge, rounded side edge, side edge porosity and side edge sinusoidal serrations.

III. Methodology

This is an experimental thesis study aimed to investigate the aerodynamic behaviour of wing tips with the following geometries:

- Baseline flat side edge
- Rounded side edge

- Side edge porosity
- Sinusoidal serrations on the side edge

These wing tips were tested on both a NACA0012 and NACA6412 base wing section. The test models were mounted to a force balance inside a wind tunnel using a manufactured mount design. Tripping was applied at 10% chord using grit tape to the airfoil models to induce turbulent boundary layers.

Normal and Axial force measurements were taken at different angles of attack and different Reynolds numbers. Coefficients of lift and drag were then calculated and plotted against the reference geometry in order to determine the effects of these wing tips.

A. Testing Facility

The experiments were conducted in UNSW’s School of Manufacturing and Mechanical Engineering’s Educational Wind Tunnel [6]. It is an open-circuit wind tunnel with a 304.8mm x 304.8mm x 609.6mm test section. The wind tunnel is capable of speeds up to 64.8 m/s. A pistol grip force beam with a sting mount is used to mount the test models in the wind tunnel. Smoke is able to flow through the test section in order to visualise the flow structure. The test section is shown below with the mounted test model in Figure 3.

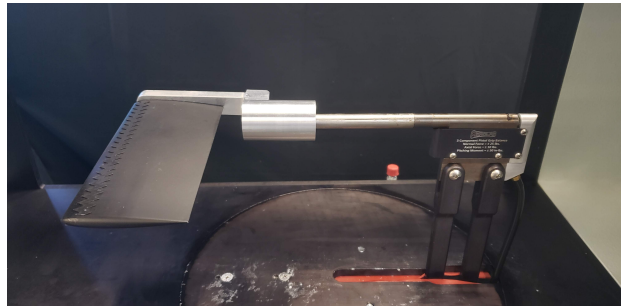


Fig. 3 Test section with mounted test model.

B. Model Airfoils

NACA0012 and NACA6412 profile wing base models and modified tip geometries have been manufactured for previous noise studies [7–9]. These base models have a span of 90 mm and allow for interchangeable tips to be assembled with a self lock mechanism and central shaft. The interchangeable tips provide the modified wing tip geometries and each have a span of 50 mm. The models have a theoretical chord length of 70 mm, a real chord length of 67 mm due to a truncated rounded trailing edge with diameter 1 mm and a span of 140 mm [9]. The assembled test models have an aspect ratio of 2. The rounded tip was defined by creating semi-circles, whose diameters are equal to the local airfoil thickness, along the camber line at 135.8 mm span [8]. 22 models were tested. All models had grit tape applied at 10% chord in order to induce turbulent boundary layers as done in previous studies [7–9].

Porosity was introduced by drilling small divots into the the top and sides of the airfoil’s wing tip of certain depth. The full details of the porous models are listed in Table 1. The sinusoidal tip edge geometries have the following specifications for each airfoil profile displayed in Table 2. Example wing tips and the assembly are shown in Appendix A below.

Table 1 NACA0012 Porous Tip Model Specifications [9]

NACA 0012 porous tips			
#	top (mm)	side (mm)	porosity %
P1	0.6	0.6	13.80
P3	1	0.8	31.24
P5	2	2	50.03

Table 2 Geometrical Parameters of Sinusoidal tips. *Peak amplitude is half of the peak-to-peak amplitude. † The varying amplitude starts from the leading edge and ends at the trailing edge. Data shown in form A:B:C corresponds to start: increment: end [9]

Airfoil profile	Tip geometry	Peak amplitude * (mm)	Wavelength (mm)	Number of chordwise wavelengths	Spanwise location of local minima (mm)
NACA0012	A3W10	3	7	10	134
	A10W10	10	7	10	120
	A3W5	3	14	5	134
	A10W5	10	14	5	120
	A3W3	3	23.3	3	134
	A10W3	10	23.3	3	120

C. Testing Apparatus

A pistol grip force balance beam was used in this study to measure the normal and axial forces produced by the airfoils. The balance is comprised of a parallelogram base and a 9.525 mm diameter cylindrical sting. A custom mount was designed and manufactured to mount the test models to the force balance beam and is shown below in Figure 4.



Fig. 4 Mount

D. Data Acquisition and Convergence Testing

When using the wind tunnel, axial and normal force data is acquired at singular points. The data at each point is an average value taken from a data set. The user is able to specify the size of the data set through specifying the sample period and sampling rate data is acquired. Convergence testing was conducted to determine the appropriate sample period and sampling rate. Convergence testing was conducted using the NACA0012 straight edge airfoil at an angle of 5° and a free-stream velocity of 10 m/s. Figure 5 below depicts the convergence test results for sample times of 10, 15 and 20 seconds. From the plot, the sampling rate and sample period are determined to be 30 Hz and 20 seconds respectively. This sample rate and period was tested on the same airfoil at an angle of 8° , a free-stream velocity of 10 m/s. Since the results also converged, these settings were used for all tests.

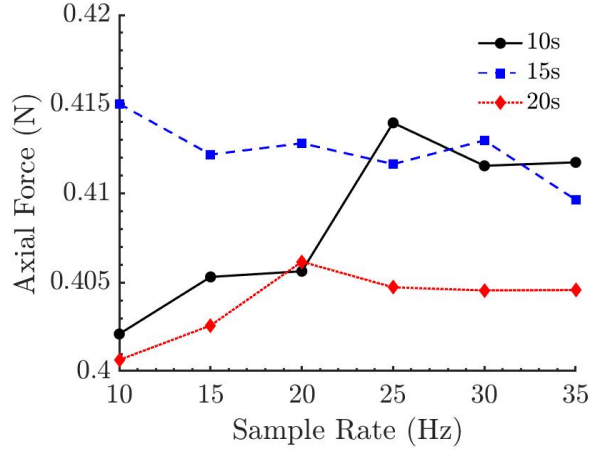


Fig. 5 $\alpha = 5^\circ$, $T = 10, 15, 20$ seconds

IV. Results and Discussion

A. Effects of Rounded Tips

The following figures Figure 6 and Figure 7 show the lift and drag coefficient plots for the NACA0012 and NACA6412 airfoils with square and rounded wing tips respectively. Figure 8 shows the lift to drag ratios these wingtips. The maximum percentage differences occurring when using rounded tips are shown below in Table 3. When comparing these results with Bashetty et al.'s there are scarce similarities. A drag increase of 0.58% is seen when using a rounded tip on a NACA23015 airfoil at $\alpha = 4^\circ$. The NACA6412 airfoil shows a much more significant increase. This could be due to the drastically different Reynolds numbers used with Bashetty using a Reynolds number of 5,000,000. However, from the plots and NACA0012 results, it is clear that the airfoil profile impacts heavily on the effects of the rounded tip. Overall, the lift and drag performance was improved by using rounded tips on the NACA0012 airfoil. As Guini, et al. concluded, the wing tip vortex reaches an axisymmetric flow condition sooner when using a rounded tip on a NACA0012 airfoil. This is believed to be the main flow phenomenon that results in the beneficial aerodynamic performance. When camber is introduced, such as Bashetty's NACA23015, this results in the wing tip vortex reaching an axisymmetric flow condition further downstream if it is reached at all. This would explain the drag increases in Bashetty's results and the larger drag increases for the NACA6412 airfoil as the camber is tripled. Additionally, the lift and drag ratio plots show that positive results for the NACA0012 airfoil while for all angles of attack, the lift to drag ratio is reduced for the NACA6412 airfoil.

Table 3 Percent Difference in lift/drag Coefficient and lift/drag ratio for the rounded tips of both NACA0012 and NACA6412 airfoils at $Re = 142,000$

Airfoil	Wing Tip	Max % ΔC_L	Max % ΔC_D	Max % $\Delta C_L/C_D$
NACA0012	Round	+8% at $\alpha = 10^\circ$	-4.6% at $\alpha = 12^\circ$	+12.4% at $\alpha = 10^\circ$
NACA6412	Round	+5.5% at $\alpha = 0^\circ$	+11% at $\alpha = 4^\circ$	-10% for $\alpha > -6^\circ$

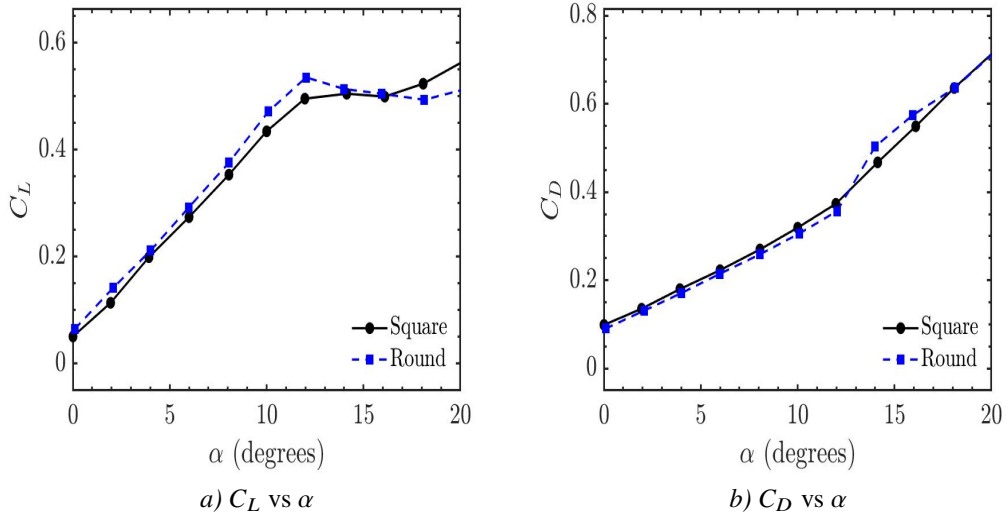


Fig. 6 Lift and drag coefficient plots for NACA0012 airfoil with square and rounded tips at $Re = 140,000$.

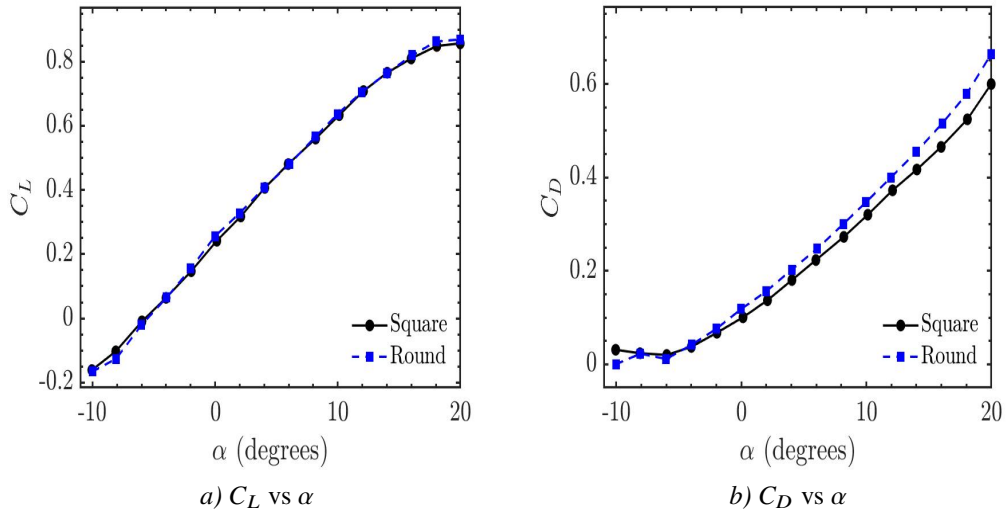


Fig. 7 Lift and drag coefficient plots for NACA6412 airfoil with square and rounded tips at $Re = 140,000$.

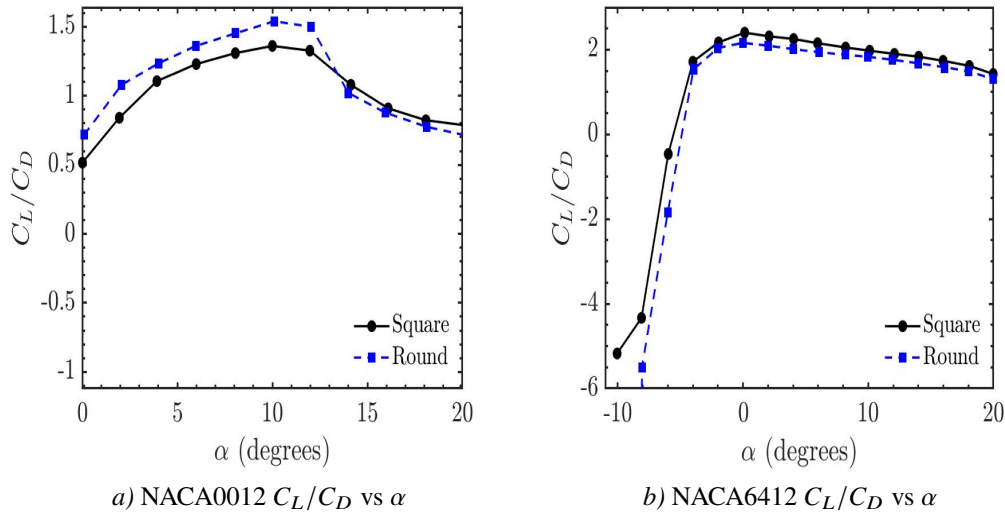


Fig. 8 Lift and drag ratio plots for NACA0012 and NACA6412 airfoils with square and rounded tips at $Re = 140,000$.

B. Effects of Sinusoidal Tips

1. Effects of Amplitude

Figure 9 shows the lift and drag coefficient plots for the NACA0012 airfoil with a square tip and sinusoidal tips of different amplitudes. Figure 10 shows the lift to drag coefficient ratio plots. Table 4 below shows the percent differences of the lift/drag coefficients and the ratios between the square and sinusoidal tip. It is clear that introducing sinusoidal serrations to the side edge of a wing tip will result in increases in lift generation. However, the drag coefficient increases as well. The lift to drag ratio results show that sinusoidal serrations result in better aerodynamic performance, however these results are heavily impacted by the amplitude of the sinusoidal peaks. When using the larger amplitude sinusoidal wingtip, the lift and drag ratio is reduced for all angles of attack. There are two aspects of the flow mechanisms that can explain this. Firstly, sinusoidal serrations disrupt the vortex formations at the wingtip. Smaller individual vortices form as the flow separates from each peak and travel further downstream. This increases vortex dissipation as these smaller vortices have lower tangential and axial velocities, leading to a less turbulent whole vortex forming off the wingtip. Secondly, the sinusoidal serrations reduces the surface area in contact within the flow field. This would predictably lead to lower lift and drag results which is not the case. However, this may contribute to how amplitude effects the impacts of the sinusoidal serrations. As shown in the results, the lower amplitude tips out perform the larger amplitude tips. This may be due to the fact that larger amplitude tips will result in larger vortices forming. Pairing this with more surface area in contact with the flow field, the drag coefficient is more significantly increased leading to the lower lift to drag ratio. This means that when using sinusoidal tips, a lower amplitude sinusoidal tip is preferable for aerodynamic performance. It is important to note that these results will be majorly impacted when using a different airfoil.

Table 4 Percent Difference in lift/drag Coefficient and lift/drag ratio for the NACA0012 airfoil with sinusoidal tips at $Re= 142,000$

Airfoil	Wing Tip	Max % ΔC_L	Max % ΔC_D	Max % $\Delta C_L/C_D$
NACA0012	A10W5	+16% at $\alpha = 14^\circ$	+14% at $\alpha = 12^\circ$	-11% at $\alpha = 10^\circ$
NACA0012	A3W5	+21% at $\alpha = 14^\circ$	+7% at $\alpha = 12^\circ$	+8.% at $\alpha > 5^\circ$

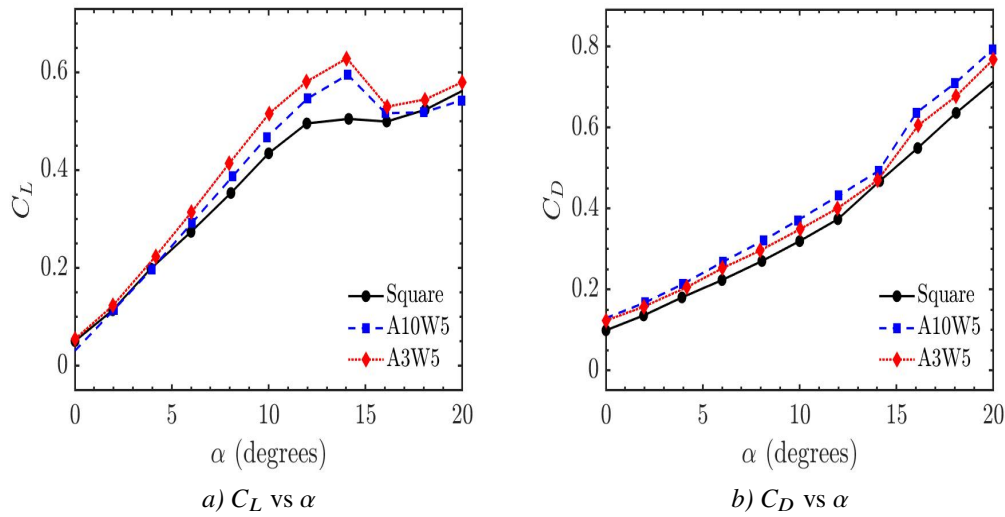


Fig. 9 Lift and drag coefficient plots for NACA0012 airfoil with square and sinusoidal tips with different amplitudes at $Re = 140,000$.

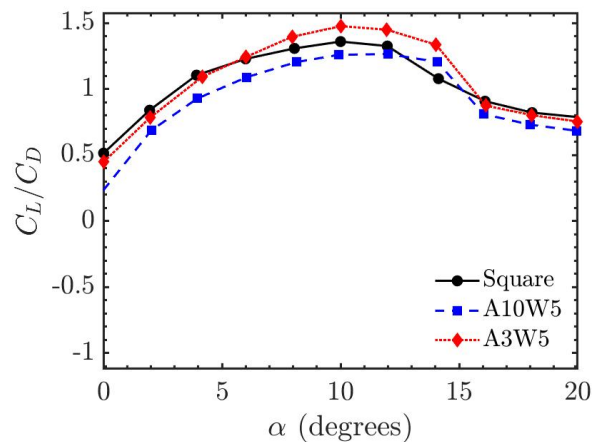


Fig. 10 Lift and drag coefficient ratio plots for NACA0012 airfoil with square and sinusoidal tips with different amplitudes at $Re = 140,000$.

2. Effects of Wavelength

Table 5 below shows the maximum changes in aerodynamic behaviour for the NACA0012 airfoils with sinusoidal tips of constant amplitude and varied wavelengths. From the previous section, a wavelength occurrence (number of peaks) of 5 is used as the reference. These results show that either increasing or decreasing the wavelength of the sinusoidal tip will result in either insignificant change or reductions in the lift coefficient and drag coefficients. These reductions are more severe for the sinusoidal tip with the larger amplitude. When you increase the wavelength of the sinusoidal tip, you increase the number of smaller vortices being generated. When adding excessive amounts of peaks, this can cause more turbulent interactions between each vortex, resulting in a non axis-symmetrical flow condition of the entirely formed wing tip vortex structure. This will lead to decreased lift and increased drag as seen in the results. By the decreasing the wavelength, the effectiveness of the sinusoidal tip is softened. Fewer smaller vortices form and a larger surface area of the airfoil will be in contact with the flow field. This impacts negatively on the aerodynamic performance on the wingtip but at a lesser impact then when increasing the wavelength. It is important to note that these

Table 5 Percent Difference in lift/drag Coefficient and lift/drag ratio for the NACA0012 airfoil with sinusoidal tips of various wavelengths at Re= 142,000

Airfoil	Wing Tip	Max % ΔC_L	Max % ΔC_D	Max % $\Delta C_L/C_D$
NACA0012	A3W3	~ 2% for all α	~ 1% for all α	~ 1% for all α
NACA0012	A3W10	~ 2% for all α	~ 2% for all α	-6% at $\alpha = 10^\circ$
NACA0012	A10W3	-14% at $\alpha = 8^\circ$	6% at $\alpha = 14^\circ$	-8% at $\alpha = 10^\circ$
NACA0012	A10W10	-9% at $\alpha = 8^\circ$	5% at $\alpha = 14^\circ$	-15% at $\alpha = 10^\circ$

Table 6 Percent Difference in lift/drag Coefficient and lift/drag ratio for the NACA0012 airfoil with porous tips at Re= 142,000

Airfoil	Wing Tip	Max % ΔC_L	Max % ΔC_D	Max % $\Delta C_L/C_D$
NACA0012	P1	+17% at $\alpha = 14^\circ$	+6% at $\alpha = 12^\circ$	+4% at $\alpha = 14^\circ$
NACA0012	P3	+16% at $\alpha = 14^\circ$	+7% at $\alpha = 12^\circ$	+2% at $\alpha = 14^\circ$
NACA0012	P5	-12% at $\alpha = 12^\circ$	+10% at $\alpha = 12^\circ$	-22% at $\alpha = 12^\circ$

results will be majorly impacted when using a different airfoil.

C. Effects of Porous Tips

Table 6 below shows the maximum percent differences in aerodynamic behaviour for the NACA0012 airfoils with porous tips. Figure 11 shows the lift to drag coefficient plots and Figure 12 shows the lift to drag ratio plots. From these results, it is clear that introducing porosity will result in improved aerodynamic behaviour. However when larger percentages of porosity is introduced, the aerodynamic performance of the airfoil worsens. Drag increases for all porosity % while the lift coefficient is only increases for the P1 and P3 wingtip. The lift to drag ratio plots show severely worse aerodynamic performance from the P5 airfoil where porosity is increased to 50%. This is related to how the flow interacts with the porous tip. As the flow hits the pressure side of the airfoil, a partial stream flows through the porous holes and reattaches with the flow field either out the side of the wingtip or through the suction side of the wing tip. This reduces the size of the wing tip vortex and the impacts on how the tip vortex may reduce lift. This can result in an axisymmetric flow condition being reached sooner downstream. The drag increases for all porous wing tips. This can be a result of blockages at the holes of the porous tip. As the stops at the pressure side of the airfoil at the porous hole, some of the flow does not enter through and instead interacts with other flow streams that don't enter the holes. This can be what leads to increased drag and as the holes grow larger at higher porosity % the flow has more chance of interacting on with each other on the pressure side of the airfoil. This can also explain the lower lift coefficient.

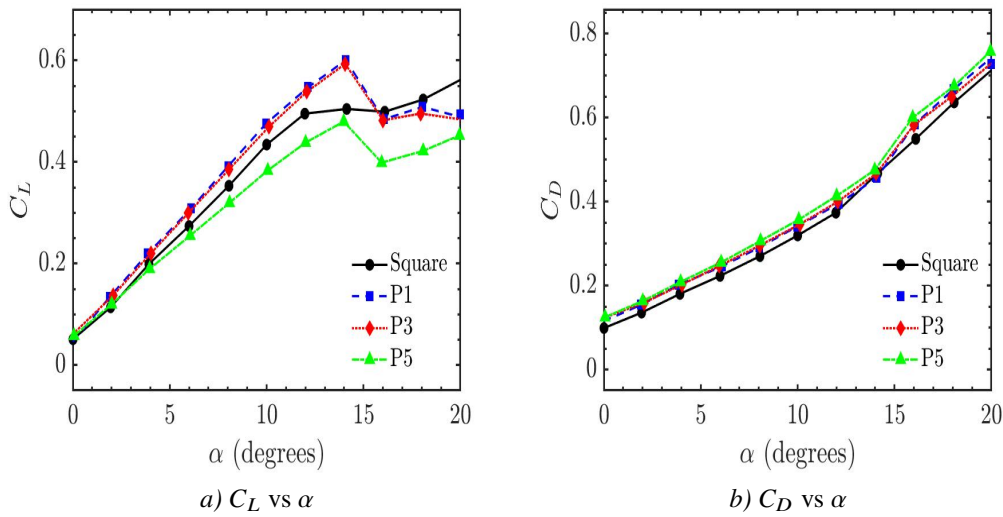


Fig. 11 Lift and drag coefficient plots for NACA0012 airfoil with square and porous tips at $Re = 140,000$.

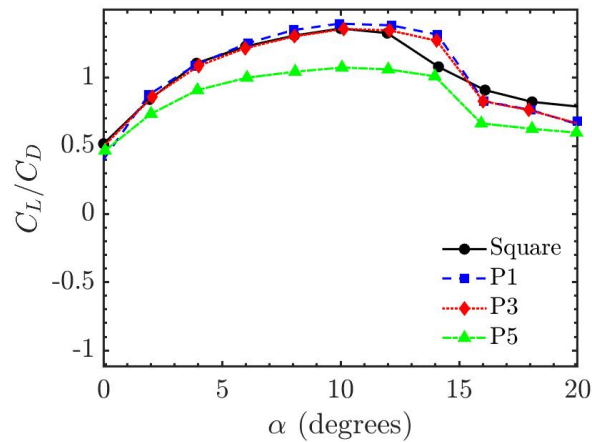


Fig. 12 Lift and drag coefficient ratio plot for NACA0012 airfoil with square and porous tips at $Re = 140,000$.

V. Conclusion

In conclusion, this study presents the aerodynamic performance of a range of wing tip devices. Rounded wing tips perform better aerodynamically for a symmetrical airfoil but will need to be tested on cambered airfoils individually to confirm their viability. Sinusoidal wingtips also lead to better aerodynamic performance when using small amplitude waves. These will need to be tested using a cambered airfoils as the results will differ. Porous wing tips improve aerodynamic behaviour but only low levels of porosity is required. These will also need to be tested on a cambered airfoil as the results will differ. In terms of reducing noise, these have been proven to be viable options as low noise wing tip devices without sacrificing aerodynamic performance. Future work may include smoke visualisation study to visualise the flow behaviour off the different tips and to record lift and drag measurements of the NACA6412 airfoils with these tips.

Appendix

Acknowledgments

I would like to firstly thank Dr. Danielle Moreau for being an invaluable mentor and supervisor during this research study. I would also like to thank Omead Saeed who mentored me in using the wind tunnels for experiments. Lastly, I would like to thank my friends and family who have supported me while writing this paper. Without you, I believe I would not have completed this paper on time.

References

- [1] Mathias, D. L., Pye, J. D., and Cantwell, B. J., "Correlation of Wingtip Noise with Mean Flow Parameters," *AIAA* 98, 1998.
- [2] Drobietz, R., and Borchers, I., *Generic Wind Tunnel Study on Side Edge Noise*, 2006. <https://doi.org/10.2514/6.2006-2509>, URL <https://arc.aiaa.org/doi/abs/10.2514/6.2006-2509>.
- [3] Revell, J., Kuntz, H., Balena, F., Horne, C., Storms, B., and Dougherty, R., *Trailing-edge flap noise reduction by porous acoustic treatment*, 1997. <https://doi.org/10.2514/6.1997-1646>, URL <https://arc.aiaa.org/doi/abs/10.2514/6.1997-1646>.
- [4] Giuni, M., and Green, R. B., "Vortex formation on squared and rounded tip," *Aerospace Science and Technology*, 2013.
- [5] Chong, T. P., Vathylakis, A., McEwen, A., Kemsley, F., Muhammad, C., and Siddiqi, S., *Aeroacoustic and Aerodynamic Performances of an Aerofoil Subjected to Sinusoidal Leading Edges, ????* <https://doi.org/10.2514/6.2015-2200>, URL <https://arc.aiaa.org/doi/abs/10.2514/6.2015-2200>.
- [6] Division, E. D., *EDUCATIONAL WIND TUNNEL*, AEROLAB, 1st ed., 2016.
- [7] Geyer, T., Moreau, D., Zhang, T., Schneehagen, E., and Ding, Y., "Experimental investigation of novel, low-noise turbine blade tip designs," 2020.
- [8] Zhang, T., Moreau, D., Geyer, T., Fischer, J., and Doolan, C., "Dataset on tip vortex formation noise produced by wall-mounted finite airfoils with flat and rounded tip geometries," *Data in Brief*, Vol. 28, 2020, p. 105058. <https://doi.org/https://doi.org/10.1016/j.dib.2019.105058>, URL <http://www.sciencedirect.com/science/article/pii/S2352340919314143>.
- [9] Zhang, T., Moreau, D., Geyer, T., Fischer, J., and Doolan, C., "Dataset on tip vortex formation noise produced by wall-mounted finite airfoils with sinusoidal and porous tip geometries," *Data in Brief*, Vol. 30, 2020, p. 105471. <https://doi.org/https://doi.org/10.1016/j.dib.2020.105471>, URL <http://www.sciencedirect.com/science/article/pii/S2352340920303656>.

Comparison of Transport Property Models For Gas Giant Planetary Entry Simulations

Igor I. Segrovets* and Rowan Gollan†
 University of Queensland, St. Lucia, Queensland 4072, Australia

The research presents a collection of methods for computation of transport properties, and examines them with respect to a CFD simulation representing a Gas Giant planetary entry. Transport properties are computed by first evaluating the collision cross section (CCS) parameter. The CCS data-sets considered share all but two interaction potentials yet it was found the transport properties computed with each differ up to 15%. For frozen thermal conductivity the Eucken method performed best and was found to remain accurate up to 15,000K and with a maximum error of 15% relative to the multi-component solution. For reactive thermal conductivity Gupta models are accurate up to 14,000K with a maximum error of 10% relative to the multi-component solution. Overall the approximate relations were increasingly inaccurate for ionised flows for which more sophisticated modelling is recommended. These models were implemented into The University of Queensland's compressible flow simulation program Eilmer to aid the study of aeroheating in Gas Giant atmospheres.

I. Nomenclature

A, B, C, D	=	fitting coefficients for Eq.(1) of [1].
$a_i, a_i(\beta), d_i, g_i$	=	fitting coefficients for Eqs.(3,5,8,9) of [2, 3].
c_N, C_N, D_N	=	fitting coefficients for Eq.(10) of [4].
$a_{l,i}$	=	stoichiometric coefficient of species i in reaction l .
C_p	=	specific heat at constant pressure (J/kg).
D	=	binary diffusion (m^2/s).
$\Delta_{ij}^{(1)}, \Delta_{ij}^{(2)}$	=	Gupta factors defined Eq. (20), Eq. (21) ($cm-s$).
η	=	viscosity ($kg/m-s$).
h	=	enthalpy (J/kg).
Δh_l	=	enthalpy of reaction l (J/mol).
k	=	thermal conductivity ($W/m-K$).
k_B	=	Boltzmann constant = 1.380649×10^{-23} (J/K) = $1380649/16021766340$ (eV/K).
λ	=	Debye shielding length (cm).
m	=	mass ($kg/particle$).
M	=	molar mass = $m \times N_A$ (kg/mol).
n	=	number density ($particles/m^3$).
N_A	=	Avogadro number = 6.0225×10^{23} ($particles/mol$).
p	=	pressure (Pa).
q	=	heat flux ($J/s-m^2$).
R_{univ}	=	universal gas constant = 8.314 ($J/mol-K$), when denoted $R' = 1.987$ ($cal/mol-K$).
ρ	=	density (kg/m^3).
σ	=	differential cross section (\AA).
T	=	temperature (K).
T^*	=	reduced temperature.
x	=	mass fraction.
X	=	mole fraction.
U	=	velocity (m/s).
$\sigma^2 \Omega_{i,j}^{(\ell,s)*}$	=	collision cross section, (\AA^2).

*Undergraduate Category, Department of Mechanical & Mining Engineering, igor.segrovets@uqconnect.edu.au. AIAA Student Member.

†Professor, Centre for Hypersonics, Division of Mechanical Engineering. Associate Fellow AIAA.

II. Introduction

IMPROVING the predictive power of computational simulations for hyper velocity flows requires the corroboration of experimental and numerical studies. As it stands in the research community those of us focusing on experimental testing in shock tunnels rarely have a chance to understand the details of the thermo-physical modelling used in the Computational Fluid Dynamic (CFD) codes developed by our colleagues. It is then the purpose of this paper to make accessible the recent efforts in modeling properties of the gas describing the transport of energy and momentum, respectively called thermal conductivity and viscosity. This comparative review should aid researchers in implementing the programs and understanding the limitations of their computations. Accurately computing *transport properties* is especially important in compressible high-speed flows—such as those encountered during planetary entry—where they strongly affect the calculated convective heat flux [1] and as a result will influence design of a spacecraft’s thermal protection system .

Upon returning data from its Jupiter entry mission the Galileo probe revealed that initial predictions of the ablation pattern resulting from its trajectory were diametrically opposed to that experienced by the craft [5]. This prediction failure set a historic precedent for the study of Gas Giant atmosphere thermo-chemistry. Today there is a renewed interest in Jovian planet exploration with Saturn and Neptune named as potential mission candidates in NASA’s decadal mission survey [6]. This has motivated the investigation of radiative and convective heating loads on Jovian atmosphere entry probes. In response, this paper conducts a comparative review of transport property models on which such studies rely upon. A six species gas mixture composition ($H_2, H, H^+, He, He^+, e^-$) is considered over the temperature range of 200K-20,000K which encompasses typical atmospheric entry conditions [1]. A cold gas Gas Giant atmosphere compositions cited in literature and used here also is 0.89 χ_{H_2} and 0.11 χ_{He} by mole fraction [1, 2]. Thermal conductivity and viscosity are evaluated under frozen and equilibrium thermo-chemical assumptions by development of a sub-program into The University of Queensland’s compressible flow simulation program Eilmer [7].

The physical phenomenology of the gas involves the interplay of thermodynamic, chemical and thermal-kinetic effects which in practical applications, especially those involving gas mixture, are approximated using mixing-rules. Mixing-rule relations trade accuracy for computational efficiency by approximating the *multi-component solution* to the Boltzmann Equation proposed by Chapman and Enskog [8]. In this study the Eucken-Hirschfelder rule [9, 10] and Yos-Gupta [11] rules are examined. These methods rely on thermophysical parameters such as the mole fractions, specific heats, enthalpy of chemical species, and *collision cross sections* (CCS) between the chemical species pairs, including neutral and ionized chemical species. The process to compute transport properties is then two stepped, first must be computed the thermo-physical parameters of the gas, including the collision cross sections of all species pairs then solve the exact or approximate multi-component equations.

To simulate a hypersonic shock-layer experiment it may be useful to understand that the Chapman-Enskog solution provides a bridge from the inter-species collision (mesoscopic) scale described by the Boltzmann Equation to a macroscopic timescale of the fluid described in terms of bulk flow and transport property coefficients. The multi-component solution is a linear symmetric NxN system of equations describing the interaction of each pair of species in the gas. The transport property equations for pure gasses are derived from this formulation, but for gas mixtures numeric methods are needed to deal with inter-species interactions.

The collision cross section parameter is collated from various chemical and quantum mechanics studies for a large number of particle species in literature. The result are usually recoverable with fitting equations and a data-set of coefficients. The contemporary data-sets for non-ionised $H_2 - He$ composition interactions, at the time of writing, are that of [1] and [2] from now on referred to as the Palmer and Bruno data-sets respectively. The Palmer data-set refit many collision cross sections of the Bruno data-set due to superior accuracy of the latter. Differences remain between treatment of $H - He$, $H_2 - He$ and charged potentials, these are investigated. For charged species the relations of Stallcop are used [4].

III. Collision Cross Section

The collision cross section depends strongly on the interaction potential between a species pair. Neutral-neutral and neutral-ion interactions are dominated by short ranged inter-molecular forces. The Bruno and Palmer data-sets evaluate the integral in the cross section form $\sigma^2 \Omega^{(\ell,s)*}$ which includes in it the squared differential cross section σ^2 , hence this is called a collision cross section.

The superscript (ℓ, s) is the order of the collision and can be thought of as a description of the discrete energy state before and after the interaction. For temperatures up to 20,000K the gas mixture is sufficiently described by first

order transport properties [12] which requires only the (1,1) diffusion, (2,2) viscosity CCS. The (1,2) and (1,3) order integrals represent second order solution and correspond to the off-diagonal terms of the multi-component solution matrix relevant at higher temperatures [2].

A. Palmer Data-set

Palmer fitting parameters can be found in [1] and the data-set supports up to a seven species model with the inclusion of H_2^+ . The source paper omits that Eq. (1) has an implicit π product in the result, the representation shown here is full and complete.

$$\begin{aligned}\pi\sigma^2\Omega_{ij}^{(\ell,s)*} &= DT^\alpha \\ \alpha &= A(\ln T)^2 + B \ln T + C.\end{aligned}\tag{1}$$

B. Bruno Data-set

The data-set of [2] has separate parameterisation functions for neutral-neutral or neutral-ion and electron-neutral species. Additionally, $He - H_2$ and $H_2 - He^+$ have separate phenomenological potentials computed with the formulation of [3]. $H - H^+$ and $He - He^+$ undergo resonant charge transfer described by Eq. (4).

1. Neutral-Neutral and Neutral-Ion Interactions

Coefficients entering Eq. (3) are found in [2].

$$\chi = \ln(T)\tag{2}$$

$$A(1) = \exp[(\chi - a_3)/a_4]$$

$$A(2) = \exp[(\chi - a_6)/a_7]$$

$$\begin{aligned}\sigma^2\Omega_{ij}^{(\ell,s)*} &= [a_1 + a_2\chi] \frac{A(1)}{A(1) + \exp[(a_6 - \chi)/a_7]} \\ &+ a_5 \frac{A(2)}{A(2) + \exp[(a_6 - \chi)/a_7]}.\end{aligned}\tag{3}$$

2. Resonant Charge Transfer Correction of $H - H^+$ and $He - He^+$

The six species model and first order transport equations only require charge transfer correction for order (1, 1) CCS of $H - H^+$ and $He - He^+$ interaction pairs. They are evaluated with Eqs.(2, 4, 5) and entering the coefficients of Table 1.

$$\sigma^2\Omega_{ij}^{(\ell,s)*} = \sqrt{\left(\Omega_{i,j}^{(\ell,s)*}\right)^2 + \left(\Omega_{ch-ex}^{(\ell,s)*}\right)^2}\tag{4}$$

$$\sigma^2\Omega_{ch-ex}^{(\ell,s)*} = d_1 + d_2\chi + d_3\chi^2\tag{5}$$

Table 1 Bruno resonant charge transfer correction fitting coefficients for order (1, 1) CCS [2].

$(i-j)_{ch-ex}$	d_1	d_2	d_3
$He - He^+$	38.6185	-3.1289	6.3410(-2)
$H - H^+$	63.5437	-5.0093	9.8797(-2)

3. Phenomenological Potentials of $He - H_2$ and $He^+ - H_2$

The data and formulation for these potentials that is found in [2, 3] has been reproduced and simplified where possible, for example by evaluating the differential cross section σ .

$$\ln \Omega_{i,j}^{(\ell,s)*} = [a_1(\beta) + a_2(\beta)x] \frac{\exp \{[x - a_3(\beta)] / a_4(\beta)\}}{\exp \{[x - a_3(\beta)] / a_4(\beta)\} + \exp \{[a_3(\beta) - x] / a_4(\beta)\}} + a_5(\beta) \frac{\exp \{[x - a_6(\beta)] / a_7(\beta)\}}{\exp \{[x - a_6(\beta)] / a_7(\beta)\} + \exp \{[a_6(\beta) - x] / a_7(\beta)\}} \quad (6)$$

$$x = \ln T^* = \ln (k_B T / \varepsilon_o) = \ln (1380649 \cdot T / (16021766340 \cdot \varepsilon_o)) \quad (7)$$

The the well depth ε_o of Eq. (7) is shown in Table 2. In Eq.7 k_B is the Boltzmann constant in eV/K . To compute the collision integral of Eq. (6) its $a_i(\beta)$ coefficients are calculated using Eq. (8) entering coefficient from Table 2 and c_j coefficients found in Table 3 and Table 4.

$$a_i(\beta) = \sum_{j=0}^2 c_j \beta^j = c_0 \beta^0 + c_1 \beta^1 + c_2 \beta^2 \quad (8)$$

Table 2 Parameters entering to Eqs.(6-8)[2, 3]

	β	ε_o [eV]	σ^2 [\AA^2]
$He - H_2$	9.290	1.865(-3)	8.1108
$H_2 - He^+$	9.220	1.775(-1)	3.7673

Table 3 Parameters of [3] entering to Eq.(8) for the $He^+ - H_2$ interaction.

	c_0	c_1	c_2	c_0	c_1	c_2
$\Omega^{(1,1)*}$				$\Omega^{(2,2)*}$		
a_1	9.851755(-01)	-2.870704(-02)	-	9.124518(-01)	-2.398461(-02)	-
a_2	-4.737800(-01)	-1.370344(-03)	-	-4.697184(-01)	-7.809681(-04)	-
a_3	7.080799(-01)	4.575312(-03)	-	1.031053(+00)	4.069668(-03)	-
a_4	-1.239439(+00)	-3.683605(-02)	-	-1.090782(+00)	-2.413508(-02)	-
a_5	-4.638467(+00)	4.418904(-01)	-1.220292(-02)	-4.127243(+00)	4.302667(-01)	-1.352874(-02)
a_6	3.841835(+00)	3.277658(-01)	-2.660275(-02)	4.059078(+00)	2.597379(-01)	-2.169951(-02)
a_7	2.317342(+00)	3.912768(-01)	-3.136223(-02)	2.086906(+00)	2.920310(-01)	-2.560437(-02)

Table 4 Parameters of [3] entering to Eq.(8) for the $He - H_2$ interaction.

	c_0	c_1	c_2	c_0	c_1	c_2
$\Omega^{(1,1)*}$				$\Omega^{(2,2)*}$		
a_1	7.884756(-01)	-2.438494(-02)	-	7.898524(-01)	-2.114115(-02)	-
a_2	-2.952759(-01)	-1.744149(-03)	-	-2.998325(-01)	-1.243977(-03)	-
a_3	5.020892(-01)	4.316985(-02)	-	7.077103(-01)	3.583907(-02)	-
a_4	-9.042460(-01)	-4.017103(-02)	-	-8.946857(-01)	-2.473947(-02)	-
a_5	-3.373058(+00)	2.458538(-01)	-4.850047(-03)	-2.958969(+00)	2.303358(-01)	-5.226562(-03)
a_6	4.161981(+00)	2.202737(-01)	-1.718010(-02)	4.348412(+00)	1.920321(-01)	-1.496557(-02)
a_7	2.462523(+00)	3.231308(-01)	-2.281072(-02)	2.205440(+00)	2.567027(-01)	-1.861359(-02)

4. Electron-Neutral Interactions

Equation (9) describes $H_2 - e^-$, $H - e^-$ and $He - e^-$ interactions [2].

$$\begin{aligned}
 G(1) &= \exp[(\chi - g_1)/g_2], \\
 \sigma^2 \Omega^* &= g_3 \chi^{g_5} \frac{G(1)}{G(1) + \exp[-(\chi - g_1)/g_2]} \\
 &\quad + g_6 \exp \left[- \left(\frac{\chi - g_7}{g_8} \right)^2 \right] + g_4.
 \end{aligned} \tag{9}$$

C. Ion-Ion Interactions

In this class of interaction long range electrostatic forces dominate the short range atomic forces. In ionised flows the interaction potential is described using a Coulomb screened potential model, where interaction forces beyond the Debye shielding length λ are effectively cancelled by equal and opposite electrostatic forces. The collision parameter is recovered from Eqs. (10 - 12) by entering the reproduced coefficients of [12] found in Table. 5. The coefficients are valid where reduced temperature $T^* \geq 4$ and the equations hold while quantum corrections are not significant. This is true in the low density regime typical to re-entry flows [4, 13].

$$\sigma^2 \Omega_{i,j}^{(N,N)*} = \left(5.0 \times 10^{15} \right) (\lambda/T^*)^2 \ln \{ D_N T^* [1 - C_N \exp(-c_N T^*)] + 1 \} \tag{10}$$

$$\lambda = 6905 \sqrt{T/n_{e^-}} \tag{11}$$

$$T^* = 4132500 [T^{1.5}/\sqrt{n_{e^-}}] \tag{12}$$

The charge density is evaluated as the electron number density n_{e^-} using an equilibrium charge assumption in units per m^3 . Bruno uses the assumption that both electrons and ions contribute to the Debye shielding length such that the effective charge density used in Eq. (11) is doubled [4]. Physically this is justified in conditions of equilibrium plasmas, which differs from the mildly ionised flow encountered in atmospheric re-entry. The impact of this was investigated for the temperature range in question.

Table 5 Fitting parameters for Eq. (10) Shielded Coulomb CCS at $T^* \geq 4$ [12].

N	Attractive			Repulsive		
	C_N	c_N	D_N	C_N	c_N	D_N
1	-0.476	0.0313	0.784	0.138	0.0106	0.765
2	-0.146	0.0377	1.262	0.157	0.0274	1.235

IV. Transport Properties

A. Mixture Thermal Conductivity

For a pure gas, calculation of the heat flux vector \mathbf{q} is shown to be directly proportional to the temperature gradient ∇T scaled by the thermal conductivity k of the gas

$$\mathbf{q} = -k \nabla T. \tag{13}$$

Physically thermal conductivity describes exchange of energy as a result of intermolecular collisions. If conditions in the flow field are such that a collision between species imparts sufficient energy for the species molecule to react, additional heat is transported by means of chemical enthalpy [14]. Heat conduction increases due to concentration gradients in the mixture, where dissociated gasses in high temperature regions are now favourably diffused into low density, low temperature regions. Here the lower temperature facilitates recombination of the diffused molecules. This reaction releases the energy carried from the high temperature region. When using macro-scale methods such as in CFD codes, this is seen as an increase in the thermal conductivity k of the gas. Non-reacting thermal *diffusion* carries negligible contribution when compared to molecular collision and chemical enthalpy and it is usually neglected [12].

A derivation of reactive and internal thermal conductivity under equilibrium thermo-chemistry can be found in [11, 15]. Relations of [16] allow for Eq.(13) to be decoupled from the flow geometry and generalised for an arbitrary reacting gas mixture. Then thermal conductivity can then be expressed as a summation of its frozen k_f and reactive k_r components as in Eq. (14) [11], where the double sum is over all binary pairs of interactions and NS is the number of total species. The frozen component can be expressed in terms of translational k_{tr} and internal k_{int} D.O.F.

$$\mathbf{q} = - \left(k_f - \frac{\rho}{M_m^2} \sum_{i=1}^{NS} \sum_{j=1}^{NS} h_i M_i M_j D_{ij} \left(\frac{\partial X_j}{\partial T} \right)_{eq} \right) \nabla \mathbf{T},$$

$$= (k_f + k_r) \nabla \mathbf{T}. \quad (14)$$

$$k = k_f + k_r = k_{tr} + k_{int} + k_r. \quad (15)$$

B. Eucken-Hirschfelder Frozen Thermal Conductivity

The Eucken-Hirschfelder approximation simplifies the treatment of polyatomic gasses for computation of frozen thermal conductivity. This is achieved by employing several assumptions.

- 1) Energy transfer between translational and internal degrees of freedom (D.O.F) is sufficiently rapid such that their distribution is equivalent to that of one at local equilibrium [10].
- 2) Each internal energy state of a molecule are modelled as a pseudo chemical species of the gas, "Eucken species" [17], all species are then mono-atomic.
- 3) Assumption (2.) implies that all species have identical mass and approximately the same interaction potential such that thermal diffusion is negligible.
- 4) Assumption (2.) implies that each D.O.F now interacts elastically through a process of translational collisions, k'_{tr} . The inelastic coupling of internal D.O.F found in polyatomic species is approximated by diffusion of Eucken species, k'_{int} , reflecting a relaxation of the collisional energy distribution.

The derivation of the Eucken-Hirschfelder approximation can be found in [17] for pure gasses, later derived by [12] for a gas mixture. In Eq.(16) subscript m denotes a property of the gas mixture, and $\rho D/\mu$ is a single term known as the reciprocal Schmidt number.

$$k = k'_{tr} + k'_{int} = \frac{15}{4} \frac{k_B \eta}{m} + \frac{\rho D}{m} \left(C_p - \frac{5}{2} k_B \right),$$

$$= \frac{R_{univ}}{M_m} \eta_m \left[\frac{15}{4} + \left[\frac{\rho D}{\eta} \right] \left(\frac{C_{p,m}}{R_{univ}} - \frac{5}{2} \right) \right]. \quad (16)$$

A value of $\rho D/\eta = 1.32$ corresponds to a Lennard-Jones 6-12 interaction potential [18], and has been shown to significantly improve model accuracy [10]. Mixture viscosity can be calculated using the kinetic theory of gases [17] or using a number of approximate mixing rules [12] to varying degrees of accuracy. The next section will present the Yos-Gupta mixing rule used for this work.

The mixture specific heat $C_{p,m}$ is calculated using Eq. (17). Species specific heat $C_{p,i}$ is retrieved from the ideal perfect gas thermodynamics model for Gas Giant compositions in the Eilmer CFD methods library [7].

$$C_{p,m} = \sum_{i=1}^{NS} X_i C_{p,i}. \quad (17)$$

C. Yos-Gupta Total Thermal Conductivity

1. Transnational and Internal Contribution

Using the derivation of [9] the reactive thermal conductivity component of Eq.(14) can be recast omitting the diffusion coefficient $D_{i,j}$, which can be otherwise understood as the simplification of the non-diagonal terms of the multi-component solution.

$$k_{tr} = \frac{15}{4} k_B \times 10^2 \sum_{i=1}^{NS} X_i \left[\sum_{j=1}^{NS} \alpha_{ij} X_j \Delta_{ij}^{(2)} \right]^{-1}, \quad (18)$$

$$k_{int} = k_B \times 10^2 \sum_{i=1}^{NS} \left[X_i \left(\frac{C_{p,i}}{R_{univ}} - \frac{5}{2} \right) \left(\sum_{j=1}^{NS} X_j \Delta_{ij}^{(1)} \right)^{-1} \right], \quad (19)$$

The Gupta factors $\Delta_{ij}^{(1)}$ and $\Delta_{ij}^{(2)}$ are computed using Eqs.(20,21), this way computation resources can be optimised as this factor is used for both frozen and reactive thermal conductivity's.

$$\Delta_{ij}^{(1)} = \frac{8}{3} \left(1.5460 \times 10^{-20} \right) \sqrt{\frac{2M_i M_j}{\pi R'_{univ} T (M_i + M_j)}} \pi \sigma^2 \Omega_{i,j}^{(1,1)*}, \quad (20)$$

$$\Delta_{ij}^{(2)} = \frac{16}{5} \left(1.5460 \times 10^{-20} \right) \sqrt{\frac{2M_i M_j}{\pi R'_{univ} T (M_i + M_j)}} \pi \sigma^2 \Omega_{i,j}^{(2,2)*}, \quad (21)$$

$$\alpha_{ij} = 1 + \frac{[1 - r_M][0.45 - 2.54r_M]}{[1 + r_M]^2}, \quad \text{where } r_M = \frac{M_i}{M_j}. \quad (22)$$

2. Reactive Contribution

Reactive thermal conductivity is then the sum over the total *number of independent reactions*, NIR in the system. Equation.(23) produces errors if reactions occur simultaneously [19] however, the Hydrogen-Helium composition is a suitable use-case as each reaction has a distinct temperature interval.

$$k_r = k_B \times 10^2 \sum_{l=1}^{NIR} \frac{(\Delta h_l / R_{univ,i} T)^2}{\sum_{i=1}^{NS} (a_{l,i} / x_i) \sum_{j=1}^{NS} (a_{l,i} x_j - a_{l,j} x_i) \Delta_{ij}^{(1)}}. \quad (23)$$

The enthalpy contribution of each reaction is calculated with,

$$\Delta h_l = \sum_{i=1}^{NS} (h_i) a_{l,i} M_i, \quad (24)$$

where $a_{l,i}$ is the stoichiometric coefficient of the i 'th species in the l 'th reaction. An independent reaction as one written such that the independent component A^j appears in only one reaction and is cast on the left hand side, with all other components divided by its stoichiometric coefficient to meet form

$$A^j = \sum_{i=1, \neq j}^{NS} a_{l,i} A^i \quad (Ref. [14]). \quad (25)$$

Dissociation of H_2 occurs at temperatures 1000K-7000K and has the chemical equation $H_2 + M \rightleftharpoons H + H + M$. (M) represents the inert interaction with any species in the mixture and drops out from the equation after applying the stoichiometric balance of Eq.(25). Proceeding to higher temperatures between 7000K-17,000K ionisation of H will occur, $H + M \rightleftharpoons H^+ + e^- + M$. Finally, above 17,000K the ionisation of He , $He + M \rightleftharpoons He^+ + e^- + M$.

D. Mixture Viscosity

Armani-Sutton and Yos-Gupta mixing rules have been shown to have favourable computational efficiency amongst the many available viscosity mixing rules [11, 12]. The Armani-Sutton scheme was shown to retain higher accuracy in the partially ionised region above 10,000K however, it relies on gas state dependent fitting factors which are yet to be optimised for a wide range of conditions in hydrogen-helium compositions [12] and as such its performance is difficult to predict.

As for the Yos-Gupta rule it approximates off-diagonal terms in the multi-component equations which means it can not account for energy transfer dominated by long range interactions such as in ionised flows. The trade off can be considered small due to the diminishing importance of viscosity to heat transfer in the radiation dominated regime [1]. As such the Yos-Gupta correlation was chosen for implementation to Eilmer. In Eq. (26) the $\Delta_{ij}^{(2)}$ is computed as before with Eq. (21).

$$\eta = \frac{1}{10} \sum_{i=1}^{NS} \left(\frac{X_i M_i / N_A}{\sum_{j=1}^{NS} X_j \Delta_{ij}^{(2)}} \right). \quad (26)$$

V. Results and Discussion

The sub-program was used to evaluate viscosity and thermal conductivity models using two CCS data-sets under conditions of equilibrium and frozen equilibrium chemistry in the temperature range of 200K-20,000K and at a constant pressure of 100kPa. Results are evaluated with respect to the NASA Chemical Equilibrium with Applications (CEA) program [18] which uses multi-parameter curve fitting to recover tabulated gas properties, and the multi-component solutions of [2] computed with the Bruno CCS data-set. For the frozen condition the multi-component solution of [10] is used which was computed with the CCS of [20].

For frozen thermal conductivity shown in Fig. 2 the Eucken rule provides the best agreement up to 15,000K and was accurate within 15% of the multi-component solution. This is because $H_2 - He$ mixtures become increasingly mono-atomic after 1000K making this composition very compatible with the mixing rules assumptions. At higher ionisation's the Gupta rule's over prediction of viscosity drives Eucken conductivity to do the same, as follows from Eq. 16. Gupta and CEA results overshoot the first dip associated with H ionisation, and are not accurate above 9,000K. This is unlike the Eucken conductivity which does not show the increase in thermal conductivity after 15,000K that occurs once long range interactions begin to dominate the flow. If used strictly for frozen thermal conductivity in flows below 15,000K the Eucken rule can be strongly recommended.

For total thermal conductivity shown in Fig. 1b all models reproduce the multi-component solution within 10% at temperatures below 14,000K. In the highly ionised region solutions diverge significantly, yet the models using Eucken frozen conductivity remain self-similar as they both use the Gupta mixture viscosity. Overall, the models have an accuracy that exceeds uncertainties achieved in experiment, and reproduce the multi-component solution better than CEA, making them a suitable choice for CFD codes.

On viscosity, shown in Fig. 1a the Gupta rule provides excellent agreement up-to 10,000K after which the characteristic overshoot is observed. Here CEA shows a better agreement at low ionisation temperatures 10,000K-15,000K. Neither CEA or Gupta performed well in the moderately ionised regime. For neutral flows the Gupta rule has been characterised in literature to outperform the commonly used Wilke rule [12] still widely used in CFD research. This is the rule used before the introduction of this works sub-program in Eilmer and the implemented Gupta rule will provide improved accuracy in the temperature range 6,000K-10,000K, yet it should be used with consideration for the over-prediction observed in ionised flows.

On collision cross sections, the Palmer CCS tend to produce higher values for transport properties in all but the region above 12,000K. There the Bruno treatment of charge density for computation of the Debye shielding length decreases the shielding length which decreases the CCS for charged interactions. This correlates inversely with transport properties, so Bruno's treatment of charged interactions increases the highly ionised thermal conductivity as seen in Fig. 1b. A similar behaviour is seen in the highly ionised region of the viscosity curve shown Fig. 1a.

The examined transport property models were compared against the Wilke mixing rules [10, 12] already incorporated to Eilmer's Gas Giant equilibrium perfect gas model. This was done by comparing the results for a simulation of a shock-tunnel test imitating a planetary entry scenario. The flow state is ($T_\infty = 377.1K$, $p_\infty = 55.0Pa$, $U_\infty = 18,201.2m/s$), the composition is ($x_{H_2} = 0.11$, $x_{He} = 0.89$) by mass fraction and the geometry is a 0.0125m radius 2D cylinder, approximating typical blunt body planetary entry probe. Results are shown with respect to the stagnation streamline at the crafts nose in Fig. 4 and Fig. 3 for thermal conductivity and viscosity respectively.

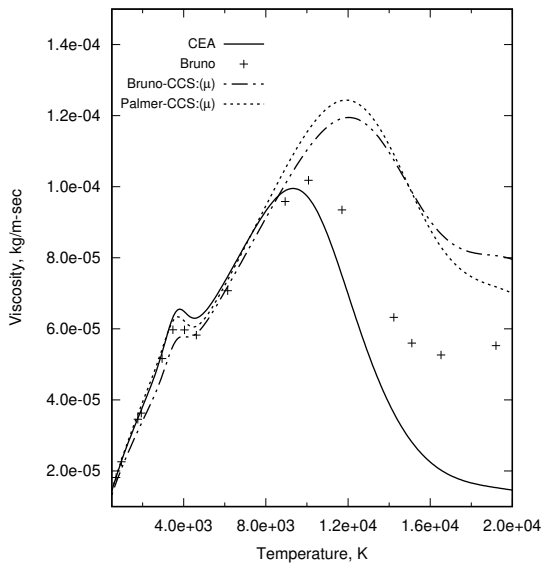
It can be observed in Fig. 3 that the temperature profile quickly enters a moderately ionised regime for which viscosity is over estimated by the Gupta model. As a result the Eucken frozen conductivity is drastically over estimated. The contribution of reaction enthalpy modelled with Gupta k_r is small. Palmer CSS are shown to produce a larger increase in transport properties at the low pressure condition, this is most prevalent on the shock side of the stagnation

line. Although the treatment of $H - He$, $H_2 - He$ potentials differs between the CCS sources, the 15% difference in temperature response of the models cannot be readily explained by the behaviour observed in the 100kPa pressure tests.

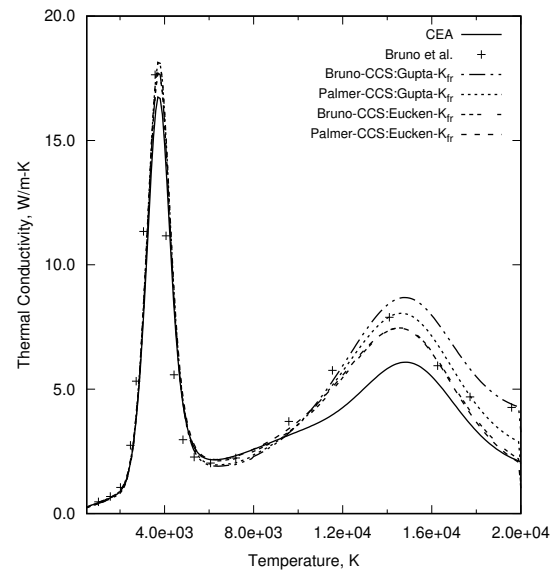
VI. Conclusion

The characterisations conducted of viscosity and thermal conductivity mixing rules provide a good point of reference for those needing to evaluate Hydrogen-Helium gas states and reveal the difficulty in approximating the behaviour of ionised flows. A recommendation can be made to incorporate a multi-component solution method into the Eilmer program, which would greatly lower the uncertainties at temperatures exceeding 10,000K. The comparative review of methods conducted here will aid researchers in utilizing the most appropriate transport property methods and to understand their performance and limitations. This non-trivial aspect has been commonly overlooked in literature where inaccurate methods are still widely employed.

Appendix



(a) Mixture viscosity using Gupta rule at 100kPa



(b) Total thermal conductivity using Gupta k_T at 100kPa

Fig. 1 Comparing CCS data-sets of Bruno [2] and Palmer [10] for computation of transport properties at equilibrium. Compared against CEA [18] and multi-component solution of Bruno [2].

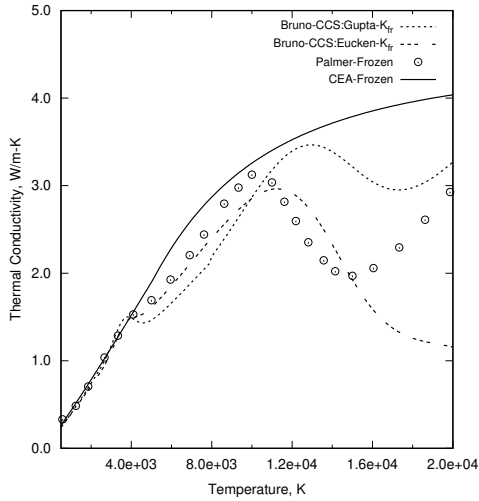


Fig. 2 Equilibrium frozen thermal conductivity at 100kPa. Compared against CEA [18] and multi component solution of [10].

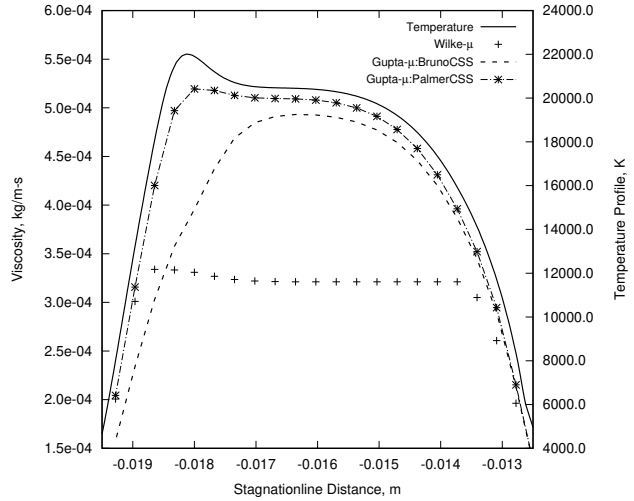


Fig. 3 Mixture viscosity along mach 14 streamline, with Eilmer's Wilke rule for comparison.

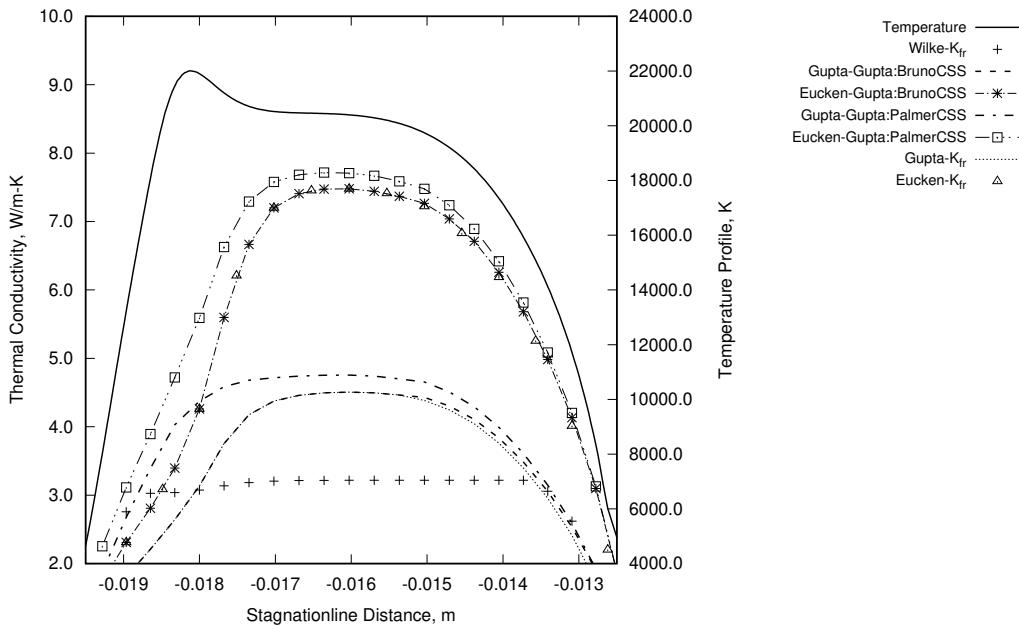


Fig. 4 Thermal conductivity along mach 14 stagnation streamline, with Eilmer's Wilke rule for comparison.

Acknowledgments

Portions of this research were done while the author was an undergraduate student at The University of Queensland's Department of Mechanical & Mining Engineering, later with the School of Mathematics and Physics and at a time a research intern at the Research School of Physics and Engineering at Australian National University. I thank Dr. Chris James, Ph. C. Kiel Hopkins and Ph. C Liu Yu, Centre for Hypersonics, University of Queensland. I especially thank Dr. Rowan Gollan, Centre for Hypersonics, University of Queensland for his supervision and guidance to this work.

References

- [1] Palmer, G., Prabhu, D., and Cruden, B. A., "Aeroheating uncertainties in uranus and saturn entries by the monte carlo method," *Journal of Spacecraft and Rockets*, Vol. 51, No. 3, 2014, pp. 801–814.
- [2] Bruno, D., Catalfamo, C., Capitelli, M., Colonna, G., De Pascale, O., Diomede, P., Gorse, C., Laricchiuta, A., Longo, S., Giordano, D., et al., "Transport properties of high-temperature Jupiter atmosphere components," *Physics of Plasmas*, Vol. 17, No. 11, 2010, p. 112315.
- [3] Laricchiuta, A., Colonna, G., Bruno, D., Celiberto, R., Gorse, C., Pirani, F., and Capitelli, M., "Classical transport collision integrals for a Lennard-Jones like phenomenological model potential," *Chemical Physics Letters*, Vol. 445, No. 4-6, 2007, pp. 133–139.
- [4] Stallcop, J. R., Partridge, H., and Levin, E., "Collision integrals for the interaction of the ions of nitrogen and oxygen in a plasma at high temperatures and pressures," *Physics of Fluids B: Plasma Physics*, Vol. 4, No. 2, 1992, pp. 386–391.
- [5] Park, C., "Stagnation-region heating environment of the Galileo probe," *Journal of thermophysics and heat transfer*, Vol. 23, No. 3, 2009, pp. 417–424.
- [6] Space Studies and National Research Council Board, et al., *Vision and voyages for planetary science in the decade 2013-2022*, National Academies Press, 2012.
- [7] Jacobs, P., Gollan, R., Potter, D., Zander, F., Gildfind, D., Blyton, P., Chan, W., and Doherty, L., "Estimation of high-enthalpy flow conditions for simple shock and expansion processes using the ESTCj program and library," *Mechanical Engineering Report*, The University of Queensland, 2014, pp. 1–15.
- [8] Chapman, S., Cowling, T. G., and Burnett, D., *The mathematical theory of non-uniform gases: an account of the kinetic theory of viscosity, thermal conduction and diffusion in gases*, Cambridge university press, 1990.
- [9] Hirschfelder, J. O., Curtiss, C. F., Bird, R. B., and Mayer, M. G., *Molecular theory of gases and liquids, Corrected Printing With Notes Added.*, Wiley New York, 1967.
- [10] Palmer, G., and Wright, M., "A Comparison of Methods to Compute High-Temperature Gas Thermal Conductivity," *36th AIAA Thermophysics Conference*, 2003, p. 3913.
- [11] Gupta, R. N., Yos, J. M., Thompson, R. A., and Lee, K.-P., "A review of reaction rates and thermodynamic and transport properties for an 11-species air model for chemical and thermal nonequilibrium calculations to 30000 K," *NASA Reference Publication*, 1990.
- [12] Palmer, G. E., and Wright, M. J., "Comparison of Methods to Compute High-Temperature Gas Viscosity," *Journal of Thermophysics and Heat Transfer*, Vol. 17, No. 2, 2003, pp. 232–239.
- [13] Hahn, H.-s., Mason, E., and Smith, F. J., "Quantum transport cross sections for ionized gases," *The Physics of Fluids*, Vol. 14, No. 2, 1971, pp. 278–287.
- [14] Butler, J. N., and Brokaw, R. S., "Thermal conductivity of gas mixtures in chemical equilibrium," *The Journal of Chemical Physics*, Vol. 26, No. 6, 1957, pp. 1636–1643.
- [15] Copeland, D. A., "New approximate formulas for viscosity and thermal conductivity of dilute gas mixtures," *AIAA journal*, Vol. 41, No. 3, 2003, pp. 525–537.
- [16] Hirschfelder, J. O., "Heat transfer in chemically reacting mixtures. I," *The Journal of Chemical Physics*, Vol. 26, American Institute of Physics, 1957, pp. 274–281.
- [17] Hirschfelder, J. O., Curtiss, C. F., Bird, R. B., and Mayer, M. G., "Molecular theory of gases and liquids," *Molecular theory of gases and liquids*, Vol. 26, Wiley New York, 1954, pp. 441–582.
- [18] Svehla, R. A., "Transport coefficients for the NASA Lewis chemical equilibrium program," *NASA Technical Memorandum*, 1995.
- [19] Gupta, R. N., Lee, K.-P., Thompson, R. A., and Yos, J. M., "Calculations and curve fits of thermodynamic and transport properties for equilibrium air to 30000 K," *NASA Reference Publication*, 1991.
- [20] Biolsi, L., "Transport properties in the Jovian atmosphere," *Journal of Geophysical Research: Space Physics*, Vol. 83, No. A3, 1978, pp. 1125–1131.

CONCEPTUAL DESIGN OF QUANTUM PROPULSION SYSTEMS

Aarya Kulkarni ^

University: DKTE's Textile and Engineering Institute, Ichalkaranji (416-115)

The idea states idea of converting the quantum energy using nuclear reactor. That later is converted into heat energy with high temperature. That energy would be helpful into the propulsion. This would create better ways to avoid pollution while we want higher Isp. Also the thrust and Isp will be ideal for deep space missions. But propulsion technique can be used in both with gravity or without gravity circumstances. For the gravity and zero gravity mediums will be totally different. This also includes the design of a particle detector, which is crucial part of the quantum propulsion systems, mentioned here. Particle detector and it's working with PPU, is also explained here in this paper. Also, it's coupling with other space propulsion systems like NTP , or Electro-Thermal Propulsion systems is also stated here.

Nomenclature

Isp- Specific Impulse

PPU- Power Processing Unit

NTP- Nuclear Thermal Propulsion

ϵ - Expansion rate for the nozzle

P_e - Exit Pressure

P_a - Ambient Pressure

Γ - Dependent of the fuel used (here it's just particle detector)

D_e - Exit Diameter

LHC- Large Hadron Collider

QPS-Quantum Propulsion System

PD- Particle Detector

CRPC- Carbon Reinforced Polymer Composites

^ Undergraduate Student, Department of Mechanical Engineering, 1181237,AIAA Student Member

I. INTRODUCTION

Quantum propulsion includes different technical terms from propulsion systems, quantum mechanics and calculus. The concept stated here works on the principle of the Fermi-Boson splitting principle and their amplitudes. The system considers following basic subsystems:

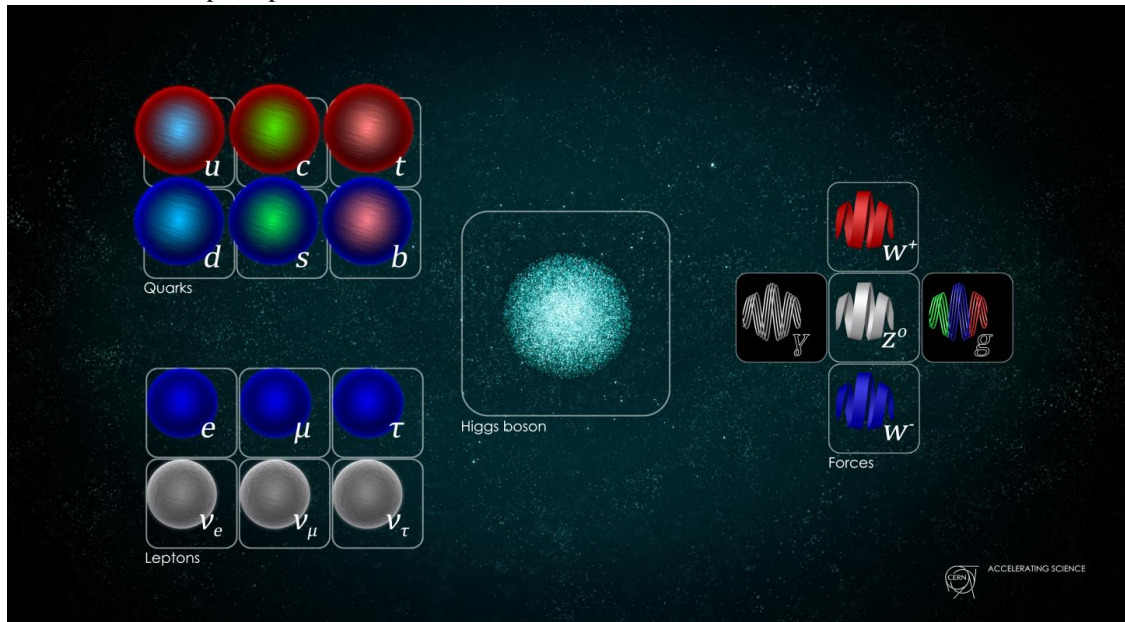
1. Particle Detector.
2. Calculations with Gravity and Zero Gravity Circumstances.
3. Mediums of Operations in Gravity and Microgravity Circumstances.
4. Explanations for Particle Detector including:
 - Material
 - Shape and Size
 - Design
 - Calculations
5. Nozzle Designing (Including calculations for Expansion Rates, Pressures, and Velocities.)

II. WORKING:

The system will work in Gravity and Zero Gravity circumstances, as stated follows:

1. In Gravity Circumstances:

- In, gravity circumstances the particle detector will work same as LHC. The detected particles will collide and release the energy.
- For the particle detection the medium used is atmosphere. The particle present in the atmosphere will be detected on the principle of the STANDARD MODEL OF PARTICLES.



• Figure1. Standard Model Of Particles

• Image Courtesy: CERN

- The particles will release certain amount of the energy, which will further passed on to the PPU. The particles will be split based on the Fermions and Bosons principle, after collision.

Formulae:

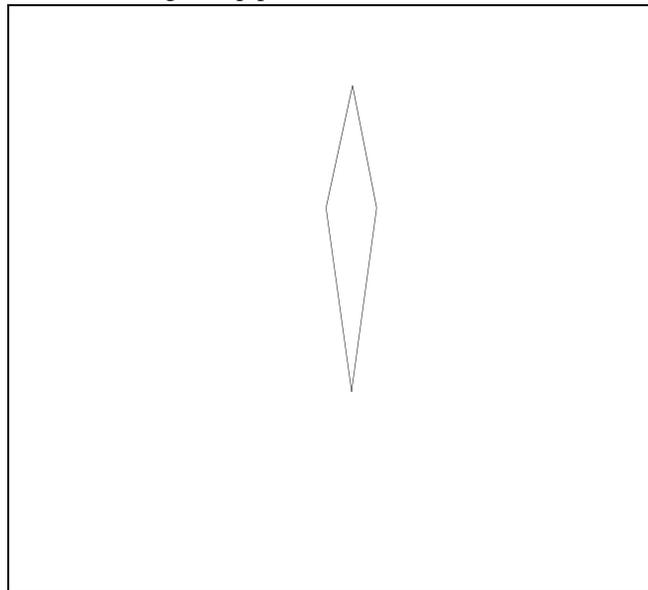
<u>FERMI PARTICLES</u>	(Amplitude Direct – Amplitude Exchanged)
<u>BOSON PARTICLES</u>	(Amplitude Direct + Amplitude Exchanged)

- PPU will have a nozzle which will increase the velocity and will decrease the pressure. And hence will give mechanical energy to the systems.
- Nozzle will be about a size of a normal car engine, which will be providing the thrust required to take off. Also the system will also have Isp about 326 sec.
- Calculations:

$\Delta V = Isp * g * \ln Mr$
$\Delta V =$ It is taken to 3000m/s.
$\ln(Mr) = \ln(Mf/Me)$, where, final mass Mf is assumed to be 100 kg and Me is initial mass round 61 kg.
$3000 = Isp * 9.81 * 0.494296321$
$3000 / 4.849046917 = Isp$
Isp = 618 Sec

2. **Zero Gravity Circumstances**

- In the absence of the gravity, medium for the particle detection will be the space dust and the unknown particles present in the space.
- Dust particles will be gone through the fan like structure designed and located outside the tube used.
- The wing rotation will also provide the drag and allow the spaceship to flow. This will provide the allowance to particles to enter through the pipe of detector and will collide.



• Figure2. Wing drawn with AutoCad-2015

- The wing shape here provides a unique drag, and sizes between 20-25 cm. This will also provide higher energy required for the spacecraft during interplanetary transfer.
- Isp provided will be same as the gravity circumstances, and upon separation of payload, lander, orbiter or any instrument, Isp will be increased.
- The energy is also stored in PPU system for further journey.

III. PARTICLE DETECTOR AND ITS SUBSYSTEMS:

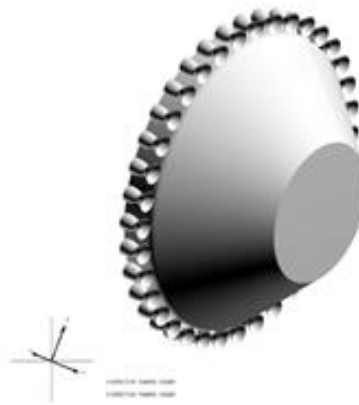
Particle detector is the most efficient part of the quantum propulsion systems.

SYSTEM SPECIFICATIONS

1. Nozzle:

- The design selected for nozzle is Plug Nozzle or Aerospike. This will provide higher expansion rates, which results into under-expansion of the nozzle.
- Due to this the weight of the nozzle and outer diameter of the nozzle is decreased, which gives allowance to increase payload weight or stay time I the orbit

Plug nozzle
("Aerospike")



• Figure 3. Aerospike Nozzle

Image Courtesy: Perdue Engineering – Ch4-89

• Calculations:

Expansion rate of the nozzle-

Gamma has been assumed to be 1.21, by combining system with AP and Aluminum combinations.

$$\epsilon = 20.23256879$$

For this, exit pressure is assumed to be the one third of the ambient pressure and ambient pressure is 1 bar.

With the same calculations, the Mach number is,

$$Me = 3.80$$

All these assumptions are derived from the literature survey.

IV. MATERIAL USED FOR THE DESIGNING OF THE OPS:

REQUIREMENTS:

- As the PD consists of the collider, it has high vibrational amplitudes. And for that we require the material which could sustain higher vibrations.
- Also while the procedure the temperature increases gradually, which may result in the cracks. To avoid these problems higher temperature sustainable material is preferred.

- As material has to undergo harsh environments, it must be non-corrosive, sustainable and reusable.
- Material should also have higher yield strengths, to bear any external drag forces.

MATERIALS TAKEN INTO CONSIDERATION:

- Names- 1. Ti-6Al-4V 2. Carbon Reinforced Polymer Composites.
- These two materials are preferred on the basis of their density, yield strength, and sustainability.
- Though the titanium alloys have high density, these materials are used for all purpose, which can be used while recovering drag, gravitational forces.
- CRPC allows to have high length, with lesser weights and higher fineness ratio for the fins and other wing shapes.

MATERIALS CHOSEN:

- Titanium alloy is chosen to build the core system of the PD.
- CRPC is selected for the wind pipe system stated before.
- Though the density for the titanium alloy is 4430gm/cm³, it will help while we have the system combined with NTP or Pulsed Plasma, where pebble bed is included.
- Also, the cost of titanium alloy is high, but the system is reusable and hence is compatible cost wise.

V. PARTICLE DETECTOR WORKING COMBINED WITH PPU

1. The particles will enter the system, when the design showed in the figure before. Firstly, fan will rotate at very low rpm, and the system will start working. Thereafter, according to the requirement of the mission rpm of the system can be changed.
2. Upon rotation, the space dust, or any other particles will enter the system and will be detected and energy conversion will be started.
3. The pipe will have a valve, where there is entry point for the PD system. This will control the flow of the particles.
4. Once they enter, collision will take place and the splitting of the particle system occurs. That will be separated in Quarks and Leptons. Upon that energy will be released and will be processed to PPU.
5. PPU will consist of the two sections:
 - Active System
 - Failure System
6. Active system works continuously, unless and until a code provided indicates the system failure of any type such as wing cracks, sudden temperature rise and cracks in PD system.
7. When the failure code gets activated, it simultaneously gives a command to the failure system to activate. This system will conclude, two solar wings with higher span and which can work like wings and provides high thrust to the system. This procedure will be activated within 3 to 5 sec of time.
8. When system is running without any failure, it follows the following sequence of the operations:
 - Once the energy is captured, it will convert the energy into the mechanical energy, with the nozzle system, which is already described.
 - When we are required to change, the amount of energy created we can increase or decrease the rpm of the system, which also results in corresponding change in the velocities also.
9. The system will take 3 seconds to activate, once it crosses the Karman line. System is estimated to be work for 3 or 3 and ½ years.
10. As system has less dry mass, it allows to increase the payload mass, with providing higher Isp.

PROCEDURE AFTER THE PD SYSTEM IS ACTIVATED:

There will be code activated after the system is activated, whether to assure the system is active or facing any failure.

CODE:

```
#include<stdio.h>
void main()
{
char system;
printf(" enter a character system");
scanf(" %system",&system);
if("system=go");
printf("%system is successfully activated");
else
printf(" %system has failure");
}
```

Code1.System Failure Code

VI. SHAPE AND SIZE FOR THE PARTICLE DETECTOR

1. System will have cylindrical shape, with amplitude measurements.
2. Amplitude measurement system, will state or estimate the rough amount of the energy, by activating a code.

CODE:

```
#include<stdio.h>
void main()
{
float AS, SF, TE;
printf(" enter AS and SF");
scanf(" %f,%f", &AS&SF);
TE= AS+SF;
printf(" TE is %f\n");
}
```

Code2. Total Energy Code

3. The size of the detector will be around 1000 cm³ volume, which is smaller compared to the other system.
4. The length of the cylindrical system is about 0.5 m, also it will consist of aerospike or the plug nozzle, with the thickness around 0.05 m, and made up of the titanium alloys.

Figure of the model on the next page due to size constraints.

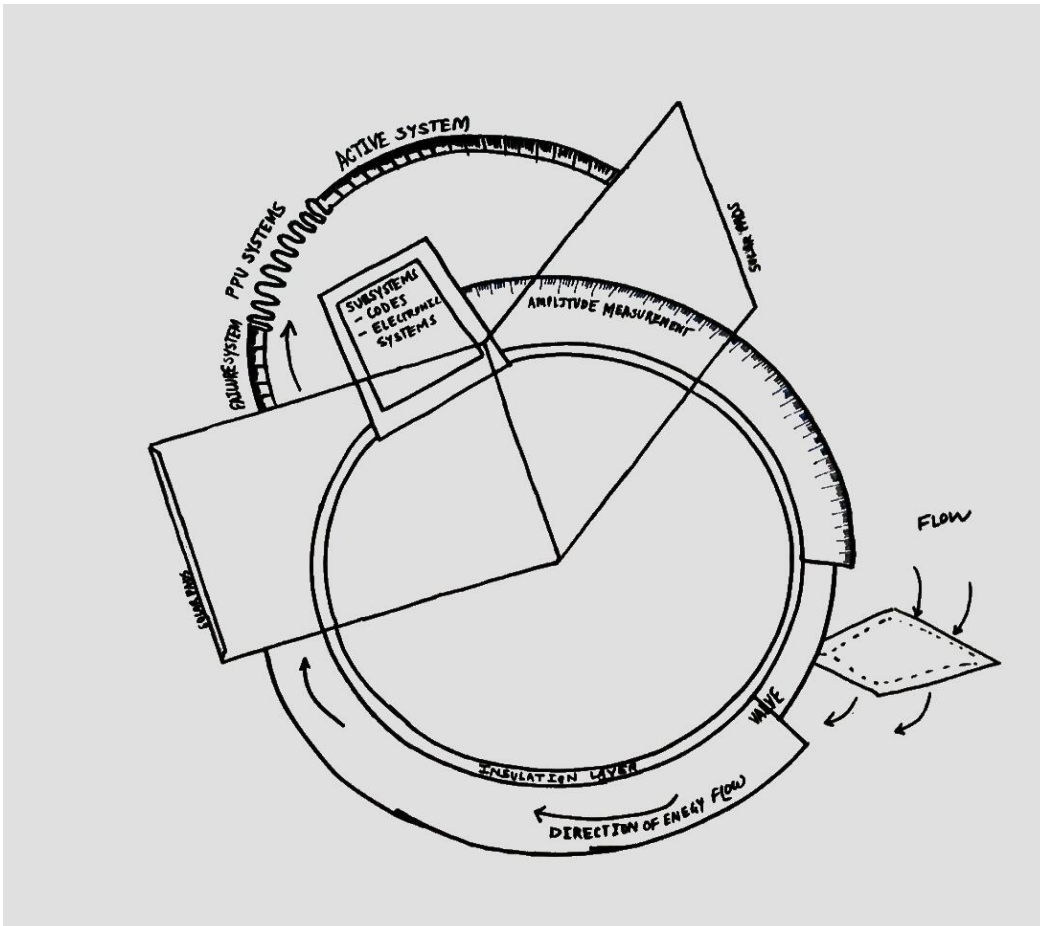


Figure 4. Top view of Quantum Propulsion Systems

VII. FURTHER PROCEDURES

1. The system can also be used to power the spaceflights on the other planets.
2. It may be useful for the 'TAG' activities, like Benu, as the system is compatible with working in low gravity or zero gravity circumstances.

VIII. ADVANTAGES

1. System provides higher supply of energy throughout the entire mission, so it can be used to power return journey of the mission.
2. The system causes very less pollution or no pollution.

IX. LIMITATIONS

1. Initial cost of the QPS is high.
2. The system is likely to fail in the cases of sudden temperature changes, breakage of the wings and cranks in PD systems.
3. Landing mode for the mission is selected to be water landing, as it gives less velocity, on re-entry as system shuts down.

X. REFERENCES

Books:

1. Richard Feynman, Robert B. Leighton, Matthew Sands., “The Feynman Lectures on Physics- Volume-3, Quantum Mechanics”. 1964. Addison-Wesley (Revised and Extended 2005)
2. R. K. Rajput., “Thermal Engineering”. 2009,Laxmi Publications Private Limited. Delhi.

Reports, Thesis, Papers:

3. NASA (National Aeronautics and Space Administration)- NTRS (NASA Technical Reports Server) Hyperlink: <https://ntrs.nasa.gov/>
4. NASA-Nuclear Thermal Propulsion-Hyperlink: https://www.nasa.gov/directorates/spacetech/game_changing_development/Nuclear_Thermal_Propulsion_Deep_Space_Exploration

OpenCourseWare and Online Lecture Notes:

5. MIT-OCW; 16.552-Space Propulsion; Spring'15
6. MIT-OCW; Quantum Mechanics; Spring'16
7. Perdue Engineering ,AAE 439- Chapter 4.7, Real Nozzle

Development and Analysis of 2D Flight Planning Search Engine considering Fusion of SWIM Data

Michael H. Sentoso¹ and Neno Ruseno²

International University Liaison Indonesia, MyRepublic Plaza 5th Floor, Jl. BSD Green Office Park, Sampora, Cisauk, Tangerang, Banten 15345, Indonesia

Flight planning is one of the essential factors of the airline operation. The selection of routes will determine the economic value of the flight. However, some conditions may prevent the flight to use the most optimum route due to airspace restriction or weather condition. The research aims to develop a search engine program that uses dynamic flight parameters that considers fusion of System Wide Information Management (SWIM) data including weather data and NOTAM to produce the most optimum route in 2D flight planning. The Dijkstra's pathfinding is implemented in Python programming language to produce the flight plan. The navigation data used is enroute airway in Indonesian FIR regions. The scenario used is a flight from Jakarta to Makassar with duration of 2 hours flight with considering the effect of restricted airspace and weather blockage during in-flight. The study also uses the optimum route produced by the algorithm to be compared with the possible alternate routes to define how optimum the route is. Adding a restricted airspace parameter will result in a new optimum flight plan that able avoids the airspace and the most minimum distance. The effect of external wind parameter could influence the optimum route which may vary depends on the speed of the wind.

I. Nomenclature

<i>2D</i>	=	Two Dimension
<i>AIXM</i>	=	Aeronautical Information Exchange Model
<i>API</i>	=	Application Programming Interface
<i>ARINC</i>	=	Aeronautical Radio Incorporation
<i>ATC</i>	=	Air Traffic Control
<i>ATM</i>	=	Air Traffic Management
<i>FIR</i>	=	Flight Information Region
<i>FIXM</i>	=	Flight Information Exchange Model
<i>FMS</i>	=	Flight Management Systems
<i>GA</i>	=	Garuda Indonesia Airline
<i>METAR</i>	=	Meteorological Aerodrome Report
<i>NOTAM</i>	=	Notice to Airmen
<i>VOR</i>	=	Very High Frequency Omni-Direction Radio Range
<i>SWIM</i>	=	System Wide Information Management
<i>USD</i>	=	United States Dollar
<i>WXXM</i>	=	Weather Exchange Model

II. Introduction

Before departure, a flight needs to have a flight plan that indicates the route that the flight will cross to reach the destination. A flight plan is usually filled by a pilot or flight dispatcher and will be sent to Air Traffic Control (ATC) authorities to be approved. Flight plan is a paper or electronic document prepared for purposes of flight planning. As

¹ Student, Aviation Engineering Department, Faculty of Engineering, AIAA membership ID: 1193327.

² Faculty Advisor, Head of Aviation Engineering Department, Faculty of Engineering.

it is mandatory for commercial aircraft to complete a flight plan and be approved by a local navigation service provider before a flight can legally depart, flight plan is an essential part of the flight planning.

Flight planning considers 2 critical parameters for the calculation to ensure the safety of the flight. First parameter is flight planning must comprehend with ATC requirements, second parameter is fuel calculation to ensure aircraft ability to safely reach designated airport or alternate airport if condition is not favorable to reach the designated airport. To find the route to destination a pilot or flight dispatcher needs to look up the aeronautical charts to determine the route that will be crossed to reach the destination. Pathfinding algorithm is used for generating the optimal route for the aircraft based on the minimum distance or minimal duration.

Flight planning is considering several parameters including departure and arrival airport, time, aircraft type, engine type, speed, flight level and weather condition. For flight planning, weather conditions during the flight will impact airplane performance and variate the fuel consumption of the aircraft. It is called a dynamic flight plan because of the dynamic parameter inside the calculation like weather conditions that could change over time.

The approved flight plan's route will then be inserted in the Flight Management System (FMS) [1]. Each FMS containing a navigation database that standardizes according to the ARINC 424. The FMS will be the guidance for the pilot to assist the aircraft to fly in the right airways. Flight plan also will be monitored by ATC, as condition on the field is dynamically changing, the ATC will react and adjust the flight plan of the aircraft to ensure the safety of the flight.

This study will focus on developing a route search engine program that consider the dynamic aspects of the flight like NOTAM release and weather that change over time. The search program will be able to generate the most optimum route using the given data. The search engine program can be used in various sectors in aviation, such as ATC, airline and other. ATC can use this search engine to update the flight plan of the aircraft when there is a NOTAM or weather problem that might risk the flight safety. Airline can use this program to search the most optimum route for the flight.

We present the Dijkstra's pathfinding algorithm in Section III, fuel required, flight time calculation and scenario presented in Section IV. Result and discussion are presented in Section V. Conclusions and recommendations for future work are provided in Section VI.

III. Dijkstra's Pathfinding Algorithm and Data Used

The main algorithm that will be used in this research will be the Dijkstra's pathfinding algorithm. The algorithm will be the core to find the best route for the aircraft to fly based on the waypoints and airways data network available. The SWIM data will be used to support this algorithm to generate the optimum flight route.

A. Dijkstra's Pathfinding Algorithm

Dijkstra's pathfinding algorithm is used to determine the shortest path from start node to finish node inside a network of nodes, the shortest path is the result of the summation of distance of the shortest path node's distance. The algorithm will stop calculating when the shortest path from a single node is able to reach the destination node. Given the network of nodes is presented by equation below [4]:

$$f(N_n) = \sum_{i=1}^n g(N_i) \quad (1)$$

$$g(N_n) = \frac{d}{v} \quad (2)$$

Note:

$f(N_n)$: Cheapest cost distance from from N_{end} to N_{start} .

$g(N_i)$: Cost distance from node N_{i-1} to node N_i

d : Distance to node from its parent node (NM)

v : Ground speed (kts)

The Equation (1) work by calculating the $f(N_n)$ by caching its parent node N_{n-1} and keep updating the $f(N_n)$ until reach the destination node, to get the nodes that being used can be done by retrieving the node stored in N_{n-1} running backward from N_{end} to N_{start} . The cost distance, Eq. 2 is the distance of a node from its parent node divided by the ground speed of the aircraft.

Dijkstra's pathfinding algorithm uses the distance between nodes which in this study is the distance between waypoints to waypoints or waypoints to airports as the search parameter. The departure airport will be the starting node and the arrival airport will be the finish node.

All the nodes will be assigned as unvisited nodes and set the distance in our starting node as zero. The starting node will be the current node and the algorithm will select all the unvisited nodes or that are connected to the current node or the neighbour node and put all the unvisited nodes to the visiting set and become the visiting node. All the visiting nodes will have their own tentative distance based on the summation of the current node tentative distance and the distance of the current node to the neighbour node, the visiting node also will store the current node as the reference route name. The current node will be marked as visited node; a visited node will never be checked again by the algorithm to avoid double calculation.

In the visiting set, the algorithm will select the node that has the lowest tentative distance and set it as the current node. The current node will again select all the neighbour nodes and add it to the visiting set. The algorithm will not add the visited nodes, if the current is also connected to the nodes that are already inside the visiting set the algorithm then will select the lowest tentative distance and it will change the value of the tentative distance of that node and will change the reference route name. This cycle will repeat until the current node is the finish node or the arrival airport. In this section will explain how the Dijkstra's pathfinding works in 3 conditions which are in normal condition, applied a restriction node and case with Headwind and Tailwind.

1. Normal Condition

Fig. 1 show How Dijkstra's pathfinding algorithm works. In Fig. 1(a) is when A node is the starting point and F node is the destination point, A node will be the current node and added to the visiting or open list with 0 cost distance. After visiting A node in Fig. 1(b), it will visit all the nodes that are connected to the A node, the A node then will be removed from the open list then will be put in the visited list, this to prevent the node A to be visited again. Nodes B, C and D will be added into the open list to which the lowest cost distance will be in the first order.

Fig. 1(c), B node will be the current node as it has the lowest cost distance then it will select all the nodes connected to nodes B to be visited except the nodes in the visited list. Node E will be added to the open list, as node C already in the open list, the algorithm will update only the cost distance if it is lower than the current cost distance, so the cost distance from A to C will be 4 instead of 6. The node B will be added into the visited list and the current list will have nodes C, D and E. Fig. 1(d), Node C will be the current node and visit node D and E, as both nodes already on the open list, this will only update the cost distance, E node will have new cost distance and D will have the same cost distance.

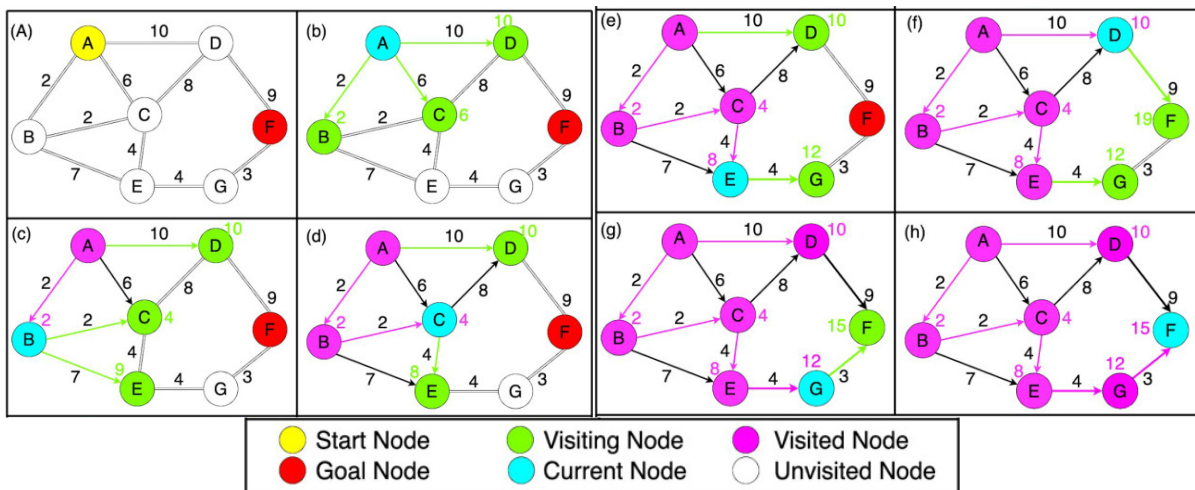


Fig. 1 Diagram of Dijkstra's pathfinding algorithm.

Fig. 1(e), Node E will be the current node, and visit node G. Fig. 1(f), the algorithm will select node D, and will visit node F or the Destination node, this will not stop the algorithm as F node have the higher cost distance of 19. Fig. 1(g), now the algorithm will visit F node again, but this time will visit it from node G, as the cost distance from node G to F is lower than from node D to F the cost distance will be updated.

Fig. 1(h), as F node is the only unvisited node left, it will be selected as the current node and it will stop the algorithm, the result of the algorithm will be A → B → C → E → G → F. The algorithm will select the shortest path possible even if it will take more nodes as it will select the lowest cost distance from starting node to goal node. This

algorithm will result the shortest path or route for the aircraft, the result will also state all the waypoints that will be flown in this route to inform the flow of the route

2. *Case with Restriction Node*

There will be time when airspace is not available for the flight to fly over it, this will need the pathfinding algorithm to be able to add restricted airspace into the algorithm before the calculation. The algorithm will work the same way as normal, but node inside the restricted airspace will be removed. For example, the node B in Fig. 1 is inside the restricted airspace. Thus it is removed from the list of available node.

The flow is still the same, except without node B. The result of the most optimum route is $A \rightarrow C \rightarrow E \rightarrow G \rightarrow F$, with 17 cost distance. The generated route has a higher cost distance than the first optimum route because of the restriction on nodes.

3. *Case with Headwind and Tailwind*

Headwind is the wind that flows in the opposite direction of the flight, this will affect the flight performance as the drag force of the aircraft will increase, so the engine needs to increase the thrust to maintain the aircraft speed or the flight will have longer duration to reach the destination. Tailwind is the opposite of the headwind as it is wind that flows in the same direction of the flight; hence it will increase airspeed and shorten the flight duration.

Headwind and Tailwind are components that will differentiate flight path calculation, this will affect most long-haul flights as it affects the aircraft performances as the longer an aircraft flies the longer will the effect of the wind to the aircraft. A route with longer flight distance can be reached in a shorter duration than the route with shorter distance if there are wind conditions that benefit the flight in the longer route.

In the program as it cannot alter the speed depending on the route, so the change will affect in the distance instead, if the speed of the aircraft in that route increase that will decrease the distance, this also happen when the aircraft is struggling to keep up the speed in particular route hence it will increase the distance in this algorithm. After entering the wind speed on a route, the algorithm will change the distance in that route depending on the wind speed input. For example, network that is used in the Fig. 1 with the wind speed decreases the distance on node A-D and D-F by 30% of the distance.

The result of the most optimum route is $A \rightarrow D \rightarrow F$, with cost distance of 13.3. From this example, it shows that the wind speed in certain routes might benefit the flight duration and become much shorter than the optimum route. If the wind speed in this example is stronger and decreases the distance even-more, the algorithm might not have to visit the below node to end the algorithm and generate the result.

B. SWIM Data

System Wide Information Management (SWIM) is a method for Air Traffic Management (ATM) to interoperable exchanging information of aeronautical, flight and weather f data from and to approved airspace users (called stakeholders). With the SWIM method the ATM will receive and read the data from other ATMs without converting the data format. With the SWIM method also, ATM will provide regulated and secure data for the stakeholder. SWIM consists of AIXM, FIXM and WXXM.

Aeronautical Information Exchange Model (AIXM) design to enable Aeronautical Information Service (AIS) and other users to supply and consume digital format of aeronautical data with higher efficiency in time, cost and safety. Information related to AIXM including aerodrome, airspace structure, flight routes, procedure, restriction and NOTAM [2].

NOTAMs (Notice to Airmen) is a notice to alert aircraft pilots with the disturbance or hazard that could risk the safety of the flight, NOTAMs are published in advance or in an emergency like volcano eruption or military emergency situation the publication reacts to the situation. NOTAMs release will notify the operating flight personnel about the alteration about the aeronautic facility, service, procedure or emergency condition that will affect the safety of the flights.

Flight Information Exchange Model (FIXM) is designed for the interoperability of stakeholder in exchanging flight and flow of aircraft data. The stakeholder will be able to subscribe, collect, verify flight data even if a different version of FIXM is implemented [2].

Weather Information Exchange Model (WXXM) is designed for the compatibility of weather data exchange even with different ATM systems. With this interoperable system weather data like Meteorological Aerodrome Report (METAR) will be accessible by various ATC or pilot, it will increase current situational awareness of the weather hence flight safety can be guaranteed [2].

SWIM able to not only reduce the time consumption but also the full potential of the SWIM which is interoperability in data sharing, semantic container consist of set of data items (NOTAM, METAR), membership condition and administrative metadata (provenance, quality, technical) [3].

IV. Flight Parameters Calculation and Scenarios

Once the flight route is defined in a flight planning, it is required to calculate some flight parameters. Two of them which are very important in a flight planning are fuel required and flight duration.

A. Fuel Required

Fuel consumption is one of the main aspects of flight planning, it is crucial to know how much fuel is needed for the flight including the additional fuel for safety measures. An optimum fuel storing will provide optimum flight economy, the optimum fuel calculation will result in no fuel shortage and no unnecessary excess fuel that will increase the aircraft weight and increase the drag of the aircraft. Fuel calculation will be affected by all the flight planning parameters, including restriction airspace, and weather condition. As increase or decrease in predicted aircraft flight performance will also alter the fuel consumption of the aircraft for the flight.

$$F_c = \frac{F_r}{D} \quad (3)$$

$$C = D * F_c * g \quad (4)$$

Note:

F_c = Fuel consumption (kg/h)

F_r = Total fuel required (kg)

D = flight duration (hour)

C = fuel cost for the flight (US dollar)

g = fuel cost per gallon (US dollar/gallon)

Equation (3) calculates the fuel consumption of an aircraft based on the total fuel required divided by the flight duration. According to the reference [5] the average fuel consumption of Boeing 737-800 is 6.123 kg/NM, as 1kg = 0.264 gallon. The fuel consumption will be 1.6175 gallon/NM.

From the fuel consumption it will be possible how much gallon of jet fuel is needed for a flight based on the flight duration. For fuel pricing, referring to Pertamina [6] one liter of jet fuel is 46.7 cent/liter, which is equal to 1.77 USD/gallon before tax. After including tax, the cost of 1 gallon of jet fuel is 1.95 USD. Equation (4) shows the fuel cost for the flight based on the aircraft, duration of flight and fuel cost per gallon in US Dollar.

B. Flight Duration

In flight planning, there are several routes that can be flown to reach the destination airport. Just like google maps or other navigation software, the goal is to give the user the quickest route possible by considering all the routes available with their parameter. For conventional road navigation software, usually considering the traffic of the possible route to reach the destination. In flight planning traffic usually occurs only when the aircraft reaches the designated airport. For flight planning the defining parameter is the weather condition. The weather condition has few parameters that should be considered for the flight planning, including current condition, en-route forecast condition, destination condition and wind aloft, wind aloft is the predicted wind and temperature at certain altitude. The wind aloft during en-route phase will certainly affect the performance of the aircraft, as aircraft spend most of the time in cruising phase.

If the wind that present during en-route is reach a certain amount, a route that have longer distance can be more economic than the shorter route if or a shorter route become more expensive because of the strong wind that increase the drag of the aircraft, this will push the aircraft to increase the engine speed to maintain the speed hence increase the fuel consumption of the aircraft.

To calculate how strong headwind or tailwind that can affect the selected route outcome, in this thesis will use the total distance of the most optimum route divided by the average speed of the aircraft for this route, the outcome will be the benchmark for analysis. Headwind and tailwind affect the speed of the aircraft, so the average speed of the aircraft will increase and decrease by 1 knot and will be divided to the total flight distance, the outcome will be the

percentage of how much percentage of flight duration will be swift by the change of the average speed. Equation (5) calculates the average speed of an aircraft.

$$FS = \frac{F\ dis}{F\ dur} \quad (5)$$

$$a = \left(1 - \left(\frac{F\ dis}{FS + 1} * \frac{FS}{F\ dis} \right) \right) * 100\% \quad (6)$$

$$A = F\ dur * (1 + (a * w)) \quad (7)$$

Note:

$F\ dis$ = Flight Distance (NM)

$F\ dur$ = Flight Duration (hours)

FS = Flight Speed (kts)

a = Percentage of flight duration change per 1 kts

A = Affected flight duration (hour)

w = winspeed (kts)

This percentage (Equation (6)) will be calculated into the optimal route to generate how strong the headwind to be present to make the route not optimal. The percentage also will be the parameter for the alternate route, to know how strong the tailwind should be generated by the weather to make the alternate route more economical. Equation (7) shows how flight distance changes with the alteration of windspeed.

In this study the wind speed range will be from -100 to 100 kts using the multiple of 5. So, there will be a total of 41 samples of flight distance consisting of 1 original sample and 40 altered samples. Each of the sample then will be divided by the average speed of the aircraft for the flight to get the flight duration based on the change of wind.

Each route will have 41 samples of flight duration then will graph in one diagram as one route will be represented as a line in the graph for comparison. The X axis will be the variation of wind speed and the Y axis will be the duration of the flight.

C. Scenario

The result of the flight route search engine will result in the route that has the lowest flight distance, this will provide the pilot or flight dispatcher the most optimal route during normal conditions. But the weather is dynamically changing. Thus, flight planning needs to dynamically change according to the current weather, as the weather change the optimum flight path can be not the most efficient path because of the weather condition.

This study uses a flight which have the starting airport of Soekarno-Hatta International Airport, which is in Tangerang, Banten. As this airport is the main hub of the all international and domestic flight in Indonesia, so there will be a lot of airways connected to this airport, with many airways connected will resulted in the substantial option for alternate route than other airports in Indonesia.

This research will use a domestic flight to analyze the effect of weather to the result in flight planning. For case study will be the medium-flight that will take around 2 hours to be reached from Jakarta, it will be the flight from Soekarno-Hatta International Airport to Sultan Hasanuddin International Airport in Makassar, South Sulawesi.

V. Result and Discussion

Each case study consist of the optimum route generated by the algorithm implemented in Python programming language, the optimum route when airspace restriction is applied and route optimization analyses comparing the optimum route with the alternate routes selected.

A. Optimum Flight Route

The distance from Jakarta to Makassar is almost 1433.26 km in great circle distance or 773.9 NM. From the calculation of the most optimum and most used flight route it accumulated a total flight distance of 788 NM. The average speed of the aircraft for this flight is 394 kts .

After putting in Soekarno-Hatta and Sultan Hasanuddin as departure and arrival airports, the search engine program will generate a navigation log and map for visualization. The Navigation log (Table. 1) stated that the flight

will take 2 hours to complete and fuel around 1275 gallons for the trip. From the navigation log it also stated the waypoints that need to be taken to fly the most optimum flight. From take-off the aircraft need to fly over Halim (HLM) VOR and continue to Cirebon (CA) before entering java sea by waypoints TELET, LUNAS, WAWAN, HEREN and OVINA to reach Makassar (Fig. 2) in 2 hours.

For comparison the flight path of Garuda Indonesia flight GA 616 on 23 July 2020 has the similar route [8]. For this flight needs approximately 1275 gallon of fuel with the ATF price is at 1.95 USD/gallon after tax, the total amount that the airlines need to spend is around 2486 USD or around Rp. 37.3 million.

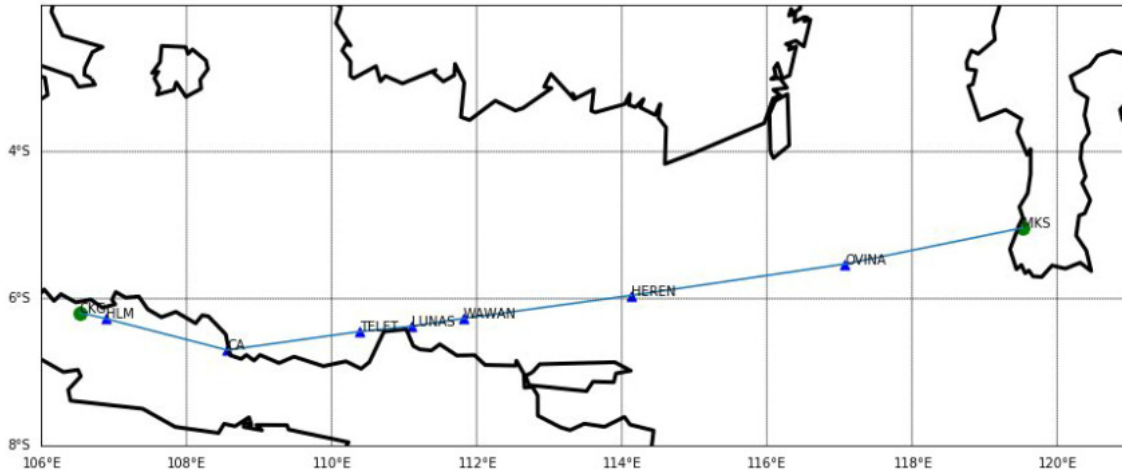


Fig. 2 The optimum route generated by the program for Jakarta-Makassar Flight.

Table. 1 Navigation Log of Optimum Route Jakarta-Makassar Flight.

Waypoints	Latitude Longitude	Distance (NM) Acc Dist (NM)	Duration Total Duration	Fuel Required (US gal) Total Fuel Required (US gal)
CKG	S 06° 11' 16" E 106° 31' 48"	0 0	0:00:00 0:00:00	0 0
HLM	S 06° 16' 19" E 106° 53' 13"	22 22	00:03:21 00:03:21	35.59 35.59
CA	S 06° 41' 53" E 108° 33' 35"	103 125	00:15:41 00:19:02	166.6 202.19
TELET	S 06° 26' 47" E 110° 23' 29"	110 235	00:16:45 00:35:47	177.92 380.11
LUNAS	S 06° 22' 33" E 111° 06' 21"	44 279	00:06:42 00:42:29	71.17 451.28
WAWAN	S 06° 16' 06" E 111° 49' 15"	42 321	00:06:24 00:48:53	67.94 519.22
HEREN	S 05° 57' 21" E 114° 08' 07"	140 461	00:21:19 01:10:12	226.45 745.67
OVINA	S 05° 31' 48" E 117° 04' 12"	177 638	00:26:57 01:37:09	286.3 1031.96
MKS	S 05° 02' 16" E 119° 31' 34"	150 788	00:22:51 02:00:00	242.62 1274.59

B. Restricted Airspace

This is the scenario when there is an airspace being restricted by the NOTAM when the aircraft is in the cruising phase. The optimum route that is generated by the program and the restricted airspace that appears in the waypoint

TELET, the restricted airspace is informed when the aircraft is making their way to Makassar and currently is approaching Cirebon.

Table. 2 is the navigation log that is generated by the program when inputting the next waypoint as the starting point and the restricted airspace into the calculation. So now the flight route will change, instead of flying from CA to TELET the flight will then fly to PIALA waypoint and Semarang before continuing to approach Makassar via Java Sea. Fig. 3 is the visualization of the new alternate generated by the program to avoid the restricted airspace.

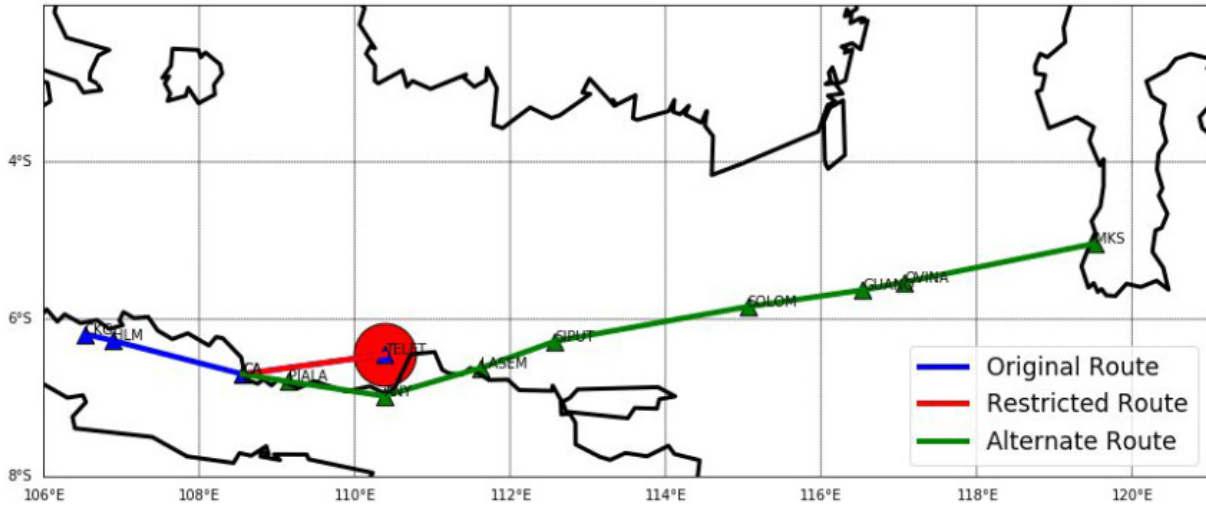


Fig. 3 Optimum route with in-flight update due to restricted airspace.

Table. 2 Navigation log with inflight update for optimum flight route Jakarta to Makassar.

Waypoints	Latitude Longitude	Distance (NM) Acc Dist (NM)	Duration Total Duration	Fuel Required (US gal) Total Fuel Required (US gal)
CA	S 06° 41' 53" E 108° 33' 35"	0 0	0:00:00 0:00:00	0 0
PIALA	S 06° 47' 24" E 109° 08' 24"	35 35	00:04:38 00:04:38	56.29 56.29
ANY	S 06° 58' 29" E 110° 22' 48"	75 110	00:09:59 00:14:38	121.15 177.44
LASEM	S 06° 37' 12" E 111° 37' 12"	77 186	00:10:14 00:24:51	124.06 301.5
SIPUT	S 06° 16' 48" E 112° 34' 48"	61 248	00:08:09 00:33:00	98.83 400.33
SOLOM	S 05° 50' 24" E 115° 03' 36"	150 398	00:20:04 00:53:04	243.43 643.76
GUANO	S 05° 37' 48" E 116° 32' 24"	89 487	00:11:55 01:04:59	144.6 788.37
OVINA	S 05° 31' 48" E 117° 04' 12"	32 519	00:04:15 01:09:14	51.6 839.97
MKS	S 05° 02' 16" E 119° 31' 34"	150 669	00:20:00 01:29:14	242.62 1082.59

C. Route Optimization Analysis

Four routes are selected to be analyzed for the flight to Makassar from Jakarta and the visualization is shown in Fig. 4. The first route or the optimal route is to fly over north of west java until reaching Cirebon and then turning left to enter the Java Seas to reach Makassar. The second route or the alternative route is the same as route 1 until reaching Cirebon, instead of fly straight to Java Sea, the aircraft continue to fly above the north coast of central java until reaching Surabaya, after reaching Surabaya the aircraft then will fly over Madura and Java Sea to reach Makassar. The third route or alternative route 3 had a different flight approach, instead of flying to Cirebon, the aircraft will fly straight crossing the java sea to reach Banjarmasin, after reaching Banjarmasin the aircraft will continue to GURNI waypoint to reach Makassar. The last route or the alternative route 3, will have same approach as alternative route 2 to straight crossing the java sea but this route will reach LAMUD waypoint, waypoint is on the Tanjung Puting National Park and the aircraft will turn to KEVOK waypoint before reaching Makassar.

The average flight duration for the optimum route is 2 hours. If it is divided by the distance of the flight distance of route 1 which is 788 Nautical Miles, we can have the average speed of the flight is 394 kts. If the same speed used to fly the other route will result in flight duration of 2 hours 3 minutes for route 2, 2 hours 4 minutes and 2 hours 8 minutes for route 3 and route 4 respectively. But all this condition is only applicable in the normal condition when the wind generated by the weather does not affect the aircraft performance. As the search engine is based on the distance between the nodes, the increase or decrease of the average speed of the aircraft will affect the increase or decrease of the air distance between nodes in the calculation. The search engine will only change the distance between waypoints in the aircraft cruising phase and descent phase.

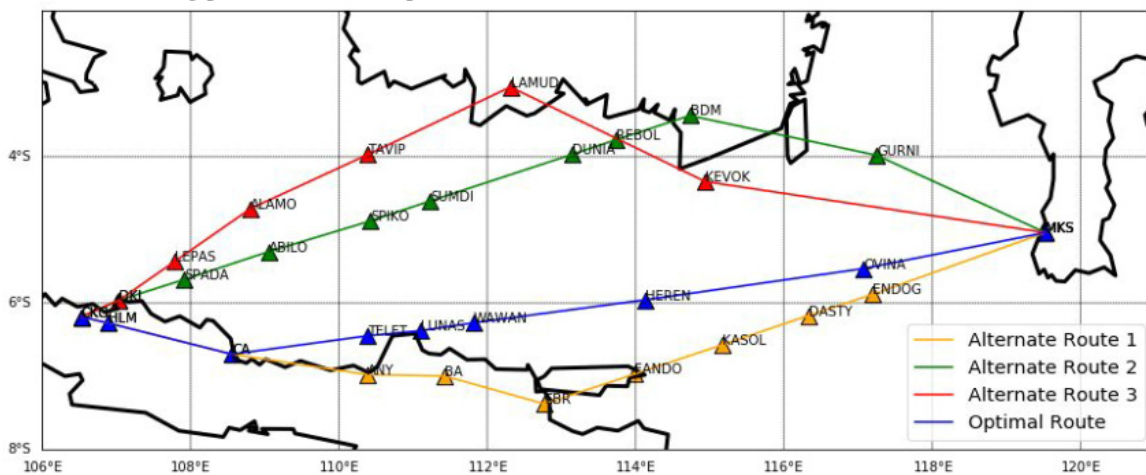


Fig. 4 Optimum and Alternate routes of Jakarta to Makassar flight.

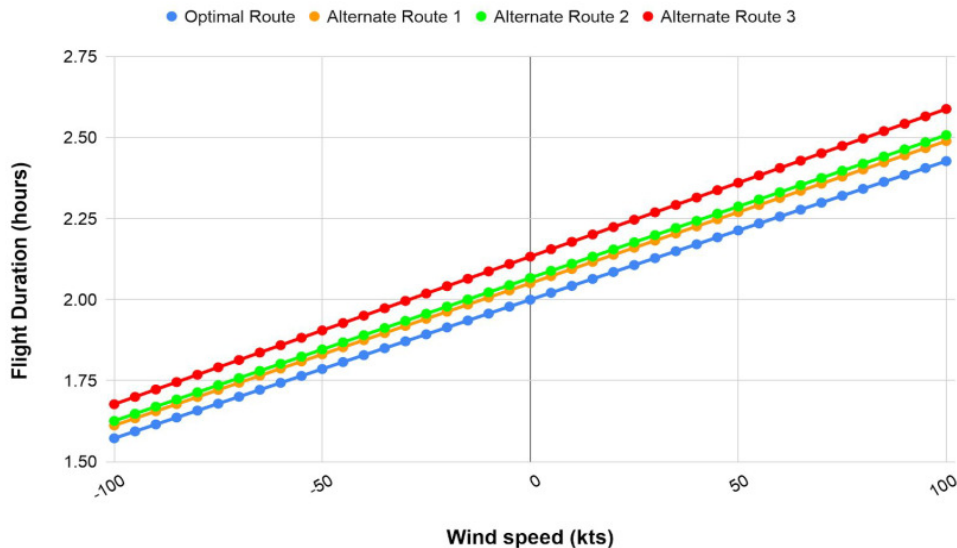


Fig. 5 Diagram of Correlation between Wind speed and Flight duration of route Jakarta to Makassar.

Fig. 5 shows the correlation between the flight duration of a flight from Jakarta to Makassar using 1 optimum route and 3 alternate routes over the change of ground speed. During normal conditions the optimal route will require 2 hour, but if there is a tailwind in average of more than 20 kts generated by the weather conditions along the waypoints in alternate route 1 and 2 it, it will cause decrease the duration of flight by less than 2 hours and the alternate route will become more profitable to fly than the original route.

For the alternate route 3, the tailwind needs to have an average bigger than 30 kts to achieve 2 hours less flight duration. The navigation log below shows the total flight duration decreased by 15 second, flight duration will continue to decrease if the tailwind becomes stronger.

Using slope rule the gradient of each route can be found, then using line equation to find the intersect. After completing the line equation then it will be able to find when will the alternate route line intersect with the optimum route line.

Table. 3 Wind speed needed for alternate routes to become optimum route for Jakarta-Makassar flight.

		Optimum Route	Alternate Route 1	Alternate Route 2	Alternate Route 3
	m	0,004	0,004	0,004	0,005
	C	2.00	2.05	2.07	2.13
If Yoptimum=Yalternate	X		-454.5454545	-500	-476.3636364
If Y = C optimum	X		-11.5660421	-15.18987342	-29.18894831

Note:

m = gradient

C = intersect

X = X value or wind speed at intersection point

From Table 3, at the wind speed of -454.55 kts or tailwind of 454.55 kts, the Optimum route and Alternate route 1 will intersect or mean both of the routes will have the exact same flight duration. For the optimum route and flight route 2 both routes need to have average speed of -500 kts or tailwind of 500 kts. For alternate route 3 the x intersection point is in -476.36 kts or tailwind of 476.36 kts. With all the windspeed need to be so massive, this condition is most likely impossible to happen as it will be too risky for the flight in to fly in such as massive wind

From the Table 4 also can be obtained the minimum speed for the alternate route to be more optimal than the optimum route. Thus, for the alternate route 1 it needs at least -11.57 kts of wind speed or 11.57 kts of tailwind in this route to be present during flight. For alternate route 2 it needs 15.19 kts of tailwind to become more optimum than the optimum route generated by the search engine program. For alternate route 3 it will need at least -29.19 of wind speed present

D. Discussion

In our case study, the resulted optimum route is the same route that had been used by many airline for flight from Jakarta to Makassar. The total flight distance for this flight is 788 Nautical Miles(NM) and with the average flight duration of 2 hours, so the average speed of the aircraft is 394 knots (kts) for the whole flight. The search engine generated a navigation log that also calculated the fuel consumption. For this flight the fuel consumption is 1275 gallons of fuel which will cost around Rp. 37.3 million.

From the restricted airspace example, the search engine calculating the ASHTAM being release and manages to get a redirected route that avoids the volcanic ash but does not have too significant increase in flight distance, the redirected route can be reached in 2 hours 4 minutes time and consume 1317 gallons of fuel that cost Rp. 38.5 million, so the redirect route will increase the operational cost by 1.2 million.

For route optimization analysis, 4 routes had been selected, 1 is the optimum route and 3 alternate routes that have similar distance as the optimum route. The analysis shows how much the flight duration of the routes differ based on the wind speed during the cruising phase of the flight, the wind speed range used in this study is from -100 kts to 100 kts with 5 kts range per analysis sample.

All the route analysis sample is plotted in the one chart and finding the gradient and the line equation of each route, using the line equation then it will be possible to know when the optimum route line and the alternate route line will intersect to show in which speed of wind will the alternate route become as optimum as the optimum route.

For the alternate route 1, the speed in both routes need to be at -454.5 kts or tailwind of 454.5 kts, and for alternate route 2 it needs to be 500 kts and 476.3 kts of tailwind for alternate route 3 to have the same flight duration as the optimum route. From the analysis, it can be obtained how many percent the alternate routes will cost based on the optimal route in normal wind condition.

If all the routes are in the zero-wind condition, when a flight takes the alternate routes, the flight duration will be 2.54% longer, to become more optimum, the alternate route 1 needs to have a tailwind of 11.57 kts. For alternate route 2, in normal condition the flight duration will be 3.35% longer and it needs to have a tailwind of 15.19 kts to have a shorter flight duration of less than 2 hours, for alternate route 3, in normal wind condition this route will be 6.65% longer than the optimum route and need a weather that generate wind that flow into the direction of the flight that is stronger than 29.19 kts.

VI. Conclusion and Recommendation

The research is able to develop a route search engine program based on the dynamic parameter such as NOTAM and weather data. The route search engine program developed in this study can generate navigation logs that contain the optimum routes. The optimum route is confirmed with the record from airlines routes for their operation. The search engine also is also capable of adding airspace restriction parameters to the calculation, the generated navigation log will avoid the restricted airspace and select the most optimum route that does not cross the restricted airspace to ensure the flight safety and obeying the NOTAM release.

The wind parameter in the weather data also affected the resulted flight route by the search engine and the route analysis show the search engine will generate the most optimum route in the given wind parameter.

In case study, during normal conditions the optimum route is 2.54%, 3.35%, 6.66% shorter than the alternate route 1, 2 and 3. Alternate route 1 needs a tailwind of 11.57 kts, alternate route 2 needs 15.19 kts and alternate route 3 needs 29.19 kts to become more optimum.

From the study, there are few recommendations to further enhance the search engine. First is to add calculation of the vertical flight phase of a flight to have more accurate flight duration. The vertical flight phase will also affect the fuel consumption as the taxi, take-off and climbing will increase the fuel consumption.

Second, the program should equip with Application Programming Interface (API) of actual weather data for each waypoint and airways. With API data the search engine will be able to generate more accurate route results, the weather data will give the wind speed to each of the waypoints, with it the route optimization will be more accurate than adding or decreasing the cruising speed with one nominal of wind speed.

References

- [1] L. Agam and D. Agam, "(54) SYSTEM FOR PRODUCING A FLIGHT PLAN," p. 21.
- [2] J. Kang, K. Choi, Y. Kim, and H. Yang, "A Method of Integrating Information for SWIM," in 2017 IEEE 13th International Symposium on Autonomous Decentralized System (ISADS), Bangkok, Thailand, Mar. 2017, pp. 195–198, doi: 10.1109/ISADS.2017.30.
- [3] B. Neumayr, E. Gringinger, C. G. Schuetz, M. Schrefl, S. Wilson, and A. Vennesland, "Semantic data containers for realizing the full potential of system wide information management," in 2017 IEEE/AIAA 36th Digital Avionics Systems Conference (DASC), St. Petersburg, FL, Sep. 2017, pp. 1–10, doi: 10.1109/DASC.2017.8102002.
- [4] J. C. H. Cheung, "Flight planning: node-based trajectory prediction and turbulence avoidance: Flight planning: node-based trajectory prediction and turbulence avoidance," *Meteorol. Appl.*, vol. 25, no. 1, pp. 78–85, Jan. 2018, doi: 10.1002/met.1671.
- [5] "Wayback Machine," Jul. 25, 2014, https://web.archive.org/web/20140725005129/http://www.boeing.com/assets/pdf/commercial/startup/pdf/737ng_perf.pdf (accessed Aug. 13, 2020).
- [6] "Pertamina Aviation." <https://www.pertamina.com/aviation/News.aspx?p=price> (accessed Aug. 14, 2020).
- [7] "SkyVector: Flight Planning / Aeronautical Charts." <https://skyvector.com/> (accessed Aug. 14, 2020).
- [8] Flightradar24, "Live Flight Tracker - Real-Time Flight Tracker Map," Flightradar24, <https://www.flightradar24.com/data/flights/ga616> (accessed Aug. 14, 2020).

Digital Image & Pressure Analysis of Supersonic Aero Spike Instability Frequency

Miguel Vila*

University of New South Wales Canberra, Canberra, ACT, 2612, Australia

Aerospikes have long been studied to improve the performance of supersonic and hypersonic vehicles. However, it has been observed that some configurations result in a flow instability with undesirable effects. A general understanding of this phenomenon exists, but there are still unknowns when it comes to a quantitative description of the instability through the relationship between spike length and oscillation frequency. There has also been a general lack in the application of digital image analysis methods to study the instability, and such techniques could provide information that has been missed with other methods. The aim of the current work was to address this by investigating the effect of aero spike length on the instability oscillation frequency with the use of pressure sensor and digital image analysis methods. Tests were conducted in the University of New South Wales (UNSW) Canberra supersonic wind tunnel at Mach 2 for various spike lengths. A pressure sensor was used in conjunction with simultaneous schlieren and shadowgraph flow visualisation, and two separate digital image analysis methods were used to process the images: edge detection and streak imaging. The results from each of the methods largely agreed, and it was concluded that they were all equally applicable for studying the instability oscillation frequency. The obtained results suggested that the Strouhal number (the non-dimensional frequency) and non-dimensional spike length trend changed behaviour near the theoretical spike length for which a steady conical shock from the spike tip would have just cleared the model base. This suggested that the instability mechanism changed for spike lengths beyond this, and a piecewise empirical equation was presented to model this trend. The instability was also observed to only occur for spike lengths which protruded past the steady bow shock from the blunt body with no spike case.

I. Nomenclature

t	=	time [s]
T	=	period of oscillation [s]
L	=	spike length [mm]
P_0	=	stagnation pressure [kPa]
T_0	=	stagnation temperature [K]
M_∞	=	free stream Mach number
P_∞	=	free stream static pressure [kPa]
T_∞	=	free stream static temperature [K]
D	=	model cylindrical base diameter [mm]
Re	=	Reynolds number
ρ_∞	=	free stream density [kg m^{-3}]
V_∞	=	free stream velocity [m s^{-1}]
μ_∞	=	free stream dynamic viscosity [$\text{kg m}^{-1} \text{s}^{-1}$]
L'	=	non-dimensional spike length
St	=	Strouhal number (non-dimensional frequency)
f	=	instability oscillation frequency [Hz]
P_{sensor}	=	pressure measured by sensor [kPa]
β	=	conical shock angle [$^\circ$]

*Pilot Officer, Royal Australian Air Force, Australian Defence Force Academy, AIAA Undergraduate Student Member (736294)

II. Introduction

SUPERSONIC and hypersonic vehicles are valued around the world due to their range of applications in both civilian and military sectors. A consistent challenge that has faced high-speed vehicles is overcoming the undesirable effects associated with shock waves, and finding solutions to problems such as high levels of drag and heat transfer would support the design of supersonic and hypersonic vehicles that could fly faster and more efficiently. An aerospike is a device that aims to overcome some of these issues by replacing the bow shock in front of a blunt body with a conical shock that occurs for pointed bodies [1]. Figure 1 illustrates the difference in the flow pattern around an object with and without an aerospike. The conical shock that occurs in Fig. 1b results in less drag and heat transfer than the bow shock in Fig. 1a, and in general the benefits of aerospikes have been widely studied in the existing literature [2–4].

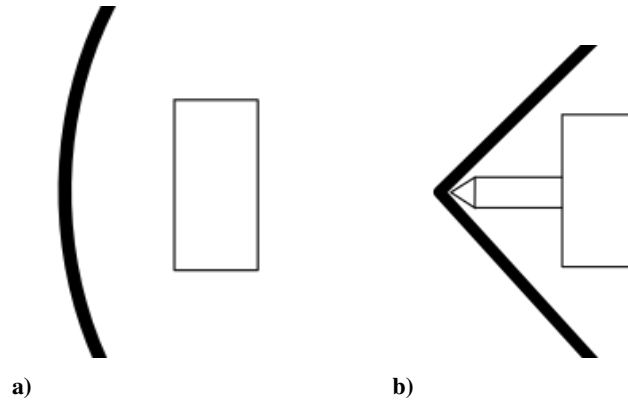


Fig. 1 Flow pattern comparison between blunt body and aerospike: a) blunt body (bow shock) and b) aerospike (conical shock).

Interestingly, it has been observed that some aerospike configurations result in a flow instability that is characterised by a shock wave that oscillates through the phases seen in Fig. 2*. This flow behaviour is undesirable as it leads to increased drag, heat transfer, and vibrations, essentially cancelling out any benefit of adding an aerospike in the first instance. This instability has been the subject of various studies, with a detailed investigation into the existing literature found in [5].

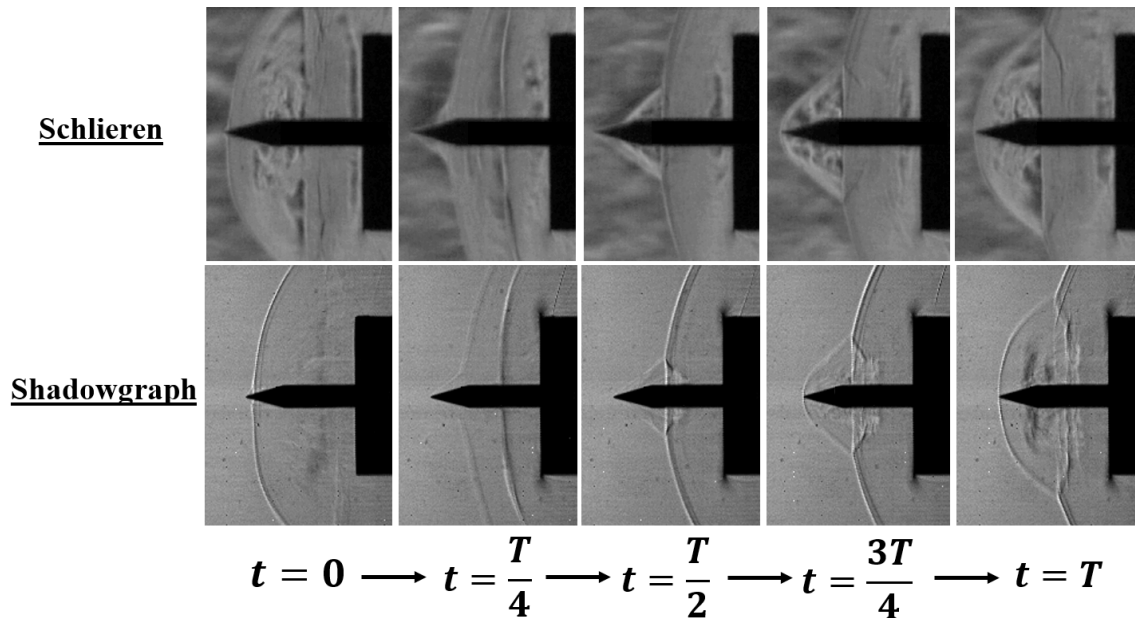


Fig. 2 Aerospike instability phases.

*Figure 2 shows flow visualisation results from the current work.

Although it is generally accepted that the instability manifests as an expanding pressure region [6], the actual mechanism that governs this process has not been explained. [7] conducted a brief investigation into the effect of spike length on the instability frequency, however short spike lengths were not considered in the empirical equation that was produced, and a more comprehensive quantitative description of the instability that includes a wider range of spike lengths would be of benefit. Additionally, of the studies that have been conducted, there has largely been a lack in the application of digital image analysis methods (with the exception of [5] who briefly implemented a single method). Such techniques are straightforward to implement, and considering that most studies already incorporate flow visualisation, could be applied with little extra experimental effort or cost. These methods also have the potential to provide new insight into the instability that could reveal elements that have been missed with other methods.

III. Project Scope

The aim of this project was to investigate the effect of aerospike length on the instability oscillation frequency with the use of pressure sensor and digital image analysis methods. The project objectives were as follows:

- 1) Investigate the effect of aerospike length on the instability frequency by using:
 - 1) Digital image analysis edge detection and streak imaging methods on schlieren flow visualisation.
 - 2) Digital image analysis edge detection and streak imaging methods on shadowgraph flow visualisation.
 - 3) Pressure sensor methods.
- 2) Evaluate the digital image analysis methods against each other and attempt to validate them with the pressure sensor method.
- 3) Compare the results and evaluate the flow visualisation methods against each other.
- 4) Attempt to quantify the instability behaviour using the relationship between aerospike length and the instability oscillation frequency.

IV. Methodology

A. Test Conditions

Tests were conducted in the University of New South Wales (UNSW) Canberra supersonic wind tunnel for spike lengths in the range $9 \text{ mm} \leq L \leq 27 \text{ mm}$ in 3 mm increments. Experiments were also conducted at some intermediate spike lengths, for a blunt body without a spike, and for a spike only. Most test cases were repeated at least once for reliability, with the experimental flow conditions as shown in Fig. 3. The stagnation pressure varied in the range $190 \text{ kPa} < P_0 < 240 \text{ kPa}$ due to the depletion of the wind tunnel reservoir pressure. This variation was reflected by changes in the Reynolds number which were shown to be too small to interfere with the results. Each test case had the instability oscillation frequency calculated with five separate methods (summarised in Table 1). Preliminary tests were conducted with varied conditions in support of parameter studies.

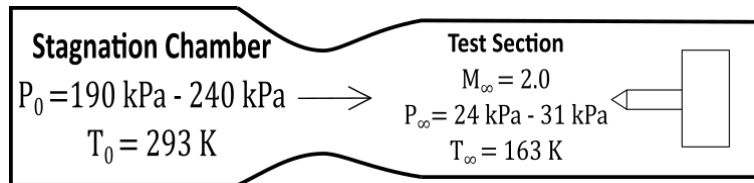


Fig. 3 Experimental flow conditions.

Table 1 Methods to determine instability oscillation frequency.

1	Pressure sensor
2	Schlieren - edge detection
3	Schlieren - streak imaging
4	Shadowgraph - edge detection
5	Shadowgraph - streak imaging

B. Aerospike Model

Two aerospike models were manufactured, one with a pressure sensor, and one without. The geometry of each model, as shown in Fig. 4a, was identical. The photo of the instrumented model in Fig. 4b clearly shows the cylindrical body and protruding spike. The models were manufactured from brass and allowed for the spike length to vary by rotating in its thread.

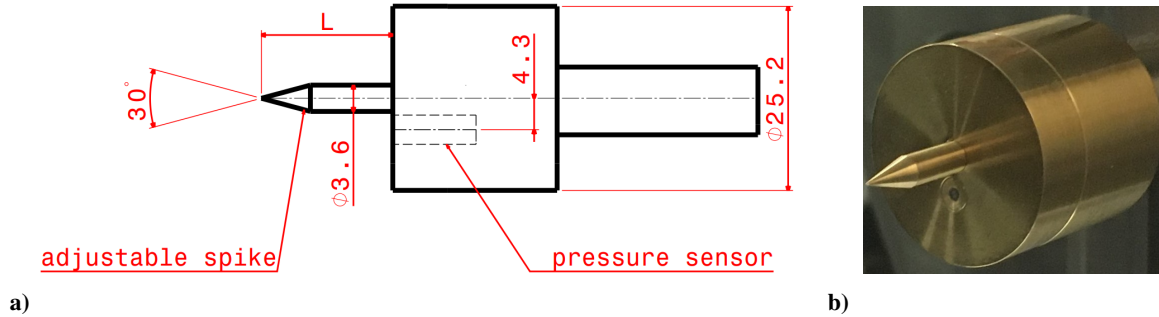


Fig. 4 Aerospike model: a) sketch and b) photo.

C. Pressure Sensor

The pressure sensor used was the EPIH-373-5B-V/10 [8]. Fig. 4 shows that the model was designed to fit the sensor flush with the face of the cylindrical base, and with its longitudinal axis 4.3 mm below the spike centreline. This was determined as the ideal sensor position based on the results of the row variation preliminary parameter study[†]. The sensor took measurements simultaneously with the flow visualisation and according to the parameters shown in Table 2. Built-in wind tunnel sensors were also used to measure the stagnation chamber and test section pressures.

Table 2 Pressure sensor parameters.

Sampling Rate	500 000 Hz
Total Number of Samples	1 000 000

D. Flow Visualisation

Schlieren and shadowgraph flow visualisation was implemented simultaneously for each test case. These techniques complemented each other and allowed for an increased amount of flow information to be collected through independent data sets. Figure 2 demonstrates the differences in the images captured by each method, with the flow visualisation parameters shown in Table 3. The total number of frames and sampling rate were determined from the results of the preliminary parameter studies[‡].

Table 3 Flow visualisation parameters.

	Schlieren	Shadowgraph
Camera	nac Image Technology Memrecam HX-3[9]	Vision Research Phantom v710[10]
Light Source	18 W LED	6 W LED
Sampling Rate	75 000 fps	75 067 fps
Exposure Time	5 μ s	10 μ s
Resolution	320 \times 312	224 \times 216
Total Number of Frames	30 000	30 000

[†]Discussed later in the report.

[‡]Discussed later in the report.

E. Digital Image Analysis

The schlieren and shadowgraph images underwent MATLAB-based digital image analysis with two separate methods: edge detection and streak imaging. Each technique was implemented along the row of pixels that coincided with the pressure sensor, as identified in Fig. 5a. The edge detection method counted the number of pixels from the start of an image frame to the shock wave edge, and doing so for every image in the data set gathered information about the shock displacement over time. The Canny edge detection algorithm was implemented [11], with a typical detected edge being as shown in Fig. 5b. The streak imaging method extracted the same row of pixels from each frame in the data set, and stacked them top-down in a single output image (similar to what is shown in Fig. 5c). The result was a final image that showed both spatial and temporal information, which was then analysed with the Canny edge detection algorithm followed by a pixel count along each row to determine the shock displacement over time.

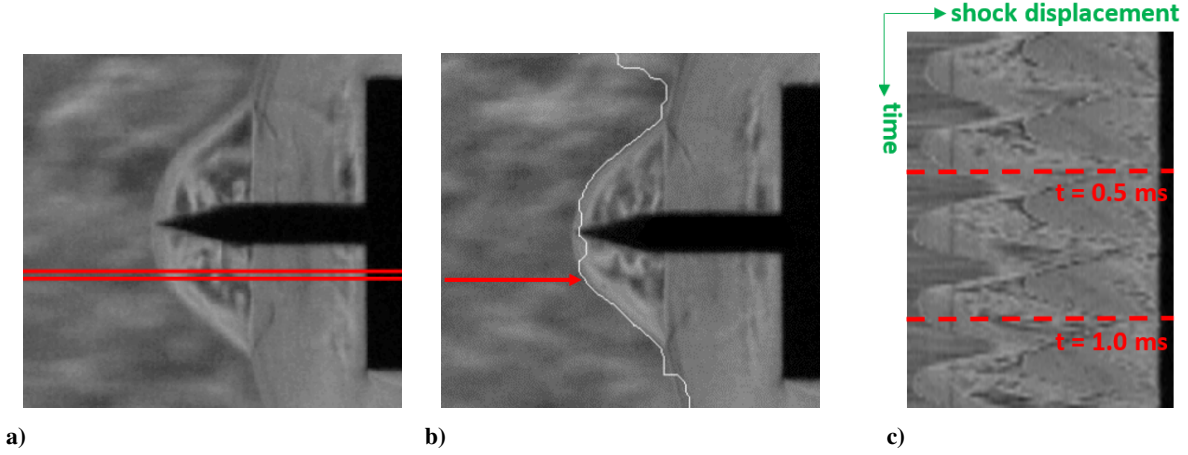


Fig. 5 Images relating to digital image analysis methods: a) pressure sensor pixel row, b) edge detection method, and c) streak image.

F. Data Processing

The data gathered from each of the five methods contained information about how either the pressure or shock displacement varied over time, with Fig. 6 showing a plot of all five signals from a single test case. Each signal had its power spectral density calculated using the MATLAB fast Fourier transform function, and the result was five separate power spectral density plots which indicated any dominant frequencies that existed in the signal. Figure 7 shows a typical power spectral density, taken from the schlieren edge detection method on the 18 mm spike length case. It can be seen that the value corresponding to the instability oscillation frequency is clearly identifiable above the noise[§], and for every test case, the oscillation frequency determined by each method was taken as the peak of each of the power spectral density plots.

G. Final Values and Dimensionless Parameters

The data across the various methods and repeated test runs were combined to deduce a single frequency value and uncertainty for each spike length. The frequency was taken as the mean, while the uncertainty was calculated as two thirds of the spread [12]. The final results were then represented in terms of three dimensionless parameters: Reynolds number (Eq. 1), non-dimensional spike length (Eq. 2), and Strouhal number (Eq. 3).

$$Re = \frac{\rho_{\infty} V_{\infty} D}{\mu_{\infty}} \quad (1) \qquad L' = \frac{L}{D} \quad (2) \qquad St = \frac{fD}{V_{\infty}} \quad (3)$$

[§]Higher orders of this frequency are also visible, with only the second harmonic being truly noticeable, and the fundamental frequency having the most significant amplitude.

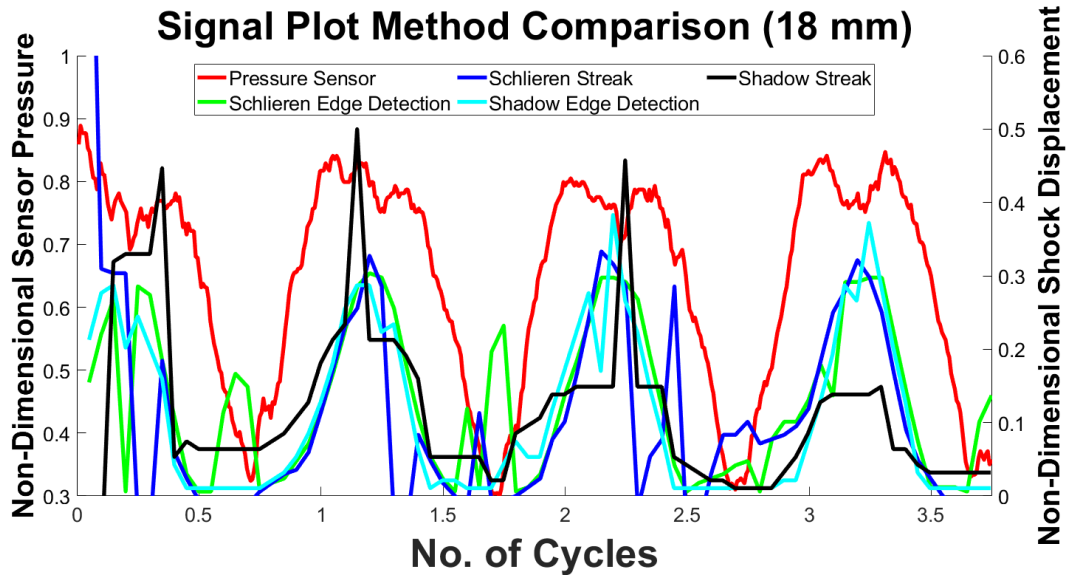


Fig. 6 Signal plot comparison for all methods (18 mm spike).

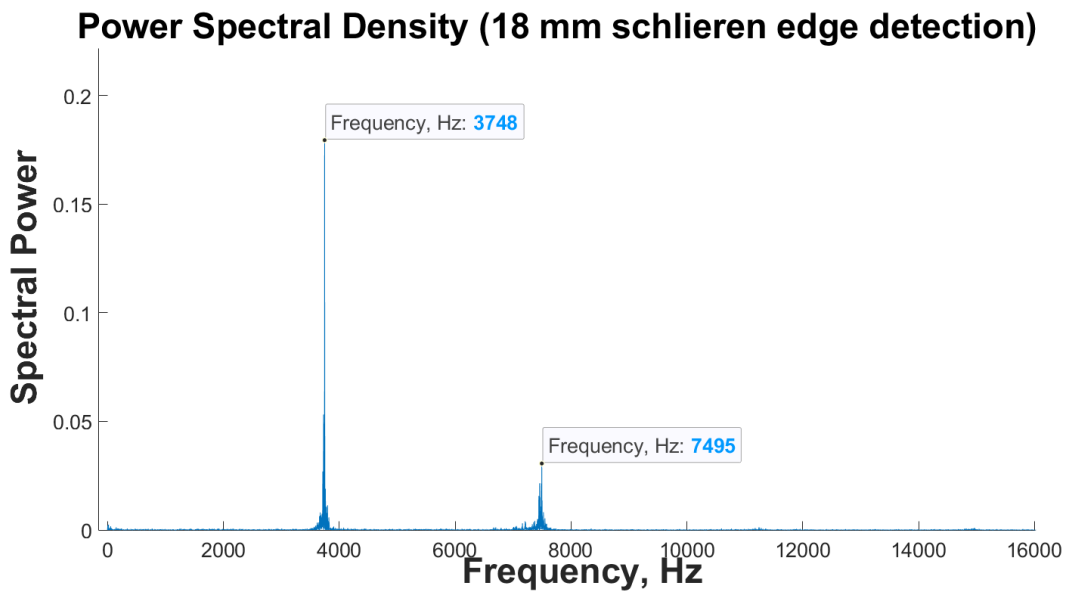


Fig. 7 Power spectral density from schlieren edge detection (18 mm spike).

V. Preliminary Parameter Studies

A series of preliminary tests were conducted using the aerospike model with no sensor at spike lengths of 12 mm, 18 mm and 24 mm for schlieren visualisation only. The data from these tests were used to conduct a series of parameter studies to identify the ideal values for the main series of tests.

A row variation study was conducted where the digital image analysis methods were run along all horizontal pixel rows of the schlieren visualisation images. It was found that the same instability oscillation frequency was measured along all rows but that the signal was weaker for the rows further away from the spike centreline. It was concluded that the ideal row for the analysis was 4.3 mm below the spike centreline, and as such the second aerospike model was designed with the sensor at this location.

A frame independence study was conducted where the digital image analysis methods were run multiple times

with various numbers of input frames of the schlieren visualisation images. It was found that a minimum of 20 000 frames was required in order to collect enough data for the instability oscillation frequency to be correctly calculated. Incorporating a safety factor, it was concluded that 30 000 frames would be used for the main series of tests (Table 3).

A sampling rate study was conducted where the digital image analysis methods were run for various sampling rates of the schlieren visualisation. It was concluded that a sampling rate of 50 000 Hz would be appropriate, with even lower sampling rates still possible[¶]. Incorporating a safety factor, it was concluded that a sampling rate of approximately 75 000 Hz^{||} would be used for the flow visualisation in the main series of tests (Table 3).

VI. Results

Figure 8 shows a plot of the individual frequencies as determined by each method. The dimensionless parameter results calculated for each spike length case are expressed in Table 4 and Fig. 9.

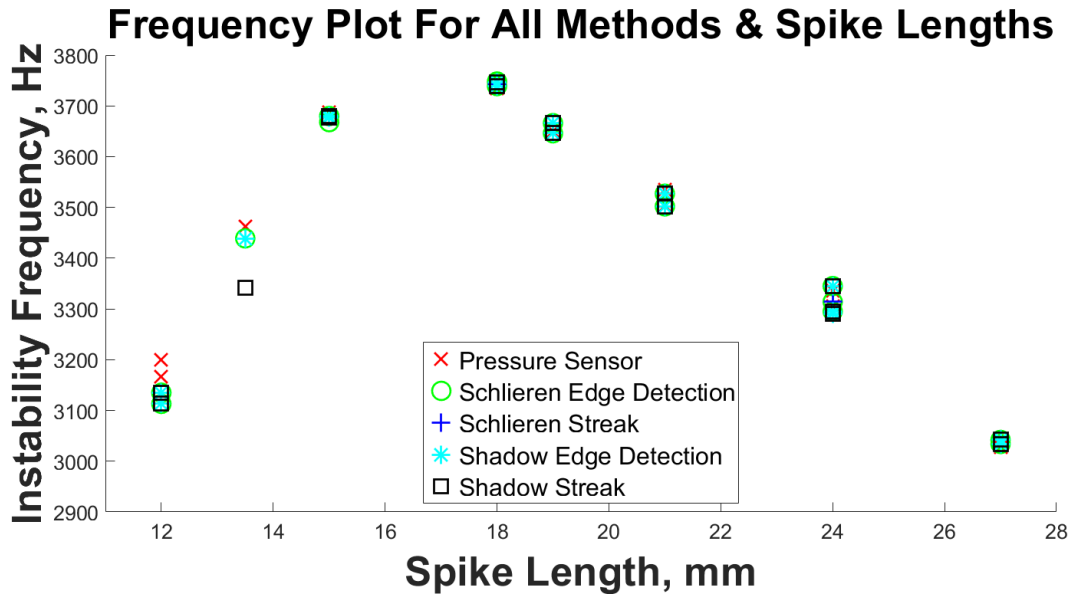


Fig. 8 Instability oscillation frequency results for all methods.

Table 4 Dimensionless parameter results.

Spike Length, mm	Non-Dimensional Spike Length	Reynolds Number, 10^5	Strouhal Number, 10^{-1}
0	0	$7.44 \pm 1.0\%$	0
9	$0.36 \pm 0.1\%$	$6.15 \pm 1.0\%$	0
10	$0.40 \pm 0.1\%$	$7.08 \pm 1.0\%$	0
12	$0.48 \pm 0.1\%$	$7.15 \pm 1.0\%$	$1.55 \pm 2.0\%$
13.5	$0.54 \pm 0.1\%$	$6.35 \pm 1.0\%$	$1.70 \pm 0.8\%$
15	$0.60 \pm 0.1\%$	$7.52 \pm 1.0\%$	$1.81 \pm 0.8\%$
18	$0.71 \pm 0.1\%$	$6.68 \pm 1.0\%$	$1.84 \pm 0.7\%$
19	$0.75 \pm 0.1\%$	$6.88 \pm 1.0\%$	$1.80 \pm 0.8\%$
21	$0.83 \pm 0.1\%$	$7.20 \pm 1.0\%$	$1.73 \pm 0.9\%$
24	$0.95 \pm 0.1\%$	$6.35 \pm 1.0\%$	$1.63 \pm 1.3\%$
27	$1.07 \pm 0.1\%$	$6.49 \pm 1.0\%$	$1.50 \pm 0.8\%$

[¶]Additional analysis would be required to confirm lower sampling rates.

^{||}The Vision Research Phantom v710 did not allow a sampling rate of exactly 75 000 Hz.

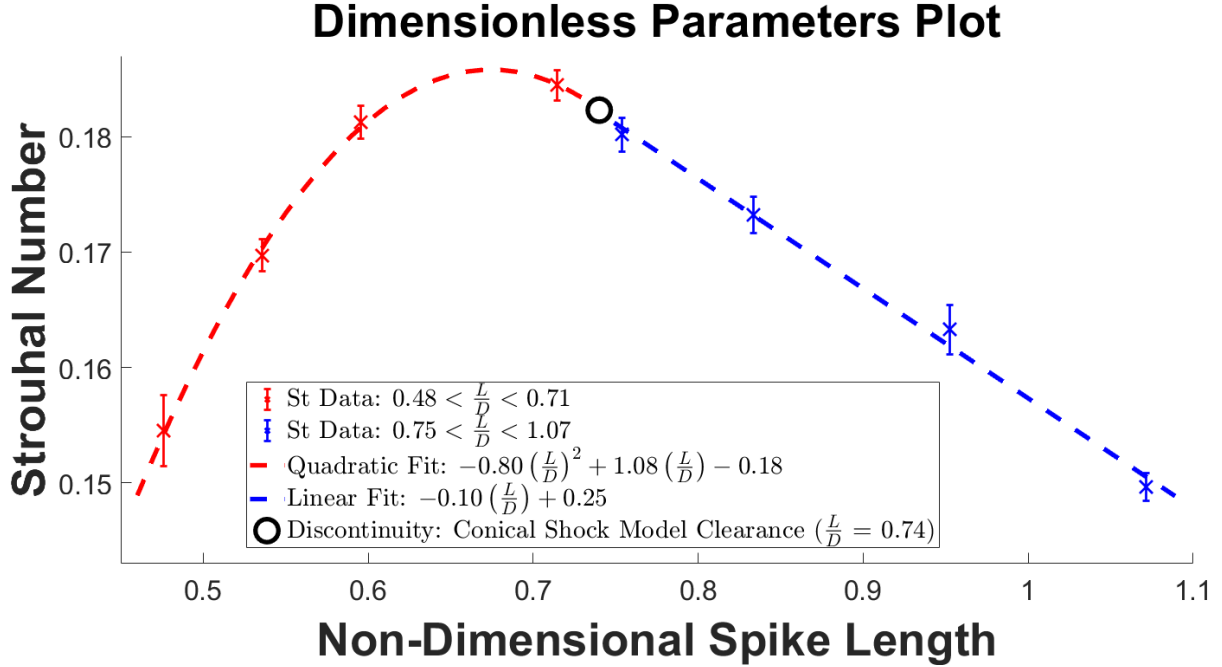


Fig. 9 Dimensionless parameter plot.

VII. Method Findings

A. Signal Plot Comparison

From Fig. 6 it can be seen that the signals detected by each method largely agree, with each curve showing a similar cycle of rising and falling at approximately the same distance between peaks. The maximum values for each of the digital image analysis method peaks are also similar, indicating that they are correctly tracking the distance of the shock wave behind the nose tip. The imperfections in the digital image analysis signals are likely due to the tolerance of the edge detection algorithm, however with such large data sets these errors become negligible. Overall it can be concluded that each method was able to correctly track the instability oscillations.

B. Frequency Comparison

As shown in Fig. 8, the frequency data points determined by each method closely agree, and in many cases are so close that the points are on top of each other and can not be distinguished**. However, the spread of frequency values appears to be worse for the shorter spike lengths. These results make it clear that each of the five methods measured the same physical property, and the fact that there was agreement across completely independent methods shows that each technique worked as intended. Overall it can be concluded that all five methods were equally applicable for studying the oscillation frequency of the supersonic aerospike instability.

C. Digital Image Analysis Methods

There was largely no difference between the results of the edge detection and streak imaging digital imaging analysis methods, exemplified by the fact that each technique returned very similar values for the instability oscillation frequency in each case. These results also agreed with those from the pressure sensor method, and as such the performance of the digital image analysis methods has been validated. The main difference between the two techniques came from the fact that every image in the data set was analysed for edge detection, however only a single image was analysed for the streak imaging approach. Since 30 000 frames were analysed in the edge detection method, it is likely that the Canny edge detection algorithm was prone to more errors as the input parameters were not optimised for every image. This was

**Some symbols appear multiple times for the same spike length due to repeated test runs.

avoided in the streak method where only a single image was analysed and the algorithm was tuned for this, reducing the amount of noise that interfered with the signal. Interestingly, this was not reflected in Fig. 6 or Fig. 8. Another difference to consider is that the computational cost of the streak imaging method was higher due to the fact that it essentially had to loop through every frame twice, once for creating the streak image, and again for the edge detection of the streak image. Overall it can be concluded that the edge detection and streak imaging digital image analysis methods were both equally applicable for studying the oscillation frequency of the supersonic aerospike instability, and that both methods were successfully validated against the results from the pressure sensor method.

D. Flow Visualisation Methods

There was largely no difference between the results of the schlieren and shadowgraph flow visualisation methods, exemplified by the fact that each technique returned very similar values for the instability oscillation frequency in each case. As shown in Fig. 2, the main difference between these methods was the detail shown in the captured images, and this comes from the fact schlieren fundamentally measures the first derivative of the flow density, while shadowgraph measures the second derivative [13]. The second derivative in shadowgraph essentially acted as a filter that removed extra detail, and as such, Fig. 2 shows that only the major flow structures were visible in the shadowgraph images. This meant that they could be seen with more clarity, however in general there were extra details visible in the schlieren images. The decrease in detail for the shadowgraph images was expected to benefit the digital image analysis, as fewer structures meant there would have been less noise to interfere with the signal. Interestingly, this was not reflected in Fig. 6 or Fig. 8. Overall it can be concluded that the schlieren and shadowgraph flow visualisation methods were both equally applicable for studying the oscillation frequency of the supersonic aerospike instability.

VIII. Aerospike Instability Findings

From Table 4 and Fig. 9 it can be seen that the Strouhal number increased as non-dimensional spike length increased in the region $0.48 < \frac{L}{D} < 0.71$, and decreased as non-dimensional spike length increased further in the region $0.75 < \frac{L}{D} < 1.07$. This difference in behaviour suggests that the physical mechanism that drove the instability was changed in the region $0.71 < \frac{L}{D} < 0.75$. A theoretical analysis of the aerospike problem shows that when a steady conical shock from the spike tip is considered, the spike length for which the conical shock just clears the model base occurs in this region. This situation is shown in Fig. 10, with the non-dimensional spike length given by Eq. 4.

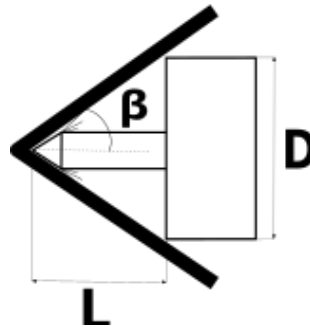


Fig. 10 Spike length for which a conical shock just clears the model base.

$$\left(\frac{L}{D}\right)_{model\ base\ clearance} = \frac{1}{2 \tan(\beta)} = 0.74 \quad (4)$$

For spike lengths beyond this, the gap between the model base and shock wave could have enabled a form of pressure escape for the flow trapped behind the instability. This could account for the change in the instability mechanism, and as such the change in the Strouhal number trend. To model this mechanism change, the data points were used to generate a piecewise fit, with a quadratic for $\frac{L}{D} < 0.74$, and a straight line for $\frac{L}{D} > 0.74$. The corresponding empirical equation is shown in Eq. 5, and when the spike geometry and flow conditions are known, it is possible to predict the instability oscillation frequency from this equation.

$$St = \begin{cases} -0.80 \left(\frac{L}{D}\right)^2 + 1.08 \left(\frac{L}{D}\right) - 0.18 & 0.48 < \left(\frac{L}{D}\right) < 0.74 \\ -0.10 \left(\frac{L}{D}\right) + 0.25 & 0.74 < \left(\frac{L}{D}\right) < 1.07 \end{cases} \quad (5)$$

Figure 9 shows that this empirical equation fits the data points closely. It is recommended that additional tests be conducted to provide more information on the exact shape of the trend near the mechanism change, and to suggest how Eq. 5 could be improved.

As indicated in Table 4, there were three test cases which did not result in an instability: the blunt body without a spike, the 9 mm spike, and the 10 mm spike. In each case, the flow manifested as a steady bow shock which had a distance at the centre of the blunt body determined from the flow visualisation records as shown in Eq. 6. Comparing this to the values in Table 4 shows that the aerospike instability did not occur until the spike was long enough to extend past the steady bow shock.

$$\left(\frac{L}{D}\right)_{steady\ bow\ shock} = 0.44 \quad (6)$$

A comparison of the results from the current work to those from previous studies shows that there is general agreement with the Strouhal number range presented in Table 4 ($0.15 < St < 0.18$). Specifically, [14] found $St = 0.15$, [7] proposed the linear empirical equation $St = 0.24 - 0.067 \left(\frac{L}{D}\right)$ (which neglects the trend change), [6] determined $St = 0.173$ and [5] found $St = 0.13$.

IX. Other Findings

As seen in Fig. 3, the stagnation pressure varied as the wind tunnel reservoir was depleted. This variation was reflected by changes of the Reynolds number in the range $6.15 \times 10^5 < Re < 7.52 \times 10^5$ (as shown in Table 4), and it was found that this had a negligible effect on the frequency values. This is exemplified by Fig. 8 where the frequency values of repeated runs at the same spike length largely agree.

Close analysis of Fig. 2 shows that there is a slight asymmetry in the aerospike instability. This is most obvious in the $t = 0$ image of each set where the bow shock appears to have a slightly larger bulge below the spike. This phenomenon is visible in the flow visualisation of other test cases, with the bulge appearing both above and below the spike. The results of the row variation study showed that the oscillation frequency was largely determined to be the same no matter which row the digital image analysis methods were applied, suggesting that the asymmetry did not interfere with the results of the current work. It is recommended that this asymmetry be the topic of a future study.

X. Conclusions

The aim of this project was to investigate the effect of aerospike length on the instability oscillation frequency with the use of pressure sensor and digital image analysis methods. Experiments were conducted in the UNSW Canberra supersonic wind tunnel for various spike lengths. Digital image analysis edge detection and streak imaging methods were applied on simultaneous schlieren and shadowgraph visualisation in conjunction with pressure sensor methods. All applied methods were evaluated as equally applicable for studying the effect of spike length on the oscillation frequency of the supersonic aerospike instability, and the digital image analysis methods were successfully validated against the results of the pressure sensor method.

The instability behaviour was quantified using the non-dimensional relationship between the aerospike length and the instability oscillation frequency. It was found that the Strouhal number increased as spike length increased in the region $0.48 < \frac{L}{D} < 0.71$ and decreased as spike length continued to increase in the region $0.75 < \frac{L}{D} < 1.07$. The theoretical spike length for which a steady conical shock from the spike tip just clears the model base occurred in the region where the Strouhal number trend changed: $\left(\frac{L}{D}\right)_{model\ base\ clearance} = 0.74$. This suggested that the instability mechanism was different for short and long spike lengths, and as such a piecewise empirical equation was used to describe the relationship:

$$St = \begin{cases} -0.80 \left(\frac{L}{D}\right)^2 + 1.08 \left(\frac{L}{D}\right) - 0.18 & 0.48 < \left(\frac{L}{D}\right) < 0.74 \\ -0.10 \left(\frac{L}{D}\right) + 0.25 & 0.74 < \left(\frac{L}{D}\right) < 1.07 \end{cases} \quad (5)$$

Additionally, it was discovered that the aerospike instability did not occur for spike lengths that did not protrude past the steady bow shock that occurred in the blunt body with no spike case: $\left(\frac{L}{D}\right)_{steady\ bow\ shock} = 0.44$. Other

supplementary findings were also made, and the results of the current work were compared to those presented in the existing literature with general agreement shown. Overall the current work sought to improve the body of knowledge surrounding the aerospikes instability in order to enable follow-on work that will ultimately lead to the improved implementation of aerospikes in supersonic and hypersonic vehicles.

Acknowledgments

The author would like to sincerely acknowledge the contributions of the project supervisor, Associate Professor Harald Kleine, who created an environment where the author was given the trust and freedom to take ownership of the project in a way that would make a real contribution to the literature. The author would also like to acknowledge the support provided by the following UNSW Canberra staff: Brendan Wallace, Geno Ewyk, and Professor Joseph Lai.

References

- [1] Anderson Jr, J. D., *Fundamentals of aerodynamics*, Tata McGraw-Hill Education, 2010.
- [2] Alexander, S. R., "Results of Tests to determine the Effect of a Conical Windshield on the Drag of a Bluff Body at Supersonic Speeds," Tech. rep., National Advisory Committee For Aeronautics, 1947.
- [3] Crawford, D. H., "Investigation of the flow over a spiked-nose hemisphere-cylinder at a Mach number of 6.8," Tech. Rep. D-118, National Aeronautics and Space Administration, 1959.
- [4] Tahani, M., Karimi, M., Motlagh, A. M., and Mirmahdian, S., "Numerical investigation of drag and heat reduction in hypersonic spiked blunt bodies," *Heat and Mass Transfer*, Vol. 49, No. 10, 2013, pp. 1369–1384.
- [5] Sahoo, D., Karthick, S., Das, S., and Cohen, J., "Shock related unsteadiness of axisymmetric spiked bodies in the supersonic flow," *arXiv preprint arXiv:1911.08326*, 2019.
- [6] Feszty, D., Badcock, K. J., and Richards, B. E., "Driving mechanisms of high-speed unsteady spiked body flows, part 1: pulsation mode," *AIAA Journal*, Vol. 42, No. 1, 2004, pp. 95–106.
- [7] Kenworthy, M. A., "A study of unstable axisymmetric separation in high speed flows," Ph.D. thesis, Virginia Polytechnic Institute and State University, 1978.
- [8] TEConnectivity, *EPIH Sub-Miniature Pressure Sensor Specification Sheet*, TEConnectivity, 2017.
- [9] nac Image Technology, *Memrecam HX-3 Specification Sheet*, nac Image Technology, 2020.
- [10] VisionResearch, *Phantom v710 Data Sheet*, Vision Research an AMTEK Company, 2009.
- [11] Canny, J., "A computational approach to edge detection," *IEEE Transactions on pattern analysis and machine intelligence*, , No. 6, 1986, pp. 679–698.
- [12] Devore, J. L., *Probability and Statistics for Engineering and the Sciences*, Cengage learning, 2011.
- [13] Kleine, H., "Flow Visualization," *Handbook of Shock Waves*, edited by G. Ben-Dor, O. Igra, and T. Elperin, Academic Press, 2001, pp. 683–740.
- [14] Mair, W., "Experiments on separation of boundary layers on probes in front of blunt-nosed bodies in a supersonic air stream," *The London, Edinburgh, and Dublin Philosophical Magazine and Journal of Science*, Vol. 43, No. 342, 1952, pp. 695–716.

Effect of a leading-edge fillet on the wall surface pressure fluctuations upstream of the leading edge of an appendage-body junction

Mudit Agrawal¹

The University of New South Wales, Sydney, NSW 2052, Australia

Junction flows occur when a boundary layer interacts with an obstacle attached to a solid surface. The velocity field and flow structure of junction flows have been extensively studied and the effect of several control mechanisms that have been investigated in past studies have been reviewed. The effect of a leading-edge fillet, specifically, on the root mean square and spectral characteristics of wall pressure fluctuations has not been sufficiently documented in past studies. Measurements of wall surface pressure fluctuating for NACA0012 airfoil with and without fillet in the upstream region of the appendage-wall junction region were performed. The measurements were performed in a closed-section benchtop wind-tunnel. The chord-based Reynolds number was approximately 139,000 and the airfoil aspect ratio was 1.0. Several geometric angles of attack ≤ 12 -deg were considered for measurements. The measurements were performed in the UNSW AF1125 wind tunnel using remote microphone method for NACA0012 airfoil with and without the leading-edge fillet for varying angles of attack. The results from measurements indicate that the presence of the leading-edge fillet increases the magnitude of pressure spectra at all angles of attack across most of the low-frequency range and suppresses high-frequency content due to an increase in large-scale recirculating structures. For any given angle of attack, the surface pressure fluctuations are most intense in regions close to the leading-edge but the effects of the presence of the leading-edge can be measured even far upstream of the leading-edge. The histograms of the surface pressure fluctuations reveal that there is no bimodal behaviour observed at any of the measurement locations. The effect of the leading-edge fillet is also observed in the production of tonal noise.

Nomenclature

α	= Angle of attack	BF	= Bluntness factor
BL	= Boundary layer	δ	= Boundary layer thickness
δ^*	= Displacement thickness	c	= Chord length
f	= Frequency	U_∞	= Freestream velocity
HSV	= Horseshoe vortex	H	= Height of the appendage body
ϕ	= Power spectral density	Re	= Reynolds number
St	= Strouhal's number	θ	= Momentum thickness
ν	= Viscosity of the fluid	T	= Thickness of the appendage
Λ	= Sweep angle of the appendage		

1 Introduction

The presence of an obstacle mounted on a wall complicates the flow resulting in the perturbation of the incoming boundary layer which induces flow vorticity, corner separation, generation of a horseshoe vortex that wraps around the airfoil and introduces three-dimensionality to the boundary layer. These flow features result in increasing the unsteady surface pressure fluctuations which can result in unfavourable noise-radiation and structural fatigue. The time-dependent fluid-structure and velocity field around the airfoil has been a subject of several past studies (Simpson, 2001), but studies on implications of these fluid structures on the surface pressure fluctuations remain scarce.

The intricacy of junction flows lies in the interaction of multiple secondary flows that can coexist in the vicinity of the corner. The basic features, horseshoe vortex and corner separation, of junction flows have been depicted in Figure 1. The velocity distribution of the main flow starts from zero at the surface of the wall due to the no-slip condition and increases to the free stream velocity through the thickness of the boundary layer. Laminar flow in case of junction flows only occurs at $Re_{\delta^*} = \frac{U_\infty \delta^*}{\nu} < 1000$. The approaching boundary layer encounters an adverse pressure gradient in the streamwise direction that is imposed by the wing which causes the inner layers of the boundary layer to slow down and roll up around itself and even become reversed. As the Reynolds number increases, a single primary horseshoe vortex changes to form steady multiple vortices, with complex dependence on the ratio of obstacle maximum thickness to boundary layer thickness and Reynolds number normalized using

¹ Student, Bachelor of Engineering (Hons), School of Mechanical and Manufacturing Engineering, AIAA Student Member (Region VII)

obstacle thickness (Baker, 1980). In the steady regime, an increase in the number of vortices could be explained by flow stability. It has been speculated that the primary vortex becomes unstable above a critical vortex core Reynolds number and begins to oscillate, which causes severing of the shear layer that feeds the vortex, thus reducing the Reynolds number. This shear layer then rolls up to create a vortex pair upstream of the primary vortex, while the primary vortex regains stability. As the Reynolds number increases, the local Reynolds number of the primary vortex core and newly created vortex will increase until one of the vortex's become momentarily unstable, which results in the formation of the third vortex pair and so on (Baker, 1991).

The dynamics of the horseshoe vortex in the vicinity of the nose of the junction can be associated with Re_θ . When Re_θ is very low ($Re_\theta \leq 100$), the HSV remains steady (Lin, et al., 2002). As Re_θ increases the primary vortex seems to have the tendency to switch periodically between zero-flow mode and back-flow mode, which refer to the condition when the vortex is detected closer to the leading-edge of the obstacle which gets stretched around the wing and when the flow that has reversed can penetrate the upstream flow results in the formation of strong wall jet that can travel upstream until its momentum is dead, respectively (Devenport & Simpson, 1989). Furthermore, due to the presence of the obstacle's streamline curves, the boundary layer is subjected to a spanwise pressure gradient, which results in a transverse secondary flow near the wall region of the boundary layer while the outer flow is still in the local streamwise direction. When the recirculated stream interacts with the incoming upstream flow, flow separation of the boundary layer occurs at some distance from the leading edge of the obstacle, it splits into minor streams around the appendage-body junction resulting in the formation of multiple horseshoe vortices that drape around the obstacle like a necklace. As described by Bradshaw (P. Bradshaw, 1987), the horseshoe vortex filaments are formed due to skewing of the shear layer, which is a quasi-inviscid process, can be defined as a secondary flow of the first kind as per Prandtl's theory.

The vortex streams seem to meander in the downstream regions of the fluid flow past the obstacle and the time-averaged vortex has an elliptical shape (Devenport, 1990). As the vortex is convected along the wing, the bimodal behaviour disappears. Horseshoe vortex system consists of a system of vortices that interact with each other in a cyclic process. The low frequency of self-induced chaotic switching results in turbulence energy and turbulent stresses in this region of vortex oscillation to be of a magnitude higher than upstream of the flow. Flow visualization studies have provided some insight into vortex systems that result in the bimodal peak of the U-velocity component and the results indicate that the direction of mean flow in the region of separated flow is mainly in reversed direction.

A stagnation point on the surface separates the boundary layer that flows around the sides of the obstacle and the upstream/downstream flow, and separation lines pass through this point on each side of the appendage around the junction. The primary vortex that is formed upstream of the obstacle has the same sense of rotation as the incoming boundary layer vorticity, while the horseshoe vortices stretched in the downstream direction satisfy vortex theorems of fluid dynamics, each leg has vorticity in the opposite sense (Baker, 1980). Upstream of the airfoil nose, the separation length has been found to be dependent on the thickness of the approaching boundary layer (Devenport, 1990).

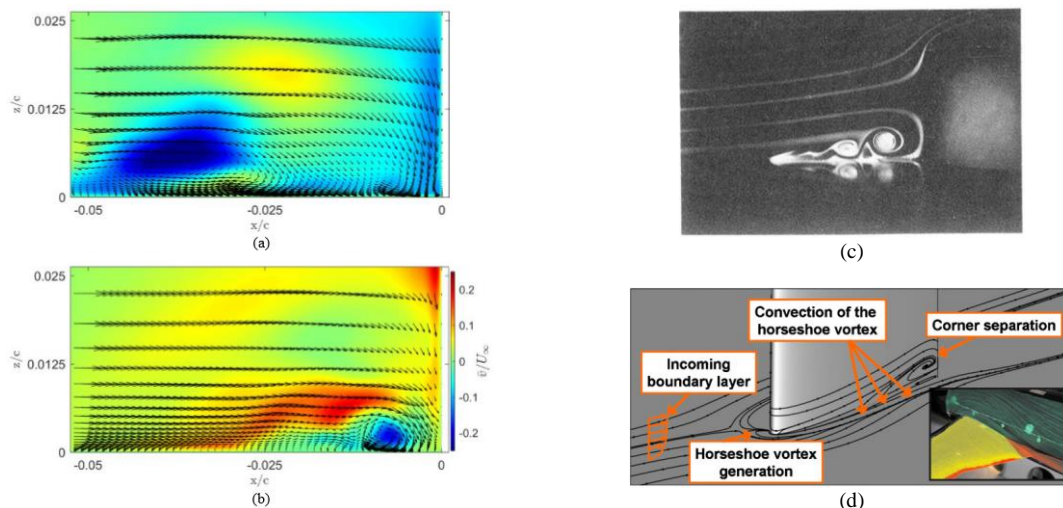


Figure 1 Bimodal behaviour upstream of the airfoil nose: (a) Back-flow mode (b) Zero-flow mode (Awasthi, et al., 2018) (c) Smoke flow visualization of junction flow upstream of the obstacle (Baker, 1991) (d) Sketch of the areas of interest of a junction flow and illustration of a technical configuration of junction flow (Gand, et al., 2010)

The horseshoe vortex system was observed in the junction flow upstream of the obstacle regardless of the shape of the appendage. The bluntness of the nose shape of the obstacle has been found to have a strong correlation with the strength and size of the horseshoe vortex that is formed at the junction. The bluntness factor (Fleming, 1991) is defined as:

$$BF = \frac{1}{2} \frac{R_o}{X_T} \left[\frac{T}{S_T} + \frac{S_T}{X_T} \right] \quad (1)$$

where R_o is the leading-edge radius, X_T is the chordwise position of the maximum thickness of the wing T , and S_T is the distance from the maximum thickness of the obstacle to the leading edge across the surface of the obstacle. It is evident from the results of past studies that the height to width ratio (H/T) of the appendage influences the amount of fluid that flows over the top of the appendage instead of going around it, particularly for cases where $H/T < 1$.

The incoming boundary layer of a fluid interacts with a body that is effectively blunter with an increasing angle of attack of the wing, which results in the formation of stronger horseshoe vortex systems. As the angle of attack, α , is increased to 15° , there is an increase in the turbulent shear stresses and kinetic energy on the suction side of the appendage, the downstream leg shifts away from the wing towards the free-stream direction, but remains at the same distance from the surface of the wall. On the pressure side of the appendage, the downstream leg stays at the same distance from the wing but moves away from the juncture. The flow characteristics of a NACA0012 airfoil with $\alpha = 10^\circ$ and an incoming boundary layer with $Re_\theta = 4200$ were studied (Shizawa, et al., 1996). It was observed that pressure fluctuations in the vicinity of the junction were only slightly affected, the horseshoe vortex on the suction side was stronger and distorted the wing wake within the boundary layer of the body and resembles a single vortex rooted far downstream in the wake within the boundary layer. Furthermore, the tail of the appendage seems to have an influence on the strength of the horseshoe vortex for an increasing angle of attack (Rood & Anthony, 1985). Size of the vortex and area across which the effects of unsteadiness are observed increases for tails that produce a greater adverse pressure gradient.

Several control mechanisms for altering the behaviour of junction flows have been extensively studied. A fairing should be designed such that it offers certain benefits: a) minimize/eliminate the separation of flow, b) minimize cross-flow within boundary layers, c) merge different streams smoothly, and d) avoid the development of thick boundary layers (Haines, 1983). A fairing downstream of the maximum thickness of the airfoil section is crucial for minimizing drag at the corners of the junction.

The effect of a leading-edge fillet on the flow characteristics at the juncture can be desirable. A study on the effect of leading-edge fillet on the junction flow in case of a NACA0020 airfoil was conducted (Devenport, et al., 1992) by comparing the measured flow characteristics of a baseline case with no leading-edge fillet with that of an airfoil with a leading-edge fillet for various angles of attack $\leq 12^\circ$. In the case of zero angle of attack, the leading edge fillet eliminated the leading edge separation of the incoming boundary layer by reducing the overall adverse pressure gradient and thus their effects on the approach boundary layer upstream of the nose. The presence of leading-edge fillet also eliminated bimodal unsteadiness of the flow by preventing the generation of a horseshoe vortex around the nose of the appendage, minimized the surface pressure fluctuations and cross-stream pressure gradients in the region around the appendage, thus controlled the skewing of the boundary layer as it flowed past the appendage.

The wall pressure fluctuations were recorded and analysed for different airfoils to develop an understanding of the relation of wall pressure fluctuations with the unsteadiness in the region (O'Connell & Simpson, 1994). The incoming boundary layer thickness (δ) was 8% of span of the airfoil and $Re_\theta \approx 4,450$ for the tests conducted on the airfoils. Six different airfoils with a leading-edge radius ranging from 5-50% of the maximum thickness of the airfoil were tested and it was observed that the root mean square (RMS) pressure levels were higher for airfoils with a larger radius. It was also found that the RMS pressure levels had also increased upstream of the flow, compared to the undisturbed boundary layer. Bimodal histograms of surface pressure fluctuations were in agreement with the bimodal histograms of the velocity field that were reported in studies conducted concerning the velocity field of junction flows (Devenport & Simpson, 1989). For airfoils with a leading-edge radius of less than 13% of the maximum thickness of the airfoil, no unsteady bimodal behaviour was observed, which is consistent with unsteadiness being a function of the airfoil bluntness. The effects of three-dimensionality on pressure fluctuations under a three-dimensional boundary layer were studied by recording and analysing the pressure fluctuations away from the region where the unsteadiness of HSV systems dominate (Goody & Simpson, 2000). The measurements reveal that there is an increase in the wall pressure fluctuations in the low-frequency spectrum at a location upstream of the airfoil, on the other hand, the pressure fluctuations downstream of the airfoil increase show an evident increase in the high-frequency levels and a decrease in low-frequency levels which can possibly be attributed to the acceleration of fluid around the nose of the airfoil.

The root mean square and spectral characteristics of the wall-pressure fluctuation have been recorded and studied for a NACA0012 airfoil (Awasthi, et al., 2018). The measurements elucidate that the magnitude and spectral shape of pressure fluctuations is modified all around the airfoil by its presence in the flow field. The wall pressure fluctuations increase across the entire frequency range due to the flow separation that occurs upstream

of the leading edge of the airfoil with an increasing angle of attack. Further downstream of the leading-edge, the pressure fluctuations increase and decrease on the suction and pressure sides respectively all around the airfoil body. At any given angle of attack, the most intense fluctuations are observed around the maximum thickness region of the airfoil on the suction, mostly in the higher frequencies. The unsteady pressure levels decay downstream of the maximum thickness of the airfoil before rising again past the trailing edge of the airfoil. The histogram of pressure fluctuations does not reveal the presence of bimodal unsteadiness upstream of the appendage-body junction.

The velocity field and flow structure of fluid flow in the vicinity of appendage-wall junctions have been extensively studied but wall pressure fluctuations and their relation to junction flows have been scarcely studied. Wall pressure fluctuations can be expected to be majorly influenced by the unsteadiness of horseshoe vortex systems, the flow separation near the airfoil leading edge, the corner separation, and the vortex legs in the streamwise direction, which are undesirable from structural and noise control aspect. In the case of an airfoil with constant radius leading-edge concave fillet, the flow dynamics, structure, and bimodal unsteadiness have been studied by Devenport et al (1992) but its effects on the frequency spectra of the wall pressure fluctuations in the airfoil-junction have not been critically studied and analysed. Thus, implications of introducing a leading-edge fillet to an airfoil at varying angles of attack on the wall pressure fluctuations in the vicinity of the appendage-wall junction region were determined to be the scope of this study.

The study aims to experimentally measure the unsteady pressure fluctuations and analyse the effects of a leading-edge fillet attached to a NACA0012 airfoil different angles of attack on the wall pressure fluctuations that are associated with the characteristics of junction flows. The study was conducted by comparing the measured flow characteristics of a baseline case with no leading-edge fillet with that of an airfoil with a leading-edge fillet for various angles of attack $\leq 12^\circ$. The study will examine the wall pressure field upstream of the leading edge. The wall pressure measurements were taken using an array of remote microphone probes in the UNSW AF1125 benchtop wind tunnel, shown in Figure 2. The measurements were taken for the tunnel operating at 30m/s while the boundary layer thickness is 3.5mm.

2 Methodology

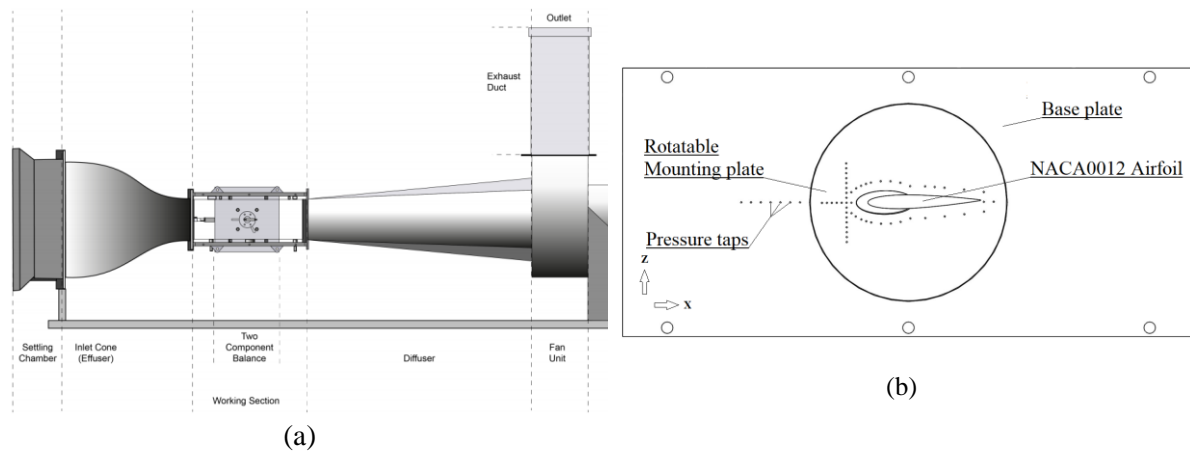


Figure 2 Schematic of the (a) AF1125 wind tunnel test facility, (b) Baseplate, mounting plate and NACA0012 airfoil assembly, coordinate system, and wall pressure measurement taps (Tecquipment, 2017)

The measurements were performed in the USNW AF1125 benchtop wind tunnel which is of the close working section and open-return suction type which is supported on a tubular structure and is compact enough to fit on top of a laboratory bench, with a 125mm×125mm×350mm test section that can operate at a flow velocity from 0 m/s to 36 m/s. Air passes through a settling chamber before entering through an aerodynamically designed effuser (cone) that accelerates the air in a linear manner, through the working section and finally passes through a grill before moving through a diffuser into the variable speed axial fan and exits into the atmosphere upwards through an exhaust duct. The test specimen, base plate and mounting plate are mounted on the left side of the closed test section. The mounting plate sits flush with the base plate. Figure 3 depicts the undisturbed boundary layer velocity profile.

Table 1 Undisturbed boundary layer parameters

	U_∞ (m/s)	δ (mm)	Re_c
Measurements	30	3.5	138,972

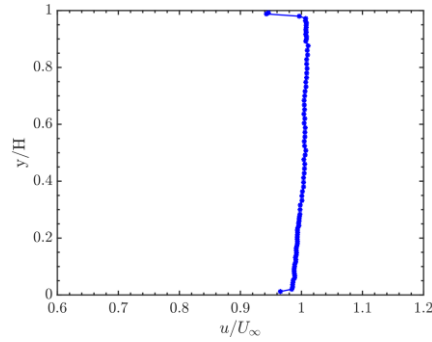


Figure 3 Velocity profile at 20mm downstream from the test section inlet at $U_{\infty} = 30\text{m/s}$. The presentation of this profile followed the coordinate system shown in Figure 2 and the coordinate (y) is normalised on the test section height ($H=125\text{mm}$) (Lu, 2018)

A 4.7mm deep counterbore with a thru-hole has been designed in the customised tunnel wall base plate on top of which a 4.7mm thick circular disc mounting plate will sit flush with the surface with a tolerance of $\pm 0.1\text{mm}$. The circular base plate has an ellipse cut-out into which the airfoil slides and sits flush with the surface. The circular disc has been designed to enable change in orientation of the pressure taps with the respect to the airfoil at different angles of attack and capture the changes that take place in the flow characteristics and unsteady surface fluctuations associated with them. The orientation of ports 1 to 7 remains fixed since they are located on the fixed base plate while the orientation of ports 8 to 28 can be changed since they are located on the rotatable mounting plate. The origin of the coordinate system is located at the tip of the leading edge of the airfoil, the x-direction is in the chordwise direction which is negative in the upstream direction and positive in the downstream direction, while the z-direction is in the spanwise direction and the coordinate system follows the right-handed rule. The flow was left to right with respect to the coordinate system in all the test cases. The leading-edge fillet has been designed to have a tapering radius leading edge fillet which has a maximum thickness twice the boundary layer at the front end of the leading edge and tapers to 0.1mm near the mid-thickness of the airfoil. The leading-edge has been optimised to be able to keep the bluntness factor of the airfoil minimum so that the primary horseshoe vortex is minimised in strength and size. The airfoil has been designed taking into consideration the design suggestion put forward by Dickenson, a fillet of twice the thickness of the boundary layer approaching an airfoil has been recommended to have desirable changes to junction flows.



Figure 4: (a) Front view of the airfoil without fillet near the junction (b) Side view of the airfoil without fillet near the junction (c) Front view of the airfoil with fillet near the junction (d) Side view of the airfoil with fillet near the junction

Table 2 Parameters of the base airfoil case

Airfoil type	Chord length (mm)	Maximum thickness (mm)	Aspect ratio of the airfoil	Blockage ratio at 12-deg AOA	Bluntness Factor	Fillet radius at leading-edge (mm)	Fillet height and length at the maximum thickness of airfoil (mm)	Distance of leading-edge from the start of test-section (mm)
NACA 0012	70	8.4	1.0	$\approx 11\%$	0.028	7	0.1 , 0.8	≈ 150.1

The unsteady wall pressure measurements were made using the remote microphone method. The measurement locations for this study are all upstream of the leading edge. The measurement locations have been tabulated in

Table 3. The pressure fluctuations at the surface of the wall were transferred remotely through a pressure tap to a GRAS 1/4-inch Type-40PH free-field microphone. To achieve this, a 10 mm long steel tube with an outside diameter of 0.8 mm and inside diameter being 0.5mm was installed downstream of the wind tunnel test section. It has been demonstrated previously by Devenport et al. that a 0.5 mm diameter thru-hole is sufficient to resolve boundary layer pressure fluctuations between the lowest measurable frequency and 20 kHz. Flexible tubing with an inside diameter of 0.8 has then been used to attach the metal tubing to a 3D printed resin prototyped housing in which a GRAS® 1/4 inch-type 40PH free-field microphone has been installed. Inside the housing, a 1.6 mm diameter channel with a T-junction has been used to split the pressure waves between the microphone and a 3 m long anechoic termination. The latter is required to dampen reflections that arise if the housing had a closed-end. The remote microphone and cavity calibration setup have been depicted in Figure 3. The GRAS® type 40 PH microphone has a flat frequency response (± 2 dB) up to around 15 kHz. The voltage output from the microphones has been acquired using National Instrument® DAQ at a sampling rate of 51,200 Hz for 32s.

The Fourier transform of the recorded data signal was obtained using a Hanning window of 4096 points and an overlap of 50% between each record. A zero-phase bandpass filter was applied to the time series pressure signal that was acquired using the microphones to filter out the noise since the data below 100Hz is possibly contaminated with background noise and above 10kHz is contaminated by noise due to reflections from the walls of the tubing.

Table 3 Wall pressure fluctuations measurement locations

Ports along axis						Pressure Side			Suction Side		
Port #	x/c	z/c	Port #	x/c	z/c	Port #	x/c	z/c	Port #	x/c	z/c
1	-1.106	0	8	-0.400	0	15	-0.143	-0.043	16	-0.143	0.043
2	-1.020	0	9	-0.357	0	17	-0.143	-0.086	18	-0.143	0.086
3	-0.934	0	10	-0.314	0	19	-0.143	-0.129	20	-0.143	0.129
4	-0.849	0	11	-0.271	0	21	-0.143	-0.171	22	-0.143	0.171
5	-0.763	0	12	-0.229	0	23	-0.143	-0.214	24	-0.143	0.214
6	-0.677	0	13	-0.186	0	25	-0.143	-0.257	26	-0.143	0.257
7	-0.591	0	14	-0.143	0	27	-0.143	-0.300	28	-0.143	0.300

The remote microphones were calibrated at the site for each of the measurement locations using the methods described by Guan et al. Refer to the remote microphone technique used by Awasthi et al. (2018) for more details on the remote microphone probe setup. The remote microphone probe and factory calibrated reference microphone were exposed to the same white noise source by applying the cavity calibration method which involves the use of a customised 3D printed calibration coupler which houses both the source and reference microphone perpendicular to each other. This coupler was placed over the tap on the base plate, while the voltage signal to the speaker microphone, the response of the reference microphone and that of the remote microphone were then recorded simultaneously to evaluate the complex transfer function using:

$$H_{cal} = \frac{\Phi_{SM}(f) \times S_{ref}}{\Phi_{SR}(f)} \quad (2)$$

where f is the frequency in Hz, S_{ref} is the sensitivity (in V/Pa) of the reference microphone, $\Phi_{SM}(f)$ is the cross-spectrum between the input voltage signal to the speaker and the remote microphone output voltage, and $\Phi_{SR}(f)$ is the cross-spectrum between the input voltage signal to the speaker and the reference microphone output voltage. The white noise signal is generated using GRAS® 40AD 1/2-inch pre-polarized microphone driven by a GRAS® 14AA electrostatic actuator amplifier.

3 Results and Discussion

The results from measurements of wall pressure fluctuations in the vicinity of the appendage-wall junction are now discussed. The root mean square (RMS) wall pressure followed by the spectral characteristics of the surface pressure fluctuations will now be discussed. Measurements were performed at a free stream velocity of 30m/s. which corresponds to a chord-based Reynolds number of nearly 138,972.

3.1 Root Mean Square (RMS) Pressure

Figure 5 depicts the root mean square wall pressure (p_{rms}) measure at each of the ports for several angles of attack as a function of the chordwise distance upstream of the leading edge and spanwise distance from the longitudinal axis of the baseplate-mounting plate assembly. The RMS pressure values at each of the ports represented in the plots have been normalized on the RMS pressure at the respective port for the undisturbed boundary layer case. The RMS pressure has been calculated by taking the RMS of the filtered time-series pressure signal using the formula:

$$p_{rms} = \sqrt{\int_{f_l}^{f_h} \phi_{pp}(f) df} \quad (3)$$

where p_{rms} is the RMS pressure in Pascals, ϕ_{pp} is the filtered time-series pressure signal. The filter applied to the data has a cut-off frequency of 100Hz to 10,000Hz.

From Figure 5 it can be inferred that the RMS pressure level at most of the ports is raised from the undisturbed boundary layer case due to the presence of an airfoil in all test cases except for the airfoil with no-fillet at the zero-lift configuration at which the RMS pressure levels remain close to the UBL case. The least RMS pressure levels can be observed for the airfoil with no-fillet at zero-lift configuration at all measurement locations. The RMS pressure levels for the airfoil with the fillet at zero-lift configuration is higher than airfoil without fillet at all measurement locations except at z/c greater than 0.25. In cases, at a 4-deg angle of attack, the RMS pressure levels at ports located on the base plate are higher for the no-fillet case than the airfoil with fillet, while the RMS pressure levels at the ports located on the rotatable mounting plate for the airfoil with fillet have higher RMS pressure levels than the case with no-fillet. In all other cases, the RMS pressure levels of the airfoil with fillet are higher than the RMS pressure levels of the no-fillet case. The RMS pressure at the ports located between x/c -0.75 and -0.4 is lesser for the 12-deg angle of attack than the 8-deg angle of attack while RMS pressure levels at the pressure taps located on the rotatable mounting plate of the no-fillet case at 8-deg and 12-deg angle of attack seem comparable, which is a deviation from the expectation of an increase in the RMS pressure levels upstream of the leading-edge with an increase in the angle of attack. It can be also be observed that the RMS pressure levels for all the test cases of the airfoil with fillet are higher than the corresponding cases without fillet except for the deviation at a 4-deg angle of attack as discussed above. RMS pressure levels between x/c -0.3 and -0.1 for the test cases with a fillet at a 0-deg angle of attack and 4-deg angle of attack are approximately equal which is a deviation from the trend of increasing RMS pressure levels with angle of attack.

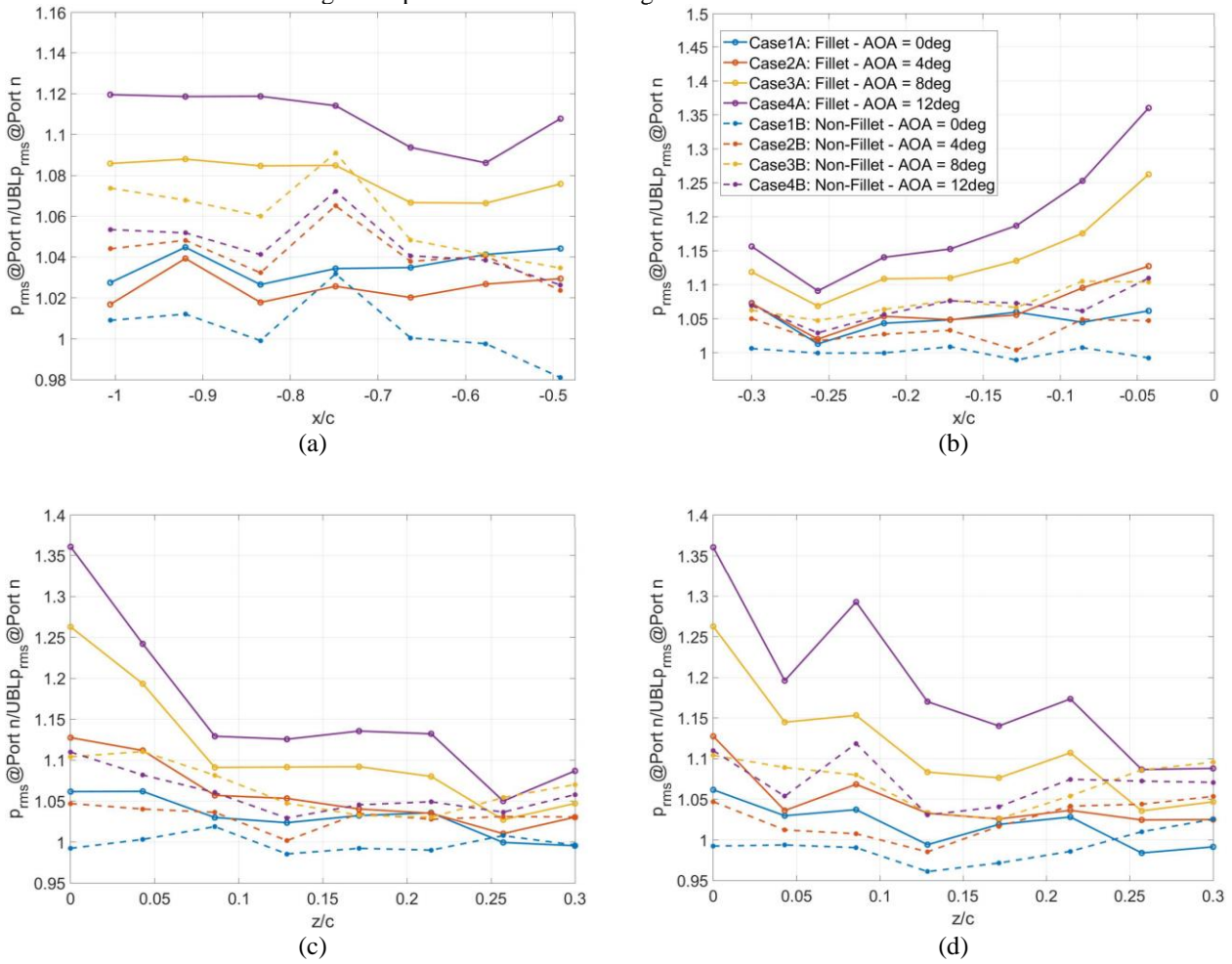


Figure 5 Chord wise variation of the RMS wall pressure upstream of the airfoil-wall junction at pressure taps (a) located on the base plate (b) located on the mounting plate along the longitudinal axis (b) located

on the mounting plate along the longitudinal axis (c) located on the mounting plate on the suction side of the airfoil (d) located on the mounting plate on the pressure side of the airfoil

The fluctuating pressure levels immediately upstream of the leading-edge increase with increasing angle of attack and the presence of an airfoil change the flow field even far upstream the leading-edge, while the effects of introducing a fillet to the leading-edge of the airfoil can too be observed far upstream of the leading-edge as can be observed from the RMS pressure plots. The RMS pressure levels increase with decreasing distance to the leading edge along the x-direction while the RMS pressure levels decrease as the distance from the center of the axis increases in the z-direction, which is following the trend that has been observed in the past research studies that have been reviewed.

3.2 Surface Pressure Spectra

Figure 6 depicts the surface pressure spectra at several locations for four angles of attack. The surface pressure spectra for the undisturbed boundary layer case at each of the measurement locations has also been represented for comparison. The spectra recorded at each of the measurement locations has been color-coded and the colour-scheme associated with each measurement location has been shown in Figure 6 (g) inset. All the data plots capture the trend of variation in surface pressure spectra for the different test cases with reasonable accuracy but differ in magnitude at some of the measurement locations due to minor error in calibration of the ports and the testing environment being in an echoic room, instead of the ideal case of having an anechoic environment for acoustic testing. Thus, comparing the pressure spectra of the undisturbed boundary layer case at each of the ports with the pressure spectra recorded for all the test cases reveals important information on the effects of introducing a fillet to a NACA0012 airfoil. The effect of introducing a fillet can be observed far upstream at all angles of attack until the farthest measurement location from the leading-edge at $x/c=-1.05$ of the leading-edge, though the spectral lines are very closely spaced when the plots were inspected and analysed the spectral lines for each of the cases followed a constant trend across all the measurement locations. The increase in overall surface pressure fluctuations can be inferred from the RMS pressure plot.

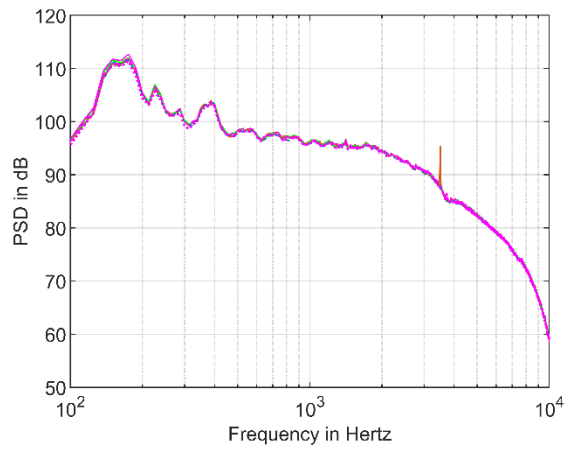
In case of all angles of attack, the presence of an airfoil raises the low frequency (less than 1000Hz) content of the surface pressure fluctuations above the undisturbed boundary layer case at all ports along the axis upstream of the leading edge, as far as the port located at $x/c=-1.10$, on the other hand, the higher frequency (above 1000Hz) content is suppressed probably due to stronger flow separation which leads to the formation of large-scale recirculating structures, the effects are more discernible at measurement locations that are closer to the leading edge than further upstream which can be inferred from Figure 6. Increasing the angle of attack increases the surface pressure fluctuations upstream of the leading edge in the low-frequency range and suppresses the higher-frequency content. The spectral plots of the fillet airfoil are higher in magnitude compared to the no-fillet airfoil at the respective angles of attack in the low-frequency range and have suppressed magnitude in the higher frequency range at the ports located on the axis. This can be attributed to the fact that the flow is encountering a blunter airfoil due to the presence of the fillet, which results in increasing the adverse pressure gradient upstream of the airfoil leading-edge to large recirculating structures.

At the ports located on both suction and pressure side of the axis, the surface pressure spectra are elevated across all the frequencies for the ports closer to the axis and as moves away from the axis in the z-direction, the frequency content above 2500Hz decreases in magnitude compared to the undisturbed boundary layer case. The fillet test cases result in an increase in the surface pressure fluctuations compared to their no-fillet counterpart at respective angles of attack.

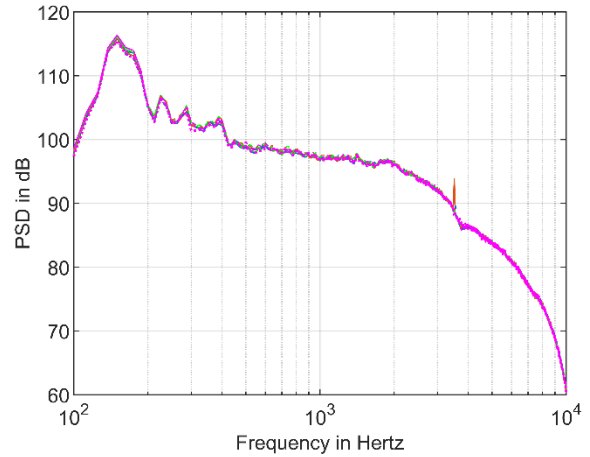
At a zero-degree angle, a spectral peak can be observed in the PSD for the no-fillet case at measurement locations further away from the leading-edge fillet between 1050Hz and 1400Hz, but the presence of leading-edge fillet results in the spectral peak at 0-deg and 4-deg angle of attack. The frequency at which the spectral peak occurs is the same for all measurement locations for a given angle of attack but the magnitude of the spectral peak decreases for measurement locations that lie closer to the potential core of the recirculating structures. The origin of this peak can possibly be attributed to the tonal noise generated by the laminar separation of the boundary layer. 2-dimensional and 3-dimensional airfoils (such as the airfoil used in this study) emanate tonal noise which can be ascribed to the acoustic feedback mechanism between the trailing-edge that scatters the acoustic waves and the laminar separation on the airfoil (Moreau & Doolan, 2016). The presence of the spectral peak at different measurement locations that are at large streamwise distances suggests that 2-D airfoil-like flow is responsible for the presence of spectral peaks. This peak was also audible while conducting the experiments and was only observed for the cases discussed above.

The presence of the leading-edge fillet did not seem to alter the flow structure in the vicinity of the junction in any favourable manner and rather increased the strength of the large-scale recirculating structures and increase the adverse pressure gradient upstream of the leading-edge fillet, which led to an increase in the power spectral density for the airfoil with fillet. The leading-edge fillet provided results contrary to what was observed by Devenport et al. mostly due to the variation in the design of leading-edge fillet. Accumulation of lower velocity boundary layers took place due to increased bluntness of the encountered nose which flowed under the higher-

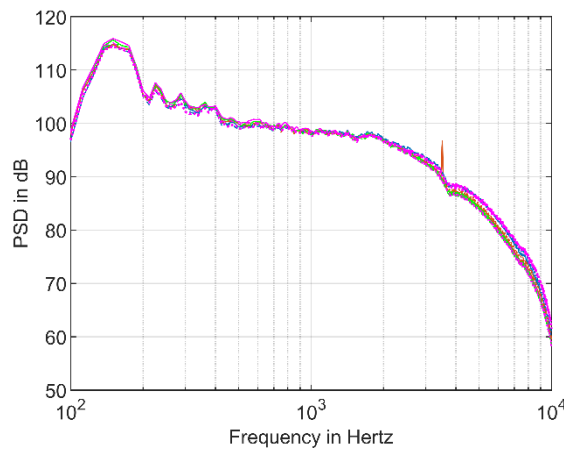
velocity boundary layers of the fluid leading to flow separation, which also increased the turbulence near the nose of the appendage. In the case of the appendage with a leading-edge fillet at a non-zero angle of attack, separation of the boundary layer probably occurs on the pressure side of the appendage due to local adverse pressure gradients, significant skewing of the approach boundary layer possibly takes place because the flow interacts with a blunter leading edge, while non-uniformity and unsteadiness of the flow on the pressure side of the appendage have been recorded to be higher than in zero angle of attack case (Devenport, et al., 1992).



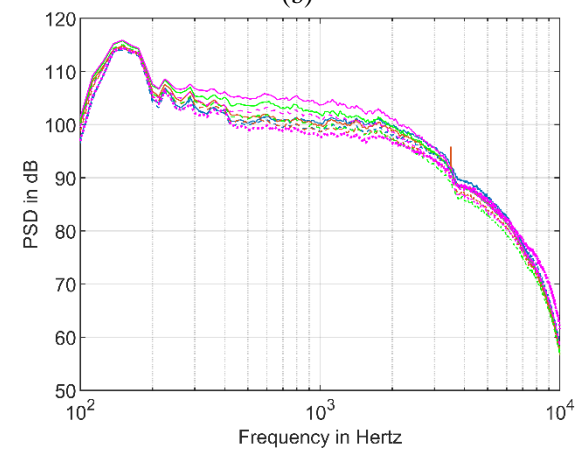
(a)



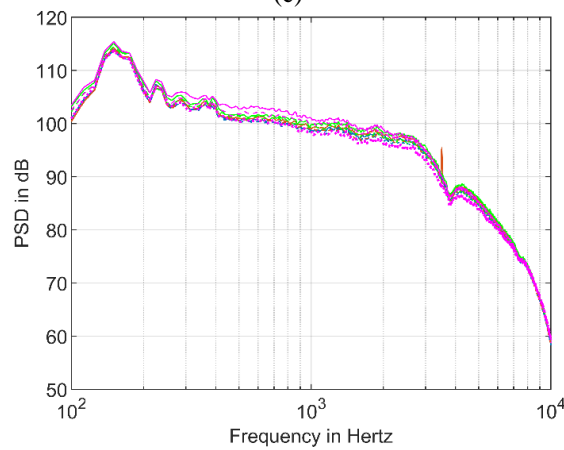
(b)



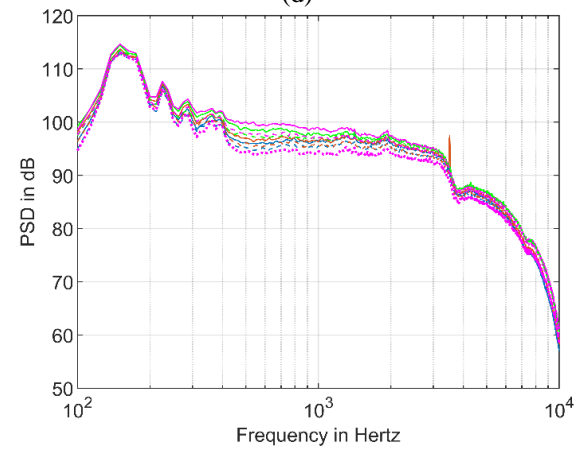
(c)



(d)



(e)



(f)

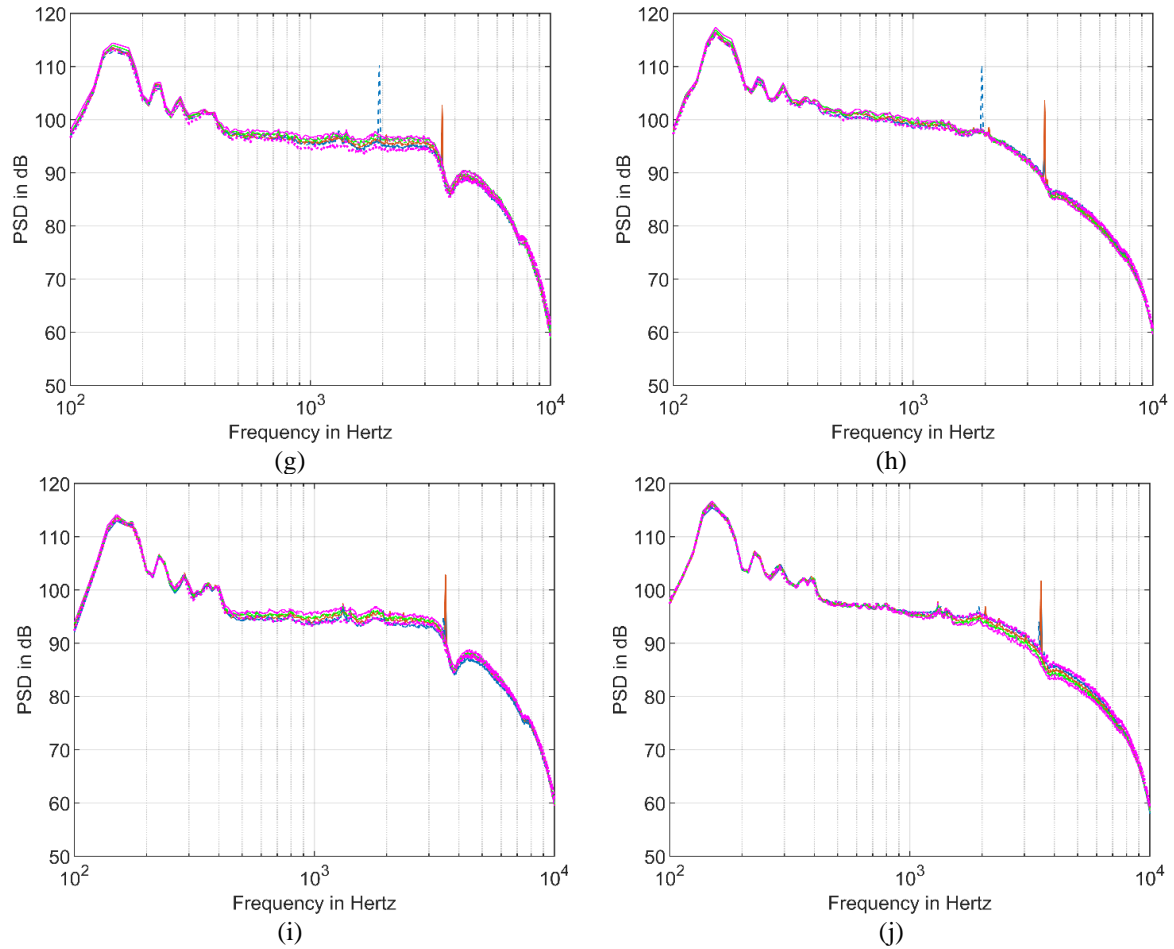


Figure 6 (a) (Port 2) $x/c = -1.020$, $z/c = 0$, (b) (Port 6) $x/c = -0.677$, $z/c = 0$, (c) (Port 10) $x/c = -0.314$, $z/c = 0$, (d) (Port 14) $x/c = -0.143$, $z/c = 0$, (e) (Port 15) $x/c = -0.143$, $z/c = -0.043$, (f) (Port 16) $x/c = -0.143$, $z/c = 0.043$, (g) (Port 21) $x/c = -0.143$, $z/c = -0.171$, (h) (Port 22) $x/c = -0.143$, $z/c = 0.171$, (i) (Port 25) $x/c = -0.143$, $z/c = -0.257$, (j) (Port 26) $x/c = -0.143$, $z/c = 0.257$

3.3 Surface Pressure Histogram

Figure 7 (a) shows the histograms of measure surface pressure fluctuations at port 13 for varying angles of attack and undisturbed boundary layer case and Figure 7 (b) represents the histograms of measured surface pressure fluctuations at port 13, 14, 15, and 16 for the zero-lift configuration. The histograms of the surface pressure fluctuations at all measurement locations do not exhibit any bimodality and have a single peak. It can be noted that this is in accordance with the findings of Devenport et al. which entail that airfoils with leading-edge radius less than 13% of the maximum thickness of the airfoil, do not exhibit unsteady bimodal behaviour, which is consistent with unsteadiness being a function of the airfoil bluntness. The baseline case of NACA0012 airfoil without fillet has a maximum thickness of 12% of the chord length, which is less than the maximum thickness recorded by Devenport et al.

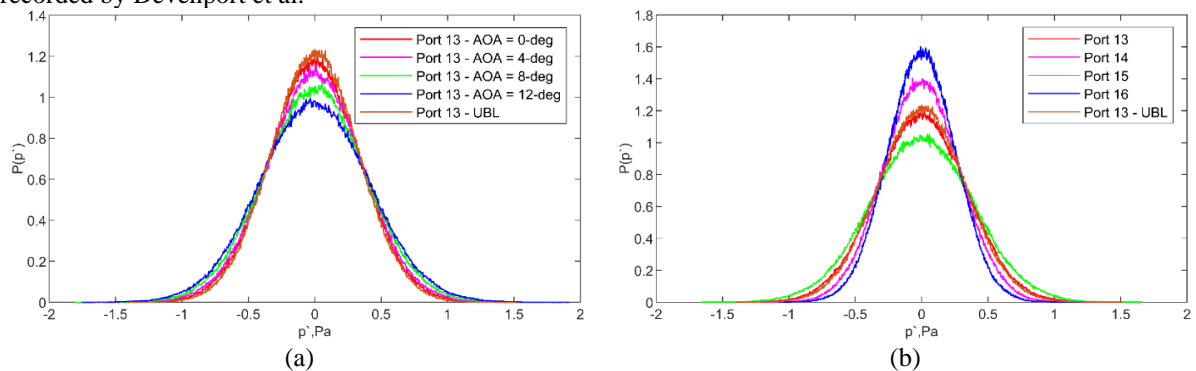


Figure 7 Histograms of wall pressure fluctuations upstream of the airfoil (a) at port 13 for varying angles of attack (b) at ports 13, 14, 15, 16 at a 0-deg angle of attack

4 Conclusion

Unsteady surface pressure measurements were performed in a wind-tunnel with closed working-section and open-return suction type to understand the behaviour of surface pressure fluctuations on introducing a leading-edge fillet to a NACA0012 airfoil by comparing it to a baseline case. The airfoil had a theoretical chord of 70mm and the Reynolds number based on chord length was approximately 139,000. The incoming wall boundary layer thickness was 3.5mm and the aspect ratio of the airfoil was 1.0. Several angles of attack were considered between 0-deg and 12-deg.

The measurements show that the presence of a leading-edge fillet did not alter the flow in the vicinity of the junction in any favourable manner and rather increases the magnitude and the spectral shape of wall pressure fluctuations across the entire upstream region of the leading-edge fillet across most of the frequency range. The flow encounters a 'blunter' object which increases the adverse pressure gradient upstream of the leading-edge. Accumulation of lower velocity boundary layers possibly took place due to the increased bluntness of the encountered nose and leads to an increase in turbulence near the nose of the appendage. The magnitude of surface pressure spectra under 1000Hz increases with an increasing angle of attack at most measurement locations upstream of the airfoil due to the flow encountering a blunter object.

At a zero-degree angle of attack, a spectral peak can be observed in the PSD for the no-fillet case at measurement locations further away from the leading-edge fillet between 1050Hz and 1400Hz, but the presence of leading-edge fillet results in the spectral peak of increased magnitude at 0-deg and 4-deg angle of attack. The frequency at which the spectral peak occurs is the same for all measurement locations for a given angle of attack but the magnitude of the spectral peak decreases for measurement locations that lie closer to the potential core of the recirculating structures, close to the leading-edge. The origin of this peak can be attributed to the tonal noise generated by the laminar separation of the boundary layer. The histograms of the wall pressure measurements do not show any indication of bimodal behaviour due to the thickness of the airfoil being less than 13%.

It would be favourable for accuracy of acoustic measurements if the measurements are recorded in an anechoic environment to be able to avoid the background noise which contaminates the pressure signal and requires extra steps for filtering. The leading-edge fillet design though did not improve the flow structure by reducing the strength of surface pressure fluctuations, the study provided an insight on the effect of the slightest change to the leading-edge on the surface pressure fluctuations around the vicinity of the wall-junction region. It would be of interest to study different configurations of leading-edge fillet airfoils, other passive devices combined with different NACA airfoils at varying angles of attack to be able to find an optimum passive device configuration to minimise the surface pressure fluctuations associated with junction flows.

References

- Ol, cmen, S. & Simpson, R., 1994. *Influence of wing shapes on surface pressure fluctuations at wing-body junctions*. *AIAA Journal*, 32(1), pp. 6-15.
- Awasthi, M. et al., 2018. *Characterization of the Fluctuating Pressure Field in the Airfoil-Wall Junction: Measurements and Computations*. Atlanta, Georgia, AIAA.
- Baker, C. J., 1980. *The turbulent horseshoe vortex*. *Journal of Wind Engineering and Industrial Aerodynamics*, vol. 6, no. 1-2.
- Devenport, W. A. N. D. M. S. R. P. K., 1990. *Effects of a fillet on the flow past a wing-body junction*. *AIAA Journal* 28(12), p. 2017–2024.
- Devenport, W. J. & Simpson, R., 1989. *Time-dependent and time-averaged turbulence structure near the nose of a wing-body junction*. *Journal of Fluid Mechanics*, 210, p. 23–55.
- Devenport, W. J., Simpson, R. L., Dewitz, M. B. & Agarwal, N. K., 1992. *Effects of a Leading-Edge Fillet on the Flow Past an Appendage-Body Junction*. *AIAA Journal*; Vol. 30,(No. 9), pp. 2177-2183.
- Dickenson, S., 1990. *Appendage hull junction flows and their application to sailboat keels*. s.l., s.n., p. 47–58.
- Fleming, J. S. R. D. W. ' . T. R. V. –. A. –. I., 1991. *An experimental study of a turbulent wing-body junction and wake flow*, Blacksburg : Aerospace and Ocean Engineering Department, Virginia Polytechnic Institute and State University.
- Gand, F., Deck, S., Brunet, V. & Sagaut, P., 2010. *Flow dynamics past a simplified wing body junction*. *American Institute of Physics*.
- Goody, M. & Simpson, R., 2000. *Surface pressure fluctuations beneath two- and three-dimensional turbulent boundary layers*. *AIAA Journal*, 38(10), p. 1822–1831.
- Guan, Y., Berntsen, C., Bilka, M. & Morris, S., 2016. *The measurement of unsteady surface pressure using a remote microphone probe*, *Journal of Visualized Experiments*. Issue 118.
- Haines, A. B., 1983. *Aerodynamic interference: a general overview. Special course on subsonic/transonic aerodynamic interference for aircraft*. s.l.:NATO-AGARD.
- Lin, C., Chiu, P. & Shieh, S., 2002. *Characteristics of Horseshoe vortex system near vertical plate-base plate juncture*. *Exp. Therm. Fluid Sci.*, 27(25).
- Lu, R., 2018. *The Aerodynamics of Shark-inspired Riblet Surfaces*, Sydney: University of New South Wales.
- Moreau, D. J. & Doolan, C., 2016. *Tonal noise production from a wall mounted-finite airfoil*. *Journal of Sound and Vibration*, Issue 363, pp. 199-224.
- P. Bradshaw, 1987. *Turbulent secondary flows*. *Annual Review Fluid Mechanics*.
- Pierce, F. J. & Shin, J., 1990. *An experimental investigation of effects of leading-edge fillets on a turbulent junction vortex*. *Kingston, s.n.*, p. 61–71.
- Rood, E. P. & Anthony, D., 1985. *Tail profile effects on unsteady large scale flow structure in the wing and plate junction*. *New York, Am. Soc. Mech. Eng., Fluids Eng. Div.* .
- Shizawa, T., Honami, S. & Yamamoto, M., 1996. *Experimental study of horseshoe vortex at wing/body junction with attack angle by triple hot-wire*. Reno, NV, AIAA.
- Simpson, R. L., 2001. *Junction Flows*. *Annual Review of Fluid Mechanics*, Volume 33, pp. 415-443.
- Tecquipment, 2017. *AF 1125 Subsonic Wind Tunnel - User Guide*. s.l.:TecQuipment Ltd.

Examining the Effects of Particle Seeding Concentration, Hologram Propagation Distance and Fluid Velocity Gradients on 4D Digital Holographic PIV/PTV Measurements

Yuan Jing Xia¹

*Laboratory for Turbulence Research in Aerospace & Combustion (LTRAC),
Monash University (Clayton Campus),
Melbourne, Victoria 3800, Australia*

I. Abstract

4D digital holographic PIV/PTV (4D-DHPIV/PTV) methods have demonstrated theoretical viability due to their relative ease of setup and high spatial accuracy per pixel. This project further improves on this technique, reducing positional error uncertainty to a thirtieth of previously realised results. Furthermore, this project investigates the effect of sensor distance and particle concentration on positional error, as well as how velocity gradients related to different flow regimes and their magnitudes affect 3-component–3-dimensional (3C-3D) displacement.

II. Nomenclature

N_x, N_y, N_z	= channel length (pixels) in x, y and z directions
<i>Pixel size</i>	= the physical length scale of a pixel
T	= particle transmission coefficient
x, y, z	= position coordinates in channel
x_0, y_0, z_0	= particle pixel position
U	= hologram amplitude
A	= Fourier transform of hologram amplitude
i	= imaginary number
λ	= light wavelength
f_x, f_y	= Fourier wave numbers in x and y directions
<i>PSF</i>	= point spread function (amplitude)
E	= error function
I	= hologram intensity
a, b	= hologram intensity scaling constants
u	= mean velocity
Δu	= change in velocity due to velocity gradient
u_i	= component-wise mean velocity
u_x, u_y, u_z	= mean velocity component in x, y and z directions
s	= strain tensor
ω	= vorticity tensor

III. Introduction

Particle image velocimetry (PIV) and particle tracking velocimetry (PTV) are modern methods used to obtain instantaneous velocity fields and particle flow paths respectively in fluids. Recent technological improvements to sensors and computers have enabled 3-component – 3-dimensional (3C-3D) and time-resolved (4D) PIV/PTV methods to become viable in macro experimental fluid mechanics and turbulence investigations [1]. Current 3D-3C PIV/PTV methods such as tomographic PIV (TPIV) require multiple cameras and extended calibration, similar to 3-component – 2-dimensional (3C-2D) stereo-PIV setups, resulting in a large source of error [2]. An alternative to TPIV is light-field PIV (LFPIV), which forgoes the lengthy calibration requirements of TPIV but resolves at a lower spatial resolution [3].

¹ Undergraduate Student, Department of Mechanical and Aerospace Engineering, AIAA Student Member 1192998.

4D digital holographic PIV/PTV (4D-DHPIV/PTV) can potentially improve upon the limitations of TPIV and LFPIV. The method has demonstrated a relatively simple calibration process whilst yielding higher spatial resolution measurements compared to TPIV and LFPIV [3]. However, as the knowledge of 4D-DHPIV/PTV techniques is limited, this project seeks to quantify the positional measurement errors under various seeding particle concentrations and light propagation distances. The effect of velocity gradients on 3C-3D vector errors are also investigated to understand and improve the reliability of this technique.

IV. Methodology

This project simulates the 4D-DHPIV/PTV technique by first randomly distributing seeding particles within a designated channel domain and simulating the resulting sensor hologram. The hologram is then post-processed to reconstruct the particle positions.

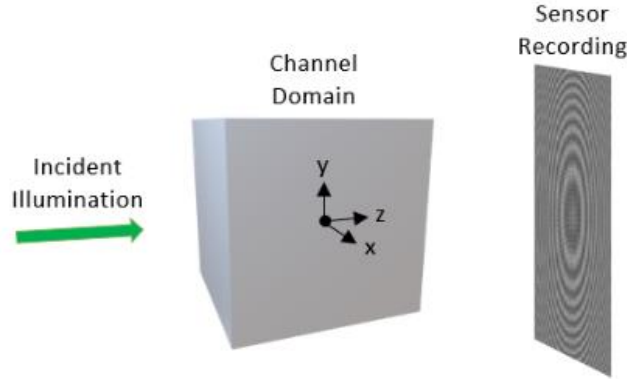


Fig. 1 Diagram of simulated 4D-DHPIV experiment

A. Distributing Seeding Particles

A flow channel is simulated between $-\frac{N_x}{2} \leq x \leq \frac{N_x}{2}$, $-\frac{N_y}{2} \leq y \leq \frac{N_y}{2}$ and $-\frac{N_z}{2} \leq z \leq \frac{N_z}{2}$ pixels. The channel is first divided into interrogation volumes, each with a fixed number of seeding particles. The x , y and z coordinates of each particle within the interrogation volumes are randomly generated and collision-checked with other particles within the interrogation volume and the volume perimeters. The particles are assumed to be neutrally buoyant and faithfully follow fluid flows.

B. Simulating the Hologram

The resulting hologram from a channel volume with its current distribution of particles is simulated by propagating incident light through the volume. The propagation of light is described by the convolution of the wave front and a diffraction kernel. Defining the z axis to be the light propagation direction, the particle can be modelled as an aperture with transmission coefficient [1]

$$T(x, y) = 1 - e^{-\frac{1}{2} \frac{(x-x_0)^2 + (y-y_0)^2}{r^2}} \quad (1).$$

As light passes a particle, the amplitude is altered as

$$U'(x, y, z) = U(x, y, z)T(x, y) \quad (2).$$

Convolution is modelled by the diffraction kernel described as

$$A\left(\frac{\alpha}{\lambda}, \frac{\beta}{\lambda}, z\right) = A\left(\frac{\alpha}{\lambda}, \frac{\beta}{\lambda}, 0\right) \exp\left(\frac{2\pi}{\lambda} i \sqrt{1 - \alpha^2 - \beta^2} z\right) \quad (3)$$

in the Fourier space, where α and β in Eq. 3 are defined by

$$\alpha = \lambda f_x \quad \beta = \lambda f_y \quad (4).$$

This method of light propagation is known as the angular spectrum method [4]. In practice, the Fourier transforms are performed using Fast Fourier Transforms (FFT) and Inverse Fast Fourier Transforms (IFFT) due to the discretised positioning of pixels within arrays. The convolution process is repeated for every particle in the channel domain until the light is finally propagated to the sensor. Furthermore, Eqs. 3 and 4 assume incident light to be monochromatic, coherent laser light. This also allows the assumption that the incident amplitude of light at the first particle encountered is 1, since only light's relative phase is important [4]. The simulations are performed using 532nm λ laser light. Sample holograms are shown in figure 2 below.

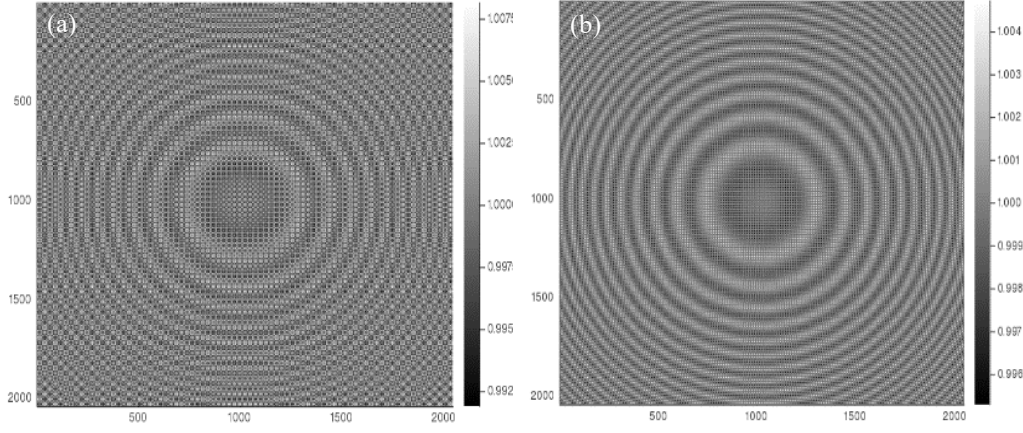


Fig. 2 Holograms of 4 micrometer particle placed 0.1m away using a pixel size of 1 micrometer. (a) shows an artifacting, simulated intensity using a 2048² pixel sensor and (b) shows intensity when calculated using 4096² pixels, with the center 2048² pixels cropped (extended).

Due to the properties of FFT and IFFT, it is important to note that longer propagation distances result in visible, non-physical artifacting occurring in simulated holograms. This can be resolved by simulating a hologram larger than the sensor itself and cropping the inner array that represents the sensor data as shown in image (b) of figure 2.

C. Reconstructing Channel Volume

To reconstruct the position of particles from the recorded hologram, the hologram's amplitude is propagated backwards at various z-planes within the original channel domain to generate a convolution volume.

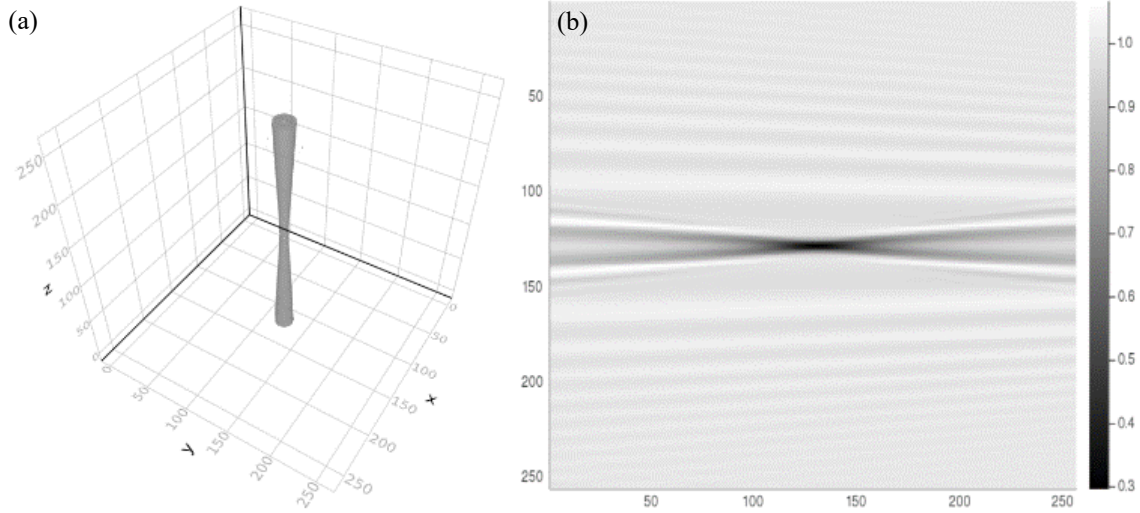


Fig. 3 Extended absolute amplitude of a centered 2 micrometer particle in a 128³ pixel volume (PSF). (a) is an iso-surface plot and (b) is a contour plot in y-z at x=0.

The contribution of the incident light is then removed from the convolution volume and point spread function (PSF) such that

$$PSF'(x, y, z) = abs(PSF(x, y, z) - 1) \quad (5),$$

$$U'(x, y, z) = abs(U(x, y, z) - 1) \quad (6).$$

The convolution PSF volume is then deconvolved with a particle's PSF using Richardson-Lucy deconvolution described by

$$U^{(t+1)} = U^{(t)} \cdot \left(\frac{U}{U^{(t)*PSF} * PSF^*} \right) \quad (7)$$

where U is the incident-light-removed initial convolution volume amplitude. $U^{(t)}$ represents the t-th iteration of the convolution volume amplitude and PSF^* is the incident-light-removed PSF amplitude reflected in the x, y and z directions across the array center [5]. The algorithm is concluded when the correlation of U between iterations exceeds a value of 0.999. The deconvolution algorithm produces a reconstructed volume with z-elongated, gaussian-like structures as particles. The stretching in the z axis is due to the z-elongated structure of the PSF.

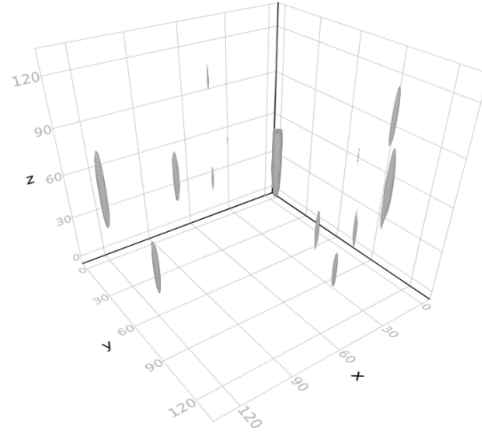


Fig. 4 Iso-surface plot of deconvolved 128^3 pixel volume, showing cluster shapes of reconstructed particles.

D. Iterative Inverse Reconstruction Method

The objective is to retrieve the particle positions from the gaussian-like structures within the reconstructed volume. The 3D Hoshen-Kopelman algorithm [3] assists by first clustering the gaussian-like structures into groups, given that they exceed a threshold value of 0.2 times the maximum value. Each cluster is then used to find its weighted centroid position.

Each particle will now undergo the inverse position-optimisation process. For each particle identified, a hologram resulting from that particle alone is then compared to that of the original, simulated hologram. The centroid position is then optimised such that the error between hologram intensities defined by

$$E = \Sigma(I_{Hologram} - I_{Particle})^2 \quad (8)$$

is minimized. The intensity of the particle hologram is also linearly scaled as described by

$$I'(x, y) = aI(x, y) + b \quad (9)$$

where a and b are scaling constants, numerically solved so that the error described in Eq. 8 is further minimised. The scaled intensity is then subtracted from the sensor hologram intensity and the finalised particle position is recorded. This is repeated for every particle centroid found in the reconstructed volume. Note that constraints on the parameter a can be utilised to reject “ghost” particles [1] when its convergent solution results in a magnitude less than 0.5 - this arises from the imperfect subtraction of particle diffraction patterns, resulting in residuals.

The deconvolution process via Eq. 7 is repeated until the light perturbations due to particle presence in the subtracted hologram fall below a predetermined error threshold when compared to incident light. The error is defined as

$$E = \Sigma(I_{Hologram} - I_{Incident\ Light})^2 \quad (10).$$

The deconvolution process is also stopped when the error decrease between subsequent reconstruction volumes is sufficiently small.

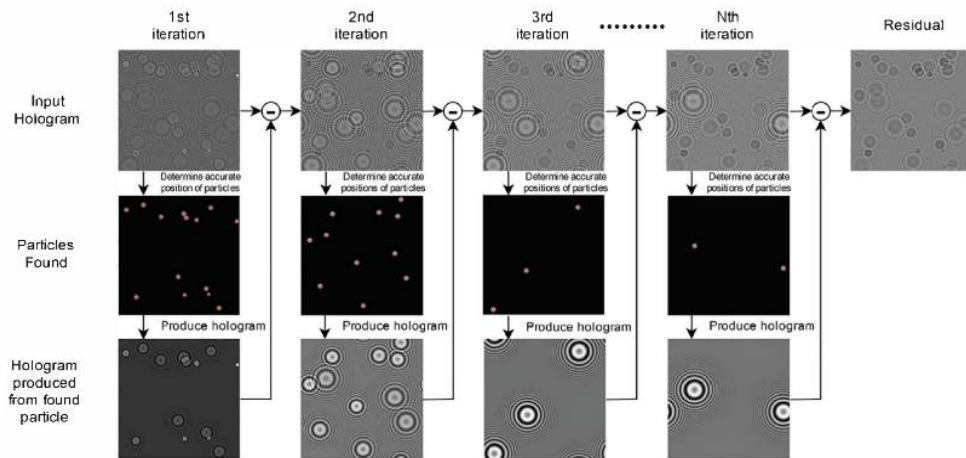


Fig. 5 Iterative particle detection process [3]

V. Results and Discussion

A. Effect of Sensor Distance on Positional Error

The effects of light propagation distance on positional error uncertainty and bias are investigated by comparing results from a repeated simulation with all parameters except sensor position being identical. A simulation using a channel size of $N_x=N_y=N_z=128$ pixels, pixel size of 1 micrometer ($128\mu\text{m}^3$ volume) and particle diameter of 2 micrometer is performed. The simulated 256^2 pixel sensor is located at distances 0.05, 0.1, 0.15, 0.2 and 0.25mm away from the channel. 10 particles are simultaneously placed within the channel and the simulation is repeated 20 times for a theoretical total of 200 particles for analysis at each distance. The following results are observed.

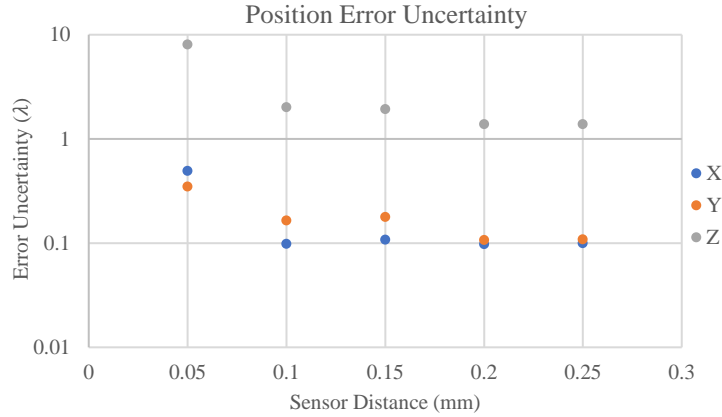


Fig. 6 Plot of position error uncertainty as a function of sensor distance, normalised by wavelength.

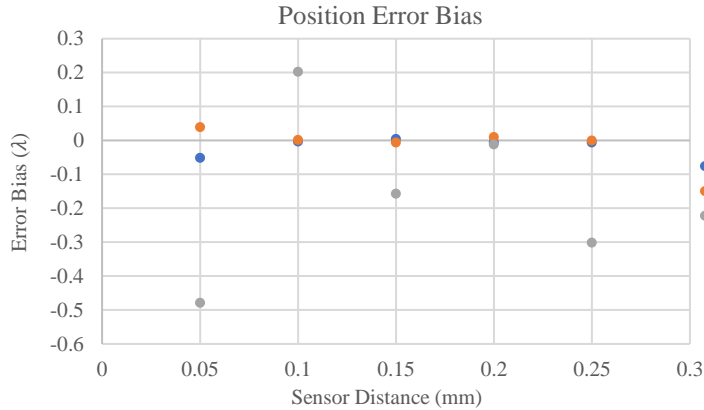


Fig. 7 Plot of position error bias as a function of sensor distance, normalised by wavelength.

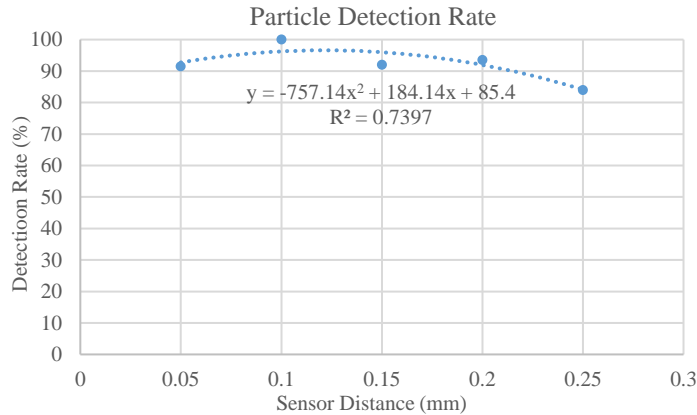


Fig. 8 Plot of inverse reconstruction method particle detection rate as a function of sensor distance.

Figure 6 suggests the expected position error uncertainties in all components decrease as sensor distance increases. This is likely because at larger distances, the hologram's diffraction patterns expand and thus enables the deconvolution algorithm to leverage supersampling to achieve greater precision. The magnitudes of error bias in figure 7 also supports this claim, with the shortest sensor distance resulting in the largest bias magnitudes.

Figure 8 portrays particle detection rate reaching a maximum at a moderate sensor distance of 0.1mm. This is likely because at short sensor distances, the diffraction patterns are the smallest and thus give the least amount of information to reconstruct the particle positions. At larger distances, the magnitude of intensity perturbations is reduced significantly, thus resulting in a lower detection rate.

Furthermore, it can be noted that the positional uncertainties are significantly larger in the z axis than in the x or y axes. This is as expected, due to the deconvolved gaussian-like peaks being elongated in the propagation axis as observed in figure 4.

B. Effect of Particle Concentration on Positional Error

The effects of particle concentration on positional error uncertainty and bias are investigated by comparing results from a repeated simulation with all parameters except particle concentration being identical. A simulation using channel size of $N_x=N_y=N_z=64$ pixels, a pixel size of 1 micrometer ($64\mu\text{m}^3$ volume), particle diameter of 2 micrometer and a sensor distance of 0.1mm is performed. The simulation is repeated with 5, 10, 20, 40 and 80 particles simultaneously and is repeated until there are 80 particles for assessment at each concentration. This corresponds to 0.00122, 0.00244, 0.00488, 0.00977 and 0.0195 particles per pixel^2 of lighting area and the results shown in figures 9-11.

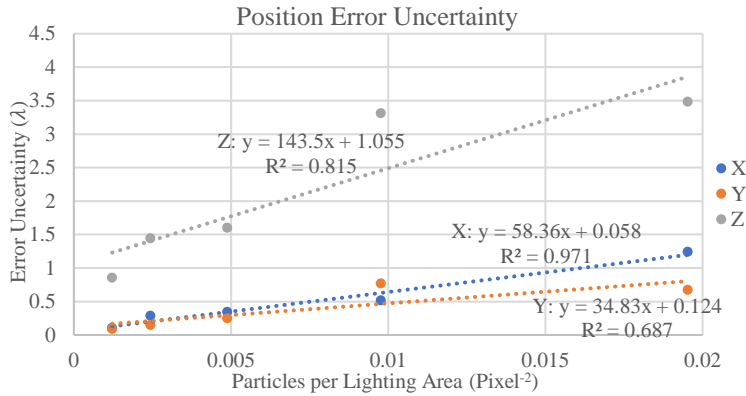


Fig. 9 Plot of position error uncertainty as a function of particle concentration, normalised by wavelength.

Figure 9 demonstrates that the uncertainty increases linearly with particle concentration. Furthermore, similar to previous findings, the error uncertainty in z position has a significantly larger minimum value and escalates quicker than x and y error uncertainties. A similar finding is observed in the figure 10 bias values as the magnitude of z bias is much more erratic and on average, significantly larger than the biases in x and y values. The lowest error uncertainty values are 0.1052, 0.0924 and 0.8573λ in x, y and z respectively, at the lowest particle concentration. Compared to literature values [1], under the same pixel size and channel domains, the simulation demonstrated it can achieve significantly lower error uncertainties - up to a 30 fold reduction at the lowest concentration in the x and y positions. The improvements are likely due to using a finely constrained (centered 0.2 pixel length box in x and y and 2 pixel length in z) numerical optimization method to prevent the numerical algorithm from iterating to adjacent minima formed by the multiple diffraction fringes.

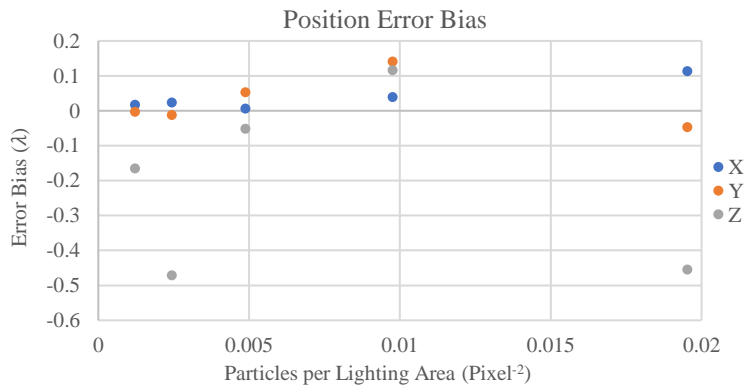


Fig. 10 Plot of position error bias as a function of particle concentration, normalised by wavelength.

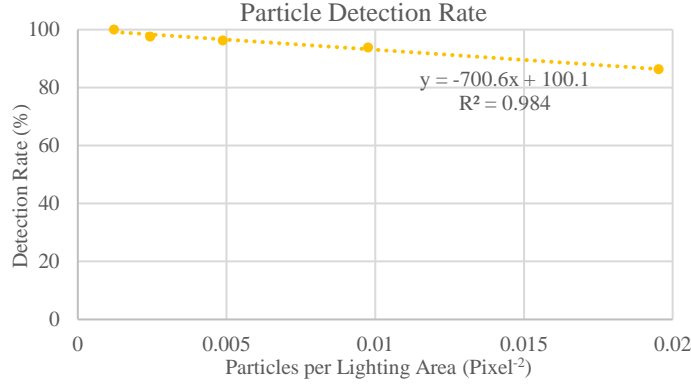


Fig. 11 Plot of reconstruction method particle detection rate as a function of particle concentration.

Figure 11 shows that particle detection rate linearly decreases as particle concentration is increased. Furthermore, the particle detection rate also appears to be significantly higher than literature values [1], particularly at the highest particle concentration - the current particle detection process is able to retrieve 86.25% as opposed to the 40% previously observed. The improvements can be attributed to the linear intensity scaling and robust reconstruction cycle stopping condition implemented.

However, as the sample sizes used for this particle concentration comparison are relatively small, further testing at the same values would be ideal to improve the reliability of the data.

C. Effects of Velocity Gradients on Particle Displacement Vector Error

The effects of velocity gradients on displacement error uncertainty and bias are investigated by comparing results of a repeated simulation with all parameters except velocity gradient and flow regime being identical. Displacement vectors are found using a simulated 128^2 pixel sensor with parameters $N_x=N_y=N_z=64$, a pixel size of 1 micrometer ($64\mu\text{m}^3$ volume), particle diameter of 2 micrometer and a sensor distance of 0.1mm. The channel domain is used to simulate a single interrogation volume with 20 particles placed in it. The channel is simulated to have a mean velocity of $u_x=4000$, $u_y=2000$ and $u_z=-3000$ pixels/s. Randomly generated particle positions are moved by their local velocity with a time stepping of 0.001s. 5 different velocity gradients were separately superimposed on the mean velocity as portrayed in figure 12.

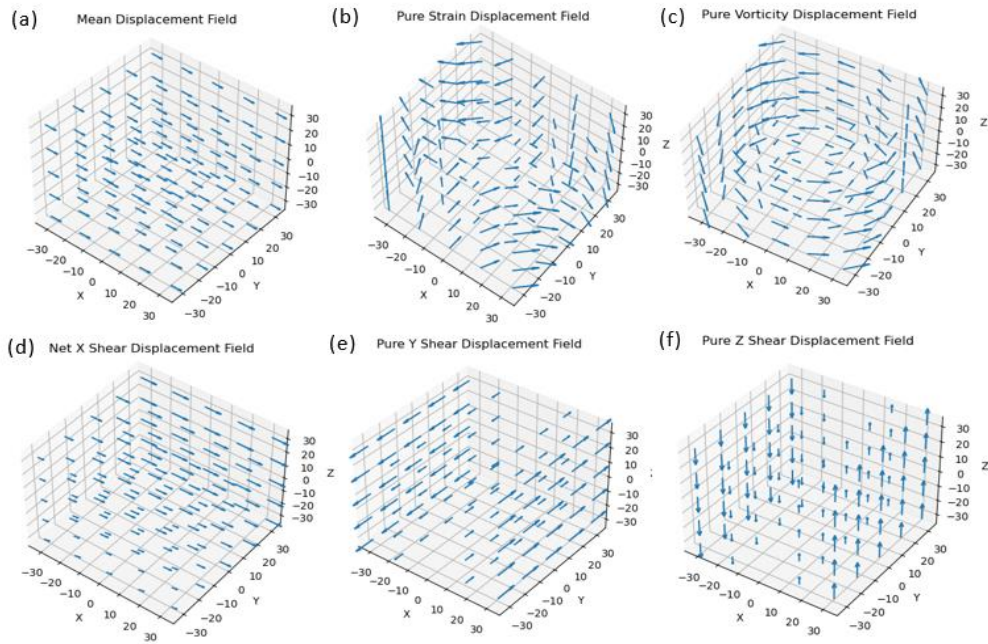


Figure 12: 3D displacement vector plot when subjected to (a) uniform mean velocity, (b) pure strain velocity, (c) pure vorticity, (d) pure x shear, (e) pure y shear and (f) pure z shear. The vector plots (b) - (e) are the vectors at $|\Delta u/u|$ ratio of 0.5 and have been scaled by a factor of 2 for visualisation.

The velocity gradients include a pure strain gradient (equal, constant and opposite s_{11} and s_{22} values), pure vorticity gradient (equal, constant, negative ω_{12} and positive ω_{21} values), and pure shearing velocity gradients in x (constant, positive $\frac{\partial u_x}{\partial y}$), y (constant, positive $\frac{\partial u_y}{\partial x}$) and z (constant, positive $\frac{\partial u_z}{\partial x}$) directions. The strength of each velocity gradient field is varied at $|\Delta u/u|$ values of 0, 0.05, 0.1, 0.2, 0.3, 0.4 and 0.5, each being repeated 100 times. The PIV displacement measurements are resolved using the sub-pixel cross-correlation method that places a 3D gaussian function at each particle center. The interrogation volume is then cross correlated across consecutive times to retrieve a mean velocity for the volume. The displacement of each individual particle is retrieved by cross-correlating its initial local volume with its predicted (via volume mean displacement vector) final volume. A detailed description of the technique was introduced by [6] and the results are shown in figures 13-16 below.

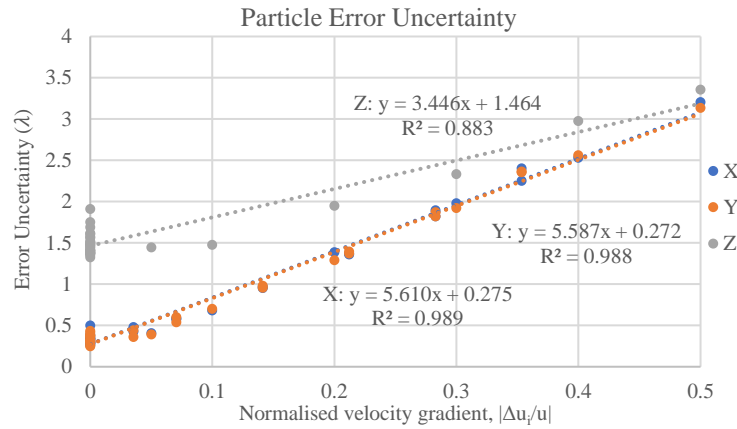


Figure 13: Compiled plot of particle displacement error uncertainty as a function of $|\Delta u_i/u|$ under all velocity gradient regimes, normalised by wavelength. Note that component-wise $|\Delta u_i/u|$ represents $|\Delta u_x/u|$ for the X series.

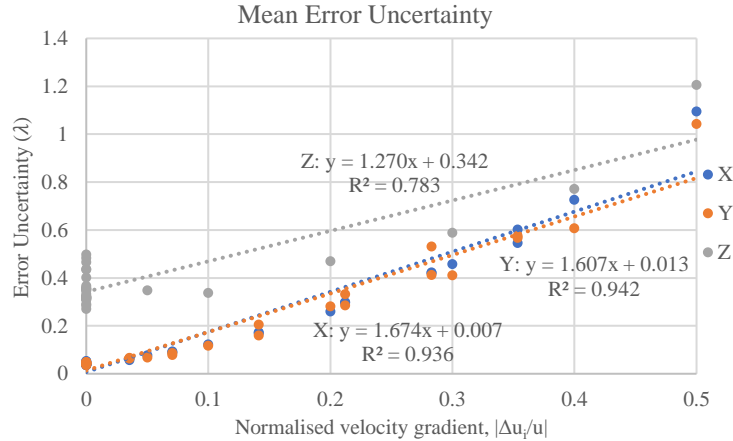


Figure 14: Compiled plot of mean displacement error uncertainty as a function of $|\Delta u_i/u|$ under all velocity gradient regimes, normalised by wavelength.

Figures 13 and 14 show that there is a strong correlation between displacement error uncertainty and the ratio $|\Delta u_i/u|$. The correlation in the x and y axes are the strongest (exceeding 0.9) whereas the correlation in z is approximately 0.8. The weaker correlation and slower error uncertainty growth can be explained by the large positional error uncertainties in the z axis. The weaker correlation in the z axis can also be attributed to the much fewer, 5 z directional velocity gradient cases being tested whereas the x and y axes each have 15 cases of varying velocity gradients, suggesting that further testing is necessary.

Moreover, it should be noted that for a uniform flow case, the particle displacement error uncertainty had values of 0.2639, 0.2526 and 1.3812 λ in x, y and z respectively, whereas the positional error uncertainty had values of 0.3469, 0.2499 and 1.6027 λ in x, y and z respectively, at the same particle concentration. The slight reduction in error uncertainty suggests that the positional errors themselves may not be random. Cancellation of errors may have occurred as performing addition of independently identical random variables during

displacement vector retrieval should result in $\sqrt{2}$ times the error uncertainty in position, contrary to the experimental data observed.

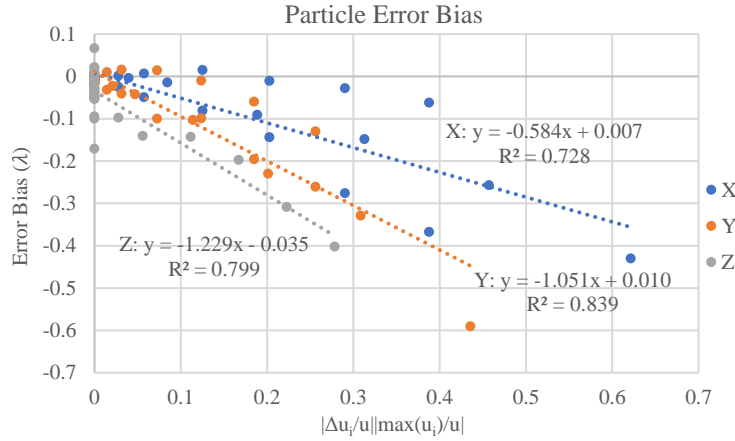


Figure 15: Compiled plot of particle displacement error bias as a function of $|\Delta u_i/u|$ under all velocity gradient regimes, normalised by wavelength.

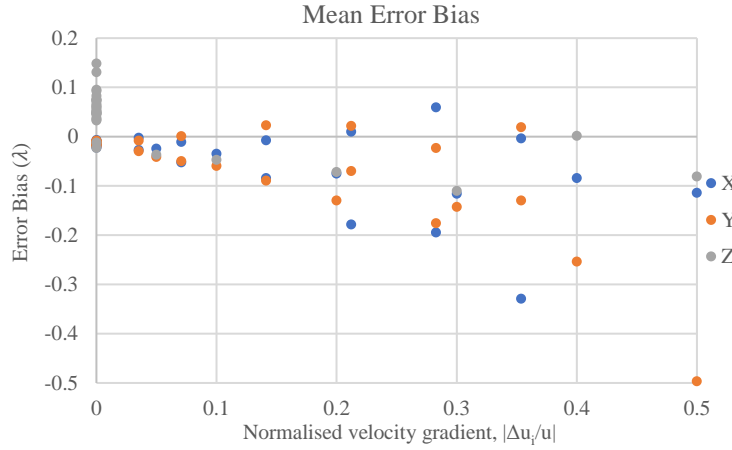


Figure 16: Compiled plot of mean displacement error bias as a function of $|\Delta u_i/u|$ under all velocity gradient regimes, normalised by wavelength.

Figure 15 shows that particle error bias is linearly, strongly correlated (approximately 0.8 correlation) to $|\Delta u_i/u| \max(u_i)/u$ in all axes, hence having a squared dependence on u_i . Larger $\max(u_i)$ and $|\Delta u_i|$ values on average increase how far the displacement values are underestimated. Figure 16 demonstrates that interrogation mean displacement is very weakly dependent on $|\Delta u_i/u|$ in all axes. This is within expectations, as the displacement biases of the interrogation volume are flow regime dependent.

VI. Conclusions

This project demonstrates that the improved 4D-DHPIV/PTV method can obtain positional error uncertainty values as low as 0.1052 , 0.0924 and 0.8573λ in x, y and z respectively. The positional error uncertainty values also increase with higher particle densities and decrease with larger diffraction pattern size, though potentially at the expense of particle detection rate. Additionally, the displacement error uncertainty and bias values increase as velocity gradients increase, as expected.

However, additional data collection is necessary to improve the reliability of positional error data as particle concentration is altered, as well as increasing the correlation of z displacement errors under a z directional velocity gradient. Further investigation into effects of sensor supersampling, pixel size and particle size on positional errors is also recommended to improve the understanding of the technique. Moreover, the algorithm can be improved through the application of machine learning to create more physically representative definitions of error, as the current definition (Eq. 8) does not properly account for the superposition of multiple diffraction patterns.

Acknowledgements

Y. J. Xia thanks Bihai Sun for the numerous, highly insightful discussion of ideas and Professor Julio Soria, for his general guidance and the access to the MonARCH supercomputing cluster.

References

- [1] Sun, B., Ahmed, A., Atkinson, C., and Soria, J., “4D Digital Holographic PIV/PTV with 3D Volume Deconvolution and Predictive Inverse Reconstruction,” *Measurement Science and Technology* [online journal], Vol. 31, No. 10, Paper 104002. DOI <https://doi.org/10.1088/1361-6501/ab8ee8> [retrieved 27 October 2020].
- [2] Atkinson, C., Coudert, S., Foucaut, J.M., Stanislas, M., and Soria, J., “The accuracy of tomographic particle image velocimetry for measurements of a turbulent boundary layer,” *Experiments in fluids* [online journal], Vol. 50, No. 4, pp. 1031–1056. DOI <https://doi.org/10.1007/s00348-010-1004-z> [retrieved 27 October 2020].
- [3] Soria, J., “Three-component Three-dimensional (3C-3D) Fluid Flow Velocimetry For Flow Turbulence Investigations,” *21st Australasian Fluid Mechanics Conference*, Australasian Fluid Mechanics Society, Adelaide, 2018.
- [4] Goodman, J., “Foundations of Scalar Diffraction Theory,” *Introduction to Fourier Optics*, McGraw Hill, New York City, 1996, pp. 55–57.
- [5] Latychevskaia, T., Gehri, F., and Fink, H.W., “Depth-resolved holographic reconstructions by three-dimensional deconvolution,” *Optics Express* [online journal], Vol. 18, No. 21, pp. 22527–22544. DOI [10.1364/OE.18.022527](https://doi.org/10.1364/OE.18.022527) [retrieved 27 October 2020].
- [6] Soria, J., “Particle Image Velocimetry - Application to Turbulence Studies,” *Lecture Notes on Turbulence and Coherent Structures in Fluids, Plasmas and Nonlinear Media*, edited by M. Shats, World Scientific, Singapore, 2006, pp. 307–347.

Performance Evaluation of Bio-mimicry inspired Whale's Fin in Cessna 172 Skyhawk Wing

Karan Kumar Shaw¹ and R. Vimalkumar²

SRM Institute of Science and Technology, Chennai, Tamil Nadu, 603203, India

This comprehensive review aims to provide a critical overview of the work on tubercles in the field of aviation. Biologists propose that the humpback whales are agile and able to perform loops and rolls due to the presence of protuberance in their fins. Protuberances on the leading edge of wings, also known as tubercles, offer several benefits during stall. Tubercles generate a unique flow control mechanism, offering the humpback exceptional maneuverability. A numerical study was performed on Cessna 172 Sky hawk's Wind Contrivances biomimicried into whales' fin to explore the aerodynamic coefficients at Reynolds number of 3×10^6 . The choice of optimal turbulence model is made by comparison of its aerodynamics characteristics calculated using three different turbulence models at ANSYS Fluent environment. Based on this computational study it can be concluded that Menter's Shear Stress Transport (K- ω SST) turbulence mode is most accurate in solving this kind of problems. The conventional wing of the selected Cessna model has its stalling angle at 18° which was further delayed to 20° degrees and it showed that the flow pattern over the tubercle wing is quite different. Research on the Tubercle Leading Edge (TLE) concept has helped to clarify aerodynamic issues such as flow separation. TLE shows increased lift by restricting spanwise separation. Analytically, for angles of attack ranging from 15° to 20° , tubercles increase lift and drag by 4-6% and by 1.7-1.9%, respectively, resulting in a 2-6% increase in the lift-to-drag ratio, and a 3% increase in the maximum lift-to-drag ratio. We have also checked for the variation in waves of tubercles for the possible scope to increase the aerodynamic efficiency.

I. Nomenclature

αAOA	=	Angle of Attack
C_L	=	Coefficient of Lift
C_D	=	Coefficient of Drag
LET	=	Leading Edge Tubercles
LEX	=	Leading Edge Extensions
P	=	Power Transmission
R/C	=	Rate of Climb
W	=	Weight of the aircraft
S	=	Planform Area of wing
η_p	=	Propeller Efficiency
ρ_∞	=	Density of free stream
L/D	=	Lift-to-drag ratio
K	=	Non-dimensional constant in induced drag
A	=	Amplitude of Wave in Tubercle
λ	=	Wavelength of Wave in Tubercle

¹ Undergraduate, Aerospace Department, and AIAA Student Member, 1083874.

² Undergraduate, Aerospace Department, and AIAA Student Member, 1204756.

- c = Chord of the wing
- C = Specific Fuel Consumption
- W_c = Weight fraction of aircraft in cruise profile

II. Introduction

Biomimicry is a method of finding inspiration by learning about natural designs, systems and processes for solving human problems. Nature has its own way of teaching us about building, processes, structures, and working. By learning how nature solves the problems that we face today, we can solve many of the problems that plague our environment. The Cessna model 172 Skyhawk is an American most popular four-seater, piston-engine, general aviation aircraft having accommodation of four. The aircraft was first launched in 1995 and has been in operation ever since. Most Cessna is made compared to other aircraft in history, about 43,000. The Cessna 172 Skyhawk is a training and teaching aircraft best known for its reliable flight features. The problem we focus on in this paper is the modification of the wing of Cessna 172 Skyhawk Wing and incorporating the tubercles of the humpback whale on to the wings to enhance its aerodynamics and fuel efficiency.

A. Humpback Whale Fins

Humpback whales are found in all deep oceans of the world. “*Megaptera novaeangliae*” is the Latin word meaning “New England’s great wing.” It was invoked owing to its giant pectoral fins, which usually grow up to 15 feet in height, because they were first spotted around the coast of New England by the European sailors. The acrobatics of humpbacks whale is makes them better than other aquatic animals [1]. It often reaches the ocean surface by hurdling belly-up thereby completely vacating its water, then rolling downwards and going to the surface with a loud smacking sound. On its way back deep into water, the animal arches its back and dives steeply forward, bringing its tail out and onto perpendicular to the water surface. These manoeuvres demonstrate its superior fluid dynamics capability and this ability has been accredited by the nature to the humpback whales through the use of its distinctive pectoral flipper. Tubercles i.e., the cavity shaped topology generate a unique mechanism of flow control, offering the humpback an exceptional manoeuverability. The leading-edge cavities act as devices which induces passive-flow control that improve the hydrodynamic performance and manoeuverability of the flipper [2]. Recent investigations of finite wing models have demonstrated that the tubercles produce a delay in the AOA until stall, which in turn maximizes lift and decreases drag. The flipper has several distinguishable characteristics; it has a unique planform shape which is quite flexible, along aspect ratio with the span being as much as 1/3 the body length of the whale, and large distinct tubercles shaped contours along the leading edge. The humpback whale flipper has a relatively large aspect ratio 6 and large-scale tubercles along the leading edge. There is variation of wavelength and amplitude of the waves [3] which constitute these tubercles on Leading side of flipper affect its flow properties, which are going to explore in this paper.

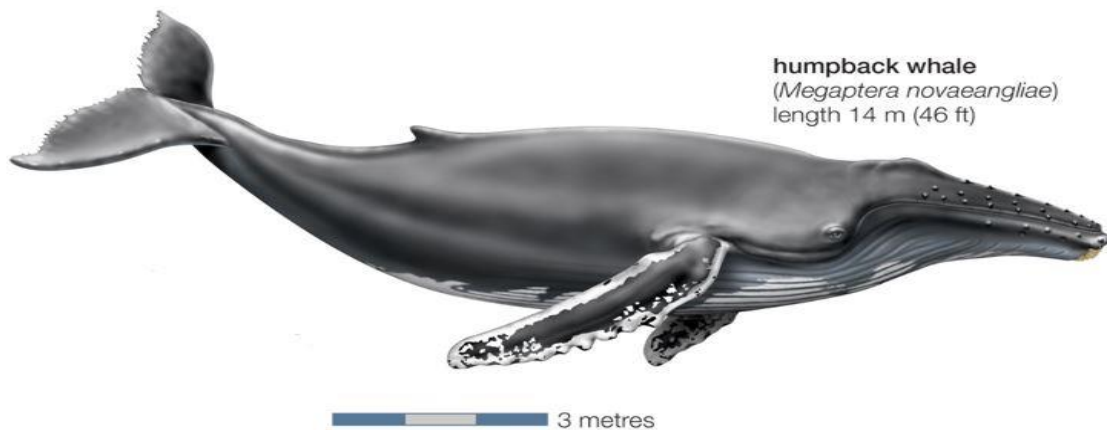


Fig. 1 Figure of Humpback Whale (*Megaptera novaeangliae*).

III. Literature Survey

Watt and Fish et al. [1] juxtapose the performance characteristics of a finite wing span having NACA airfoil of 5th series 63-021 between curved shaped tubercles and unmodified airfoil using a numerical technique. Their research showed a 4.8% lift surge up, 10.9% induced drag surge down, and 17.6% increment in lift-to-drag ratio L/D at a 10° AOA. It was culminated that tubercles have no such significant effect on drag at 0° AOA, but there was 11% rise in

form drag at a 10° AOA. The Reynolds-averaged Navier-Stokes was used with the identical airfoil at certain AOA. The streamlines images showed the formation of huge stream-wise vortices in the region of curves in tubercles. Reynolds number of numerical simulations was not clearly mentioned in their research.

Bolzon and Kelso et al. [2] discussed the tubercled effect on Swept Wing at very low angle of attack. He experimented with two different semi-span wings of Aluminium series 6061, one with smooth LE (leading edge) while the other was tubercled at an amplitude of 7.7mm. Force measurement was procured in Re of 221,000 for angle of attack extending from 1° to 8° . Through flow visualization techniques they observed that tubercles seem to act like vortex generators and there is a significant rise in the lift and drag forces with increment in Lift-to-Drag ratio. They concluded that their wing had produced induced drag at 0° due to symmetry of the airfoil, however when the leading edge was modified, it showed a 9.5% reduction in drag, which must be due to a backslide of the friction drag.

Miklosovic et al. [3] performed an experimental study where he compared the forces of idealized scale models redesigned into humpback whale flipper having airfoil NACA 0020 altered and unaltered with tubercles at Re ranging from 505,300-510,300. Their results divulged a 40% rise in stall angle, a 6% surge up in the maximum coefficient of lift. The lift-to-drag ratio was larger for the airfoils with tubercles for all angles except $10^\circ < \alpha < 12^\circ$. The researchers agreed with the correlation between tubercles and ordinary vortex generators that was aforementioned by Watt and Fish [1]. But later it was found that tubercles don't replicate vortex generators due to its aerodynamic characteristics in a higher angle of attack.

David Shormann et al. [4] investigated the performance of humpback whale -inspired short board surfing fins as it manoeuvres in the ocean's wave fieldwork. They reviewed different passive flow past humpback fins including leading edge tubercles and implemented them into surfboard fins. It was the first time when the tuberculated body was dynamically evaluated in all three axes. Researchers used standard instrumentation such as GPS & 9-axis motion sensors to collect survey data and it was attached to truster style 3-fin configurations designed at low aspect ratio. The deduced that shortboards equipped with LE design showed a ubiquitous increase in characteristics, i.e. 89% of the performance means improvement in results, with 44% of these being statistically important. It was also inferred that these modified fins would actually improve a surfer's performance.

Velkova and Branger et al. [5] tried to establish the best turbulence models in ANSYS Fluent 18 for the purpose of studying the aerodynamic features of aircraft wing airfoil NACA 2412. They performed the numerical analysis of typical airfoil of Cessna 172 sky hawk at Reynolds Number of 3×10^6 in three different turbulence model namely Spalart-Allmaras, $k-\omega$ SST model, and DES $k-\omega$ SST model models with CFD code Fluent. They finally concluded that the DES $k-\omega$ SST model was the most appropriate approach as it showed results close to theoretical calculations with some inaccuracy. Nevertheless, their results of 57% for stall angle isn't representative of the real environment in which the airfoil is immersed and they considered the wing speed to be uniform which was inappropriate.

IV. Methodology

A. CAD Modelling

The wing CAD was designed in SOLIDWORKS 2020. The basic dimension of Cessna 172 wing span - 35 feet 10 inches, Root chord – 5 feet 4 inches, Tip chord – 3 feet 8.5 inches. These dimensions were used to make a half span unmodified wing which was used to establish proper values for the simulation. The dimensions of the tubercles of the whale was scaled approximately to the size of our wing. Many variations were simulated to give the best results.

Table 1. The variation in Leading Edge with respect to Amplitude and Wavelength

Amplitude (A) / chord (c)	Wavelength (λ) / chord (c)	Amplitude (A) / Wavelength (λ)	Tag
0.082	0.307	0.266	A2 λ 7.5
0.086	0.307	0.254	A4 λ 7.5
0.089	0.369	0.241	A6 λ 15
0.089	0.399	0.223	A6 λ 30
0.089	0.43	0.207	A6 λ 60
0.09	0.461	0.206	A8 λ 62

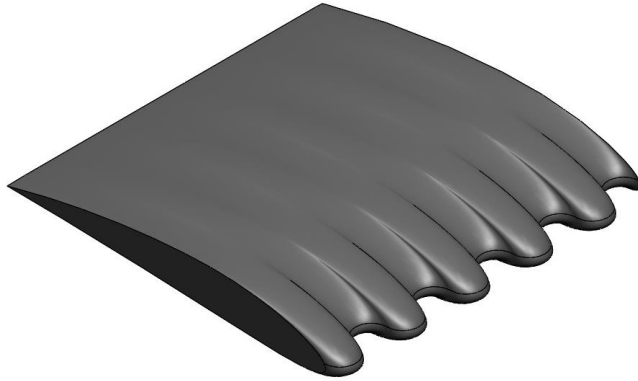


Fig 2. Isometric View of CAD Model of Wing Section

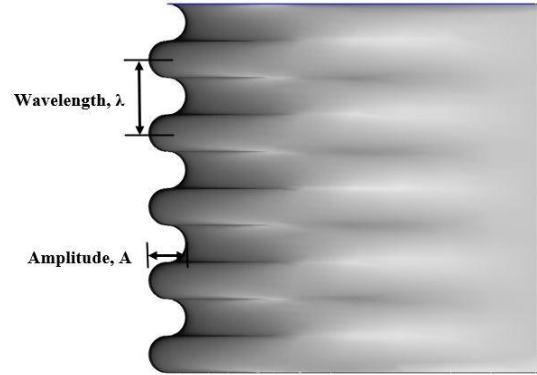


Fig 3. Top View of Wing Section

B. Meshing

A mesh quality plays a crucial role in the precision and efficiency of the numerical study. We should strive to maintain an optimal balance between the computational cost and the level of fineness achieved. Henceforth, we decided to use ICEM platform as it provides a fine mesh with lesser elements and better controllability in mesh quality. The CAD model of the Cessna Wing is imported into ICEM CFD in IGES format. The following images imprints the section view of the boundary box showing the detailed meshing in and around the Cessna 172 wing. Special attention is the leading edge of wing since it is our area of interest.

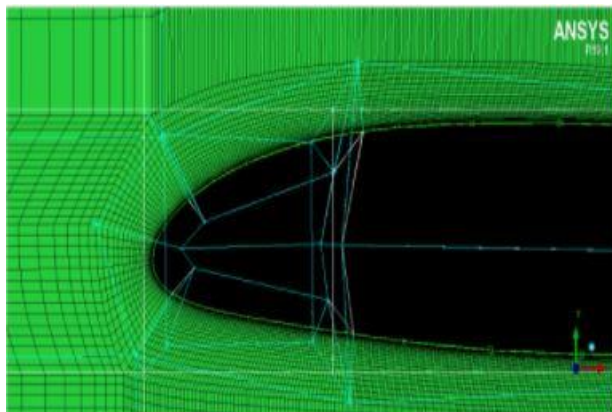


Fig 4. Applying Y+ values near surface of wing

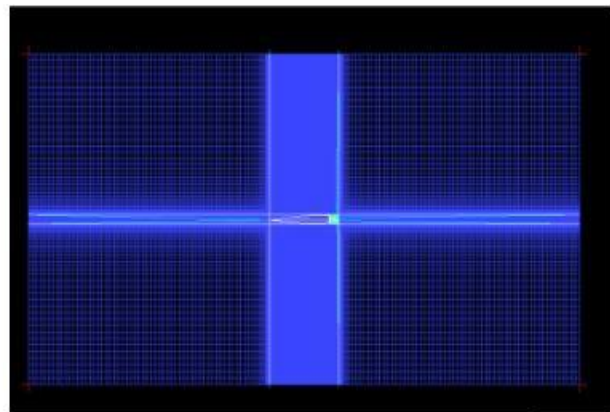


Fig 5. Overall Meshing view of boundary box

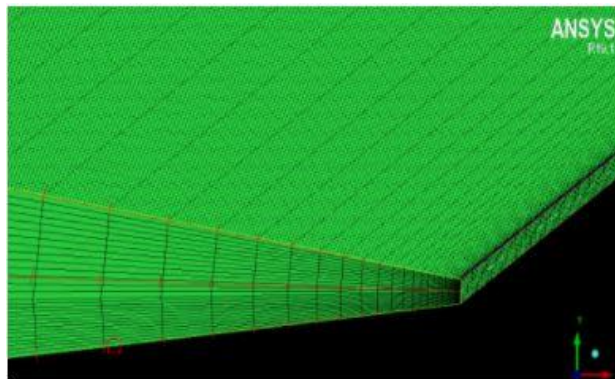


Fig 6. Meshing Refinement at trailing edge

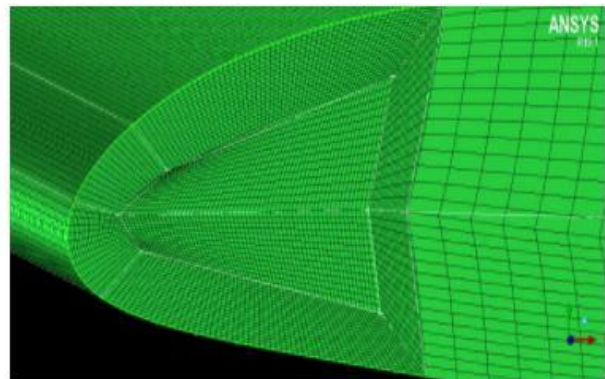


Fig 7. Meshing Refinement in leading edge

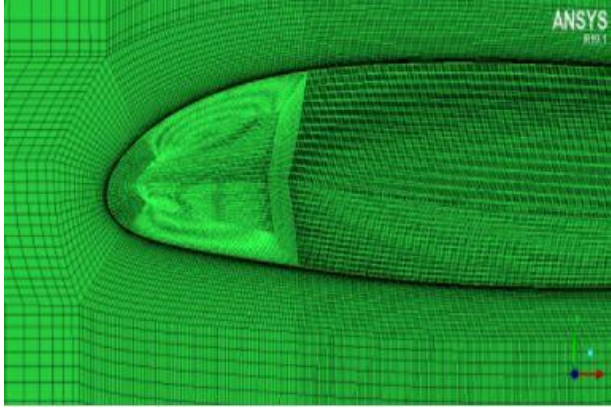


Fig 8. Grid Formation around the airfoil shape

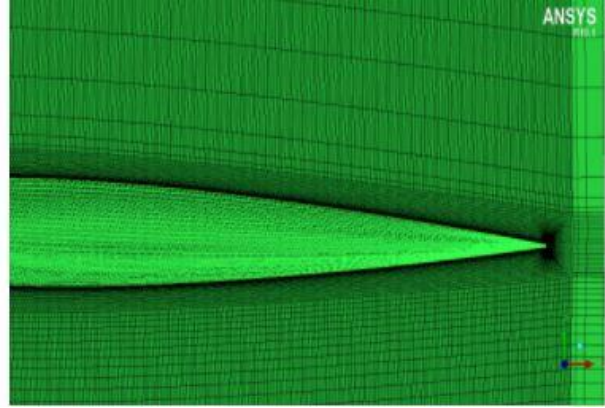


Fig 9. Refinement close to the surface of wing

C. Simulation

The simulations were performed in the ANSYS 19.1 CFD Fluent. The first part of simulations to select the correct viscous model for our research. Next part to compare the normal Cessna wing with wing modified with Leading Edge extensions for both 2D & 3D cases by simulating the model under cruising conditions.

1. Preprocessing

The pre-processing starts with defining the appropriate boundary box (28.2m x 19.74m x 34m) inside the ICEM CFD, which was then uploaded in the CFD Fluent. In Meshing setup, the quality of mesh was verified by skewness & Orthogonality. Under the Fluent setup section in the general tab we have specified the type of solver as pressure - based because Cessna 172 operates in subsonic regime and time as steady. The default values of density and viscosity of the air were considered. The basic criterion stowed to meet are the residual RMS error values should be at least 10^{-4} and overall imbalances inside the domain should be less than 1% for all the variables [6]. The grid independent study was performed until the force coefficient became independent of meshing refinement. The basic boundary conditions involved were the cruising speed (80 m/s) of the Cessna at inlet while the zero-gauge pressure at outlet. The same conditions were maintained for different turbulence models in order to select the most fitting one.

2. Choosing the appropriate Turbulence model

1) Spalart-Allmaras Model

Spalart-Allmaras models can be applicable for low-Reynolds numbers, it uses a single equation to solve the kinematic eddy turbulent viscosity. It mainly focuses on the region where shear dominates. On the other hand, this particular model cannot determine the behaviour of flow in separation and decaying turbulence as well.

2) k- ω SST Model

It comes under Reynolds-averaged Navier-Stokes (RANS) group. In this turbulence model two transport equations will be used, which will predict the energy in turbulence and specific turbulent dissipation rate. These two parameters will help to estimate the rate of dissipation in per unit turbulent kinetic energy [5]. This model can be used in the condition where the relative boundary layer is thicker at low Reynolds numbers, due to which this Turbulence model is mostly suggested for predicting the flow characteristics near the wall. Even though the boundary layer is under adverse pressure gradients and separations, this turbulence model predicts the early separations of the flow. In addition, $k-\epsilon$ characteristics will improve the inlet free stream turbulence properties [8].

3) Detached Eddy Simulation k- ω SST Model

This model is known for reducing the turbulent viscosity in the particular area where large turbulence models have fine mesh. It is mostly based on the K- ω SST which deals with the flows with pressure induced separation and adverse pressure gradient flows as well. It is actually a mix of two types of turbulence models namely k-epsilon and the k-omega, which is mostly used in both outer region of the boundary layer and in the inner part as well. Blending functions are used to switch between the two formulations in order to solve the transport equations. The main advantage is using two different models at two different regions, so that each turbulence model will have its own strength and weakness.

We compared these three models under the same boundary conditions and the $k-\omega$ SST is most appropriate for it illustrates behaviour close to the theoretical approach especially at stalling angles.

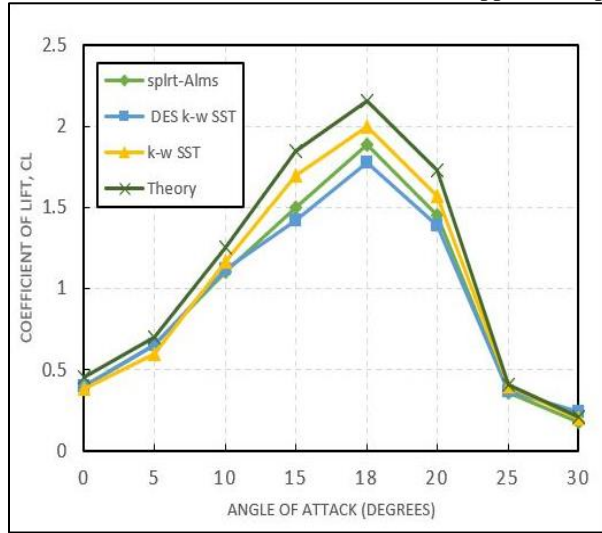


Fig 10. Comparing the C_L for different turbulence model along with theoretical calculation

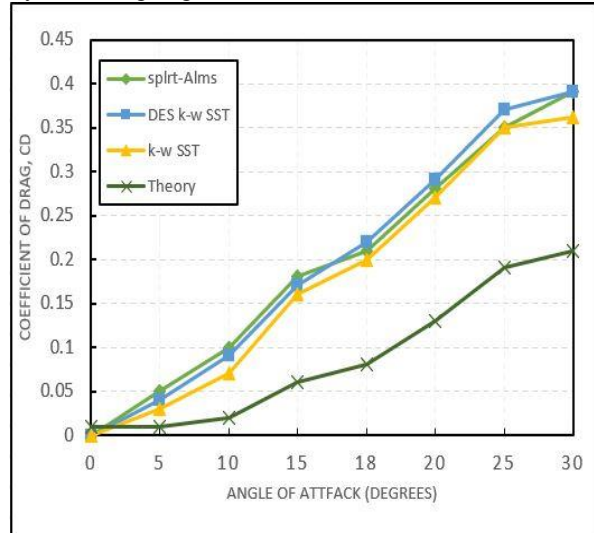


Fig 11. Comparing the C_D for different turbulence model along with theoretical calculation

V. Results

A. Document Contours & hydrodynamic Flow Pattern of Wing with Leading Edge Tubercle (LET)

The images show the contours of pressure distribution & streamlines across a small wing section with LETs. The images obtained as a result of post-processing in ANSYS Fluent 19.

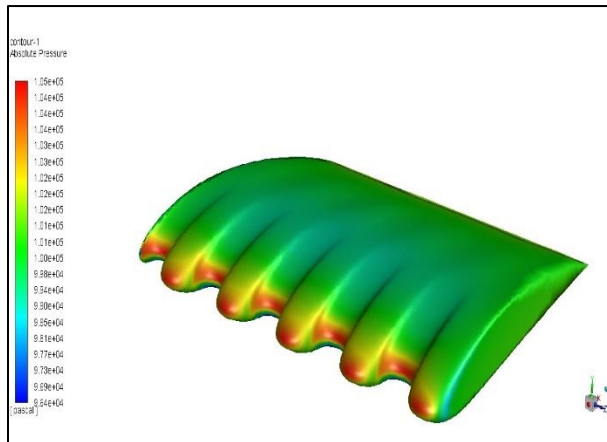


Fig 12. Comparison of C_L for both 2D & 3D Wings of Different Leading Edge

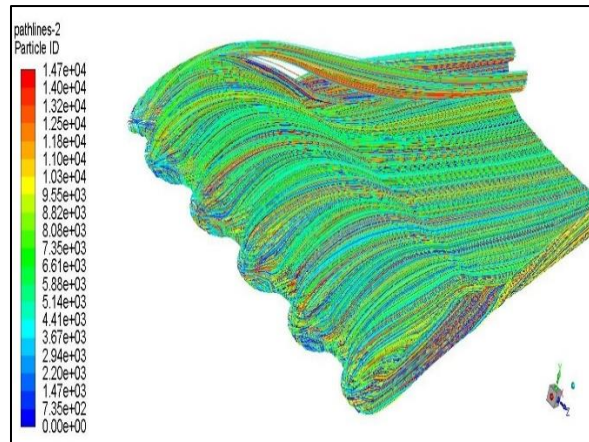


Fig 13. Comparison of C_D for both 2D & 3D Wings of Different Leading Edge

B. Nomenclature Comparison of Unmodified Wing to Wing with Leading Edge Tubercle (LET)

Detailed collation of the nominally unmodified wing at both two-dimensional (2D) and three-dimensional (3D) shows the potent angle of attack and the maximum coefficient of lift are due in 3D case due to skin friction drag & downwash [9]. Lift plots are linear with the increasing angle of attack till $\alpha = 4^\circ$.

It was observed through numerical study that even the smallest amplitude and smallest wavelength tubercle demonstrates better aerodynamics characteristics. The stalling characteristics which typically starts at $\alpha = 18^\circ$ was delayed to $\alpha = 20^\circ$, for 3D wing [5]. There might be a little decrease in lift for LET wing, the Lift -to-drag ratio is more for LET wing than unmodified wing. There is trifling difference in the proportion of drag for 3D and 2D NACA

2412 wings at lower angle of attack. As the AOA increases, there is reduction in drag LET modified wing typically at $\alpha = 14^\circ$. However, as the stalling angle approaches, the airfoil with modified LET experiences increase in Drag. Therefore, the differences in performances of wings with tubercles is similar for both 2D and 3D bodies suggesting there is no additional benefit for finite wings with tubercles.

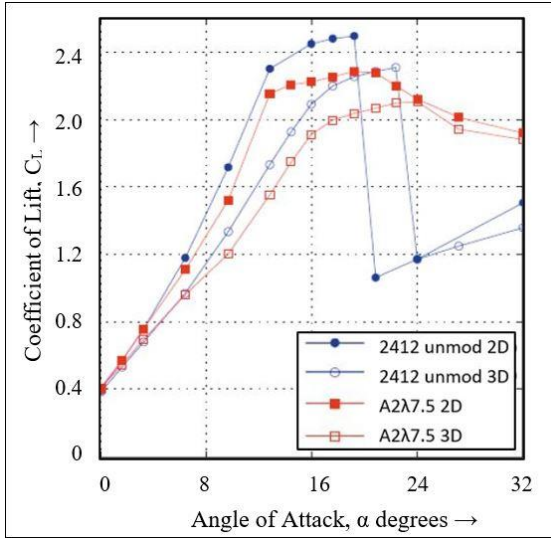


Fig 14. Comparing the C_L for both 2D & 3D Wings of Different Leading Edge

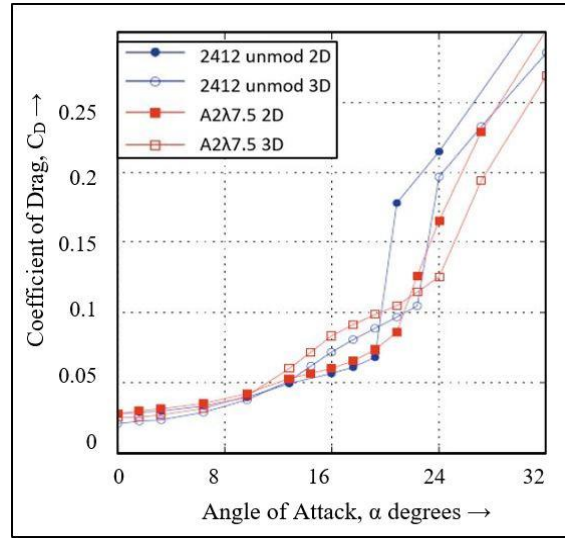


Fig 15. Comparing the C_D for both 2D & 3D Wings of Different Leading Edge

C. Change in force Coefficients due to Variation in Tubercle Amplitude

The 2D and 3D NACA 2412 wing modified with LET having fixed wavelength while the amplitude is diversified. It is noticed that in smaller amplitude, there is the significant increase in maximum lift coefficient at $\alpha = 12^\circ$, around stalling angle in addition to post-stall lift at $\alpha = 24^\circ$ are both finite & infinite cases. There is high interconnection between the lift characteristics for full-length and half-length airfoils for tubercled arrangement [11]. At lower AOA, the LET wing with sizeable amplitude has slightly elevated drag value. The 2D airfoil experiences a bigger amount of drag at low amplitude when stall angle approaches. The behaviour pattern is more pronounced in 3D at higher angle attack. This occurs due to downwash effects due to delayed stall which happens in the 3D wing.

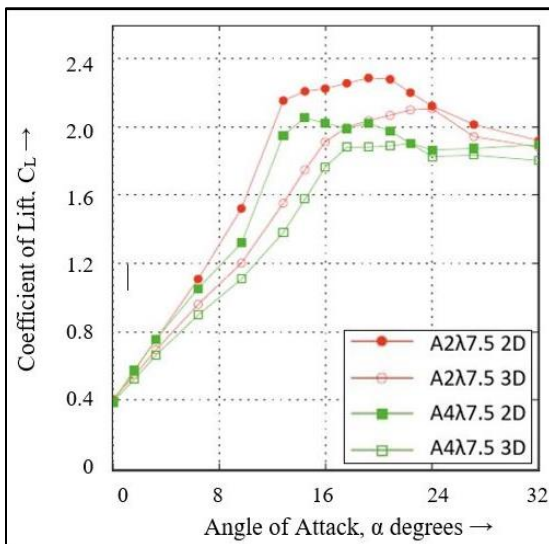


Fig 16. Comparing the C_L for both 2D & 3D Wings of Different LET Amplitude

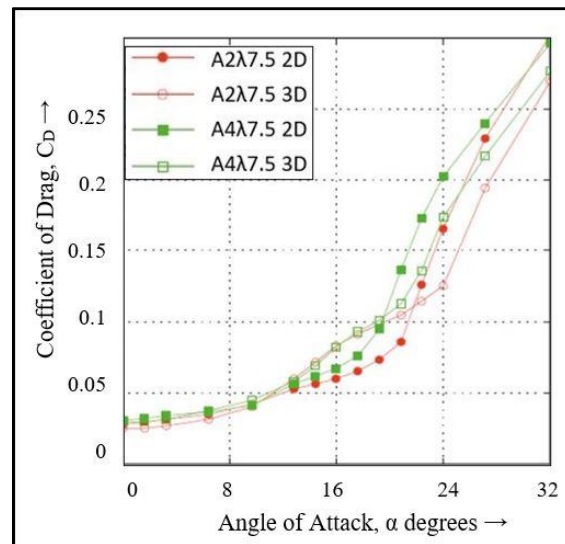


Fig 17. Comparing the C_D for both 2D & 3D Wings of Different LET Amplitude

D. Change in force Coefficients due to Variation in Tubercle Wavelength

Through previous study, we noted that as the cavity between consecutive tubercled leading edge decreases, the aerodynamic properties enhances. Nevertheless, through our research, we found that it is true upto certain point after which further chopping down the wavelength will lead to decrease in performance trait. For the current research, it is spotted that, tubercle with A/c of 0.089 showed the most optimized aspect in designation of maximum coefficient of lift, lowest vale of drag and topmost possible stalling-lift accomplished at wavelength, $\lambda/c=0.369$.

The graph advocates that the wing with the largest wavelength encounters early stalling, which is defined as the unexpected loss of lift. Yet, this pattern is not followed in the lowest wavelength. Similar attributes were also observed in 2D airfoils. This suggests that wingtip has almost trivial effect on wavelength variation. The drag differences were eminent for varying wavelength LET wings nearby stalling angle. Stall occurs earlier for large wavelength tubercles, the point at which higher drag increment occurs at lesser angles [15]. The optimized tubercle design in form of lowest drag for greater ranges of AOA is identical to same configurations that demonstrated better lift characteristics.

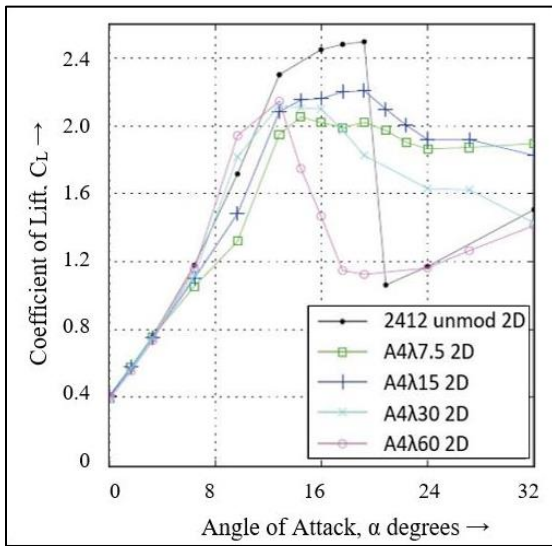


Fig 18. Comparison of C_L for 2D Wings having Variations in LET Wavelength

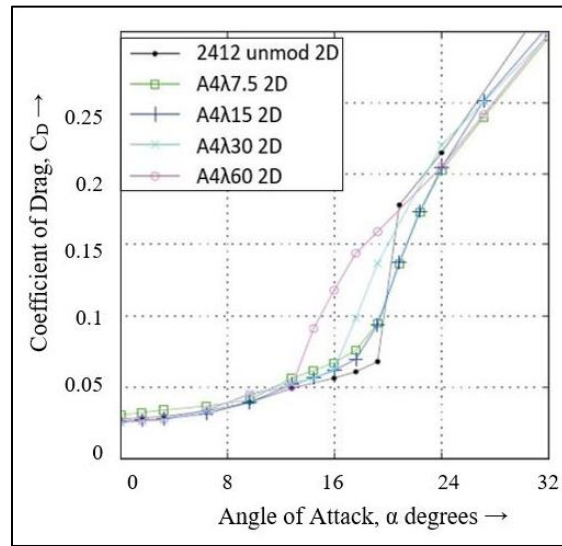


Fig 19. Comparison of C_D for 2D Wings having Variations in LET Wavelength

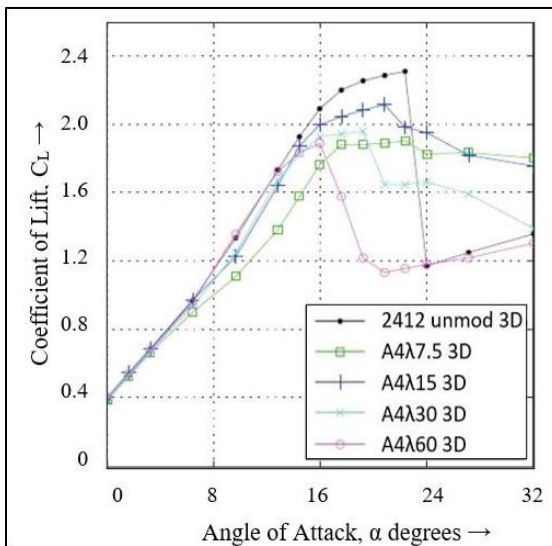


Fig 20. Comparison of C_L for 3D Wings having Variations in LET Wavelength

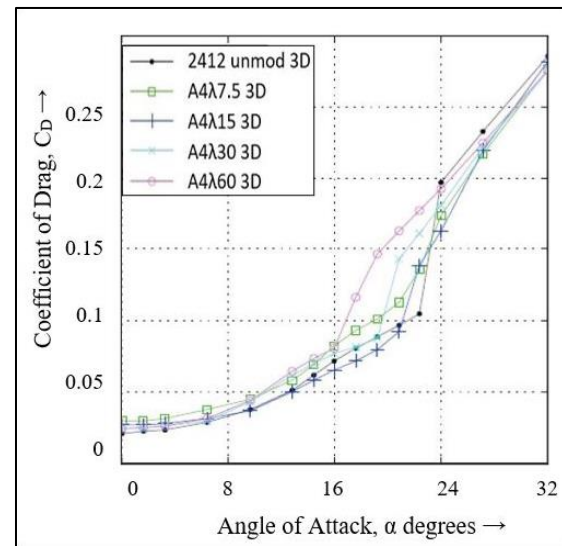


Fig 21. Comparison of C_D for 3D Wings having Variations in LET Wavelength

E. Effect of Bio-Inspired Technology on Cruise Performance and Rate of climb (RoC) of Cessna

The vertical component of velocity with which an airplane climbs up in the air is apparently called the Rate of Climb. RoC depends on several factors and its dependency varies with the type of aircraft like jet, propeller driven etc. Cessna 172 Skyhawk is a propeller driven aircraft and its equation of rate of climb is given by:

$$(\text{RoC})_{\max} = \frac{\eta_p P}{W} - \left[\frac{2}{\rho_{\infty}} \sqrt{\frac{K}{3C_{D,0}}} \left(\frac{W}{S} \right) \right]^{1/2} \frac{1.155}{\left(\frac{L}{D} \right)_{\max}} \quad (1)$$

This implies that with increase in lift-to-drag rate, the negative component of the right-hand side decreases, thereby increasing the RoC. Based on previously obtained results, we found that wing refashioning with leading edge extensions of certain wavelength & amplitude demonstrates a rise in maximum L/D ratio. Therefore, the change in Rate of Climb is addressed through the graph.

Cruise is that phase of flight profile when aircraft moves with level altitude before it begins to descend. In this phase, the pilot decreases the power, the rpm of the propeller decreases, the weight fraction of aircraft is more dependent on lift-to Drag ratio than thrust. The equation that vividly describes the weight fraction in cruise phase.

$$W_c = \exp\left(\frac{-RC}{V\left(\frac{L}{D}\right)_{\text{cruise}}}\right) = \text{values} \quad (2)$$

So, with the increment in lift-to-drag ratio, we find that the denominator on the left-hand side increases which in turn decreases the weight fraction in the cruise region. Therefore, the amount of fuel required to maintain level altitude decreases. The fuel consumption in terms of gallons per hour is compared for both normal & modified wings. For propeller driven aircraft, the L/D ratio in the loiter phase happens to be 86.6% of the L/D ratio in the cruise phase. So, arguably, there are some economizing in fuel consumptions in those phases of profile where L/D ratio is the significant factor.

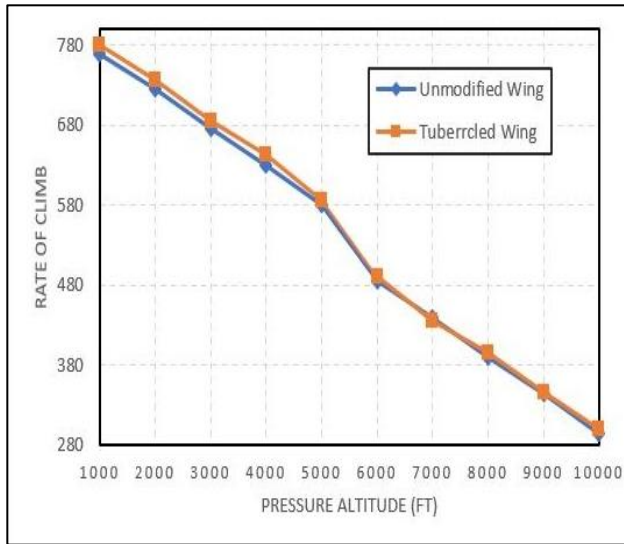


Fig 22. Comparison of Rate of Climb between Normal & LET wing of Cessna 172

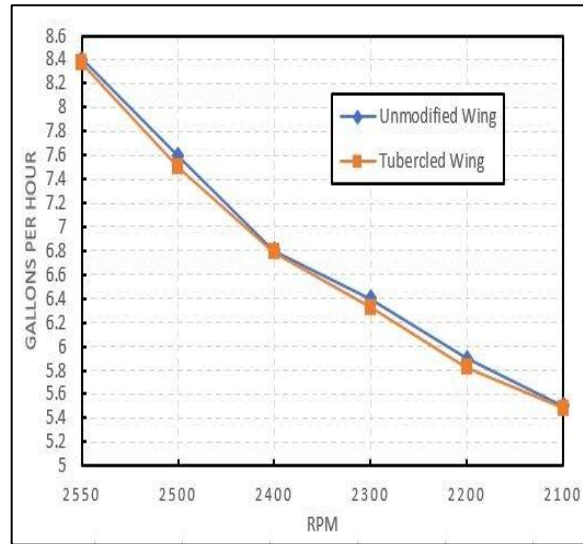


Fig 23. Comparison of Fuel Consumption between Normal & LET Wing at 2000 ft Altitude

F. Effect of Tubercle on Pressure drag, Friction drag & Induced drag

At zero-degree angle of attack, tubercled wing shows reduction in drag, it must be because of pressure drag or skin-friction drag. From streamline's contours, it is observed that vortices move away from each other having recurrent downwash, while exactly opposite happens with a recurrent upwash [16]. Therefore, the expected net outcome of tubercle is to enlarge the total boundary layer momentum, thereby reducing the pressure-drag. At lower AOA, pressure drag is usually less than friction drag. Therefore, it is unclear that overall drag reduction is accompanied with reduction in friction drag. The strength of the vortex at wingtip directly indicates the magnitude of induced drag. The pressure

distribution figure shows the reduction in magnitude of the tip vortex of wing. Therefore, there has to be the reduction of induced drag due to the presence of tubercles [17].

VI. Conclusion

Through literature, we noted that redesigning the leading edge with tubercles had shown significant performance enhancement in [9, 11, 12, 15]. However, the other previous researches didn't show such optimistic results [2, 5, 6, 7]. The important factor due to difference in aerodynamic results for former & latter research is the wingtip. In the former cases, the wings were infinite while in later cases, the wings were semi-infinite. This clearly indicates that the effect of tubercles is comprehend better for three -dimensional cases. All the studies done in this paper related to the aerodynamic characteristics were carried out at $Re \geq 300,000$.

The case study of a simple NACA 2412 wing of Cessna Skyhawk remodeled with leading edge tubercles showed quality performance improvement. This augmentation in aerodynamics characteristics are of the same nature for both full spans and half-spans with no swept & taper. We have also observed that alteration of tubercle amplitude (A) and wavelength (λ) steers the changes in aerodynamic traits for the half-span length and full-span length wings. In both of the cases, the best configuration was with the smallest amplitude and certain range of wavelength.

The hydrodynamic flow pattern was found to be intriguing and different from the conventional flow over the wing. The coefficient of lift was little higher when the 2D wing is compared to modified 2D airfoil conversely, the 3D modified wing showed high lift values (4%-6%) when compared with its conventional equivalent. But for both 2D and 3D wing, there was an increase in L/D ratio when its leading edge had tubercles by 2%-6%. There was increase in stalling angle from $\alpha=18^\circ$ to $\alpha=20^\circ$, thereby, indicating that boundary layer separation closing to the stalling angle was delayed. There might be increase in drag, typically at $\alpha=10^\circ$ for both 2D and 3D models but they eventually decreased with increase in angle of attack. The consequences of tubercle on various type of drag is also being reflected.

We found through performance calculation in Cessna that this bio-inspired technology escalates the cruise & RoC performance of aircraft. In other words, with this improvised technology, we do have a scope to reduce the amount of fuel burned to reach a certain altitude or cover a certain range, even though the amount of fuel saved is trivial. Other factors which can be taken into account when working is the three-dimensional effect of the sweep and taper ratio. It is believed that success of tubercles is somewhat connected to stall progression along span-wise and it ought to offer more benefits with swept & tapered wing having larger amounts of spanwise flow.

The ability of tubercle technology to alter fluid flows around any curved structure thereby, delaying the boundary layer separation which results in increase in lift & reduction in drag at same time has found several applications in recent researches. These bio-inspired flippers were found to be much useful in marine based control surfaces like rudders of boats, propellers, stabilizers, fans etc. Many Surfboard fin is improvised on its Leading edge like that of whale's flippers and a field test shows the increase in the performance of the surfer. The Wind Energy Institute of Canada has developed windmill blades utilizing the Leading-Edge Tubercle and at moderate wind speeds, it appears to indicate better electrical output than its equivalent standard windmill.

References

Proceedings

- [1] Watts, P. and Fish, F.E., "The influence of passive, Leading Edge Tubercles on Wing Performances" proceedings of *Unmanned Untethered Submersible Tech.* (UUST), Durham, NH, Aug 2001.
- [2] M.D. Bolzon, R.M. Kelso and M. Arjomandi, "The effect of Tubercles on Swept Wing Performance at Low Angles of Attack", *Australian fluid Mechanics Conference*, December 2003.

Books

- [3] Miklosovic, D.S & Murray, M.M., Howle, L.E., and Fish, "Leading Edge Tubercles Delay Stall on Humpback Whale Flippers", *Physic Fluids* 16(5): L39-L42,2004.

Reports, Theses, and Individual Papers

- [4] David Shormana and Marc in het Panhuis, "Performance Evaluation of Humpback Whale-Inspired Shortboard Fins based on Ocean Wave Fieldwork" PLoS ONE 15(4): e0232035, Texas, April 2020.
- [5] Cvetelina Velkova, Terence Branger, Francesco Motta Calderon and Camille Soulier, "The Impact of different turbulence models at ANSYS Fluent over the aerodynamic characteristics of Ultra-light wing airfoil NACA 2412", *Journal of Aerospace Engineering*, 2014.
- [6] Fish FE, Battle JM., "Hydrodynamic design of the humpback whale flipper.", *J of Morphology*. 1995;225: 51-60.
- [7] Bushnell DM, Moore KJ., "Drag reduction in nature.", *Ann Rev Fluid Mech*. 1991;23: 65-79.

- [8] Aftab SMA, Razak NA, Mohd Rafie AS, Ahmad KA., “Mimicking the humpback whale: An aerodynamic perspective.”, *Progress in Aerospace Sciences*. 2016; 84:48–69.
- [9] Kaya M, Elfarrar M., “Effect of taper distribution on the torque and thrust generated by a wind turbine rotor blade.” *Proc of the 10th International Renewable Energy Congress*, Sousse, Tunisia, 26–28 March 2019.
- [10] Shormann DE, in het Panhuis M. Performance evaluation of a humpback whale-inspired hydrofoil design applied to surfboard fins. *Proc of OCEANS 2019 MTS/IEEE Seattle*. 2019.
- [11] Wang Y, Zhao K, Lu XY, Song YB, Bennett GJ., “Bio-inspired aerodynamic noise control: a bibliographic review.”, *Applied Sci*. 2019;9, 2224.
- [12] Rocha FA, de Paula AA, Cavaliere AVG, Kleine VG, Sousa MS., “Lift enhancement by wavy leading edges at Reynolds numbers between 700,000 and 3,000,000.” *AIAA Aviation Forum*, Atlanta, Georgia, USA, 25–29 June 2018.
- [13] Butt FR, Talha T., “A parametric study of the effect of leading-edge tubercle geometry on the performance of aeronautic propellers using computational fluid dynamics (CFD).” *Proc of the World Cong on Eng. Vol II, London, UK*, 4–6 July 2018.
- [14] Stein B, Murray MM., “Stall mechanism analysis of humpback whale flipper models. Unmanned Untethered Submersible Technology (UUST).” *Autonomous Undersea Systems Inst., Lee, NH*, Aug. 2005.
- [15] Hansen KL, Kelso RM, Dally BD., “Performance variations of leading-edge tubercles for distinct airfoil profiles.”, *AIAA Journal*. 2011;49(1): 185–194.
- [16] Stanway MJ., “Hydrodynamic effects of leading-edge tubercles on control surfaces in flapping foil propulsion.”, Master’s Thesis, Massachusetts Institute of Technology. 2008.
- [17] Johari H., “Applications of Hydrofoils with Leading Edge Protuberances.”, Final Technical Report for the Office of Naval Research contract N00014-08-1-1043. 2012.
- [18] Levshin A, Custodio D, Hensch C, Johari H., “Effects of leading-edge protuberances on airfoil performance.”, *36th AIAA Fluid Dynamic Conference and Exhibit*, 2006.
- [19] Edel RK, Winn HE., “Observations on underwater locomotion and flipper movement of the humpback whale *Megaptera novaeangliae*.”, *Marine Biology*, 1978;48: 279–287.
- [20] Jurasz CM, Jurasz VP., “Feeding modes of the humpback whale, *Megaptera novaeangliae*.”, *Southeast Alaska Sci. Rep. Whales Res. Inst.* 1979;31: 69–83.
- [21] Hain JHW, Carter GR, Kraus SD, Mayo CA, Winn HE., “Feeding behaviour of the humpback whale, *Megaptera novaeangliae*”, in the *Western North Atlantic. Fishery Bulletin*, 1982;80(2); 259–268.
- [22] Fish FE, Howle LE and Murray MM., “Hydrodynamic flow control in marine mammals.”, *Integral. Comp. Biology*, 2008;48, 788–800. pmid:21669832.

Powerplant Hybridization of a High-Altitude Mountain Rescue Helicopter

Jarrold C. Moonen¹

RMIT University, Melbourne, Victoria, 3000, Australia

I. Nomenclature

A	=	Portionality Coefficient
B	=	Portionality Coefficient
E	=	Energy
g	=	Gravity
I	=	Electric Current
m	=	Mass
$P2W$	=	Power to Weight Ratio
$PSFC$	=	Power Specific Fuel Consumption
R	=	Ideal Gas Constant
T	=	Temperature
t	=	Time
V	=	Voltage
v	=	Velocity
W	=	Weight
ρ	=	Density
μ	=	Figure of Merit
η	=	Efficiency

II. Introduction

The world's highest peak, Mt. Everest, stands 8848m tall, while the current record for the highest rescue by use of a rotorcraft is 7010m, completed in 2010 by Daniel Aufdenblatten on Nepal's Annapurna Summit Trek [1]. This leaves a zone of 1838m for which rescue by helicopter is not available to trekkers, leading to what may have been the otherwise preventable deaths of almost 300 trekkers on Mt. Everest alone in the past half- century [2].

The challenges facing rotorcraft at these altitudes are primarily economical; while it can be analytically shown that a specialist rotorcraft can perform a rescue at these altitudes this rotorcraft would need to be exceedingly light with a powerplant comparable to a military-grade heavy lift helicopter. This excessive level of power is due to the power-lapse experienced by any combustion-based engine in a low-oxygen environment. This results in a poor fuel consumption in low-power legs of the rotorcraft's mission profile as well as a grossly oversized powerplant for all mission legs but the final rescue.

It is perceived that the excess mass associated with an excessively overpowered turboshaft engine could be offset by the implementation of a hybrid-electric powerplant, such that the vehicle could operate only under power of a justifiably sized turboshaft engine for all low-power mission legs before supplementing the maximum power output with an electric engine for the high-power final rescue operation, where the electric power is not sensitive to the low atmospheric density that plagues combustion engines at altitude. This may not only decrease the mass of the powerplant but also improve the fuel economy of the vehicle by allowing the turboshaft engine to operate at closer to its nominal state for a longer period of the mission.

Therefore, a model was developed to perform a trade-off between a turboshaft engine and electric motor hybrid powerplant with the objective of minimizing powerplant and power source weight. It shall be initially sized under the following assumed mission profile: Take off at 1402m with 405kg payload, climb to 3780m, cruise for 135km, land, refuel. Takeoff at 3780m, climb to 8870m, cruise 28km, hover for 30 minutes, take on an additional 170kg payload to rescue the climber, cruise 28km, descent to 3780m, land, refuel. Takeoff at 3780m, cruise for 135km, descend to 1402m, land.

The results of the model shall be presented alongside those for the same helicopter powered exclusively by means of a turboshaft engine do demonstrate any mass savings, if available. The model enables the identification of technologies that may further increase the mass savings generate a technology roadmap that may enable the development of this life- saving vehicle.

¹ Undergraduate Aerospace Student, RMIT School of Engineering, AIAA Student Member

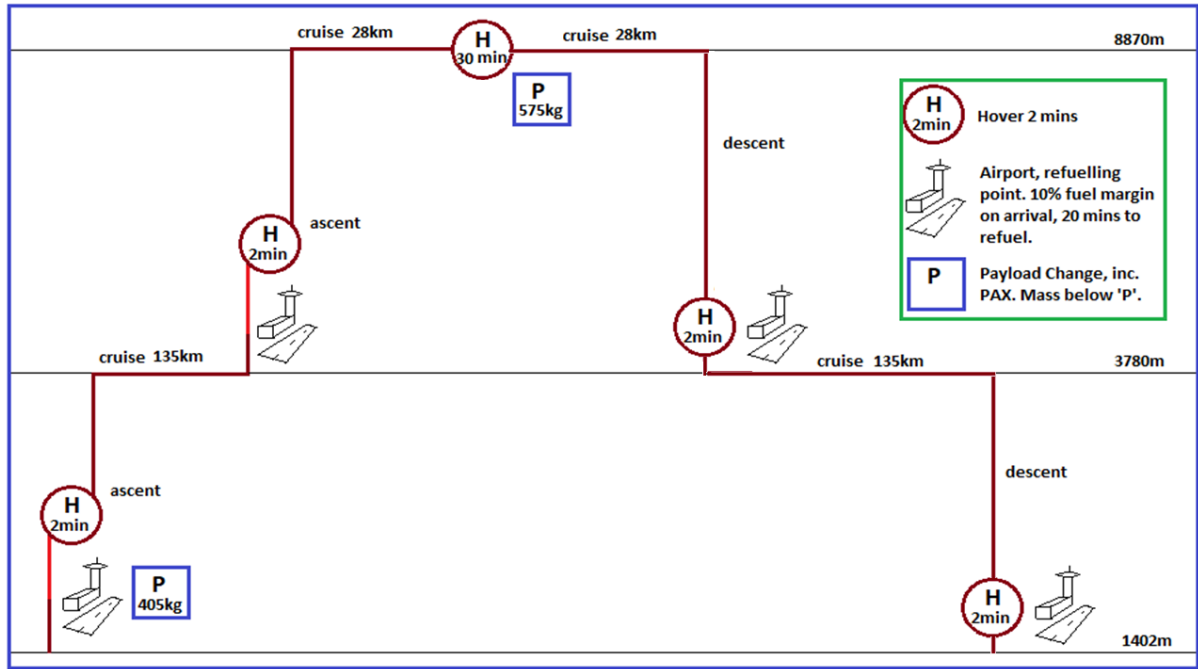


Fig. 1 Conceptual Rotorcraft's Assumed Mission Profile

III. Rotorcraft Preliminary Design

To define the characteristics of a powerplant for purposes of performing the mission profile given as Figure I, the requirements of the powerplant must first be defined. This can only be accomplished by the preliminary design of the rotorcraft, as follows.

The cornerstone assumption of this report is that the rotorcraft shall be of a Coaxial configuration. This assumption was based on a trade performed by another student team from RMIT University [3] for the 2019 VFS Design Contest. It was for this team that the work to follow was initially intended before expanding beyond their mandate.

Matlab 2016 under student license was used in conjunction with Xfoil to write an optimization program to determine the optimum number of rotors, rotor length, chord and airfoil via the Blade Element Method as described in Prouty's 1995 Textbook *Helicopter Performance, Stability and Control* [4]. This information was then used to infer the vehicle's Power Requirements and mass at the point of peak power requirement, also guided by Prouty. The vehicle characteristics and power requirement chart are given as Table 1. and Fig. 2, respectively.

Parameter	Value
Configuration	Coaxial
Airfoil	NACA23012
Number of Rotors	6
Rotor Length	5.5 m
Chord	0.27 m
Lift to Drag Ratio	78.31
Coaxial Correction (k)	1.28
Thrust per blade	4710 N
Total Thrust (T)	28,262 N
Swept Area (A)	95 m ²
Figure of Merit (F.M.)	0.732
Peak Power Requirement	938.6 kW
Max Mass at Peak Power Req.	2881 kg

Table 1. Rotorcraft Characteristics

Note from Fig. 2 the powers required for hover are given as the y-intercepts of the chart and the optimum cruise velocities at altitude are the troughs of the relevant lines. These power requirements may then be used in conjunction with the Breguet Range and Endurance Eqns (Eqns 1a & 1b) to determine the mission's fuel requirement.

$$R = W_{Fuel} \frac{V}{P_{req} * PSFC} \quad (1)$$

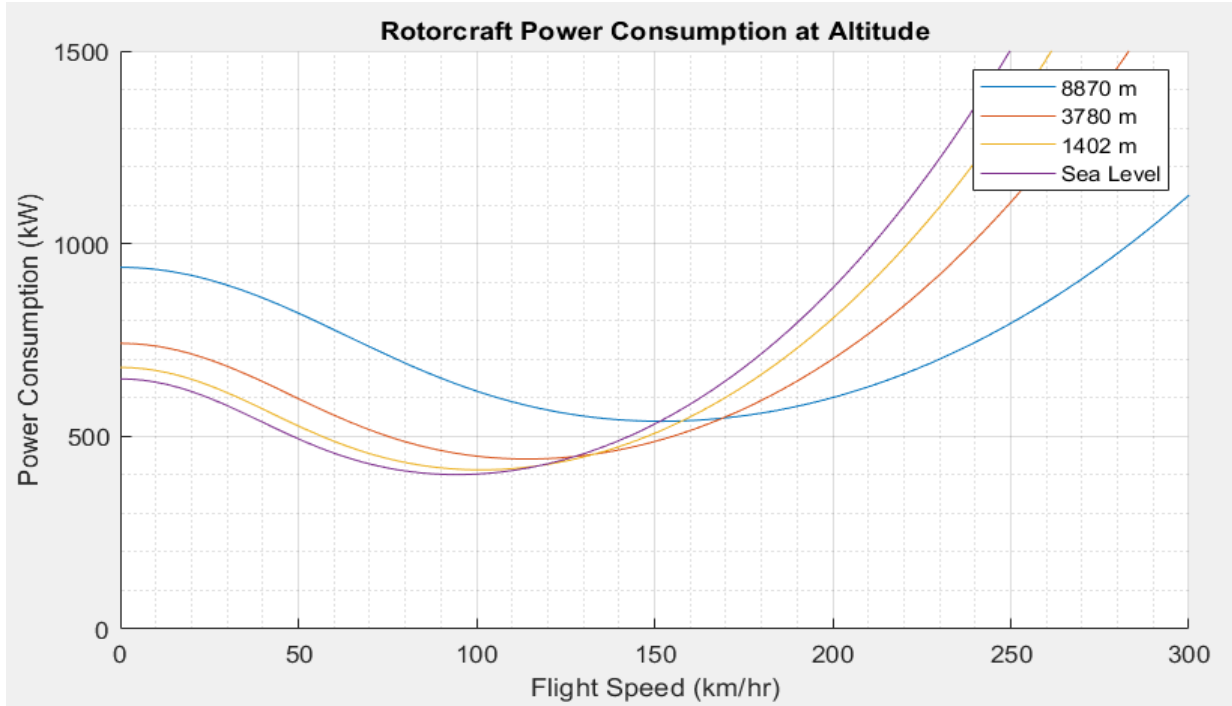


Fig. 2. Vehicle Characteristic Power Curves at relevant Altitudes

$$E = W_{Fuel} \frac{1}{P_{req} * PSFC} \quad (2)$$

Where the Power Specific Fuel Consumption was approximated as:

$$PSFC = \frac{1}{h_{comb} * \eta_{comb} * \eta_{trans}} \quad (3)$$

With the enthalpy of combustion of aviation fuel known to be 42,700kJ/kg, the efficiency of combustion capped at 0.45 and the transmission efficiency assumed to be 0.8. This gives an approximate PSFC of 0.065MW/kg, with some variation on atmospheric properties and engine characteristics.

Taking the most power intensive leg of the mission profile, being the second leg between refuelings and including the rescue operation, the mass of fuel required for each mission leg could be determined, giving the maximum take-off and dry mass of the rotorcraft including a 10% fuel margin and 1% allowance for fuel in lines.

Parameter	Value
Maximum Take-off Mass	2946kg
Dry mass	2130kg
Fuel Fraction	0.277

Table 2. Continued Rotorcraft Characteristics

IV. Hybridization Model Development

Before an analysis of combined electrical and turboshaft powerplants at altitude may be performed, the Power Lapse of turboshaft engines at altitude shall be defined to inform the following work.

The power lapse of a turboshaft engine is known to be directly proportional to the mass flow rate of air travelling through the engine's combustion chamber [5]. That is to say:

$$\frac{P_{alt}}{P_{SL}} = \frac{\dot{m}_{alt}}{\dot{m}_{SL}} = \frac{\rho_{alt} v_{in} A_{in}}{\rho_{SL} v_{in} A_{in}} \quad (4)$$

Where ' v_{in} ' denotes the intake air velocity and ' A_{in} ' denotes the engine intake area. Note that the intake area does not change throughout the flight so these terms can be cancelled. However, the intake velocity is the sum of the engine's static intake velocity and forward flight velocity which are variable on the flight condition so may

not be cancelled. However, as a turboshaft's ideal sea level power output is usually defined in the static condition, it can be stated that the forward cruise velocity at sea level is zero. Therefore, Eq 4. may be rewritten as:

$$Lapse = \frac{P_{alt}}{P_{SL}} = \frac{\rho_{alt}(v_c + v_0)}{\rho_{SL}v_0} \quad (5)$$

Now, an expression for the static intake velocity, i.e. the engine's induced velocity, must be derived. Prouty [4] gives the definition of induced velocity as:

$$v_0 = \sqrt{\frac{T}{2\rho A_{in}}} \quad (6)$$

And the static thrust as:

$$T = P_0^{2/3} (2\rho A_{in})^{1/3} \quad (7)$$

The substitution of Eq 5. and Eq 6. into Eq 3. and manipulating to get the equation in terms of the Power ratio yields the following expression:

$$\frac{P_{alt}}{P_{SL}} - \left(\frac{\rho_{alt}}{\rho_{SL}}\right)^{1/3} \left(\frac{P_{alt}}{P_{SL}}\right)^{2/3} = \frac{v_c(2\rho_{SL}A_{in})^{1/3}}{P_{SL}^{1/3}} \quad (8)$$

As expected, when the cruise velocity of the aircraft is zero, (i.e. hover condition) Eq 8. can be simplified to:

$$\frac{P_{alt}}{P_{SL}} = \frac{\rho_{alt}}{\rho_{SL}} \quad (9)$$

However, when the cruise velocity is non-zero the expression is not straight forward and requires a numerical solution to solve. Doing so however yields the adjusted Sea Level Power requirements to meet the power demands at altitude, given in Table 3 where the power requirements are taken from Figure 2:

Mission Stage	Power Requirement	Lapse	Adjusted SL Power
259km/hr cruise at 3780m	1206 kW	2.556	471.8 kW
2 min Hover at 3780m	741.3 kW	0.684	1083.8 kW
Ascent from 3780m to 8870m	840.0 kW	0.519	1618.5 kW
28km Cruise at 8870m	539.1 kW	1.553	347.1 kW
30 min Hover at 8870m	938.6 kW	0.387	2425.3 kW

Table 3. – Lapsed Power Requirements

It can now be seen that when the power requirements are adjusted relative to the equivalent power output at Sea Level, the engine power necessary to hover at 8870m is by far the greatest requirement of the mission profile when completed by a turboshaft engine powerplant.

Now the development of the Hybridization model shall begin in earnest. Note at this stage that the assumed configuration of powerplant is given as Figure 3.

Energy sources alternative to Lithium Ion Batteries were considered when deciding upon this powerplant, specifically being Diesel Propulsion Units (DPUs) and Hydrogen-Oxygen Fuel Cells. The metric for comparison was the Specific Energy of the energy sources, given for DPUs as Eq 10 and Fuel Cells as Eq 11 [6, 7].

$$E_{specific} = \frac{\eta_{comb} h_{diesel}}{m_{fuel} + m_{DPU}} \quad (10)$$

- η_{comb} = efficiency of combustion
- h_{diesel} = enthalpy of combustion for diesel
- m_{fuel} = mass of fuel
- m_{DPU} = mass of Diesel Propulsion Unit

$$E_{specific} = \frac{3661\eta\mu}{3661\eta\mu(ViAt_d)^{-1} + 83.3RT + \mu} \quad (11)$$

- t_d = discharge time (s)
- R = Ideal Gas Constant
- T = Temperature (K)
- μ = Fuel Tank Figure of Merit (FOM)
- η = Fuel Cell Efficiency
- A = Area density of Cell Stack (m^2/kg)
- V_i = Output Voltage (V)

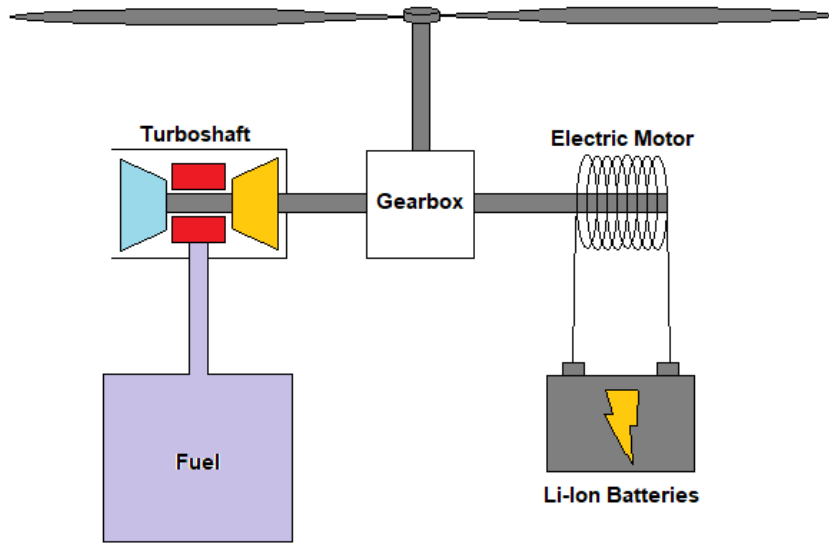
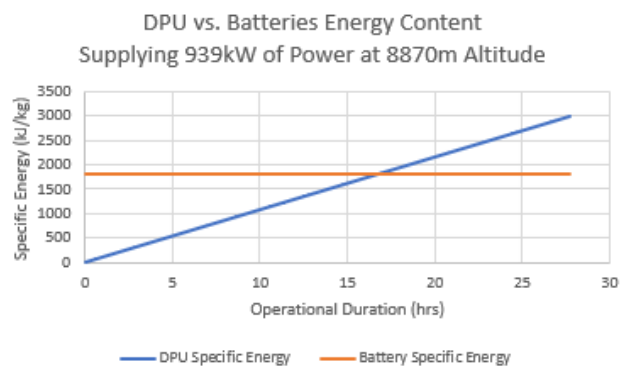
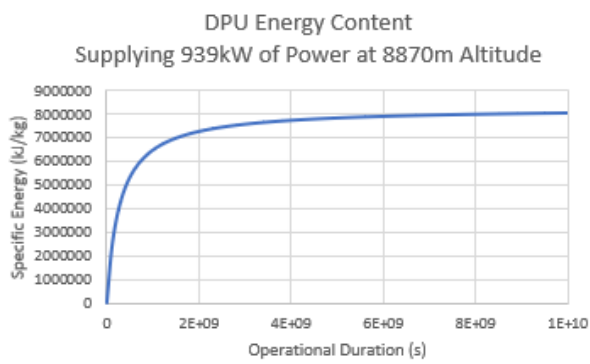


Fig 3. – Hybrid Powerplant Configuration



Figures 7. 1.2a and 7.1.2b – DPU Performance over long- and relevant-time frames

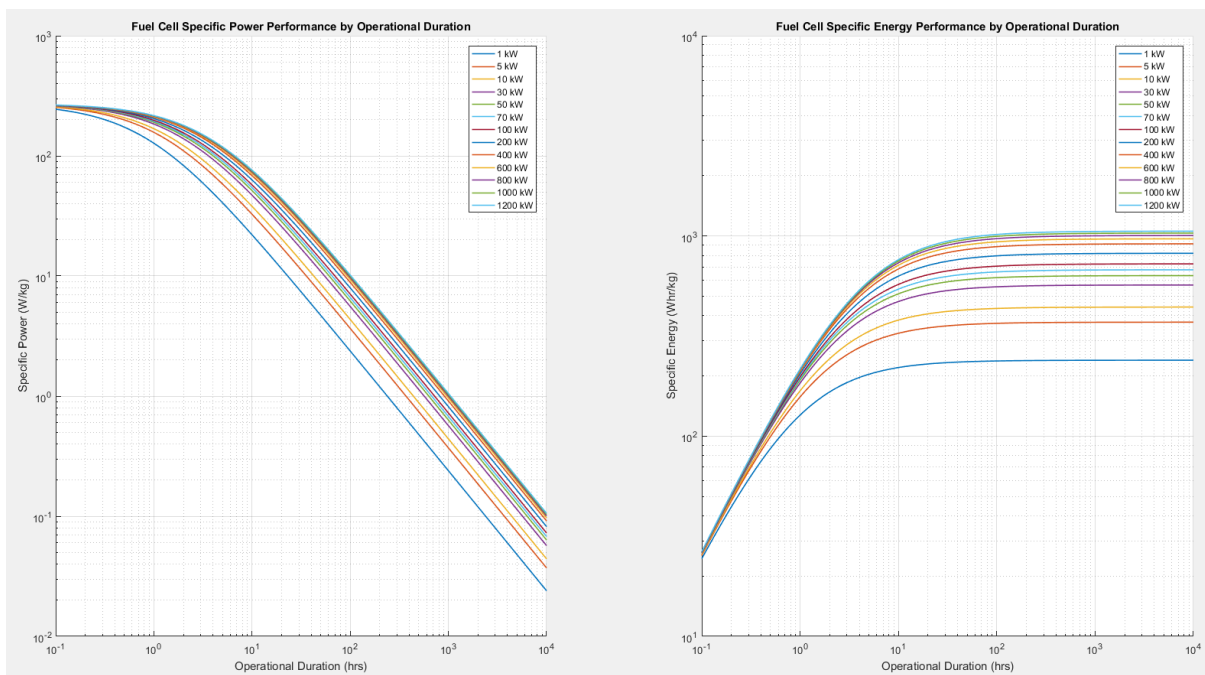


Figure 5. – Specific Energy against Discharge Time

The results of the evaluation of Eqns 10 and 11 are given as Figures 4 and 5. Note at this stage that the specific energy of a state-of-the-art Li-Ion Battery is 500Whr/kg, equivalent to 1800kJ/kg [8]. The specific energies of both DPUs and Fuel Cells are dependent on their operational duration, which can be interpreted as the high specific energy of fuel outweighing the initial mass investment of the power generation infrastructure as more fuel is added to enable a longer generation period. However, both means of power generation have specific energies inferior to Li-Ion Batteries at operation durations in the order of 10^0 to 10^1 hours, the operational duration of interest. Therefore, it can be stated that the configuration depicted in Figure 3 is the most economical in terms of mass.

Now that the configuration has been confirmed, the model may be developed. The model was developed to estimate the overall mass of the powerplant in Figure 3. as a function of the power and energy supplied by each means of mechanical power generation. Overall, the model is based upon the following equations:

$$\begin{aligned} P_{req} &= A * P_T + B * P_E \\ E_{req} &= C * E_f + D * E_B \end{aligned} \quad (12a,b)$$

Such that:

$$\begin{aligned} A + B &= 1 = C + D \\ A, B, C, D &\leq 1 \end{aligned} \quad (13a,b)$$

Where:

- P_{req} = Total Power Required
- P_T = Power supplied by turboshaft
- P_E = Power supplied by electric motor
- E_{req} = Total energy required
- E_f = Energy available from the fuel
- E_B = Energy available from the batteries

Furthermore, as:

$$E_{req} = P_{req} * t$$

Where 't' is the operational duration, it may be demonstrated that:

$$A = C, \quad B = D \quad (14)$$

This model shall be developed using the design case of a 30-minute hover at 8870m altitude requiring 939kW of Power. Now that the fundamental characteristic equations of the power plant have been defined, it is necessary to convert them into mass, as this is the metric that shall be used to determine its suitability over a turboshaft only configuration

The mass of the overall power plant may be described as:

$$m_{PP} = m_T + m_F + m_{FT} + m_{EM} + m_B \quad (15)$$

Where:

- m_{PP} = Total mass of the power plant
- m_T = Mass of the turbine
- m_F = Mass of the on-board fuel
- m_{FT} = Mass of the fuel tank
- m_{EM} = Mass of the electric motor
- m_B = Mass of the batteries

To proceed, each of the above terms must be described in terms of Eqns 12a and 12b. This shall be done in the order that they appear.

The mass of the turbine may be approximated as:

$$m_T = A P_{req} \frac{m_T}{P_{req}} \frac{1}{Lapse} = A * \frac{P_{req}}{P2W_T * Lapse} \quad (16)$$

Where 'P2W_T' is the Power to Weight ratio, also the Specific Power, of the turbine in question. Note that all the terms in Equation 9.1.5. can be defined, as the Power to Weight Ratio is known from Appendix Item X to be between 2285W/kg and 6540W/kg, depending on the turboshaft. For this exercise, the Power to Weight Ratio of the Safran Engines MTR390-2C shall be used, giving a value of 6530W/kg. The Lapse Rate as it varies with flight speed and altitude is defined previously., and the Power Requirement is known from Figure 2.

The mass of fuel required to perform what was determined to be the two ascension legs (therefore the most energy intensive) of the mission as calculated from Eqns 1 and 2 and is given in Table 4.

Mission Stage	Leg	Fuel Req
2 min Hover at 3780m	5	9.42 kg
Ascent from 3780m to 8870m	6	94.55 kg
28km Cruise at 8870m	7	36.16 kg
30 min Hover at 8870m	8	171.22 kg
28km Cruise at 8870m	9	36.16 kg
2 min hover at 3780m	10	9.42 kg
<i>Total</i>		356.93 kg

Table 4 – fuel requirement over mission

Note however that it cannot be stated that the Mass of the Fuel as it appears in Equation 15. cannot be defined as the total fuel masses shown in Table 4. Consider the profile: The time of interest begins at Leg 8, therefore the fuel associated with Legs 5-7 will have been consumed before the point of analysis so must be neglected. Furthermore, it is assumed that the batteries will be depleted when the 30-minute hover has concluded, so the fuel mass for Legs 9 and 10 must not vary with the turbine power requirement. Lastly, according to Equation 12b, the fuel mass associated with Leg 8 must vary with turbine power requirement. Therefore, the mass of the fuel may be expressed as:

$$m_F = m_{L9} + m_{L10} + A * m_{L8} \quad (17)$$

The mass of the fuel is now defined.

The mass of the tank may be geometrically approximated to be:

$$m_{FT} = 4\pi\rho_{Al}t_{tank} \left(\frac{3m_{FT}}{4\pi\rho_F} \right)^{\frac{2}{3}} \quad (18)$$

Where ‘ m_{FT} ’ is the larger total mass of fuel between refueling. The mass of the fuel tank must be able to accommodate the total fuel required by the mission profile:

$$m_{FT1} = m_{L5} + m_{L6} + m_{L7} + A * m_{L8} + m_{L9} + m_{L10} \quad (19)$$

The mass of the fuel tank is now defined.

By method similar to the turbine mass, the mass of the electric engine may be characterized as:

$$m_{EM} = B * P_{req} \frac{m_{EM}}{P_{req}} = B * \frac{P_{req}}{P2W_{EM}} \quad (20)$$

The Power-to-Weight Ratio of the Electric Engine was taken to be 5200W/kg inline with the characteristics reported by both Siemens/Airbus in Europe and Magnix in the U.S.A., both developing engines of this ilk and report them to be at TRL 7 and 6 respectively [9-11].

Lastly, the mass of the batteries may be defined as:

$$m_B = B * \frac{E_{Req}}{0.72 * SE_B} \quad (21)$$

Where ‘ SE_B ’ is the Specific Energy of Li-Ion Batteries, given as 1800kJ/kg previously and the factor of 0.72 accounts for a 10% fuel margin and the tendency of Li-Ion Battery Power Output to drop rapidly when below 20% of its capacity [12].

All variables in Eq 15. have now been defined, and the complete model is gained by the substitution of Eqns 16 – 21 into Equation 15.

V. Results

The plotting of the total mass of the powerplant against variable ‘A’ as they appear in Eqns 12-15 yields the chart given as Figure 6.

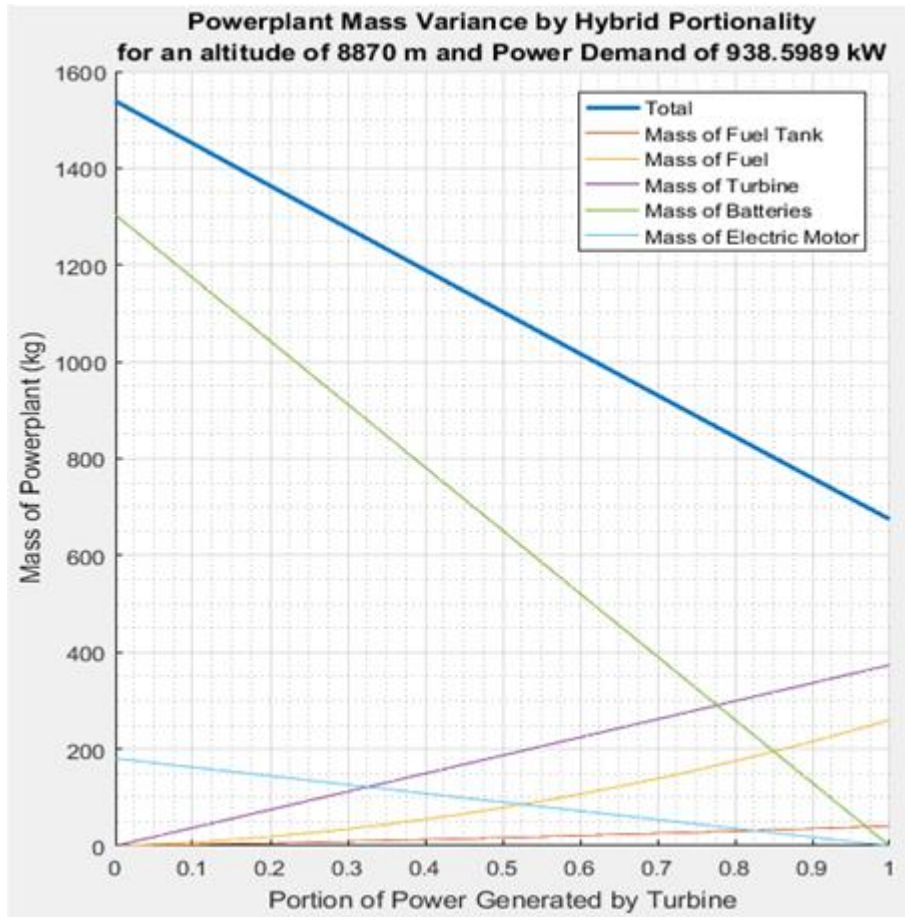


Fig 6. – Mass of a Hybrid Rotorcraft Powerplant

VI. Discussion

It can be seen from Figure 6 that the minimum mass is achieved at $A=1$, indicating that the minimum possible mass is achieved when all power is met by a turboshaft-only powerplant. Therefore, it can be stated that for the input parameters used there is no hybrid configuration that generates a net mass saving at the current level of technology.

However, a closer look at Figure 6 shows that, as expected, the mass of the Electric Engine is far lower than that of the Turboshaft Engine. Therefore, mass savings are available here as expected. Unfortunately, the mass of the batteries washes these savings away and then some, resulting in the overall failing of the hybrid configuration. This begs the question; what if batteries were lighter?

To answer this question, the model was iterated with increasing Battery Specific Energy and instructed to cease when a net mass saving has been found. The results of this endeavor are given as Figure 7.

It can be seen from this figure that modest mass savings, approximately 24.5kg, become available if approximately 33% of the power required during the hover/rescue at 8870m leg of the mission is provided by an electric engine when the electrical energy storage specific energy is 2980kJ/kg. This represents an increase of 66% over the current achievable specific energy of 1800kJ/kg in Li-Ion Batteries.

This power plant is barely capable of meeting all power requirements met throughout the mission with the turboshaft alone except for the 8870m hover condition, where the difference is made up by the electric motor. The electric motor is then supplied by the batteries with sufficient energy to operate for 30 minutes at the required power output. This allows for mass savings of 24.5kg off what otherwise would have been a 674.7kg power plant, or 3.6% of the total mass, giving a total mass of 650.2kg. This may not seem like much, but will also lead to savings in fuel consumption in other legs of the mission due to the more appropriate size of the turboshaft engine(s), as they need to operate at extremely low powers relative to their design condition less often. This will serve to decrease the running costs of the vehicle over its lifetime. However, operating costs were not given as a primary customer requirement and so will not be analysed in detail for this exercise. The specifications of the power plant are given in Table 5:

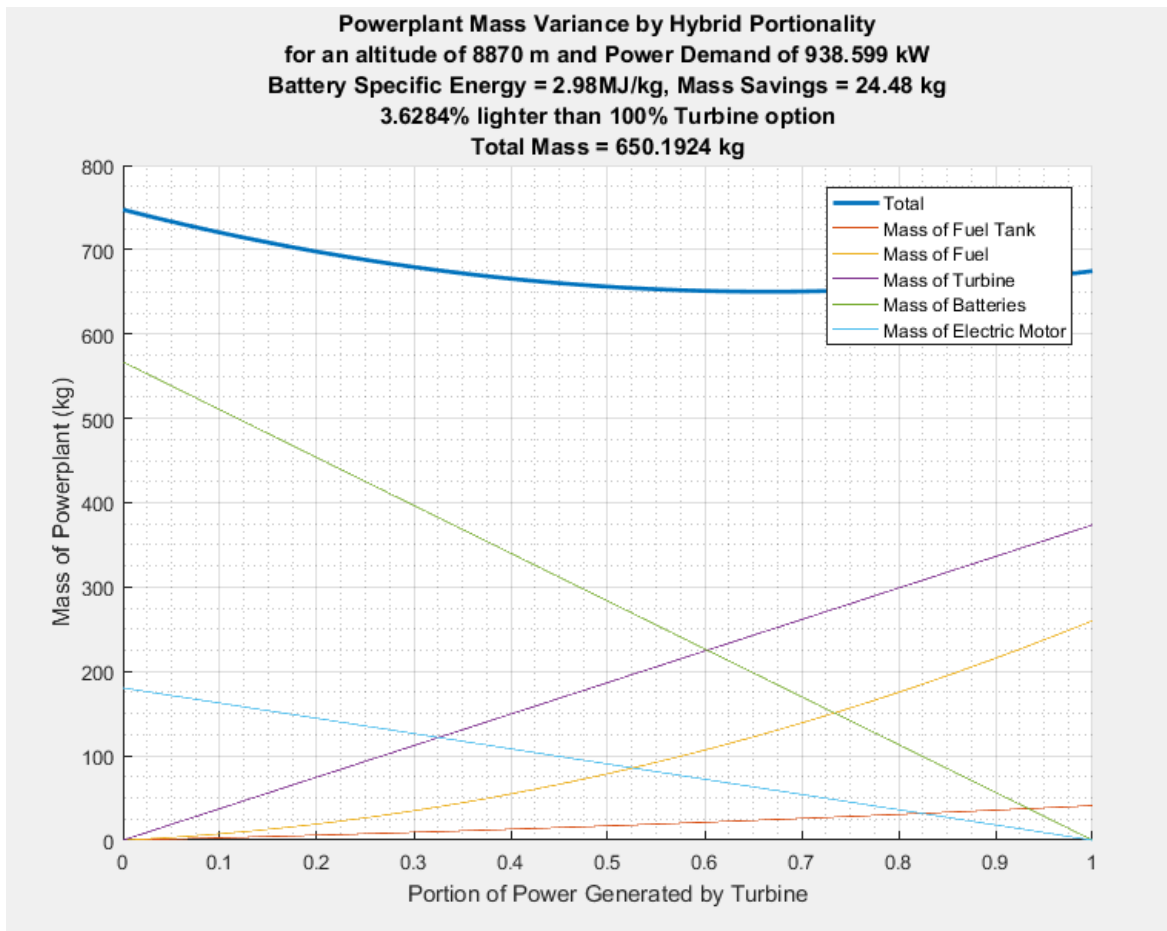


Fig 7. – Minimum Characteristic Hybrid Mass Chart for a mass saving

<i>Component</i>	<i>Characteristic</i>
<i>Turboshaft Mass</i>	248kg
<i>Max. Fuel Mass</i>	284kg
<i>Fuel Tank Mass</i>	24kg
<i>Electric Motor Mass</i>	61kg
<i>Li-Ion Battery Mass</i>	190kg
<i>Maximum Powerplant Mass</i>	807kg
<i>SL Turboshaft Power Output</i>	1619 kW
<i>Electric Motor Power Output</i>	314 kW

Table 5. – Powerplant Characteristics

However, it is expected that the 24.5kg of savings shall be consumed by increased transmission architecture. Furthermore, for this result to be valid it is necessary that Li-Ion Battery Technology improve such that their Specific Energy increases from the current value of 1800kJ/kg to 2980kJ/kg, an increase of 66%. Furthermore, increases in Li-Ion energy storage or alternative technologies to the same end beyond this identified minimum point shall lead to further mass savings in the described configuration of Hybrid-Electric Power Plant.

VII. Conclusion

This report has seen the conceptual sizing of a hybrid-electrical powerplant for a high-altitude mountain rescue helicopter. Using the given mission profile (Appendix Item I) and the first principles of helicopter design given in Prouty's [4] '*Helicopter Stability, Performance and Control*', an upper limit for the vehicles dry mass (2881kg) and the vehicle's spectrum of power requirements (Figure 4.4.1) was defined.

This power spectrum was then compared against the vehicle's thrust lapse rate with altitude in order to determine the peak power requirement of the vehicle in the given mission profile, found to be 2425.3kW at the 8870m hover condition.

This was used to inform a model was developed to express the mass of a hybrid-electric powerplant suitable for the 30-minute hover at 8870m mission period only, where it was assumed that the batteries would be depleted thereafter. Logic then dictated the addition of the requirement that the turboshaft engine be suitably large to

perform all other mission phases without assistance from the electric engine. The model was then developed to return the mass of a hybrid powerplant for known specific energies, specific powers power requirement and flight condition where the total mass was given by the summation of a variably sized turboshaft powerplant and a sufficiently sized electric powerplant to make the up the power deficit. Plotting this mass over the power-fraction made up by the turboshaft engine was hoped to return a trough, indicating a minimum mass of a hybrid configuration. Instead, the minimum was shown to be at the point where 100% of the power is generated by the turboshaft (Figure 6), indicating that at current levels of technology there is no hybrid configuration that will outperform a pure turboshaft powerplant.

Some analysis of the returned data showed that the driver of the electric powerplant's failings were still the low Specific Energy of the Li-Ion Batteries compared to aviation fuel; therefore the model was iterated with increasing battery specific energy in the attempt to determine the minimum Li-Ion Battery Specific Energy at which hybridization becomes economical. This exercise was successful in determining that the Specific Energy of Li-Ion Batteries or comparable energy source needs to increase by 66% to 2980kJ/kg (Figure 7). This would result in a modest 24.5kg mass saving but increases from there as battery technology further improves.

However, In order to reliably identify the point at which batteries will sufficiently improve to make hybridization of a powerplant to perform the given mission profile viable, it is necessary to quantify all mass advantages and penalties incurred by the hybridization process. The penalty, if indeed one does exist, associated with excess transmission architecture was not reliably quantified. It is recommended that this be analyzed in more detail in further research.

Furthermore, the developed model likely over penalizes the electrical propulsion system by not accounting for the offset in fuel consumption and, therefore, mass that its presence generates. That is to say, by eliminating a higher power requirement on the turboshaft at the highest altitude, the turboshaft will be able to operate at closer to its nominal power output at the lower altitude components of the flight, reducing the PSFC of the engine in these operating regimes. This effect was not captured in this method and its quantification could be the subject of further work.

Acknowledgements

I would like to acknowledge my academic supervisor, Prof. Cees Bil, for his guidance and assistance throughout the completion of this work.

References

- [1] P. Veillette. (2016, 12/10). *World's Highest Helicopter Rescue*. Available: <https://aviationweek.com/businessaviation/world-s-highest-helicopter-rescue>
- [2] E. Barone and L. Tweeten. (2019, 12/10). *Greed, Weather and Inexperience: See How Mount Everest's Deadly Season Compares to Past Years*. Available: <https://time.com/5604758/mount-everest-deaths/>
- [3] D. Lynch, J. Lekakis, and M. Celeste, "Conceptual Design of an Extreme High Altitude Rescue Helicopter," RMIT, Melbourne, Australia 2019.
- [4] R. W. Prouty, *Helicopter performance, stability, and control*. 1995.
- [5] C. A. Snyder, "Defining Gas Turbine Engine Performance Requirements for the Large Civil Tiltrotor (LCTR2)," 2013.
- [6] I. P. Sahu, G. Krishna, M. Biswas, and M. K. Das, "Performance study of PEM fuel cell under different loading conditions," *Energy Procedia*, vol. 54, pp. 468-478, 2014.
- [7] K. Burke, "Fuel cells for space science applications," in *1st International Energy Conversion Engineering Conference (IECEC)*, 2003, p. 5938.
- [8] C. A. Snyder, "Exploring propulsion system requirements for more and all-electric helicopters," 2015.
- [9] F. Ismagilov, V. Vavilov, D. Farrahov, V. Bekuzin, and A. K. Miniyarov, "Fault-tolerant brushless external-rotor motor for fuel pumps," in *2019 26th International Workshop on Electric Drives: Improvement in Efficiency of Electric Drives (IWED)*, 2019, pp. 1-5: IEEE.
- [10] Anonymous. (2018, 25/5). *Siemens Global Website - Information for the Press*. Available: <https://www.siemens.com/press/en/feature/2015/corporate/2015-03-electromotor.php?content%5B%5D=Corp#event-toc-2>
- [11] J. Stewart. (2018, 25/5). *A Better Motor is the First Step Toward Electric Planes*. Available: <https://www.wired.com/about/press/>
- [12] D. A. Pola *et al.*, "Particle-filtering-based discharge time prognosis for lithium-ion batteries with a statistical characterization of use profiles," *IEEE Transactions on Reliability*, vol. 64, no. 2, pp. 710-720, 2015.

Research on rotor blades and their optimum shapes in Mars exploration

Danishi Ai¹

University of Tsukuba, Tsukuba, Ibaraki, 305-8577, Japan

Tatsuki Horii²

University of Tsukuba, Tsukuba, Ibaraki, 305-8577, Japan

This year, NASA has sent Mars helicopter “Ingenuity” to the Mars. It uses coaxial rotors to fly on Mars. The Mars exploration UAV performs missions such as measuring from the sky and assisting the course of the rover by flying. It is also expected to conduct exploration in places where the rover cannot enter, such as vertical holes. In UAV of the helicopter type, there are single rotors, tandem rotors, intermeshing rotors, coaxial rotors. In the coaxial rotors type, rotors of the same size but in different rotation directions rotate coaxially. In the intermeshing rotors type, the two rotors rotate in opposite directions with two rotors crossing each other. In this study, we consider which rotor types are most suitable for Mars UAV. In addition, the size of Mars UAV is one of the important elements when loading it onto rocket. The tandem rotors are excluded in this section because they are structurally difficult to miniaturize as a Mars UAV. Flight efficiency and weight are important factors when flying in the harsh atmospheric environment of Mars.

I. Nomenclature

F	= aerodynamic lift, N
W	= watt = power, W
w	= aerodynamic lift per system weight
m	= system weight, kg
η	= Flight efficiency = F/W

¹Student Member, Undergraduate, AIAA Membership Number 1037197.

²Student Member, Undergraduate, AIAA Membership Number 1205091.

II. Introduction

Research on Mars exploration UAVs represented by Mars helicopter “Ingenuity” (NASA) is being conducted all over the world. Coaxial rotors and multi rotors are attracting attention as types of rotor types. In this Study, we have focused on single rotor type, coaxial rotors type and intermeshing rotors type aside from multi rotors type. We have conducted basic lift measurement experiment and CFD analysis in order to clarify the characteristics of each rotor type. We defined each factors as follows.

$$\eta=F/W$$

$$w=F/m$$

At first, we have conducted preliminary experiments comparing coaxial rotor model with single rotor model. The comparison was lift per number of rotations. For the comparison experiment, we have used simple experimental equipment that is capable of measuring rotor speed and aerodynamic lift. Also, when it comes to test coaxial rotor, it can control anti-torque and measure interval between rotors. Two motors with an output of 150w are installed in this experimental equipment so that they are less affected by downwash effect. In the first test, we have used rotor that is designated for this motor. As a result, it was found that there was almost no difference in aerodynamic lift between coaxial rotor and single rotor at low rotation speeds (1000 to 3000rpm). Considering this result, it can be said that at least under these conditions, single rotor is superior in both η and w . At maximum output rotation speeds (6000 rpm), the coaxial rotor had aerodynamic lift of about 1.6 times that of the single rotor. As a conclusion for all these experiment results, coaxial rotor does not show excellent efficiency, especially at low speeds. It should be noted that the Atmospheric conditions of Mars and Earth is quite different, but in this study, we decided to conduct basic experiments under the Earth atmospheric condition as being applicable to the Mars atmospheric condition in the future. Flight conditions on Mars is harsh. Also it is desirable to be able to fly for a long time for exploration on Mars. Therefore, it is meaningful to study the rotor types for Mars UAV. In addition, the results of this study can be used to UAVs on Earth.

III. Experiment

1) Experiment equipment

We made experiment equipment “Fig.1”, “Fig.2” and conducted basic lift measurement experiment. In order to reproduce the situation during flight, this equipment has free yaw axis direction and rotates due to the reaction of the rotor. Also to exclude the influence of the ground effect, we made the equipment produces lift power in the downward direction as showed in “Fig.1”.

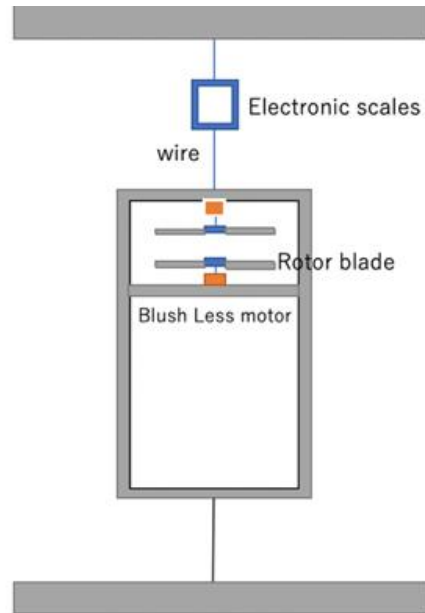


Fig. 1 Outline of experimental equipment

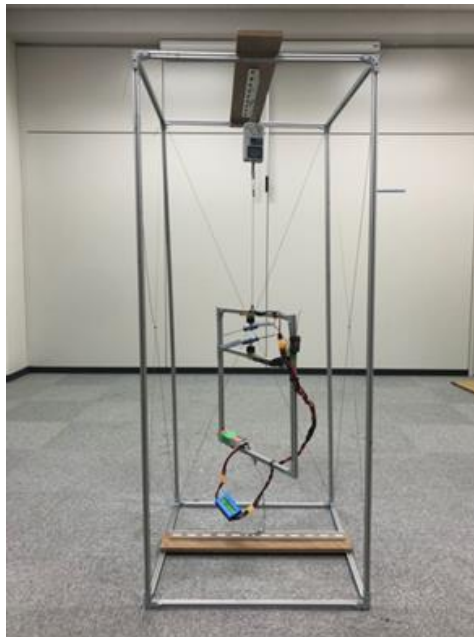


Fig. 2 Whole experimental equipment

Each rotor speed, power consumption, and lift power can be measured. Using this experiment equipment, we have tested three rotor type models, single rotor model, coaxial rotors model, and intermeshing rotors model in the same condition (Fig.3).

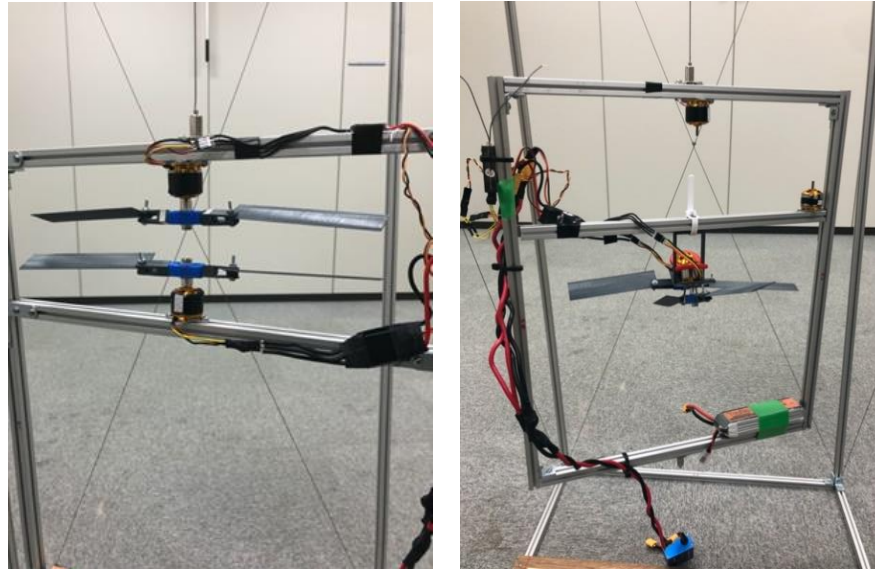


Fig. 3 Coaxial rotors model (left) and Intermeshing rotors model (right)

In this experiment, it was necessary to prevent the rotation of the yaw axis in each model, so a rotation suppression method was devised for each model. When experimenting single rotor model, we fixed yaw axis direction. When experimenting coaxial rotors model, we adjusted the elevation angles of two rotor blades to a difference of two degrees. When experimenting intermeshing rotors model, the rotors were rotated in opposite directions.

2) Experiment and consideration on rotor blade elevation angle and lift power

We have attached single rotor model, coaxial rotors model, and intermeshing rotors model to the experimental equipment, and measured lift power by changing rotor blade elevation angle from 0deg to 22deg. In this experiment, we set up revolution number to be constant for all models. The conditions are shown in “Table1”.

Table1	Experiment condition
Temperature	28 °C
Rotor speed	2000 rpm
Blade length	120 mm
Radius of rotation	155 mm
Chord length	30 mm
Blade airfoil	NACA0006

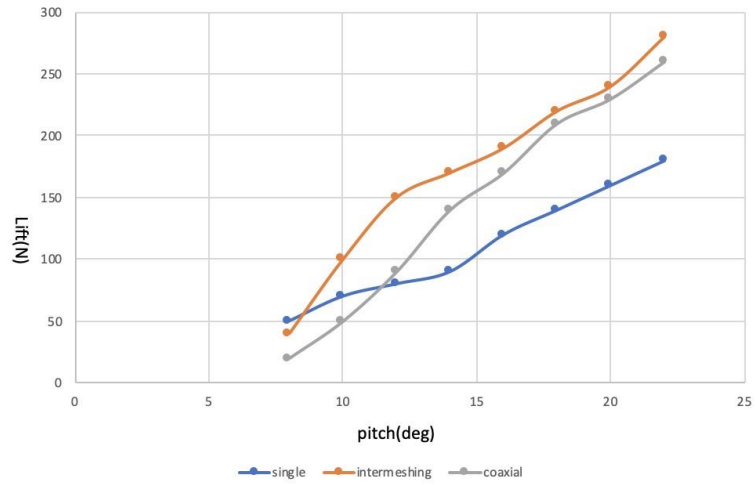


Fig. 4 Relationship between blade elevation angle and lift power for each model

From this result, it was found that in the case of models with two rotors, intermeshing rotors model can generate more lift power in the same rotation speed.

3) Experiment and consideration on rotor blade rotation speed and lift power

For all models, we set up the blade elevation angle to 16 degrees and measured lift power respect to rotation speed. The result is shown in “Fig.5”.

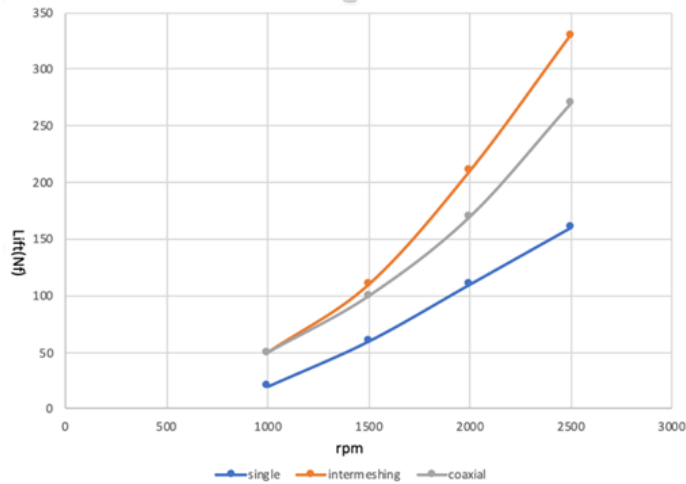


Fig. 5 Relationship between blade rotation speed and lift power

From this result, in the low rotation speed range, (less than 1500 rpm), there is almost no difference between the coaxial rotors model and intermeshing rotors model, but in the high rotation speed range (1500 rpm or more), the intermeshing rotors model produces larger lift power. Also from this result, the coaxial rotors model requires higher rotation to generate the same lift power than intermeshing rotors model. For rotorcraft where blade tip speed is important, the intermeshing

rotors model which can reduce the rotor speed for same lift power, is considered to be a great advantage in harsh flight conditions like Mars UAV.

4) Consideration on the relationship between system weight (m) and lift power

Rotors and batteries make up a large proportion of UAV aircraft weight. In this study, we mainly focused on the motor, battery and its peripherals. We considered the lift power generated with respect to the system weight. The results are shown in “Table2, Table3”.

Table2

Rotor type	System weight (m)
Single	271
Intermeshing	342
Coaxial	342

Table3

Rotor type	w (F/m)
Single	0.442
Intermeshing	0.555
Coaxial	0.497

From this result, it is shown that the intermeshing rotors type can obtain the most lift power per system weight at least in this experiment. Also it is considered that the weight of the payload can be increased using intermeshing rotors model.

5) Experiment and consideration on energy efficiency

Next, we investigated the relationship between power consumption and lift power. Although the power and power consumption for obtaining lift power are different, it is possible to compare them because the same motor is used in all models in this experiment. The result is shown in “Fig.6”.

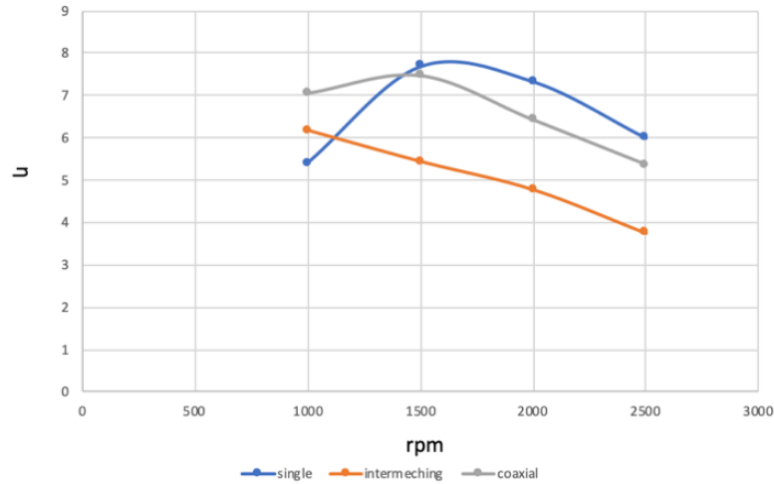


Fig. 6 Relationship between rotor speed and efficiency

This result shows that the models with two rotors was inferior to the single rotor model. Also it shows that intermeshing rotors model is inferior to coaxial rotors model.

IV. CFD analysis review

So far, we have assessed three models by actually conducting experiments. In addition, CFD analysis by SolidWorks 2019 Flow Simulation was performed to confirm the correctness of the experiment. The result of CFD analysis and experiment on single rotor model is shown in “Fig.7”

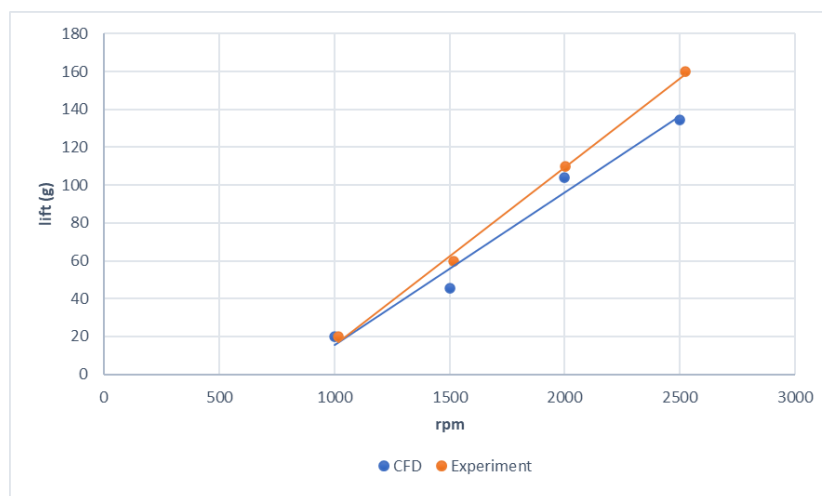


Fig. 7 Relationship between rotor speed and efficiency

As can be seen from “Fig.7”, the experimentally measured values are slightly lower than the CFD result, but they show almost the same behavior.

We also conducted CFD analysis “Fig.8” of the coaxial rotors model under exactly the same conditions as in the experiment.

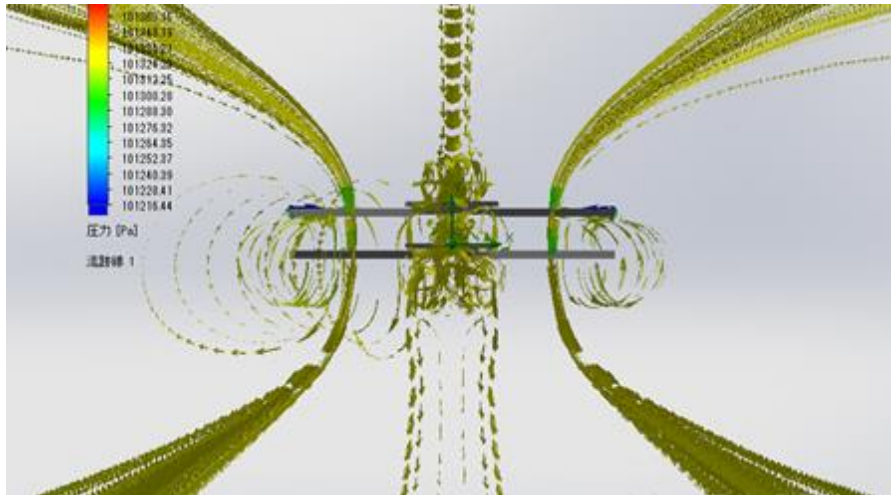


Fig. 8 Pressure distribution and airflow on coaxial rotors model viewed from side

From “Fig.8”, it can be seen that the airflows between rotor interfere with each other, especially near the tip of the blade. This is considered to be case of lowering η . Regarding the intermeshing rotors model, there were few precedents that could be used as a reference, and CFD analysis could not be performed. In the future, it will be necessary to develop a method for performing CFD analysis on intermeshing rotors model.

V. Conclusion

In this study we have investigated the single rotor type, coaxial rotors type and intermeshing rotors type in multiple items. All the results are briefly shown in “Table4”. They are ranked with number. “1” is the best performance and “3” is the lowest.

Table4 review of all the results

item/rotor type	single	coaxial	intermeshing
rotor blade elevation angle and lift power	3	2	1
rotation speed and lift power	3	2	1
system weight (m) and lift power	2	3	1
power consumption and lift power (η)	1	2	3

Through this study, it was found that each method has its advantages and disadvantages. In particular, it can be seen that the intermeshing rotors type has good performance in items other than the relationship between power consumption and lift power (η). This suggests the possibility of using the intermeshing rotors aside from coaxial rotors type used by the current Mars exploration UAV “Ingenuity” (NASA). For example, when the performance of the battery is dramatically improved in the future, or when the payload weight is more important than energy efficiency, the advantages of the intermeshing rotors type can be utilized to many extent. In addition, the intermeshing rotors type has very few prior examples and adoption examples. Therefore, there are still plurality of factors that can be considered for intermeshing rotors type. Such as angle formed by rotor shafts and appropriate distance between the two rotors. We will continue to study these elements in the future.

References

Periodicals

- [1] Fu-Shang (John) Wei. Edward Moore. Alfred Gates ., ”An Intermeshing Rotor Helicopter Design and Test” ,The AIAA SciTech 2015
- [2] Koning, W. J., Johnson, W., & Allan, B. G. , “Generation of Mars Helicopter Rotor Model for Comprehensive Analyses”, Document ID 20180008645.
- [3] VK Lakshminarayan, JD Baeder., ”Computational Investigation of Microscale Coaxial-Rotor Aerodynamics in Hover”, Journal of Aircraft 2010
- [4] M. Rida Mokhtari, Brahim Cherki, Amal Choukchou Braham, “Disturbance observer based hierarchical control of coaxial-rotor UAV”, ISA Transactions, Volume 67, March 2017, Pages 466-475

Computer Software

- [5] SOLIDWORKS 2019-2020, SOLIDWORKS Flow simulation Dassault Systems SolidWorks

The Effect of Riblets on Trailing Edge Noise

E. R. Wotherspoon*

The University of New South Wales, Sydney NSW 2052, Australia

The effect of riblets on turbulence passing the trailing edge of an airfoil was investigated, with the aim to see if a drag reduction and a noise reduction can be achieved simultaneously with one passive technology. The riblet geometry tested was optimised for drag reduction yielding a predicted drag reduction of 8%. The riblet film was applied to a NACA0018 airfoil and tested in a wind tunnel at a Reynolds number of 160,000 for angles of attack ranging from 0 to 10 degrees. Two measurements were taken; the total drag force using a load cell, and unsteady wall pressure measurements near the trailing edge using the remote microphone technique. The aerodynamic force measurements yielded a drag reduction of 8% at an angle of attack of 0 degrees, verifying the riblet optimisation. The respective wall pressure spectra demonstrated a maximum sound pressure level (SPL) reduction on the order of 10 dB for mid range frequencies at 1kHz, a smaller SPL reduction of 2 dB at lower frequencies (< 300 Hz), and a slight increase of 1.5 dB at higher frequencies (> 3 kHz). Therefore, the mechanism of drag reduction by riblets alters the flow regime to reduce low-mid range surface pressure sound levels near the trailing edge.

I. Introduction

RIBLETS are a biomimetic drag reducing passive technology, inspired by shark skin. Fast swimming sharks have tiny scales covering their skin, known as dermal denticles, which are micro-structures aligned in the direction of fluid flow [1]. Riblets are artificially manufactured to resemble dermal denticles, however modified as continuous streamwise micro-structures with constant cross sectional profiles, instead of scales. They are known to reduce skin friction by altering the flow structures in the turbulent boundary layer [2]. A simplified depiction of how two common riblet cross sectional profiles; triangular and blade like, alter vortices is shown in Fig. 1 [3].

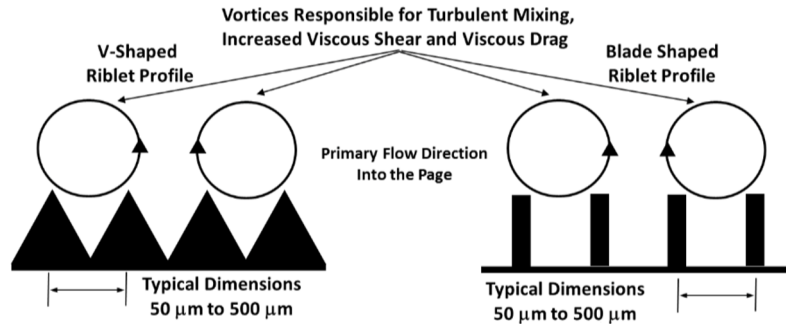


Fig. 1 Conventional riblet geometry and commonly proposed drag reduction mechanism [3]

Drag reducing riblets have been investigated for various areas including road transport vehicles, marine applications like ship hulls, aircraft and even Olympic swimsuits [2]. Relatively large drag reductions, on the order of 10% have been proven possible for certain riblet designs using wind tunnel testing and modelling [2]. The fabrication of riblets is predominately driven by commercial aerospace, where the technology has the potential to significantly improve the fuel efficiency of aircraft.

Another area important to commercial aerospace is aeroacoustics. The trailing edge of an airfoil is the dominant source for self noise production [4] and many passive noise reduction technologies have been developed. Finlets and serrations are both biomimetic technologies taken from the aeroacoustic properties of an owl's wing [5, 6]. Finlets and serrations have been proven to reduce turbulent boundary layer trailing edge noise, through altering the turbulent

*Undergraduate Honours Student, School of Mechanical and Manufacturing Engineering, AIAA Student Member

boundary layer flow structures [5, 6]. However, in both cases the reduction in noise is accompanied by an increase in drag. Thus for applications on aircraft, finlets and serrations will increase fuel consumption.

Therefore, the effect of riblets on trailing edge noise is an area to investigate, to understand if the mechanism of drag reduction by riblets has an effect on trailing edge noise. The scope of this paper is to understand the effect of riblets on boundary layer turbulence passing the trailing edge. This research is motivated by the practical application of riblets to aircraft in order to improve fuel efficiency and reduce noise pollution.

II. Methodology

Two experimental campaigns were taken in the AF1125 Bench Top Wind Tunnel at the University of New South Wales, to understand the effect of drag reducing riblets on the trailing edge noise of a NACA0018 airfoil; the lift and drag force and unsteady wall pressure. Amiet [7] proposed an empirical model for the far field sound produced by turbulent flow passing the trailing edge, where the input is the ‘convecting surface pressure spectrum upstream of the trailing edge’ [7]. The far field noise ‘is regarded as generated almost totally by the induced surface dipoles near the trailing edge’ [7]. Therefore, the unsteady wall pressure measurements demonstrate the source of the far field sound and it can be expected that a reduction in the unsteady wall pressure will be seen in the far field noise. Additionally, the wall pressure spectra provide insight into how the riblets altered the turbulent boundary layer structures to reduce drag, and how that translates to trailing edge noise reduction.

The AF1125 Bench Top wind tunnel is open return suction type with a closed working section. Air is directed into a settling chamber and then enters the tunnel through an effuser. This accelerates the air in a linear manner into the working section. The air is moved back to the atmosphere through a diffuser and variable speed axial fan with an exhaust duct [8]. The tunnel has a square cross section of 125 mm x 125 mm and is 350 mm long with a maximum freestream velocity of 36 m/s [8].

The following sections will describe the methodology; Section A will describe the test models used and the test conditions, Section B will present the riblet geometry and optimisation by resolvent analysis. Section C describes the aerodynamic force measurement instrumentation and Section D the remote microphone technique which was used to measure the unsteady wall pressure.

A. Test Models

The airfoil used was a NACA0018, Fig. 2(a) shows the model mounted in the wind tunnel with the riblet film applied and labeled pinholes and Fig. 2(b) shows the isometric CAD view with hidden edges. The chord was 69 mm with a span of 121 mm in order to simulate 2D flow. The airfoil was tripped on the pressure side and suction side at 10% chord using turbulator tape. Surface treatments were applied on the pressure side and suction side; one airfoil with a smooth surface treatment and the other with riblet film. In Fig. 2(b) the grey area defines the area with the surface treatment. The film was applied at 6% chord up to 85.5% chord, leaving the trailing edge untreated. Three pinholes were on the suction side, located 0.06 mm downstream of the surface treatments in an ‘L’ shape configuration. PVC tubing was inserted into the pinholes with an outer diameter of 1.2 mm and inner diameter of 0.8 mm, yielding an effective pinhole diameter of 0.8 mm.

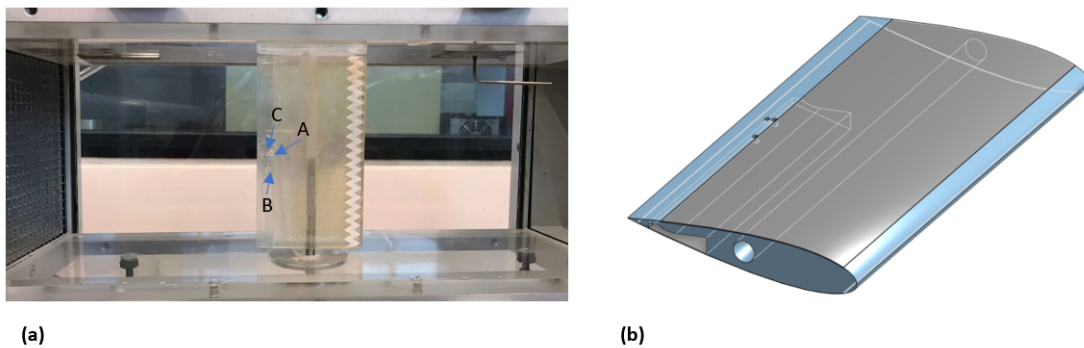


Fig. 2 NACA0018 Model (a) Side view of model mounted in the wind tunnel with the riblet film, (b) Isometric CAD view with hidden edges

The lift and drag measurements were performed at a chord Reynolds number of 160,000 for angles of attack of 0, 2, 4, 6, 8, 10 degrees. The pressure spectra were measured at the same Reynolds number however for angles of attack of 0 and 2 degrees.

B. Riblet Optimisation

The optimisation of riblet geometry is dependent on the thickness of the turbulent boundary layer and the width of the streamwise vortices [1]. Riblet geometry is commonly referred to in non dimensional wall units, non dimensionalised by the shear velocity and the kinematic viscosity of the fluid; Eq. (1) is the non dimensional height, Eq. (2) is the non dimensional spacing and Eq. (3) is the non dimensional thickness.

$$h^+ = \frac{hu_\tau}{\nu} \quad (1)$$

$$s^+ = \frac{su_\tau}{\nu} \quad (2)$$

$$t^+ = \frac{tu_\tau}{\nu} \quad (3)$$

It is known that if the riblet height protrudes out of the buffer layer into high velocity flow, drag is increased [1, 2]. If the spacing is larger than the streamwise vortices drag is also increased [1]. Therefore, riblet optimisation is a function of the flow regime.

Optimisation was performed via resolvent analysis which was developed by Chavarin and Luhar [9]. This form of CFD interprets the Navier-Stokes equations as a forcing-response system [9]. A pressure and velocity response is generated by interpreting the nonlinear convective term as a feedback forcing on the remaining linear terms. The velocity and pressure modes are amplified by a 'gain-based decomposition of the linear forcing-response transfer function' [9]. This generates the key components of the turbulent flow field. The effect of riblets is simulated using a 'linear spatially varying body force' [9] which is added to the governing equations. The performance metric for riblet profiles is the gain mode identified from the governing equations. It has been shown that drag decreases linearly with increasing riblet size in the viscous regime, which is consistent with a monotonic decrease in gain [9]. Therefore to minimise drag, the gain must also be minimised which is obtained through a series of iterations.

To simulate the turbulent flow regime the Friction Reynolds number, Eq. (4) was used as the input for resolvent analysis.

$$Re_\tau = \frac{u_\tau \delta_x}{\nu} \quad (4)$$

The Friction Reynolds number is a function of the shear velocity u_τ , local boundary layer thickness δ_x and kinematic viscosity ν of the working fluid. To obtain the Friction Reynolds number multiple calculations were necessary. Firstly, the wall shear stress was estimated using the local skin friction coefficient for turbulent flow, Eq. (5). Since the focus of this paper is the trailing edge of the test model, the local location was $x = 0.06$ m.

$$C_{f,x} = \frac{0.059}{Re_x^{0.2}} \quad (5)$$

This was then used to calculate the shear velocity, Eq. (6).

$$u_\tau = \sqrt{\frac{\tau_w}{\rho}} \quad (6)$$

where τ_w is the wall shear stress and ρ is the fluid density. The local boundary layer thickness for turbulent flow was then calculated for the trailing edge of the test model using Eq. (7).

$$\delta_x = \frac{0.385x}{Re_x^{0.2}} \quad (7)$$

These calculations yielded a Friction Reynolds number of $Re_\tau = 272$. The resolvent analysis optimised the geometry to be $h^+ = 16$, a base thickness of $t^+ = 1.13$ and $s^+ = 17.72$. Figure 3(a) demonstrates the initial and optimised profile generated by resolvent analysis, where the profile outlined in red is the optimised geometry. Figure 3(b) shows the

time step iterative process to minimise the gain to a final value of 0.712. However, since the riblet height behaves as a monotonically decreasing function, the predictions favor taller riblets over shorter riblets. Therefore the riblet height manufactured and tested was $h^+ = 10$, to ensure the riblet is within the viscous regime.

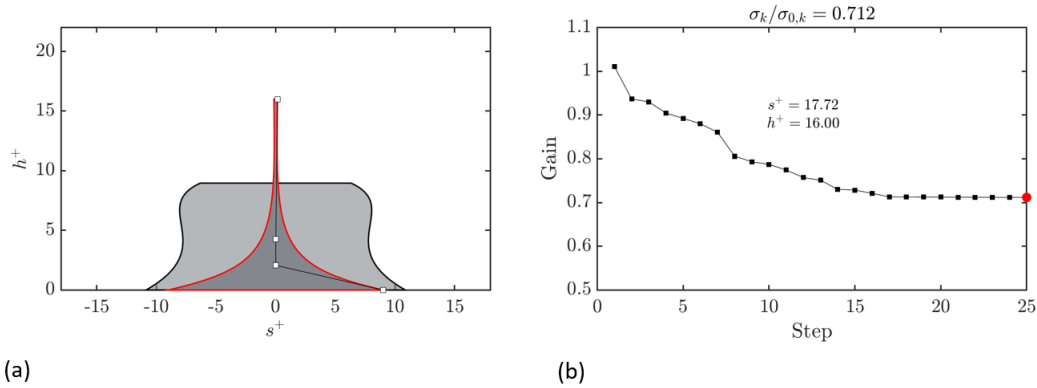


Fig. 3 Optimised blade riblets: (a) Riblet profile in wall units, (b) Gain iterations

The riblet film was then manufactured at MicroTau Pty. Ltd, Fig. 4(a) depicts a microscope image of the riblet cross sectional profile and Fig. 4(b) shows a microscope image of a top down view of the riblet film. The average measured height was $78 \mu\text{m}$, with a base width of $26 \mu\text{m}$ and a spacing of $140 \mu\text{m}$. These values in wall units are; $h^+ = 9.8$, $t^+ = 3.2$ and $s^+ = 17.4$. The height and spacing are thus equivalent to the optimised values, however the thickness of the riblet was larger to ensure durability of the micro-structures.

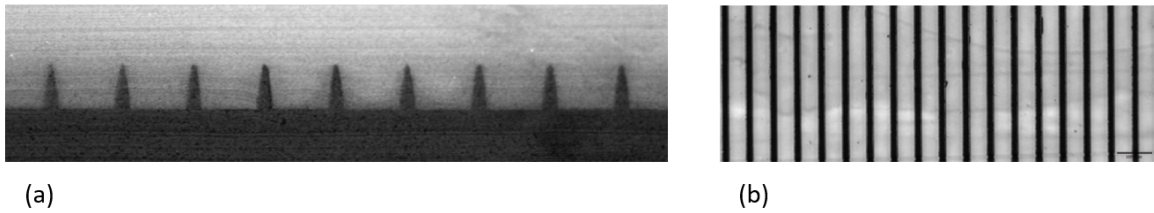


Fig. 4 Blade riblet film; (a) Microscope image taken of a mould of the cross sectional profile using a 10x objective lens, (b) Top down view of the riblet film using a microscope with 5x objective lens.

Dean and Bushan [1] generated performance curves for different riblet geometries for flow over a flat plate. Figure 5 demonstrates the performance curve for blade riblets and it can be seen that for a geometry of $h^+ = 9.8$ and $s^+ = 17.4$, the predicted drag reduction is approximately 8%. Since the geometry is specified in wall units which are non dimensionalized by the flow regime, the performance curve can be extrapolated to other flow conditions.

C. Aerodynamic Force Measurements

The lift and drag force was measured with a two component balance. The resolution of the two component balance was 0.1 N with noticeable fluctuations at 0.01 N thus restricting the accuracy. The balance was connected to a control box which measured the applied aerodynamic forces during the experiment. The angle of attack was varied via the mount and a protractor.

D. Remote Microphone Technique

The unsteady wall pressure was measured using the remote microphone technique described by Awasthi et al. [10]. A flexible tubing approximately 100 mm long with an inside diameter of 0.8 mm was inserted into the pinholes on the model and connected to the microphone housing [10]. The housing had a 3 m long anechoic termination tube. This minimised surface pressure reflections back to the housing. The microphone was a GRAS 1/4 inch type 40PH, with a flat

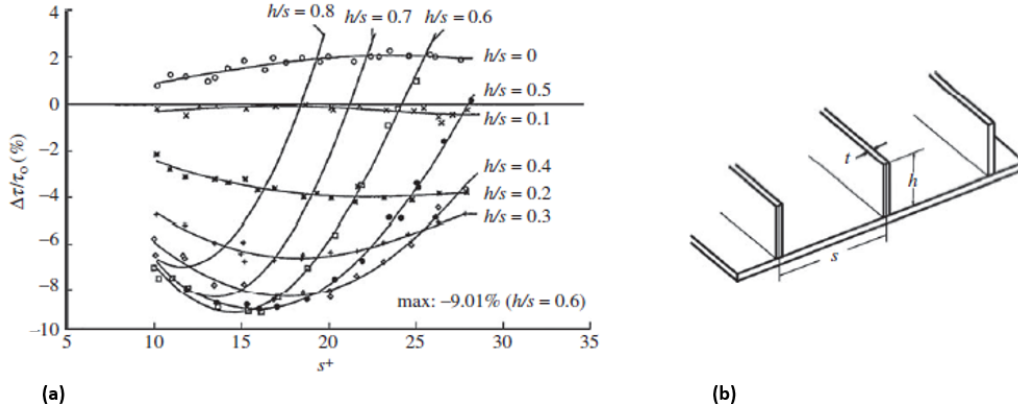


Fig. 5 (a) Blade riblet dimensions and drag-reduction dependence, (b) Schematic of blade riblet geometry [1]

response of ± 1 dB and a frequency up to 12 kHz [10]. This method requires calibration to ensure the pressure measured by the remote microphone is indeed the pressure at the surface, Fig. 6 depicts a CAD schematic of the experimental setup for the remote microphone calibration. This was done by mounting a reference microphone perpendicular to a speaker in an anechoic housing, over the pinholes on the model. The reference microphone was the same model as the remote microphone and both were exposed to the same white noise voltage signal from the speaker. The response of both microphones was measured and the calibration found by calculating the remote microphone transfer function, Eq. (8) [10].

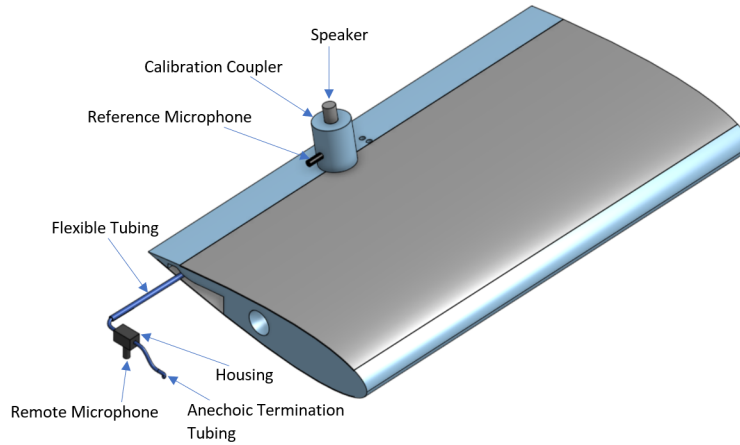


Fig. 6 CAD schematic of remote microphone calibration with labels

$$H_{cal}(f) = \frac{\phi_{(SM)} S_{Ref}}{\phi_{(SR)}} \quad (8)$$

where f is the frequency in Hz, S_{Ref} is the reference microphone sensitivity in V/Pa, $\phi_{(SM)}$ is the cross spectrum between the input voltage signal to the speaker and the remote microphone and $\phi_{(SR)}$ is the cross spectrum between the input voltage signal to the speaker and the reference microphone [10].

III. Results and Discussion

Section A presents and discusses the lift and drag results and Section C the airfoil wall pressure spectra measurements.

A. Lift and Drag Results

The lift and drag measurements were repeated a minimum of four times for each test case to ensure repeatability. The lift and drag coefficients were calculated using the 2D lift and drag equations, Eq. (9) and Eq. (10), respectively using the forces provided by the load cell.

$$C_L = \frac{2L}{\rho V^2 c} \quad (9)$$

$$C_D = \frac{2D}{\rho V^2 c} \quad (10)$$

where L is the lift force in N, D is the drag force in N, V is the freestream velocity and c is the chord length. An analysis of variance table was generated to visualise and filter out any outliers. Figure 7 presents the coefficient of drag data against angle of attack (α) for the smooth airfoil and the airfoil with riblet film with standard error bars, compared to 2D XFOIL simulations. The XFOIL simulations were done at the test case chord Reynolds number with a forced transition point at $x/c = 0.1$ on both the top and bottom surface, an N_{crit} value of 9 and a Mach number of 0.

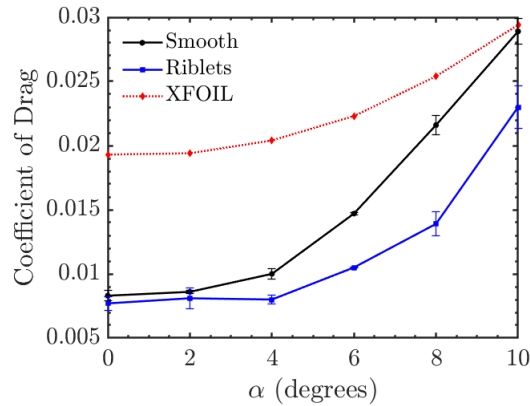


Fig. 7 Drag polar for smooth and riblet film measurements with standard error bars, compared to XFOIL.

Fig. 7 demonstrates that similar trend lines exist between the theoretical and experimental data. However, the measured values for both surface treatments are less than the XFOIL prediction. This difference is likely to be due to the assumption that the wind tunnel model is experiencing two dimensional flow. Since the models had a 2 mm allowance on either side of the wind tunnel wall; wing tip vortices induced a downwash and reduced the angle of attack effectively seen by the local airfoil section. This effect resulted in a percentage of the drag force being due to induced drag, resulting in a discrepancy between theoretical and experimental results.

At angles of attack less than 4° a drag change of -8% is achieved by the riblets, which was theorised by Dean and Bushan [1] based on the riblet wall units. Above $\alpha = 4^\circ$, the drag change increased to a maximum of -36%. Traub [11] demonstrated in 2011, that at moderate angles of attack, in low Reynolds number flow, trip tape can contract or eliminate the laminar transition bubble [11]. Traub's [11] research showed that trip tape at 10% chord at $Re = 100,000$ caused the laminar transition bubble to produce less pressure drag, which in turn increased the extent of turbulent flow and thus the skin friction [11]. Since the mechanism of riblet drag reduction occurs within the turbulent boundary layer, this more established turbulent flow over the surface of the airfoil could be exaggerating the effect of riblets on drag reduction as seen in Fig. 7.

A study by Subashchandar et al. [12] demonstrated a similar relationship where the drag reduction by riblets increased with angle of attack. Their research was on the effect of drag reducing riblets on a NACA0012 airfoil at various angles of attack. The wind tunnel flow was approximated to be 2D at a Reynolds number of 1,000,000 with an airfoil trip at 10% chord [12]. The riblets used on the airfoil had a triangular cross section with a wall unit height of $h^+ = 13$. Subashchandar et al. [12] proposed that the increased drag reduction with increasing angle of attack was due to the flow alteration by riblets in adverse pressure gradients, then when the boundary layer starts to progress towards flow separation, the drag reduction decreases [12]. Figure 8 compares the data from the Subashchandar et al. [12] study with the results obtained in this paper.

The drag reduction curve at angles of attack less than 3° agree with Subashchandar et al. [12]. The reduction of the blade riblets is 1% greater than the triangular riblets, which is likely due to the optimisation of the blade riblet wall units. Dean and Bushan [1] also found that blade riblets yielded higher drag reductions than triangular. Figure 8 shows that as the angle of attack increases, the curves deviate, but follow a similar trend of reaching a maximum drag reduction at a moderate angle of attack, and as the angle of attack progresses to stall, the drag reduction becomes smaller.

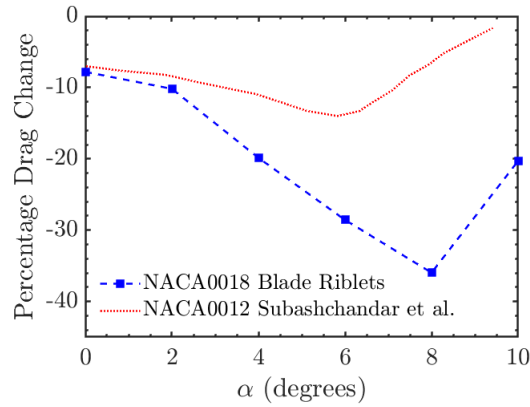


Fig. 8 Drag reduction for various angles of attack compared to the results of a NACA0012 airfoil from Subashchandar et al. [12].

Figure 9 demonstrates the lift measurements for both surface treatments with standard error bars. The data follows the expected linear trend for a pre-stall lift polar, with reasonable error due to the resolution of the two component balance. The riblets have increased the lift coefficient by 24% at $\alpha = 0^\circ$. This effect was seen by Viswanath in 2002 [13]. In a summary of the effect of riblets on aircraft drag reduction, it was found that riblets increased the lift coefficient by 1% for a study on a Do-228 commuter aircraft model [13]. Viswanath [13] found that the increase was due to riblets reducing the boundary layer displacement thickness distribution. The lift increase observed in this paper is much greater than Viswanath [13] but is likely due to the same effect. The lift coefficient measurements are also likely to be impacted by the assumption of 2D flow. In comparison to XFOIL, the lift coefficient measured was 2 orders of magnitude smaller. This discrepancy could be due to wing tip vortices generated by the 3D flow which are not accounted for in the XFOIL simulation.

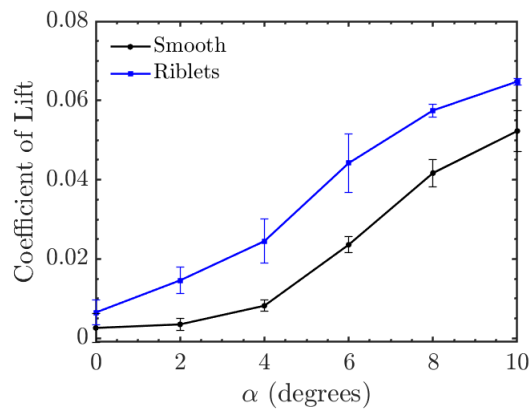


Fig. 9 Lift polar for smooth and riblet film measurements with standard error bars.

The drag results for low angles of attack agree with multiple previous studies [1, 2, 12] that have investigated the effect of riblets on the flow structures in the turbulent boundary layer. Dean and Bushan [1] found that riblets lift the turbulent structures off the surface of the body and only interact with the riblet tips. This reduces the effective wetted surface area and thus reduces the skin friction coefficient. The interaction with the riblet tips was found to induce

small secondary vortices however they were small enough to have a negligible effect on drag [1]. Additionally, ‘by keeping the vortices above the riblet tips, the cross-stream velocity fluctuations inside the riblet valleys’ [1] were much less than a flat plate. Since the results obtained in this paper for low angles of attack agree with Dean and Bushan [1] and Subashchandar et al. [12], it is likely that the mechanism described above is applicable to the results obtained at $\alpha = 0^\circ, 2^\circ$ in Fig. 7.

However, the larger drag reductions at higher angles of attack in Fig. 7 are most likely not due to the same mechanism and further research is required to visualise the effect on the flow structures in the turbulent boundary layer. Therefore, to understand how the above mechanism of drag reducing riblets effects trailing edge noise, the unsteady wall pressure was measured only for $\alpha = 0^\circ, 2^\circ$.

B. Wall Pressure Spectra

Gruber [6] as a part of a study on the effect of serrations on trailing edge noise, measured the trailing edge wall pressure spectra of a tripped NACA0012 airfoil at zero angle of attack and a Reynolds number of 247,000. The results from Gruber [6] were used to validate the trailing edge wall pressure spectra measured on the smooth NACA0018 airfoil. Figure 10 shows the sound pressure level (SPL) measured at $\alpha = 0^\circ$ for all microphones on the smooth airfoil compared to the results of Gruber [6]. It can be seen that the curves follow the same slope, verifying the wall pressure spectra. However, the NACA0018 produces a higher SPL which is likely due to the thickness of the airfoil and different tripping devices.

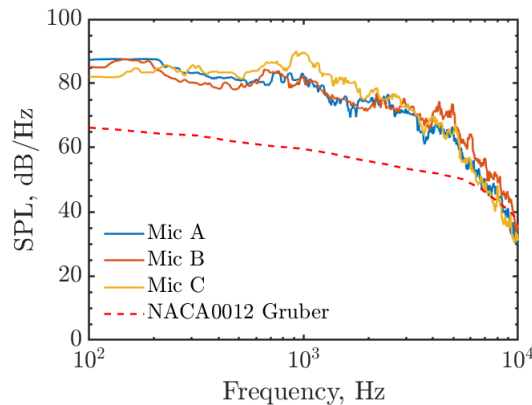


Fig. 10 SPL with a reference pressure of $20\mu\text{Pa}$ of all microphones on the smooth airfoil at zero angle of attack compared to Gruber [6]

Figure 11 compares the SPL on the smooth airfoil to the airfoil with riblet film at zero angle of attack. It can be seen across all microphones that the SPL has a substantial reduction in the mid frequency range (300 Hz - 3 kHz), with an on average maximum reduction of 10 dB at 1kHz. Smaller SPL reductions of about 2 dB at lower frequencies (< 300) Hz) are evident with a slight increase of about 1.5 dB at higher frequencies (> 3 kHz).

It is likely that the increase at higher frequencies is due to the riblet tips inducing secondary smaller vortices as observed by Dean and Bushan [1]. This also demonstrates that drag reducing riblets have little effect on small, high frequency structures in the turbulent boundary layer. The maximum reduction around 1 kHz demonstrates that the riblets have a strong effect on the energy of mid frequency turbulent structures and less of an effect on lower frequency structures.

The surface pressure spectra analysis of $\alpha = 2^\circ$ provides further insight into how riblets are affecting the flow regime in adverse pressure gradients. Figure 12 presents the SPL for each microphone comparing the riblet and smooth airfoils. The SPL plots for $\alpha = 2^\circ$ show similar trends as Fig. 11 with a maximum SPL reduction of 10 dB at 1 kHz. There is a slightly greater increase of 3 dB for high frequencies, and a greater reduction of 4 dB at lower frequencies. The similar trends observed for $\alpha = 0^\circ$ and $\alpha = 2^\circ$ indicate that the effect of the riblets on the flow regime for both angles of attack is similar.

A coherence study was performed for both angles of attack in order to understand the effect of riblets on low - mid range frequency streamwise structures. The coherence was calculated using Eq. (11)

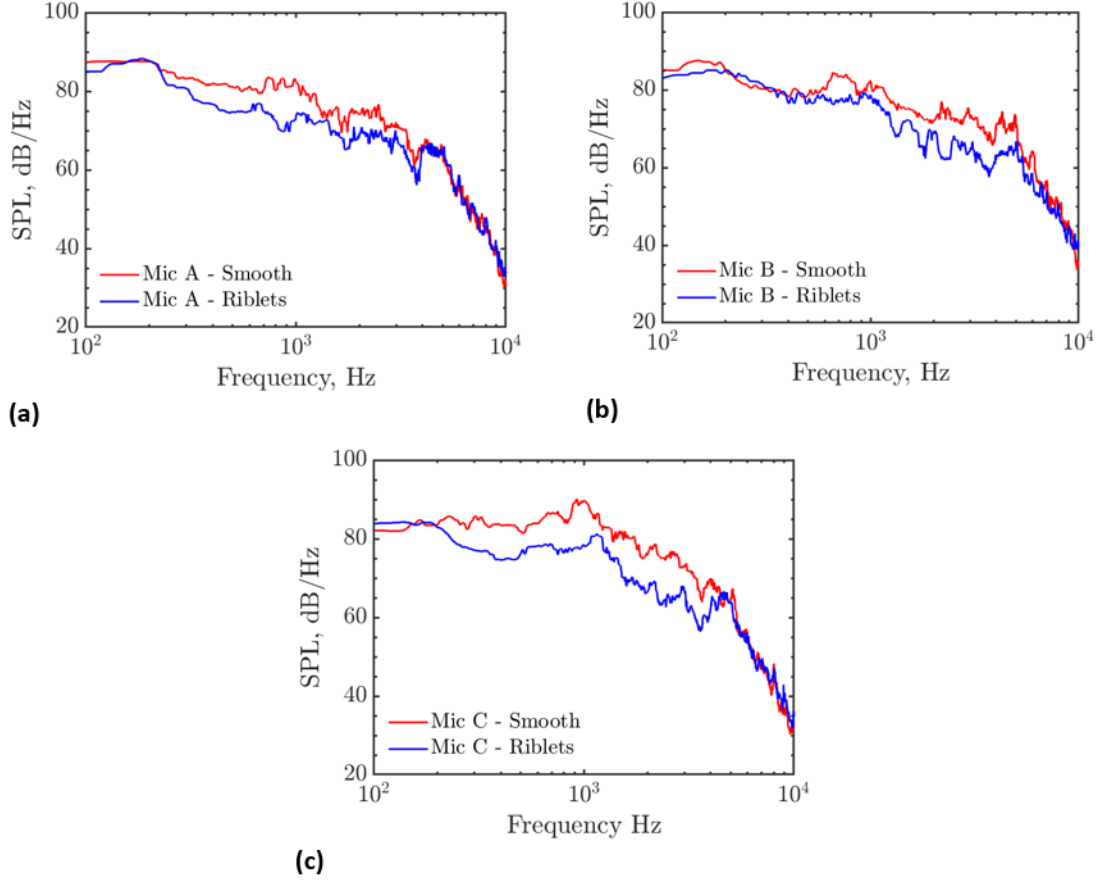


Fig. 11 SPL with a reference pressure of $20\mu\text{Pa}$ of the smooth airfoil compared to the airfoil with riblet film at $\alpha = 0^\circ$, (a) Microphone A, (b) Microphone B, (c) Microphone C

$$\gamma^2(f) = \frac{|\phi_{12}(f)|^2}{\phi_{11}(f)\phi_{22}(f)} \quad (11)$$

where $\phi_{12}(f)$ is the cross spectrum of two microphones, $\phi_{11}(f)$ is the auto spectrum of one microphone and $\phi_{22}(f)$ is the auto spectrum of the second microphone. Figure 13 demonstrates the coherence of streamwise microphones A and C for the smooth airfoil compared to the riblet airfoil, Fig. 13(a) is for $\alpha = 0^\circ$ and Fig. 13(b) is for $\alpha = 2^\circ$. It can be seen for both angles of attack that at low frequencies (< 240 Hz) the riblets have minor effect on the coherence. At mid range frequencies (240 Hz - 4 kHz) the riblets have reduced the coherence, introducing a peak in coherence at 1.2 kHz. Martin and Bushan [2] proposed that riblets optimised for drag reduction reduce the dimensions of surface vortices in the buffer layer, in comparison to a flat plate. Martin and Bushan [2] theorised that because riblets protrude into the turbulent boundary layer, vortex rotation and growth becomes obstructed [2].

The peak in coherence at 1.2 kHz for both angles of attack, could indicate that the flow regime over the surface of the riblets is dominated by vortices of consistent dimensions, where the vortex size is related to the riblet size [2], and varies insignificantly for small angles of attack. The reduction on either side of 1 kHz seen in Fig. 13 is less for the $\alpha = 2^\circ$ case than $\alpha = 0^\circ$, which could be an effect of riblets in adverse pressure gradients. However, the reduction in both cases is likely due to the obstruction of streamwise vortex rotation and growth.

It is apparent that the way drag reducing riblets alter the turbulent boundary layer results in a reduction of the surface SPL by 10 dB for mid frequencies, 2 dB for low frequencies and an increase of 1.5 dB for high frequencies. It is proposed that these trends are a result of mechanisms proposed by other papers on how riblets alter the turbulent boundary layer to reduce drag.

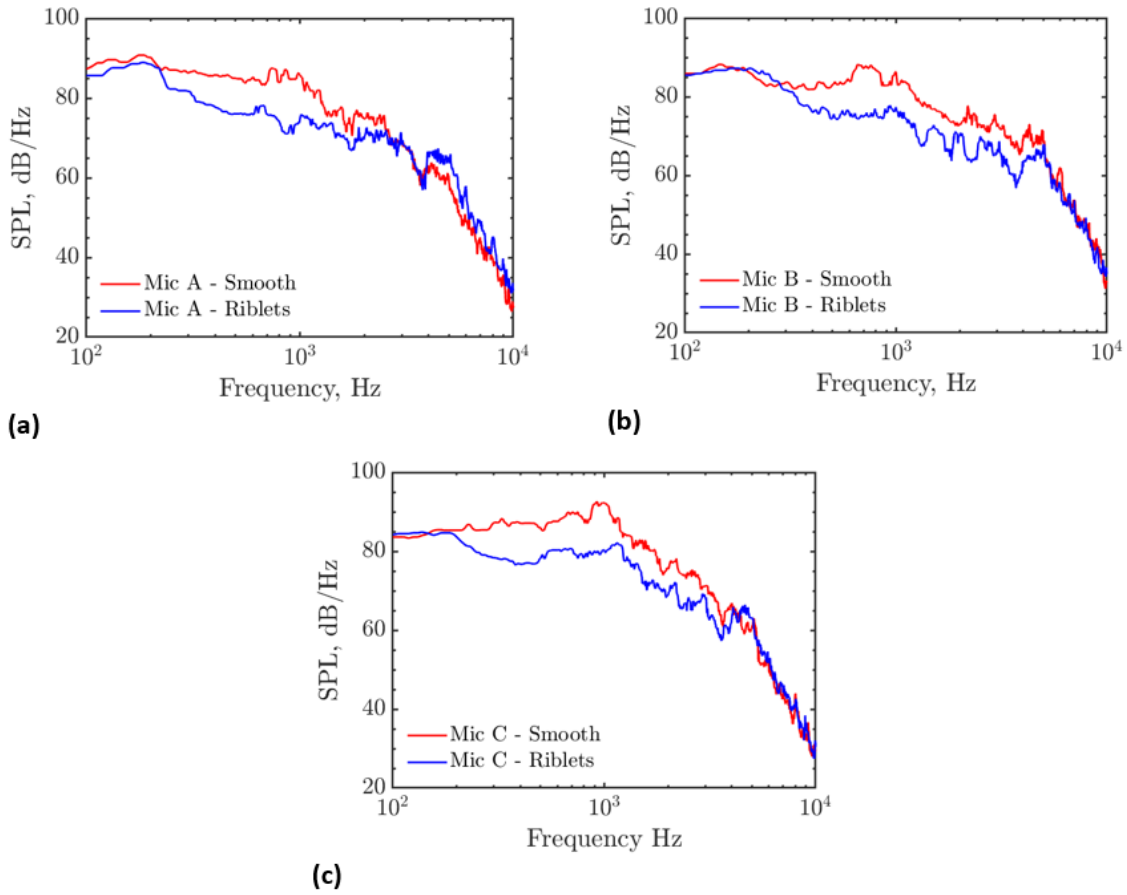


Fig. 12 SPL with a reference pressure of $20\mu\text{Pa}$ of the smooth airfoil compared to the airfoil with riblet film at $\alpha = 2^\circ$, (a) Microphone A, (b) Microphone B, (c) Microphone C

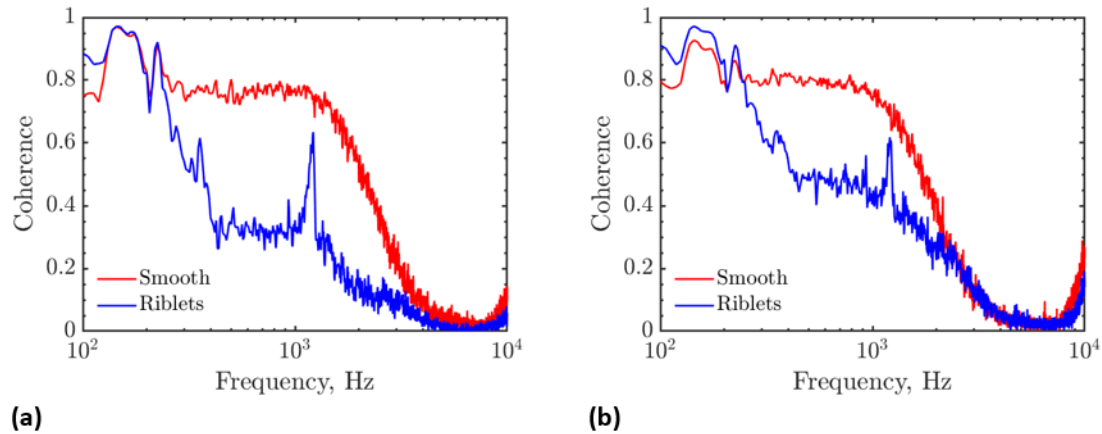


Fig. 13 Streamwise coherence of microphones A and C of the smooth airfoil compared to the airfoil with riblet film at (a) $\alpha = 0^\circ$, (b) $\alpha = 2^\circ$

IV. Conclusion

This paper found that riblets optimised for drag reduction, reduce mid frequency surface sound pressure levels near the trailing edge for low angles of attack. Amiet's theory [7] demonstrated that the surface pressure is the source of trailing edge far field sound and therefore, it can be expected that a reduction in the surface pressure would be seen in the far field sound. This work is important to the aerospace industry as it holds the potential to passively reduce drag and noise simultaneously.

Acknowledgments

The guidance and assistance of Danielle Moreau is gratefully acknowledged.

References

- [1] Dean, B., and Bhushan, B., "Shark-skin surfaces for fluid-drag reduction in turbulent flow: a review," *The Royal Society Journal*, 2019.
- [2] Martin, S., and Bhushan, B., "Fluid flow analysis of continuous and segmented riblet structures," *Royal Society of Chemistry*, 2016.
- [3] McClure, P., Smith, B., Baker, W., and Yagle, P., "Design, Testing and Analysis of 2-D and 3-D Riblets," *AIAA SciTech Forum*, 2020.
- [4] Brooks, T., Pope, S., and Marcolini, M., "Airfoil Self-Noise and Prediction," *NASA*, 1989.
- [5] Shi, Y., and Lee, S., "Numerical Study of 2-D Finlets Using RANS CFD for Trailing Edge Noise Reduction," *AIAA Aviation Forum*, 2018.
- [6] Gruber, M., "Airfoil noise reduction by edge treatments," *University of Southampton*, 2012.
- [7] Amiet, R. K., "Noise due to Turbulent Flow Past a Trailing Edge," *Journal of Sound and Vibration*, 1976.
- [8] TecQuipment, "AF1125 Subsonic Wind Tunnel User Guide," *TecQuipment Ltd*, 2017.
- [9] Chavarin, A., and Luhar, M., "Resolvent Analysis for Turbulent Channel Flow with Riblets," *AIAA JOURNAL*, 2019.
- [10] Awasthi, M., Rowlands, J., Moreau, D. J., and Doolan, C. J., "Two-step hybrid calibration of remote microphones," *Acoustical Society of America*, 2018.
- [11] Traub, L. W., "Experimental Investigation of the Effect of Trip Strips at Low Reynolds Number," *Journal of Aircraft*, 2011.
- [12] Subashchandar, N., Kumar, R., and Sundaram, S., "Drag Reduction Due to Riblets on a NACA 0012 Airfoil at Higher Angles of attack," *National Aerospace Laboratories*, 1995.
- [13] Viswanath, P. R., "Aircraft viscous drag reduction using riblets," *Progress in Aerospace Sciences*, 2002.

The Influence of Inlet Geometry of Circular Reflectors on Pressure Amplification in Shock Wave Focusing

Nathan S. Reed¹

University of New South Wales, Canberra, Australian Capital Territory, 2600, Australia

The interaction of a plane shock wave with a concave cavity generates complex shock focusing phenomena, with past research indicating that the bluntness and size of reflector inlets influences this shock focusing process. The current research investigates the extent to which circular inlets affect the maximum pressure amplification and focus location of shock waves for circular reflector profiles. A numerical parameter study is conducted using an adaptive, unstructured, finite-volume Euler solver, simulating Mach 1.35 shock-cavity interactions into compound profiles of varying inlet radius and joining angle. It is found that increasing the size of profile inlets raises the maximum pressure amplification achieved at focus, whilst shifting the location of gasdynamic focus towards the profile base. A profile with an inlet ratio of 9 and joining angle of 30° is observed to have a focal pressure 2.4 times greater than that of the circular reflector for a Mach 1.35 incident shock. Simultaneous flow visualisation using schlieren imaging and shadowgraphy is used to validate and examine shock focusing mechanisms for the studied compound profiles at Mach numbers of 1.2 and 1.35. The creation and collision of an additional shear layer pair not present in the shock focusing process of a standard circular reflector is observed for compound profiles with large inlets, leading to an increase in focal pressure and a shift in focus location away from the profile base. The spatial and temporal separation of shear layer collisions, largely determined by profile geometry and shock Mach number, is shown to significantly influence peak pressure amplification. Development of these shear layer pairs during shock focusing is shown to be crucial in achieving high pressure amplification; profiles where no Mach reflections occur at the wall perform substantially worse than the circular reflector under equivalent conditions, and have a larger focal region. A novel experimental pressure measurement technique is implemented allowing simultaneous recording of shadowgraph images and pressure sensor readings. This technique shows reasonable agreement to corresponding numerical pressure traces, and permits visualisation of a large portion of the shock focusing process.

I. Nomenclature

α	= joining angle [deg]	P	= static pressure [Pa]
A	= profile aperture [m]	r_{ir}	= inlet ratio
C	= Courant number	r_i	= inlet radius [m]
D	= profile depth [m]	r_r	= reflector radius [m]
D_r	= reflector depth [m]	x	= horizontal coordinate
L_{sc}	= length scaling factor [m]	y	= vertical coordinate

¹Undergraduate, School of Engineering and Information Technology. AIAA Student Member 1192981.

II. Introduction

Since the discovery of the myriad of special effects and phenomena intrinsic to compressible flows, researchers have maintained a keen interest in studying supersonic flow, long before applications for such knowledge were established [1]. Initial applications relating to the flight of bullets has since evolved into a wide field of academia with extensive applications in aeronautics, acoustics, and medicine (primarily in extracorporeal shock wave lithotripsy or ESWL). In particular, the process by which shock waves may be concentrated to create regions of high temperature and pressure has found use beyond the study of gas dynamics, notably within the medical industry [2].

The process of shock wave focusing has been investigated by researchers since the mid-20th century, when Guderley [3] conducted the first study, later revisited by Ramsey et al. [4]. Results predicted in this study were first visualised using schlieren images by Perry and Kantrowitz [5], and validated experimentally by Dennen and Wilson [6]. Subsequent advancements in this field were reviewed by Grönig [7], who also identified potential areas of application of the technology, where the generation of high pressure regions is desired. Such applications include the initiation of detonations [2], study of material behaviours at high pressure [8], and mitigation of the ‘superboom’ phenomenon for supersonic aircraft [9]. Shock wave focusing is a highly non-linear process dominated by strong gasdynamic effects, and was analysed by Sturtevant and Kulkarny [10] using geometric shock dynamics.

The shock focusing process and effectiveness for planar, cylindrical, and parabolic cavities is well understood; improvements in simulation methods and flow field visualisation techniques have allowed the complex flow features of reflectors to be resolved in great detail [11], permitting the study of compound profiles, where convex inlet shapes are blended with the main reflecting surface. The incorporation of inlets has been shown to significantly affect the mechanism of focus and pressure amplification, though research in this area is limited. MacLucas [12] investigated compound profiles that use a combination of circular, parabolic, and catenary shapes for profile reflectors and inlets, demonstrating that the addition of inlets resulted in increased maximum pressure amplification. A novel investigation into shock focusing by Babinsky et al. [13] studied the effect of incorporating inlets onto circular reflecting profiles. This study, conducted using holographic interferometry on experimental setups and an Euler-based Godunov finite volume solver, established a qualitative link between the relative size of circular inlets and the peak pressure measured at focus. A recent review by MacLucas et al. [14] of previously studied profiles indicated that, despite an acknowledged link between the presence of an inlet and the maximum pressure amplification at focus, the role of the inlet is not well characterised.

A. Research Objectives

The objective of this study was to characterise the relationship between relative inlet size, maximum pressure amplification, and focus mechanism resulting from a Mach 1.35 plane shock wave interacting with a compound profile constructed from circular arcs. A representative range of circular compound profiles was investigated in a numerical parameter study, supplemented by findings from experimental testing of several compound profiles in which changes to the mechanism of gasdynamic focus were identified. A limited investigation into the Mach number dependency of amplification effectiveness for the tested profiles was conducted, and a simultaneous flow visualisation and pressure measurement technique was used to corroborate numerical and experimental findings.

Findings from this study may be used to inform the development of more efficient, shallower profiles capable of achieving higher pressure amplification than traditional cavity shapes. Identification of such geometries has the potential to inform future development in the fields of shock wave lithotripsy, detonation initiation mechanisms, and pressure amplification. The observation of new shock focusing mechanisms in the studied compound profiles also improves understanding of the highly nonlinear processes present in shock wave dynamics.

III. Background

A. Shock Wave Reflection

Discontinuities in the flow properties of pressure, density and temperature occur over moving normal shock waves, which can be formed from a sudden release of energy (such as in an explosion or bursting of a pressure vessel), or by the coalescing of acoustic waves formed in front of translating objects, as occurs with objects moving faster than the local speed of sound. An important dimensionless parameter when considering shock waves is the Mach number, defined as the ratio of fluid/object velocity to the local speed of sound. The movement and reflection of normal shock waves along surfaces can generate a wide range of transient reflection phenomena; the precise nature of which is dependent on the strength of the incident shock and surface profile. Unsteady flow and rapidly changing boundary conditions causes shocks produced by the reflection to be curved, with non-uniform shock strength along their length.

Extensive analytical descriptions of shock reflection phenomena are performed by Courant and Friedrichs [15] and Ben-Dor [16]. The two most common reflection types are the Mach reflection and regular reflection, both discovered by Ernst Mach in the late 1800s. For a plane shock wave reflecting within a concave profile, the regular reflection mode consists of an incident shock (I) producing a curved reflected shock (R), as shown in Fig. 1. The Mach reflection mode is similar, differentiated by the addition of another shock, known as the Mach stem (H), and a contact discontinuity (L), which grows from the intersection of the three shocks, or triple point [12].

The type of reflection observed is largely determined by the strength of the incident shock and the wall angle, with strong shocks and large angles leading to regular reflection modes. For smaller angles and weaker shocks, Courant and Friedrichs [15] demonstrated that three classes of Mach reflection may occur, depending on whether the triple point moves towards, parallel to, or away from the reflection surface. Another notable reflection mode is the transitioned regular reflection (TRR) first defined by Ben-Dor [16]. This reflection mode may also be observed in concave cavity flows, occurring when the incident shock wave encounters an ever-increasing wall angle. As the triple point of an inverse Mach reflection collides with the reflection surface, a TRR develops, consisting of a regular reflection immediately followed by a Mach reflection that causes development of a shear layer (S) from the motion of the triple point between shocks (F), (R) and Mach stem (W), also shown in Fig. 1.

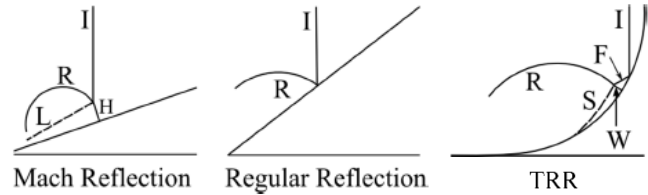


Fig. 1 Mach, regular and transitioned regular reflection modes [12].

B. Shock Wave Focusing

Gas dynamic focus resulting from the coalescence of shocks is capable of generating a small region of high pressure and temperature efficiently and at reduced cost when compared with other methods. The gasdynamic focusing process is commonly studied by reflecting a normal shock from a concave reflector, shown below in Fig. 2 for a circular profile. The reflection process is typically made up of four stages, as defined in Fig. 2.

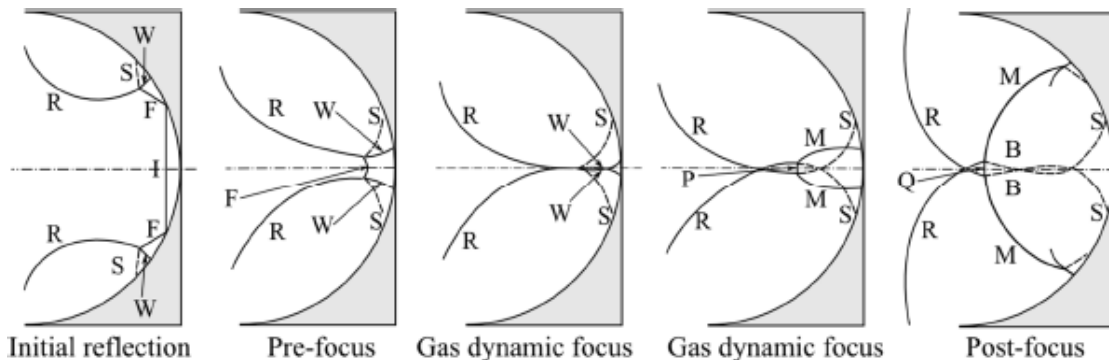


Fig. 2 Four stage focusing process of a plane shock wave with a concave profile [12].

Initially, the incident shock wave (I) moves towards the profile base, with the reflection at the profile wall changing from a regular reflection, to Mach reflection, to TRR [17]. During pre-focus, the shear layers (S) and triple points are moving towards the profile centreline, and the reflected initial wave (F) diminishes in size. The collision of the reflected wave and triple points defines the beginning of gasdynamic focus. During gasdynamic focus, the original wall shocks (W) join, forming the main reflected wave (M), which undergoes a Mach reflection with the original reflected waves (R), producing a new Mach stem (P). The triple points of this Mach reflection enclose a small region as the Mach stem first grows, then diminishes in length. Gasdynamic focus concludes when the triple points collide for the second time, defining the focal region as the area enclosed by the path of the shear layers (B).

In-depth focusing behaviours for several cavity shapes are provided by MacLucas [12], as the precise nature of the shock sequence is strongly dependent on reflector geometry [14], though the principle of shocks coalescing to create a small focal region is evident in all concave profiles designed to focus shocks.

C. Compound Profiles

The shock focusing process has been studied extensively for simple reflecting profiles, with established focusing mechanisms explored in literature for planar, circular, parabolic, catenary, and log-spiral profiles [12,18,19].

Comparatively little research has been conducted into compound profiles, which incorporate convex inlets blended into a traditional reflector profile.

Initial findings by Babinsky et al. [13] identified an increase in maximum pressure amplification achieved by the addition of inlets to a circular profile, a trend also evident when inlets were added to parabolic and catenary reflectors [12]. MacLucas et al. [14] confirmed that inlets can be used to reach higher pressure amplifications at lower depth-to-aperture ratios and incident shock strengths, and recognised that a complete performance map quantifying the extent to which inlets affect pressure amplification is lacking in literature.

IV. Numerical Simulation

A. Numerical Scheme

The numerical solver used for the parameter study was Masterix 3.40, an adaptive, unstructured finite-volume Euler solver [20]. Data collected from simulations was exported to MATLAB for analysis. Masterix is custom-designed to solve unsteady compressible flows, in particular the interaction of moving shocks with objects, and is thus highly suitable to analyse the shock focusing process within concave compound profiles. An Euler-based approach to numerical simulation has been shown in Taieb et al. [21] to be in excellent agreement with full Navier-Stokes computations and experimental findings; the influence of viscosity on observed reflection patterns and triple point movement is typically negligible [22]. Some viscous flow phenomena can be resolved using the selected scheme due to numerical dissipation introduced when computing the density gradient error within mesh elements. The scheme uses explicit time integration, while the flow solver has second-order spatial and temporal accuracy. Wall boundary conditions were used for the symmetry plane and profile wall, while a Dirichlet-type inlet boundary condition was specified for the flow inlet/outlet. The solutions calculated by Masterix were computed using flow and physical properties scaled with respect to user-defined reference values, allowing for direct comparisons between simulations.

For all simulated profiles, the cavity depth D , as defined in Fig. 3, was set to 50 units, and flow was simulated up to 100 units upstream of the cavity to allow the resolution of shock features post-focus. A scaling factor of $L_{sc} = 0.001\text{m}$ is used to dimensionalise the geometry for comparison with similarly-sized shock tube models. Profile wall geometry is comprised of several circular arcs, and the shape of a typical compound cavity, along with its defining parameters is shown in Fig. 3. An important parameter in subsequent analysis, the inlet ratio r_{ir} , is defined in Eq (1) as the ratio of inlet to reflector radius.

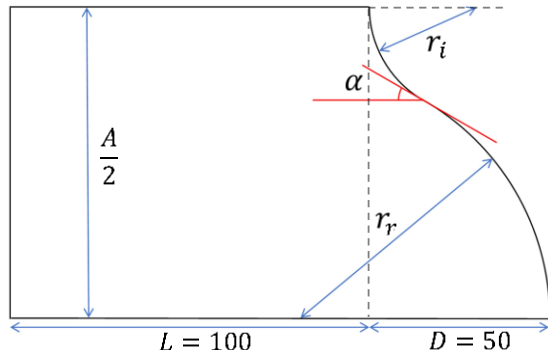


Fig. 3 Simulated compound cavity geometry with circular inlet and reflector.

$$r_{ir} = \frac{r_i}{r_r} \quad (1)$$

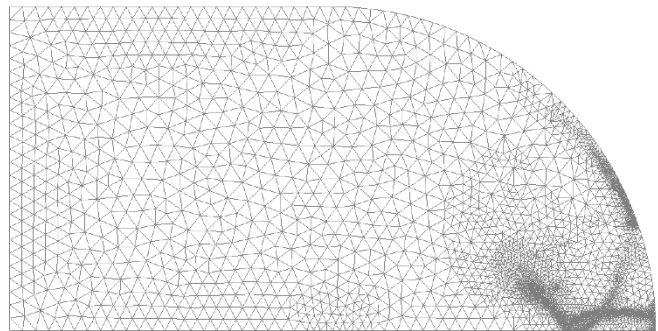


Fig. 4 Circular profile dynamic mesh with 5 levels of refinement, shown during gasdynamic focus.

Fig. 4 shows an example mesh, where varying levels of mesh refinement are clearly visible. Dynamic meshing allows the resolution of flow features of interest such as shock waves and shear layers in greater detail, up to a maximum mesh refinement level specified during initial meshing. Simulations are reduced to a two-dimensional area consisting of the top half of the profile, due to geometric symmetry, in order to reduce the number of mesh elements and computational resources required for each simulation. The minimum timestep is defined using the Courant-Friedrichs-Lewy condition, where the Courant number C was set to 0.5 to ensure solution convergence [23].

B. Verification

As the resolution of the mesh over key flow features is only directly controllable by varying the maximum level of mesh refinement, a mesh independence study was conducted to find the refinement level needed for solution

independence. A simulation of a Mach 1.35 incident shock into a circular cavity profile, shown in Fig. 4, was conducted on eight meshes with increasing levels of mesh refinement. Flow properties were recorded at three locations designed to record the mesh behaviour at the focal point, cavity wall, and towards the profile entrance. The performance of a given mesh did not vary significantly between sampled locations, however increasing the maximum level of mesh refinement markedly improved performance across shocks. The pressure history at a point near the profile wall where the incident shock undergoes a transitioned regular reflection is shown in Fig. 5.

At this location, two shock waves pass over the region in rapid succession, as the reflected wave and Mach stem are in close proximity, shown in the inset of Fig. 5. Distinction between these two shocks is not seen in meshes 1-4, and is only weakly present in mesh 5. Though the peak pressure varies with the choice of mesh [24], the remainder of the solution is mesh-independent for a mesh refinement level of 6 and higher. The timing of the pressure rises is also affected by the choice of mesh, with coarse meshes anticipating the pressure rise immediately preceding shocks. The duration of this anticipation decreases as finer meshes are used, and is negligible for a mesh refinement level of 6, which was therefore used for the remainder of numerical simulations.

C. Validation

Shock focusing tests conducted by MacLucas [12] on a parabolic profile cavity, $x = -10y^2$, with an aperture of 160mm and depth-to-aperture ratio of 0.4, involving pressure traces obtained from PCB transducers placed at various sites within the cavity were used to validate the Masterix mesh and numerical scheme. Flow conditions, profile geometry, and sensor locations from MacLucas [12] were replicated using Masterix, and the resulting numerical pressure traces, averaged over the same area as the pressure transducers, were compared at a selection of transducer locations and incident shock Mach numbers. Fig. 6 shows a comparison between the numerical and experimental pressure traces at one of the transducers, with an indicative image of the flow field and pressure transducer location shown in the inset. Excellent agreement between the traces is observed, allowing clear identification of the flow features passing over the transducer, including the incident wave (I), initial reflected wave (R) and main reflected wave (M). Deviations between the traces post-focus are attributed to the interaction of weak transverse waves present during tests.

D. Parameter Study Design

Previous studies into the shock focusing process of cavities consisting of an inlet and reflector section, known as compound profiles, have demonstrated that the ratio of inlet to reflector radius has a significant effect on the maximum pressure amplification achieved at the point of gasdynamic focus [13]. For a compound cavity where both the inlets and reflector are circular arcs, as shown in Fig. 3, there are three key parameters that define the geometry: the depth-to-aperture ratio D/A , the inlet ratio r_{ir} , and the joining angle α . The effect of depth-to-aperture ratio on the shock focusing process is understood for a wide range of pure reflector profiles, and for circular compound profiles, the depth-to-aperture is determined by the joining angle.

In the present work, simulations were conducted encompassing a wide range of compound geometry configurations. The joining angle of tested geometries was varied from 0° to 60° in increments of 15° , with each selection yielding a unique depth-to-aperture ratio. Ten different inlet ratios were tested for each joining angle, resulting in a total of 50 different profile geometries. To develop a representative range of inlet sizes, for a given joining angle, the inlet radius was systematically increased by 10% of the reflector radius for the inlet-free geometry, and the reflector radius was decreased by the same amount.

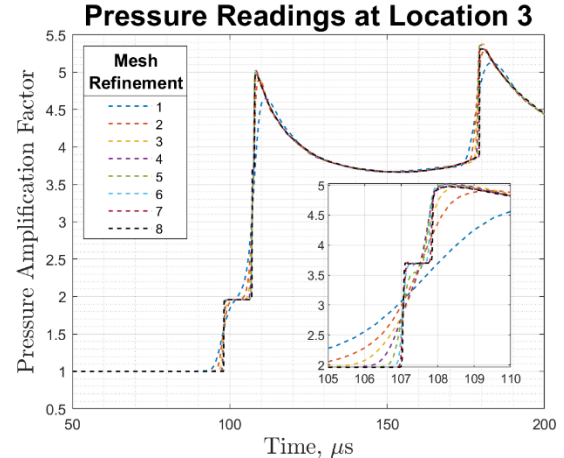


Fig. 5 Pressure amplification history at region undergoing TRR for each mesh refinement level.

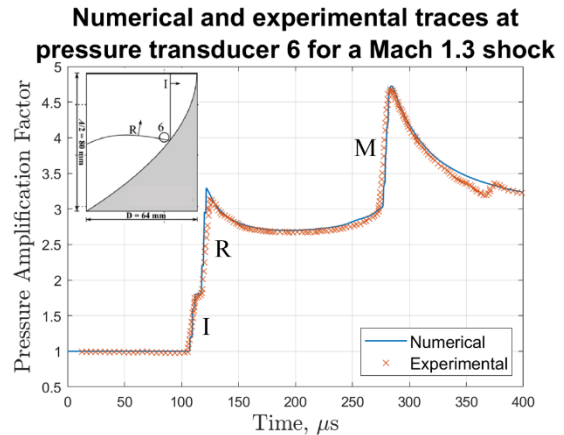


Fig. 6 Numerical and experimental pressure traces at indicated transducer location (inset) at an incident Mach number of 1.3 and atmospheric pressure of 83.1kPa.

V. Experiments

Experiments were conducted at the shock tube facility located at UNSW Canberra at ADFA, which is a conventional diaphragm-operated shock tube with a 150mm high by 75mm wide rectangular test section. Test profiles were subjected to Mach 1.2 and Mach 1.35 normal shocks, and high-speed time-resolved video photography was used to observe the evolution of flow features. Shock wave velocity was measured via time-of-travel measurements with three staggered pressure transducers mounted flush to the tube wall ahead of the test section. Diaphragm thicknesses of $25\mu\text{m}$ and $50\mu\text{m}$ were used to control the burst pressure to achieve the desired flow velocities.

Simultaneous shadowgraphy and schlieren imaging was used to capture qualitative information concerning the location and evolution of flow features, and validate the numerical scheme. The optical system was arranged in a Z-type configuration using a single-source, multiple-camera visualisation concept similar to the second setup described by Kleine et al. [25]. A Shimadzu HPV-1 high-speed camera was used to record shadowgraph images with a resolution of 312×260 pixels and frame rate of 500,000 fps. Schlieren visualisation was captured using a Shimadzu HPV-X2 high-speed camera with a resolution of 400×250 pixels and frame rate varying between 500,000 and 2,000,000 fps. This simultaneous recording technique allowed the observation of the miniscule flow features that occur during gasdynamic focus, with the schlieren system providing a magnified view of the focal region, whilst shadowgraphy of the entire test profile ensured control of test consistency. The optical setup and camera arrangement used in the shock tube facility at UNSW Canberra at ADFA is shown in Fig. 7.

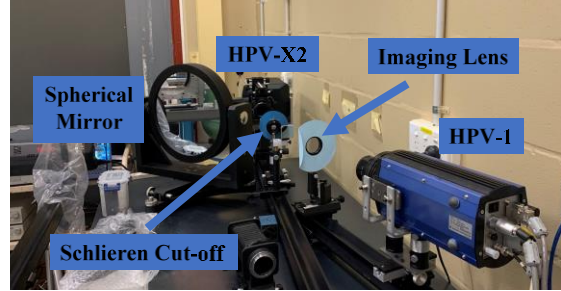


Fig. 7 Camera and optical arrangement for simultaneous time-resolved flow visualisation.

Additional tests were performed using a novel combination of shadowgraphy and a mirror-mounted pressure sensor to generate quantitative and qualitative flow data simultaneously. One of the test section walls was replaced with a plane mirror with an 8mm hole in which a Kistler 603B pressure sensor [26] was mounted.

Three profiles were manufactured for experimental testing from solid aluminium blocks each having a cross-sectional depth of 74.5mm, which were wirecut to yield accurate reflecting face geometries. Cavity profiles were smoothed to reduce surface roughness, that may have caused interference in the form of acoustic perturbations. The details of these profiles are included in Table 1. Fig. 8 shows each of the experimental test profiles secured to the shock tube using two bolts in the rear of each profile.

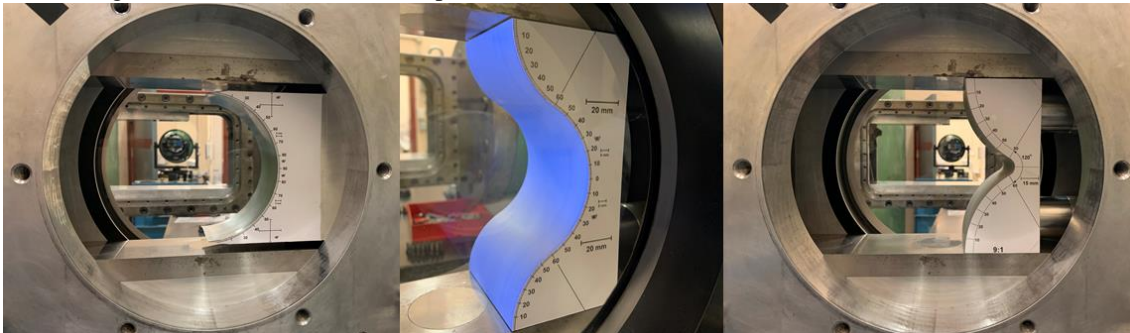


Fig. 8 Shock tube mounting of Control (left), Model B (centre), and Model A (right) test profiles.

Table 1. Test Model Geometry

Model Name	Inlet Ratio	Joining Angle ($^{\circ}$)	Reflector Radius (mm)	Inlet Radius (mm)	D/A
Control	0	0	140	—	0.5
A	9	30	8.6	77.42	0.289
B	1	30	43.01	43.01	0.289

VI. Results

A. Compound Circular Profiles

The work of Babinsky et al. [13] investigated the incorporation of circular inlets to the standard circular reflector profile, and identified that the inlet ratio had a significant effect on the reflection mechanism, peak focusing pressure,

and the shape and extent of the high pressure region generated. That study was limited to numerical and experimental testing of three compound geometries, having inlet ratios of 0.5, 1, and 2. Numerical simulations of similar compound profiles having inlet ratios varying from 0.11 to 9 were conducted as part of the current parameter study to corroborate and augment the findings of Babinsky et al. [13].

The effectiveness of the compound profiles was determined by calculating the magnitudes and locations of pressure maxima along profile centrelines. Pressure values along the profile centreline were saved at each timestep, allowing the construction of pressure trace curves for each profile, which show the spatial extent of the focal regions. Pressure readings were normalised to the focal pressure of the simple circular reflector, and spatial coordinates were normalised to the distance of gasdynamic focus of the circular reflector, to show the shift in pressure amplification and focus location from the simple, well-studied case. Equations (2) and (3) reflect this process, with $P_{(0,0)}$ and $x_{(0,0)}$ indicating peak pressure and focus location for the circular reflector respectively.

$$\text{Pressure Amplification Factor} = \frac{P}{P_{(0,0)}} \quad (2)$$

$$\text{Normalised Distance} = \frac{x}{x_{(0,0)}} \quad (3)$$

Traces of pressure maxima for compound profiles with a joining angle of 0° , comparable to the family of profiles analysed by Babinsky et al. [13], are shown in Fig. 10, which includes the base case of a simple circular reflector. It is apparent that the addition of convex inlets results in an increase in the focal pressure achieved by the profile, as well as a shift in the focal location towards the profile base. The focal region also becomes smaller, with the focal pressure peaks being sharper and more spatially localised.

As suggested by Babinsky et al. [13], the configuration and relative size of the reflector entrance alters the mechanism of focus by introducing additional shocks to and increasing the strength of existing shocks involved in focusing. In all cases with a blunt inlet, the initial reflection mode of the oncoming shock wave is regular, producing a reflected wave (R) which travels towards the profile centreline. As the initial shock passes over the remainder of the inlet, it transitions to a Mach reflection, generating a Mach stem (W). As can be seen in the left image of Fig. 9, once this shock enters the main reflector, it too undergoes a Mach reflection, generating a second Mach stem (H), which collides with the profile wall and becomes a TRR as the wall angle rapidly increases.

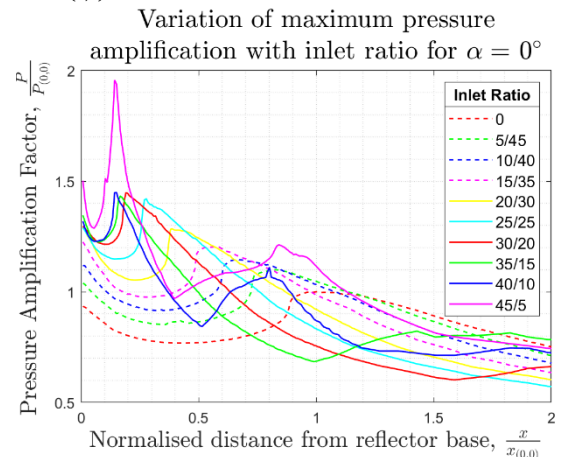


Fig. 10 Normalised pressure traces taken along the centreline for compound profiles with a 0° joining angle for a Mach 1.35 shock.

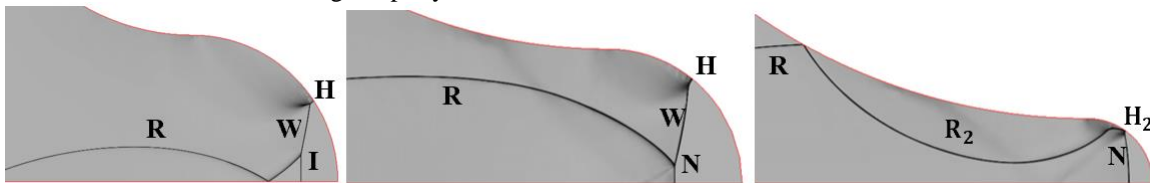


Fig. 9 Pre-focus shock development for compound profiles having a joining angle of 0° and inlet ratios of 1.5 (left), 4 (centre), and 9 (right) for a Mach 1.35 incident shock.

Three different behaviours of the first Mach stem (W) are observed across the tested profiles, determined by profile inlet ratio. For all tested cases with an inlet ratio of 1.5 or less, the Mach stem collides with the profile wall and contributes to the development of the wall TRR; this motion is seen in the left image of Fig. 9. Profiles having inlet ratios larger than 1.5 were observed to generate a longer Mach stem (W) which reaches the reflector centreline before the profile wall, forming a new normal shock (N), which passes over the location of gasdynamic focus before the collision of triple points instead of the reflected wave (R), shown in the centre image of Fig. 9.

For the tested inlet ratio of 9, the focusing mechanism changes again, with the reflected wave (R) undergoing an additional reflection from the opposite wall (R_2) overtaking the Mach stem (W) and undergoing a TRR at the wall to produce a new Mach stem (H_2). This shock (R_2) also crosses over the profile centreline as gasdynamic focus occurs,

as can be seen in the right image of Fig. 9; this second extra shock, along with the strengthened Mach stem (H_2) involved in the gasdynamic focus process, causes a significant increase in peak focal pressure compared to other tested profiles. It can be clearly seen that the time of arrival of each shock involved in the focusing process plays an important part in driving the peak focal pressure, as strong expansions behind each shock counteract the pressure increases of each shock front. Effective amplification is achieved by profiles where shocks reach the focus in rapid succession.

B. Variations in Joining Angle

Numerical simulations were conducted across the same range of inlet ratios for profiles with joining angles of 15° , 30° , 45° and 60° to determine the effect of α on the focusing process, peak pressure, and focal point location.

1. 60° Profiles

Simulations at and beyond a 60° joining angle showed no significant gasdynamic focusing, as the reflection of the incident shock remained regular throughout the interaction, thus no triple points converged at the profile centreline. Both the sonic criterion and experiments tracking the transition from regular to Mach reflection for convex circular surfaces indicate that this change in reflection mode does not take place until after a relative wall angle of 55° is experienced for a Mach 1.35 shock [27]. Instead of the standard gasdynamic focus mechanism of converging triple points, a simpler interaction takes place. For the case with no inlet, the initial shock and its reflection from the profile base cause two pressure jumps in rapid succession, followed by a gradual pressure rise as a weak compression wave travels towards the profile centreline. As the addition of inlets does not change the initial reflection mode at the profile lip, the reflection process remains the same, though as the inlet ratio increases the strength of the compression wave builds, eventually becoming a shock front post-focus in the case of profiles with large inlet ratios. This shock front behaves similarly to the main reflected wave of previously studied profiles, propagating away from the profile base and generating a Mach stem.

Focal regions for profiles of this type are not highly localised, instead a large region of elevated pressure is present along the profile centreline. The maximum pressure amplification of all tested profiles with a 60° joining angle was less than 80% of the focal pressure of the circular reflector, as shown by the pressure trace in Fig. 11.

2. 15° , 30° , and 45° Profiles

The remaining three tested joining angles were all small enough to cause the initial shock to transition from a regular to a Mach reflection as it entered the concave portion of the profile, exceeding the transition criteria detailed in Skews and Kleins [27]. For a given inlet ratio, the maximum Mach stem length decreased as joining angle increased, as the length of the profile wall over which a Mach reflection mode was possible decreased. Thus, the reflection behaviour seen for large inlet ratios and a joining angle of 0° described earlier was observed with decreasing frequency in profiles with non-zero joining angles. Like compound cavities with a joining angle of 0° , arrival timing of shocks at the focal region plays a significant role in determining the peak pressure amplification achieved for a given configuration. Normalised pressure traces along the profile centreline for a joining angle of 30° is shown in Fig. 12.

Across each family of compound profiles, it can be seen that although for small inlet ratios the location of peak pressure amplification is coincident with the location of shear layer collision, there is a rearward shift in the location of the focal point for larger inlet ratios. A sequence of schlieren images of Model B subjected to a Mach 1.35 shock, shown in Fig. 13, illustrates the additional shock interactions taking place during gasdynamic focus to cause the pressure amplification to reach a maximum further from the base than point of shear layer collision.

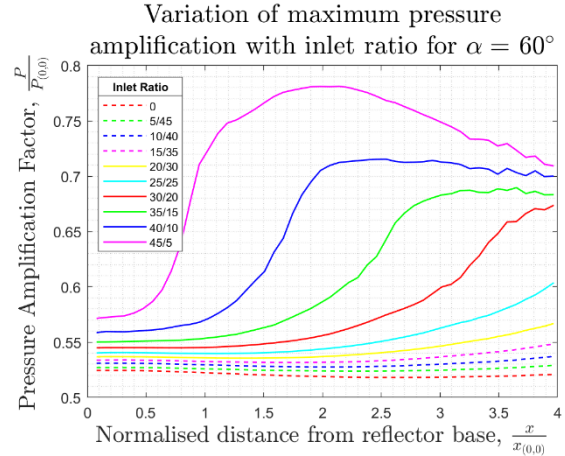


Fig. 11 Normalised pressure traces taken along the centreline for compound profiles with a 60° joining angle for a Mach 1.35 shock.

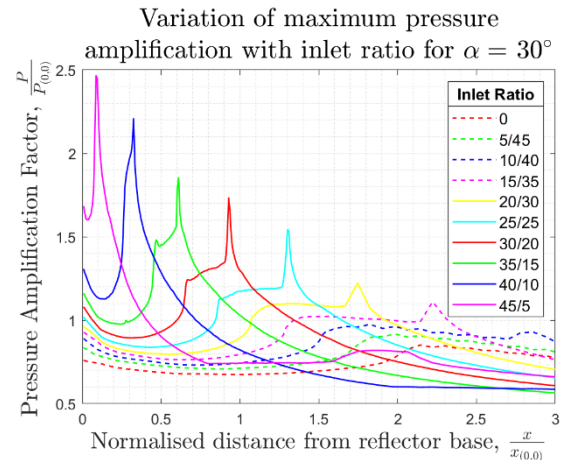


Fig. 12 Normalised pressure traces taken along the centreline for compound profiles with a 30° joining angle for a Mach 1.35 shock.

Behaviour of the main shear layer pair (S), Mach stem (W) and reflected wave (F) remains the same as the base case of the circular reflector. Figures Fig. 13a and Fig. 13b show that the curvature of the reflected wave (R) near the shear layer (S) changes rapidly, becoming a new shock (R') and causing the development of a second set of shear layers (S₂) and triple points. An additional shock front (L) forms as signals from the profile base coalesce.

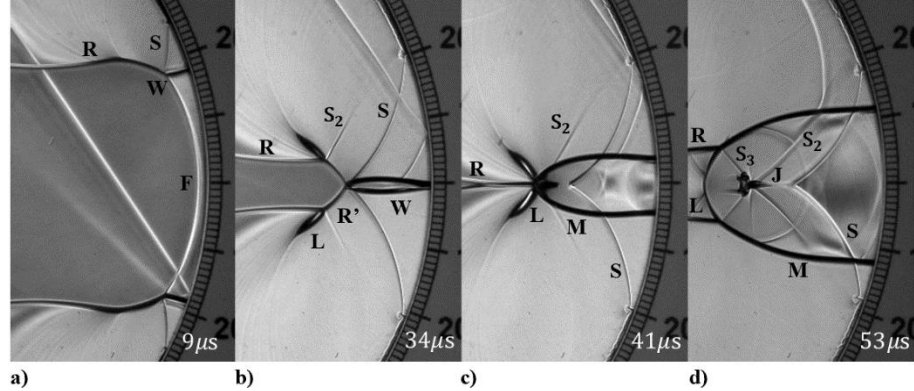


Fig. 13 Monochrome schlieren images of shock focusing behaviour for a Mach 1.35 shock with Model B. Timestamp shows instance of flow field from beginning of image capture. The weak disturbance wave (white) was observed to have a negligible effect on the flow field.

Significant pressure amplification occurs when the shear layers (S) collide, with the wall shocks (W) forming the main reflected wave (M). Gasdynamic focusing continues as the second set of shear layers (S₂) collide shortly thereafter, creating the highest pressure along the profile centreline, shown in Fig. 13c. Figure Fig. 13d shows that post-focus, a strong jet (J) is formed, which quickly develops into a mushroom-shaped vortex flow. A third pair of shear layers (S₃) forms as the main reflected wave (M) and initial reflected wave (R) propagate away from the profile centreline, while the shock front (L) is eventually overtaken by the main reflected wave (M).

A similar focusing process was also observed for Model A under the same conditions, however it occurred much closer to the profile base, leading to crowded schlieren images during focus and high pressure amplification along the profile centreline. Post-focus wall shear layer development for Model A also caused high pressures at the model surface, as the main reflected wave (M) underwent a TRR as it exited the reflector portion of the profile.

The spatial separation between shear layer collision plays an important role in determining the peak focal pressure for the profile, as strong expansion subsequently occurs at each point. Decreasing the spatial, and therefore temporal, separation of these two processes reduces the detrimental effect of expansions on the peak focal pressure. It can be seen in Fig. 12 that increasing the inlet ratio tends to decrease the spatial separation of the two pressure amplification processes, with the highest pressure amplification for a given joining angle occurring when the two collisions are coincident. The highest pressure amplification of all tested profiles occurs at an inlet ratio of 9 and joining angle of 30°, achieving a peak pressure over 2.4 times greater than that of the standard semicircular reflector, hence its selection as Model A for experimental testing in the shock tube. Model B was selected to show the two sets of shear layers more clearly than Model A, to aid in understanding the shock process underpinning the large pressure amplification.

C. Quantitative Analysis of Circular Inlets

For each simulation, the magnitude and location of maximum pressure were calculated from gathered pressure data, and are graphed in Figs Fig. 14 and Fig. 15, normalised to the case of the simple circular reflector. It can be seen that increasing the inlet ratio increases the maximum pressure achieved at focus. Furthermore, truncating the circular reflector to present an initial angle to the incoming shock (ie $r_{ir} = 0$), has the effect of reducing the peak pressure amplification of the profile. Compound profiles with small inlets quickly overtake the circular reflector in terms of maximum amplification, with the 0°, 15°, and 30° profiles having an inlet ratio greater than 0.3 all performing better than the base case. The change in focus mechanism as the incident shock no longer undergoes a Mach reflection is clearly evident in Fig. 14 by the comparatively poor performance of the 60° joining angle geometries.

The importance of arrival timing of each set of shear layers can be clearly seen with the variation in profile performance at high inlet ratios; while the best performing profile has an r_{ir} of 9 and α of 30°, the best performing profile from the

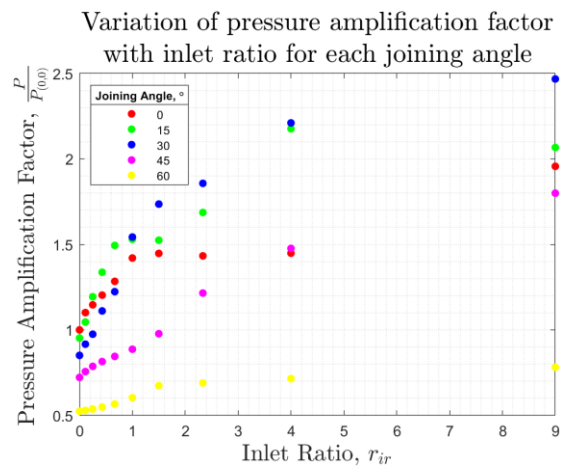


Fig. 14 Focal pressure of each compound profile relative to that of the control, for a Mach 1.35 shock, presented as a function of inlet ratio.

15° joining angle family has an r_{ir} of 4, corresponding to the tested geometry with the smallest separation in the collision of each shear layer pair. The peak pressure achieved in Model A is 2.4 times greater than that generated in a cylindrical cavity, but in a profile with less than 60% the value of depth-to-aperture ratio, highlighting the influence of the inlets on pressure amplification. Pressure amplification for profiles of set depth can be greatly optimised from the case of the circular reflector through the use of large inlets and a small reflector.

Furthermore, experimental data collected for Mach 1.2 incident shock waves found that the focusing mechanism remained unchanged for the studied compound profiles, though the location and separation of shocks and shear layer collisions changed from the Mach 1.35 tests. These findings indicate that optimisation of compound profiles is only possible across a narrow range of Mach numbers, as the expansions following each shear layer collision reduce focal pressure significantly when they do not occur simultaneously or in rapid succession.

From Fig. 15, the location of peak pressure is seen to shift closer to the profile base as reflector diameter decreases and inlet ratio increases, regardless of joining angle. Several changes to this trend, shown by the line discontinuities in Fig. 15, are attributed to the point of peak pressure changing from the initial collision of shear layers (S) to that of the collision of shear layers (S_2) detailed previously. For the case of truncated reflectors, the focal location is shifted away from the profile base as joining angle is increased. The change in focus mechanism for the 60° joining angle cases shifts the focal region significantly further away from the reflector base, with only three of the simulated profiles having a focus location within the profile geometry (and hence the data collection region).

Experimental data collected using the simultaneous pressure measurement and shadowgraphy technique shows reasonable levels of agreement to corresponding numerical pressure traces; a comparison between the traces for a Mach 1.2 shock in Model B is shown in Fig. 16, with the location of the pressure transducer shown in the shadowgraph inset (green). Numerical traces were developed by simulating pressure readings across a number of point determined using an equal-area decomposition of the physical pressure sensor [28]. Rise time across shock fronts is captured well, though the data suffers from strong averaging effects due to the large (5.5mm) diameter of the sensor. Peak pressure is captured well for Model B, though the level of agreement is lower for Model A, and in all tests, the corresponding shadowgraphs show significant image doubling due to the quality of the glass mirror used.

VII. Conclusion

Increasing the inlet ratio of compound circular profiles was shown to increase peak pressure amplification, confirming the results of Babinsky et al. For small inlet ratios, increasing the joining angle causes a decrease in pressure amplification, though for large inlet ratios focal pressure is greatly amplified even at large joining angles. For a Mach 1.35 shock, a compound profile with an inlet ratio of 9 and joining angle of 30° was seen to have a peak focal pressure over 2.4 times greater than that achieved in a circular reflector under the same conditions. Maps of focal point location indicate that increasing the inlet ratio causes gasdynamic focus to occur closer to the profile base. Profiles in which no transition from regular-to-Mach reflection modes occur reach lower peak pressures and have a wider focal region than the base case of the circular reflector.

The gasdynamic focusing process for compound profiles with large inlet ratios is observed to involve the creation and collision of an additional pair of shear layers, generated as the initial reflected wave undergoes a rapid change in curvature. This pair of shear layers causes a second pressure rise during focus, the effectiveness of which is largely determined by Mach number, as well as the spatial and temporal separation of triple point collisions. A novel pressure measurement and shadowgraph technique provides simultaneous quantitative and qualitative flow data, showing

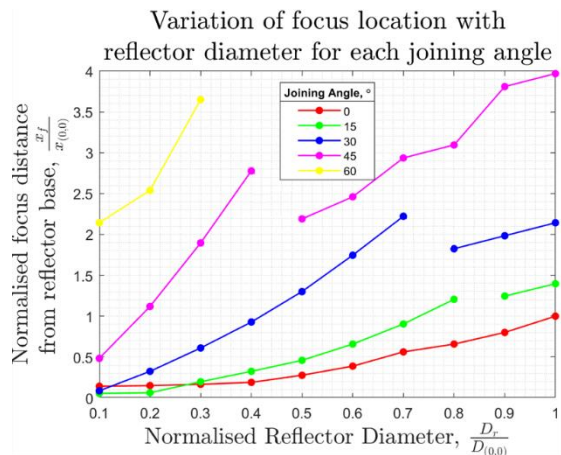


Fig. 15 Focus distance from reflector base relative to the focal distance of the control profile for each profile for a Mach 1.35 shock.

Experimental and numerical pressure traces for Model B subjected to a Mach 1.2 shock

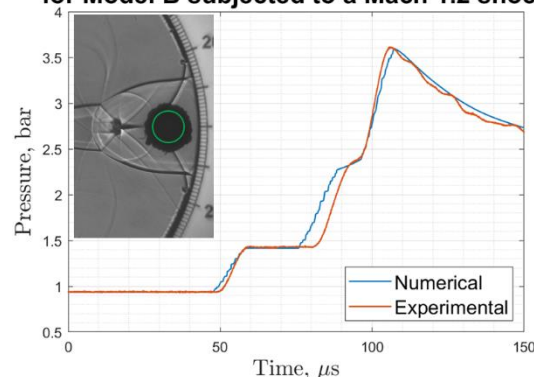


Fig. 16 Numerical and experimental pressure traces for Model B subjected to a Mach 1.2 shock.

reasonable agreement to numerical methods. Findings from this study confirm that inlets can be used to develop profiles that achieve higher pressure amplification at lower depth-to-aperture ratios than simple reflecting profiles, which may improve the design of shock focusing devices used in ESWL and other applications.

Future work would involve testing the compound profiles across a wider range of Mach numbers, improving upon the simultaneous pressure measurement and shadowgraph technique employed in this project by decreasing the size of the pressure sensor and improving the quality of the reflecting surface to reduce the doubling of flow images.

Acknowledgments

The author acknowledges the efforts of Brendan Wallace for his work in manufacturing the reflector models, and the efforts of the project supervisor, Associate Professor Harald Kleine, who set up and calibrated the optical systems, assisted in the operation of shock tube tests, and provided significant support and expertise throughout the project.

References

- [1] Bar-Meir, G., 2007. *Fundamentals Of Compressible Fluid Mechanics*. Orange Grove Texts Plus, pp.5-6.
- [2] Smirnov, N., Penyazkov, O., Sevrouk, K., Nikitin, V., Stamov, L. and Tyurenkova, V., 2017. Detonation Onset Following Shock Wave Focusing. *Acta Astronautica*, 135, pp.114-130.
- [3] Guderley, G. 1942. Starke Kugelige und Zylindrische Verdichtungsstöße in der Nähe des Kugelmittelpunktes bzw. der Zylinderachse. *Luftfahrtforschung*, 19: 302–312.
- [4] Ramsey, S., Kamm, J. and Bolstad, J., 2012. The Guderley Problem Revisited. *International Journal of Computational Fluid Dynamics*, 26(2), pp.79-99.
- [5] Perry, R. and Kantrowitz, A., 1951. The Production and Stability of Converging Shock Waves. *Journal of Applied Physics*, 22(7), pp.878-886.
- [6] Dennen, R. and Wilson, L., 1962. Electrical Generation of Imploding Shock Waves. *Exploding Wires*, 2, pp.145-157.
- [7] Grönig, H., 1985. Shock Wave Focusing Phenomena. In: *Fifteenth International Symposium on Shock Waves and Shock Tubes*.
- [8] Apazidis, N., Kjellander, M. and Tillmark, N., 2013. High Energy Concentration by Symmetric Shock Focusing. *Shock Waves*, 23(4), pp.361-368.
- [9] Marchiano, R., Coulovrat, F. and Grenon, R., 2003. Numerical Simulation of Shock Wave Focusing at Fold Caustics, with Application to Sonic Boom. *The Journal of the Acoustical Society of America*, 114(4), pp.1758-1771.
- [10] Sturtevant, B. and Kulkarny, V., 1976. The Focusing of Weak Shock Waves. *Journal of Fluid Mechanics*, 73(4), pp.651-671.
- [11] Skews, B. and Kleine, H., 2007. Flow Features Resulting from Shock Wave Impact on a Cylindrical Cavity. *Journal of Fluid Mechanics*, 580, pp.481-493.
- [12] MacLucas, D., 2012. *Shock Wave-Induced Flow Features In Concave Profiles*. Ph.D. University of the Witwatersrand.
- [13] Babinsky, H., Onodera, O., Takayama, K., Saito, T., Voinovich, P. and Timofeev, E., 1998. The Influence of Entrance Geometry of Circular Reflectors on Shock Wave Focusing. *Computers & Fluids*, 27(5-6), pp.611-618.
- [14] MacLucas, D., Skews, B. and Kleine, H., 2020. Shock Wave Interactions Within Concave Cavities. *Experiments in Fluids*, 61(3).
- [15] Courant, R. and Friedrichs, K., 1948. *Supersonic Flow And Shock Waves*. New York: Interscience Publishers Inc.
- [16] Ben-Dor, G., 2007. *Shock Wave Reflection Phenomena*. 2nd ed. Berlin: Springer-Verlag Berlin Heidelberg.
- [17] Ben-Dor, G. and Takayama, K., 1985. Analytical Prediction of the Transition from Mach to Regular Reflection over Cylindrical Concave Wedges. *Journal of Fluid Mechanics*, 158, pp. 365–380.
- [18] Bond, C., Hill, D., Meiron, D. and Dimotakis, P., 2009. Shock Focusing in a Planar Convergent Geometry: Experiment and Simulation. *Journal of Fluid Mechanics*, 641, pp.297-333.
- [19] Inoue, O., Imuta, S., Milton, B. and Takayama, K., 1995. Computational Study of Shock Wave Focusing in a Log-Spiral Duct. *Shock Waves*, 5(3), pp.183-188.
- [20] Masterix, 2010. *Masterix*. Toronto: RBT Consultants.
- [21] Taieb, D., Ribert, G., Hadjadj, A., 2010. Numerical Simulations of Shock Focusing over Concave Surfaces. *AIAA Journal*, 48(8), pp.1739-1747.
- [22] Kleine, H., Timofeev, E., Hakkaki-Fard, A. and Skews, B., 2014. The Influence of Reynolds Number on the Triple Point Trajectories at Shock Reflection off Cylindrical Surfaces. *Journal of Fluid Mechanics*, 740, pp.47-60.
- [23] De Moura, C.A. and Cumbrouly, C.S., 2013. *The Courant-Friedrichs-Lewy (CFL) Condition*. AMC, 10, p.12.
- [24] Izumi, K., Aso, S. and Nishida, M., 1994. Experimental and Computational Studies Focusing Processes of Shock Waves Reflected from Parabolic Reflectors. *Shock Waves*, 3(3), pp.213-222.
- [25] Kleine, H., Hiraki, K., and Nonaka, S., 2019. Simultaneous Time-Resolved Density-Sensitive Visualization of High-Speed Flows. *32nd International Congress on High-Speed Imaging and Photonics*.
- [26] Kistler, 2010. *Quartz Pressure Sensor for High Frequencies Type 603B*. [PDF] Winterthur: Kistler Group. Available at: <<https://www.process-controls.com/intertechnology/Kistler/indexPressure.htm>>.
- [27] Skews, B. and Kleine, H., 2010. Shock Wave Interaction with Convex Circular Cylindrical Surfaces. *Journal of Fluid Mechanics*, 654, pp.195-205.
- [28] Gringorten, I. and Yezpey, P., 1992. *The Division of a Circle or Spherical Surface into Equal-Area Cells or Pixels*. (No. 343). Phillips Laboratory, Directorate of Geophysics.

Failure Identification for Passenger Aircraft with Multimodel Approach

Adam Adila Arif¹ and Rianto Adhy Sasongko²
Institut Teknologi Bandung, Bandung, Jawa Barat, 40135, Indonesia

Passenger aircraft is one of aircraft type that mostly used in last few years. Most of the time it follows common mission profile which including takeoff and landing procedure. Those two procedures are so critical and it contribute to most of accident happened in recent years. In this paper, passenger aircraft will be modeled based on ATR-72 using semi empirical data in MATLAB and SIMULINK environment. The aircraft will be simulated as if in takeoff condition with few control surface's performance is degraded and will affect aircraft overall performance. To detect the failure, aircraft model will be compared with linear databases consist of Kalman Filter bank, and when one of the estimation has the closest responses to aircraft model, identification model will determine which mode of failure that occurred at the mean time.

I. Nomenclature

e	= error
y	= measurement
y^*	= estimate
j_i	= error of i -th estimation model
$f(s)$	= transfer function
HM	= Hinge moment
δ_e	= elevator deflection
\hat{x}	= state estimation
\hat{y}	= output estimation
P	= covariance matrix
Q	= process noise matrix
R	= measurement noise matrix
X	= actuator distance traveled
Z	= aircraft position in Z-axis inertial frame

II. Introduction

Passenger aircraft is one of aircraft type that mostly used in last few years compared to another type of aircraft such as utility, cargo, and others. Most of the time, passenger aircraft fly following common mission profile which are engine-on – taxi out – takeoff – climb – cruise – descent – approach – landing – taxi in – engine off. Passenger aircraft well known as safest transportation mode beside other transports seen from casualty per distance traveled. Even so, there are two phases in aircraft flight that extremely crucial that called Critical Eleven (Magazine, 1990) which are takeoff and landing phases. Based on latest report by Boeing, those two phases contribute 63 percent of incident with takeoff 14 percent and approach-landing 49 percent as shown in Fig. 1 (Boeing, 2018), so safety measurement on those two phases are extremely important to look into.

¹ Student, Department of Aerospace Engineering – Faculty of Mechanical and Aerospace Engineering, AIAA Student Member

² Lecturer, Department of Aerospace Engineering – Faculty of Mechanical and Aerospace Engineering, AIAA Professional Member.

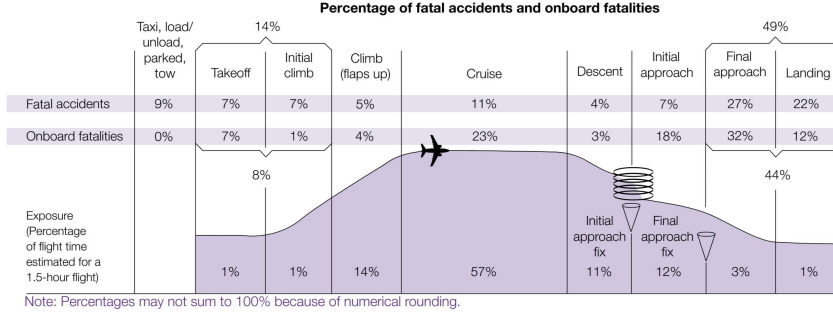


Fig. 1 Aircraft Incident Data in 2008-2017(Boeing,2018)

To examine aircraft performance, behavior, and controller parameter needed when failures present, simulation will be conducted in MATLAB and Simulink environment with ATR-72 aircraft as the basic model, and actuator modeled as transfer function referring to previous research. The actuator itself consist of 4 operation modes which is normal/nominal condition, pressure loss, high friction, and floating to imitate common failure that occurred on the actuators. The aircraft will be simulated on takeoff condition with elevator actuator performance degrade in a certain time. To identify the failure, Kalman Filter (Grimble, 1994) will be used as an estimator to estimate aircraft responses when there was a failure as well as to nullify noise, and the amount of Kalman Filter as estimators proportional to failure cases because in this method the failures are predefined. To detect the failures, the plant (aircraft non-linear model and actuator model) responses will be compared with estimation output from Kalman Filters, when one of the estimation output has closest values to the plant it will be detected as failure occurring at the mean time and determine which mode of failure that occurred. This method aims to detect and isolate control surfaces failures so that aircraft performance will not degrade even there are failures occurred.

III. Failure Identification with Multimodel Approach

Failure identification method that used in this paper is multimodel switching and tuning (MMST) which utilized linear model to estimate aircraft responses when there is failure occurred (Kumpati S. Narendra, 2003). In this paper, linear model that will be used are Kalman Filter with A, B, C, D matrices obtained from linearization of aircraft nonlinear model and actuator condition in certain operating point. Because of the failures are predefined, so there will be a number of models depends on the failure defined as shown in Fig. 2.

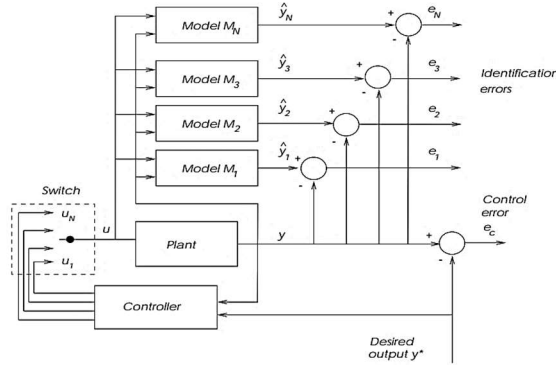


Fig. 2 MMST Block Diagram

To identify failures, the responses from plant (aircraft and actuator) then compared with estimation of model banks and defined as responses error. The model that has smallest error will be selected and the information will be used to determine which mode of failure occurred at the mean time. The equation to define error stated in equation (1) with e is difference between plant and estimated model, J_i is i -th model error which selected model will be one with minimum value of J . But in this paper it will mainly discussed on identification method first,

$$e_c = (y - y^*) \quad (1)$$

$$\begin{aligned}
J_i(t) &= e_i^2(t) \\
J_i(t) &= \int_0^t e_i^2(\tau) d\tau \\
J_i(t) &= \alpha e_i^2(t) + \beta \int_0^t e_i^2(\tau) d\tau \\
J_i(t) &= \alpha e_i^2(t) + \beta \int_0^t e^{-\lambda(t-\tau)} e_i^2(\tau) d\tau
\end{aligned} \tag{2}$$

A. Failure Model

In order to depict failure of control surfaces in takeoff phase, this paper will focus on failure of elevator only since elevator is one of main control for climbing beside of thrust from the engine. To generate asymmetrical effect on failure condition, only one elevator will have failure condition so that it will generate roll rate from elevator deflection difference. Based on aircraft model discussed in chapter IV, each elevator will produce lift as well as pitching and rolling moment as shown in equation (3)-(5) with term $\frac{1}{2}\rho V^2 SC_{l_{\delta_e}}(\delta_{e_r} - \delta_{e_l})b = 0$ if both elevator deflection have same value.

$$L = \frac{1}{2}\rho V^2 SC_L + \frac{1}{2}\rho V^2 SC_{L_{\delta_e}} \delta_e \tag{3}$$

$$M = \frac{1}{2}\rho V^2 SC_{M\bar{c}} + \frac{1}{2}\rho V^2 SC_{M_{\delta_e}} \delta_e \bar{c} \tag{4}$$

$$l = \frac{1}{2}\rho V^2 SC_{l_b} + \frac{1}{2}\rho V^2 SC_{l_{\delta_a}} \delta_a b + \frac{1}{2}\rho V^2 SC_{l_{\delta_e}} (\delta_{e_r} - \delta_{e_l}) b \tag{5}$$

To model the actuators failure condition, first it will be simulated using non linear model which the deflection output is a function of deflection command and hinge moment acting on the surfaces as shown in diagram in and Eq. (3) – Eq. (6). Using nonlinear model, it will be simulated on small deflection and hinge moment value to linearize the model using Low Order Equivalent System (LOES) so that the model can be represented with transfer function. To validate the model, non-linear and linear model disturbed by sinusoidal input and the result presented in Fig. 4 shown significantly small difference.

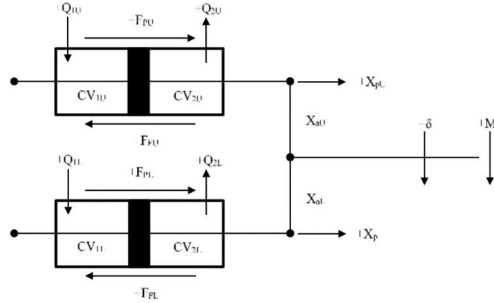


Fig. 3 Non-linear Model Scheme of Actuator (Ndaomanu & Sasongko, 2019)

$$X_{aU} = f(\delta) \tag{6}$$

$$X_{aL} = f(\delta) \tag{7}$$

$$\dot{X}_{pU} = X_{aU} \dot{\delta} \tag{8}$$

$$\dot{X}_{pL} = -X_{aL} \dot{\delta} \tag{9}$$

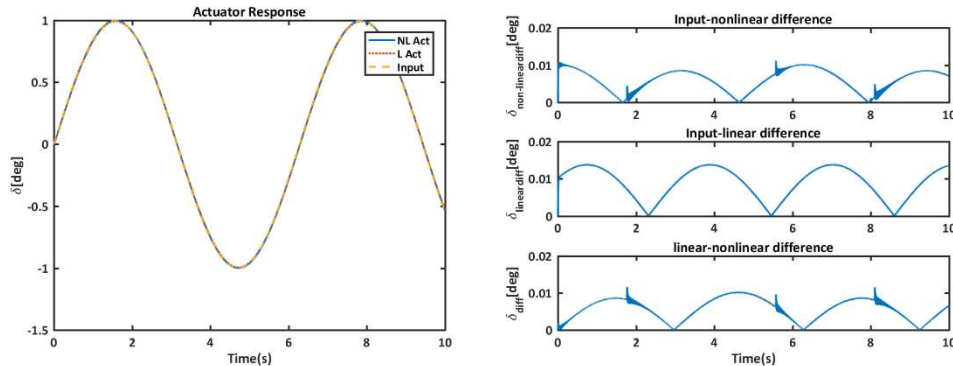


Fig. 4 Non-linear and Linear Response Comparison

Failure case for elevator actuator will be based on related research with 4 operating condition as mentioned in Table 1. Elevator deflection itself will be affected by deflection command and hinge moment acting on the elevator surface as shown in equation (6) with $f_{\delta_{ec}}(s)$ and $f_{HM_e}(s)$ are transfer function representing nonlinear model (Ndaomanu, 2019).

Table 1 Actuator Operating Condition

No	Operating Condition
Case 1	Operating normally/nominal condition
Case 2	Hydraulic pressure reduced by 50%
Case 3	Piston friction 35 times larger
Case 4	Both upper and lower actuators are in standby so it is in floating condition

$$\delta_{e_{actual}} = \delta_{e_{command}} * f_{\delta_{ec}}(s) + HM_e * f_{HM_e}(s) \quad (10)$$

Elevator failure case that will be simulated is right elevator will be operating normally while left elevator will switching to operating condition 1-2-3-4 each 40 seconds as shown in Fig. 5. Difference between right and left elevator deflection on climb openloop flight shown in Fig. 6. Condition 2-3 will have slight difference on deflection while condition 4 will deviate abruptly since it cannot be commanded and only depends on hinge moment at the mean time.

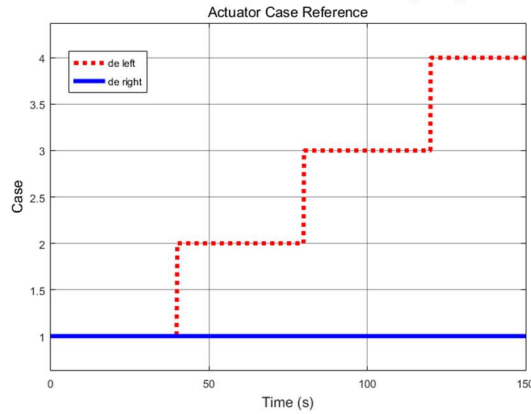


Fig. 5 Elevator Failure Case

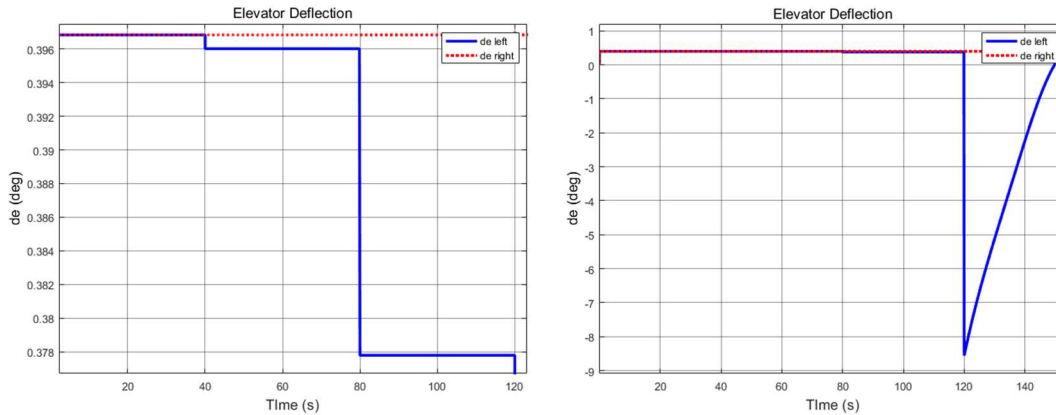


Fig. 6 Elevator Deflection Difference on Failure Condition (red=right, blue=left)

B. Identification Model

As mentioned in this chapter earlier, identification method will utilize kalman filter to estimate aircraft responses when failure occurred, so that there will be kalman filter bank model since the failures are predefined. Kalman filter model will consist of A, B, C, D matrices as state estimation model with elevator deflection and plant measurement as the input. A, B, C, D matrices parameter value are obtained from linearization result of aircraft series with actuator to plant model. Kalman filter equation that used to estimate aircraft response on failure is shown in equation (7)-(8),

$$\begin{aligned} L &= (PC^T + \bar{N}) \\ \dot{P} &= AP + PA^T + \bar{Q} - L\bar{R}L^T \\ \hat{x} &= A\hat{x}Bu + L(y - C\hat{x} - Du) \end{aligned} \quad (11)$$

$$\begin{aligned} \hat{y} &= C\hat{x} + Du \\ \bar{Q} &= GQG^T \\ \bar{R} &= R + HN + N^TH^T + HQH^T \\ \bar{N} &= G(QH^T + N) \end{aligned} \quad (12)$$

In this simulation case, there will be 4 kalman filter estimator with each estimator has different parameter to emulate aircraft response when failure occurred. Identification flow diagram is shown in Fig. 7 with both plant and identification models receive same input, but there will be 4 estimated response since there are 4 cases for actuator condition. Each estimated response will be compared using equation (1) to define error, and using equation (2) model that has minimum value of J will be chosen as closest one with plant. If identification model yield model 1 so that there is no failure occur, while otherwise, there is failure occur at the mean time. In this simulation, since the difference of actuator failure mode is quite small, the noise defined in this simulation is small as well and the matrices related to noise (Q, R, and N) will be defined as identity.

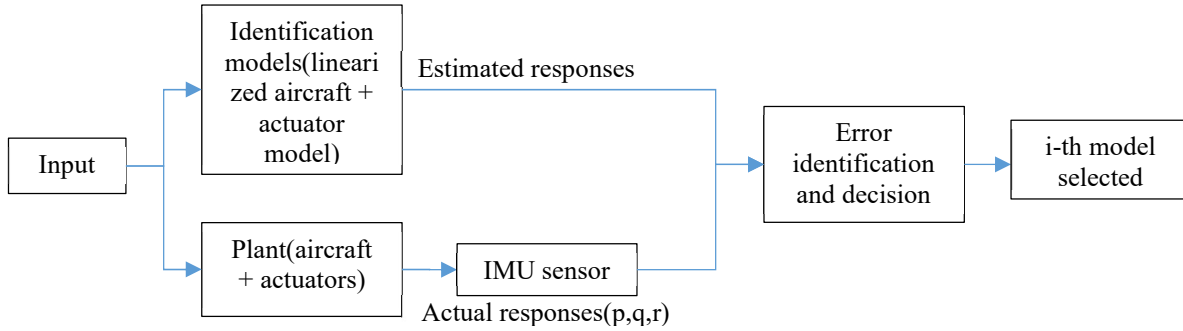


Fig. 7 Failure Identification Flow Diagram

IV.Numerical Model

The aircraft modeled in this paper are based on semi empirical data which using DATCOM+ to obtain aerodynamical data (Mihaela Florentina Niță, 2008), and the actuators are based on previous research that representing actual model with transfer function (Ndaomanu, 2019)that consist of four operational cases, nominal/normal, pressure loss, high friction, and floating as discussed in previous chapter. Below are few aerodynamical data that used in this model as well as thrust model which obtained from simulation on X-Plane software as shown in Fig. 8 and Fig. 9. The other aircraft data like reference dimension, mass, inertia, are obtained from drawing and other source as shown in Table 2. The aircraft simulated numerically in Matlab and Simulink environment represented by nonlinear mathematical equation (Allerton, 2009).

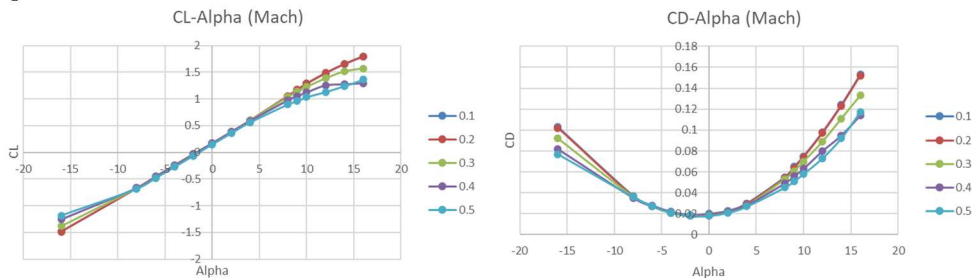


Fig. 8 Lift and Drag Coefficient Data

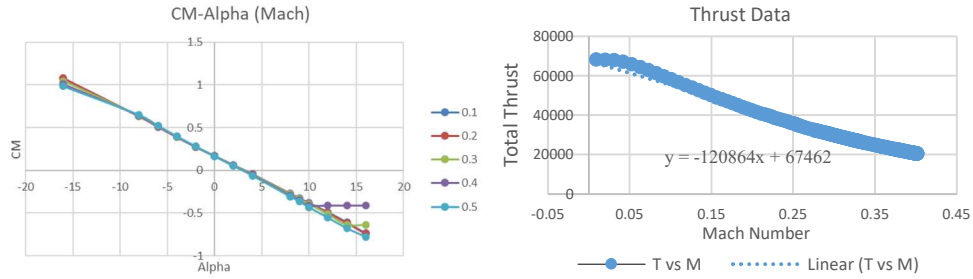


Fig. 9 Moment and Thrust Data

Table 2 Aircraft Model Data

No	Parameters	Value	Unit
1	Mass (m)	18000	Kg
2	Inertia-x (Ixx)	385000	Kg.m ²
3	Inertia-y (Iyy)	719000	Kg.m ²
4	Inertia-z (Izz)	1040000	Kg.m ²
5	Reference Area (S)	69	m ²
6	Wingspan (b)	27.8	m
7	Mean Aerodynamic Chord (\bar{c})	2.5	m
8	Gravity	9.8	m/s ²
9	Atmosphphere	ISA Model	MKS

As explained in previous chapter that discuss about failure identification, it will utilize Kalman Filter as an estimator that estimate plant (aircraft+actuator) response, here the aircraft model will be linearized at several operating point (speed and altitude) to represent nonlinear model (The MathWorks, 2020) and series with actuator model to produce estimation model with aircraft and actuator dynamic included. To validate estimation model, both plant and estimation model response will be compared by disturbing both model with elevator impulse as shown in Fig. 10 and the responses shown in Fig. 11 which have similar responses both its magnitude and dynamics in nominal condition.

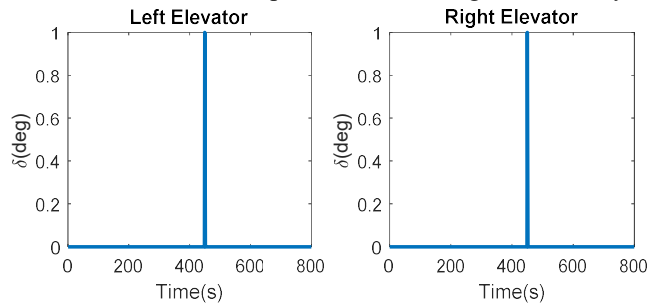


Fig. 10 Elevator Impulse to Test Both Model Responses

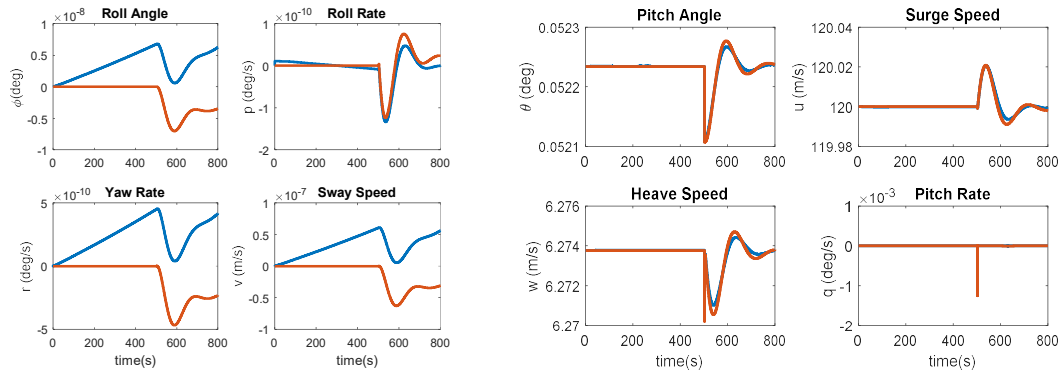


Fig. 11 Plant and Identification Model Responses Comparison in Nominal Condition

V. Simulation Result and Analysis

In this simulation case, fail identification method will be tested in openloop climb case first with aircraft flying in steady climb flight in nominal condition and then elevator actuator condition will be degraded and asymmetrically every few seconds that affect aircraft flight variables. The block diagram of fail identification presented below with both plant and identification model receive same input with identification model parameters are based on linearization result with dynamics of aircraft and actuator represented in Kalman Filter model. The implementation of this block diagram in Simulink also presented below with ‘u’ and ‘y’ are input and measurement from plant..

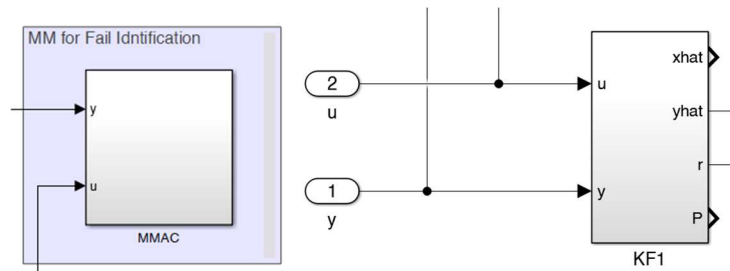


Fig. 12 MMST Subsystem in Simulink Environment

Here are the results of open loop case study with elevator actuator failure is asymmetrical. The failure case will be determined as actuator condition goes from condition 1 until 4 each 40 second. From IMU sensor, the variables that will be observed are pitch rate(q), roll rate(p), and yaw rate(r) since elevator failure will mostly affect body rate. In Figures below, roll rate output from estimation model has different value for each failure case and the result of identification can determine which failure that occurred at the mean time. For fourth case there is spike on the roll rate, it is caused by elevator cannot be given any command so that hinge moment at the mean time makes failed elevator suddenly deflected with such a large value.

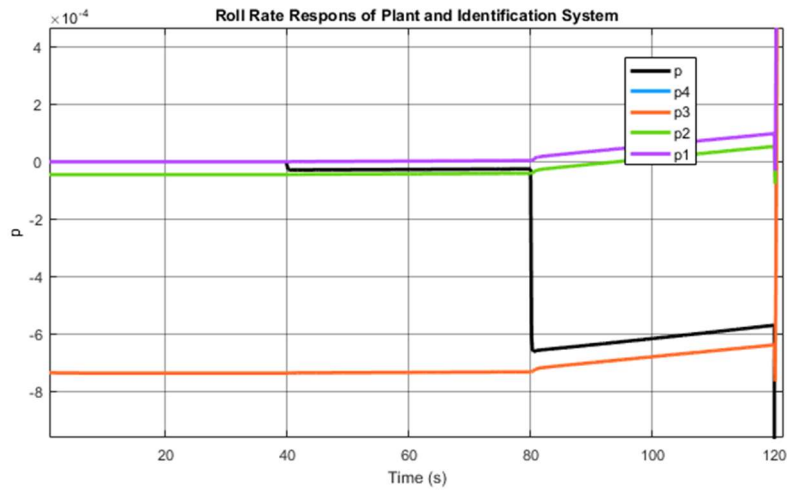


Fig. 13 Plant and Estimated Response for Roll Rate

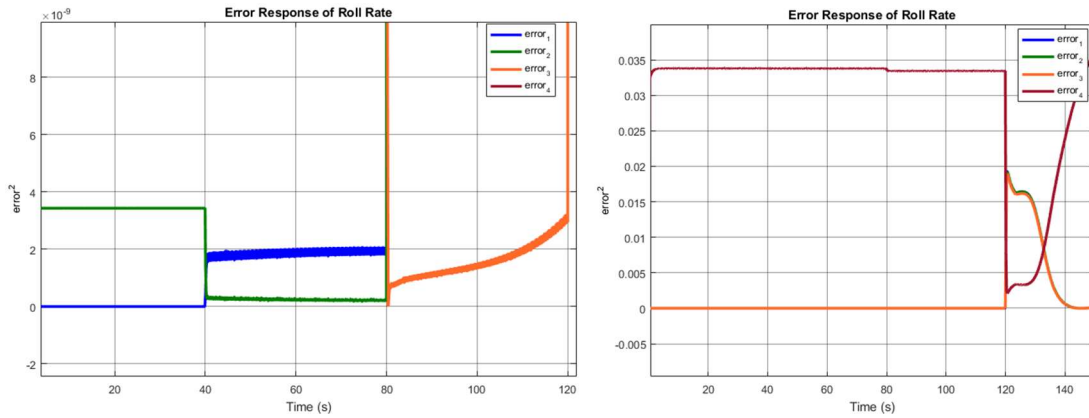


Fig. 14 Error Response of Roll Rate from Identification model

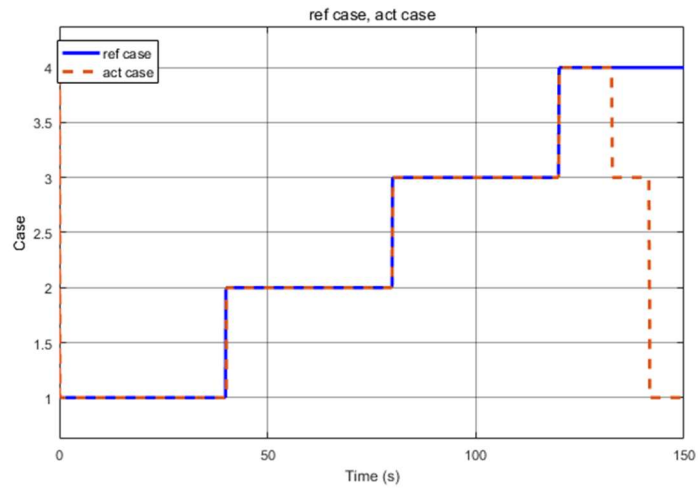


Fig. 15 Identification Result for Asymmetrical Openloop Case

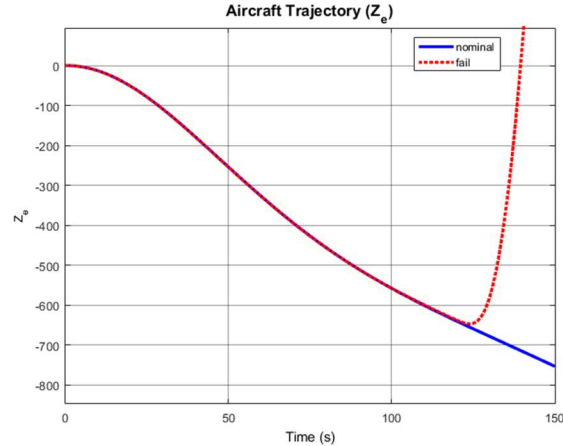


Fig. 16 Aircraft Trajectory in Z direction (blue=nominal, red=fail sequentially)

Using multimodel method which utilize predefined kalman filter estimation model it shows that identification model can identify failure on asymmetrical elevator deflection on openloop climb flight based on IMU sensor(body rate) data that shows increased value of roll rate when there is failure on one of elevator as shown in Fig. 13. Aircraft roll rate for each identification model has different value since each elevator operating condition result in different value of deflection as well. Using equation (2) (first error criteria) it can be seen that when plant has similar value to certain identification model the error will close to zero as shown in Fig. 14. So that based on calculation of error response for 4 identification model, minimum value from those model will be selected to identify which mode of error that occurring at the moment as shown in Fig. 15. In this result as well when there is asymmetrical failure on one elevator, not only body rate that affected, it will affect aircraft climbing performance as well especially when failure condition 4 occurred as shown in Fig. 16 that aircraft altitude will drop rapidly while failure mode 2 and 3 yield slightly difference climbing performance

VI. Conclusion

In this paper there are already discussed about aircraft failure identification method and its result on climbing phase of flight. The method that used to identify failure is multimodel approach which the model parameter obtained from linearization of aircraft and actuator condition so that each identification model will represent plant failure on certain condition. Aircraft variable that used for identification is body rate from IMU sensor since control surface mainly affect aircraft body rate. The result of simulation in Matlab and Simulink environment shows the method can identify asymmetrical deflection on elevator while climbing. Further research needed to finely tune feedback parameter to maintain aircraft performance when there is failure occurred so that the aircraft can climbing or return to origin safely.

References

- [1]. Allerton, D. (2009). *Principles of Flight Simulation*. Chichester, UK: John Wiley and Sons.
- [2]. Boeing. (2018). *Statistical Summary of Commercial Jet Airplane Accidents Worldwide Operations | 1959 – 2017*. Seattle: Aviation Safety, Boeing Commercial Airplanes.
- [3]. Grimble, M. (1994). *Robust Industrial Control: Optimal Design Approach for Polynomial Systems*. Prentice Hall.
- [4]. Kumpati S. Narendra, O. A. (2003). Adaptive Control Using Multiple Models, Switching, and Tuning. *International Journal of Adaptive Control and Signal Processing*, 1-16.
- [5]. Lewis, F. (1986). *Optimal Estimation*. John Wiley & Sons, Inc.
- [6]. Magazine, T. E. (1990). *CABIN CREW SAFETY*. FLIGHT SAFETY FOUNDATION.
- [7]. Mihaela Florentina Niță, P. D.-I. (2008). *Aircraft Design Studies Based on the ATR 72*. Brno: Brno University of Technology.

- [8]. Ndaomanu, Y.A, Sasongko, R. A. (2019). LOES Derivation of Non-Linear Actuation System for Flight Control Synthesis Purpose. *Proceedings of the 2019 IEEE 6th Asian Conference on Defence Technology, ACDT 2019*, 142-148.
- [9]. The MathWorks, I. (2020). *Linearize Nonlinear Models*. Retrieved from Mathworks: <https://www.mathworks.com/help/slcontrol/ug/linearizing-nonlinear-models.html>

RLS-based Indirect Adaptive Model Predictive Control for a MIMO Aircraft Flight Dynamic Model

Yusuf K. Asalani¹ and Rianto A. Sasongko²
Institut Teknologi Bandung, Bandung, West Java, 40132, Indonesia

Adaptive model predictive control (adaptive MPC) combines parameter adaptation and control input calculation feature as an integrated control method. Parameter adaptation uses system past output-input series to construct equivalent model of the system with specific configuration and environment condition. Then, control input is calculated by minimizing the cost function formulated as system model-based prediction error of the output to its reference in certain window horizon. Moreover, the optimization also considers system constraints, e.g. input amplitude and incremental input constraints are used in this paper. Therefore, obtained control input is calculated based on model with lower level of model mismatch compared to unadjusted model. Furtherly, the controller can be utilized for broader configurations and conditions. This advantage motivates the usage of adaptive MPC in aerospace engineering, i.e. aircraft may fly in unideal conditions and various configuration. In this paper, recursive least-squares (RLS) is selected as parameter adaptation method. RLS is used to estimate system model parameter as state-space model which refers to indirect scheme of adaptation process. However, all state variables must be available. This consequence is resolved by assuming all state variables are measured. ADMIRE linear model is used as aircraft flight dynamic model for this paper purpose.

I. Nomenclature

$A(k), \widehat{A}(k)$	=	actual and estimated state matrix
a	=	Laguerre poles
$B(k), \widehat{B}(k)$	=	actual and estimated input matrix
Δu	=	incremental input vector
K_{RLS}	=	RLS gain
N	=	number of Laguerre expansion terms
N_c	=	control horizon
N_p	=	predicted horizon
φ	=	regressor matrix
$r(k)$	=	reference signal
$\hat{\theta}$	=	estimated parameter vector
$u(k)$	=	input vector
$x(k), \hat{x}(k)$	=	actual and estimated state vector
$y(k)$	=	output vector

¹ Student, Department of Aerospace Engineering – Faculty of Mechanical and Aerospace Engineering, AIAA Student Member.

² Lecturer, Department of Aerospace Engineering – Faculty of Mechanical and Aerospace Engineering, AIAA Professional Member.

II. Introduction

Model predictive control (MPC) is advanced control method that utilizes system model to predict how the system behave in the future as the basis of control input optimization. MPC optimizes the control input online for every time interval based on several prediction points of system output. This control method becomes current interest of academic and industrial fields [1]. The reasons why MPC becomes current interest are (1) input-output constraints are able to be directly included in formulation, (2) MPC is able to handle diverse system models and types, (3) providing optimal control online, (4) ability to handle uncertainty effectively, and (4) easily reconfigured as applied control objective [1-3]. Based on those advantages, MPC can be implemented for broad system configurations and conditions. Furthermore, to enhance the capability of uncertainty handling, adaptation mechanism can be added to MPC to form adaptive model predictive control (AMPC) [2]. An example of the areas that has various configurations and conditions in its operation is aerospace engineering. Aircraft may fly in unideal environment or experience actuator fault that alters aircraft behavior.

Several researches related to adaptive MPC have been performed. There are several parameter adaptation methods applied to support adaptive ability. Set membership identification was applied by Tanaskovic et. al. as the adaptation method for linear time varying systems [4]. Zhu et. al. [5] and Dhar et. al. [6] implemented gradient descent to adjust system parameters model for MPC problem without and with constraints, respectively. Dual MPC for finite impulse response (FIR) systems was developed by Heiring based on recursive least-squares [7]. Moreover, Schofield [8] and Mardi [9] developed adaptive MPC based on subspace identification.

In this paper, recursive least-squares (RLS) is selected as parameter adaptation feature with indirect scheme. RLS is used to adjust system parameter model based on available state and input variables information. The state variables are assumed available through measurement. MPC is utilized to perform reference tracking as state-feedback controller by considering input and its incremental constraints. To sum up, adaptive MPC is constructed to control linear time-varying aircraft model with input-related constraints hence aircraft behaves as desired reference.

This paper is arranged as follows. Problem statement of this paper is presented in Section III. Afterward, formulation of adaptive model predictive control is discussed in Section IV. Then, Section V describes the simulation example and its results. Lastly, conclusion is described in Section VI.

III. Problem Statement

Suppose that aircraft dynamics is represented as deterministic linear time-varying (LTV) dynamics model in form of discrete-time state-space which is expressed by

$$\begin{aligned} x(k+1) &= A(k)x(k) + B(k)u(k) \\ y(k) &= Cx(k) \end{aligned} \tag{1}$$

where $x(k) \in \mathbb{R}^l$ is system state vector, $u(k) \in \mathbb{R}^p$ is system input vector, and $y(k) \in \mathbb{R}^q$ system output vector. $A(k) \in \mathbb{R}^{n \times n}$ and $B(k) \in \mathbb{R}^{l \times p}$ are system state and system input matrix at time k and initially assumed as known parameter, while $C \in \mathbb{R}^{q \times l}$ is system output matrix which is known and constant along the time. It is assumed that the pair of $[A(k) B(k)]$ is controllable and the pair of $[A(k) C]$ is observable. The controller is constructed as state-feedback which the state variables are supposed to be available by measurement. The presence of controller is to manipulate system output hence its value tracks the desired reference $r(k)$ with the presence of system input and its incremental constraints as presented below.

$$y(k) \rightarrow r(k) \text{ as } k \rightarrow \infty \tag{2}$$

$$u_{\min} \leq u(k) \leq u_{\max}; \quad \Delta u_{\min} \leq \Delta u(k) \leq \Delta u_{\max} \tag{3}$$

To implement integral part in model predictive control formulation, the state-space is formed as augmented state-space with incremental input vector $\Delta u(k)$ as follows [1].

$$\begin{aligned} x_A(k+1) &= A_A(k)x_A(k) + B_A(k)\Delta u(k) \\ y_A(k) &= C_A x_A(k) \end{aligned} \tag{4}$$

B. Recursive Least-Squares as Adaptation Law

The estimated state $\hat{x}(k)$ which corresponds to Eq. (1) is described as

$$\hat{x}(k+1) = \hat{A}(k)\hat{x}(k) + \hat{B}(k)u(k) \quad (7)$$

where $\hat{A}(k)$ and $\hat{B}(k)$ are estimated state matrix and estimated input matrix, respectively. As presented earlier in Eq. (6), estimated state $\hat{x}(k)$ is also able to be described as

$$\hat{x}(k) = \varphi^T(k)\hat{\theta}(k-1)$$

where $\hat{x}(k) = [\hat{x}_1(k) \ \hat{x}_2(k) \ \cdots \ \hat{x}_q(k)]^T$, $\varphi^T(k) = [\hat{X}_m(k) \ U_m(k)]$, and $\hat{\theta}(k) = [a_{tot} \ b_{tot}]^T$. The notations $\hat{X}_m(k)$ and $U_m(k)$ are defined as

$$\hat{X}_m(k) = \begin{bmatrix} -\hat{x}^T(k) & 0 & \cdots & 0 \\ 0 & -\hat{x}^T(k) & \cdots & 0 \\ \vdots & \vdots & \ddots & \vdots \\ 0 & 0 & \cdots & -\hat{x}^T(k) \end{bmatrix} \in \mathbb{R}^{q \times q^2}; \quad U_m(k) = \begin{bmatrix} u^T(k) & 0 & \cdots & 0 \\ 0 & u^T(k) & \cdots & 0 \\ \vdots & \vdots & \ddots & \vdots \\ 0 & 0 & \cdots & u^T(k) \end{bmatrix} \in \mathbb{R}^{q \times pq}$$

Then, the notations a_{tot} and b_{tot} are defined as

$$a_{tot} = [a_{1,1} \ \cdots \ a_{1,q} \ a_{2,1} \ \cdots \ a_{q,q}]; \quad b_{tot} = [b_{1,1} \ \cdots \ b_{1,p} \ b_{2,1} \ \cdots \ b_{p,p}]$$

The definitions of regressor matrix $\varphi^T(k)$ and estimated parameter vector $\hat{\theta}(k)$ shown above are built to consider the interaction between each state variable and all inputs [11] which becomes the characteristics of multi-input, multi-output (MIMO) system. Actually, ARX-model can also represent MIMO model as combination of several multi-input, single-output (MISO) systems [12]. However, in indirect scheme, this method is possible to generate non-minimal realization model which has different matrices $\hat{A}(k)$ and $\hat{B}(k)$ dimension compared to the actual parameter dimension.

Afterward, the estimated parameter vector $\hat{\theta}(k)$ is calculated using recursive least-squares (RLS) with forgetting factor method. The RLS with forgetting factor method is presented as follows.

$$\hat{\theta}(k) = \hat{\theta}(k-1) + K_{RLS}(k) [\hat{x}(k) - \varphi^T(k)\hat{\theta}(k-1)] \quad (8)$$

$$K_{RLS}(k) = P(k)\varphi(k) = P(k-1)\varphi(k) [\lambda I + \varphi^T(k)P(k-1)\varphi(k)]^{-1} \quad (9)$$

$$P(k) = [I - K_{RLS}(k)\varphi^T(k)] \frac{P(k-1)}{\lambda} \quad (10)$$

Where $P(k) \in \mathbb{R}^{l \times l}$ is estimated parameter covariance matrix and λI is multiplication of forgetting factor and identity matrix ($I \in \mathbb{R}^{(q^2+pq) \times (q^2+pq)}$).

From the RLS method, estimated parameter vector $\hat{\theta}(k)$ is obtained and should be formed as estimated parameter matrices $\hat{A}(k)$ and $\hat{B}(k)$. The estimated parameter matrices are reformed as

$$\hat{A}(k) = - \begin{bmatrix} a_{1,1} & \cdots & a_{1,q} \\ \vdots & \ddots & \vdots \\ a_{q,1} & \cdots & a_{q,q} \end{bmatrix}; \quad \hat{B}(k) = \begin{bmatrix} b_{1,1} & \cdots & b_{1,p} \\ \vdots & \ddots & \vdots \\ b_{q,1} & \cdots & b_{q,p} \end{bmatrix} \quad (11)$$

C. Model Predictive Control Design for Estimated Model

Incremental input $\Delta u(k)$ is calculated based on estimated system $[\hat{A}(k) \hat{B}(k)]$ by optimizing a cost function J with considering applied constraints. The formulation of model predictive control is referred to Ref. [1]. After the estimated system is obtained, augmented state-space is formed as referred to Eq. (4). Afterward, the prediction of future state variables is described as

$$\begin{aligned}
\hat{x}_A(k+1|k) &= \hat{A}_A(k) \hat{x}_A(k) + \hat{B}_A(k) \Delta u(k) \\
\hat{x}_A(k+2|k) &= \hat{A}_A(k) \hat{x}_A(k+1|k) + \hat{B}_A(k) \Delta u(k+1) \\
&= \hat{A}_A^2(k) \hat{x}_A(k) + \hat{A}_A(k) \hat{B}_A(k) \Delta u(k) + \hat{B}_A(k) \Delta u(k+1) \\
\hat{x}_A(k+N_p|k) &= \hat{A}_A^{N_p}(k) \hat{x}_A(k) + \hat{A}_A^{N_p-1}(k) \hat{B}_A(k) \Delta u(k) + \hat{A}_A^{N_p-2}(k) \hat{B}_A(k) \Delta u(k+1) + \\
&\quad \dots + \hat{A}_A^{N_p-N_c}(k) \hat{B}_A(k) \Delta u(k+N_c-1)
\end{aligned} \tag{12}$$

Then, to compute the value of incremental input $\Delta u(k)$ without excessive computational burden due to prediction stage calculation which depends on prediction horizon N_p and control horizon N_c , incremental input $\Delta u(k)$ is defined as Laguerre networks which have orthonormal property.

$$\Delta u(k+i) = L(i)^T \eta \tag{13}$$

Where $L(k)$ is Laguerre network and η is Laguerre coefficients. Then, cost function is formulated as

$$J = \sum_{i=1}^{N_p} \left[\left[\hat{x}_A(k+i|k) - x_r(k) \right]^T Q \left[\hat{x}_A(k+i|k) - x_r(k) \right] \right] + \eta^T R \eta \tag{14}$$

Where Q and R are weighting matrices. ΔU and $x_r(k)$ are incremental input vector and reference signal vector as

$$\Delta U = \left[\Delta u(k)^T \quad \Delta u(k+1)^T \quad \dots \quad \Delta u(k+N_c-1)^T \right]^T; \quad x_r(k) = \left[\underbrace{0 \quad \dots \quad 0}_n \quad \underbrace{r_1(k) \quad \dots \quad r_q(k)}_q \right]^T$$

The variables a and N are Laguerre poles and number of Laguerre expansion terms to define $\Delta u(k)$. The value of a must be $0 \leq a < 1$. Afterward, to obtain optimal $\Delta u(k)$ at k , estimated state of augmented state matrix $\hat{x}_A(k)$ in Eq. (14) is substituted by Eq. (12). Afterward, first derivative of the result which is equal to zero yields

$$\eta = -\Omega \Psi \left[\hat{x}_A(k) - x_r(k) \right] \tag{15}$$

Where

$$\begin{aligned}
\Omega &= \sum_{i=1}^{N_p} \left[\sum_{j=0}^{i-1} \hat{A}_A(k)^{i-j-1} \hat{B}_A(k) L(j)^T \right] Q \left[\sum_{j=0}^{i-1} \hat{A}_A(k)^{i-j-1} \hat{B}_A(k) L(j)^T \right]^T + R \\
\Psi &= \sum_{i=1}^{N_p} \left[\sum_{j=0}^{i-1} \hat{A}_A(k)^{i-j-1} \hat{B}_A(k) L(j)^T \right] Q \hat{A}_A(k)^i
\end{aligned}$$

Hence, incremental input $\Delta u(k)$ has formed as $\Delta u(k) = L(0)^T \eta$ when constraints are met. However, if input and incremental input constraints are considered, the value of incremental input sequence ΔU needs to fulfill this following inequality.

$$\begin{bmatrix} -C_2 \\ C_2 \\ -I \\ I \end{bmatrix} \Delta U \leq \begin{bmatrix} -U_{\min} + C_1 u(k-1) \\ U_{\max} - C_1 u(k-1) \\ -\Delta U_{\min} \\ \Delta U_{\max} \end{bmatrix} \quad \text{with} \quad I \in \mathbb{R}^{N_c p \times N_c p} \quad (16)$$

Where

$$C_1 = \begin{bmatrix} I \\ I \\ \vdots \\ I \end{bmatrix} \in \mathbb{R}^{N_c p \times p} \quad \text{and} \quad C_2 = \begin{bmatrix} I & 0 & \dots & 0 \\ I & I & \dots & 0 \\ \vdots & \vdots & \ddots & \vdots \\ I & I & \dots & I \end{bmatrix} \in \mathbb{R}^{N_c p \times N_c p} \quad \text{with} \quad I \in \mathbb{R}^{p \times p}$$

The inequality shows in Eq. (16) is solved using Hildreth's quadratic programming procedure [1].

D. Adaptive Model Predictive Control Algorithm

In this paper, adaptation mechanism of adaptive model predictive control is based on recursive least-squares method with forgetting factor. The adaptation feature requires all state variables information at time k to construct system parameters with suitable dimension n . Therefore, the assumption that state variables is available from measurement is used. The adaptation feature is run continuously to calculate the estimated parameter. However, the estimated parameter is utilized by the controller and the several steps of future state estimation when the estimated parameter error is lower than its threshold ε_θ . The algorithm is presented in Fig. 1 and summarized as follows.

- At time $k = t_0$, initialize parameter covariance matrix P , input vector $u(t_0)$ estimated system vector $\hat{\theta}(t_0)$ as available information of estimated system matrices $[\hat{A}(t_0) \hat{B}(t_0)]$.
- At time k , collect estimated state variables $\hat{x}(k-1)$ and system input $u(k)$ to calculate estimated parameter vector $\hat{\theta}(k)$ using Eqs. (8)-(10).
- Update estimated system matrices $[\hat{A}(k) \hat{B}(k)]$ as shown in Eq. (11) if estimated parameter error is lower than estimated parameter error threshold ε_θ .
- Calculate and implement $u(k)$ based on estimated system matrices $[\hat{A}(k) \hat{B}(k)]$ using Eqs. (15)-(16).
- Continue to next k and go to step b.

V. Simulation Example

A. Aircraft Linear Model and Simulation Scenarios

Aircraft linear model for this purpose is ADMIRE model (ADMIRE ver. 3.4h 2003) which is developed and maintained by Swedish Defence Research Agency (FOI) [13]. The linear model is trimmed at Mach 0.22. altitude 3000 m. This aircraft model is equipped by canard, right-elevator, left-elevator, and rudder as its control devices ($u = [\delta_c \ \delta_{re} \ \delta_{le} \ \delta_r]^T$). The dynamics of aircraft is modelled as function of $x = [\alpha \ \beta \ p \ q \ r]^T$. The state and input matrices at this condition are described as follows.

$$A = \begin{bmatrix} -0.5432 & 0.0137 & 0 & 0.9778 & 0 \\ 0 & -0.1179 & 0.2215 & 0 & -0.9661 \\ 0 & -10.5128 & -0.9667 & 0 & 0.6176 \\ 2.6221 & -0.0030 & 0 & -0.5057 & 0 \\ 0 & 0.7075 & -0.0939 & 0 & -0.2127 \end{bmatrix}; \quad B = \begin{bmatrix} 0.0069 & -0.0866 & -0.0866 & 0.0004 \\ 0 & 0.0119 & -0.0019 & 0.0287 \\ 0 & -4.2423 & 4.2423 & 1.4871 \\ 1.6532 & -1.2735 & -1.2735 & 0.0024 \\ 0 & -0.2805 & 0.2805 & -0.8823 \end{bmatrix} \quad (17)$$

Each control device performance is limited by its deflection amplitude and deflection rate shown as follows.

$$\begin{aligned} u_{\min} &= [-55^\circ \ -30^\circ \ -30^\circ \ -30^\circ]^T; \quad u_{\max} = [25^\circ \ 30^\circ \ 30^\circ \ 30^\circ]^T \\ \Delta u_{\min} &= [-50^\circ/s \ -150^\circ/s \ -150^\circ/s \ -100^\circ/s]^T; \quad \Delta u_{\max} = [50^\circ/s \ 150^\circ/s \ 150^\circ/s \ 100^\circ/s]^T \end{aligned} \quad (18)$$

This aircraft linear model has a pair of complex poles and three real poles. Its poles are $[-2.1258, 1.0769, -0.1990, -0.5491 \pm 5.2731i]$. By separating the model for its longitudinal and lateral-directional axes, it is known that the first two poles represent longitudinal and the rests are lateral-directional. Hence, the unstable pole comes from longitudinal axis behavior. In this paper, simulation is presented for comparing aircraft response by equipping model predictive control only and adaptive model predictive control. Sideslip angle β , pitch angle θ , and yaw rate r are selected as the controlled states. At initial time, system parameters $A(k)$ and $B(k)$ are known. Therefore, to trigger the adaptation, at $t = 30$ s, the aircraft right elevator δ_{re} performance decreases into 60% of its initial performance. The aircraft is controlled to have square wave trajectory of its pitch angle with zero sideslip and yaw angle. Hence, the aircraft is expected to have straight level flight with minimum horizontal deviation even though there may be forces and moments difference due to inequal value of right and left elevator input matrices components as initial one.

For this simulation, the controller parameters are chosen as $N_p = 30$, $N_c = 15$, $a = 0.3$, and $N = 8$. While for the parameter estimation, the parameters are $\lambda = 0.95$, $P_0 = 100I$, and $\varepsilon_\theta = 1E-4$. Lastly, the weighting matrices for optimization process are $Q = 1I$ and $R = 2I$. Afterward, the comparisons are done qualitatively by observing the plot and also quantitatively using measures of integral squared error (ISE), integral absolute error (IAE), and integral time-weighted error (ITAE) [14].

$$\begin{aligned}
 ISE &= \int (x(k) - x_r(k))^2 dk \\
 IAE &= \int |x(k) - x_r(k)| dk \\
 ITAE &= \int k |x(k) - x_r(k)| dk
 \end{aligned} \tag{19}$$

B. Comparison of Model Predictive Control and Adaptive Model Predictive Control

To identify advantage of adaptive model predictive control (AMPC) over model predictive control in case of system parameter change, this subsection presents the simulation results when the input matrix which corresponds to right elevator value changes at $t = 30$ s. From Fig. 2, MPC and AMPC are able to maintain the aircraft as desired value even though the input matrix change appears. Fig. 3 presents full version of output variables comparison between aircraft with MPC-only and AMPC equipped. The differences are clearly seen since $t = 60$ s when the parameter estimation have obtained the condition of estimated parameter error threshold. Both MPC and AMPC generates new equilibrium point when the aircraft input matrix and reference signal changes, also the estimated parameter converges.

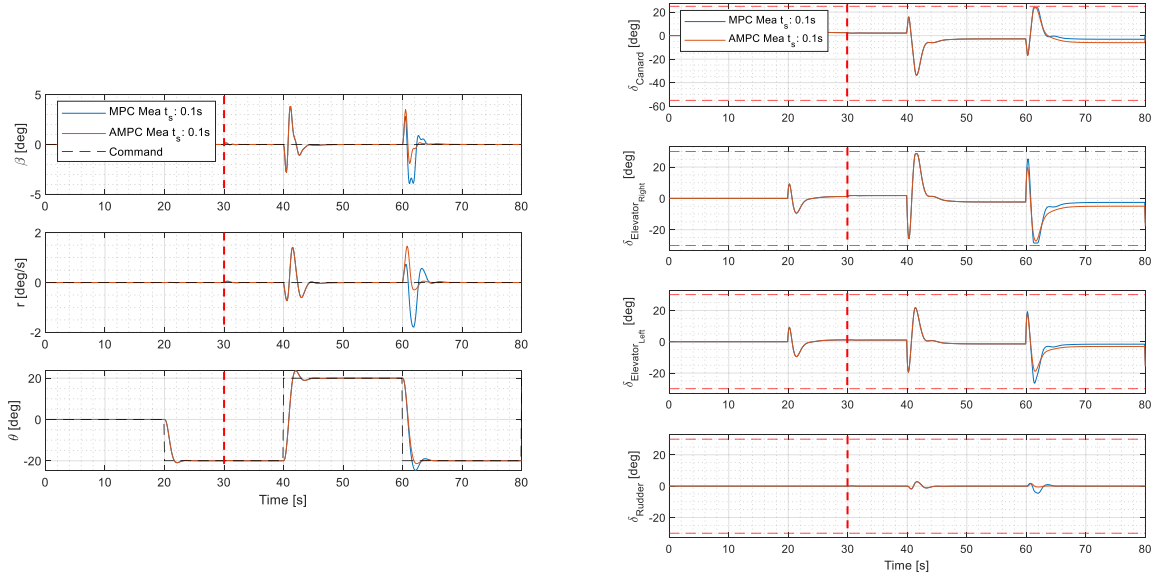


Fig. 2 Comparison between MPC and Adaptive MPC with fully measured state variables: aircraft state (left) and input variables (right).

By observing the state variables, AMPC has superiority to quickly damp the controlled states to its desired value or the response has shorter settling time. Furthermore, from Table 1, IAE and ITAE values of AMPC are lower than MPC's even though its ISE value is higher than MPC's. It means that AMPC may be able to decrease the deviation between actual and desired value in shorter duration. However, this characteristic makes AMPC's ISE value of pitch angle θ bigger since AMPC has longer rise-time and pitch angle θ has big value which create higher square deviation. Afterward, by comparing input variables performance using sum of square-manipulated variables [15]

$$\sum_{k=0}^{k_{fin}} \Delta u^2 \quad (20)$$

it is known that the performance for MPC and AMPC are 3448.77 and 3077.72. It means AMPC is more efficient in manipulating the input device compared to MPC. This characteristic is the advantage of parameter adaptation usage that creates model with lower model-mismatch level compared to unadjusted version used by MPC.

Table 1 Quantitative comparison between MPC and AMPC equipped aircraft.

State	ISE		IAE		ITAE	
	MPC	AMPC	MPC	AMPC	MPC	AMPC
β	29.34	16.61	12.09	8.33	640.76	407.23
r	5.25	3.21	5.56	3.96	295.88	195.40
θ	2647.71	2696.99	104.41	103.36	4735.07	4665.34

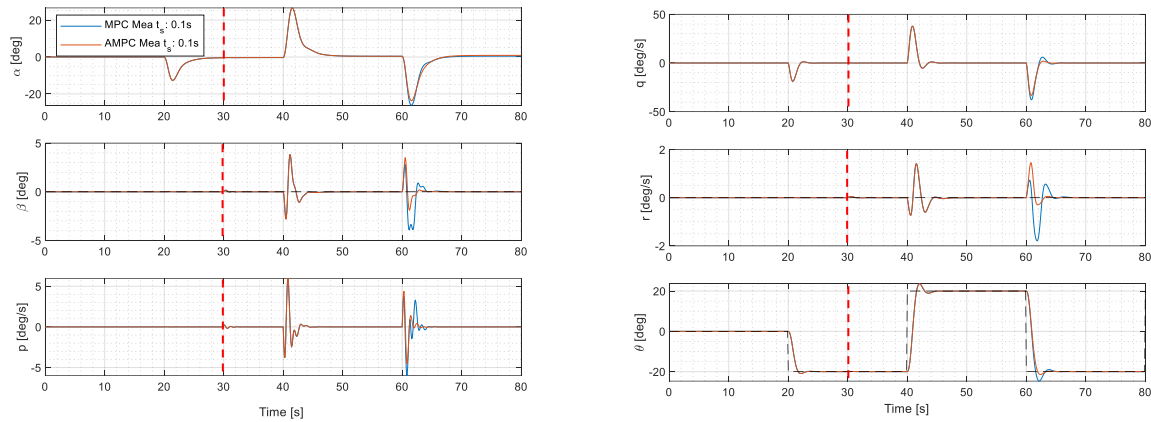


Fig. 3 Comparison between MPC and Adaptive MPC with fully measured state variable: output variables.

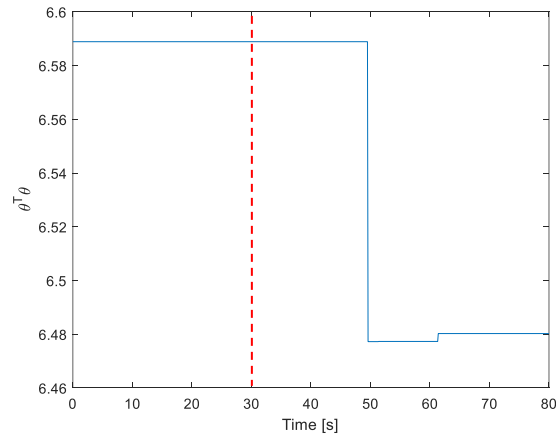


Fig. 4 Parameter estimation history.

Parameter estimation history is presented as quadratic value of estimated parameter vector $\hat{\theta}(k)$. In Fig. 4, it can be seen that system parameter starts adjusting at $t = 50$ s and convergent around $t = 61$ s. However, the effect of this adjustment is seen clearly after $t = 60$ s. From this paper, it means the adaptation process is performed and the advantage of adaptation is able to be observed if there is change of reference value.

VI. Conclusion

In this paper, adaptive model predictive control with assumption of all state variables are measured or estimated is discussed. The control objective in this paper is reference tracking with varying reference signal and input constraints. The applied adaptation mechanism is based on recursive least-squares with forgetting factor for MIMO system. The adaptation mechanism injects new estimated parameter matrices in indirect scheme. To provide state variables for adaptation purpose, it is assumed that aircraft is able to measure all state variables. In this paper case, aircraft with AMPC equipped has better performance in terms of IAE and ITAE, also its input variable performance. Its ISE has higher value than MPC's as the result of big reference tracking and longer rise-time of pitch angle θ .

To obtain more knowledges about the advantages and application of adaptive MPC, these two future works may be performed: (1) usage of observer to provide aircraft unmeasured state variables and (2) application of adaptive model predictive control for nonlinear aircraft model.

References

- [1] Wang, L., *Model Predictive Control System Design and Implementation Using MATLAB®*, Advances in Industrial Control Series, Springer London, London, 2009.
- [2] Eren, U., Prach, A., Kocer, B. B., Rakovic, S., Kayacan, E., and Acikmese, B., "Model Predictive Control in Aerospace Systems: Current State and Opportunities", *Journal of Guidance, Control, and Dynamics*, Vol. 40, No. 7, 2017, pp. 1541-1566. doi: 10.2514/1.G002507
- [3] Simon, D., "Fighter Aircraft Maneuver Limiting Using MPC Theory and Application", Dissertation, Dept. of Electrical Engineering, Linköping Univ., No. 1881, Linköping, Sweden, 2007.
- [4] Tanaskovic, M., Fagiano, L., and Gligorovski, V., "Adaptive Model Predictive Control for Linear Time Varying MIMO Systems", *Automatica*, Vol. 105, 2019, pp. 237-245. doi: 10.1016/j.automatica.2019.03.030
- [5] Zhu, B. and Xia, X., "Adaptive Model Predictive Control for Unconstrained Discrete-Time Linear Systems with Parametric Uncertainties", *IEEE Transactions on Automatic Control*, Vol. 61, No. 10, 2016, pp. 3171-3176. doi: 10.1109/TAC.2015.2505783
- [6] Dhar, A. and Bhasin, S., "Adaptive MPC for Uncertain Discrete-Time LTI MIMO Systems with Incremental Input Constraints", *IFAC PapersOnLine*, Vol. 51, No. 1, 2018, pp. 329-334. doi: 10.1016/j.ifacol.2018.05.040
- [7] Heirung, T. A. N., Ydstie, B. E., and Foss, B., "Dual MPC for FIR Systems: Information Anticipation", *IFAC PapersOnLine*, Vol. 48, No. 8, 2015, pp. 1033-1038. doi: 10.1016/j.ifacol.2015.09.104
- [8] Schofield, B., "Subspace Based Identification for Adaptive Control", Master Thesis, Dept. of Automatic Control, Lund Institute of Technology., ISRN LUTFD2/TFRT--5706--SE, Lund, Sweden, 2003.
- [9] Mardi, N. A., "Data-Driven Subspace Model Predictive Control", Ph. D. Thesis, School of Electrical and Computer Engineering, RMIT Univ., Melbourne, 2010.
- [10] Astrom, K. J. and Wittenmark, B., *Adaptive Control*, Dover Publications, 2nd ed., New York, 1994.
- [11] Halldin, A., "Control of a Multivariable Lighting System", Master Thesis, Dept. of Electrical Engineering, Linköping Univ., LiTH-ISY-EX--17/5022--SE, Linköping, Sweden, 2017.
- [12] Kumar, K., Heirung, T. A. N., Patwardhan, S. C., and Foss, B., "Experimental Evaluation of a MIMO Adaptive Dual MPC", *IFAC PapersOnLine*, Vol. 48, No. 8, 2015, pp. 545-550. doi: 10.1016/j.ifacol.2015.09.024
- [13] Håckegård, O., "Backstepping and Control Allocation with Application to Flight Control", Dissertation, Dept. of Electrical Engineering, Linköping Univ., No. 820, Linköping, Sweden, 2003.
- [14] Marzaki, M. H., Tajjudin, M., Rahiman, M. H. F., and Adnan, R., "Performance of FOPI with error filter based on controllers performance criterion (ISE, IAE and ITAE)", *2015 10th Asian Control Conference (ASCC)*, IEEE, Kinabalu, Malaysia, 2015, pp. 1-6. doi: 10.1109/ASCC.2015.7244851
- [15] Marlin, T. E., *Process Control Designing Processes and Control Systems for Dynamic Response*, McGraw-Hill, 2nd ed., London, 2015.

A Swashplateless Bicopter Using Underactuated Propulsion Unit

H. Guan*

University of Sydney, Camperdown, NSW, 2008, Australia

In this paper a platform design, system implementation and prototyping of a swashplateless bicopter using underactuated propulsion is presented. The vehicle achieves attitude and translation motion control authority through two groups of propellers. The only two actuators are pulse modulated torque main drive, and no extra actuators are required in this design. In the end of this paper, a comparison was made between the component weight fractions of typical multi-copters and current prototype.

I. Introduction

VERTICAL take-off and landing unmanned aerial vehicles (VTOL-UAVs) are recently becoming publically focused for multiple directions including surveillance, rescues, agriculture [1] or even recreations. They have high applicability in wide ranges of researches, industries and departments [2] [3]. For missions when a hovering platform or an aerial operator is required but highly constrained by terrain, risks or costs, small sized VTOL UAV platforms are usually the best choices. Among VTOL platforms miniature sized UAVs especially quad-rotors are also options for indoor operations [4]. Typical classes of autonomous VTOL platforms are either single-rotor copters or multi-rotor copters. Platform with only one or two rotors usually has designs with more complex structures to contain extra actuators to fulfill its control. Fully articulated rotors usually involves swashplate mechanisms [5]. In most of the current situations, multi-copter platforms are the focused ones among all options due to its higher mechanical and structural simplicity as well as the simplicity of its controller design[6]. In 2013, a prior research was first done by James Paulos for a type of a single degree of freedom (DoF) underactuation rotor blade without using swashplate mechanisms[7], which shows the feasibility to design a MAV with greatly reduced complexity. In later developments, a further developed rotor design concept involves an additional teetering hinge[8]. In the prior researches, the MAV platform was designed in coaxial layout. In this work a different design principle is used to design the underactuated swashplateless UAV. Under the same design principle, the platform usually need a distinctive outer-ring landing gear for VTOL missions. In 2019, another team reviewed the dynamics of the same design, calculated and validated its stability boundary[9].

Following a similar process, the practicality, manufacturability and applicability is considered during the platform design, system integration and prototyping. In many cases, mission that miniature or micro sized VTOL-UAVs are deployed missions carrying payload with specific requirements, i.e. cameras that requires an open operating line of sight or carrier bay with ease of access. Typical twin rotor platforms aim for ground missions are either fore-back layout (Tandem rotors layout as Chinook) or left-right rotor layout (Tilt-rotor layout as Osprey), while under coaxial propulsion category, helicopters such as Sikorsky (Top located paired counter rotor) also has high adaptability to situations with ground missions.

Aiming for high structural simplicity, the underactuation active control method for thrust vectoring is using modulated torque that pulse a cycle per revolution. However, the design supports using identical multiple rotor blades without changing blade pitch for control. Therefore, the kinematic model in this design is highly similar as 2-DoF thrust vectoring tilt-rotors instead of cyclic pitch helicopter rotors. This characteristics further reduces the limitations and possible difficulties for its application on other platforms.

The concept of operation will be described in Section III with sketches. In Section IV, the externally sourced materials for the construction of prototype is listed. Section V shows the platform design and discuss the design principles of such platform. The comparisons of the mass budgets between different platforms is stated in Section VI. The applicability and manufacturability of the platform is evaluated in section VII. Finally, the article is concluded in Section VIII.

*MPhil Student, School of Aerospace, Mechanical and Mechatronic Engineering, Student Member AIAA.

II. Operation Concept

Designing bi-copter propulsion layout has multiple aims. From the operation concept, the bi-copter is able to take-off and land with conventional landing gear and operation attitude. Around its hovering point, the platform is also applicable to an attitude linearized model of a vectorized (tiltrotor) propulsion. The detailed control concept of the platform is as shown in figure 1. Overall, the roll pitch and yaw control for the system can be obtained from thrust vectoring differences between two rotors. The platform altitude is controlled through both rotors' thrust, the planar motions are controlled by the rolling, pitching and yawing of the system. Yaw control authority is achieved by having different vectoring on both rotors.

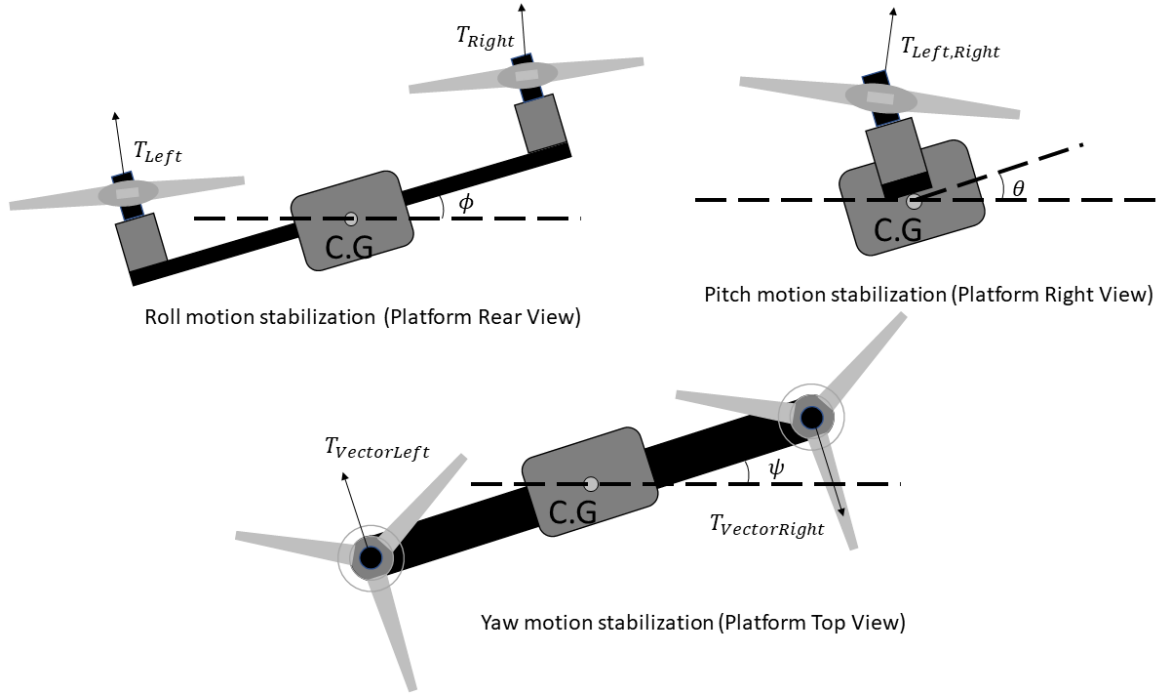
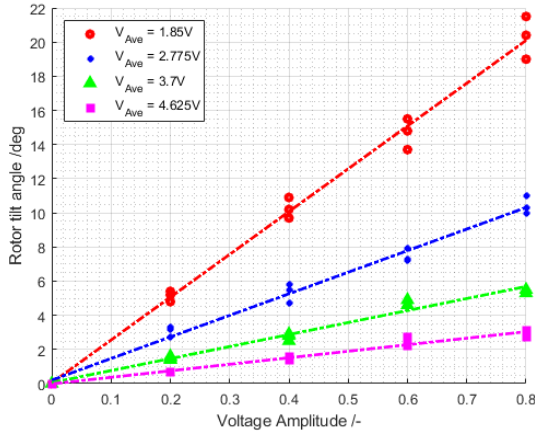


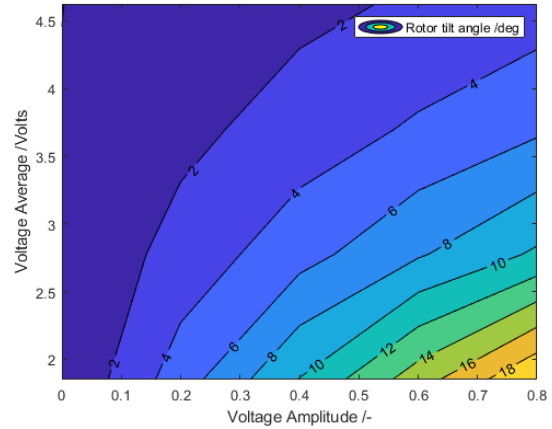
Fig. 1 Bicopter attitude motions stabilization principles.

From the experiment attitude control of Bi-Rotor tilt-rotor UAV design by Christos Papachristos, the linearized attitude dynamic model of this platform can be obtained given the platform (tilt-rotor model) inertial parameters, including its roll, pitch and yaw subsystems[10]. Using this process, a PID (In Papachristos's model for conventional tilt-rotors, a PD controller is also applicable) controller model for tilt-rotor bicopter can be implemented for its hovering state. However, to fly the new platform like a typical rotorcraft, it needs a signal mapping model from input (usually linearly mapped) to its tilt-rotor angle (related to amplitude and rotation speed), the relation of pulse torque amplitude and the equivalent rotor tilt angle is mapped through tests and shown in figure 2a with a limited maximum modulation amplitude. Maintaining same average voltage, the amplitude of rotor tilting changes along a linear line. Taking consideration of the change of rotor speed, figure 2b can be derived to represent the change of rotor tilt angle given rotor voltage and amplitude in this design. Therefore, the slope of field in figure 2b (A 2D data of rotor tilting) is written in the signal converter to ensure that when motor average speed (voltage difference induced due to roll commands) does not impact rotor tilt-angle.

This conversion indicated that a bridging electronic can be integrated to convert the control signal of an underactuated rotor into a similar model that is applicable on other open-source autopilots to operate as a tilt-rotor platform. Although the stabilized signal-to-angle model has been addressed, during the laboratory experiments for hovering, a time-response model difference was identified between actuator-connected rotor-tilting and underactuated rotor-tilting, which as a result observed reduces the effective control frequency from the flight controller to the platform and thereby affects the correct PID gain value to stabilize the platform as derived from conventional tilt-rotor platforms. Currently, the hovering PID gain values were obtained by manual tuning during its hovering state. A detailed parameter-based solution to optimize rotor time-response will be discussed in future work.



(a) Amplitude signal to rotor tilt-angle map.



(b) Contour of tilt-angle for Amplitude to Average voltage.

Fig. 2 Rotor tilt mapping from experimental data.

III. Material Preparation

Using the underactuated propulsion allows a platform design to be built as shown in figure 3. It has axial distance of 226mm between both rotors. The rotor diameter is 135mm and the disk area is 286.1 cm^2 . The overall weight of the prototype is 341 grams including the battery which is 108 grams. To prototype this platform, the listed materials below are sourced externally:

- 1) Motors: two IQ motion 2306 speed module with pulse modulation firmware.
- 2) Rotor blades: six 5"x3" fold-able propeller for generic multi-copters (Pairs of CW/CCW 5"x3" propeller x3).
- 3) Flight controller: Pixfalcon (FMUv2) flight controller (Bi-copter tilt-rotor firmware).
- 4) Evaluation (Bridging) board: Arduino Mega 2560 dev board.
- 5) WiFi Module: ESP8266 WiFi module.
- 6) Battery: 3 Cell 1000mAh Lipo Battery Pack.



Fig. 3 Bicopter UAV with only two underactuated propulsion unit as actuators.

In current prototype, pulse modulation firmware specialized IQ motion 2306 speed module is selected as the pulsed torque generator. Although the pulse modulation from a motor can be generated from other sources, considering for the prototyping step, using identical existing motors and control the modulation signal with firmware can eliminate the impact of construction error. Given the fact that self-made rotor mechanism is used in the design, during prototype testing, with same signal for both rotors, reasons for any different behaviors between these rotors can be quickly identified

Table 1 Component mass summary of the Underactuated Swashplateless Bicopter

Component	mass
Underactuation mechanism and propellers	2×10 grams
Power distribution board with wired XT60 connectors	22 grams
Flight controller	16 grams
IQ2306 Motor (with ESC)	2×38 grams
Evaluation Board	37 grams
1000mAh 3-Cell Lithium polymer battery	108 grams
Main structure (Plate)	33 grams
Undercarriage (Landing gear frame)	9 grams
ESP8266 (Wifi Module)	7 grams
Misc. hardware (RC Receiver, other connectors, wires, cable-ties etc.)	13 grams
Total mass	341 grams

and resolved. With identical motors, the modulation-to-angle amplitude can be measured with identical models for both motors which simplifies the calibrating procedure. Each IQ2306 motor has weight of 38 grams, integrating an electronic speed controller (ESC) and Hall effect sensor with capability to read the orientation of the motor shaft and therefore form a feedback control loop within the motor unit.

In this work, Arduino 2560 Mega is used as the evaluation board which is oversized for total connections required in the design in exchange for ease of platform assembly and disassembly in multiple design cycles. In terms of connections, it requires a group of digital ports to communicate with flight controller (4 pins) and two pairs of serial ports to communicate with IQ2306 motor ESCs. In fact, using a bridging board with capability of two pairs of UART connectors is functionally equivalent. Such as using Teensy 3.2 is able to save up to 30 - 40 grams of weight from avionics and connecting wires. However, adaptability is considered more important in first design cycle.

The evaluation board has two important roles under this circumstances. The first function is to connect between the motor and the source of signal (Evaluation board) using IQ Motion Control communication package. The control signal has different protocols comparing with that the open source autopilot can generate, as it contains data of rotor speed, rotor modulation direction and amplitude on one serial port. Using a bridging evaluation board, without changing the format of autopilot I2C ports or UART ports, the control signal can be mapped and processed by bridging board.

The second function is to integrate the control mapping of tilt-rotor models in flight controllers, the evaluation board carries the mapping model for equally spaced rotor-tilt angle to voltage-amplitude map as shown in figure 2b.

IV. Platform Design and Prototyping

Since the design principle of this platform is to aim for the high structural simplicity. The structural component of platform is modelled as a single rigid plate. For most multi-copters, this structure is also solid but with higher geometric complexity. In rotor mechanisms, multiple individual components are required, however no actuation is to be integrated among the rotor components therefore 3D printed parts are selected during prototyping.

In current prototype, the platform main structure has uniform thickness 5.5 mm. Structure (planform view) CAD model is as shown in figure 4. The weight of component for the assembly including both self-made material and externally sourced materials are listed in table I.

In this prototype, the avionics are mounted near the center of main structures (refer to figure 3 and 4). The overall connections between each components are illustrated in figure 5. The hovering power of this platform under current design point (Take-off weight 341 grams without extra payload) is measured over 5 runs that hovers for average 2-3 mins. The mean power consumption of the platform in its hovering state is around 60-70 Watts. In future design cycles, the platform design will take further consideration of optimising forward flight performance.

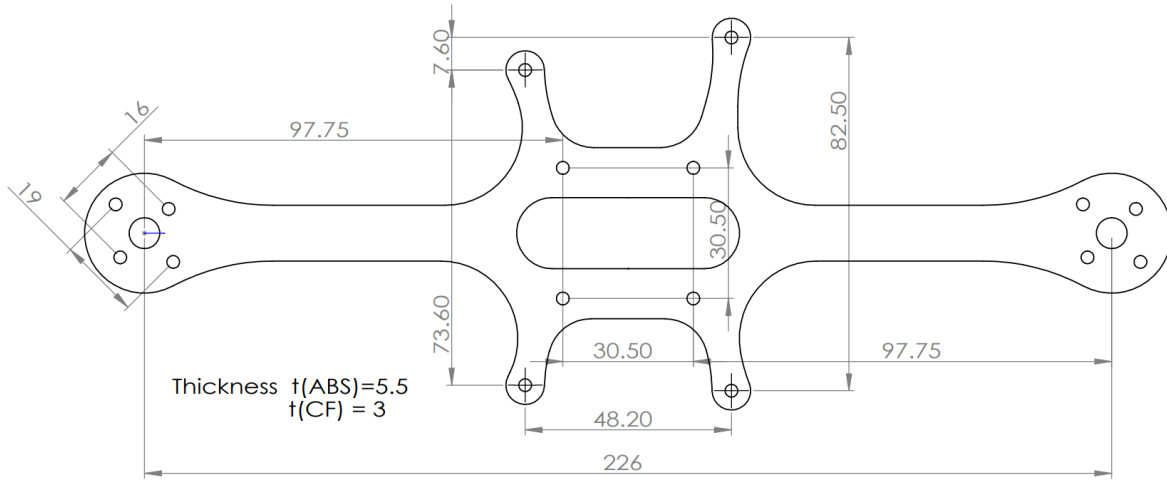


Fig. 4 Underactuated Bicopter main structure platform.

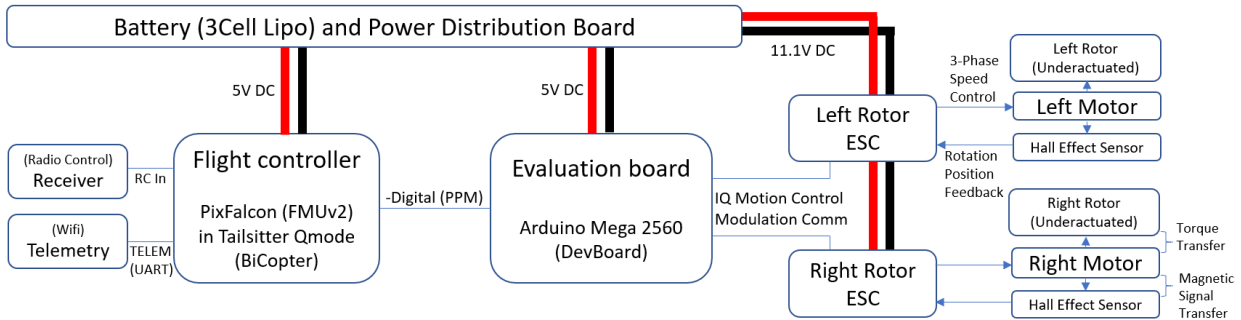


Fig. 5 Underactuated Bicopter main hardware diagram.

V. Mass Budget Comparisons

Since the mass distribution on current platform is generally affected by first design cycle procedures. It does not have high validity to compare avionics weight fractions with other types of platform. However, considering the weight of excess avionics weight combined with misc. materials as payload, the overall weight of the platform provides a relatively firm comparison with quad-copters. In the survey for typical quad-rotor platforms, the heaviest part are actuators as presented in [11]. Average quad-rotor platforms have Motors and propellers taking a weight fraction of 29% while for this Bi-copter design, this value is 28.2% which is relatively close. However, the weight fraction of frame for quad rotors are usually 17% while in current design, Bi-copter is able to operate with 12.3% structural weight fraction, which increases the overall usable weight for electronics, batteries and other payloads. From the comparisons of mass budget, the future development in this direction will be further reduction of avionics weight and therefore maximize effective payload.

VI. Applicability and Manufacturability

Since the major issue aimed to resolve in this work is the platform complexity, the reduction of size of structures and numbers of actuators shows a success. But based on current design principle and hardware diagram, it is expected that to extend the same design principle to other flight controllers without specifications requires an additional signal converter board. Otherwise, both hardware and software supporting for pulse modulation is required either on flight controller design or on ESC designs for open-source applications.

In terms of manufacturing, the single plate platform layout in current design brings significant advantages of simplicity. This propulsion layout overcome the main structure complexity issues that widely exists on other twin-rotor, tilt-rotor hover platforms. As a contrast, among other tilt-rotor platforms, multiple actuators are commonly required. In terms of rotor mechanisms, to achieve direct thrust vectoring, only two pairs of components need to be 3D printed (Current precision 2.0mm). Comparing with the conventional 2-blade underactuated rotor proposed by James Paulos in 2018, the design in this work does not induce cyclic blade pitch on each blades and instead can be applied to rotors with more than two blades to provide direct thrust vectoring. These characteristics also enable design applicability on other aerial platforms that requires thrust vectoring.

VII. Conclusions and Future Work

The design of the underactuated swashplateless bicopter prototype as a demonstration model for its design principle was presented in this article. With manually tuned gain values, the rotor-tilt conversion model provides the capability to control the platform. In the following work, the conversion method will be addressed for the rotor-parameter based solution to optimize the underactuated rotor time-response and thus further improve the applicability of this model operating with vectored thrusts. After addressing the time-response model and its control, side thrust vectoring will be implemented to fully apply its roll control authority into lateral movements.

Acknowledgments

This paper is based upon the work in UAVLab of University of Sydney as part of Swashplateless Underactuated Platform Design Research.

References

- [1] S. R. Herwitz, S. E. D. R. G. H. D. V. S. J. Z. B. M. L. J. G. L. B. A. G. M. A. R. E. S. J. A. B., L. F. Johnson, "Imaging from an unmanned aerial vehicle: agricultural surveillance and decision support," *Computers and Electronics in Agriculture*, Vol. 44, 2004, pp. 49–61.
- [2] K. Alexis, A. T. L. D., G. Nikolakopoulos, "Coordination of helicopter UAVs for aerial Forest-Fire surveillance," *Applications of Intelligent Control to Engineering Systems*, 2009, p. 169–193.
- [3] D. Murphy, J. C., "Applications for mini VTOL UAV for law enforcement," *Information and Training Technologies for law enforcement*, Vol. 3577, 1999. <https://doi.org/10.1117/12.336986>.
- [4] M. Cutler, B. M. J. H., N. K. Ure, "Comparison of fixed and variable pitch actuators for agile quadrotors," *AIAA Guidance, Navigation, and Control Conference (GNC)*, 2011. <https://doi.org/10.2514/6.2011-6406>.
- [5] Johnson, W., "Helicopter Theory," *Newburyport: Dover Publications*, 2012, pp. 26–31.
- [6] D. Mellinger, V. K., "Minimum snap trajectory generation and control for quadrotors," *IEEE International Conference Robotics and Automation (ICRA)*, 2011, pp. 2520–2525.
- [7] J. Paulos, M. Y., "An Underactuated Propeller for Attitude Control in Micro Air Vehicles," *2013 IEEE/RSJ International Conference on Intelligent Robots and Systems (IROS)*, 2013, p. 1374–1379.
- [8] J. Paulos, M. Y., "Flight Performance of a Swashplateless Micro Air Vehicle," *2015 IEEE International Conference on Robotics and Automation (ICRA)*, 2015, pp. 5284–5289. <https://doi.org/10.1109/ICRA.2015.7139936>.
- [9] Y. Jin, Y. W., L. Yong, "Dynamics research on actively controlled swashplateless rotor," *Part G: Journal of Aerospace Engineering*, 2019, pp. 4492–4508.
- [10] C. Papachristos, A. T., K. Alexis, "Design and Experimental Attitude Control of an Unmanned Tilt-Rotor Aerial Vehicle," *2011 IEEE International Conference on Advanced Robotics (ICAR)*, 2011, p. 465–470.
- [11] Y. Mulgaonkar, B. M. C. M. K. A. M. H. V. K., M. Whitzer, "Power and weight considerations in small, agile quadrotors," *Proc. SPIE*, Vol. 9083, 2014. <https://doi.org/10.1117/12.2051112>.

Advanced Tether-Net Device for Removing Space Debris from LEO

Jiaqi. Liu¹ Shufan. Wu²

Shanghai Jiao Tong University, Shanghai, 200240, China

The objective of this paper is to design a device to catch space debris about 30 centimeters for the international space station (ISS). The device is combined with four small satellites connected by tether-net. The four small satellites capture device is an advanced tether-nets device (ATND), and it's designed based on the traditional tether-nets device. The concept of tether-net's insulting material is Kevlar, the conductive material is 8030 aluminum alloy, and electromagnets inserted in the tether for adsorbing the small satellites and shrinking the tether-net. Only one small satellite installs special payloads, others install necessary payload that can decrease the total mass of this device and carry more propellers. In the ATND, each small satellite owns one propeller, it can implement several times capture tasks. Two methods of removing the space debris are proposed, one is taking the debris to 280km LEO orbit after ATND capturing the debris, then the space debris is deorbited by natural dynamics and the debris destroys by air resistance producing a large amount of heat; the other is taking the debris to the graveyard orbit. This concept of ATND is novel, environmental and functional, it's aimed to remove space debris in the LEO where ISS is settled, and will not produce new space debris, once finished its task, it will be maneuvered back to the earth.

I. Nomenclature and Acronyms

ATND	=	Advanced Tether-Net Device
ISS	=	International Space Station
LEO	=	Low Earth Orbit
PCB	=	Printed Circuit Board
ADR	=	Active Debris Removal
GPS	=	Global Positioning System
EPS	=	Electrical Power Supply
SSS	=	Student Small Satellite
SSTC	=	Student Satellite Technology Centre
SJTU	=	Shanghai Jiao Tong University

II. Introduction

There are thousands of pieces of space debris flying around LEO. Most orbital debris are man-made space debris, such as debris from spacecraft, tiny paint spots on spacecraft, rocket parts, satellites that no longer work or space debris from spacecraft exploding in space at high speed. Indeed, LEO is already an orbital space dump. The ISS serves as a microgravity and space environment research laboratory in which scientific experiments are conducted in astrobiology, astronomy, meteorology, physics, and other fields. It is the largest artificial object in space and the largest satellite in low Earth orbit (LEO), regularly visible to the naked eye from Earth's surface. Space debris could cripple the ISS and kill its crew. These objects are travelling around the earth at ten times the speed of the average firearm bullet, so space debris is a high risk for the ISS.

The removal of space debris is a hot topic in the international space field. The Active Debris Removal (ADR) strategy proposed in the National Space Policy released in 2010. The task of clearing space debris is widely recognized

¹ Master student and School of Aeronautics and Astronautics, and Student, AIAA.

² Professor, School of Aeronautics and Astronautics, and Member, AIAA.

as an important task in preserving the space environment for decades to come. The topic was on the agenda of the International Scientific and Technical Subcommittee and consultations were held among the space agencies. ESA proposed an active removal method of space debris based on expanding foam application for ADR, the "RemoveDebris"[1] project, led by the University of Surrey, has designed a "harpoon" to be used to capture debris in orbit. Japanese "electric tether-net" scheme, carrying a 700m-long electric tether-net on board[3], to lock and grab the space debris and drag it into the Earth's atmosphere and burn it up. the Russian space agency, Roscosmos, is developing a powerful laser gun that vaporizes space debris directly by focusing a powerful laser beam. Therefore, it is of great scientific and engineering significance to discuss and conceive a new spacecraft device for capturing space debris[4,5,6].

ATND aims to capture space debris which size about 30 centimeters, the concept bases on traditional tether-net spacecraft[2]. It is designed to remove space debris in LEO to protect spacecraft in service with LEO and the International Space Station (ISS).

III. Concept of Overall Design

ATND will be working in the low earth orbit which altitude is about 400km, the main function is to protect the International Space Station from impacting by space debris. As shown in Figure 1, it's the concept of overall operating process. Before ATND launched, it should be passed ground test, after that ATND can be launched, ATND will be launched into orbit when it's in a shrinking state. Then ATND will have an in-orbit check, to make sure every payload is working normal and make sure ATND can be deployed be a big "net". When everything working normal, ATND entry nest step, it will be operated at LEO (400km) to find a space debris, every time ATND meeting ISS in the LEO, it will operate evade maneuver. Once it found a space debris the small satellites will be restructured be a big "net" to do the capture tasks. After ATND captured the space debris, small satellites will be restructured again, four small satellites will be combined together, and the space debris is packaged in the net. There are two methods to remove the space debris, one is let ATND bring the space debris back to 280km-LEO, the space debris will be lowering their orbit by itself, then burns in the atmosphere, the other removal method is in virtue of manifold, ATND will bring the space debris into grave orbit. The ATND will back to LEO (400km) to find a new space debris, capture process, removal space debris. If the ATND runs out of fuel, it can run close to ISS and let ISS to capture it, and the astronauts refuel it, so the ATND can keep working in LEO (400km).

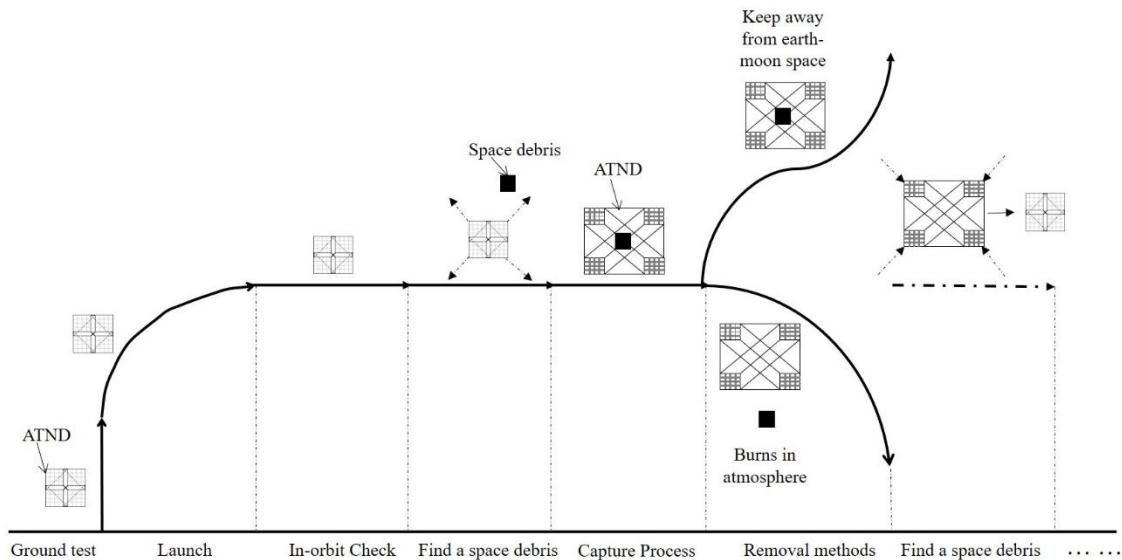


Fig.1 A concept map of space debris' capture process

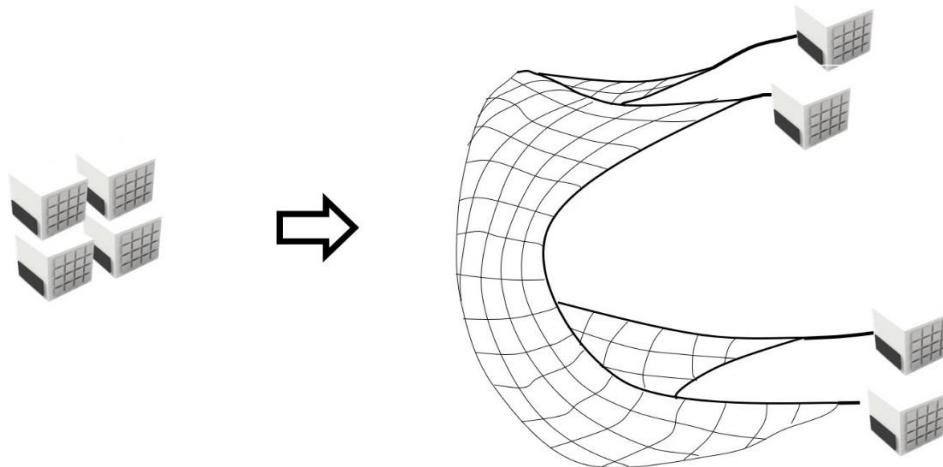


Fig.2 The concept of ATND deploying process

IV. Advanced Tether-Net Device Design Details

A. External Layout Design of ATND

Figure 3 shows the structure of ATND, the four small satellites are located at the four corners of the tether-net respectively. The four small satellites are mainly connected by the main tether and electromagnet, and the main tether with the main tether are connected by deputy tethers, as shown in Figure 4. Electromagnets are mounted at the surface of each small satellite, when ATND doesn't find a space debris, small satellites can absorb each other by magnet force. Compared with the traditional Tether-net spacecraft[2], ATND doesn't need to eject a net to do the capture work and the ejection process maybe produce new space debris, ATND can be restructured as a big net to capture a space debris and no new space debris produced.

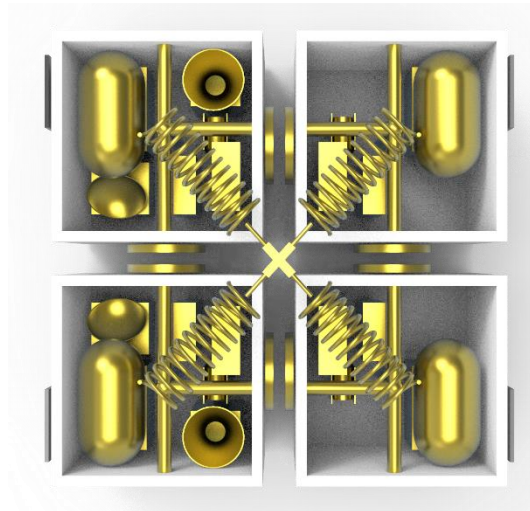


Fig.3 The unexpanded state of the four small satellites

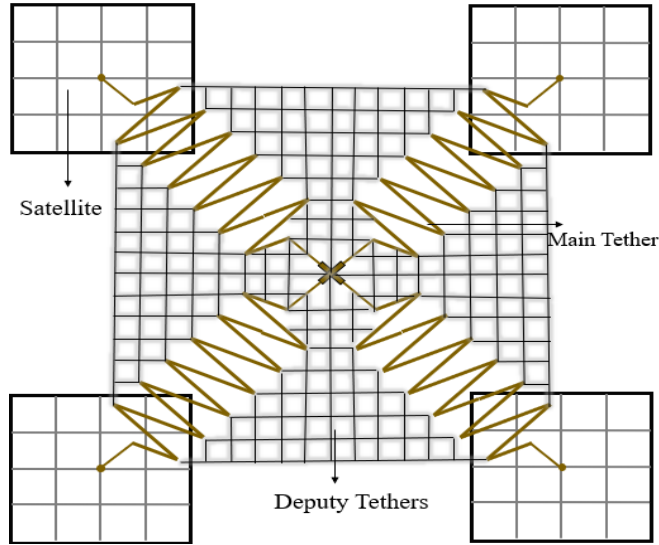


Fig.4 States of the four small satellites after expansion

According to the thermal analysis of ATND, cooling panel will be installed on the hottest side of small satellites to keep the internal thermal circumstance of ATND, make sure every payload operating normal. Almost all surface of small satellite is covered with solar panel to store energy when there is sunlight. In the Figure 5, it's the state when small satellite is extended the solar panel. In the ATND, each small satellite has two solar panels, and if ATND under solar light, the solar panel will be extended to store energy, when no solar light or once find a space debris, the solar panel will be shrinkable.

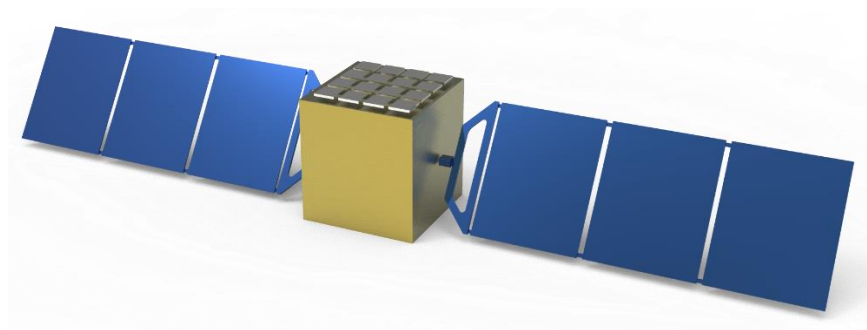


Fig.5 Solar panel of small satellite

Table.1 The total carrying weight and the envelope of ATND

Item	ATND
Mass of small satellite	3000g
Size of small satellite	$168 \times 168 \times 234mm^3$
Length of one solar panel (expanded)	380mm
Mass of solar panel	2880g
Dry mass of propeller	1520g
Wet mass of propeller	1900g

B. Internal design of small satellites

As for the internal design of small satellite, we considered to different small satellites carry different payloads, for example, ATND just need one camera to find the space debris and it need one U/V transceiver to get information from

earth, so we just choice one small satellite to carry camera and U/V transceiver. However, the necessary payloads, like thrusters, OBC, battery, and so on, must be settled at each small satellite.

There is serval system are necessary for each small satellite, power supply system, attitude control system, thermal control system, propeller, OBC. As for power supply system of ATND, small satellite has the characteristics of small size, light weight and complex load. It is proposed to choose a highly efficient combined power supply scheme of potassium arsenide solar cell and lithium ion battery. The power supply system comprises a solar array, which is used to convert solar energy into electricity and then charge or output the battery for the load. The battery bank, in parallel with a solar cell array, is used to store electric energy converted by the solar cell array or to output electric energy to supply power for a load; A power controller is used for regulating and stabilizing the transfer of current or voltage between solar arrays, batteries and loads; The battery bank and the power controller are connected directly by an electrical connector. Due to the mission's off-orbit requirements, the power consumption cannot be met by simple bottom panel. Moreover, in the solar system, sufficient solar light can provide sufficient energy for the satellite, so solar panels are proposed to be used. The maximum power point tracking is adopted for energy supply and distribution, and the time-sharing of the payload is arranged, so as to realize the multi-track balance of the battery.

The main functions of the small satellite power supply subsystem are as follows:

- a. During the illumination in orbit, solar battery array is used to generate electricity, power the payloads of small satellites and charge the battery.
- b. During no illumination in orbit as for thermal control system, the battery releases electric energy to supply power to on-board equipment.
- c. Implement the management and control of primary power supply. Power supply subsystem includes the control of the charging of the lithium-ion battery pack, the telemetry required for the energy module, and the provision of remote control and interface.
- d. Implement the management and control of secondary power supply. Power supply subsystem includes 5V, 3.3V secondary power conversion to meet the load requirements and switch control of gyro, single machine of attitude control, digital transmission, visible light camera and other equipment.



Fig.6 Schematic of solar panels

As for thermal control system, in the small satellite uses passive thermal control is enough for keeping the thermal environment of small satellite. In addition, ATND is proposed to use the multi-layer insulation (MLI) component, which can protect the spacecraft from the sun or a planet by excessive heating also prevent ATND exposure to excessive cooling caused by deep space. At the same time, black anodized thermal control coating is intended to be used on the surface of in-star structural parts, while single-machine PCB board has a high emissivity, so there is no need to spray black paint. Multi-layer insulation material consists of a multi-layer reflective screen and a spacer laminate to reduce heat loss, the basic structure of the multilayer insulation material consists of a reflective layer that emits radiant heat and a spacer layer that isolates heat. The main tasks of OBC system are as follows: whole star management, on-board data processing and analysis, subsystem communication, micro-nano satellite attitude determination and control, science unit management, on-board time function, on-board state monitoring, data storage function, command remote control function, etc.

Following are those special payloads which don't install at every small satellite. Camera, the passive imaging and laser ranging system, which is composed of large field telescope, small field telescope and laser rangefinder, can be used to discover, capture and track tiny objects in space. The observation camera is CMOS plane array visible light

camera. Its main function is to image debris in the cosmic environment and provide initial data for debris movement recognition and channel planning. Meanwhile, it has large-capacity data storage and management functions, including image data of the camera itself. The design scheme of UV band communication equipment uses high integration modular. It adopts a board card, which is the standard size of small satellite. It can connect power supply, data and telecommand and telemetry interface. There are multiple modules, such as radio frequency receiver, transmitter, digital processing board and low speed data communication interface, to combined to different functional boards.

C. The concept of tether-net

The core of the main tether, as shown in Figure 7, is made of conductive aluminum. The outer layer of aluminum is covered with insulating material Kevlar, and an electromagnet is placed at the same interval of the main tether, which is responsible for shrinking the main tether. Figure 8 and 9 show the states when the main tether is expanded and contracted respectively. The material of deputy tethers is insulating material Kevlar, and deputy tethers will be moving as main tethers' movement.

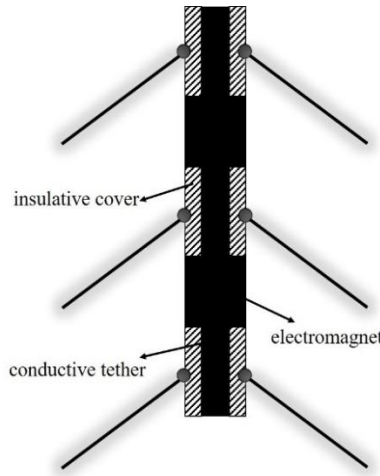


Fig.7 The main tether structure

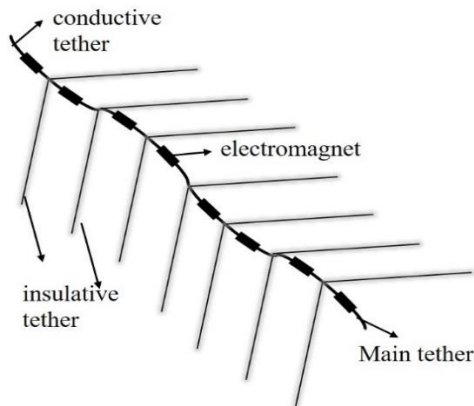


Fig.8 The unfurling state of the main tether

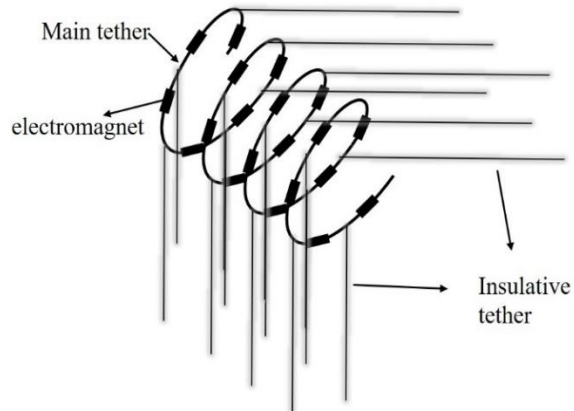
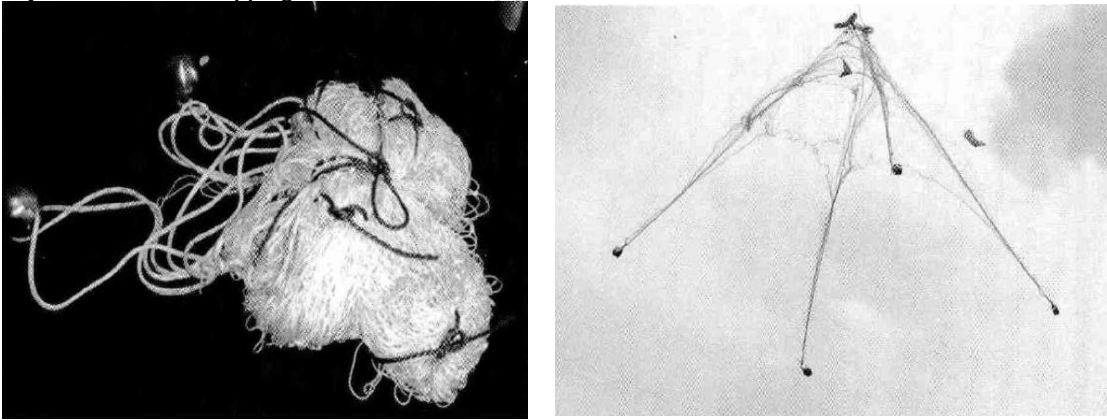


Fig.9 The shrinkable state of the main tether

When no space debris is found, electromagnets located on the close sides of the satellites are electrically magnetic, and the satellites adsorb onto each other, meanwhile, tether-net is in the shrinkable state. When a space debris be discovered, electromagnets located on the close sides of the satellites power off and lose the magnetic so small satellites can be moved as the attitude control system and the electromagnet inlay in main tether all power off too, electromagnet lose magnetism, main tether can be moved as the satellites' movement, ATND will be restructured be a big "net" to capture space debris.

In the design of tether-net, the choice of material is particularly important, for the main tethers, should be used with good electrical conductivity of material, at the same time, has high strength, wear resistance and tear resistance characteristics. Considering that the main tether needs to have electrical conductivity, so referring to the structure of optical fiber, the woven material of the rope network is finally selected as the inner core of 8030 aluminum alloy, and the outer wrapping material is Kevlar[10]. In previous designs, the tether-net made of Kevlar material has been proved to have a good application prospect. In addition, Kevlar materials in tank armor, body armor, has been widely used in the design of motor shell, it is worth mentioning, because of its volume between-196°C ~+182°C size stability[9], there is no significant change of performance Kevlar often used in the aerospace manufacturing industry, it's an ideal material used in aviation and space flight. Therefore, the main tethers of ATND also inner material use 8030 aluminum alloy and the outer wrapping material is Kevlar[8].



(a) A tether-net made of Kevlar

(b) Expansion experiment of tether-net

Fig.9 Tether-model and ground test

The electromagnetic docking technology of small satellites is characterized by light weight, simple structure and autonomous control, etc. The main device to generate electromagnetic force is electromagnet, which is mainly composed of armature, iron core and coil. As the force between electromagnets decreases exponentially with the increase of distance, the electromagnetic force or torque that meets the requirements of formation flight and rendezvous and docking can be provided under certain range, power consumption, mass and other constraints. Therefore, it is more suitable to choose ferric nickel alloy (Permalloy) for making magnetic bar with iron core. Considering the coerced force and saturated magnetic induction intensity, 1J50 fe-Ni alloy can be selected as the core material.

The Table 2 is the specification of tether-net, it promised that when the tether-net is expanded, the size of tether-net can wrap a size of 30cm's space debris.

Table.2 Specifications of ATND's tether-net

The area of tether-net (m^2)	The thickness of tether-net (cm)	The density of tether-net (g/cm^3)	The mass of tether-net (kg)
0.793	0.5	1.44 (Kevlar)	0.8208
		2.7 (8030 aluminum alloy)	

V. The Measure after Capturing Space Debris

After ATND caught a space debris, the electromagnets settled on the side of small satellites will be work, let the four small satellites gather together again, and the space debris will be fixed in the tether-net. There are two methods about removing space debris, the first is ATND transferring the space debris into 280km altitude orbit. The space debris will be deorbited by natural movement, as time going when the space debris entre to atmosphere it will be burning due to air resistance produces a large amount of heat. The other option is to transfer the space debris into graveyard orbit[7], the graveyard orbit are long-term stable orbits where the evolution of the orbital elements due to natural perturbation, and the space debris will not back with in the 30-year period.

Once the space debris was captured by ATND, the space debris will be fixed in the tether-net and moved as four small satellites' movement. ATND will be maneuvered into 280km orbit, then ATND will release space debris let it

move by natural force. After those action, ATND will be maneuvered back to LEO (400km) enter next period. And the space debris removal process of graveyard is same with transferring the space debris into 280km orbit.

VI. Conclusion

Based on the traditional tether-net spacecraft, this paper proposed a novel device of the space debris removal spacecraft. Compared with the traditional tether-net spacecraft, ATND will not generate new debris when in the removing process, and there is more accurate capture device than the traditional tether-net. When ATND finds space debris, four small satellites will be deployed to capture space debris, and each small satellite is equipped with positioning equipment. By the way ATND has more propellers than the traditional tether-net spacecraft because each of the small satellites is equipped with a propulsion system that enables multiple space debris capture missions. In addition, the equipment can be returned to Earth after completing the space debris removal mission, so there is no potential risk of creating new space debris. ATND reduces unnecessary payloads which don't influent the normal work of small satellites, some special payloads that to operate special work, like camera, U/V transceiver, just need one small satellite to carry. This method saves the space of small satellite to carry more propellers and reduces the total mass of ATND meanwhile saving the thrust. The concept of tether-net design of ATND is a novel idea. An electromagnet is inset at the same interval to the tether to control the deploy or shrinkable state of tether-net. There is difference between main tethers and deputy tethers, the core of main tether is conductive material covered by insulting material-Kevlar, the deputy tethers just consist with insulting material. As the reason of using conductive material be the core of main tethers is to control the magnetism of electromagnets.

At present, space debris bring a big risk to space environment especially for the low earth space, by the way low earth space has very high frequency of using for human space activities. Active removal is the inevitable choice and the only way out. The acquisition of space debris by small satellites shows good economic benefits and future prospects. Compared with the high cost of space tug catch-up removal technology, using small satellites for space capture can greatly reduce the cost.

In the future, the technology of space debris capture by small satellites shows a very broad application prospect. First of all, the reuse technology of space debris capture technology of small satellites can be further studied, such as the launch and recovery of tether-net, which can effectively reduce the cost. Secondly, in addition to capturing space debris, its core capture technology, tether-net technology and multi-satellite collaborative formation net technology can also be used to capture asteroids in space in the future, and carry out a series of scientific experiments, which have a good prospect for scientific research and exploration.

Acknowledgments

The authors would like to thank the other students and teachers from SSTC of SJTU, Zhou Zhiwei, Cao Xin, Duan Yuxiao, Huang Yixin who contributed to ATND. Author got a lot of knowledge about the layout of small satellites from SSS (Student Small Satellite) program which proposed by SSTC, about this design we got a lot of suggests from Research Professor. Liqiang Hou. This design is inspired by Dr Ivan Rudoj who is the tutor of the first author when the first author got her first master degree in Moscow Aviation Institute. There is a special person we would like to thanks is Mr. Mingzhi Li who is the husband of the first author, he gives a lot of help and support to this paper.

References

- [1] G. S. Aglietti et al., "The active space debris removal mission RemoveDebris. Part 2: In orbit operations," *Acta Astronaut.*, vol. 168, no. June 2019, pp. 310-322, 2020.
- [2] M. Lavagna, R. Armellini, A. Bombelli, R. Benvenuto, and R. Carta, "Debris Removal Mechanism Based on Tethered Nets," *Proc. i-SAIRAS 2012*, no. September, pp. 1–6, 2012.
- [3] S. Nakasuka, T. Aoki, I. Ikeda, Y. Tsuda, and Y. Kawakatsu, 'Furoshiki satellite' - A large membrane structure as a novel space system," *Acta Astronaut.*, vol. 48, no. 5–12, pp. 461–468, 2001.
- [4] UNCUPOS, "Active Debris Removal — An Essential Mechanism for Ensuring the Safety and Active Debris Removal — An Essential Mechanism for Ensuring the Safety and Sustainability of Outer Space," vol. V.12-50395, no. January, pp. 1–50, 2012.
- [5] Erin J. C. Active Debris Removal — An Essential Mechanism for Ensuring the Safety and Sustainability of Outer Space[C]. A/AC.105/C.1/L.310. V.12-50395 (E).
- [6] N.L. Johnson. Orbital debris: The growing threat to space operations. *Advances in the Astronautical Sciences*, 137:3–11, 01 2010.
- [7] Colombo C, Alessi E M, Willem V D W, et al. End-of-life disposal concepts for Libration Point Orbit and Highly Elliptical Orbit missions[J]. *Acta Astronautica*, 2015, 110(may-jun.):298-312.

- [8] Chen Yunjin, Liu Chang. Application and development of 'Kevlar' materials in weapons and equipment [J]. Modern weapons,1990(02):19-21.
- [9] Fan Xiangze. Study on microstructure and properties of 8030 aluminium alloy conductive material for wire and cable [D]. Chongqing University, 2019.
- [10] Alex Mak, P. Eng. General Cable AA8030 Aluminum Alloy Conductors: A Successful Counter-Measure against Theft of Copper Street Lighting Cable [EB/OL].

Aeroacoustics and aerodynamics of flow over a forward-backward facing step

Chung-Hao Ma¹

University of New South Wales, NSW 2052, Australia

A combined experimental and numerical study on aeroacoustics of low Mach number flow over a forward-backward facing step (FBS) is presented. The aeroacoustic and aerodynamic behaviors of a two-dimensional FBS immersed in an incompressible turbulent boundary layer were investigated. The height of the step being considered was 50% of the incoming boundary layer thickness ($h/\delta \cong 0.5$). The step aspect ratio (step length to step height L/h) was 4. The Reynolds number based on the step height Re_h in the experiments ranged from 1.4×10^5 to 2.8×10^5 while the Re_h in the simulation was 1.2×10^5 . The experiment was conducted in the UNSW Anechoic Wind Tunnel (UAT), where far-field sound radiated by the step was measured. The sound spectra show that the sound level with the step is higher than background (flat plate) at between 1k to 10k Hz. Acoustic beamforming was applied to locate the source of the sound. The beamforming map implies the noise was originated from the top of the step, where the separation and reattachment of the shear layer happened. The large-eddy simulation (LES) was performed to model the unsteady turbulent characteristics and visualize the flow field. The wall pressure fluctuations were calculated to understand the unsteady force acting on the surface. The unsteady velocity components $u'u'$, $v'v'$ and $u'v'$ as well as the turbulent kinetic energy (TKE) were plotted to identify the highest turbulence generation in the flow field. The results indicate that the peak flow excitation was consistent with the occurrence of the separated shear layer from the leading edge of the step.

I. Introduction

Surface discontinuities are often found in engineering applications, such as the uneven plate joints on the surface of the vehicles or gaps between panels. When exposed to fluid flow, these surface irregularities will separate the incoming boundary layer and modify the flow field. The flow excitation will induce the turbulent behaviors further downstream and create wall pressure fluctuations which might cause the vibration. These turbulent activities and pressure fluctuations could affect the structure fatigue life and generate undesirable noise. Some previous studies [1-5] have considered the forward-facing step (FFS) and Backward-facing step (BFS). Awasthi [2] concluded that the geometry of the leading edge is the critical factor of the flow field modification as well as the far field noise production in such situation. Ji & Wang [5, 6] performed a large-eddy simulation (LES) for both FFS and BFS with different h/δ and found that the sharp corners are critical in flow alteration and sound generation in both scenarios. Pure FFS or BFS cases have been widely investigated; however, flow over a FBS has not yet been comprehensively understood.

The flow configuration for the forward-backward facing step (FBS) is different from FFS as the trailing edge of the step is involved. Fig.1 illustrates the general flow field of a forward-backward facing step. Flow separation occurs upstream of the edge owing to the adverse pressure gradient induced by the step. The flow reattaches on the vertical face of the step and separates again on the sharp edge, forming the first separation bubble. The excited separated shear layer will then reattach on top of the step (if the step is long enough) and forms the second separation bubble. Further downstream, the existence of the trailing edge causes the third separation in this flow configuration. The shear layer encompassing those separation bubbles induces intense turbulence, which is responsible for the high-levels of surface pressure fluctuation [7].

¹ Master student, School of Mechanical and Manufacturing Engineering, student member AIAA, 1192752

Leclercq and Addad [8, 9] considered a large FBS ($h/\delta < 1$) with aspect ratio = 10, which was long enough to keep the reattachment point upstream of the step trailing edge. The corresponding Re_h is 1.7×10^5 . The backward reattachment length was affected by the upstream flow and reduced by $3h$ compared to a typical backward-facing step flow where only one backward-facing edge is considered. The acoustic results revealed that the forward edge dominated the noise production, and the source was located at the forward step separation region, where high velocity and pressure fluctuations were measured. The shear layer generated by flow separation significantly contributed to the pressure fluctuation.

Doolan and Moreau [10] presented an experimental study of noise generated by sub-boundary layer forward-backward facing steps. The study considered various geometries of the step, such as triangular and rectangular steps with different aspect ratios. Step height to boundary layer height ratio $h/\delta = 26.3\%$, 52.6% and 79% , and the aspect ratios were 8, 4, 2.67. The measurements indicated that the slanted leading edge generated less noise. However, the location of the sound source in these cases was not identified.

Springer [11] consider a square FFS ($l/h = 1$) with $Re_h = 2.6 \times 10^5$. The trailing edge of the step was completely immersed in the wake region, and it was unclear if reattachment occurred on top of the step or not. A numerical calculation identified that the source term to be the shear layer behind the upper edge.

In summary, separation and reattachment, which were affected by the sharp corners in the flow field, were concluded to be critical factors controlling flow modification. The separation bubble downstream of the leading edge of the forward-facing step is highly sensitive to the step geometry, such as the shape of the edge or the step height. The separated shear layer is found for both forward- and backward-facing steps. It is responsible for downstream pressure fluctuation and far-field noise generation. Previous research showed that sound production is mostly affected by the front edge geometry. Yet the location of the source was found to vary as aspect ratio presumably because the trailing edge further alters the downstream flow field.

To address the knowledge gap, a combined experimental and numerical study of a forward-backward facing pair step with medium aspect ratio ($l/h=4$) is presented. The far-field sound was measured by a 64-microphone phased array. The measurements were carried out at free stream velocities = 20,30,40 m/s ($1.4 \times 10^5 < Re_h < 2.8 \times 10^5$). Large-eddy simulation (LES) was performed to visualize the turbulent flow characteristics and the shear layer structure. The Mach number for all cases were below 0.12.

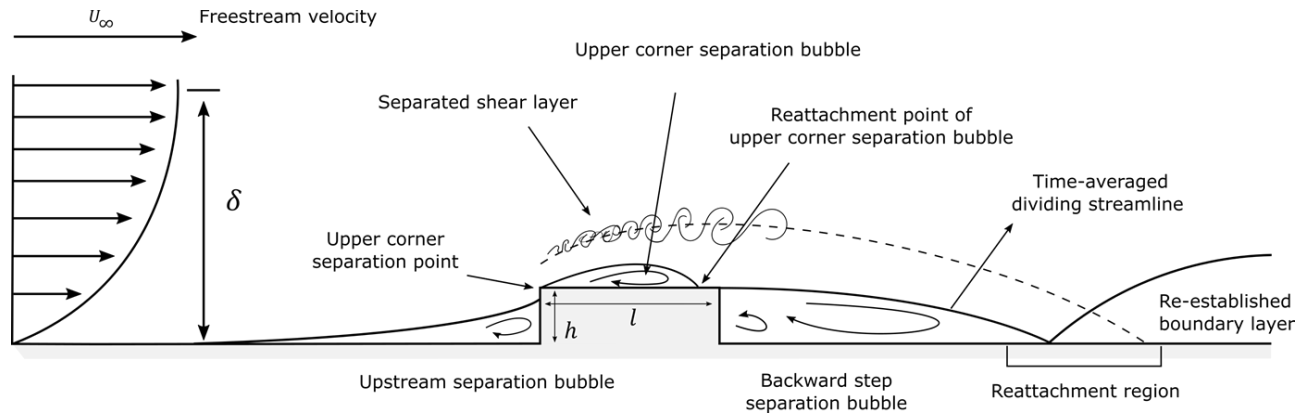


Fig. 1 Flow configuration of FBS.

II. Instrumentation and Methodology

A. UNSW Anechoic Wind Tunnel (UWT)

The measurement was conducted in UNSW Anechoic Wind Tunnel, which is an open-jet type wind tunnel facility with a $0.455\text{m} \times 0.455\text{m}$ test-section enclosed by a $3\text{ m} \times 3.2\text{ m} \times 2.15\text{ m}$ anechoic chamber. The maximum test speed of the wind tunnel is around 70 m/s and the acoustic foam attached on the surrounding wall provides an anechoic condition above 300Hz. The facility is a suction type tunnel where an axial fan is placed downstream of the test-section and connected to the anechoic chamber through a diffuser. More details of the facility can be found in Ref. [12].

B. Microphone acoustic array

Acoustic measurements were carried out using a 64-microphone phased array. The array consists of 64 1/4" GRAS 40PH phase matched microphones with frequency response range between 50 Hz to 20 kHz. The nominal sensitivity of each microphone at 250 Hz is 50 mV/Pa (± 20 dB). The microphones are mounted on a 2 m \times 2 m perforated steel grid. The array has an optimal design for beamforming applications [13]. The acoustic data were beamformed by using conventional beamforming algorithm. The background noise was removed by frequency domain subtraction and the far-field sound spectra were obtained by the center microphone in the array.

C. Experimental setup

Figure 2a shows the experimental setup of the testing rig. A forward-backward facing step with aspect ratio = 4 was mounted on the endplate which sit on the side of the wind tunnel test section. The free stream velocity U was set to be 20, 30 and 40m/s and the corresponding Reynolds number based on step height varied from 1.4×10^5 to 2.8×10^5 . The step leading edge was 400mm away from the jet exiting plane. The undisturbed boundary layer thickness was measured in the absence of the step using hot wire anemometry. The boundary layer information at $x = 400$ mm was given in table 1. The boundary layer thickness was 20 mm at $U = 40$ m/s and the step height was 10 mm ($h/\delta = 0.5$). The spanwise length of the step was longer than the test section to ensure flow two-dimensionality. The array was settled 1.3m above the model and the center microphone is 150 mm downstream of the leading edge of the step which results in an 83.4° observation angle θ (Fig. 2b). A correction method was applied to correct effect of the shear layer forming on the other side of the test section [14].

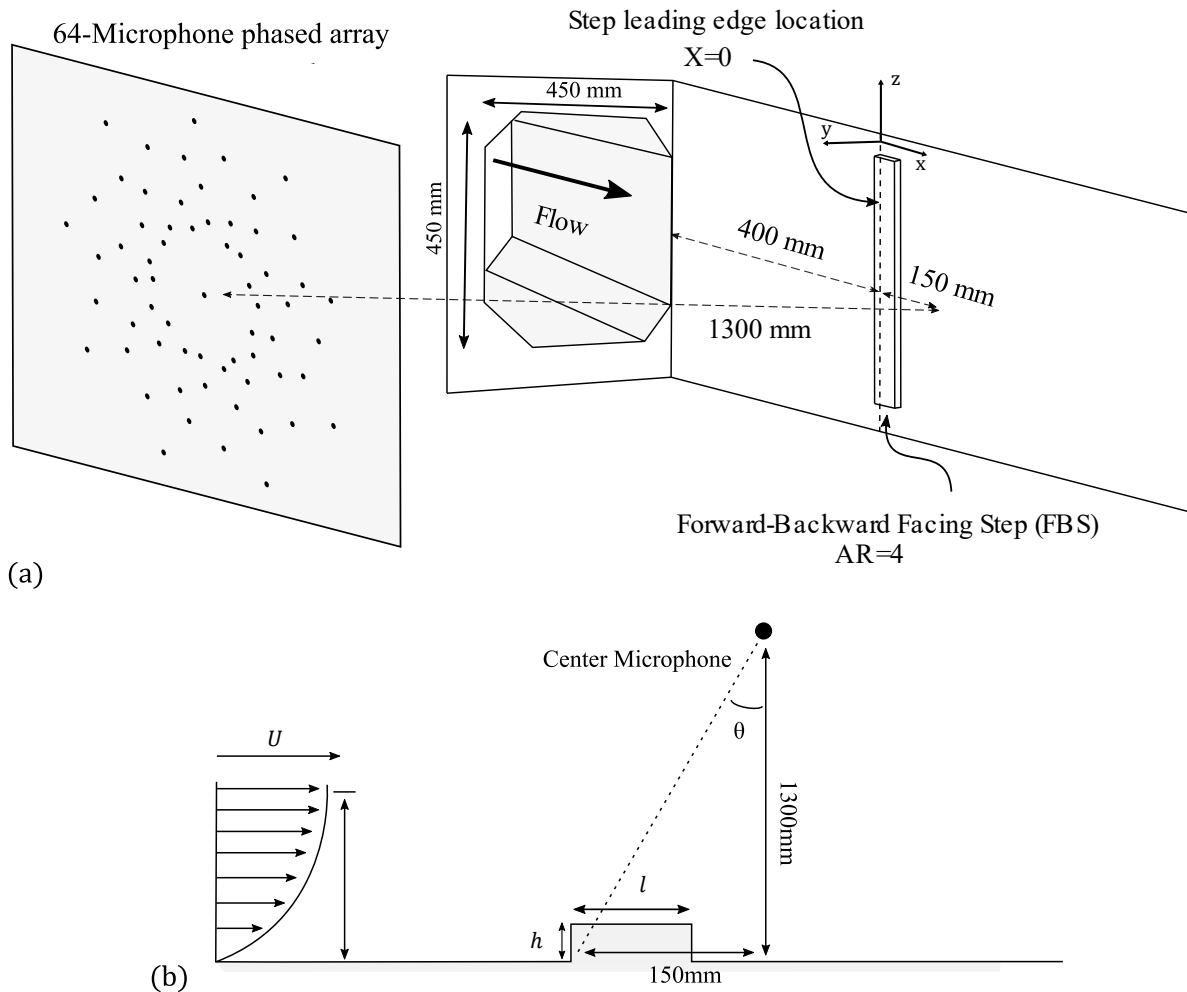


Fig. 2 Sketches of the test section and experiment setup. (a) Anechoic test section with FBS mounted on the side and phased-microphone array sitting on the other side. (b) Side view of the experimental setup.

Table 1 Flat plate boundary layer information

U	Position	δ	δ^*	θ	H	Re_δ	Re_{δ^*}	Re_θ
20	400	19	1.98	1.57	1.27	25851	2691	2127
30	400	19	1.82	1.47	1.24	38776	3697	2988
40	400	20	1.77	1.45	1.23	54422	4793	3923

D. Numerical setup

The large-eddy simulation (LES) was adopted to resolve the incompressible turbulent flow field. In LES, the governing equations are derived by applying a spatial filter instead of time averaging as is done in RANS, which makes the instantaneous quantities available above the grid cut-off frequency. The equations were solved using ANSYS FLUNT 19.1 finite-volume solver. Wall-Adapting Local Eddy-viscosity Model (WALE model) was selected to model the unresolved flow scale. Second-order schemes were used for both time and space discretisation. The velocity-pressure coupling was conducted with SIMPLE method. The calculations were performed on Australia National Computational Infrastructure (NCI)'s supercomputer Gadi.

The computational domain size is $L_x = 60h$, $L_y = 30h$, $L_z = 5h$ in streamwise (x), wall normal (y), and spanwise (z) directions. A similar domain size has been found to be adequate [5, 15, 16]. Streamwise domain length was cut by the front edge of the step with $20h$ before it. The structured mesh was employed in the simulation. The grid size in each dimension is determined by the normalized values. The Δx^+ in streamwise direction is varying from 5 to 50 with the smallest mesh created at the vertical faces of the step. Δy^+ is set to be 1 on all horizontal surfaces and grows to 40 at $y/h \cong 3$. Δz^+ value is a constant 25 in the spanwise direction. The number of total cells is around 16.5 million. The time step size was 8×10^{-7} seconds with the corresponding CFL number < 1 throughout the entire computational domain cells. A separate RANS calculation adopting the $k - \omega$ SST turbulence model of a flat plate is used to generate the turbulent boundary layer for inlet velocity profile. The constant total pressure is arranged at the outlet boundary. A periodical boundary condition is used at the spanwise direction and no-slip boundary condition is used on the walls. The symmetry boundary condition is employed on the top of the domain.

E. Grid independence study

A grid independence study was performed to demonstrate the grid spacing convergence. The grid convergence index (GCI) was calculated to estimate the spatial discretization error [17]. Three different grid resolutions with mesh refinement concentrated on the wake region and the vicinity of the step were considered. The aforementioned Δy^+ and Δz^+ value remain the same in all three cases. The grid refinement ratio was estimated by $r = (k_i/k_{i+1})^{1/3}$, where k is the number of cells in each case and $i = 1, 2, 3$ represents the coarse mesh, medium mesh and fine mesh, respectively.

The r.m.s. wall pressure at $x = 3h$ downstream of the leading edge and the mean velocity magnitude in the wake region at $x = 6h$ and $y = 0.5h$ were chose to evaluate grid convergence. The results are shown in Table 2. $GCI_{3,2}$ and $GCI_{2,1}$ are the grid convergence indices for medium-to-fine and coarse-to-medium refinements, respectively. The Richardson error estimator ϵ was calculated to quantify the discretization error between the value predicted by the Richardson extrapolation method [18] and by the medium resolution grid when the grid spacing approaches zero. The error estimator ϵ for medium resolution grid were 1.1% and 2.47% for r.m.s. wall pressure and mean velocity magnitude, respectively. The $GCI_{3,2}$ were lower than $GCI_{2,1}$ for both variables, which implies the flow parameters are indeed converging as the computational cells size reduced. The medium resolution grid was adopted in this study as it provides reasonable estimation of the flow properties, while requiring relatively lower computational cost.

Table 2 Results of grid convergence study

	$GCI_{2,1}$ (coarse-to-medium)	$GCI_{3,2}$ (medium-to-fine)	ϵ
Velocity Magnitude	34.19%	3.21%	2.47%
r.m.s. wall pressure	11.8%	1.36%	1.1%

III. Results and Discussion

A. Far-field noise radiated from FBS

Figure 3 shows the beamforming results at 4000Hz with free stream velocity from 20 to 40. The flow direction in the figures was from the left to the right and the black lines represent the leading and trailing edges of the FBS. Since the microphone array was placed outside of the flow, the effect of acoustic propagation must be taken into consideration. A correction term [14] was included in the beamforming algorithm to take account of sound refraction [19] and convection due to the shear layer. The background noise was pre-subtracted in frequency domain to remove the acoustic contamination cause by the tunnel. The beamforming maps suggest that the sound was essentially originated from the top of the step where flow separation and reattachment occurred. Inside this region, high levels turbulence was generated which contributes to the noise production [5, 20]. As the free stream velocity increased, the source became more distinct. Meanwhile, the source location remains the same regardless of the incoming flow speed. The sound source location agrees with some previous studies regarded FFS.

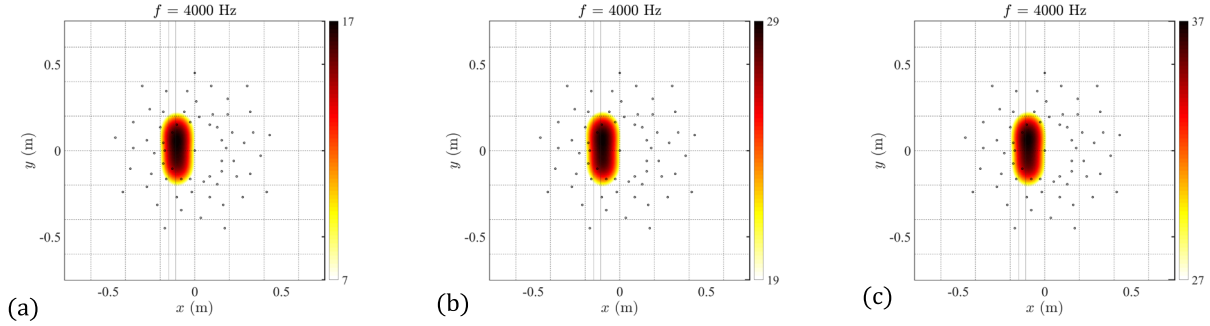


Fig. 3 Acoustic beamforming maps. Black dots represent the positions of each microphone in the array. Black lines indicate the location of the edges of the step. (a) $U = 20$ m/s. (b) $U = 30$ m/s. (c) $U = 40$ m/s. The source strength is shown in dB.

The signal to noise ratio SNR was introduced to identify the noise produced by FBS [21]. SNR between step noise and background noise was calculated as

$$SNR = 10 \log_{10} \left[\frac{\Phi_{pp}(f)}{\Phi_{pp, no\ step}(f)} \right]$$

,where Φ_{pp} is the spectral density measured with a FBS and $\Phi_{pp, no\ step}$ is the spectral density measured at the same flow velocity but without the step. Fig. 4 shows the SNR at $U = 40$ m/s. It can be seen that $SNR > 1$ dB at between 1kHz to 10kHz, which indicates the influence of the step in far-field sound radiation mainly locates in this frequency range. Thus, the following discussion and the sound spectra results will only focus on this frequency range.

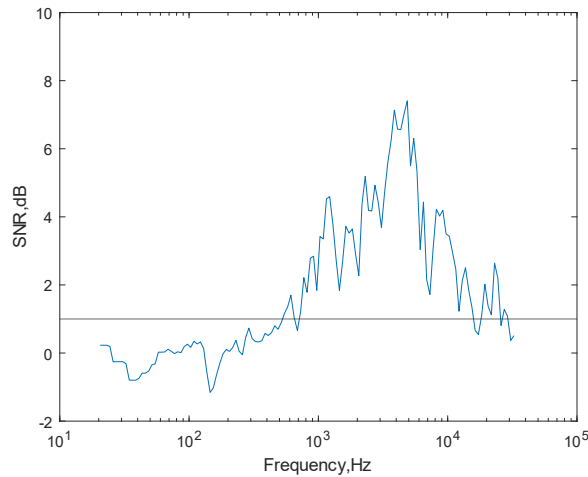


Fig. 4 Signal to noise ratio between step noise and background noise (without step). Black line locates at 1 dB.

The 1/12-octave band sound pressure spectra for FBS at 3 different mean flow velocity are shown in Fig. 5 The observation angle was 83.4° from the leading edge. The noise produced by the step is generally broadband without any distinct tonal noise. The sound spectra at different velocity have nearly identical shape throughout the frequencies of interested. The spectra shows an almost flat shape at low frequencies followed by two small humps peak at around 4500Hz and 10kHz respectively. Awasthi [1] suggested the step may become acoustically non-compact and result in a spectral dip when the wavelength is close to the step height, which in this case the corresponding frequency is 32-34k Hz. Such frequency is outside of the concerned frequency region, yet a decline trend can be observed at high frequencies.

The result shows a strong influence of mean flow velocity. At highest mean flow velocity, the sound level exceeds that at $U=30\text{m/s}$ and 20m/s by 8 dB and 18 dB between 1kHz to 10kHz, respectively. A scaling law for the pressure spectrum of FBS at a fixed observation angle was proposed by [10]. The non-dimensional model was given as

$$St_L \text{ vs. } 10 \log_{10} \left(\frac{\Phi r^2}{\rho_0^2 M^3 L l} \right)$$

,where Φ is the acoustic pressure spectrum, r is the distance from the step leading edge and the microphone, l is the step length, M is Mach number, and $p_0 = \rho U^2$. St_L is the Strouhal number based on the characteristic length L of the flow, which was selected to be the step height in this study. The scaled acoustics data are shown in Fig. 5b. A great collapse of the data can be seen at St_h below 1. At a similar observation angle, Doolan and Moreau [10] observed an impressive data collapse at St between 0.3 to 2. It is worth noting that in [10], the boundary layer thickness downstream of the step was chosen as the flow characteristic length whereas the step height was selected here.

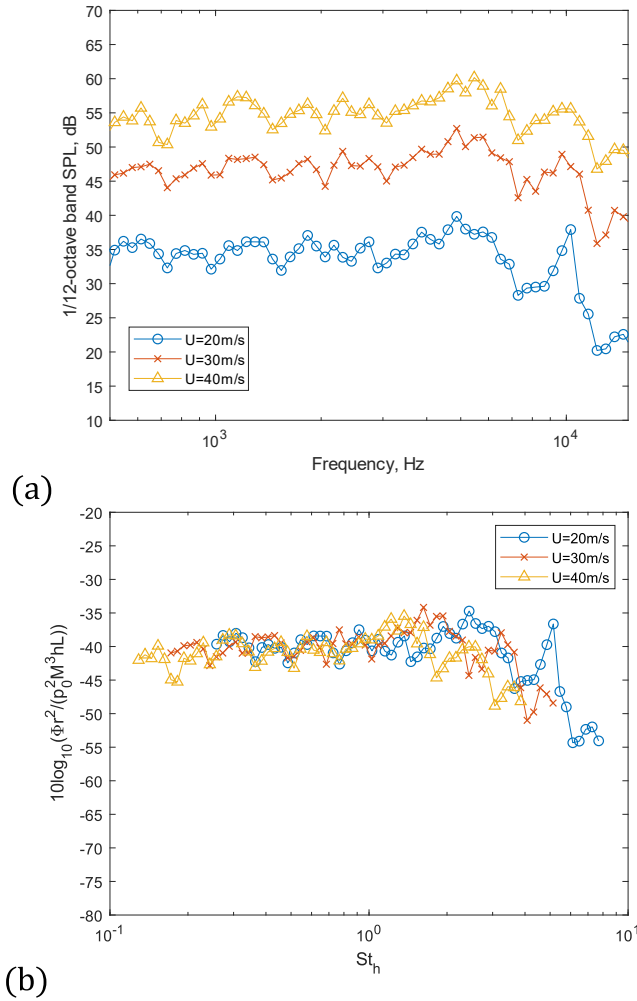


Fig. 5 Step sound spectra at center microphone $\theta = 83.4^\circ$. (a) 1/12 Octave sound pressure level under different mean flow velocity. (b) Scaled 1/12 octave band sound spectra.

B. CFD results

1. Flow field

The velocity field near the FBS is given in Fig. 6a. In the figure, the mean streamwise velocity U/U_∞ was contoured with mean streamlines placed overlaid. The flow deflected upward of the step, separated at the leading edge and reattached downstream of the edge. After the quick reattachment on the step, the boundary layer detached again at the trailing edge and formed the largest separation bubble. Three separation bubbles can be observed in the flow field. As the step length was long enough to accommodate the first downstream separation bubble, the second downstream separation bubble preserved some the backward-facing step nature. The downstream mean reattachment length x_{r1} and x_{r2} were determined by the zero-crossing location of the wall shear stress. The separated flow reattached $2h$ from the leading edge and $4.8h$ from the trailing edge ($8.8h$ from the leading edge). The first reattachment length x_{r1} was found comparable to $1.3h$ to $2.5h$ reported by [6, 22-25] but shorter than $3.47\sim 5h$ observed by [26-28]. It is claimed by Sherry [29] that the reattachment length of FFS is highly sensitive to step height to boundary layer thickness h/δ and Reynolds number. While the second separation bubble retained the BFS flow feature, the upstream perturbation due to the upper corner of the step altered the flow field after all. The reattachment length x_{r2} was found smaller than $5.5\sim 7h$ noticed by [6, 16, 30, 31] in pure BFS. However, this value was comparable to $5.1h$ noted by [23] who considered a FBS with aspect ratio = 2.36.

Fig.6b shows the turbulent kinetic energy distribution. The higher level of turbulent kinetic energy (TKE) can be seen concentrates along the shear layer around the separation bubbles. The maximum value 0.09 is found on top of the step($(x/h, y/h) = (1, 1.2)$) where the flow was extensively excited by the leading edge. The TKE associated with the first separation bubble is in general two to three times higher than that with the second separation bubble, which indicates the leading edge plays a critical role in turbulence generation.

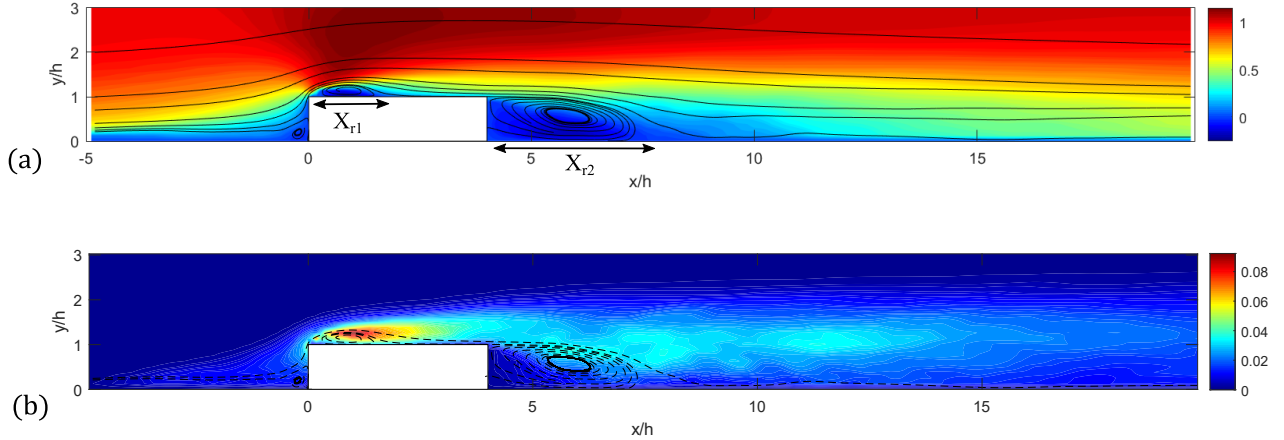


Fig. 6 Velocity fields for forward-backward facing step. (a) Mean streamwise velocity U/U_∞ . Black lines denote the mean streamlines. X_{r1} , X_{r2} indicate the reattachment length on top of the step and downstream fo the step, repectively. (b) Turbulent kinetic energy $((\overline{u'^2} + \overline{v'^2} + \overline{w'^2})/2U_\infty^2)$, black dashed lines denote the mean streamlines surrounding the circulation bubbles.

The Reynolds stress components in $x - y$ plane ($\overline{u'u'}$, $\overline{v'v'}$ and $\overline{u'v'}$) are plotted in Fig. 7a-c for $-2 < x/h < 10$. It is apparent that the overall contours for each component are similar to the turbulent kinetic energy distribution, which is highly associated with the separated shear layer. The highest magnitude of each velocity fluctuations were all found on top of the step with the second highest group located downstream of the trailing edge. The velocity fluctuations in streamwise direction $u'u'$ are mostly greater than that in wall-normal direction $v'v'$. The maximum value of $u'u'$ was found nearly 2 times of the maximum value of $v'v'$. The most intensive velocity fluctuation region for $v'v'$ located at the rear part of the first separation bubble, which is observed slightly downstream than that region for $u'u'$. Meanwhile, the fluctuations downstream of the step in wall-normal direction was found extending longer distance. This could be attributed to the reattachment phenomenon and the blend of two separated shear layer emanating from the first and second separation bubble.

The Reynolds stress $u'v'$ exhibits small positive values near the leading edge. This has also been reported by several previous studies [23-25]. Hattori and Nagano [24] believed it was caused by the counter-gradient diffusion phenomenon (CDP), whereas Nematollahi and Tachie [25] explained the occurrence of this region is due to the

interaction between the high-momentum convection in the streamwise direction and the upwash along the vertical face.

It can be noticed that the area covered by the first separation bubble shear layer contains the strongest velocity fluctuations and turbulent kinetic energy. This region has also been identified as the location of acoustic source from beamforming maps.

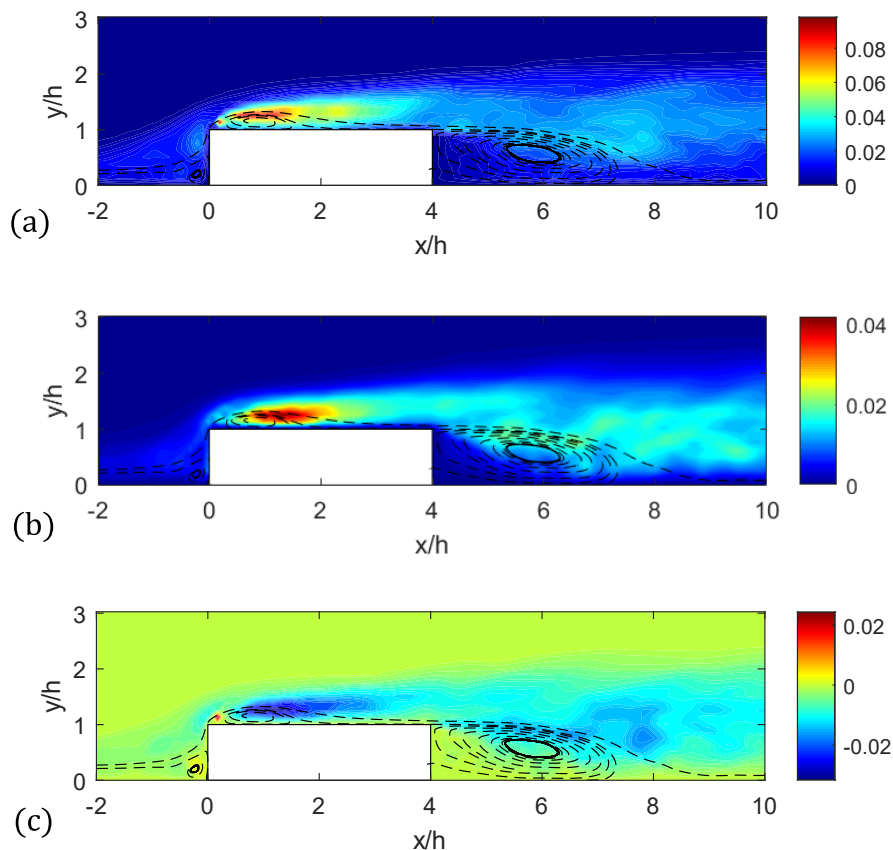


Fig. 7 Contours of Reynolds stresses. (a) $\overline{u'u'}/U_\infty^2$. (b) $\overline{v'v'}/U_\infty^2$ (c) $\overline{u'v'}/U_\infty^2$. black dashed lines denote the mean streamlines surrounding the circulation bubbles.

2. Mean and unsteady wall pressure

Computed wall pressure coefficient and r.m.s. of wall pressure fluctuations distributions are shown in Fig. 8. Red dashed lines and blue dashed lines in the figure indicate the leading edge and trailing edge of the step, respectively. The C_p curve follows the similar pattern with the FFS [28] where a roll-up can be observed upstream of the step and plunges immediately after the upper corner, coincides with the first downstream recirculation region. Downstream of the trailing edge, the C_p value drops again in the second recirculation region and then slowly returns to zero. An overshoot is generally observed in the BFS C_p curve ; however

Figure 8b reveals that the highest values of r.m.s. wall pressure occurs at $x/h = 1.08$ with the peak value of 0.148. The value downstream of the step is in general greater than that in upstream with the highest value found near the reattachment region ($x_{r2} = 8.8h$). Similar features are observed in the distributions of r.m.s. wall pressure fluctuation, TKE and Reynolds stresses. Highest values were all detected on top of the step where the separated shear layer was induced due to the sharp corner at the leading edge. Downstream of the step, disturbed flow remains the fluctuations at certain level but lower than that in the first separation bubble.

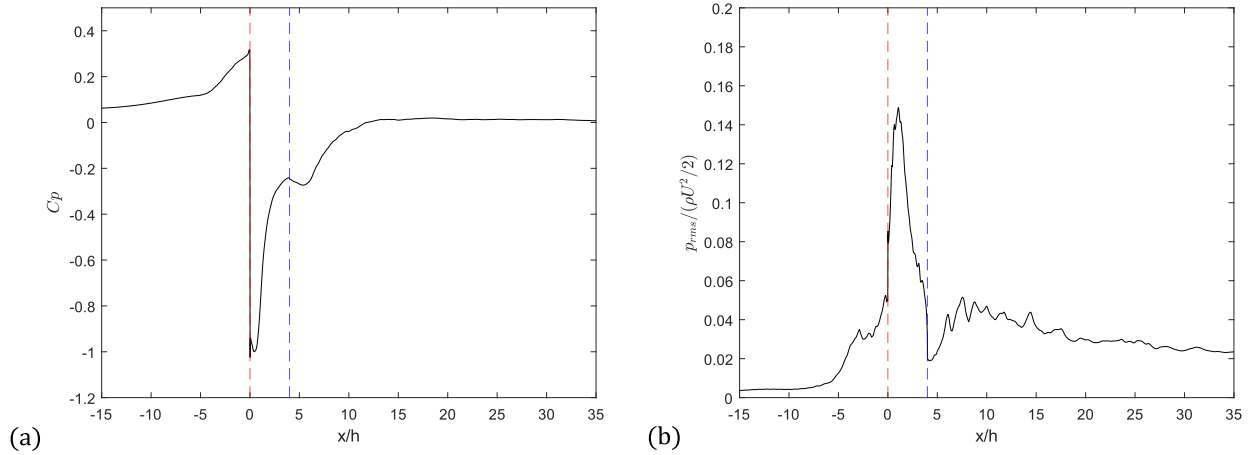


Fig. 8 Pressure coefficient and root mean square wall pressure fluctuation distributions for FBS. (a) Pressure coefficient. (b) r.m.s. wall pressure fluctuation. Red dashed line, leading edge of the step; blue dashed line, trailing edge of the step.

Frequency spectrum of wall pressure fluctuations along streamwise direction at the center of the span is shown in Fig. 9. The normalized wall pressure spectrum $\Phi_{pp}U/(\rho U^2)^2h$ quantified the fluctuation strength at different frequency and different streamwise locations. It is obvious that the fluctuations on top of the step were consist of components with higher energy across wider range of frequency ($0.01 < St_h < 1$). The maximum value in this region was found 0.025 at $St_h = 0.03$ at $1h$ downstream of the leading edge. Other local maximum values in this region were recorded as 0.017 and 0.015 at $St_h = 0.14$ and 0.23, respectively. Downstream of the trailing edge, the wall pressure fluctuations were mostly induced by low frequency components with the corresponding Strouhal number between 0.02 and 0.15.

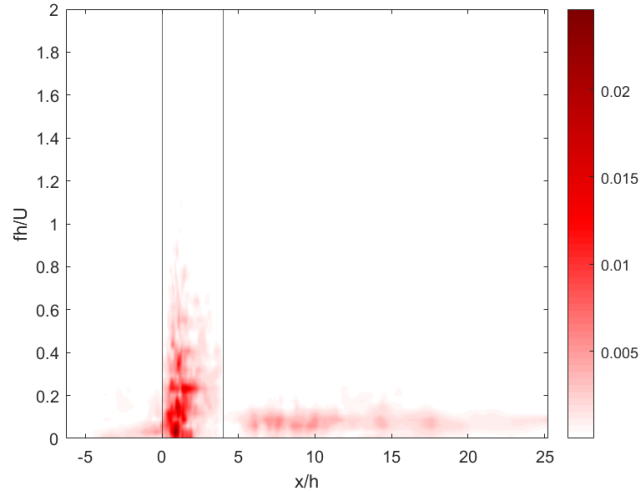


Fig. 9 Frequency spectrum of wall pressure fluctuations for $-7 < x/h < 25$.

IV. Conclusion

The acoustics measurements for a FBS were conducted to examine the far-field sound radiation. The acoustic beamforming maps reveals that the noise source located on top of the step, where the separated layer was induced by the leading edge of the step. Far-field sound was collected by the center microphone of the array with 83.4° observation angle. The 1/12 octave band sound spectrum presented a broadband nature between 1k to 10k Hz without any apparent tonal noise. The spectra under 3 different mean flow velocities collapse well when $St_h < 1$ by applying the scaling

model proposed by [10]. It has been noted that the step noise is directive, therefore measurements at different observation angles still needed to be conducted to gain a comprehensive understanding of this geometry.

LES of flow over a FBS has been performed to study the flow modification caused by the obstacle. The mesh sensitivity study has been carried out to verify the convergency of the calculation. However, the LES model still requires a further experimental validation to confirm the prediction. The model predicted the highest turbulence generation happened on top of the step, where the flow was separated by the upper corner of the step. Flow excitation remained downstream of step but at a lower level. The wall pressure fluctuations spectra displayed a similar pattern with maximum r.m.s. value was observed immediately downstream of the leading edge. The region of highest turbulent generation and wall pressure fluctuations was found consistent with the noise source indicated by beamformed maps, which associated with the separated shear layer emanated from the first separation bubble. It is worth noted that in this case, the step was long enough to keep the whole first separation bubble on top of the step, which allows some of the backward-facing step features to be preserved. FBS with smaller aspect ratio still needed to be investigated.

References

- [1] Awasthi, M., W.J. Devenport, W.N. Alexander, S.A.L. Glegg, “Aeroacoustics of Rounded Forward-Facing Steps: Far-Field Behavior”. *AIAA Journal*, 2019. **57**(5): p. 1899-1913.
- [2] Awasthi, M., W.J. Devenport, and S.A.L. Glegg, “Sound radiated by turbulent flow over unrounded and rounded forward-facing steps.” *Journal of Sound and Vibration*, 2020. **488**: p. 115635.
- [3] Becker, S., Schaefer, F., Grabinger J., Kaltenbacher, M., “Simulation of Broadband Noise Behind a Backward Facing Step”. in *16th AIAA/CEAS Aeroacoustics Conference (31st AIAA Aeroacoustics Conference)* 2010.
- [4] Jacob, M.C., Louisot, A., Juvé, D., Guerrand, S., “Experimental Study of Sound Generated by Backward-Facing Steps Under Wall Jet”. *AIAA Journal*, 2001. **39**(7): p. 1254-1260.
- [5] Ji, M. and M. Wang, “Sound generation by turbulent boundary-layer flow over small steps”. *Journal of Fluid Mechanics*, 2010. **654**: p. 161-193.
- [6] Ji, M. and M. Wang, “Surface pressure fluctuations on steps immersed in turbulent boundary layers”. *Journal of Fluid Mechanics*, 2012. **712**: p. 471-504.
- [7] Awasthi, M., W.J. Devenport, W.N. Alexander, S.A.L. Glegg, “Aeroacoustics of Rounded Forward-Facing Steps: Near-Field Behavior.” *AIAA Journal*, 2019. **57**(3): p. 1237-1249.
- [8] Addad, Y., Laurence, D., Talotte, C., Jacob, M. C., “ Large eddy simulation of a forward-backward facing step for acoustic source identification”. *International Journal of Heat and Fluid Flow*, 2003. **24**(4): p. 562-571.
- [9] Leclercq, D., Jacob, M., Louisot, A., Talotte, C., “ Forward-backward facing step pair - Aerodynamic flow, wall pressure and acoustic characterisation”. 2001.
- [10] Doolan, C. and D. Moreau, “ Flow-induced noise generated by sub-boundary layer steps”. *Experimental Thermal and Fluid Science*, 2015. **72**.
- [11] Springer, M., C. Scheit, and S. Becker. “ Flow-Induced Noise of a Forward-Backward Facing Step”. in *New Results in Numerical and Experimental Fluid Mechanics X*. 2016. Cham: Springer International Publishing.
- [12] Con Doolan, D.M., Manuj Awasthi and Chaoyang Jiang. “THE UNSW ANECHOIC WIND TUNNEL”. in *WESPAC*. 2018.
- [13] Z. Prime, B.Z., and C. Doolan., “ Beamforming array optimisation and phase averaged sound source mapping on a model wind turbine”., in *Internoise*. 2014: Melbourne, Australia.
- [14] Bahr, C., Zawodny, Nikolas S., Yardibi, T., Liu, F., Wetzels, D., Bertolucci, B., Cattafesta, L., “Shear Layer Time-Delay Correction Using a Non-Intrusive Acoustic Point Source”. *International Journal of Aeroacoustics*, 2011. **10**(5-6): p. 497-530.
- [15] Akselvoll, K. and P. Moin, “Large-eddy simulation of turbulent confined coannular jets”. *Journal of Fluid Mechanics*, 1996. **315**: p. 387-411.
- [16] Le, H., P. Moin, and J. Kim, “ Direct numerical simulation of turbulent flow over a backward-facing step.” *Journal of Fluid Mechanics*, 1997. **330**: p. 349-374.
- [17] Roache, P.J., “ QUANTIFICATION OF UNCERTAINTY IN COMPUTATIONAL FLUID DYNAMICS”. *Annual Review of Fluid Mechanics*, 1997. **29**(1): p. 123-160.

- [18] Richardson, L.F. and J.A. Gaunt, “The Deferred Approach to the Limit. Part I. Single Lattice. Part II. Interpenetrating Lattices”. *Philosophical Transactions of the Royal Society of London Series A*, 1927. **226**: p. 299.
- [19] Amiet, R.K., “Refraction of sound by a shear layer”. *Journal of Sound and Vibration*, 1978. **58**(4): p. 467-482.
- [20] Lighthill, M.J., “On Sound Generated Aerodynamically. I. General Theory”. *Proceedings of the Royal Society of London. Series A, Mathematical and Physical Sciences*, 1952. **211**(1107): p. 564-587.
- [21] Awasthi, M., “Sound Radiated from Turbulent Flow over Two and Three-Dimensional Surface Discontinuities”, in *Aerospace and Ocean Engineering Department*. 2015, Virginia Polytechnic Inst. and State Univ., Blacksburg: Vol. Ph.D. Dissertation.
- [22] Camussi, R., Felli, M., Pereira, F., Aloisio, G., Di Marco, A., “Statistical properties of wall pressure fluctuations over a forward-facing step”. *Physics of Fluids*, 2008. **20**(7): p. 075113.
- [23] Fang, X. and M.F. Tachie, “On the unsteady characteristics of turbulent separations over a forward-backward-facing step”. *Journal of Fluid Mechanics*, 2019. **863**: p. 994-1030.
- [24] Hattori, H. and Y. Nagano, “Investigation of turbulent boundary layer over forward-facing step via direct numerical simulation”. *International Journal of Heat and Fluid Flow*, 2010. **31**(3): p. 284-294.
- [25] Nematollahi, A. and M.F. Tachie, “Time-resolved PIV measurement of influence of upstream roughness on separated and reattached turbulent flows over a forward-facing step”. *AIP Advances*, 2018. **8**(10): p. 105110.
- [26] Awasthi, M., Devenport, WilliamJ, Glegg, StewartA L., Forest, JonathanB, “Pressure fluctuations produced by forward steps immersed in a turbulent boundary layer”. *Journal of Fluid Mechanics*, 2014. **756**: p. 384-421.
- [27] Bergeles, G. and N. Athanassiadis, “The Flow Past a Surface-Mounted Obstacle”. *Journal of Fluids Engineering*, 1983. **105**(4): p. 461-463.
- [28] Farabee, T.M. and M.J. Casarella, “Effects of surface irregularity on turbulent boundary layer wall pressure fluctuations”. *ASME Journal of Vibration Acoustics*, 1984. **106**: p. 343.
- [29] Sherry, M., Jacono, D., Sheridan, J., Mathis, R., Marusic, I., “Flow separation characterisation of a forward facing step immersed in a turbulent boundary layer”. *Sixth International Symposium on Turbulence and Shear Flow Phenomena*, 2009.
- [30] Eaton, J.K. and J.P. Johnston. “Low-frequency unsteadiness of a reattaching turbulent shear layer. 1982.
- [31] Kim, J., S.J. Kline, and J.P. Johnston, “Investigation of a Reattaching Turbulent Shear Layer: Flow Over a Backward-Facing Step. ”, *Journal of Fluids Engineering*, 1980. **102**(3): p. 302-308.

Computational Aerodynamic Analysis of Hypersonic Flow over 2D Axisymmetric Space Re-Entry Vehicle with Euler and RANS Models

Ahsan Uz Zaman*

School of Engineering and Material Science, Queen Mary University of London, Mile End Road, London, E1 4NS, United Kingdom.

Computational modelling of re-entry vehicles at hypersonic speed is conducted using inviscid Euler and RANS turbulence models on Queen Mary's High-Performance Computing, Apocrita. The geometry considered is a modification of NASA's Orion Crew Exploration Vehicle which is based on the Apollo crew module and has become a reference design for modern re-entry vehicles. The analysis is restricted to the flow around the re-entry vehicle and does not take into consideration parameters such as thermochemical changes, structural integrity and materials selection. Inviscid Euler and RANS $k-\omega$ SST Menter turbulence models have been implemented in Siemens STAR-CCM+ software. Spatial and temporal discretization are carried out by implementing MUSCL 3rd-order/CD and 1st-order implicit Euler time differencing schemes, respectively. AUSM+ FVS and Roe-FDS schemes have been implemented for flux splitting. AUSM+ FVS is found to be most suitable and robust flux splitting scheme for hypersonic flows compared to Roe-FDS. Inviscid model is found to be in reasonable agreement with $k-\omega$ SST results for capturing shock ahead of the re-entry vehicle. However, for capturing accurate aft-body flow features, viscous modelling is necessary.

I. Nomenclature

AoA	=	Angle of Attack
BC	=	Boundary Condition
C_D	=	Drag Coefficient
C_L	=	Lift Coefficient
C_P	=	Pressure Coefficient
L/D	=	Lift-to-drag Ratio
NS	=	Navier-Stokes
RANS	=	Reynolds averaged Navier-Stokes
REV	=	Re-entry Vehicle

II. Introduction

The development of re-entry vehicles (REVs) has allowed humans unprecedented access to space; from first manned spaceflight of Vostok 1 to the first human landing on the Moon on Apollo 11, and the continuous operation of the International Space Station via Soyuz capsule. The surge in recent times in proposed space missions ranging from exploration to extra-terrestrial colonization will see ever-increasing dependence on REVs.

The velocity ranges within which REVs enter Earth's atmosphere during the descent are of extreme hypersonic regimes. Typically, an REV would travel around Mach 25 when it encounters the atmosphere with Apollo capsule reported to be travelling at even Mach 36. At these speeds, REVs undergo immense aerodynamic loads which, coupled

* Master of Science, School of Engineering and Material Science, AIAA Student Member.

with continuously changing environment (density, pressure, and temperature), make their flight unstable. Investigating the compressibility effects that dominate the flow field surrounding the REV is essential in improving its design and performance. However, flow complexities in extreme hypersonic regimes cannot be predicted using standard mathematical models and recreating such a harsh environment in wind tunnels carries significant physical and financial challenges. Hence, CFD is needed to simulate and predict the fluid dynamics around space vehicles during re-entry.

This research paper aims to investigate the flow characteristics around an Orion-based REV at Mach 5 using Euler and RANS models in STAR-CCM+. The effects of introducing viscosity in the flow-field are analyzed, and comparison is made with the theoretical prediction of hypersonic flow around blunt-nosed bodies.

III. CFD Setup

A. Geometry and Mesh Generation

REV geometry and the mesh are created using ANSYS ICEM R19.2 package. ICEM is preferred over other packages due to its user-friendly interface, a high degree of control in blocking, e.g. automatic O-grid feature to increase mesh density in the region surrounding the REV, quality mesh production, and mesh diagnosis ability. The REV simulated is based on IDAT modified version of Orion capsule [1] and is shown with dimensions in Fig. 1.

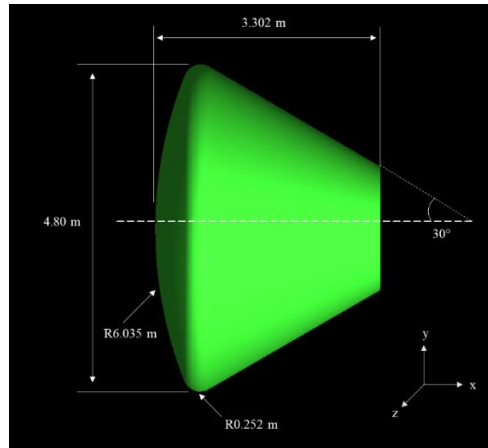


Fig. 1 Axisymmetric REV's dimensions with the defined global coordinate system

The computational domain is kept at $\sim 6x$ the chord length upstream (from leading edge) and vertically, and $\sim 20x$ the chord length downstream from the trailing edge. Structured quadrilateral meshing strategy has been adopted due to several advantages it offers over the unstructured mesh. Other than efficiency and simplicity, structured grids are less computationally intensive, offer grid alignment to the principal flow direction, and provide higher resolution in the regions of interest within the flow domain. To obtain a high-quality structured mesh, all meshes generated are validated for five quality metrics; Aspect Ratio, Angle, Eriksson Skewness, Orthogonal Quality, and Determinant (2x2x2) Stencil. Table 1 lists these metrics with the obtained values for each of them:

Table 1 Mesh quality metrics with their acceptable and obtained values

Metric	Range	Target Value	Achieved Value
Aspect Ratio	-	from unity to the order of tens	1 close to the body, 37.9 away
Angle	$0^\circ - 90^\circ$	$18^\circ - 90^\circ$	$47.88^\circ - 90^\circ$
Eriksson Skewness	0 – 1	0.5 – 1	0.742 – 1
Orthogonal Quality	0 – 1	close to unity	0.963 – 1
Determinant	0 – 1	close to unity	0.963 – 1

B. STAR-CCM+ Setup

Siemen's STAR-CCM+ (version 2019.3.1) is preferred due to its enhanced workflow environment, task automation using Java macros, and excellent post-processing capabilities. Initially, [2] and [3] are referred to set up hypersonic simulations in STAR-CCM+. Any modifications that needed to be made for this research are built mostly upon these two resources.

1. Euler Model

Inviscid modelling is used to obtain an initial approximation of flow around the REV. Euler equations are a set of hyperbolic quasi-linear equations that govern inviscid and adiabatic fluid flows. Euler equations govern compressible gas flows and provide practical simplifications in many cases, such as hypersonic regimes. In such instances, the primary goal of the simulation is to capture discontinuities in the flow, such as shock and expansion waves.

2. RANS Model

Reynolds Averaged Navier Stokes (RANS) are a family of turbulent models that close ensemble-averaged Navier-Stokes (NS) equations. This typically involves modelling the turbulent stress by taking the mean value of fluctuating velocity as identically 0. It is used in this research to obtain key flow characteristics that are not captured by inviscid setups such as boundary layer formation, flow separation, and wake characteristics. Compared to other turbulence models such as LES and DNS, RANS are computationally much less expensive. Within the RANS, $k - \omega$ SST is the most robust from the family of two-equation turbulent models and is used and is recommended for hypersonic analysis [2].

C. Initial Conditions

Physics node in STAR-CCM+ sets up initial conditions under which a fluid needs to be simulated. Model selections to define the physics of the fluid for this research are listed in the table below.

Table 2 Initial physics setup for simulations

Model	Selection
Space	Axisymmetric
Time	Implicit Unsteady
Material	Gas
Flow	Coupled Flow
EoS	Ideal Gas
Viscous regime	Inviscid/Turbulent

The finite volume discretization option selected is MUSCL 3rd-Order/CD (MUSCL stands for Monotonic Upstream-centered Scheme for Conservation Law, and CD for Central Differencing). It is a hybrid between 3rd order upwind MUSCL and 3rd order central differencing reconstruction scheme. Other than its higher-order spatial accuracy, MUSCL 3rd-Order/CD scheme ensures boundedness by reducing the accuracy to 2nd order near regions of strong shocks, and 1st order in the region of non-smooth flows. Elsewhere in the flow, the scheme is constructed as a combination of 3rd order upwind MUSCL and 3rd order central differencing [4]. This ensures that the scheme remains less dissipative while also staying robust to solve for discontinuities in the flow.

1. Roe-FDS

Roe's Flux Difference Splitting scheme, commonly known as Roe-FDS, uses Riemann approximation to calculate inviscid fluxes from non-linear governing equations. Obtaining an exact solution of the Riemann problem can be computationally expensive and, in some cases, not possible at all. Therefore, the system of conservation laws is converted into a quasi-linear hyperbolic system with the flux vector represented by a Jacobian matrix. Roe [5] presented a method to approximate the Jacobian matrix across the interface of two cells using parameter vectors, which if satisfies conditions of diagonalizability, consistency and conservation, would solve the quasi-linear system in a linear manner [6]. Although this approach is accurate for low Mach numbers, for high Mach number flows, Roe-FDS may introduce instabilities such as carbuncle phenomena and expansion shocks. Also, conducting the mathematical steps associated with solving the Jacobians and Roe averaged variables for each cell can still make Roe-FDS computationally demanding.

2. AUSM+ FVS

Advection Upstream Splitting Method flux vector splitting, AUSM FVS, is an alternate to flux differencing schemes to calculate inviscid fluxes of Euler and RANS equations. It splits the inviscid flux into two components; numerical convective flux and numerical pressure flux. The convective flux is determined in terms of flow convective speed, M , whereas the pressure flux is defined solely in terms of pressure terms. The splitting functions for Mach number and pressure introduced by Liou [7] makes AUSM FVS computationally less expensive, capable of capturing stationary shocks precisely and removes carbuncle phenomena, even at high Mach number flows.

D. Boundary Conditions

Boundary conditions (BC) assigned to each boundary of the computational domain are; *Axis* to the bottom boundary, *Freestream* to the inlet, outlet, and top boundaries, and *Wall* to REV geometry. Freestream BC in STAR-CCM+ requires three parameters to be defined; Mach number, pressure and temperature. These are defined as 5, 101325 Pa and 300 K, respectively. Freestream BC sets up flow conditions at far-field from the geometry and outside the domain. It is a non-reflective BC that is implemented to prevent any spurious reflections modelling of shock waves may cause at the boundaries. In the absence of shear force, i.e. inviscid flow, slip condition is imposed on 'wall' type BC. For turbulence modelling, the no-slip condition is imposed on the REV. This sets fluid velocity at the REV to zero and represents it as a solid stationary wall.

BC sensitivity analysis is performed using various BCs and are listed in Table 3. For velocity inlet BC, velocity and temperature are set to 1715 m/s and 300 K respectively, symmetry plane BC does not require any user input, whereas, for pressure outlet boundary conditions, the pressure and temperature are set to 101325 Pa and 300 K, respectively.

Table 3 Boundary condition settings for sensitivity analysis

	Inlet	Top	Outlet
BC1	Velocity Inlet	Symmetric Plane	Pressure Outlet
BC2	Velocity Inlet	Freestream	Pressure Outlet
BC3	Freestream	Symmetric Plane	Freestream

E. Solver Settings

1. CFL and Time-step Size

Unlike explicit solvers, implicit schemes do not have a strict restriction of having $CFL \leq 1$ condition for stability as they are unconditionally stable [8]. Having a larger CFL number for implicit schemes can result in quicker convergence (lower residual values) but with higher inaccuracies in the solution, while keeping a low CFL requires a lot more iterations to converge. Thus, there is a need to calculate, or estimate, a CFL number that provides a balance between convergence and accuracy while keeping the simulations stable[‡]. Furthermore, time-step size and CFL have a significant impact on the computational resources required for simulations of this scale and complexity. To obtain an initial estimate, CFL 1 is used to calculate the time-step size using following compressible gas dynamics CFL formula:

$$CFL = (u + c) \frac{dt}{\Delta x_{min}} \quad (1)$$

where Δx_{min} is the smallest cell size and is found using *X size* parameter within ICEM, dt is the time-step, and u is the characteristic velocity of 1715 m/s, and c is the speed of sound as 343 m/s. All meshes generated in this research have the same min x size of 0.00868 m. The time-step size using Eq. (1) is therefore 4.22×10^{-6} s. Corresponding physical simulation time and the number of time-steps are easily obtained using the following equations:

$$Physical\ time = \frac{Domain\ length}{Velocity} \quad (2)$$

$$No\ of\ time\ steps = \frac{Physical\ time}{dt} \quad (3)$$

[‡] One of the primary indicators of solver instability in STAR-CMM+ is the pressure and temperature correction and/or limitation errors that do not disappear themselves within the span of few iterations.

where domain length is rounded up to 89 m and velocity is 1715 m/s. Physical flow time works out as 0.052 s and number of time-steps required for a time-step size of 4.22×10^{-6} s as approximately 12,322. Since the flow is being initialized at 1 m/s, it is necessary that flow can develop completely before extracting results. Therefore, initially, the simulations are run for a physical time that covers the length of the domain around 1.5x, i.e. 0.078 s, at characteristic velocity. This increases the number of time-steps required to approximately 18,484. Running a simulation that takes over 18,000 time-steps, each in the order of 10^{-6} s, is found to be significantly demanding even for Apocrita. As [2] verifies, implicit schemes along with expert initialization and CFL ramping features in STAR-CCM+ allow CFL of 10 or even higher without compromising on the solution accuracy. Various CFL numbers are calculated using Eq. (1) and are shown in the following table:

Table 4 CFL number calculation for different time-step sizes

dt, s	CFL
4.22E-06	1.0
1.00E-05	2.0
5.00E-05	9.9
1.00E-04	19.8

After running test simulations with all the above time-step sizes, it is found that the time-step size of 5E-05 s performs best in terms of residuals, convergence and computational resources. Table 5 offers an insight into how time-step size affects the computational requirements.

Table 5 Time-step size sensitivity on computational resources

dt, s	No of dt	Max Total Iterations	Physical Time, s	Distance Covered, m	% Distance
4.22E-06	18484	1848400	0.078	137.20	154.16
1.00E-05	7500	750000	0.075	128.63	144.52
5.00E-05	1500	150000	0.075	128.63	144.52
1.00E-04	750	75000	0.075	128.63	144.52
5.00E-05	6000	600000	0.3	514.50	578.09

Physical time of 0.078 s is found to be inadequate to completely develop the flow in the domain. With the time-step size of 5E-05 s, it is found that simulations need to run for 6000 time-steps for the flow to be developed completely. Further, CFL used is 5, instead of 10 as in Table 4 due to AMG linear solver diverging after around 75000 iterations. CFL linear ramp feature is used from 1st iteration to 210000th iteration (with a starting value of 0.1). The aggressive CFL values at the beginning of simulations ensure convergence rate for complex hypersonic flows is maximized while solver remains stable throughout the entire simulation.

F. Turbulence Model Settings

For viscous flow model, AUSM+ FVS is chosen for flux splitting reconstruction. Recommended modifications for SST Menter model in STAR-CCM+ as found in [2] are; Constitutive option as QCR (Quadratic Constitutive Relation), Compressibility correction deactivated, and a1 coefficient as 0.355.

G. Stopping Criteria

Table 6 Stopping criteria set for all simulations

Criteria	Logical Rule	Values
Continuity, kg/s	AND	min 1.0E-04
X-momentum, kg m/s	AND	min 1.0E-04
Y-momentum, kg m/s	AND	min 1.0E-04
Max Inner Iterations	OR	100
Max Physical Time, s	OR	0.3
Max Steps	OR	6000

Minimum limits for continuity, x, and y momentum are kept to their STAR-CCM+ default values. For low-velocity flows, satisfactory residual convergence can be achieved with 15 to 20 inner iterations per time-step. For hypersonic flows, this is found to be quite inadequate. After running several test simulations at 50, 75, 100 and 150 inner iterations per time-step, it was observed that 100 inner iterations provided adequate residual convergence while keeping computational times within acceptable limits.

H. Mesh Independence

Mesh independence study aims to obtain a mesh refinement limit after which solution to governing equations and solver setup does not change the result by a significant margin. C_D and C_L are chosen as the parameters against which the mesh independence study is carried out.

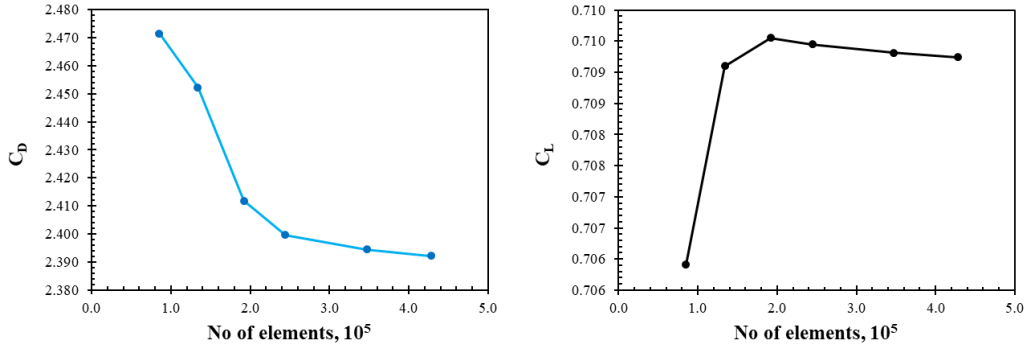


Fig. 2 Mesh independence study with C_L^\ddagger and C_D for all meshes

Fine mesh is chosen to conduct all simulations on since the percentage differences between *Fine* and *Fine 2* for both C_L and C_D are sufficiently small. However, computational resources needed to simulate a mesh with almost 79000 more elements would be much higher. For turbulent analysis, the same number of mesh elements have been used; however, the mesh bias around REV is modified to capture boundary layer effects. The first cell height is calculated to be 3.15×10^{-7} m using an online Pointwise calculator [9] for wall y_+ value of 1.

IV. Results

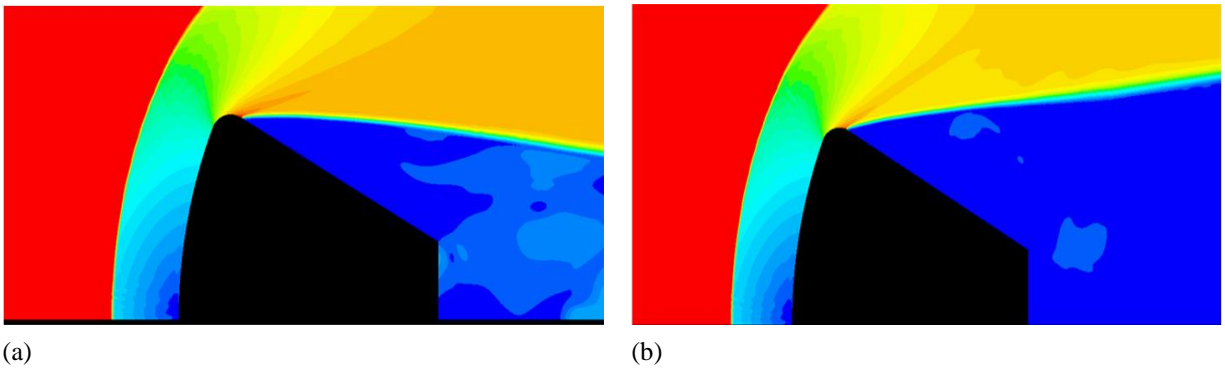


Fig. 3 Comparison of near body velocity contours for BC sensitivity analysis; (a) Freestream BC on top wall, (b) Symmetry plane BC on top wall

\ddagger Note that all C_L values have been multiplied by -1 to keep the C_L axis in +ve range

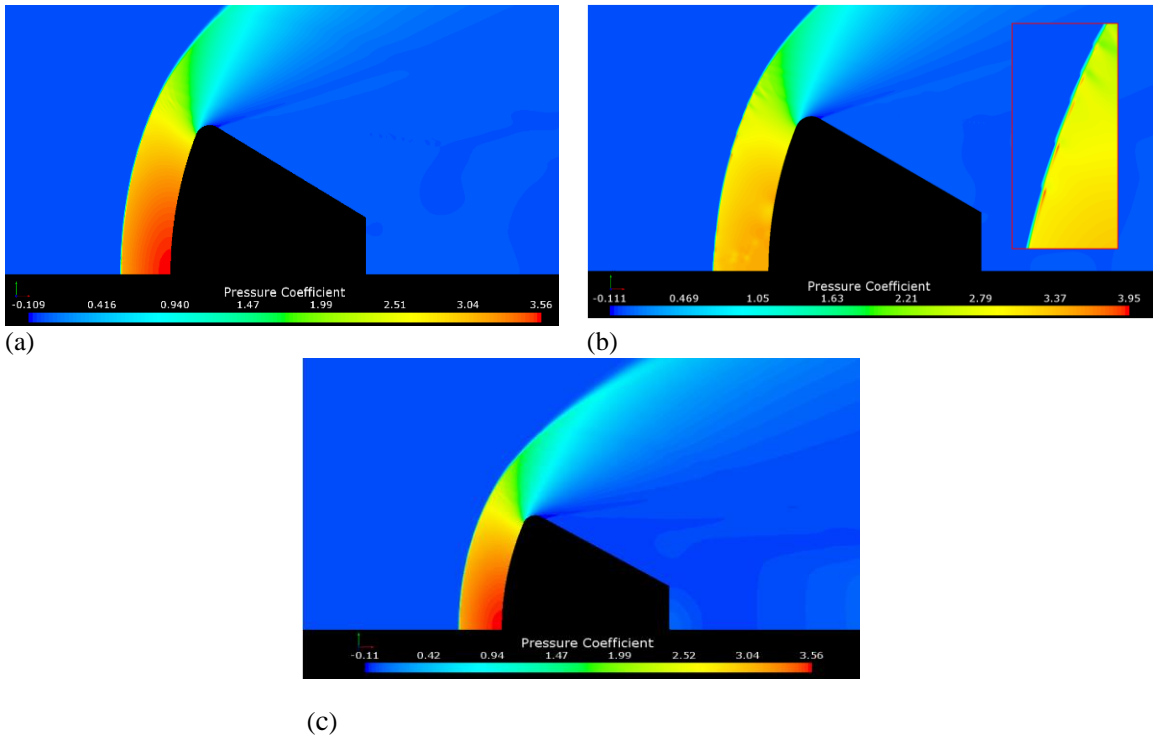


Fig. 4 C_p contours around REV body using (a) AUSM+ FVS scheme, (b) Roe-FDS scheme, and (c) $k - \omega$ SST model

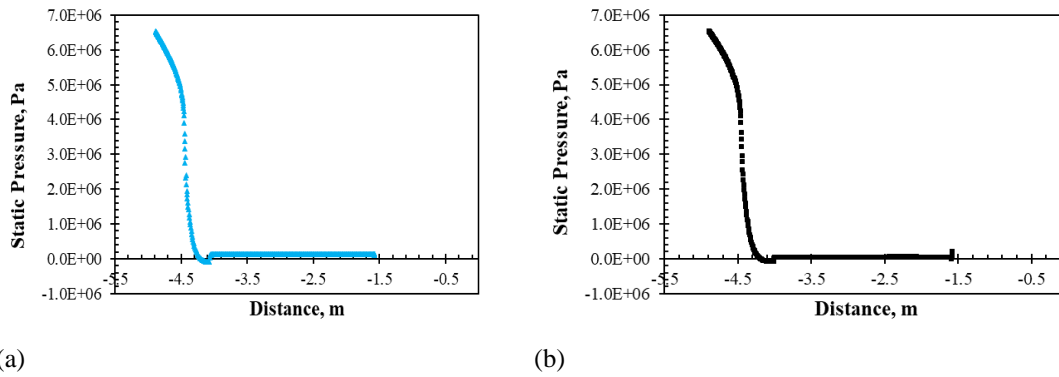


Fig. 5 Static pressure distribution over the REV body; (a) inviscid and (b) viscous regimes

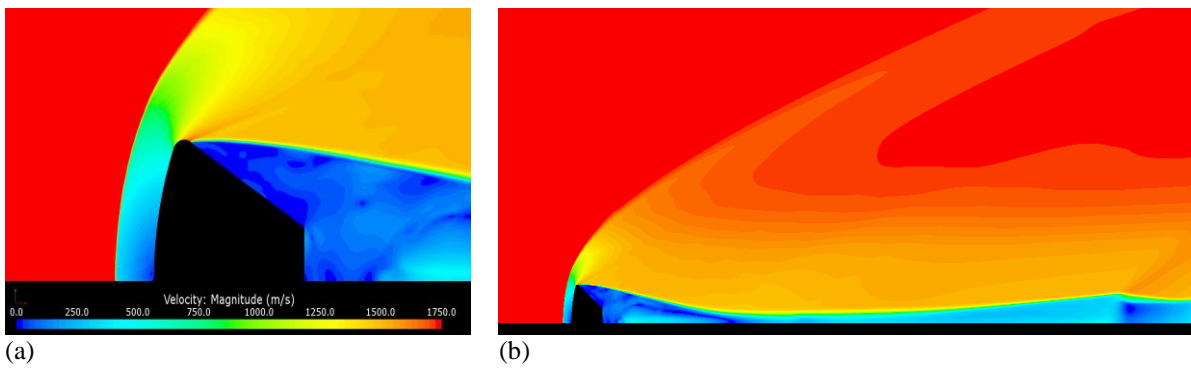


Fig. 6 Inviscid velocity magnitude contours using AUSM FVS scheme

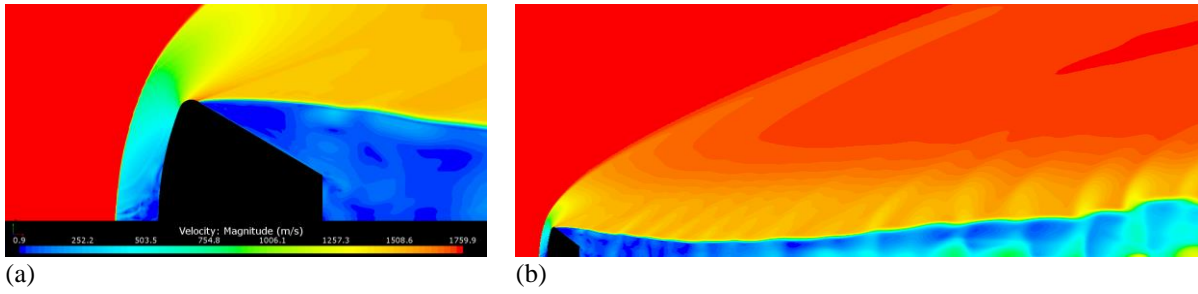


Fig. 7 Inviscid velocity magnitude contours using Roe-FDS scheme

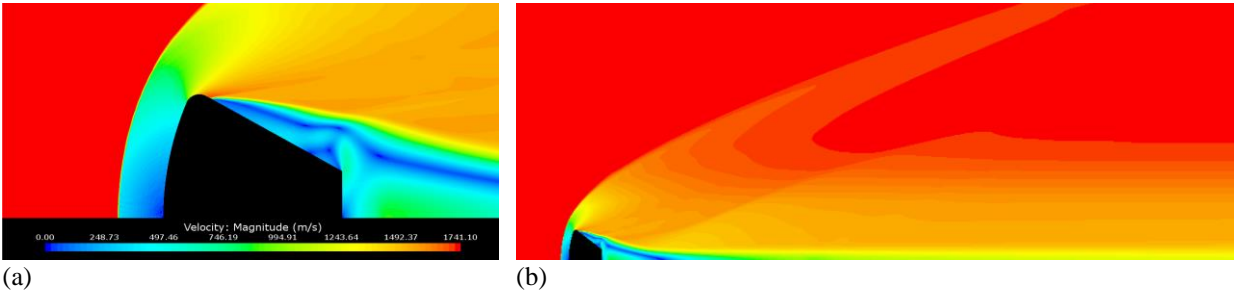


Fig. 8 Viscous velocity magnitude contours using $k - \omega$ SST model

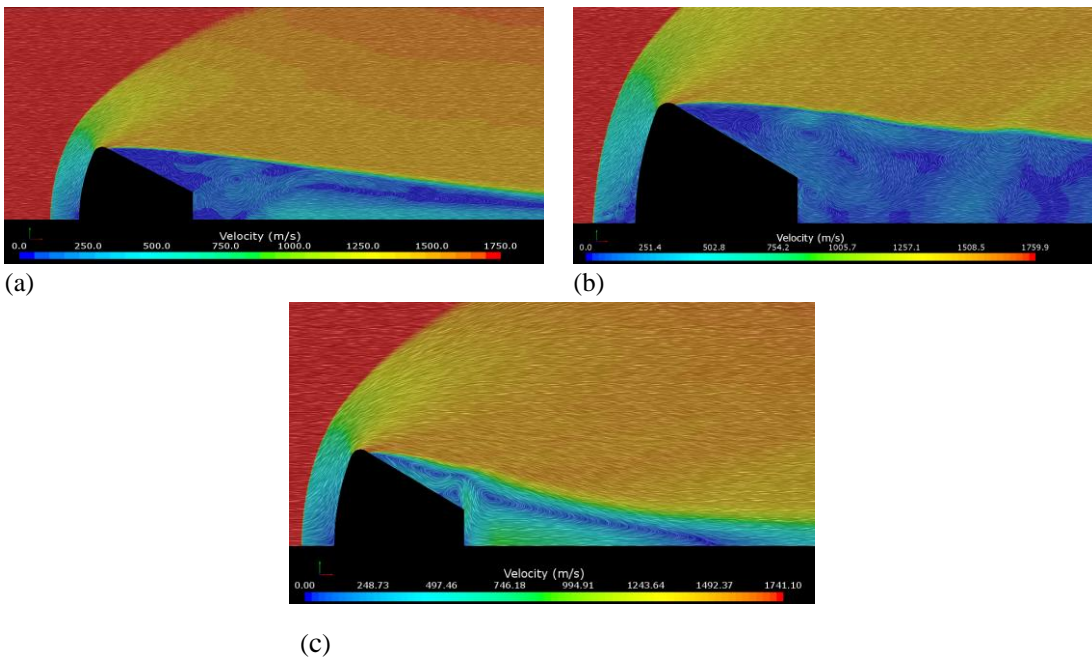


Fig. 9 Velocity vectors around REV body; (a) AUSM FVS scheme, (b) Roe-FDS scheme, (c) $k - \omega$ SST model

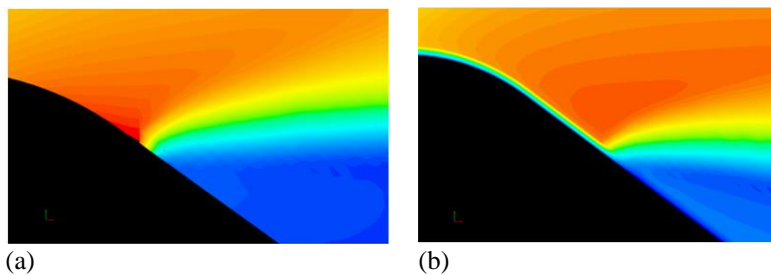


Fig. 10 Flow separation point using velocity magnitude contours; (a) inviscid and (b) viscous regimes

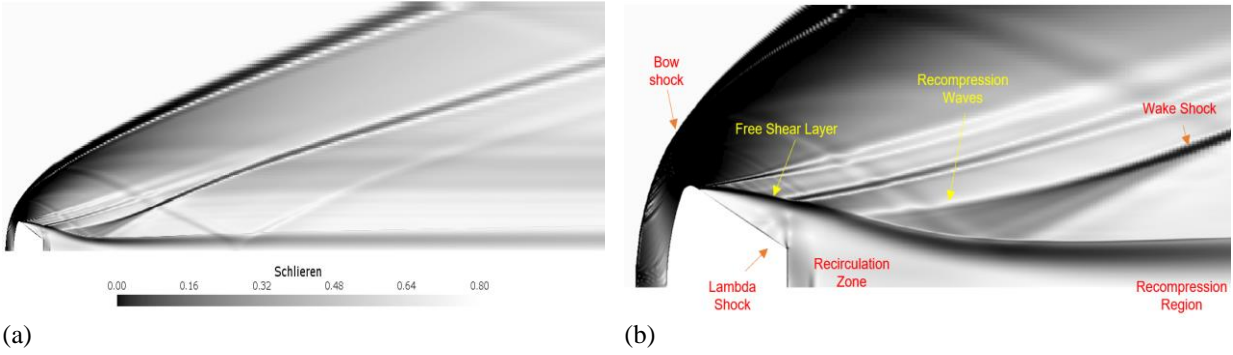


Fig. 11 Numerical Schlieren for flow field obtained using $k - \omega$ SST model

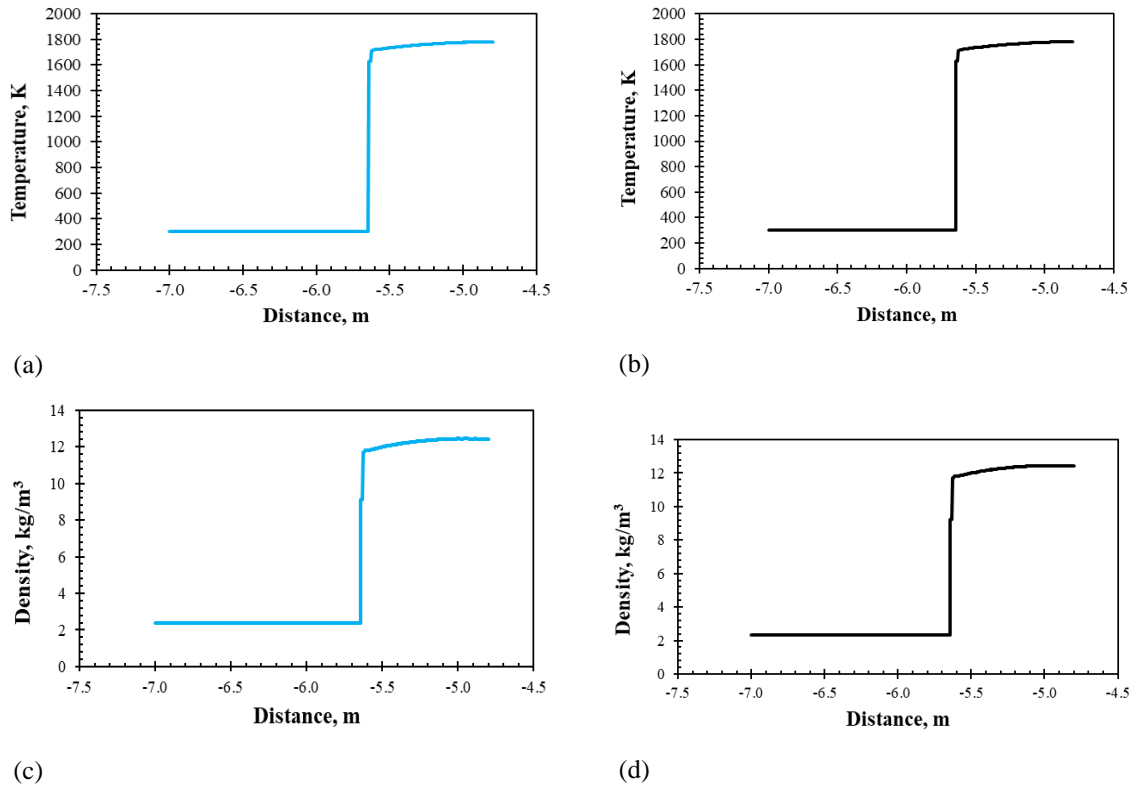


Fig. 12 Temperature gradient in (a) inviscid and (b) viscous regimes; Density gradient in (c) inviscid and (d) viscous regimes; across front bow shock wave

Table 7 Parameters used for validation of CFD results

	Theoretical	CFD
M_1	5	5.06
P_1 , MPa	0.101325	0.101325
ρ_1 , kg/m^3	1.225	2.353
P_{01} , MPa	53.61	53.61
P_{02} , MPa	3.31	3.56
P_{02}/P_{01}	0.062	0.066
ρ_2/ρ_1	5.00	5.02
T_2/T_1	5.80	5.73

V. Discussion

BC sensitivity analysis is carried out to determine the correct BCs to impose (see Table 3). BC1 and BC2 encounter floating point errors around 50,000 and 52,000 iterations whereas BC3 performs similarly in the near body region, as shown in Fig. 3, to Freestream settings given in Table 2. Velocity inlet BC (BC1 and BC2) only defines the directional velocity magnitude and static temperature of the incoming flow. For solving equations of incompressible flows to which the governing equations would converge at $\text{Mach} \ll 0.3$ this information is enough. However, as compressibility effects begin to take place at higher velocities, pressure must also be defined. Imposing symmetry plane BC on top wall extrapolates the 'outside' fluid quantities from adjacent cells while reducing the normal component to 0. Hence, freestream BC is imposed on the inlet, top and outlet boundaries.

Figure 4 compares the C_p contours from inviscid and viscous simulations. A thin shock layer, one of the main characteristics of hypersonic flow, can be observed ahead of the REV. This indicates the presence of a strong shock, causing rapid density increase, leading to reduced volume in accordance with conservation of mass. This also means that the bow shock angle is almost same as that of REV forebody. Between AUSM FVS and Roe-FDS, latter fails to capture the bow shock and pressure gradients after the shock accurately. As shown in Fig. 4(b) inset, Roe-FDS introduces saw-toothed patterns on the bow shock. In terms of pressure gradients aft shock, unlike Roe-FDS, AUSM FVS captures smooth, rapid increase in pressure as expected with a clear stagnation point at the mid-tip of REV at centerline. Further, Roe-FDS also introduces spurious spots within the thin shock layer. C_p profiles produced by both AUSM FVS and $k-\omega$ SST model have no discernable difference. This is further confirmed from Fig. 5 where, as expected, introduction of viscosity has not impacted the static pressure distribution over the REV body.

Velocity magnitude contours in the vicinity of REV body in Fig. 6 and Fig. 7 show formation of rapid expansion fans over REV shoulder as flow begins to turn around the convex corner for inviscid setup. This is followed by flow separation from REV body leading to eddies underneath and high-speed flow above (see Fig. 9(a) and Fig. 9(b)). For same flow conditions and number of contours, AUSM FVS clearly resolves the flow feature with higher sensitivity. Since parts Fig. 6(a) and for Fig. 7(a) contain solution to inviscid setup, the flow separation is caused due to non-physical CFD artifact; numerical viscosity arising due to discretization of numerical schemes. Compared to AUSM FVS, Roe-FDS is further producing spurious artifacts in the thin shock layer as well as throughout the far wake region (see Fig. 7(b)). Comparing the inviscid (AUSM FVS) velocity profiles with viscous velocity profiles (see Fig. 8(a)), both setups show similar distributions ahead of the REV body. However, formation of boundary layer can be seen impact of which magnifies as the flow reaches the shoulder (see Fig. 10). The separation point has moved further downstream compared to inviscid flow. This is because the effects of shear forces are now included in the flow. After the separation point, a complex flow region is captured by the $k-\omega$ SST model.

The effect of viscosity in the wake can be observed in Fig. 11. A weak lambda shock due to viscous effects seem to be present near the trailing edge of the REV. Recompression waves are created at the free shear layer which eventually form into trailing shock. Weak shock reflections also seem to be present before recompression waves and on top of free shear layer. The flow around the lambda shock is highly rotational and can be observed in Fig. 9(c). In the same figure, rear stagnation point is also seen labelled as 1. This stagnation point forms a division between recirculation region to its left and recompression region to its right. The difference due to viscosity can also be made with respect to the angle that the free shear layer makes with the aft-REV body (see Fig. 9).

Figure 12 contains density and temperature gradients across the bow shock captured by inviscid and viscous setups. The horizontal axis refers to the location of REV forebody on the computational domain with respect to the origin. As the Mach number increases, the strength of bow shock needs to increase as well to bring hypersonic flow down to the subsonic regime. This results in a sudden and significant increase in temperature and density across the shock wave. In line with the theory, both setups capture this significant increment and do so with exact same magnitudes.

Table 7 compares the theoretical and experimental ratios of stagnation pressure, density, and temperature across the bow shock wave for validation of results. Theoretical values have been calculated using the 2D shock relations, whereas experimental values have been taken from simulated results. All three experimental ratios show excellent proximity to theoretical values.

VI. Conclusion

Successful simulations were carried out in capturing aerodynamic flow characteristics around a REV in hypersonic flow regime using Euler and RANS models. Roe-FDS scheme is found to be producing non-physical artefacts and hence unsuitable for high Mach number flows due to lack of robustness of Roe's differencing scheme. Although wake modelling with RANS model was generally in reasonable agreement with theoretical predictions, it did contain some erroneous predictions such as weak lambda shock and extra layer just underneath the free shear layer. Overall, this study has provided useful guidelines for performing engineering calculations of hypersonic flows around bluff bodies.

Features like the unattached bow shocks can be well simulated by an inviscid shock-capturing method while for capturing of wake effect downstream of the body RANS model based on AUSM scheme is recommended.

Acknowledgments

The author would like to extend profound gratitude towards Professor Sergey Karabasov for his excellent support and guidance. This research utilized Queen Mary's Apocrita HPC facility, supported by QMUL Research-IT <http://doi.org/10.5281/zenodo.438045>.

References

- [1] K. L. Bibb, E. L. Walker, G. J. Brauckmann and P. E. Robinson, "Development of the Orion Crew Module Static Aerodynamic Database, Part II: Supersonic/Subsonic," in *29th AIAA Applied Aerodynamics Conference*, Honolulu, 2011.
- [2] P. G. Cross and M. R. West, "Simulation of Hypersonic Flowfields Using Star-CCM+," China Lake, 2019.
- [3] Siemens PLM Software, "Coupled Flow Controls and General Setup Recommendations," Siemens, [Online]. Available: <file:///D:/14.06.013-R8/STAR-CCM+14.06.013-R8/doc/en/online/index.html#page/STARCCMP/GUID-72FFFC1E-AF81-4348-A010-D96D554C2763.html>. [Accessed June 2020].
- [4] Siemens PLM Software, "Finite Volume Discretization," Siemens, [Online]. Available: <file:///D:/14.06.013-R8/STAR-CCM+14.06.013-R8/doc/en/online/index.html#page/STARCCMP%2FGUID-A806D14C-6833-458E-89B7-8B273EE048B7.html>. [Accessed August 2020].
- [5] P. L. Roe, "Approximate Riemann Solvers, Parameter Vectors, and Difference Schemes," *Journal of Computational Physics*, vol. 43, pp. 357-372, 1981.
- [6] ChimeraCFD.com, "Roe Flux Differencing Scheme: The Approximate Riemann Problem," ChimeraCFD, 6 March 2010. [Online]. Available: <http://chimeracfd.com/programming/gryphon/fluxroe.html>. [Accessed September 2020].
- [7] M. Liou, "A sequel to AUSM: AUSM+," *Journal of Computational Physics*, vol. 129, no. 2, pp. 364-382, 1996.
- [8] G. Caminha, "The CFL Condition and How to Choose Your Timestep Size," Simscale, 17 October 2019. [Online]. Available: <https://www.simscale.com/blog/2017/08/cfl-condition/>. [Accessed August 2020].
- [9] Pointwise, "Compute Grid Spacing for a Given Y+," [Online]. Available: <https://www.pointwise.com/yplus/>. [Accessed September 2020].
- [10] LearnCAx, "CFD Meshing with ANSYS ICEM CFD," Centre of Computational Technologies Private Limited (CCTech), [Online]. Available: <https://www.learncax.com/class/cfd-meshing-with-ansys-icem-cfd-detail>. [Accessed June 2020].
- [11] ANSYS, Inc., "Pre Mesh Quality Options," Ansys, 2018. [Online]. Available: https://ansyshelp.ansys.com/account/secured?returnurl=/Views/Secured/corp/v192/icm_help/iblock_premeshqualityoptions.html. [Accessed June 2020].
- [12] ANSYS, "4.5.2 Shear-Stress Transport (SST) k-w Model," ANSYS, 23 January 2009. [Online]. Available: <https://www.afs.enea.it/project/neptunius/docs/fluent/html/th/node67.htm>. [Accessed September 2020].
- [13] Siemens PLM Software, "Coupled Flow Solver," Siemens, [Online]. Available: <file:///D:/14.06.013-R8/STAR-CCM+14.06.013-R8/doc/en/online/index.html#page/STARCCMP%2FGUID-BBC28794-4C63-429F-BB47-8C1866AA13DF.html%23wwID0ELKR1C>. [Accessed July 2020].
- [14] Simcentre STAR-CCM+, "Modeling hypersonic cases in STAR-CCM+ (Mach >10)," Siemens, 12 February 2018. [Online]. Available: https://support.sw.siemens.com/knowledge-base/KB000020896_EN_US. [Accessed July 2020].
- [15] Siemens PLM Software, "Setting Convergence Accelerators," Siemens, [Online]. Available: <file:///D:/14.06.013-R8/STAR-CCM+14.06.013-R8/doc/en/online/index.html#page/STARCCMP/GUID-ADEC93AE-B9FC-4C56-9996-5411D3E22F28.html#wwID0ECAIHB>. [Accessed July 2020].

Computational Modelling of Imperfectly Expanded Supersonic Jets

Akash Kini^{*}

School of Engineering and Material Science, Queen Mary University of London, Mile End Road, London, E14NS, United Kingdom

Underexpanded jets have been the subject of keen investigation in aerodynamics and aeroacoustics. The complex flow patterns that take place in Underexpanded jets are still not completely understood. One of the measures taken in this respect is to analyze the problem using computational fluid dynamics. This paper aims at investigating the effects of various CFD parameters on the jet flow, such as boundary conditions and turbulence modeling, using ANSYS Fluent package. Mass flow inlet and pressure inlet boundary conditions were imposed at the inlet of the supersonic nozzle whereas pressure far field and pressure outlet conditions were imposed on the outlet of the computational domain. The combination of pressure inlet at the inflow region, pressure outlet at outflow region, and pressure far field conditions at the top and side of the domain showed the best results. The simulations were carried out using 5 turbulence models: standard k epsilon, realizable k-epsilon, standard k-omega, k-omega SST, and Reynolds Shear. It was found that the k omega SST model performed the best in capturing the flow physics of the jet. The scope of using the Reynolds Shear model must further be investigated before making final remarks on its appropriateness.

I. Nomenclature

D_j	=	nozzle diameter
M_{fe}	=	fully expanded Mach number
NPR	=	Nozzle Pressure Ratio
TTR	=	Total temperature Ratio
P_∞	=	Ambient Pressure
P_0	=	stagnation pressure
U_j	=	jet velocity at the nozzle throat
T_0	=	stagnation temperature
T_∞	=	ambient temperature
κ	=	turbulent kinetic energy

II. Introduction

The performance and success of a nozzle can only be determined by how much one can predict the behaviour of the processes that are to take place. One such important aspect is the shock produced when the flow is imperfectly expanded. This occurs when the nozzle pressure at the exit and the back pressure acting on the nozzle is different. In the case of underexpansion, there is a series of expansion fans and compression waves that equalize the pressure at the exit to the back/ambient pressure. This continuous process forms quasi-periodic shock cells inside the shear layer. This Paper will focus on computational modelling of these jets to examine shocks cells and compare the results to other findings.

The importance of studying the imperfect expansion of jets applies in many engineering aspects such as aircraft design, screech noise reduction in civilian aircraft, etc. [1]. The aeroacoustics behavior can be predicted by studying the noise generated in the jet however the sources of these noises occur in different regions of the exhaust flow and

^{*} Master of Science, School of Engineering and Material Science, AIAA Student Member

must be studied individually. This calls for a focused area of importance that can be brought upon by computational modelling as, if modelled correctly, there is the flexibility of resolving the flow differently at different places.

A complete description of the facility and the PIV system can be found in [2]. A strongly under-expanded jet case corresponding to $\text{NPR} = 4.2$ and $M_{je} = 1.59$ from the LTRAC experiment [2] is simulated on Ansys Fluent. The obtained results are compared with existing RANS simulations and experimental PIV data.

III. CFD Setup

A. Geometry and Mesh Generation

The geometry and design of the nozzle are shown in Figure 1a. A $60D_j$ (axial direction) by $20D_j$ (transverse direction) domain is made considering the setup used in the paper [3]. Due to continuous limitation in the simulation caused by flow reversal affecting the jet formation, the referred domain size was modified to a square domain. The new domain was extended $100 D_j$ in both the axial and transverse dimensions as shown in Figure 1b. A domain/boundary condition sensitivity check is conducted to ensure that the reversed flow limitation occurring does not affect the results obtained in the area of interest (near nozzle exit). The area before the converging section of the nozzle is extended upstream to ensure stability.

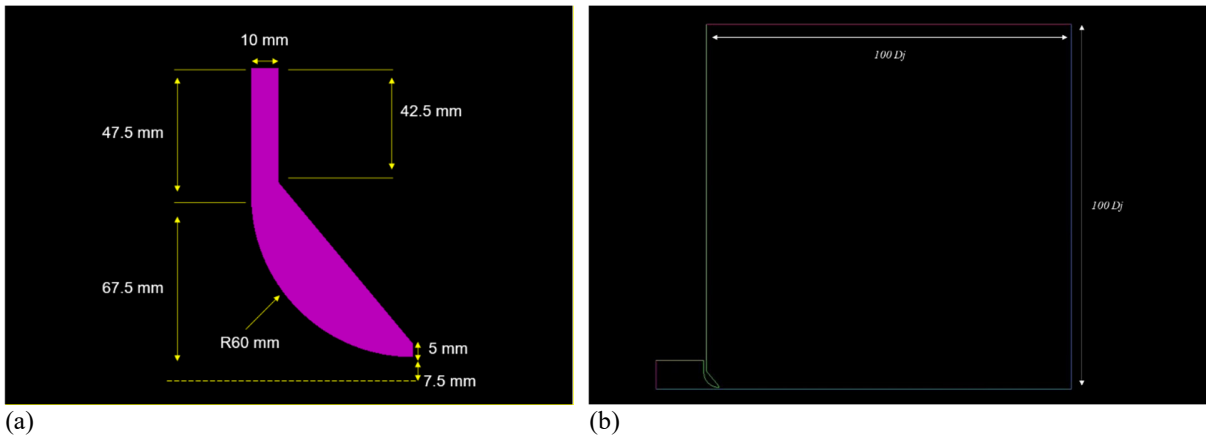


Fig. 1 Nozzle geometry with dimensions (a), computational domain (b)

A domain to boundary condition sensitivity check is performed to ensure that changes in the domain size would not affect the solution obtained. First, a solution is obtained for the square mesh in which the jet formed agrees with the theoretical understanding of the process. Then a larger domain ($200D_j$ to $100D_j$) with the same number of cells is made by expanding the mesh in the radial direction. It is found that there is a negligible difference in the values obtained by both cases. This shows that the square mesh can be considered as accurate enough to conduct the simulations on and be used as the basis for further study.

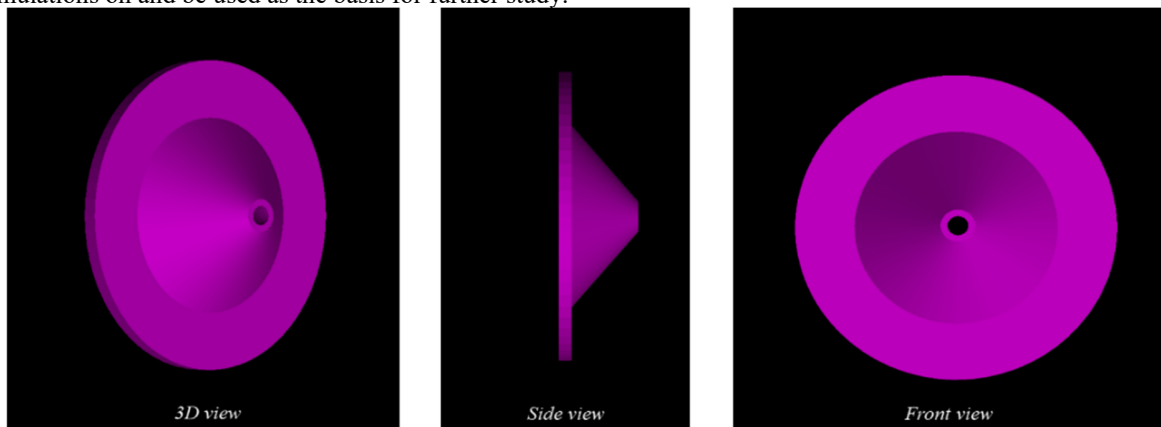


Fig. 2 Different View of nozzle geometry

ICEM CFD software is used to generate the mesh as it allows for more flexible options to concentrate the mesh in the area of interest. The mesh contains $210 * 10^3$ cells and is concentrated streamwise from the nozzle lip to obtain a well resolved shear layer. The aspect ratio of the cells within the area of interest is maintained at 1 but increases thereafter away from the region of interest. The lowest grid spacing in both the axial and transverse direction is 0.0001m. The small size of the cell ensures that the flow is capture and well resolved. The skewness of the cells is kept above 0.8 throughout the mesh and the maximum angle between the cells are above 18° . All these aspects are necessary for establishing a good mesh for Fluent. Figure 3a shows the mesh on the whole domain, as the elements are concentrated at the nozzle. Figure 3b shows the mesh closer to the nozzle. Figure 4 shows the mesh at the nozzle lip and the area of interest.

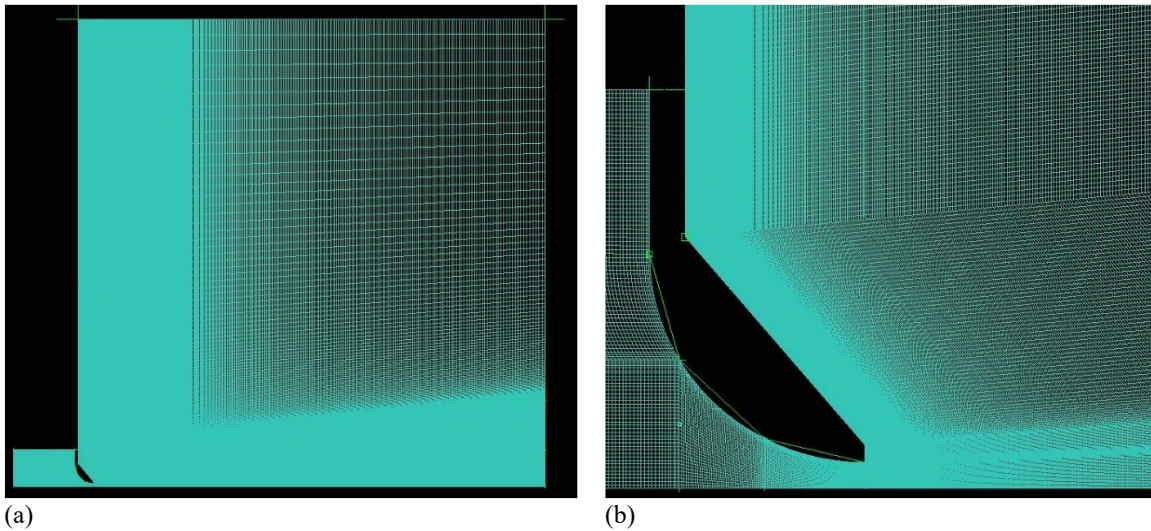


Fig. 3 Fine mesh of the full domain(a), Mesh closer to the nozzle(b)

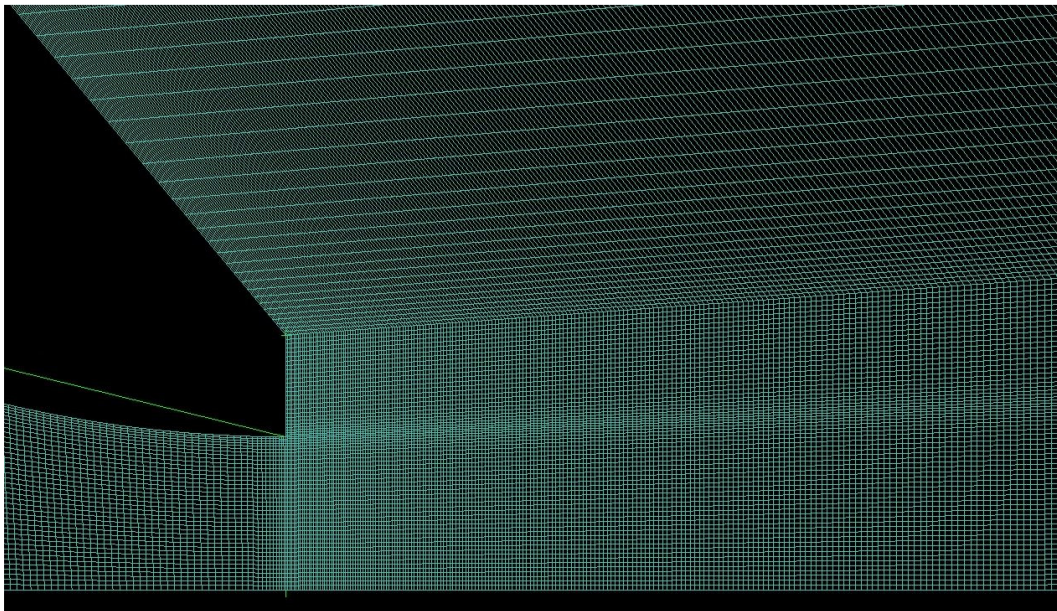


Fig. 4 Mesh at the area of interest

A mesh independence study is done based on the velocity profile captured in the first 3 shock cell by the mesh compared to the solution obtained from the RANS solution in paper [3]. Mesh 1 underpredicted the velocity of the

flow after the shock and the area of shock was not resolved correctly. Mesh 2 and 3 compared well compared to the RANS solution obtained from the literature. Mesh 2 was used as the primary mesh for all the simulations as it gave the best result for the least computational effort.

B. Boundary Conditions

The boundary conditions used for the simulations are shown in Figure 5. The figure is not up to the scale of the original domain used. The boundary conditions include an inlet boundary condition at the inflow region, outlet pressure condition downstream for the jet outflow, axis boundary condition at the bottom wall and freestream boundary conditions at the other parts of the domain, i.e. top and side.

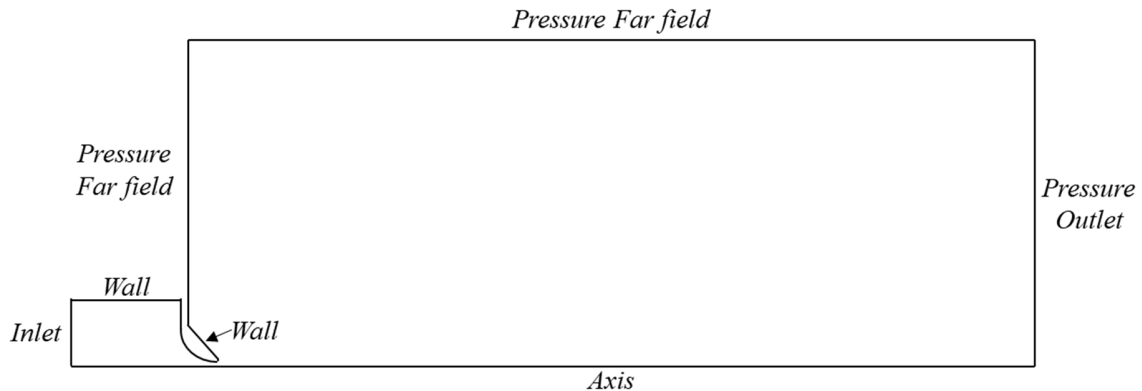


Fig. 5 Domain Boundary Conditions

A pressure inlet boundary condition is applied at the inflow region where the stagnation pressure and temperature, obtained by the NPR and the TTR, is defined. Wall boundary conditions are used for the top wall extending from the inlet to the converging section of the nozzle, and the body of the nozzle as shown in Figure. No slip conditions are applied throughout the wall conditions. An axis boundary condition is applied to the bottom wall of the domain because of the axisymmetric nature of the nozzle geometry. The top and side wall of the domain use a pressure far-field boundary condition. Ambient pressure, ambient temperature and free stream Mach number are defined as per the simulation requirements. A very low free stream Mach number, 0.0003, is defined to ensure the stability of the solution [4]. A pressure outlet boundary condition is used at the right end of the domain. Only the back pressure, equal to the ambient pressure, is required to be defined at the outlet. The operating pressure is set to zero from its default setting as there is no need for roundoff error corrections for high speed compressible flows. All the inputs for pressure are in terms of absolute pressure.

C. Fluent Setup

Ansys Fluent software is used to conduct the simulations for this research. Ansys Fluent numerically solves the Navier-Stokes equations by converting them into algebraic equations using a control volume-based technique [5]. Density-based solver is used as the flow is compressible and supersonic. As the nozzle being simulated is symmetric about the center line, axisymmetric conditions are used. To ensure stability in solution, Transient formulation is implemented.

Simulations are carried out for inviscid and different RANS turbulence models. Inviscid model is used to study the formation of the jet neglecting viscosity. The presence of a very thin shear layer is obtained when using the inviscid model. The inviscid model was used to get a primary understanding of the solution as its simulation are quick. ANSYS Fluent computes this model by solving the Euler equations in which the momentum and energy equations are simplified with the absence of viscosity.

Reynolds Averaged Navier Stokes (RANS) turbulence model is used in this simulation because it is computationally cheap when compared to other methods like Large Eddy Simulations or Direct Numerical Simulation, and has fast return time [6]. Standard k epsilon, realizable k-epsilon, standard k-omega, k-omega SST, and Reynolds Shear turbulence models are studied. As the shear layer formed by using the different turbulent models affect the formation of the shock cell and Mach disk, mean axial velocity along the centerline is considered for comparison. The turbulent dissipation rate along the lip line is also used for comparison as it is used for acoustic modelling of jets.

The fluid is setup as Ideal gas air model to consider compressibility effects in supersonic flow. Implicit formulation is used for both spatial and temporal discretization. Advection Upstream Splitting Method (AUSM) type convective flux scheme is used for this simulation since it performs better at resolving contact and shock discontinuities. Least Squares Cell-Based Gradient Evaluation method is used to compute gradients. A Second-order upwind scheme is used to solve flow and other transport equations from the turbulence model, i.e. turbulent kinetic energy, and the specific dissipation rate equations. The second-order upwind scheme provides more accuracy and stability than the first-order scheme. First-order implicit scheme is used in time as its unconditionally stable with respect to time step size. Both Standard and Hybrid Initialization methods are used for solution initializing. As Hybrid initialization shows less stability and accuracy, standard initialization method is used for the simulations.

All values are computed from the inlet. The Maximum inner iteration is set to 50. As the simulation includes compressible high-speed flow, more iterations are needed to achieve timestep convergence. Having a lower number of iterations reduces convergence stability of the residuals. Convergence criteria is set to 10^{-4} for all equations but due to flow reversal limitation occurring at intervals of time steps the solution fails to converge. Regardless, the flow is studied for local convergence as the residuals seem to stagnate at same values every time step. All simulations are run until this criterion is established. This local convergence is achieved as the flow reversal does not affect the solution of the jet which can be seen by conducting the domain – BC sensitivity check.

IV. Results and Discussion

Figure 6a shows the axial velocity fields of the jet. It is seen that the RANS simulations predict the flow structure nicely as it contains features of heavily Underexpanded jets as discussed in the literature. The quasi-periodic shock cells are seen in the core of the jet. The interaction with the shear layer and the formation of the jet core is also very evident. A relatively long Mach disk is present at the center of the first shock cell as the high and low velocity regions between the Mach disk are clearly seen. There is a formation of an internal shear layer after the Mach disk as expected from the literature. Shock-turbulence interaction is generated inside this internal shear layer. Fig 6b, c and d show the transverse velocity, pressure and temperature contours of the jet. The results of these contours show the formation of flow structures such as shock, Mach disk and the internal shear layer and are hence well resolved.

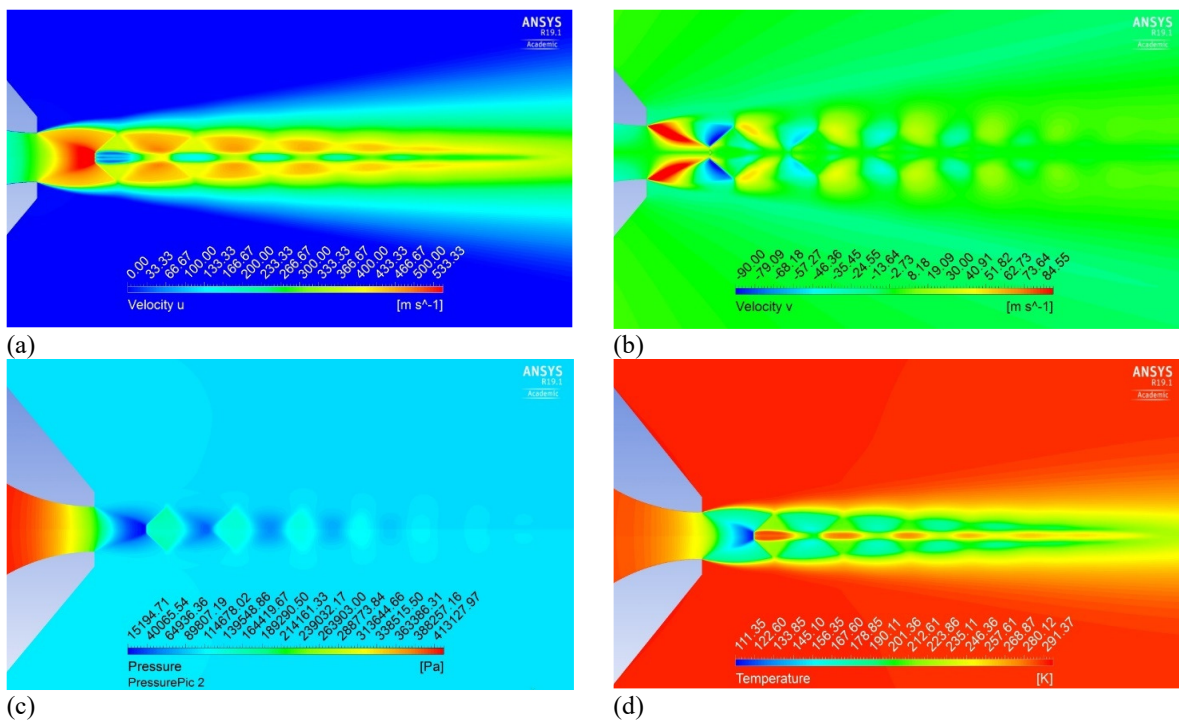


Fig. 6 Axial velocity contour of the jet (a), Radial velocity contour of the jet (b), Pressure contour in the jet (c), Temperature contour of jet (d)

The mean axial flow velocity for the experimental PIV data [7], the RANS literature results [3] and the RANS simulation results from this thesis are shown in Fig 7. It is seen that the RANS simulation shows an acceptable agreement with the PIV data. The first 2 shock cells of the PIV data are predicted well by the RANS simulation after which even though the simulation follows the trend of the mean axial velocity, it fails to accurately predict the experimental solution. The main RANS solution completely follows the trend of the RANS result obtained from literature and is accurate upto 4 shock cells. The results obtained indicate that the RANS solution is well resolved at the jet centre line.

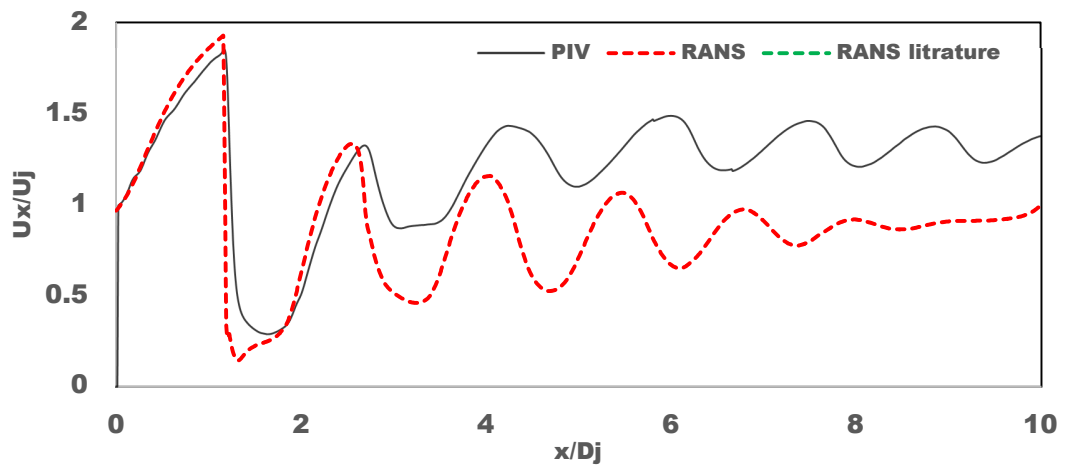


Fig. 7 Mean axial velocity at the center line of the RANS solution, experimental results, and results from literature

Figure 8 shows the mean axial flow velocity of the experimental PIV data, the RANS literature results, and the RANS simulation at the nozzle lip line. The solution of the RANS simulations compares nicely with both the literature and the experimental data. It is seen that the solution accurately predicts the velocity for the initial shock cell after which it slightly underpredicts the velocity of the flow. This could be due to a requirement of more refinement of the mesh at the lip line. It could also be caused due to error in the initial value of the turbulence model.

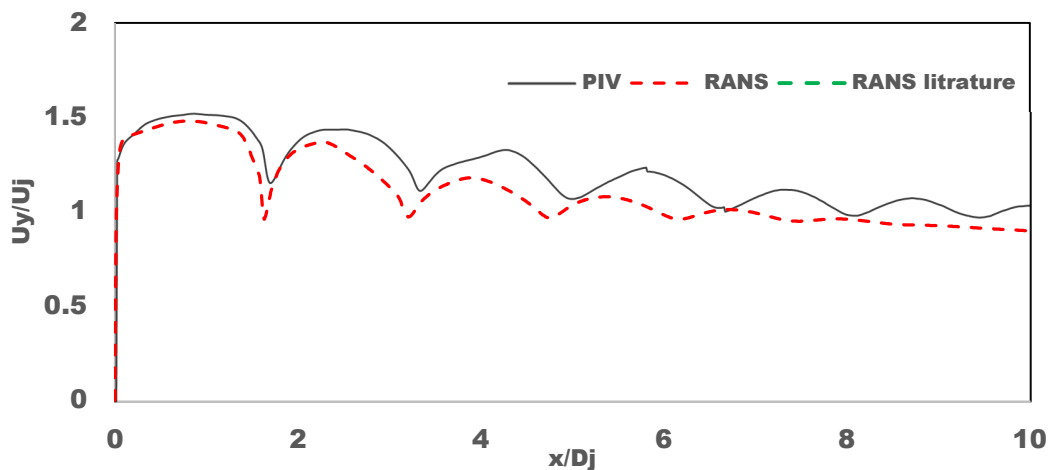


Fig. 8 Mean axial velocity at the lip line of the RANS solution, experimental results, and results from literature

Mean pressure distribution at the center line of the RANS literature results and the RANS simulation is shown in Fig 9. It is seen that the shock pressure along the centre line is in reasonable agreement with the solution from the literature.

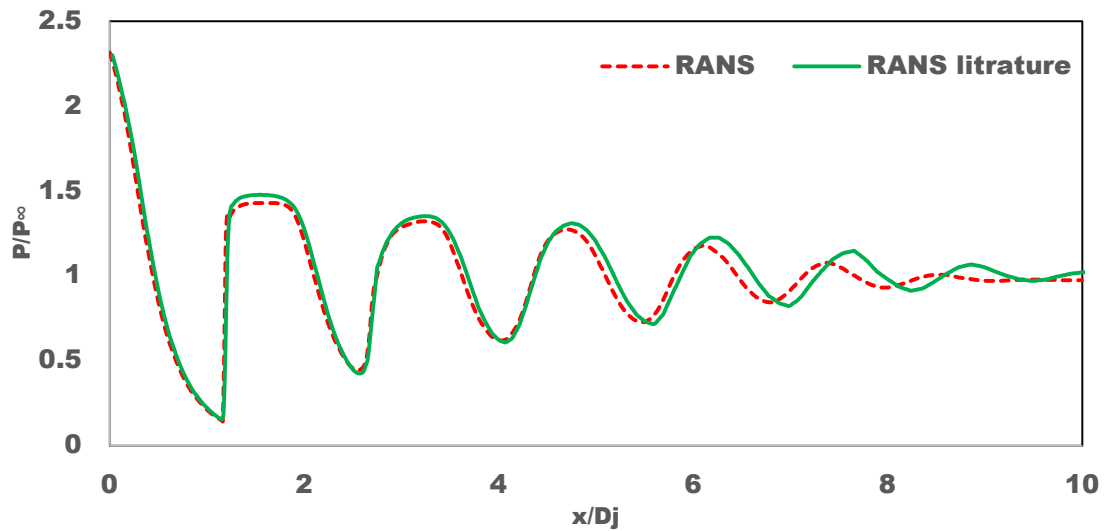


Fig. 9 shock pressure along the center line of the RANS solution, experimental results, and results from literature

The mean turbulent kinetic energy of the RANS literature results and the RANS simulation at the nozzle lip line is shown in Fig 10. The RANS solutions reasonably predict the TKE obtained by the literature for $x/D < 2$ above which it overpredicts the solution. It is seen that the solution match the trend entirely but scales the value by an amount. This could be caused by the initial condition of the $k - \omega$ SST model set up.

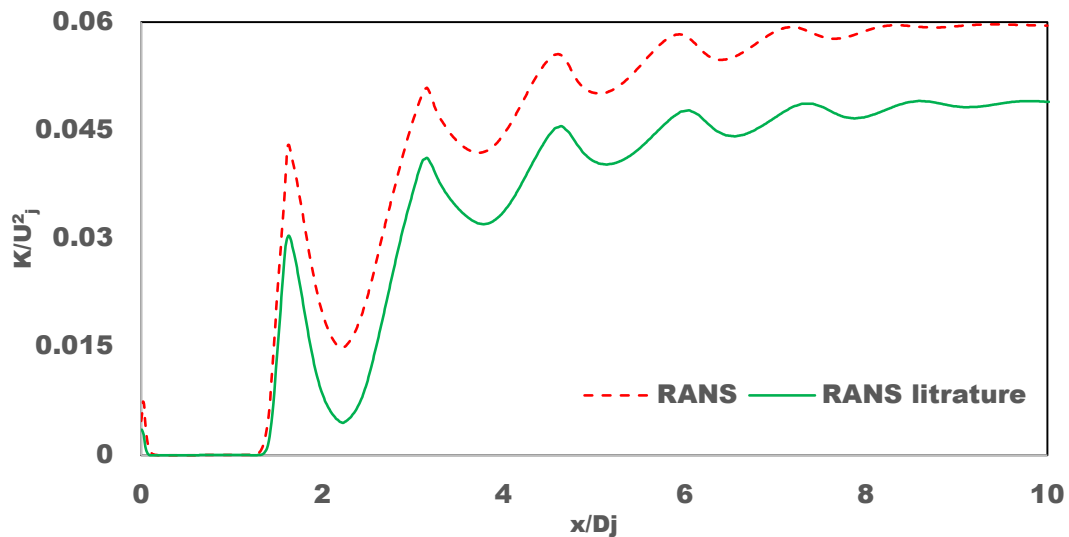


Fig. 10 Mean Turbulent kinetic energy at the lip line of the RANS simulation and the results from the literature

Figure 11 shows the mean axial flow velocity at the center line for the five different turbulence models used. It is evidently seen that the $k - \epsilon$ model fails to predict the flow as it does not contain the contribution of a strong shock in its flow. The trend throughout the jet is supersonic and only has sonic region at the nozzle exit. It is also seen the amplitude of the velocity after the shocks are smaller when compared to other models. This is caused as the shear layer is larger and decays the shock cells quicker because the $k - \epsilon$ model considers the flow as fully turbulent.

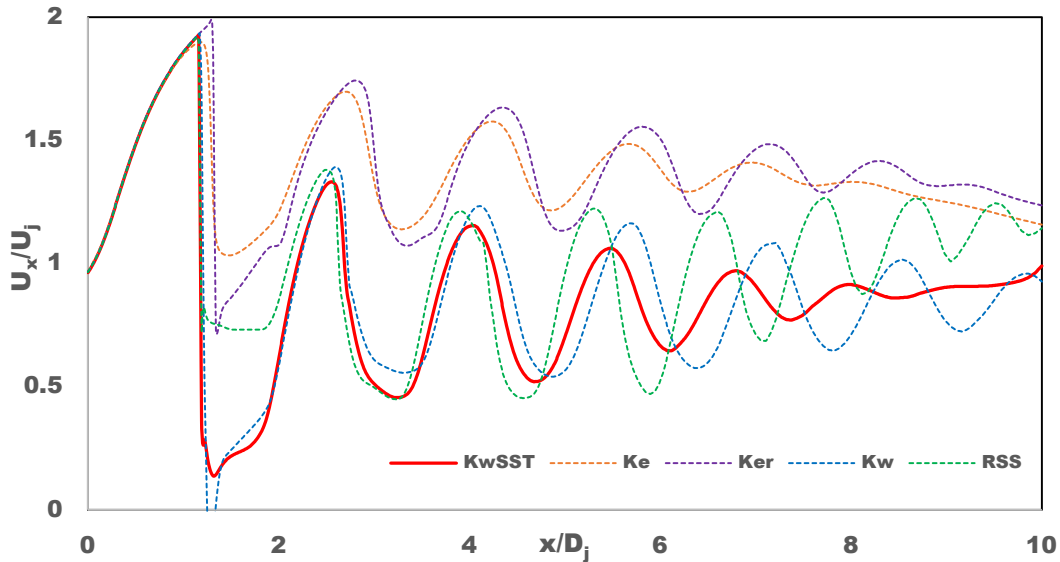


Fig. 11 Mean axial velocity at the center line using different turbulence models

Similar to the $k - \epsilon$ model the realizable $k - \epsilon$ model also fails to predict the flow accurately as large variations are seen from the true solution. It is seen that there exists a Mach disk in the solution as there is a significant drop in the velocity across the first shock cell. As this is not seen in the velocity contour this Mach disk must be small of a few computational cell sizes. Along the center line, the realizable $k - \epsilon$ model overpredicts the solution but follows the trend of the true solution.

The $k - \omega$ model shows most accuracy to the true solution in the first 3 shock cells as seen from Fig 11. An interesting point to note with the $k - \omega$ model is that it predicts a very strong shock across the first shock cell. The solution is predicted to have reversed flow inside the internal shear layer immediately after the Mach disk. This is could be the vortices formed inside the shear layer as discussed in the literature. The accuracy is only true for the first 3 shock cells after which the flow is still relatively fast compared to the true solution because of a thinner shear layer.

The Reynolds shear stress turbulence model shows an acceptable agreement with the true solution for $x/D_j < 5$. The model predicts the existence of strong shock and therefore the formation of the Mach disk. The first 3 shock cells are predicted well after which the model predicts the formation of an additional shock wave at $x/D_j > 8$. Theoretically, this model is supposed to be most accurate as it ignores the isotropic eddy viscosity hypothesis. However, due to close coupling of equations, it is much tougher to converge. Overall, the results show a possible use of this model as it has a reasonable agreement with the true solution in the first three shock cells.

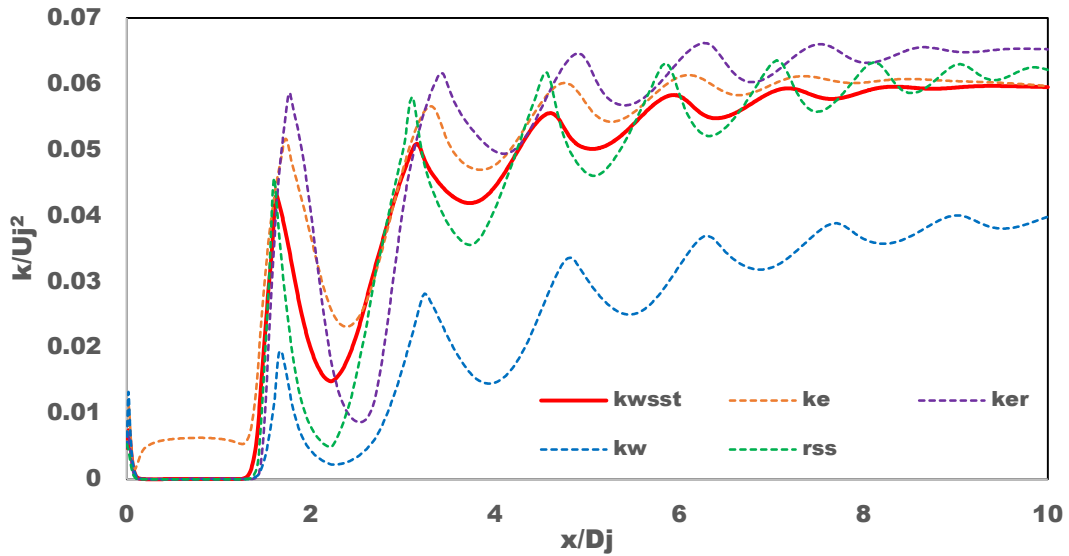


Fig. 12 Mean TKE at the lip line using different turbulence models

Figure 12 shows the mean TKE at the nozzle lip line of the turbulence model used in this thesis. The $k - \epsilon$ model shows a reasonable agreement with the true solution. It overpredicts the value of the mean TKE at the first few shock cells after which it follows the true solution closely. The realizable $k - \epsilon$ model seems to be inaccurate as it overpredicts the value from the true solution. The $k - \omega$ model also seems to be highly inaccurate in predicting mean TKE as it significantly underpredicts the value from the true solution. The Reynolds shear stress model shows sharp mean TKE gradients at every shock cell compared to the other models and the true solution. Overall, it predicts the true solution fairly well throughout the lip line.

V. Conclusion

SST $k - \omega$ model proved to be the most suitable turbulence model for the problem setup in this research. This is because of its superior performance around the shear layer which leads to a more accurate prediction of shock waves, Mach disk and the turbulence in the shear layer. $k - \epsilon$ model proved to be insufficient for this research due to weaker performance in flows with large pressure gradient. On the other hand, the suitability of the Reynold Stress model in problems such as this research needs further investigation. It remains to be seen whether the additional computational resources required, compensates for results with higher accuracy.

In addition to exploring Reynold Stress suitability in future, the results of this simulation can be built upon with incorporating acoustic modelling. The accuracy of the results could further be improved by implementing higher order discretization schemes and/or by using other turbulence models such as LES and DNS.

Acknowledgments

The Author would like to thank Professor Sergey Karabasov for his help, superb guidance, and outstanding support.

The Author would also like to thank Dr Tan and Professor Edgington-Mitchell for the access to the PIV data.

This research utilized Queen Mary's Apocrita HPC facility, supported by QMUL Research-IT <http://doi.org/10.5281/zenodo.438045>.

References

- [1] B. Emami, M. Bussmann and H. N. Tran, "A mean flow field solution to a moderately under/over-expanded turbulent supersonic jet," *Comptes Rendus Mecanique*, vol. 337, pp. 185-191, 2009.
- [2] D. E. Mitchell, K. Obereleithner, D. R. Honnery and J. Soria, "Coherent structure and sound production in the helical mode of a screeching axisymmetric jet," *Journal of Fluid Mechanics*, vol. 748, p. 822–847, 2014.
- [3] S. Karabasov, A. Kalyan, V. Gryazev and S. N. Gurbatov, "When is Nonlinear Sound Propagation Important for Broad Band Shock Associated Noise?," in *AIAA AVIATION Forum and Exposition 2020*, 2020.
- [4] S. A. E. Miller , J. Veltin, P. J. Morris and D. K. McLaughlin, "Assessment of Computational Fluid Dynamics for Supersonic Shock Containing Jets," *AIAA JOURNAL*, vol. 47, no. 11, pp. 2738-2746, 2009.
- [5] ANSYS , "ANSYS FLUENT 12.0 Theory Guide," ANSYS, [Online]. Available: https://www.afs.enea.it/project/neptunius/docs/fluent/html/th/main_pre.htm. [Accessed 30 10 2020].
- [6] A. Kalyan, "Theoretical modelling of broadband shock-associated noise in supersonic jets," 2018.
- [7] D. J. Tan, A. Kalyan, V. Gryazev, A. P. Markesteijn and S. A. Karabasov, "Supersonic Axisymmetric Jet Noise," 2016.

Filename: Paper for AIAA
Directory: C:\Users\Akash\Desktop
Template: C:\Users\Akash\Desktop\Updated AIAA Meeting Papers
Template_02192019.dotx
Title: Preparation of Papers for AIAA Journals
Subject:
Author: Akash
Keywords: TP Template 2017
Comments:
Creation Date: 01-11-20 12:20:00
Change Number: 10
Last Saved On: 01-11-20 12:37:00
Last Saved By: Akash Kini
Total Editing Time: 21 Minutes
Last Printed On: 01-11-20 12:39:00
As of Last Complete Printing
Number of Pages: 10
Number of Words: 8,114 (approx.)
Number of Characters: 46,255 (approx.)

Effective Implementation of Microblowing Technique on Airfoils

Aideal Czar Zohary*

International Islamic University Malaysia, 50728 Kuala Lumpur, Malaysia

This paper demonstrates evidence through numerical investigation that a proper implementation of micro-blowing technique (MBT) on a S1223 airfoil improves its lift-to-drag ratio by 16.5%. A simple and effective CFD modelling of MBT on a Clark Y airfoil shows trends similar to published experimental data involving hot wire and wake pressure measurements. The Clark Y CFD results are also validated against XFOIL. MBT simulation results on the S1223 airfoil consist of the effect of varying blowing fraction and angle of attack on the L/D ratio. Our findings indicate that total drag reduction is heavily dependent in the manner in which MBT affects the pressure distribution around the airfoil. A proper selection of the region in which micro blowing is located will lead to a significant reduction in pressure drag. Drop in pressure drag reached nearly 30% across a range of angles of attack. It is concluded that the integration of properly located MBT in aft-loaded airfoils should produce significant improvement in their performance.

I. Introduction

Hwang pioneered the concept of micoblowing technique (MBT) and showed that more than 70% of skin friction drag in subsonic and 80% in supersonic flows were reduced on a flat plate [1]. In detailed experimental works later with a similar setup that of Hwang's, it was proven that a drag reduction of up to 90% is possible in subsonic flows [2]. The ability of this method to be successfully implemented depends greatly on the MBT skin. Hwang concluded that an altered skin can be considered fit for MBT when it contributes to only a maximum addition of 10% of the skin friction drag of a solid skin so that any contribution due to blowing will actually give significant reduction in the overall drag on a flat plate [1]. The term "micro" means that the blowing hole diameter is much smaller than the boundary layer thickness. Thus, the designated hole dimensions depend on the boundary layer characteristics. Physical parameters which outlined the necessary constraints of the skin were then determined [3]. An interesting review on a handful of research on the early developments of MBT can be seen in Ref. [4] which also mentioned the adverse effect of MBT on pressure drag.

Early numerical studies focused on the local effect of MBT, without taking into account its influence on the surrounding flow [5-7]. Many years later in 2014, a new method named the Microporous Wall Model (MPWM) was proposed to model the effect of the MBT skin [8]. It features a boundary condition which include the integration of microjets to imitate the effect of micro blowing. It was then adopted to study the performance of a supercritical airfoil RAE 2822 in the presence of MBT at transonic speeds [9]. With certain placement of MBT which was considered essential in ensuring improved performance, numerical results indicate that a 12.8–16.8% reduction of total drag, and 14.7–17.8% increase of lift could be achieved with a blowing fraction of 0.05.

Experimental work resurfaced in 2012 where the details of the boundary layer over the permeable surface was of interest and validated upon the work of Hwang [2]. Valuable theoretical information as described earlier was demonstrated in the experiment where due to blowing, the momentum thickness of the boundary layer increases and additional observation of a recovery region. To optimize the usage of the MBT skin, the introduction of permeable-impermeable surfaces on a flat plate was done to study the efficiency of alternating blowing to take advantage of the recovery region discovered earlier [10]. Results showed that this configuration is able to provide reduction of the net aerodynamic drag of about 15–25% at the same airflow rate as for a completely permeable surface and was subject to improve with higher blowing fractions. MBT integration on wings in subsonic flows have also been attempted in Ref. [7, 11-15] but to date any reduction in total drag in experiments has not been observed, instead it was found to increase.

* Graduate Student, Department of Mechanical Engineering. Student Member AIAA 1180148.

After over 30 years since the first reported work of this technique, researchers have yet to relate the pressure drag mechanism in subsonic flows when MBT is used and this is the reason why its implementation on airfoils have never reported to be successful in reducing total drag. However, based on a detailed in-depth analysis of their work and reasons for earlier disappointments, we arrived at a novel hypothesis that MBT may prove effective on aft-loaded airfoils. Thus, the objective of this paper is to perform numerical studies on the successful application of MBT on a S1223 high lift low Reynolds number airfoil. The numerical approach will be validated with previous experimental data followed by the aerodynamic performance assessment of the MBT integration at a chord-based Reynolds number from 0.3×10^6 and a range of angle of attack from 0-10 degrees. Corresponding details on the drag reduction mechanism will be discussed.

II. Total Drag Reduction with MBT

A. Effect of MBT on Pressure Drag

MBT has long been known to adversely affect pressure drag despite its undoubted success in the literature in reducing skin friction drag. The general effect on how MBT affects the pressure distribution on airfoils can be seen numerically and experimentally [9, 13]. It is clear that in the presence of blowing, generally C_p increases upstream especially as it reaches the MBT region and then decreases downstream. The change in C_p to some degree is due to the increase of the effective airfoil thickness, since in the presence of blowing, the overall thickness of the boundary layer increases. Consequently the flow “sees” the airfoil having a slightly distorted geometry [16]. Due to this, it is possible to control the pressure forces acting on the airfoil via MBT with using design considerations on the proper location and size of the MBT region. In deciding the MBT location, information about the C_p vector distribution around the original airfoil is vital.

B. Implementation of MBT on the S1223 airfoil

Selection of airfoils is crucial in determining successful implementation of MBT. Due to the reasoning mentioned earlier, aft-loaded airfoils which feature high pressure drag contribution near the trailing edge should perform well with the integration of MBT. The S1223 high lift-low Reynolds number airfoil is a great candidate for this study since the application of high efficiency airfoils in the low Reynolds number regime is increasingly attractive for UAVs. Figure 1, illustrates the C_p vector along the S1223 baseline airfoil with divided segments showing the contribution of pressure forces towards positive or negative drag.

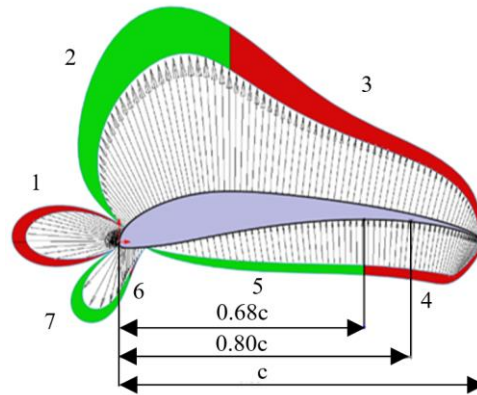


Fig. 1 Baseline pressure vector for the S1223 from XFOIL at Reynolds number: 0.3×10^6 , and ($\alpha=0^\circ$): green portion indicates negative pressure drag and red portion indicates pressure drag.

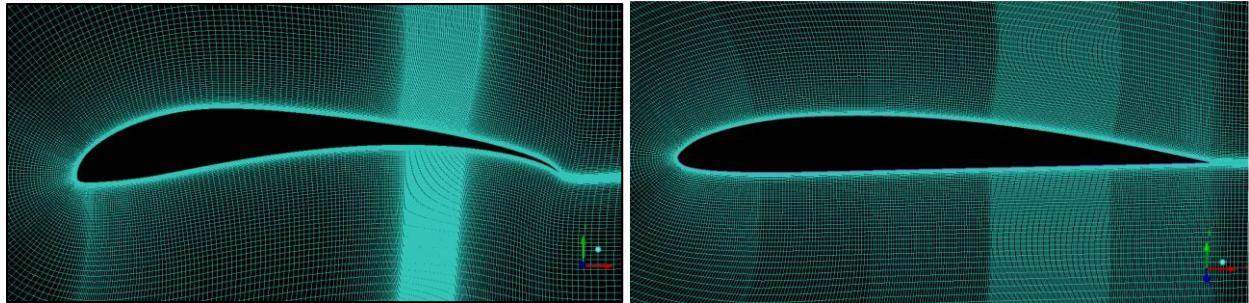
The direction of the vectors is governed by the flow condition, angle of attack as well as the geometry of the airfoil. Recall from the literature that the C_p upstream of the blowing region will increase and decrease downstream. Thus, using this as a rule of thumb, the onset for MBT was selected to be at $x/c: 0.68$ on the lower surface, so that segment 5 experiences an increase in C_p thus supposedly increasing the contribution towards lift as well as negative pressure drag. The blowing region ends at $x/c: 0.8$ to reduce the pressure drag contribution in segment 4 and to take advantage of the recovery region in skin friction reduction as reported in the literature. It is important to note that since C_p changes

with angle of attack, the design process should take into account the most strategic location of the MBT region depending on the intended mission.

III. Numerical Method, Procedure and Validation

A. Numerical Method

In this paper, the Shear Stress Transport $k - \omega$ model which is a two-equation eddy-viscosity model developed in Ref. [17] will be adopted. This SST formulation was devised to effectively blend the robust and accurate formulation of the $k - \omega$ model in the near wall region with the free-stream correct behavior of the $k - \epsilon$ turbulence closure. Apart from that, since available wind tunnel data in Ref. [15] was not reported to be corrected, the baseline simulation will also be compared with the XFOIL code [18]. The code combines a panel method and an integral boundary layer formulation for the analysis of potential and viscous flows around airfoils. The code was developed to rapidly predict the airfoil performance at low Reynolds numbers and its accuracy is well recognized [19]. During validation, 200 panels were used to represent the airfoil and to match experimental conditions in Ref. [15], a forced transition at chord-based location of 0.05 was selected on the top surface. The structured meshes for this study and the validation work were generated using a C-type topology in ICEM with 30 chordlength in radius and 60 chordlength downstream. The designated value for y^+ in both cases was chosen to be 1 which is lower than the suggested 3 so that sufficient information is captured in the boundary layer [17]. The mesh near the airfoils are shown in Fig. 2. ANSYS 2019 R3 software package was used to carry out the simulations. Fluent double precision with parallel processing was selected. CFD simulations were performed using a steady-state pressure-based solver. The pressure-velocity coupling scheme was set to coupled and the least squares cell based was chosen for the spatial discretization gradient. Second order upwind was preferred for the pressure, momentum, turbulent kinetic energy and specific dissipation rate for improved accuracy. Convergence is decided when there is insignificant change in c_l and c_d and the residual errors are below 10^{-6} for all governing equations.



a) S1223.

b) Clark Y.

Fig. 2 Near airfoil mesh generated using ICEM.

B. Procedure

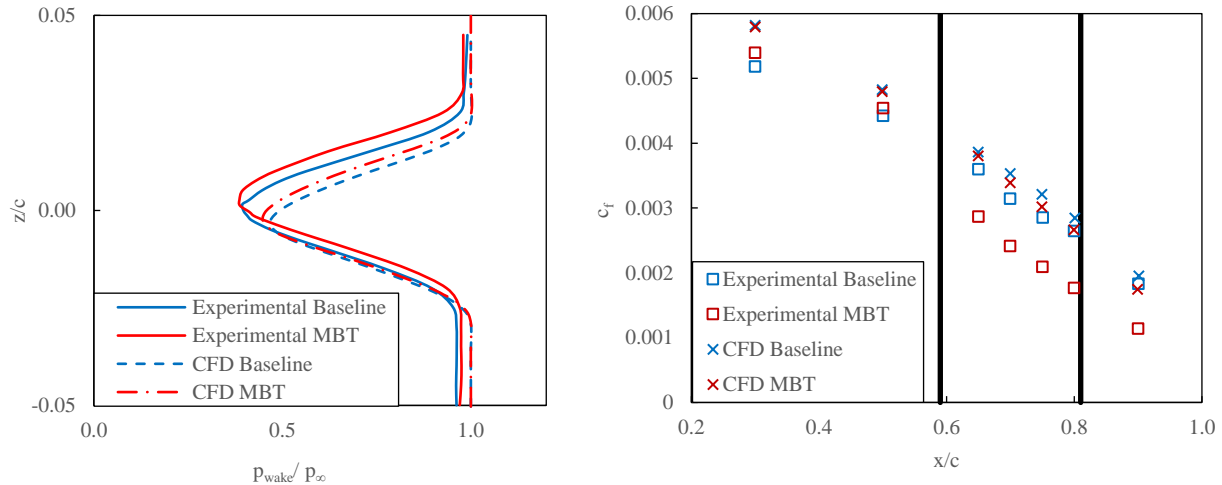
To simulate the effect of MBT, a rather simple approach is being implemented and it is viable since the MBT skin used in the experimental data is reported to closely resemble that of a smooth wall [15]. This will allow flexibility in the simulation since governing effective roughness parameters such as hole size and porosity are no longer of importance. In the case where the effective roughness is significant, this approach may not be as reasonably accurate since it is not able to imitate the effect of the holes in resulting additional roughness. In modelling the smooth skin, the region in which MBT is applied will then be divided into equal segments where individual length is sufficiently small within available computational capabilities. In both cases here, the individual segment length is $0.001x/c$ making the “modelled” holes to be 0.3mm. The segments will then be grouped and defined as a wall and a velocity inlet alternatingly. Freestream condition for turbulence intensity was selected to be 0.1% to represent the average wind tunnel and the turbulence viscosity ratio will be calculated according to the Reynolds number as reported in Ref. [20]. Further simplification is needed since the velocity inlets in the simulation do not report any forces and this is not true in real world applications. Due to this, even though in the baseline model all segments are set as “wall”, the contribution of forces imposed by the segments which are grouped as velocity inlets, in cases where MBT is being applied, will be omitted.

C. Validation of CFD modelling using Clark Y

The results from the numerical approach is examined against the experimental MBT data on a Clark Y airfoil [15]. Chord-based Reynolds number is 1.54 million and hot wire measurement at $z/c: 0.05$ above the blowing region reveals that the blowing velocity was 0.08m/s . The total drag was computed from wake pressure measurements located at $x/c: 1.125$. However, wind tunnel correction which include buoyancy, solid blockage, wake blockage, streamline curvature and additional velocity corrections were not being reported thus resulting in published data for drag not to be comparable with CFD [19, 21]. Nevertheless, the objective of this study is not to evaluate the actual data of the airfoil, rather to build confidence in the capability of the current numerical approach in estimating the aerodynamic performance of the airfoil in the presence of MBT. Supportive data for the baseline CFD simulation is therefore done via XFOIL. In the code, the number of panel nodes was set to 200 with a bunching parameter of 1 and amplification factor value of 9. Artificial tripping was designated at $x/c: 0.05$ on the top surface to match the experimental setup. Results from Table 1 indeed proves that the baseline CFD model is reliable. Difference may be due to the effect of tripping that can easily be modelled in XFOIL as opposed to FLUENT. Similar trend of increasing drag due to MBT can also be seen in Table 1 when compared against experimental data. The effect of thickening of the boundary layer due to blowing which increases the size of the wake as mentioned in Ref. [12] can be seen in Fig. 3a. This is evident especially on the upper surface as shown in the wake total pressure profile. In addition to that, as expected local skin friction coefficient dropped in the MBT region and there exists a recovery zone extending further aft depicted in Fig. 3b as reported by [2, 22]. Data in Fig. 3 show that the CFD results agree with the trend of the experimental data of [15]. It is therefore reasonable to claim that the proposed MBT simulation is consistent with actual application

Table 1 CFD MBT comparison against Clark Y airfoil experiment data [15]

	C_l	$C_{d,\text{pressure}}$	$C_{d,\text{friction}}$	$C_{d,\text{baseline}}$	$C_{d,\text{MBT}}$	Drag increment, %
XFOIL	0.3581	0.0020	0.0076	0.0096	-	-
FLUENT	0.3232	0.0022	0.0083	0.0105	0.0113	5.14
Experiment	-	-	-	0.0162	0.0169	3.86



a) Total pressure distribution in the wake ($\alpha = 0^\circ$).

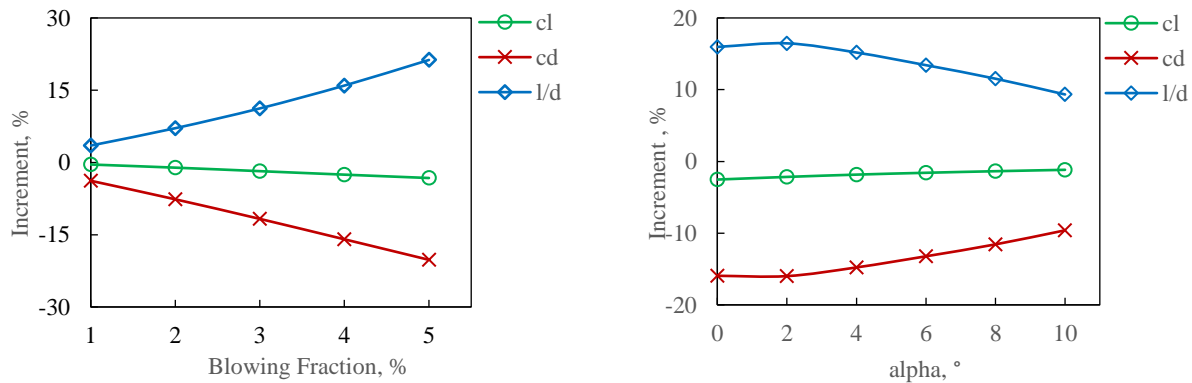
b) Local skin friction coefficient c_f as a function of streamwise coordinate x ($\alpha = 0^\circ$): vertical black lines represent onset and offset of the blowing region.

Fig. 3 CFD and experimental data in Ref. [15] comparison.

IV. Results and Discussion

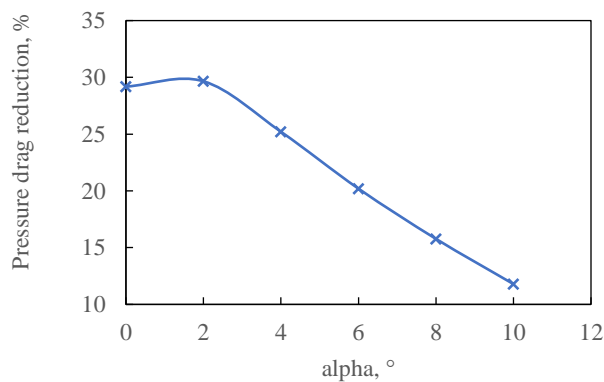
The aerodynamic performance while varying the blowing fraction and angle of attack was investigated for the S1223 airfoil. Since there is no ceiling value for the blowing fraction to counter the increase in pressure drag as described in Ref. [23], the blowing fraction is selected to be in the range of 1-5%. The angle of attack will be varied from 0-10 degrees at a Reynolds number of 0.3×10^6 . Figure 4a demonstrates the performance of MBT on the S1223 airfoil at 0 degrees angle of attack with different blowing fractions. Improvement on both drag and l/d ratio can be related with increasing blowing velocity. As previously mentioned, the improvement of drag results from the increment of the contribution of negative pressure drag upstream of the blowing region in addition to the reduction of pressure drag near the trailing edge. In the same figure, it can also be seen that the production of lift deteriorates with increasing blowing fraction. This is due to the increase of C_p upstream of the blowing region was unable to compensate the degeneration of lift near the trailing edge. The change in both lift and pressure drag can be linked to the modification of the effective thickness of the airfoil which affects the variation of static pressure along the chord. The effective thickness of the airfoil is sensitive towards surface curvature therefore it can be expected that the trade-off between the degree to which C_p is affected is dependent on the location, geometry, and maximum thickness of the airfoil.

The direction of pressure forces which act normal either towards or outwards of the airfoil surface is determined by the local static pressure, whether it is lower or higher than the freestream static pressure. Aside from this, geometrically, there exists a line which is perpendicular to the airfoil surface which separates the pressure forces into contributing either towards positive drag or negative drag. The starting point on the airfoil due to this line will then be referred as the critical point from here onwards. The described information should allow us to intuitively understand the drag mechanism caused by pressure forces as well as identify portions on the airfoil which generate positive pressure drag or negative pressure drag as shown in Fig. 5.



a) Aerodynamic performance as a function of blowing fraction at $\alpha = 0^\circ$.

b) Aerodynamic performance as a function of angle of attack with blowing fraction of 4% at $\alpha = 0^\circ$.



c) Pressure drag reduction as a function of angle of attack.

Fig. 4 Effect of MBT towards aerodynamic performance of S 1223 airfoil at $Re: 0.3 \times 10^6$.

At zero angle of attack, on the lower surface, the first critical point is located at $x/c: 0.03$ and the second is located at $x/c: 0.68$. At 10 degrees of attack, the first critical point has shifted downstream to $x/c: 0.18$ and the second being shifted upstream to $x/c: 0.32$. Hence for a fixed location of blowing region, the potential of MBT is most likely to depreciate when being operated at an angle of attack other than the design angle of attack as shown in Fig. 4b. The change in effectiveness of MBT at different angle of attack due to the shifting of the critical points can be seen in Fig. 4c. At 10 degrees, the blowing region is no longer capable to significantly improve the negative pressure drag since the critical point has shifted further upstream. Nevertheless, pressure drag is shown to decrease as the C_p aft of the blowing region is still being reduced. Other than that, when comparing the effect of angle of attack on the pressure distribution as shown in Fig. 5, the component of drag in the pressure vectors near the trailing edge at 10 degrees has increased which explains how improvement in pressure drag can still be attained at off-design condition. In general, stronger blowing fraction should be able to decrease drag and improve l/d ratio even more. With the current placement, a 4% blowing fraction corresponded to a maximum reduction in drag of 16%, reduction in lift of 2.5%, and an increase of 16.5% in l/d ratio. This proves that the geometry of the airfoil is crucial in deciding its compatibility with MBT.

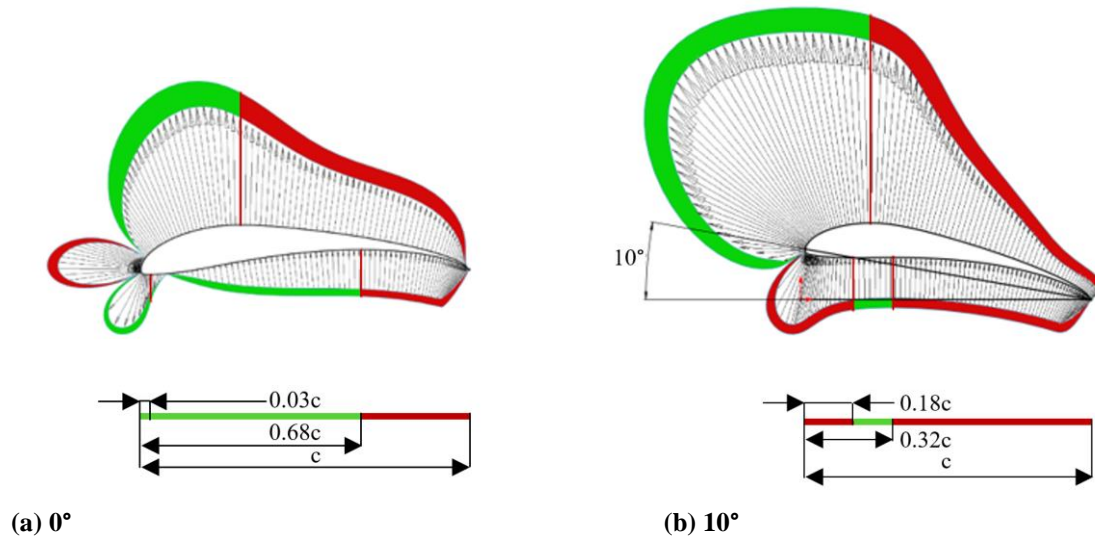


Fig. 5 Baseline pressure vectors for the S1223 from XFOIL at Reynolds number: 0.3×10^6 . Green portion indicates negative pressure drag and red portion indicates positive pressure drag. Red lines represent normal lines on the airfoil that are perpendicular to the flow (critical point).

V. Conclusion

Numerical simulation and analysis on the application of the microblowing technique (MBT) on a high lift low Reynolds number airfoil S1223 was performed. Blowing was applied on the lower surface at $x/c: 0.68-0.80$. CFD validation work shows agreement with published experimental data in the characteristics of c_f , wake, and total drag for a Clark Y airfoil. Integration of MBT on the S1223 airfoil has proven to be a success in total drag reduction of 16% as well as increase in l/d ratio by 16.5% for a chord-based Reynolds number of 0.3×10^6 . As discussed, the placement of the region of MBT depends on the C_p distribution, geometry of the airfoil, and angle of attack. Optimal location of the MBT region should be designed based on cruise or loiter angle of attack to obtain best results. Further investigation on the effect of MBT on transition characteristics, and leading-edge separation prevention at very low Reynolds number will disclose further potential of MBT as an effective drag reduction technique.

References

- [1] Hwang. "A proof of concept experiment for reducing skin friction by using a micro-blowing technique," *35th Aerospace Sciences Meeting and Exhibit*. 1997, p. 546.
- [2] Kornilov, V. I., and Boiko, A. V. "Efficiency of air microblowing through microperforated wall for flat plate drag reduction," *AIAA journal* Vol. 50, No. 3, 2012, pp. 724-732.

- doi: 10.2514/1.J051426
- [3] Hwang. "Experimental study of characteristics of micro-hole porous skins for turbulent skin friction reduction," 2002.
- [4] Hwang. "Review of research into the concept of the microblowing technique for turbulent skin friction reduction," *Progress in Aerospace Sciences* Vol. 40, No. 8, 2004, pp. 559-575.
doi: 10.1016/j.paerosci.2005.01.002
- [5] Menon, S. "Large-eddy/lattice Boltzmann simulations of micro-blowing strategies for subsonic and supersonic drag control," 2003.
- [6] Lin, Y.-L., Chyu, M., Shih, T., Willis, B., and Hwang, D. "Skin-friction reduction through micro blowing," *36th AIAA Aerospace Sciences Meeting and Exhibit*. 1998, p. 359.
- [7] Parkhe, V. "A parametric study on flow over a flat plate with microblowing." University of Akron, 2009.
- [8] Li, J., Shen, J., and Lee, C. "A micro-porous wall model for micro-blowing/suction flow system," *Scientia Sinica Physica, Mechanica & Astronomica* Vol. 44, No. 2, 2014, pp. 221-232.
doi: 10.1360/132013-158
- [9] Gao, Z., Cai, J., Li, J., Jiang, C., and Lee, C.-H. "Numerical study on mechanism of drag reduction by microblowing technique on supercritical airfoil," *Journal of Aerospace Engineering* Vol. 30, No. 3, 2017, p. 04016084.
doi: 10.1061/(ASCE)AS.1943-5525.0000685
- [10] Kornilov, V. I., and Boiko, A. V. "Flat-plate drag reduction with streamwise noncontinuous microblowing," *AIAA journal* Vol. 52, No. 1, 2014, pp. 93-103.
doi: 10.2514/1.J052477
- [11] Choi, N. S. *A study of micro-blowing technique*: University of Toronto, 1999.
- [12] Kornilov, V. "Implementation of air injection into the turbulent boundary layer of aircraft wing using external pressurized flow," *Thermophysics and Aeromechanics* Vol. 24, No. 2, 2017, pp. 175-185.
doi: 10.1134/S0869864317020032
- [13] Kornilov, V. "Control of turbulent boundary layer on a wing section by combined blowing/suction," *Thermophysics and Aeromechanics* Vol. 25, No. 2, 2018, pp. 155-167.
doi: 10.1134/S0869864318020014
- [14] Eto, K., Kondo, Y., Fukagata, K., and Tokugawa, N. "Friction drag reduction on a clark-Y airfoil using uniform blowing," *2018 Flow Control Conference*. 2018, p. 3374.
- [15] Eto, K., Kondo, Y., Fukagata, K., and Tokugawa, N. "Assessment of friction drag reduction on a Clark-Y airfoil by uniform blowing," *AIAA journal*, 2019, pp. 2774-2782.
doi: 10.2514/1.J057998
- [16] Anderson Jr, J. D. *Fundamentals of aerodynamics*: Tata McGraw-Hill Education, 2010.
- [17] Menter, F. R. "Two-equation eddy-viscosity turbulence models for engineering applications," *AIAA journal* Vol. 32, No. 8, 1994, pp. 1598-1605.
doi: 10.2514/3.12149
- [18] Drela, M. "XFOIL: An analysis and design system for low Reynolds number airfoils," *Low Reynolds number aerodynamics*. Springer, 1989, pp. 1-12.
- [19] Selig, M. S. *Summary of low speed airfoil data*: SOARTECH publications, 1995.
- [20] Rumsey, C. L., and Spalart, P. R. "Turbulence model behavior in low Reynolds number regions of aerodynamic flowfields," *AIAA journal* Vol. 47, No. 4, 2009, pp. 982-993.
doi: 10.2514/1.39947
- [21] Awbi, H. "Wind-tunnel-wall constraint on two-dimensional rectangular-section prisms," *Journal of Wind Engineering and Industrial Aerodynamics* Vol. 3, No. 4, 1978, pp. 285-306.
doi: 10.1016/0167-6105(78)90034-X
- [22] Junxuan, C., and ZhenXun, G. "Numerical study on drag reduction by micro-blowing/suction compounding flow control on supercritical airfoil," *Procedia Engineering* Vol. 99, 2015, pp. 613-617.
doi: 10.1016/j.proeng.2014.12.579
- [23] Hwang, and Biesiadny. "Experimental evaluation of penalty associated with micro-blowing for reducing skin friction," *36th AIAA Aerospace Sciences Meeting and Exhibit*. 1997, p. 677.

Artificial Intelligence Explanation for Decision Supporting System in Low Level Air Traffic Management

Yibing Xie¹, and Nichakorn Pongsakornsathien²

School of Engineering, RMIT University, Bundoora, VIC 3083, Australia

The emerging interest in Urban Air Mobility (UAM) and in unrestricted Unmanned Aircraft Systems (UAS) challenges the conventional Air Traffic Management (ATM) methodologies. In order to overcome the outstanding obstacles, the ATM systems need to be highly automated and intelligent, hence increasing efficiency and increase capacity. An highly automated ATM/ UAS Traffic Management (UTM) system based on artificial intelligence (AI) is technically feasible, however, the opacity and inexplicable characteristics of intelligent algorithms restrict the usability of such systems in environments where human operators are still involved in making safety-critical decisions. A relatively inexplicable recommendation by the system is not conducive to the interaction and cooperation between the Air Traffic Controller (ATCo) and the system. This not only reduces the efficiency of the entire operation but also increases the risk. This research investigates the adoption of ATM AI for incidents and accident risk prediction through the XGBoost algorithm. The study focuses on explaining the trained AI model and the predicted results. Moreover, considerations are made on the most promising strategies to strengthen the trust between the ATCo and the system through the redesign of the interface of Human Machine Interaction (HMI).

I. Introduction

Unmanned Aircraft Systems (UAS) have begun to spread, but there is no mature infrastructure and management model to enable UAS to operate safely and efficiently in low-altitude airspace [1]. In response to the need for a safe and efficient UAS operational framework, NASA and Europe have proposed UAS Traffic Management (UTM) and U-Space plans, respectively [2]. However, UTM still needs to adapt to ATM rules and regulations, including the flexible use of airspace regulations. UTM and ATM need to coordinate with each other and cannot be completely independent because the airspace still needs human supervision [3]. A seamless ATM/UTM system requires not only the interoperability of system components but also of the information exchange and management used by different processes and services [4, 5]. The traditional air traffic control model puts a heavy burden on Air Traffic Controller (ATCo) and cannot meet the demand for high-volume traffic. UAS operations need to be safely integrated into isolated/non-isolated airspace. It is impossible to use the existing ATM system to manage the high density and diversified flight equipment in single airspace [6]. Therefore, a more efficient Decision Support System (DSS), a support system for air traffic control based on AI technology, is introduced to implement in UTM system, which has more improves the control level of ATCo and reduces the workload, to dynamically balance the demand for air transportation. The decision-making system developed based on Machine learning (ML) can already solve complex mass data analysis problems by identifying the interaction patterns between variables [7]. At the same time, using the general algorithm of the open source platform to create an auxiliary prediction system can simplify the deployment of the program and reduce the barriers to entry [8, 9]. Decision-making needs to be transparent, especially when the profit or loss caused by the decision is seriously concerned. That is especially critical when AI systems are deployed in areas where humans have long dominated [10]. Therefore, it is necessary to build the trust of human operators in the system by understanding the conclusions of the AI system and the reasons behind the results. The collaboration

¹ Student Member, Masters, 1192575

² Student Member, Masters, 11084304

between ATCo and auxiliary systems, mutual trust and workload have a significant positive correlation [11]. It is necessary to assist decision-makers to trust the conclusion of the system through XAI [12]. Therefore, the human-machine system needs to be adjusted and developed to handle the high-level information of the future UTM. However, the responsibilities and tasks of the UTM operator are not fully identified. It is therefore very challenging to properly design such HMI and choosing the suitable ML/AI and XAI for UTM operations. Thus, the preliminary UTM operator task analysis was performed and also proposed human-machine interactions workflow for HMI design [13]. This research aims to improve the development of ATM/UTM DSS applications by using open source AI algorithms and exploring the explanation methods of the results given by the model, and the purpose of the research is to enable non-AI experts to understand the results of the model, to achieve the trustworthiness and reliability of the AI system.

II. Literature Review

A. AI algorithm

The structure of the AI algorithm is flexible, while it needs to assume that the input data is very limited. Thus, it is suitable for dealing with complex and highly nonlinear relationships in data [14]. Ensemble learning is one of the most popular and promising machine learning methods. Its fusion methods include boosting, bagging and stacking [15]. Ensemble learning not only explains the interaction between input variables and predictive models but also identifies the relative importance of key factors. Gradient Boosted Decision Tree (GBDT) is an integrated learning method based on decision trees. Unlike traditional Decision Tree (DT), the enhanced design enables GBDT to iteratively train a series of weak learners and strategically generates the best tree set to improve prediction accuracy [16]. Ramon [17] demonstrated the take-off time prediction system based on the GBDT model, which provided more accurate prediction results than Enhanced Tactical Flow Management System (ETFMS). GBDT is applied to more scenarios at the same time; for example, Zhou [18] proposed based on GBDT and LR (logistic regression). Zhang [19] presented a spatiotemporal gradient-enhanced regression tree model, which extracts the spatiotemporal correlation of neighbouring and target links from historical and real-time traffic data, thereby providing higher prediction accuracy. For non-stationary and nonlinear features, the ML algorithm is generally more accurate [20]. However, most ML models lack the explainability of the algorithm itself and the output results.

B. Explainable AI (XAI)

According to Arrieta et al. [21], the XAI method is systematically analysed, and its importance is divided into two-step classification. The first classification, which includes interpretable models and model explainability techniques, divides XAI into two methods: model transparency and post-hoc explainability. When the ML model cannot satisfy its transparent explanation, a particular method is needed to explain its decision, so that the second classification is generated based on the first classification: model-agnostic and model-specific method. Model-agnostic methods can be applied to any AI model, while the model-specific methods are a post-hoc explanatory technique developed for a specific AI model. Generally, the black box model will use the post-explanation method. The Local Interpretable Model-Agnostic Explanations (LIME) method is used to explain the prediction of any classifier or regression model [22]. It does not interfere with the algorithm inside the black-box but randomly disturbs the input data to form analog data. The feature importance is obtained by comparing with the prediction result between the disturbing data and original example, thereby generating an explanation for a single prediction of any ML model. The SHapley Additive exPlanations (SHAP) is a method based on the concept of game theory to calculate the importance of additive features for each specific prediction [23]. Similar to the "feature correlation explanation", the method describes the function of the opaque model by ranking or measuring the impact, relevance or importance of each feature in the prediction output. Lundberg et al. [24] developed TreeExplainer based on SHAP, which is a visual local explanation method. While assigning the weight and value to each feature, the local explanation is extended to capture the interaction of the features directly, and a large amount of local explanations are used to understand the global structure.

C. Human-Machine Interaction (HMI)

With the increasing role of AI, the pre-existing problems, such as trust, over-dependence, and loss of situational awareness and control, not only have not been eliminated but also been further amplified [25]. Traditional Human-Machine Interaction (HMI) focuses on the visual display, and system information mainly relies on display output [26]. In ATM applications, additional physiological sensors are exploited to improve the effectiveness of HMI, such as voice recognition [27], gesture recognition [28], and eye-tracking sensors [29]. One emerging concept that aims to enhance cognitive states of the human operator in real-time during the complex and time-critical operations with a high level of automation is Cognitive Human Machine Interfaces and Interactions (CHMI²) [30]. A human cognitive state monitoring/enhancement by machine prevents cognitive overload and human-oversight when increasing the level

of autonomy in decision support systems. The CHMI² framework comprises of three main modules: sensing, inference and adaptation. Similar to other proposed HMI concepts in the literature, CHMI² sensing module also uses advanced neurophysiological sensors, but in this framework, they are used to collect the responses in real-time. The collected and pre-filtered data is passed through the inference module to estimate the cognitive state of the operator. This inferred cognitive state is the key driver to dynamically adapt the HMI formats/functions and automation behaviour [31]. However, such adaptation must occur in a human-comprehensible manner, promoting trustworthiness and understandability by the user of the system.

III. Methodology

The first section is the dataset preparation. The second part is the prediction model developed with the open-source XGBoost algorithm. The third part is explaining the post-explanation method with SHAP. The fourth part is information interaction combiner. The last part is the framework of predictive and explanation models.

A. Data Preparation

In order to verify the model, the meteorological data used in the research comes from the open-access database of Bureau of Meteorology (BoM); all incidents and accidents report data to obtain from Australian Transport Safety Bureau (ATSB) National Aviation Occurrence Database. The date of weather and incidents and accidents, which is from 1 April 2018 to 31 March 2019, and from 1 July 2019 to 30 November 2019. The location of the weather data is Melbourne Airport, and the site number is 086282. The incidents and accidents data are based on Melbourne Airport as the centre, within a 15 kilometres radius of the report, and the types of reports are all weather-related. The record of meteorological data is divided into three parts, which is the synthetic daily data, the observation data at 9 am, and the observation data at 3 pm. The entire data is divided into five sectors. The first sector is ID and Date. The second to the fourth sector are meteorological data, which are the synthetic daily data including the observation data at 9 am and the observation data at 3 pm. Lastly, the fifth sector is the incidents and accidents report.

B. Prediction Model - XGBoost

XGBoost model is essentially a GBDT model, which is proposed by Chen and Guestrin [32]. Its goal is to maximize the speed and efficiency of the model. The algorithm combines multiple weak learners through the boosting method, and its basic algorithm is the CART decision tree. The DT method has good interpretability and transparency [33].

$$Obj^{(t)} = \sum_{i=1}^n L \left[y_i, \hat{y}_i^{(t-1)} + g_i f_t(x_i) + \frac{1}{2} h_i f_t^2(x_i) \right] + \left(\gamma T + \frac{1}{2} \lambda \sum_{j=1}^T w_j^2 \right) + Constant \quad (1)$$

where $g_i = \partial_{\hat{y}^{(t-1)}} l(y_i, \hat{y}^{(t-1)})$, $h_i = \partial_{\hat{y}^{(t-1)}}^2 l(y_i, \hat{y}^{(t-1)})$. Equation 1 is based on the first-step of Taylor expansion, while the second-step of Taylor expansion is performed on the error part. Also, the algorithm itself adds L1 and L2 regularization terms to prevent over-fitting and enhance generalization ability. The core concept is to continuously perform feature splitting and learn new functions to fit the residuals of the previous prediction. Therefore, the objective function is essentially divided into two parts. The first part is the loss function, whose goal is to reveal the training loss, that is, the difference between the predicted score and the real score. The second part is the regularization term, which defines the complexity of the algorithm to avoid overfitting. When let the $G_j = \sum_{i \in I_j} g_i$, $H_j = \sum_{i \in I_j} h_i$, and after the $w_j^* = -\frac{G_j}{H_j + \lambda}$ is substituted, the final function is shown as Equation 2. Also, Equation 3 is the calculation expression of Gain, which represents the contribution degree of each leaf node to the current model loss.

$$Obj = -\frac{1}{2} \sum_{j=1}^T \frac{G_j^2}{H_j + \lambda} + \gamma T \quad (2)$$

$$Gain = \frac{1}{2} \left[\frac{G_L^2}{H_L + \lambda} + \frac{G_R^2}{H_R + \lambda} + \frac{(G_L + G_R)^2}{H_L + H_R + \lambda} \right] - \gamma \quad (3)$$

XGBoost provides seven hyper-parameters, which can be adjusted to improve the algorithm's progress, robustness, and reduce overfitting. The experiment adjusts only part of the hyperparameters, which is the learning rate, the maximum depth, and the minimum child weight. The remaining hyperparameters are all set to fixed values, the maximum number of iterations is set to 800, the Lambda regularization is 1, the Alpha regularization is 0.85, the gamma value is 0.2, and the sub-sample is 0.85. Finally, the parameter configuration with the highest predicted value

is selected for the explanation. The prediction model train on Python 3.7.8 with computing libraries. These computing libraries include Numpy 1.18.5, Pandas 1.0.5, Scikit-learn 0.23.1 and XGBoost 1.3.0.

C. Explanation Model

SHAP is an additive feature attribution method, which attributes the output value to the shapely value of each feature. In other words, it calculates the Shapley value of each feature and then measures the impact of the feature on the final output value [34, 35], which is expressed as Equation 5.

$$g(z') = \phi_0 + \sum_{j=1}^M \phi_j z'_j \quad (5)$$

where g represents the explanation model; M is the number of input features; z represents whether the feature exists; ϕ is the attribution value of each feature (Shapley value). The output S of the tree conditioned on the feature subset is defined as $f_x(S)$. The SHAP value is based on game theory to average all possible conditional expectations. For a certain feature j , it is necessary to calculate the Shapley value for all possible feature combinations (including different orders) and then weighted summation. The formula is Equation 6.

$$\phi_j = \sum_{S \in N \setminus \{j\}} \frac{|S|!(p - |S| - 1)!}{M!} [f_x(S \cup \{i\}) - f_x(S)] \quad (6)$$

where S is a subset of the features used in the model, x is the vector of feature values of the sample to be explained, and p is the number of features. Similarly, the explanation model is trained on Python 3.7.8 with a computing library. These calculation libraries include SHAP 0.36.0.

D. HMI Mode

The design of the HMI system under the highly automated ATM/UTM system mainly includes the following three key points: monitoring of automated programs; awareness of abnormal information; handling of emergencies. Therefore, in this research, the information interaction of the prediction system is divided into two states and three modes. Which the two states are PNIA (Predict Non-Incidents and Accidents) and POIA (Predict Occur Incidents and Accidents). The three methods comprise of Silent Predicting Mode when no Incidents and Accidents are predicted; Condensed Prompt Mode when an incident or accident is predicted; Detailed Information Mode that can be viewed regardless of status. The interaction input methods are operating via a traditional keyboard, mouse, and other physical buttons. There are two interaction output methods, output visual images through monitors, which is divided into the main and secondary displayer, and output prompt sounds and alarms through audio.

E. Process Framework

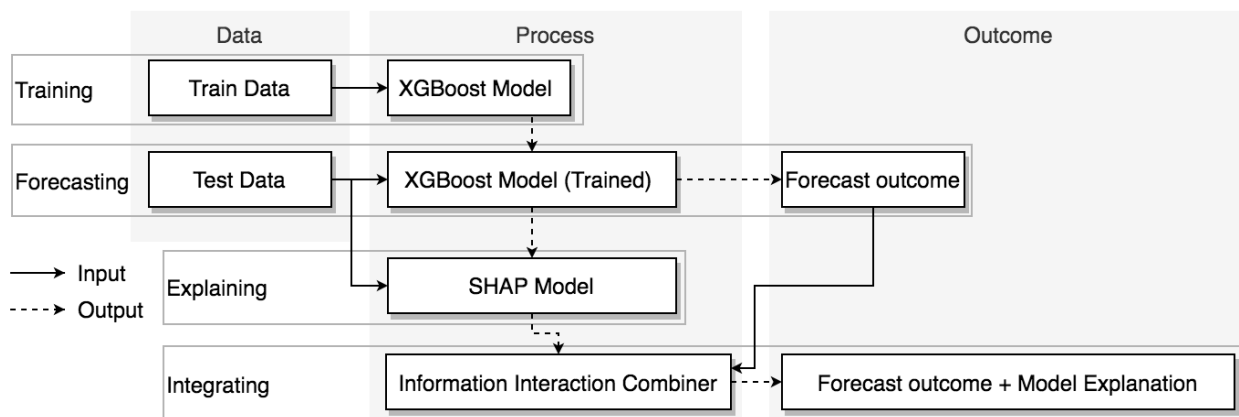


Figure 1. Process framework of prediction model.

The processing flow of the program is illustrated in Figure 1. The training data set is input into the XGBoost model for training, and the trained prediction model is obtained. Then the test data set is predicted, and the output result is compared with the test data set to obtain the model prediction accuracy. Then input the trained prediction model and test data set into the SHAP model to generate SHAP values and interpret the data afterwards. Finally, post-hoc-

explanation data are re-edited in the information interaction combiner, and then output the prediction results and related explanations.

IV. Result and Discussion

A. Model generation

A total of 518 days of data were input to the model and split into two data sets. The system randomly selects 67% of the data as the training set for training the model, that is 347 days of data. 33% of the data is the test set used to test the accuracy of the model, that is, 171 days of data. The test sets up three hyperparameters to compare the results. The three hyperparameters are learning rate, maximum depth, and minimum child weight. The role of the learning rate is to prevent overfitting by shrinking the step size of the iteration. In other words, by reducing the weight of each step, the robustness of the model is improved. In this test, a total of four values were taken, which are (1, 0.1, 0.01, 0.001). The maximum depth value is the maximum depth of the tree, and its function is also used to avoid overfitting. The larger the maximum depth value, the more specific and local samples the model can obtain. In this test, a total of 4 values were taken, which are (3,5,8,10). The minimum child weight determines the sum of the minimum leaf node sample weights. This parameter is also used to avoid overfitting. When its value is large, it can prevent the model from learning local special samples. However, if this value is too high, it will lead to underfitting. In this test, a total of 4 values were taken, which are (1,3,4,7). The remaining hyperparameters are fixed values, and no adjustments were made in this experiment to obtain more experimental data.

B. Model performance evaluation

A total of 518 days of data are the inputs of the model and split into two data sets. The system randomly selects 67% of the data as the training set for training the model, that is, 347 days of data. 33% of the data is the test set used to test the accuracy of the model, that is, 171 days of data. The test sets up three hyperparameters to compare the results. The three hyperparameters are learning rate, maximum depth, and minimum child weight. The role of the learning rate is to prevent overfitting by shrinking the step size of the iteration. In other words, by reducing the weight of each step, the robustness of the model is improved. In this test, a total of 4 values were taken, which are (1, 0.1, 0.01, 0.001). The maximum depth value is the maximum depth of the tree, and its function is also used to avoid overfitting. The larger the maximum depth value, the more specific and local samples the model can obtain. In this test, a total of 4 values were taken, which are (3,5,8,10). The minimum child weight determines the sum of the minimum leaf node sample weights. This parameter is also used to avoid overfitting. When its value is large, it can prevent the model from learning local special samples. However, if this value is too high, it will lead to underfitting. In this test, a total of 4 values were taken, which are (1,3,4,7). The remaining hyperparameters are fixed values, and no adjustments were made in this experiment to obtain more experimental data.

C. Identify influencing variables

The highest positive correlation between the two variables is 0.98, and the highest negative correlation is -0.69. The most relevant features are the temperature in each period and Mean Sea-Level (MSL) pressure. There is no close correlation between the remaining features. The XGBoost develops ML algorithms based on a tree model which are different from the combination of linear models; tree models are naturally robust to related variables [36]. For XGBoost, the existence of relevant variables will only increase the calculation time, but it will not have a great impact on the accuracy of the model. When preparing the data in this experiment since there were less than 20 types of variables, the relevant variables were not screened.

D. SHAP Explanation

All variables in the model are considered "contributors". In each prediction sample, the model produces a prediction value, and the value assigned to each feature in the sample is the SHAP value. The part A of Figure 2 shows the summary plot, which combines feature importance and feature effect to help understand the variables in the model globally. Each point in the Figure 2 represents one aspect of data. The ordinate represents the variable, and the abscissa is the SHAP value. The redder the colour represents the larger the value and the bluer the colour represents the smaller the value. The overlapping points jitter in the y-axis direction so that we can understand the distribution of Shapley values for each feature. As shown in the figure, the higher the wind speed, the higher the output of the predicted value of the model. In other words, the more incidents and accidents will occur, and the impact at low wind speeds will be

lower. The opposite is sunshine time and MSL pressure. The higher the value of these two variables, the smaller the effect on the output value. This means that the longer the sunshine hours and the higher the mean sea level pressure, the lower the probability of incidents and accidents. The part B shows the SHAP feature dependence plot for maximum gust wind speed, which shows feature dependency. Compared with the summary graph, the dependency graph is a more specific global explanation. It focuses on the impact of a single variable on the overall model. For each data instance, draw a point with a characteristic value on the x-axis, and draw a corresponding Shapley value on the y-axis. Taking the wind speed of 60km per hour as the dividing line, when the gust wind speed exceeds this value, the output of the SHAP characteristic value will rise rapidly. However, when it reaches 70km per hour. No matter how the wind speed value increases, the contribution to the forecast value will no longer continue to increase. In other words, wind speeds exceeding 70km/h tend to be the same threat to aircraft. Part C presents the description of a single sample output, that is, sample No. 42 of the test set. The predicted base value of the training model is 0.114. The displayed length of each feature is the absolute contribution value of that feature. When the wind speed is 48km per hour, the system judges that its contribution to the prediction result is negative, which means that the probability of an accident will decrease. When the rainfall is 1.2 mm, the system determines that the probability of an accident will increase. However, the contribution of rainfall is much smaller than wind speed.

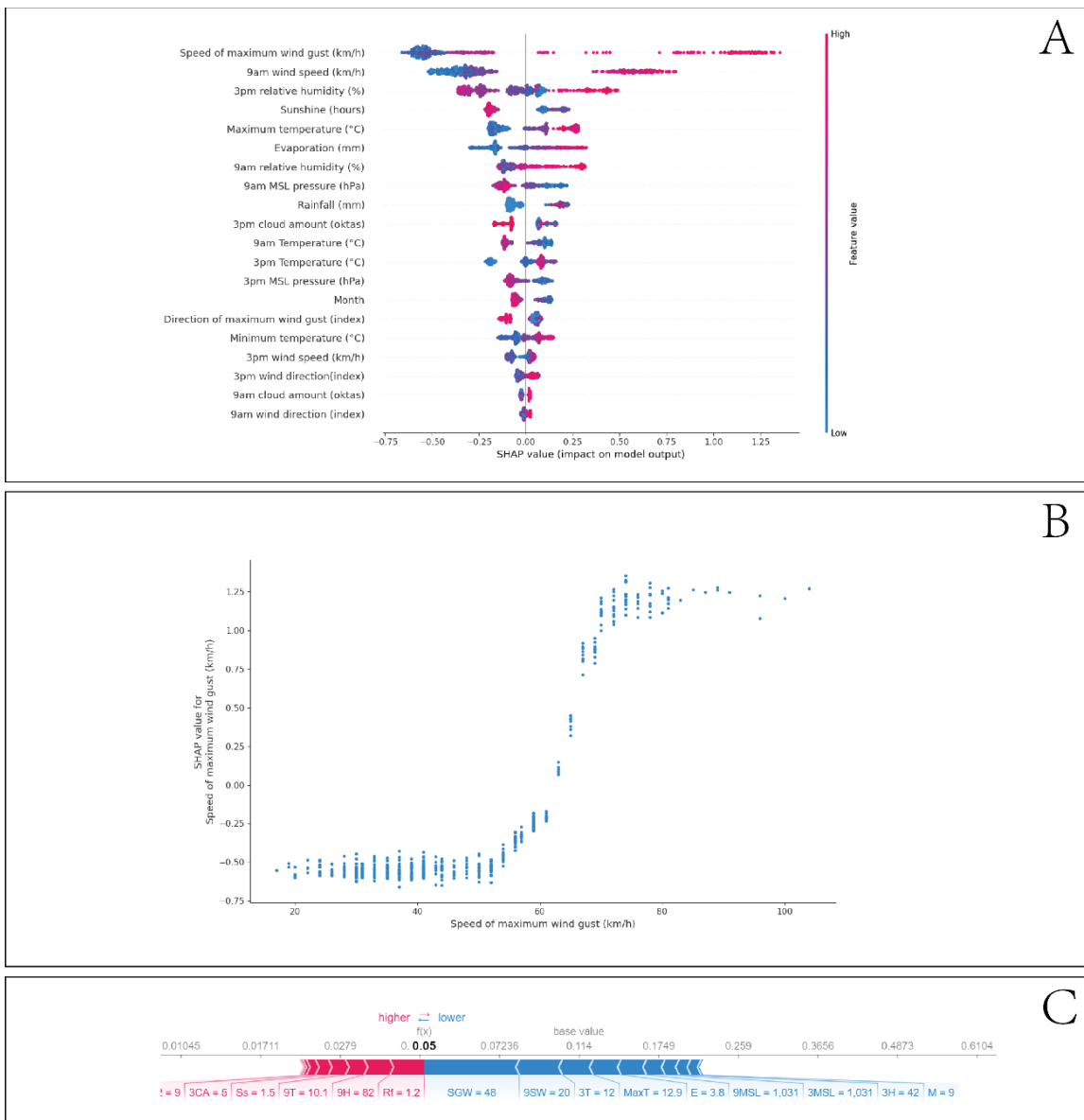


Figure 2. SHAP explanation of summary plot, dependence plot and force plot.

E. Information Interaction Mode

The information interaction of the prediction system is divided into two states and three modes. When no accident occurs, the mode is silent predicting mode. In this state and mode, the system will display "Predictive Alert: Active" in the information list area (top left of the main screen) and make predictions periodically. When the system predicts that there is no accident, the system will maintain this model, which is characterized by almost no displayed information to hinder or distract ATCo's attention. When the system predicts that an accident will occur, the mode switches from silent predicting mode to condensed prompt mode. In this mode, the system and ATCo begin limited interaction. In the information list area, "Predictive Alert:" changes from "Active" to "Warning" and flashes the alert. At the same time, the label of the corresponding aircraft flickered to guide ATCo to deal with emergencies. In addition to visual images, when the label flashes, the system will output an alarm through audio to assist the system to get ATCo's attention.

Based on the original information, the label adds the predicted probability and the type of incident/accident, and at the same time prompts ATCo to inform the pilot. In order to open the information on the label, the system needs to receive ATCo operations. There are two input methods, one is a physical button, and the other is eye tracking. The physical button requires ATCo to click on the label of a single aircraft with the mouse to view more information and end the flashing and alarm prompts. Figure 3 shows the detailed information mode, which has no status restrictions, and information can be viewed at any time. This mode is displayed on the secondary monitor and does not occupy the space of the primary monitor. The display layout in this mode is divided into three parts. The left part is the global explanation of the training model, that is, explaining the weight and priority of each feature after the model is trained, which is similar to the summary plot of SHAP. Moreover, ATCo can view more feature information by sliding up and down. The right part shows the local explanation of the training model, explaining the numerical distribution and weight of the specified feature in the training model. The display of this part is not fixed, and ATCo needs to click on the feature list in the left part. Up to 3 local feature explanations can be displayed at the same time, one is the main display and two are the secondary display, that is, data can be displayed without dragging the features. The part at the bottom explains the predicted results of each target. Different from the explanation of the training model, the data input for target prediction in real-time. The left side of this section provides data series, forecast results, forecast values and basic values. In addition, the right side of this part explains the prediction target in a visual method and provides the features name and real-time value of the features. Also, this area requires ATCo input operation to switch explanation information of different targets. The physical key input quickly switches to the target through the input window on the left.

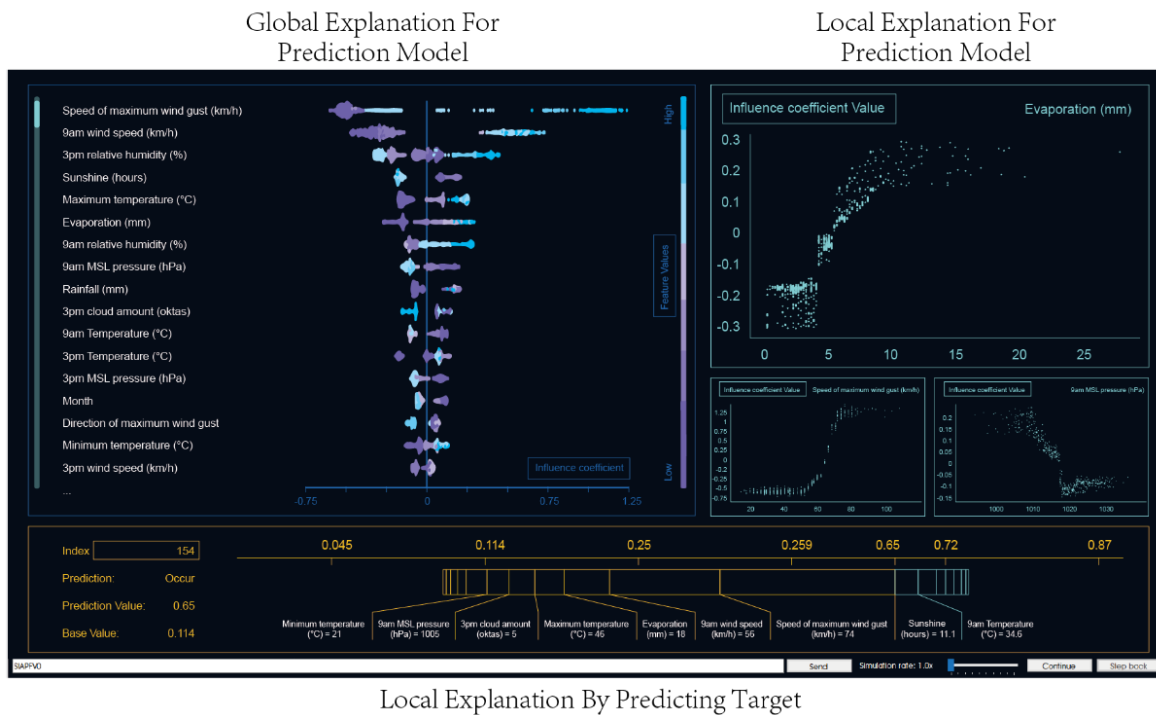


Figure 3. Prototype of detailed information mode.

V. Conclusion

A high level of automation support has been increasingly adopted to support tactical deconfliction duties in traditional Air Traffic Management (ATM). It is expected to further increase in the shortcoming UAS Traffic Management (UTM) framework. With the increasing role of Artificial Intelligence (AI), the complexity of machine learning black box has been increasing, which then raises the need for greater transparency through an Explainable AI (XAI). The research introduces the aviation incident and accident prediction model adopting the XGBoost algorithm, which is part of the ATM/UTM Decision Support System (DSS). The predicted results of the XGBoost model are well within the acceptable range with overall high accuracy. In terms of the explainability of the model, this study uses the SHAP interpretation method, which is a post-explanation model. The SHapley Additive exPlanations (SHAP) model provides an efficient explanation of the weight distribution of various features during the algorithm training, and also the explanation of the global and local output results. It was found that when the gust wind speed is greater than 65km/h, it will have a key positive impact on weather-related aviation events and accidents, while when it is less than 50km/h, it will have a negative impact. The accuracy and explainability of the predicted results have proved the reliability of the model. In the future work, the model not only needs to improve the accuracy further and reduce the processing time but also needs to shorten the prediction interval, so that the model can be further used in actual operations. To prove the efficiency of the proposed AI explanations and Human-Machine Interactions (HMI), ATCo-in-the-loop experimental verification activities are targeted.

Acknowledgments

The authors wish to thank and acknowledge Dr. Alessandro Gardi and Prof. Roberto Sabatini for their valuable supervisory guidance, and THALES Australia for supporting this work under the collaborative research project RE-02544-02003-15666.

References

- [1] Y. Kim, J. Jo, and M. Shaw, "A lightweight communication architecture for small UAS Traffic Management (sUTM)," ed: IEEE, 2015, pp. 1-29.
- [2] EUROCONTROL. (20 September). *European Network of U-space Demonstrators*. Available: <https://www.eurocontrol.int/product/european-network-u-space-demonstrators#:~:text=On%2019%20October%202019%2C%20the.operations%20safe%2C%20secure%20and%20green>
- [3] U. AIRSPACE. (2020, 20 September). *Progress on UTM and U-space regulations under the spotlight in high level GUTMA regulatory webinar*. Available: <https://www.unmannedairspace.info/latest-news-and-information/progress-on-utm-and-u-space-regulations-under-the-spotlight-in-high-level-gutma-regulatory-webinar/>
- [4] A. Gardi, R. Sabatini, and S. Ramasamy, "Multi-objective optimisation of aircraft flight trajectories in the ATM and avionics context," *Progress in Aerospace Sciences*, vol. 83, pp. 1-36, 2016.
- [5] T. Kistan, A. Gardi, R. Sabatini, S. Ramasamy, and E. Batuwangala, "An evolutionary outlook of air traffic flow management techniques," *Progress in Aerospace Sciences*, vol. 88, pp. 15-42, 2017.
- [6] B. Syd Ali, "Traffic management for drones flying in the city," *International journal of critical infrastructure protection*, vol. 26, p. 100310, 2019.
- [7] C. Krittanawong, H. Zhang, Z. Wang, M. Aydar, and T. Kitai, "Artificial Intelligence in Precision Cardiovascular Medicine," *J Am Coll Cardiol*, vol. 69, pp. 2657-2664, 2017.
- [8] M. Stephen, "Open-Source AI Bionic Leg Offers a Unified Platform for Prosthetics," *Machine Design*, 2019.
- [9] C. Huang, R. Mezencev, J. F. McDonald, and F. Vannberg, "Open source machine-learning algorithms for the prediction of optimal cancer drug therapies," *PLoS One*, vol. 12, p. e0186906, 2017.
- [10] L. Ding, "Human Knowledge in Constructing AI Systems — Neural Logic Networks Approach towards an Explainable AI," *Procedia computer science*, vol. 126, pp. 1561-1570, 2018.
- [11] J. Langan-Fox, M. J. Sankey, and J. M. Canty, "Human Factors Measurement for Future Air Traffic Control Systems," *Hum Factors*, vol. 51, pp. 595-637, 2009.
- [12] T. Kistan, A. Gardi, and R. Sabatini, "Machine Learning and Cognitive Ergonomics in Air Traffic Management: Recent Developments and Considerations for Certification," *Aerospace*, vol. 5, p. 103, 2018.
- [13] N. Pongsakornsathien, A. Gardi, R. Sabatini, T. Kistan, and N. Ezer, "Human-Machine Interactions in Very-Low-Level UAS Operations and Traffic Management," *the 39th Digital Avionics System Conference (DASC)*, Virtual Conference, 2020.
- [14] X. Ma, Z. Tao, Y. Wang, H. Yu, and Y. Wang, "Long short-term memory neural network for traffic speed prediction using remote microwave sensor data," *Transportation research. Part C, Emerging technologies*, vol. 54, pp. 187-197, 2015.
- [15] J. Elith, J. R. Leathwick, and T. Hastie, "A working guide to boosted regression trees," *J Anim Ecol*, vol. 77, pp. 802-813, 2008.
- [16] Y. Zhang and A. Haghani, "A gradient boosting method to improve travel time prediction," *Transportation research. Part C, Emerging technologies*, vol. 58, pp. 308-324, 2015.
- [17] R. Dalmau and F. Ballerini, "Improving the Predictability of Take-off Times with Machine Learning", SESAR, 2019.

- [18] S. Zhou, S. Wang, Q. Wu, R. Azim, and W. Li, "Predicting potential miRNA-disease associations by combining gradient boosting decision tree with logistic regression," *Comput Biol Chem*, vol. 85, p. 107200, 2020.
- [19] F. Zhang, X. Zhu, T. Hu, W. Guo, C. Chen, and L. Liu, "Urban Link Travel Time Prediction Based on a Gradient Boosting Method Considering Spatiotemporal Correlations," *ISPRS international journal of geo-information*, vol. 5, p. 201, 2016.
- [20] J. Cheng, G. Li, and X. Chen, "Research on Travel Time Prediction Model of Freeway Based on Gradient Boosting Decision Tree," *IEEE access*, vol. 7, pp. 7466-7480, 2019.
- [21] A. Barredo Arrieta, N. Díaz-Rodríguez, J. Del Ser, A. Bennetot, S. Tabik, A. Barbado, *et al.*, "Explainable Artificial Intelligence (XAI): Concepts, taxonomies, opportunities and challenges toward responsible AI," *Information Fusion*, vol. 58, pp. 82-115, 2020/06/01/ 2020.
- [22] M. T. Ribeiro, S. Singh, and C. Guestrin, "'Why Should I Trust You?': Explaining the Predictions of Any Classifier," 2016.
- [23] E. Strumbelj and I. Kononenko, "An Efficient Explanation of Individual Classifications using Game Theory," *Journal of Machine Learning Research*, vol. 11, pp. 1-18, 01/01 2010.
- [24] S. M. Lundberg, G. Erion, H. Chen, A. DeGrave, J. M. Prutkin, B. Nair, *et al.*, "Explainable AI for Trees: From Local Explanations to Global Understanding," 2019.
- [25] L. Onnasch, C. D. Wickens, H. Li, and D. Manzey, "Human Performance Consequences of Stages and Levels of Automation: An Integrated Meta-Analysis," *Hum Factors*, vol. 56, pp. 476-488, 2014.
- [26] D. B. Kaber, J. M. Riley, and K.-W. Tan, "Improved Usability of Aviation Automation Through Direct Manipulation and Graphical User Interface Design," *The International journal of aviation psychology*, vol. 12, pp. 153-178, 2009.
- [27] N. Campbell and M. Rojc, *Coverbal synchrony in human-machine interaction*. Boca Raton, Florida: CRC Press, 2014.
- [28] N. Zengeler, T. Kopinski, and U. Handmann, "Hand Gesture Recognition in Automotive Human-Machine Interaction Using Depth Cameras," *Sensors (Basel)*, vol. 19, p. 59, 2018.
- [29] M. Xu, Y. Guo, B. Yang, W. Chen, P. Lv, L. Fan, *et al.*, "Improving Aviation Safety using Synthetic Vision System integrated with Eye-tracking Devices," 2018.
- [30] Y. Lim, S. Ramasamy, A. Gardi, T. Kistan, and R. Sabatini, "Cognitive Human-Machine Interfaces and Interactions for Unmanned Aircraft," *Journal of Intelligent and Robotic Systems*, vol. 91, pp. 755-774, 2018.
- [31] N. Pongsakornsathien, Y. Lim, A. Gardi, S. Hilton, L. Planke, R. Sabatini, *et al.*, "Sensor Networks for Aerospace Human-Machine Systems," *Sensors*, vol. 19, p. 3465, 2019.
- [32] T. Chen and C. Guestrin, "XGBoost: A Scalable Tree Boosting System," in *International Conference on Knowledge Discovery and Data Mining*, ed: ACM, 2016, pp. 785-794.
- [33] P. Patidar and A. Tiwari, "Handling Missing Value in Decision Tree Algorithm," *International Journal of Computer Applications*, vol. 70, pp. 31-36, 05/17 2013.
- [34] W. Zhao, T. Joshi, V. N. Nair, and A. Sudjianto, "SHAP values for Explaining CNN-based Text Classification Models," 2020.
- [35] Y. Chen, "Understanding Machine Learning Classifier Decisions in Automated Radiotherapy Quality Assurance," ed: ProQuest Dissertations Publishing, 2020.
- [36] Laurae. (2016, 28 September). *Ensembles of tree-based models: why correlated features do not trip them — and why NA matters*. Available: <https://medium.com/data-design/ensembles-of-tree-based-models-why-correlated-features-do-not-trip-them-and-why-na-matters-7658f4752e1b>

Numerical Model of Radiative and Convective Heat Flux for Fuel Regression Rate of Wax-based Hybrid Rocket

Genya Naka¹ and

The University of Tokyo, Tokyo, 113-0033, Japan

Toru Shimada²

*Japan Aerospace Exploration Agency (JAXA),
Sagamihara, Kanagawa, 252-5210, Japan*

A numerical set up has been developed to predict the axial distribution and time history of fuel regression rates. The numerical approach is based on a quasi-one-dimensional CFD strategy, which is coupled with chemical equilibrium combustion; the wax-fuel regression rate has been simulated with the liquefying fuel theory developed by Karabeyoglu. Local radiation heat transfer from both the hot gas combustion molecules and soot particles is considered. To investigate the effect of radiative and convective heat transfer further, following two model are introduced. Three-dimensional soot radiation model is introduced in our numerical model. The effect that radiation enhances the blocking effect is introduced. It is shown that, when radiation heating of the fuel and blocking effect are taken into account, the calculated fuel regression rates exhibit values and axial profiles close to the ones observed experimentally.

I. Nomenclature

A	= port area	E_a	= activation energy for soot oxidation rate
A_{ave}	= average value in each 1000 iteration	F_r	= correction term of surface roughness
A_f	= pre-exponential factor accounting for the sooting propensity	G	= local mass flux
A_o	= pre-exponential factor for soot oxidation rate	I_b	= black-body radiance
$A_{residual}$	= residual of pressure or internal energy	L	= latent heat
A_s	= soot particulate surface ratio	L_{sp}	= laminar soot point
B	= blowing parameter	P, p	= pressure
B_g	= vapor blowing parameter	\dot{Q}	= heat flux
C	= constant for soot radiation	R	= port radius, or gas constant
C_{B1}, C_{B2}	= blowing correction coefficient	R_{he}, R_{hv}	= ratio of effective heats of gasification for entrainment and vaporization
C_H, C_{H0}	= Stanton number with and without blowing	T	= temperature
C_l	= heat capacity of liquid	ΔT_1	= temperature difference between melting point and vapor point
C_p	= specific heat at constant pressure	T_a	= activation temperature
$(C/O)_C$	= critical carbon and oxygen ratio where stop soot oxidation	V	= small section volume of soot area
		W_α	= atomic weight for element α , or molecular weight for chemical species α

¹ Master's Course Student, Aeronautics and Astronautics, School of Engineering, The University of Tokyo. Student Member AIAA. 1087003

² Professor, Institute of Space and Aeronautics, JAXA. Associate fellow AIAA.

Y_i	= mass fraction of chemical species i	ρ	= density
Y_s	= soot mass fraction	σ	= Stefan-Boltzmann coefficient
Z	= elemental mass fraction	$\bar{\tau}$	= transmissivity
a_{ent}	= entrainment parameter	τ_{sp}	= soot formation time
b_c, b_{c1}, b_{c2}	= carbon moll number per unit mass at local, fuel oxidizer	ϕ	= nondimensional axial velocity in boundary layer
e	= internal energy, or radiative energy from small section of soot area	Ψ_c	= ratio of soot inception oxidizer-to-fuel ratio to stoichiometric oxidizer-to-fuel ratio
f_s	= soot volume fraction	Ω	= solid angle
h	= enthalpy	ω_s	= net soot volume formation rate
h_f	= enthalpy of blowing fuel gas from port	ω_{sf}	= soot volume formation rate
h_m, h_e	= total heat of melting and boiling point at the liquid	ω_{so}	= surface soot oxidation rate
h_v	= effective heat of gasification		
k_s	= absorption coefficient of soot	<i>Subscripts</i>	
l	= column length	c	= convection
\dot{m}	= mass flow rate	$center$	= center of the hybrid rocket engine
\dot{r}	= regression rate	cl	= classical
t	= time	$e, edge$	= boundary edge
x	= coordinate, or carbon number in wax	ent	= entrainment
y	= distance from fuel surface, or hydrogen number in wax	$ethylene$	= ethylene
z	= axial distance from injector	f	= fuel
α, β	= parameter for entrainment, that of soot model, or absorptivity	fl	= flame
γ	= exponent for soot oxidation rate	g	= gas
δ	= boundary layer thickness	i	= molecular species, nodes number, or ray number
δ_g	= concentration boundary layer thickness	l	= liquid
ζ	= mixture fraction	k	= ray mesh point
ζ_c, ζ_{so}	= soot inception limits	m	= melt, or mean
η	= nondimensional radial distance in boundary layer	$norad$	= value in the absence of the radiation
η_g	= nondimensional radial distance in concentration boundary layer	o, ox	= oxidizer
θ	= elevation angle of ray	$q1d$	= quasi one dimensional
ε	= emissivity	r	= radiation, or reference
κ	= absorption coefficient	s	= soot
μ	= viscosity	st	= stoichiometric
ξ	= mixture fraction	v	= vapor
		$wall$	= wall
		wax	= wax
		0	= values in the fuel streams, or reference
		1	= values in the oxidizer streams

II. Introduction

A hybrid rocket often uses a solid fuel and a liquid or a gaseous oxidizer. Hybrid rocket is studied and developed actively for future space transportation with the hope for the benefit of its inherent safety characteristics. Because of the low regression rate of conventional hybrid rocket fuels, the solid grains tend to be long or with a complex geometry (like a multi-port fuel) in order to achieve a high thrust output. One method to increase the regression rate is to use liquefying fuels including paraffin-wax fuel. Karabeyoglu et al. [1] revealed that the droplet entrainment from unstable liquefying layer formed over the fuel surface would increase the regression rate. They also extended the classical theory of fuel regression rate [2] to a liquefying fuel hybrid rocket. In order to use the wax-based fuel hybrid rocket practically, predicting the time history and space distribution of the regression rate is essential for designing and controlling propulsion characteristic. In the case of paraffin wax fuel hybrid rockets, it is needed to predict both vapor and entrainment regression rates individually in order to estimate the degree of the deterioration of combustion efficiency due to unburned wax fuel droplets. The radiative heat transfer to the surface of the fuel grain is significant when the mass flux is small and consequently the convective heat transfer is relatively small [3]. Radiation can play

a significant role especially with paraffin wax which is known to be a heavily sooty fuel. There are few previous researches to predict the effect of the radiation numerically.

In this study, we developed a reduced spatial dimension model to predict the regression rate for a relatively long combustion time for a small computational cost. To evaluate the local fuel regression rate of paraffin-wax, we apply the Karabeyoglu model [1] of liquefying hybrid rocket (which will be recalled in the section III.A) in a quasi-one-dimensional CFD simulation. Chemical equilibrium, and radiation are considered to calculate the steady-state solution at given time instants in the burn. In this study, these two new model are applied to previous research [4] to further investigate the radiative and convective heat transfer. Three-dimensional soot radiation model is applied. The effect that radiation enhances the blocking effect [5] is also introduced. After calculation of the steady-state solution at each time step, the fuel port is updated, and the process is repeated until the combustion ends. We compare numerical results with experimental ones of Messineo et al. [6] to evaluate the validity of this prediction model. In addition, comparison will be made between numerical results and reconstructed time-dependent results [7] from experimental data [6].

III. Numerical set up

A. Regression rate theory of liquefying hybrid rocket

We first recall the results of the liquefying hybrid rocket fuels model which Karabeyoglu et al.[1] proposed. The total regression rate is expressed by the sum of the regression rates respectively due to the fuel vaporization and droplet entrainment as:

$$\dot{r} = \dot{r}_v + \dot{r}_{ent} . \quad (1)$$

Marxman pointed out that radiation and convection are not independent. [5] Radiation increase the rate of vaporization and aerodynamic blowing parameter and reduce the convective heat transfer. In this study, We apply this effect to the previous numerical model [4]. Marxman derived this following equation,

$$\dot{Q}_{total} = \dot{Q}_{C,norad} \exp\left(-\frac{\dot{Q}_r}{\dot{Q}_{C,norad}}\right) + \dot{Q}_r , \quad (2)$$

where the subscript 'norad' is the value when radiation is not assumed. To calculate the convection heat transfer which occurs under the given flow conditions in the absence of the radiation, the Karabeyoglu theory [1] is applied. The heat balance of liquid-gas surface is given as:

$$\dot{r}_{v,norad} + \left[R_{he} + R_{hv} \left(\frac{\dot{r}_{v,norad}}{\dot{r}_{norad}}\right)\right] \dot{r}_{ent} = \frac{\dot{Q}_{C,norad}}{\rho_f h_v} = F_r \frac{0.03\mu_g^{0.2}}{\rho_f} B \frac{C_H}{C_{H0}} G^{0.8} Z^{-0.2} , \quad (3)$$

$$R_{hv} = \frac{C_l \Delta T_1}{h_e + L_v}, \quad R_{he} = \frac{h_m}{h_e + L_v} . \quad (4)$$

In Eq. (3) the correction term of surface roughness, F_r , which is made by the ripple of liquefying layer because of a high momentum flow is given by

$$F_r = 1 + \frac{14.1\rho_g^{0.4}}{G^{0.8}(T_g/T_v)^{0.2}} . \quad (5)$$

The ratio of Stanton number with and without the blowing is described as follows:

$$\frac{C_H}{C_{H0}} \cong \frac{2}{2+1.25B^{0.75}} = \frac{C_{B1}}{C_{B1}+C_{B2}(\dot{r}_{v,norad}/\dot{r}_{cl})} , \quad (6)$$

$$C_{B1} = \frac{2}{2+1.25B^{0.75}} \quad C_{B2} = \frac{1.25B^{0.75}}{2+1.25B^{0.75}} . \quad (7)$$

Note that, differently from non-liquefying hybrid theory, only the vapor regression rate is taken into account for the aero dynamic blowing parameter. To relate the classical aerodynamic blowing parameter and the vapor blowing parameter, the following regression rate expression from classical analysis is needed,

$$\dot{r}_{cl} = \frac{0.03\mu_g^{0.2}}{\rho_f} B C_{B1} G^{0.8} Z^{-0.2} . \quad (8)$$

In this study, the blowing parameter is set to 5. This value was estimated by Karabeyoglu et al. [8].

After calculating the convection in the absence of the radiation, the vapor and the entrainment regression rates are calculated by:

$$\dot{r}_v + \left[R_{he} + R_{hv} \left(\frac{\dot{r}_v}{\dot{r}}\right)\right] \dot{r}_{ent} = \frac{\dot{Q}_{total}}{\rho_f h_v} = \frac{1}{\rho_f h_v} \left(\dot{Q}_{C,norad} \exp\left(-\frac{\dot{Q}_r}{\dot{Q}_{C,norad}}\right) + \dot{Q}_r\right) . \quad (9)$$

The entrainment regression rate is given by

$$\dot{r}_{ent} = a_{ent} (G^{2\alpha} / \dot{r}^\beta) . \quad (10)$$

According to Karabeyoglu et al. [1], the entrainment parameter of wax is $6.88 \times 10^{-14} \text{ m}^{8.5} \text{ s}^{0.5} / \text{kg}^3$, both α and β are 1.5. Di Martino et al. [9] pointed out that the entrainment parameter is influenced by the gas phase density [9] and they estimated it as $2.1 \times 10^{-13} \text{ m}^{8.5} \text{ s}^{0.5} / \text{kg}^3$. The gas density of the results of Karabeyoglu et al. is about 4.0 kg/m^3 . That of Di Martino et al. is about 1.0 kg/m^3 . In our experiments, the gas density is about 0.6 kg/m^3 , when the oxidizer mass flow rate is 50 g/s . The entrainment parameter in our experiments should be larger than these two experimental results. In this research, we estimate the entrainment parameter as $2.3 \times 10^{-13} \text{ m}^{8.5} \text{ s}^{0.5} / \text{kg}^3$ from Refs. [1,9].

B. Fuel properties

In this study, paraffin-wax chemical formula is $\text{C}_{35}\text{H}_{72}$. We made the following assumptions: paraffin fuel immediately decomposes into ethylene and hydrogen after wax evaporates with the following chemical reaction: $\text{C}_{35}\text{H}_{72} \rightarrow 35/2 \text{C}_2\text{H}_4 + \text{H}_2$; the enthalpy of the fuel gas is the same as the boiling point of gaseous wax. The fuel properties are listed in Table 2. The melting point, the boiling point, and the heat of fusion of HiMic-1080 (Nippon Seiro Co. Ltd.) are used. The standard enthalpy of formation of FT-0070 (Nippon Seiro Co. Ltd.) is used. The fuel density is measured before each burning test, and make an average is used. Other properties of wax were retrieved from Ref. [1].

Table 1 Wax properties

Melting point, K	Boiling Point, K	Heat capacity of solid, kJ/kg/K,	Heat capacity of liquid, kJ/kg/K	Heat of fusion, kJ/kg	Heat of vaporization, kJ/kg	Fuel density, kg/m ³	Standard enthalpy of formation, kJ/mol
357	745	2.03	2.92	180	163.5	896	-710

C. Computational fluid dynamics and chemical equilibrium

The combustion gas properties are computed by a quasi-one-dimensional CFD simulation and a chemical equilibrium analysis. The following 9 molecule species (CO , CO_2 , H_2 , H_2O , H , O , OH , O_2 , C_2H_4) are assumed in the combustion mixture, temperature and velocity are in equilibrium among each chemical species.

In this study, entrained wax droplets are assumed to be vaporized immediately and contribute to the gas mixture in the chamber. The fluid dynamics and carbon-element mixture fraction of the corresponding non-reactive flow are computed by solving the governing equations described by Eqs. (11-14), in which fuel mass and energy addition due to the fuel vaporization are handled as the product source terms:

$$\frac{\partial A\rho}{\partial t} + \frac{\partial \rho u A}{\partial x} = \rho_f \dot{r} l, \quad (11)$$

$$\frac{\partial A\rho u}{\partial t} + \frac{\partial (\rho u^2 A + P A)}{\partial x} = P \frac{dA}{dx}, \quad (12)$$

$$\frac{\partial (e + \frac{u^2}{2}) \rho A}{\partial t} + \frac{\partial (h + \frac{u^2}{2}) \rho u A}{\partial x} = \rho_f \dot{r} l h_f, \quad (13)$$

$$\frac{\partial A\rho\xi}{\partial t} + \frac{\partial A\rho u\xi}{\partial x} = \rho_f \dot{r} l. \quad (14)$$

In the case of this study, $\dot{r} = \dot{r}_v + \dot{r}_{ent}$ is used in Eqs.(11-14). Eq. (11) represents the conservation of mass, Eq. (12) the conservation of momentum, Eq. (13) the conservation of energy, and Eq. (14) the conservation of carbon element-base mixture ratio. The specific enthalpy of a gas mixture and the equation of state for an ideal gas are expressed as:

$$h = \sum Y_i h_i, \quad h_i = h_{i0} + \int_{T_r}^T C_{pi} dT, \quad e = h - \frac{p}{\rho} \quad (15)$$

$$p = \sum \frac{Y_i}{W_i} \rho RT, \quad (16)$$

Assuming that the transport velocities of carbon, hydrogen and oxygen are equal, other element mixture ratio can be obtained by only solving the transport equation of carbon-element based mixture ratio. By describing the fuel as C_xH_y , a carbon element mixture fraction of carbon, ξ , is defined as:

$$\xi = \frac{b_{C1} - b_{C2}}{b_{C1} - b_{C2}}, \quad (17)$$

$$b_{C1} = \frac{x}{12x+y}, \quad b_{C2} = 0, \quad (18)$$

Regarding the discretization of the governing equations, the numerical flux is calculated by SLAU scheme [10] with a second-order scheme MUSCL approach [11] with a limiter.

To calculate the local area averaged chemical equilibrium state, Helmholtz energy or Gibbs energy is minimized for the given gas properties. Both free energies are minimized by solving Euler-Lagrange equations [12]. The

calculation cost of chemical equilibrium is high because it is needed for repeated calculations. In this study, we have devised a table lookup method instead of repeated calculations in order to accelerate the calculation of this process. Look up tables are prepared before starting calculation. The gas phase viscosity is calculated by the polynomials, the viscosity is assumed to be the function of the gas temperature [12].

D. Effect of radiation and radiation from hot gas molecules

The radiative heat transfer from hot gas molecular and soot particles in the flame was estimated in this study. The absorptivity of the wax fuel grain is assumed to be 1. The net radiative heat flux is given by:

$$\dot{Q}_{r,total} = \alpha_{wax}\dot{Q}_{r,flamegas} + \alpha_{wax}\dot{Q}_{r,soot} - \dot{Q}_{r,wall} = \sigma(\varepsilon_g\alpha_{wax}T_{fl}^4 - \varepsilon_{wax}T_{wall}^4) + \alpha_{wax}Q_{r,soot} \quad (19)$$

Statistic narrow band model (SNB) [13] is used to investigate the effect of radiation from hot gas molecules. In the SNB model, we can evaluate the radiation from CO, CO₂, and H₂O, which are the main sources of the combustion products radiation. Marxman observed the flame thickness is about 0.06 inches [5]. It turned out that the flame emissivity was relatively insensitive to the particular choice of the reaction zone thickness [14]. In this study, the flame thickness is assumed 1mm and the oxidizer to fuel ratio is assumed to be stoichiometric. The hot gas molecular radiation from the other region assumed to be negligible.

E. Radiation from soot particles

In this study, the radial distribution of soot and the volume radiation from soot particles were estimated. We developed a soot volume radiation model and applied it to our numerical simulation. In this study, we develop the three-dimensional soot radiation model that can take into account the radiation from all directions and applied this model to the previous research [4]. (See section III.E.3) By using this model, we do not need to assume the view factor.

1. Global soot model

In this section, we will provide more details about the global soot model [15–18]. In the global soot model, we can estimate the upper and the lower soot inception limits of the oxidizer to fuel ratio. We can also estimate the volumetric soot formation rate, and surface oxidation rate. By using these values, we can estimate the soot volume fraction.

The upper and the lower soot inception limits of oxidizer to fuel ratio can be written as:

$$\zeta_c = \Psi_c \zeta_{st} \quad \Psi_c = 2.5, \quad (20)$$

$$\zeta_{so} = \frac{(C/O)_c}{(C/O)_c + \left(\frac{1}{\zeta_{st}} - 1\right) / \left(2 + \frac{1y}{2x}\right)} \quad (C/O)_c = 0.6, \quad (21)$$

where Ψ_c is assumed to be fuel-independent constant [15], $(C/O)_c$ is the critical carbon to oxygen ratio at which soot oxidation stops. This latter for wax has not been investigated yet, so $(C/O)_c$ is assumed to be 0.6 [15,19].

ζ and ξ both represent oxidizer to fuel ratio, but definitions are different. The relation between ζ and ξ can finally be written as: [4]

$$\zeta = \frac{\xi + \alpha\beta\xi^2}{1 + \alpha + \beta}, \quad \alpha = \frac{W_O}{2W_H} \frac{Z_{H,1} - Z_{H,0}}{Z_{O,0} - Z_{O,1}}, \quad \beta = \frac{2W_O}{W_C} \frac{Z_{C,1} - Z_{C,0}}{Z_{O,0} - Z_{O,1}}, \quad (22)$$

Next, we will explain the soot formation and oxidation rates. The net soot formation rates can be written as [15]:

$$\omega_s = \begin{cases} \omega_{sf} - \omega_{so}'' \rho Y_s A_s & (\zeta \in [\zeta_{so}, \zeta_c]) \\ -\omega_{so}'' \rho Y_s A_s & (\zeta \in [0, \zeta_{so}]) \end{cases}, \quad (23)$$

Previous researchers experimentally investigated the soot particle surface area per unit mass, and they found that it can vary from 20m²/g to 270m²/g [15]. In this study, the soot particle surface area per unit mass is assumed to be 100 m²/g. The soot volumetric formation rates and the surface soot oxidation rates can be written as:

$$\omega_{sf} = A_f \rho^2 \left(Y_{Fu,0} \frac{\zeta - \zeta_{st}}{1 - \zeta_{st}} \right) T^\gamma e^{-\frac{T_a}{T}}, \quad (24)$$

$$\omega_{so} = A_o [O_2] T^{1/2} e^{-\frac{E_a}{RT}}, \quad (25)$$

The activation temperature is equal to 2000 K and is fuel independent [16]. A_o is the pre-exponential factor which equals to 120 [20]. E_a is the activation energy for soot oxidation rate and is equal to 163,540 kg/m²/s [15]. $[O_2]$ is the molar concentration.

To determine A_f , the laminar soot point (LSP) is used. LSP means the flame height. The soot formation time is proportional to the LSP, and the soot propensity A_f is inversely proportional to LSP.

$$\begin{aligned} L_{sp,fuel} &\propto \tau_{sp}, \\ A_{f,fuel} &\propto L_{sp,fuel}^{-1}. \end{aligned} \quad (26)$$

$A_{f,fuel}$ of ethylene is equal to 4.0×10^{-5} [16] and $L_{sp,fuel}$ of ethylene is equal to 0.106 m [18]. From these values, $A_{f,fuel}$ for the wax can be obtained by Eq. (27) [15].

$$\frac{A_{f,fuel}}{A_{f,ethylene}} = \frac{L_{sp,ethylene}}{L_{sp,fuel}}. \quad (27)$$

$L_{sp,fuel}$ is calculated by Eq. (28) [21].

$$L_{sp,fuel} = -1.03x + 88.3 \text{ mm}, \quad (28)$$

where x is the carbon number. Please notice that when the LSP is used for evaluation of $A_{f,fuel}$, the LSP of wax and ethylene must be evaluated under the same test condition. For example, smoke points for each fuel are seen to increase with wick diameter [21].

2. Radial distribution of soot volume fraction

Marxman et al. [2] assumed that momentum diffusion and concentration diffusion are similar (Reynolds analogy). In our model, we also apply this assumption. In their study [2], they assumed the following radial profile of axial velocity:

$$\phi = \frac{\eta^n [1 + (\frac{1}{2}B)\eta^n]}{1 + \frac{1}{2}B}, \quad \eta = \frac{y}{\delta}, \quad \phi = u/u_{edge}, \quad n = \frac{1}{7}, \quad (29)$$

where y is the distance from fuel grain, and u is the axial velocity at y . For the Reynolds analogy, thus, the radial profile of carbon molar fraction, ξ , can be written as:

$$\xi(\eta_g) = \xi_{wall}(1 - \phi(\eta_g)) + \xi_{edge}\phi(\eta_g) \quad \eta_g = \frac{y}{\delta_g}, \quad (30)$$

where ξ_{wall} is the carbon molar fraction at the fuel grain wall, which is assumed to be 1, and ξ_{edge} is the carbon molar fraction at the edge of the concentration boundary layer, which is assumed to be 0. By area integrating $\xi(\eta_g)$, the following relation stands:

$$\xi_{Q1D} = \frac{1}{\pi R^2} \int_0^R 2\pi r \xi(r) dr = \frac{\delta_g}{\pi R^2} \int_0^1 2\pi (R - \delta_g \eta) \xi(\eta) d\eta. \quad (31)$$

The concentration boundary layer thickness is obtained from Eq. (31). When the concentration boundary layer thickness is larger than the port radius, the carbon molar fraction at the center is determined by Eq. (32).

$$\xi_{Q1D} = \frac{1}{\pi R^2} \int_0^R 2\pi r \xi(r) dr = \int_0^1 2\pi (1 - \eta) (\xi(\eta)) d\eta, \quad \xi(\eta_g) = \xi_{wall}\phi(\eta_g) + \xi_{center}(1 - \phi(\eta_g)), \quad (32)$$

where ξ_{center} is the carbon molar fraction at the center of the chamber. From these calculations the radial distribution of ξ can be calculated from the local port diameter and the quasi-one-dimensional carbon molar fraction.

When the diffusion of the soot is neglected, the soot balance equation in the steady state and neglecting the axial and circumferential directions can be written as:

$$\frac{\partial \rho Y_s v}{\partial y} = \omega_s. \quad (33)$$

Eq. (34) can be discretized as:

$$\rho_{i+1} v_{i+1} Y_{s,i+1} - \rho_i v_i Y_{s,i} = \omega_{s,i} \Delta y. \quad (34)$$

When $Y_{s,i+1}$ is smaller than 0, we assume that net soot formation rate is zero and $Y_{s,i}$ is written as:

$$Y_s = \frac{\omega_{sf}}{\omega_{so} \rho A_s} \quad (35)$$

In this model, we must assume the profile of the radial velocity. We assume that the fuel gas is a wax. The temperature of fuel gas is assumed to be the boiling point of wax. The radial velocity is assumed to decrease linearly from the fuel grain surface to the edge of the concentration boundary layer and be zero at the edge of the boundary layer. The gas velocity radial component at the grain surface grain is written as:

$$v_{wall} = \dot{r}_v \frac{\rho_{fuel}}{\rho_{wall_gas}} \quad (36)$$

3. Calculate the soot radiation

Gray body radiation is assumed in this study. To evaluate the radiation on the surface, soot area is divided into small sections and add up all radiation from the small sections. The effect that radiation is absorbed in the middle of the ray is also taken into account. Radiation energy emitted from soot clouds of volume ΔV to the solid angle $\Delta \Omega$ is written as;

$$e = k_s I_b \Delta V \Delta \Omega. \quad (37)$$

Integrating the soot emission over all wavenumber, the absorption coefficient of soot is calculated by Eq. (38) [18].

$$k_s = C f_s T . \quad (38)$$

C is assumed to be a constant equal to $1226 \text{ m}^{-1}\text{K}^{-1}$ [18]. The radiation emitted from soot is absorbed in the middle of the ray. The energy at the middle point of the k is written as;

$$e_k = e_{k-1} \bar{\tau}_{k-1 \rightarrow k}, \quad \tau_{k-1 \rightarrow k} = \exp(-k_s l_{k-1 \rightarrow k}) \quad (39)$$

where $l_{k-1 \rightarrow k}$ is the mesh size of ray at point k. Radiant heat flux on the fuel surface considering the radiation from all the ray is as follows;

$$\dot{Q}_r = \sum_i e_{end,i} \sin \theta_i \quad (40)$$

where i is each direction of the ray from small section and e_{end} is the radiative energy at the end of the ray. θ_i is the elevation angle of each ray i.

F. Boundary and convergence conditions, calculation process

The conditions at the oxidizer inlet and the flow outlet are listed in Table 4. and 5

Table 4 Inlet condition		Table 5 Outlet condition	
Properties	conditions	Properties	conditions
Pressure	Extrapolation	Pressure	Extrapolation (Supersonic flow) 0.1MPa (Subsonic flow)
Temperature	300K	Density	Extrapolation
Mass flow rate	Arbitrarily	Velocity	Extrapolation
Mixture ratio	0 (Only GOX)	Mixture ratio	Extrapolation

The geometry of the port is determined by the experiment [6]. The initial port diameter is 40mm, the fuel port length is 100mm, and the nozzle throat diameter is 14mm. The computational region is equally divided and each grid spacing is 2mm. The time step for the calculation of the steady state for each geometry is set to 10^{-7} s.

First, CFD and CEA are solved and properties about the gas in the combustion chamber are obtained for the initial geometry. From them, the local regression rates are calculated. The criterion of convergence is checked at every 1000 iterations. We judge the flow is stable when the following criterion is satisfied.

$$A_{residual} < 10^{-5}, \quad A_{residual} = \frac{A_{ave_new} - A_{ave_old}}{A_{ave_old}} \quad (41)$$

The average of pressure and internal energy at every 1000 iterations are used to calculate the residuals. When Eq. (41) is met, the time is increased, and the fuel port is updated. The time step for geometry updates is 0.5 s. The soot radiation is calculated every 200 steps and the regression rate every 15 steps.

IV. Results and discussion

A. The numerical results of heat flux and regression rate

The numerical results of the local heat flux and the regression rate at the beginning of combustion are shown in Fig. 1. The oxidizer mass flow rate is 50g/s.

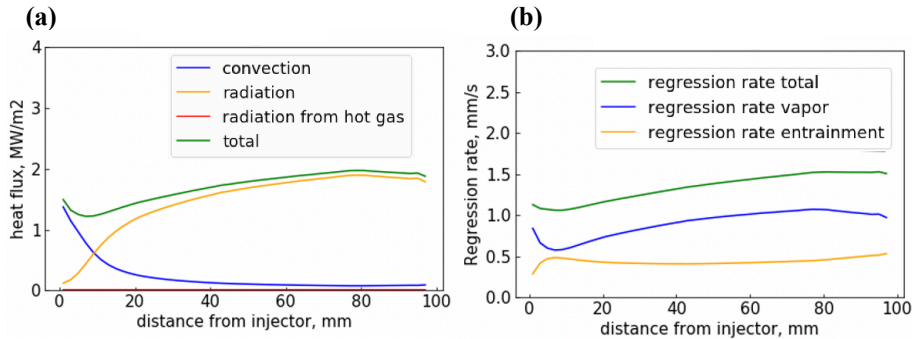


Fig. 1 (a) The numerical results of axial distribution of convective heat flux, radiative heat flux from hot gas molecular and total heat flux at $t=0$ s. (b) The numerical results of axial distribution of vapor, entrainment, and total regression rate at $t=0$ s. The oxidizer mass flow rate is 50 g/s.

Fig. 1 (a) shows that the convective heat transfer is dominant and the radiative heat transfer is small at the injector side. Radiative heat transfer increases as you go downstream because soot area is developed. On the other hand, the convective heat transfer becomes negligibly small as you go downstream because of the radiative heat transfer enhance the blocking effect. The numerical results of the time history of the history of the history of spatial-averaged heat flux and regression rate is shown in Fig.2.

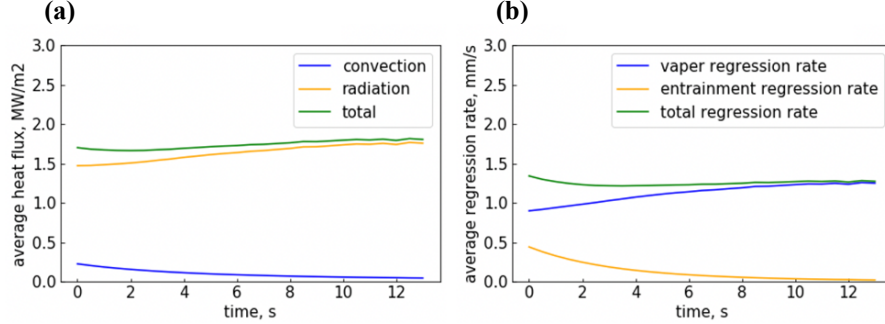


Fig.2 (a) Numerical result of the history of spatial-averaged heat flux. (b) Numerical result of the history of spatial-averaged regression rate. The oxidizer mass flow rate is 50 g/s.

Fig.2 (a) shows that radiative heat transfer accounts for most of the total heat flux. Convective heat flux is negligibly small because the blocking effect is enhanced by radiation. Fig.2 (b) shows that the entrainment regression rate is relatively important at first, but the entrainment is near zero at the end of burning because mass flux is small.

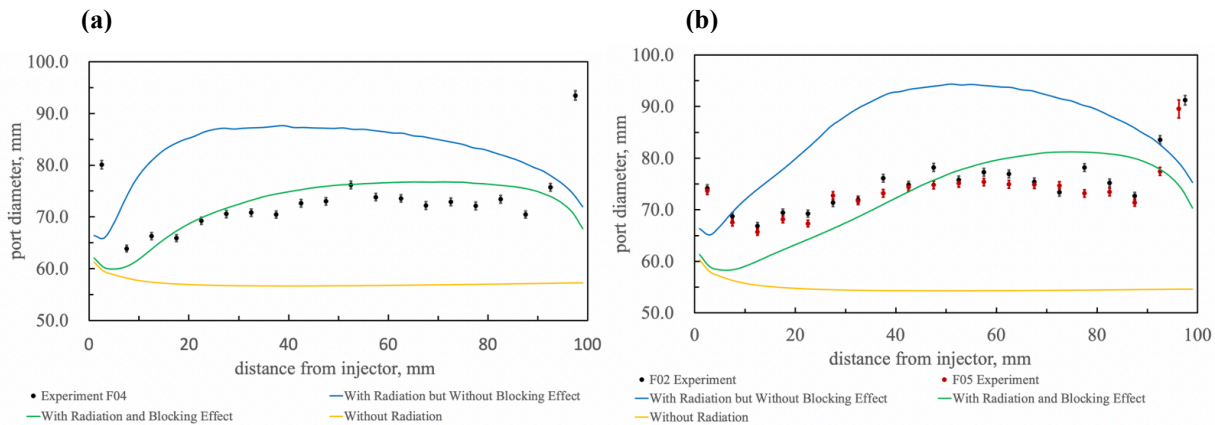
B. Compare with numerical results and experimental results.

In this section, we compare the numerical results and the experimental results of Messineo et al. [6]. Experimental conditions are listed in Table 2.

Table 2 Test conditions [6]

No.	Average oxidizer mass flow rate, g/s	Combustion duration, s
#F01	20.04	22
#F02	29.79	18
#F03	44.91	5
#F04	48.85	13
#F05	29.62	18

The numerical results and the experimental results [6] of port diameter are shown in Fig. 3. The numerical results which is not considered the radiation and is considered the radiation but not considered the blocking effect are also shown in Fig.3.



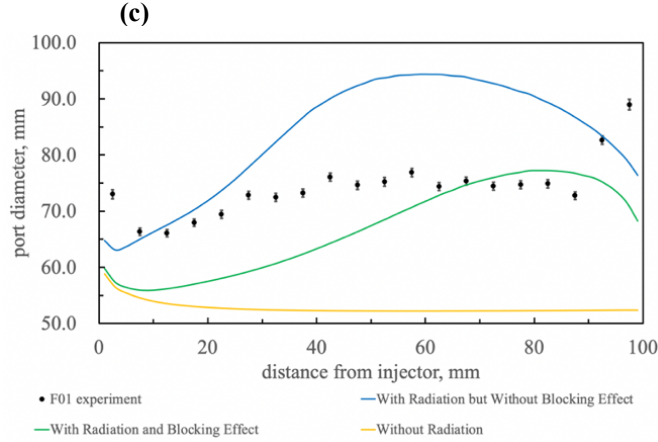


Fig. 3 Numerical results of final port diameter and the experimental result. The oxidizer mass flow rates are (a) 50 g/s, (b) 30g/s, and (c) 20 g/s. The combustion durations are (a) 13 s, (b) 18 s, and (c) 22 s. The numerical models are the models without radiation, with radiation but without blocking effect, and with radiation and blocking effect.

Fig. 3 clearly shows that when the radiation heating is not considered, the numerical results of the regression rate are underestimated and the distribution of the local regression rate deviates significantly at the downstream region. Fig. 3 also shows that when the radiation heating is considered and blocking effect is not considered, the numerical results of regression rate are overestimated. On the other hand, when both the radiation heating and the blocking effect are considered, the numerical results on the distribution of the local regression rate qualitatively agrees well with the experiments and numerical results can estimate the minimum consumption which is appeared in experimental results. The regression rate at the nozzle side is decreasing probably because flame outside the fuel grain is not considered. When the oxidizer mass flow rate is 20g/s, the regression rate is underestimated. As I mentioned at the section III. A, the entrainment parameter is influenced by gas density [9] and inversely proportional to the 1.5th power of the gas density. The gas density when the mass flow rate is 20g/s is about 0.25kg/m³. Probably entrainment parameter for oxidizer mass flow rate of 50g/s is larger than that of 20g/s. Other effects such as recirculation [22] or acceleration of main flow [23] probably affect the regression rate.

C. Compare with numerical results and reconstruction technique results

The reconstruction estimation of spatial averaged regression rate and the oxidizer to fuel ratio (Ref. [6]) and the numerical regression rate data are shown in Fig. 4. The oxidizer mass flow rate is 50g/s, and the combustion duration is 13 sec.

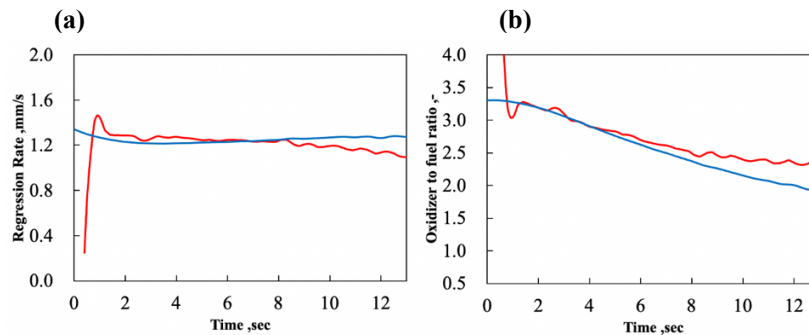


Fig. 4. Numerical result and the reconstruction result of (a) regression rate and (b) oxidizer to fuel ratio. The blue line is the numerical results that radiative heat transfer and blocking effect are considered. Red line is reconstruction result (Experiment number is F04 [6]).

From Fig. 4, the numerical results approximately agree well with the numerical results. Fig. 4 (b) clearly shows that the oxidizer to fuel ratio is decreasing over time. Such decreasing trend is also shown in other experiments [6].

The numerical result of the history of the oxidizer to fuel ration is shown in Fig. 5. When the radiation is not considered, the oxidizer to fuel ratio is increasing over time. Whereas when the radiation is considered, the oxidizer to fuel ratio is decreasing over time with or without blocking effect. From these facts, it is suggested that the

phenomenon that the oxidizer to fuel ratio is decreasing over time is due to the radiative heat transfer. It is also suggested that the effect of radiative heat transfer plays significant role in the experiments by Messineo et al. [6], which is done in a low mass flux region.

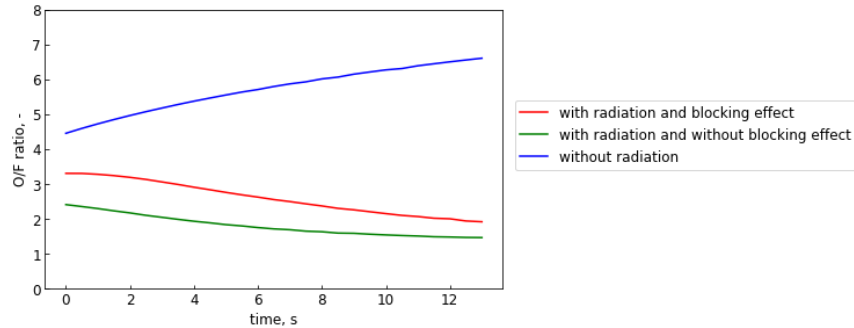


Fig.5 Three numerical model result of oxidizer to fuel ratio. The blue line is the model without radiation. The green line is the model with radiation but without blocking effect. The red line is the model with radiation and blocking effect. The oxidizer mass flow rate is 50g/s.

Finally, it can be said that although the reconstruction technique cannot calculate the exact solution because of the multiple solution problem [6], our numerical method seems efficient to calculate the regression rate.

V. Conclusions

In this research, we developed a numerical method to predict the internal ballistics of hybrid rocket burning liquefying fuels and validated it by comparison with experimental combustion test results. The regression rate model for liquefying fuel proposed by Karabeyoglu et al.[1] is combined with a quasi one-dimensional CFD and chemical equilibrium analysis to calculate the axial distribution and time history of both vapor regression rate and entrainment regression rate. Local radiation from high temperature gas molecules and soot particles is considered. We improve radiative and convective heat transfer model and these two new model are applied to the previous model [4]. Three-dimensional soot radiation model is introduced in our numerical model. The effect that radiation enhances the blocking effect is also introduced. When the effect of radiation and blocking effect are taken into account, the numerical results show good agreement with the experimental data. This observation demonstrates that the radiation effect is important because convective heat transfer is negligibly small because of the blocking effect, when the mass flux is small. The entrainment parameter may be affected by the gas properties such as gas density. Further investigation of the entrainment phenomenon should be investigated. Other effects such as recirculation or acceleration of the main flow should also be investigated further.

Acknowledgments

I would like to thank to Dr. Messineo, Dr. Kitagawa, and Dr. Carmicino for providing the experimental data [6] and discussing our researches. I would also like to thank Mr. Takeshita and Mr. Sicat for discussing our researches.

References

- [1] Karabeyoglu, M. A., Altman, D., and Cantwell, B. J. "Combustion of Liquefying Hybrid Propellants: Part 1, General Theory." *Journal of Propulsion and Power*, Vol. 18, No. 3, 2002, pp. 610–620. <https://doi.org/10.2514/2.5975>.
- [2] Marxman, G., and Gilbert, M. "Turbulent Boundary Layer Combustion in the Hybrid Rocket." *Symposium (International) on Combustion*, Vol. 9, No. 1, 1963, pp. 371–383. [https://doi.org/10.1016/S0082-0784\(63\)80046-6](https://doi.org/10.1016/S0082-0784(63)80046-6).
- [3] ESTEY, P., ALTMAN, D., and MCFARLANE, J. "An Evaluation of Scaling Effects for Hybrid Rocket Motors." *27th Joint Propulsion Conference*, Reston, Virginia, 1991. <https://doi.org/10.2514/6.1991-2517>.
- [4] Naka, G., Messineo, J., Kitagawa, K., Carmicino, C., and Shimada, T. "Prediction of Space and Time Distribution of Wax-Based Fuel Regression Rate in a Hybrid Rocket." *AIAA Propulsion and Energy 2020 Forum*, Reston, Virginia, 2020. <https://doi.org/10.2514/6.2020-3768>.

- [5] Marxman, G. A. "Combustion in the Turbulent Boundary Layer on a Vaporizing Surface." *Symposium (International) on Combustion*, Vol. 10, No. 1, 1965, pp. 1337–1349. [https://doi.org/10.1016/S0082-0784\(65\)80268-5](https://doi.org/10.1016/S0082-0784(65)80268-5).
- [6] Messineo, J., Kitagawa, K., Carmicino, C., Shimada, T., and Paravan, C. "Reconstructed Ballistic Data Versus Wax Regression-Rate Intrusive Measurement in a Hybrid Rocket." *Journal of Spacecraft and Rockets*, 2020, pp. 1–14. <https://doi.org/10.2514/1.A34695>.
- [7] Wernimont, E. J., and Heister, S. D. "Reconstruction Technique for Reducing Hybrid-Rocket Combustion Test Data." *Journal of Propulsion and Power*, Vol. 15, No. 1, 1999, pp. 128–136. <https://doi.org/10.2514/2.5401>.
- [8] Karabeyoglu, A., Cantwell, B., and Stevens, J. "Evaluation of the Homologous Series of Normal Alkanes as Hybrid Rocket Fuels." *41st AIAA/ASME/SAE/ASEE Joint Propulsion Conference & Exhibit*, Reston, Virginia, 2005. <https://doi.org/10.2514/6.2005-3908>.
- [9] Di Martino, G. D., Mungiguerra, S., Carmicino, C., and Savino, R. "Computational Fluid-Dynamic Modeling of the Internal Ballistics of Paraffin-Fueled Hybrid Rocket." *Aerospace Science and Technology*, Vol. 89, 2019, pp. 431–444. <https://doi.org/10.1016/j.ast.2019.04.019>.
- [10] Shima, E., and Kitamura, K. "Parameter-Free Simple Low-Dissipation AUSM-Family Scheme for All Speeds." *AIAA Journal*, Vol. 49, No. 8, 2011, pp. 1693–1709. <https://doi.org/10.2514/1.J050905>.
- [11] Van Leer, B. "Towards the Ultimate Conservative Difference Scheme. IV. A New Approach to Numerical Convection." *Journal of Computational Physics*, Vol. 23, No. 3, 1977, pp. 276–299. [https://doi.org/10.1016/0021-9991\(77\)90095-X](https://doi.org/10.1016/0021-9991(77)90095-X).
- [12] Gordon, S., and McBride, B. J. Computer Program for Calculation of Complex Chemical Equilibrium Compositions and Applications. *NASA Reference Publication 1311*.
- [13] Rivière, P., and Soufiani, A. "Updated Band Model Parameters for H₂O, CO₂, CH₄ and CO Radiation at High Temperature." *International Journal of Heat and Mass Transfer*, Vol. 55, Nos. 13–14, 2012, pp. 3349–3358. <https://doi.org/10.1016/j.ijheatmasstransfer.2012.03.019>.
- [14] Chiaverini, M. J., Kuo, K. K., Peretz, A., and Harting, G. C. "Regression-Rate and Heat-Transfer Correlations for Hybrid Rocket Combustion." *Journal of Propulsion and Power*, Vol. 17, No. 1, 2001, pp. 99–110. <https://doi.org/10.2514/2.5714>.
- [15] Yao, W., Zhang, J., Nadjai, A., Beji, T., and Delichatsios, M. A. "A Global Soot Model Developed for Fires: Validation in Laminar Flames and Application in Turbulent Pool Fires." *Fire Safety Journal*, Vol. 46, No. 7, 2011, pp. 371–387. <https://doi.org/10.1016/j.firesaf.2011.06.004>.
- [16] Beji, T., Zhang, J. P., and Delichatsios, M. "Determination of Soot Formation Rate from Laminar Smoke Point Measurements." *Combustion Science and Technology*, Vol. 180, No. 5, 2008, pp. 927–940. <https://doi.org/10.1080/00102200801894398>.
- [17] Beji, T., Zhang, J. P., Yao, W., and Delichatsios, M. "A Novel Soot Model for Fires: Validation in a Laminar Non-Premixed Flame." *Combustion and Flame*, Vol. 158, No. 2, 2011, pp. 281–290. <https://doi.org/10.1016/j.combustflame.2010.08.017>.
- [18] Lautenberger, C. W., de Ris, J. L., Dembsey, N. A., Barnett, J. R., and Baum, H. R. "A Simplified Model for Soot Formation and Oxidation in CFD Simulation of Non-Premixed Hydrocarbon Flames." *Fire Safety Journal*, Vol. 40, No. 2, 2005, pp. 141–176. <https://doi.org/10.1016/j.firesaf.2004.10.002>.
- [19] Kumfer, B. M., Skeen, S. A., and Axelbaum, R. L. "Soot Inception Limits in Laminar Diffusion Flames with Application to Oxy-Fuel Combustion." *Combustion and Flame*, Vol. 154, No. 3, 2008, pp. 546–556. <https://doi.org/10.1016/j.combustflame.2008.03.008>.
- [20] Leung, K. M., Lindstedt, R. P., and Jones, W. P. "A Simplified Reaction Mechanism for Soot Formation in Nonpremixed Flames." *Combustion and Flame*, Vol. 87, Nos. 3–4, 1991, pp. 289–305. [https://doi.org/10.1016/0010-2180\(91\)90114-Q](https://doi.org/10.1016/0010-2180(91)90114-Q).
- [21] Allan, K. M., Kaminski, J. R., Bertrand, J. C., Head, J., and Sunderland, P. B. "Laminar Smoke Points of Wax Candles." *Combustion Science and Technology*, Vol. 181, No. 5, 2009, pp. 800–811. <https://doi.org/10.1080/00102200902935512>.
- [22] Carmicino, C., and Sorge, A. R. "Role of Injection in Hybrid Rockets Regression Rate Behaviour." *Journal of Propulsion and Power*, Vol. 21, No. 4, 2005, pp. 606–612. <https://doi.org/10.2514/1.9945>.
- [23] Boyarshinov, B., Volchkov, E. P., and Lukashov, V. V. "Heat Transfer in an Accelerated Chemically Reacting Boundary Layer." *Doklady Akademii Nauk*, Vol. 350, No. 6, 1996, pp. 763–769.

Statistical Reliability Analysis of Interplanetary Spacecraft Operating at Different Interplanetary Extremity

Malaya Kumar Biswal M*

Department of Physics,

School of Physical Chemical and Applied Sciences,

Pondicherry University, Kalapet, Puducherry - 605 014, India.

Reliability of the spacecraft determines the extent of success probability and mission accomplishment. Despite effective testing and integration, the complexity of the space environment affects reliability. In this paper, we investigate the reliability behaviour of interplanetary spacecraft operating at different interplanetary extremities. So, our investigation assesses spacecraft in interplanetary space with the context of the interplanetary boundary (between distinct planetary orbit or within the bounds of heliopause). From the perspective of spacecraft reliability in interplanetary space, we have excluded planetary landers, atmospheric probes, and satellites maneuvering earth orbit. Thus, we have identified 131 spacecraft (includes 82 probes within the bounds of Sun and the Earth, and 49 within the bounds of Earth and Heliopause) along with their gross mass at launch and lifespan. Based on acquired data, we first conduct a non-parametric analysis of spacecraft reliability to obtain two reliability curves for distinct interplanetary extremity. We then perform a parametric fit (Weibull Distribution) over the data to show the analogy of reliability behaviour. Results showed that the spacecraft operating beyond the extremity of the Earth and the Mars exhibits increased reliability than any other interplanetary extremity. In addition to this, we execute reliability analysis over spacecraft of various mass categories (Small-Medium-Large) to testify the reliability effect interpreted by Dubos in 2010. Finally, we discuss the possible factors and causes accountable for the difference in reliability behaviour concerning the spacecraft design and integration, testing, and constraints in considering spacecraft mass.

I. Nomenclature

\bar{R}	= Mean Reliability of the Spacecraft	Var	= Variance
$\hat{R}(t)$	= Reliability function (Kaplan-Meier)	Γ	= Gamma function
$S_r(t)$	= Weibull Distribution function for the spacecraft	$\lambda(t)$	= Hazard function / Hazard rate
EH	= Earth-Heliopause	β	= Shape parameter
LCL	= Lower Confidence Level	UCL	= Upper Confidence Level
$R(t)$	= Weibull Reliability function	η	= Scale parameter
SE	= Sun-Earth	σ	= Standard Deviation
t	= Lifespan of the Spacecraft (Years)	τ	= Mean life of the spacecraft
AU	= Astronomical Unit	ESA	= European Space Agency

A. Interplanetary Boundary Condition

- **SE-Extremity:** The region of interplanetary space extending from the proximity of the Sun to the Earth.
- **EH-Extremity:** The region of interplanetary space extending from the proximity of the Earth to the farthest point of the Solar System say Heliopause.

* Master of Science Student, Department of Physics, Pondicherry University, Kalapet, Puducherry, India. Student Member AIAA (Membership No: 908157). Email: malaykumar1997@gmail.com; mkumar97.res@pondiuni.edu.in

II. Introduction

Reliability of the spacecraft is the key parameter to determine the extent of mission accomplishment and any disruption in reliability may result in spacecraft failures. Scientists and Data analysts have limited their reliability analysis to earthbound satellites [1-6] and their studies to on-orbit spacecraft failures [3]. From the perspective of spacecraft reliability operating at different interplanetary boundary and space environments, no statistical analysis has been found in any of the past technical literature. So, to sustain the stride of reliability analysis and to assert the reliability effect established by Dubos in 2010, we have collected the spacecraft data (in terms of gross mass at launch and lifespan in years) that were launched between 1960 to 2020 from [7-9] and appropriate online resources of space agencies to perform the non-parametric and parametric estimation. Our analysis showed that the spacecraft operating beyond the extremity of the Earth and Mars exhibits maximum reliability as compared to any other interplanetary extremity. Finally, we represent the graphical results and discuss the potential causes responsible for the substantial increase in the reliability behaviour of the spacecraft at EH-Extremity and reduced reliability at SE-Extremity.

III. Research Methodology and Data Description

A. Research Methodology

- Our analysis uses spacecraft data of success, partial success, failed (lifespan estimated until its last active state), and ongoing active spacecraft (lifespan estimated based on the elapsed time as of October 2020) in hered in interplanetary space. The data were gathered in terms of spacecraft's gross mass in kilograms and lifespan in years.
- Overall data were categorized under SE and EH extremity. The categorization excludes the data of planetary landers, sample return and atmospheric probes, impactors, and rovers.
- Statistical analysis of non-parametric (Kaplan-Meier estimation) and parametric (Weibull probability) estimation were performed over the spacecraft's data in terms of iteration-1 (for SE extremity) and iteration-2 (for EH Extremity).
- Then, we perform the same procedure of reliability analysis over the spacecraft data of various mass category [Small (0-500kg) - Medium (500-2500 kg) - Large (>2500kg)] to compare and assert the reliability effects found by G.F.Dubos.
- Finally, with reference to the results obtained, we discuss the possible causes accountable for variance in reliability behaviour of spacecraft operating in the different interplanetary environment.

B. Data Description and Categorization

For our analysis, we gathered spacecraft data from [7-9] in terms of spacecraft's gross mass in kg and lifespan in years from the time frame of 1960 to 2020. The sample template of data collection is shown in table-1. And our database has a total of 131 spacecraft of successful, partial success, failed, and active missions. To ensure homogeneity, sister spacecraft with a similar lifespan is considered as one. Similarly, en-route space missions and eliminated from our database for further analysis (i.e., Emirates Mars Mission and Mars 2020 Rover). Finally, overall data were categorized under extremity conditions (i.e. out of 131 spacecraft, 82 spacecraft falls under SE-Extremity, and 49 under EH-Extremity).

Table 1 Sample Template of Data Collection

Spacecraft Name	Launch Date	Failure/Decay Date	Launch Mass (kg)	Lifespan (Years)
Pioneer 5	11 Mar 1960	26 Jun 1960	63	0.30
Pioneer 6A	16 Dec 1965	08 Dec 2000	63	34.94
....
New Horizons	19 Jan 2006	XX Oct 2020*	401	14.66

*lifespan estimated for ongoing missions as of October 2020

IV. Formulations

A. Kaplan-Meier Estimation

Kaplan-Meier is a non-parametric statistical estimation used to determine the survival function from the lifetime measurement of data. Here, we modify the equation to estimate the spacecraft reliability at different interplanetary boundaries based on their lifespan data. From the equation of Kaplan-Meier estimation [10], the modified expression for the reliability function of the spacecraft can be defined as

$$\widehat{R}(t) = \prod_{t_i \leq t} \left(1 - \frac{s_i}{n_i}\right) \quad (1)$$

s_i - number of spacecraft operating or accomplished its mission intent

n_i - number of spacecraft failed at time t

t_i - initial time after leaving low earth orbit

t - time elapsed for the spacecraft to accomplish its intent/ time elapsed at the current operating state.

B. Weibull Distribution

Similar to Kaplan-Meier estimation, Weibull probability distribution (parametric function) is used to estimate the reliability analysis for electronic components and spacecraft subsystems. Here, we define the Weibull distribution function [11] for the spacecraft at appropriate extremity as

$$S_f(t) = \frac{\beta}{\eta} \left(\frac{t}{\eta}\right)^{\beta-1} e^{-\left(\frac{t}{\eta}\right)^\beta} \quad (2)$$

where β is the shape parameter, η is the scale parameter, and t is the lifespan of spacecraft in years.

Relation of Failure rate with β : (i) $\beta < 1$ defines that the failure rate decreases with time (lifespan), (ii) for $\beta \approx 1$ the spacecraft has a fairly constant failure rate, and (iii) for $\beta > 1$ the failure rate of the spacecraft increases with time(lifespan).

Reliability of the Spacecraft

Weibull Reliability expression for the spacecraft from parametric estimation can be defined as

$$R(t) = e^{-\left(\frac{t}{\eta}\right)^\beta} \quad (3)$$

where the reliability is the exponential function of scale parameter η and shape parameter β .

Hazard Function of the Spacecraft

The hazard function or hazard rate $\lambda(t)$ of the spacecraft can be defined as the ratio of Weibull distribution function to Weibull reliability that can be mathematically written as

$$\lambda(t) = \frac{\beta}{\eta} \left(\frac{t}{\eta}\right)^{\beta-1} \quad (4)$$

Mean Reliability and Median life of the Spacecraft

The expression for the mean and median life of the spacecraft can be defined from the Weibull distribution function that can be written as

$$\text{Mean Reliability } \bar{R} = \eta \Gamma\left(\frac{1}{\beta} + 1\right) \quad (5)$$

$$\text{where } \Gamma \text{ is the gamma function } \Gamma(n) = \int_0^\infty e^{-t} t^{n-1} dt \quad (6)$$

$$\text{Median Life } \tau = \eta (\ln(2))^{\frac{1}{\beta}} \quad (7)$$

Variance from Weibull Distribution Function

$$\text{Variance} = \eta^2 \left[\Gamma\left(1 + \frac{2}{\beta}\right) - \left(\Gamma\left(1 + \frac{1}{\beta}\right)\right)^2 \right] \quad (8)$$

V.Non-Parametric and Parametric Analysis of Spacecraft Reliability

A. Non-Parametric Kaplan-Meier Estimation

Our database holds three types of data samples 1) time to the successful mission accomplishment, 2) time to the failure of spacecraft, and 3) time to the ongoing/active missions. This study intends to understand the reliability behaviour of the spacecraft when exposed to the distinct interplanetary environment. So, we have performed a powerful Kaplan-Meier estimation with random data censoring. The lifespan of the spacecraft in years was inputted as time range with random data censoring.

B. Parametric Weibull Probability Distribution

To understand the analogy of reliability behaviour exhibited by interplanetary spacecraft by the Kaplan-Meier method, we perform the Weibull probability distribution function over the spacecraft data. The procedure follows random data censoring and Weibull analysis over the lifespan (in years) of spacecraft by maximum likelihood estimation of single Weibull fit. Relevant equations and formulations are shown in equation (1-8).

VI. Results of Non-Parametric and Parametric Analysis

A. Non-Parametric Results for SE-Extremity: Kaplan-Meier estimation shows that the spacecraft operating within the boundary of Sun and Earth exhibits 48% reliability after 2 years of functioning and can extend their performance to $\approx 30\%$ reliability after 6 years. At this extremity, the spacecraft experiences a hazard rate of 10% after 4 years and 20% after 15 years of operation. The reliability behavior of spacecraft at SE-Extremity is shown in Fig 1.

B. Non-Parametric Results for EH-Extremity: Comparably for the spacecraft operating between the bounds of Earth and the farthest point of the Solar System (say Heliopause) exhibits 60% reliability after 2 years of operation and extends up to 40% reliability after 6 years. Spacecraft within this extremity is exposed to a hazard rate of 10% after 6 years and 20% after 18 years. It can be understood from Fig 2.

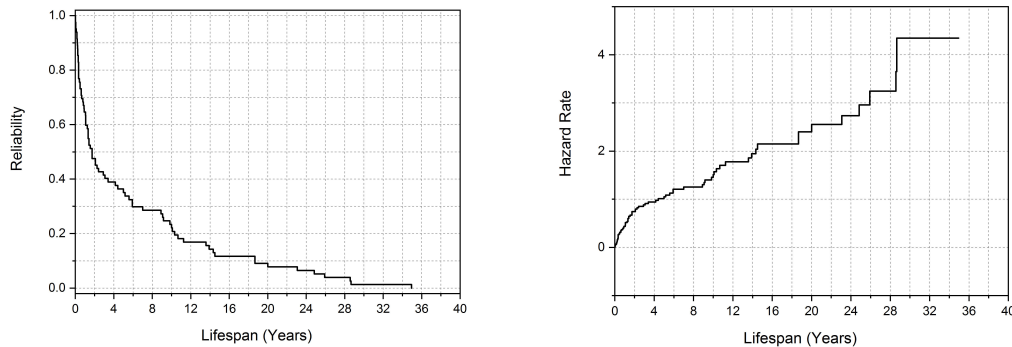


Fig 1 Kaplan-Meier Curve for Reliability and Hazard Rate of Interplanetary Spacecraft at SE-Extremity

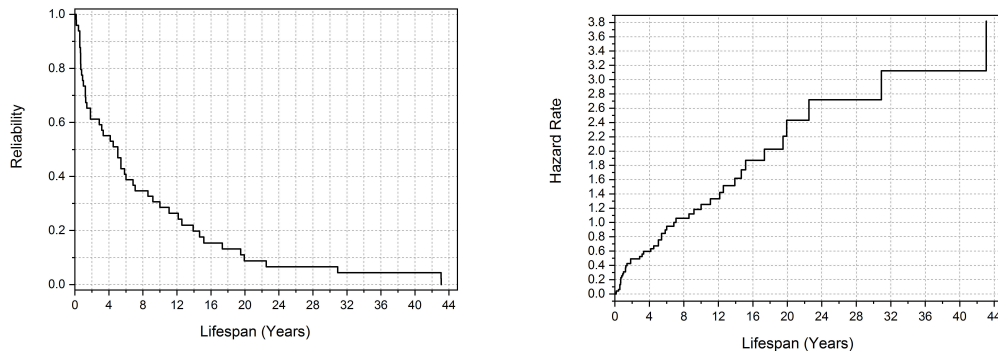


Fig 2 Kaplan-Meier Curve for Reliability and Hazard Rate of Interplanetary Spacecraft at EH-Extremity

C. Parametric Results for SE-Extremity: Parametric estimation using Weibull Distribution showed that the spacecraft operating within the boundary of SE-Extremity reflects 35% reliability after 4 years of operation with 95% upper confidence of 48% and lower confidence of 30%. The spacecraft can function up to a maximum extent of 36 to 38 years. At this extremity, the spacecraft encounters a 20% hazard rate after 2.5 years that gradually decreases with an increase in lifespan of space probes shown in Fig 3.

D. Parametric Results for EH-Extremity: Contrary to the SE-Extremity, the spacecraft functioning between the boundary of Earth and to a limited extent of Solar System shows 52% reliability after 4 years of operation with 95% upper confidence of 70% and lower confidence of 48%. The spacecraft at this extremity experiences a 10% hazard rate after 12.5 years of operation which readily decreases relative to an increase in lifespan. This effect can be realized from Fig 4. Further, the spacecraft at this boundary can last up to an upper limit of 48 years of operation.

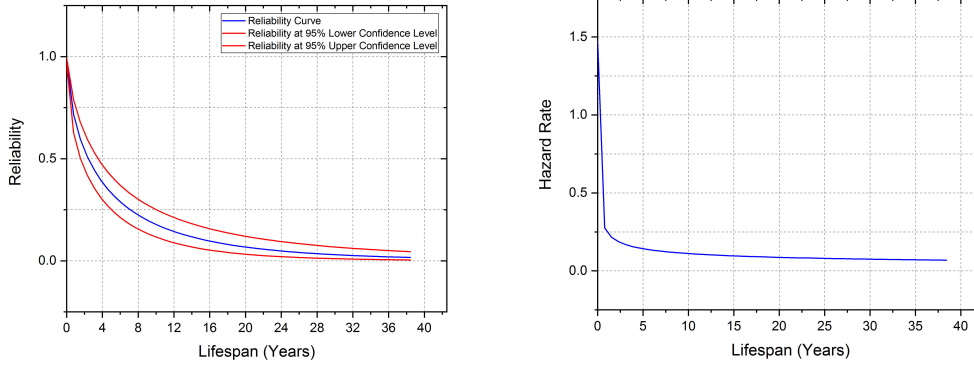


Fig 3 Weibull Curve for Reliability and Hazard Rate of Interplanetary Spacecraft at SE-Extremity

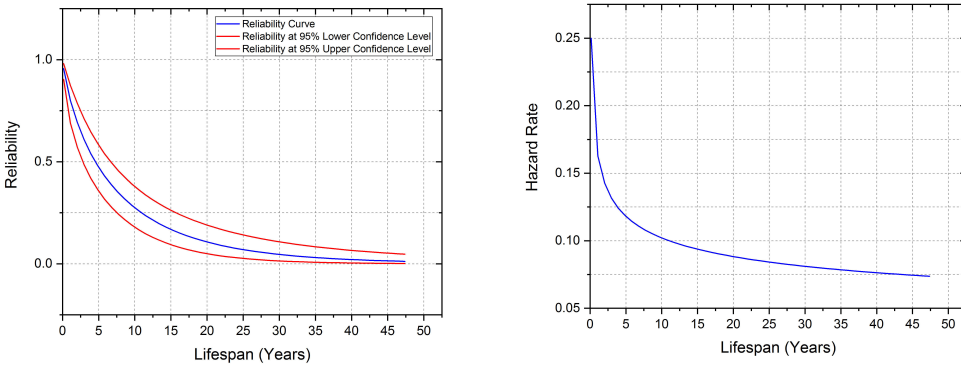


Fig 4 Weibull Curve for Reliability and Hazard Rate of Interplanetary Spacecraft at EH-Extremity

E. Comparison of Results

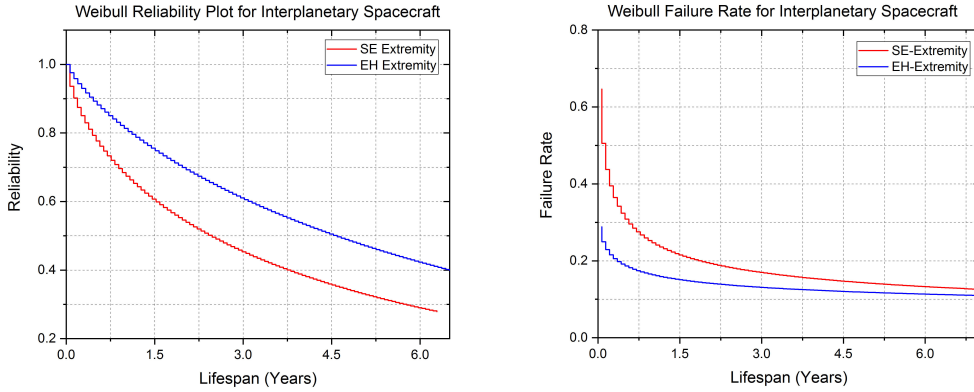


Fig 5 Weibull Reliability and Failure Rate Plot for Interplanetary Spacecraft at SE & EH-Extremity

Comparing both parametric and non-parametric results in terms of reliability behaviour and hazard rate of interplanetary spacecraft inherited in two interplanetary boundaries, we have found that the boundary limit from the Earth to the Heliopause renders a promising environment for substantial reliability than the Sun-Earth boundary. Our analysis shows that the approximate mean reliability of spacecraft at SE-Extremity is 58% which is smaller than 74% at EH-Extremity with a variance of $Var_{SE}=0.0238$ to $Var_{EH}=0.0145$ shown in table 4. More precisely the reliability behaviour can be understood from the equations

$$R(t)_{SE}=e^{-\left(\frac{t}{4.29271}\right)^{0.64439}} \quad \text{and} \quad R(t)_{EH}=e^{-\left(\frac{t}{7.23227}\right)^{0.79025}} \quad (9) \text{ and } (10)$$

Similarly, both extremity shows a shape parameter ($\beta=0.644$ at SE-Extremity) and ($\beta=0.790$ at EH-Extremity) shown in table 4. And overall shape parameter is found to be less than unity (i.e. $\beta < 1$). The parameter $\beta < 1$ depicts the failure rate or the hazard rate decreases with an increase in lifespan that can be precisely understood from the expressions,

$$\lambda(t)_{SE}=0.150 \left(\frac{t}{4.29271}\right)^{0.64439-1} \quad \text{and} \quad \lambda(t)_{SE}=0.109 \left(\frac{t}{7.23227}\right)^{0.79205-1} \quad (11) \text{ and } (12)$$

Further, the results and estimates from the non-parametric and parametric analyses are shown in the table-2. Estimated values calculated from equation (5, 7,8) are shown in table 4.

Table 2 Mean and Quartile Estimate from Kaplan-Meier Analysis

Quartile Estimate	SE-Extremity			EH- Extremity			Mean Estimate	SE-Extremity	EH-Extremity
Percent Failures	25	50	75	25	50	75	Estimate	5.9393	8.2871
Estimate	0.49	1.74	9.16	1.00	5.05	12.16	Standard Error	0.9128	1.4950
95% LCL	0.31	1.08	5.00	0.66	1.83	6.83	95% LCL	4.1501	5.3568
95% UCL	0.92	3.41	13.58	1.83	7.08	17.33	95% UCL	7.7284	11.2174

Table 3 Estimate from Weibull Probability Distribution Function

Weibull Parameters	SE-Extremity				EH-Extremity			
DF	1	1	1	1	1	1	1	1
Estimate	1.4569	1.5518	4.2927	0.6443	1.9785	1.2654	7.2322	0.7902
Standard Error	0.1820	0.1356	0.7816	0.0563	0.1918	0.1422	1.3875	0.0888
95% LCL	1.1000	1.3075	3.0043	0.5429	1.6025	0.0152	4.9656	0.6340
95% UCL	1.8137	1.8417	0.5429	0.7647	2.3545	1.5772	10.5336	0.9849

Table 4 Parametric Results of Spacecraft Reliability

Results	Notation	SE-Extremity	EH-Extremity
Shape Parameter	β	0.64439	0.79025
Scale Parameter	η	4.29271	7.23227
Variance	Var	0.0238	0.0145
Mean Reliability	\bar{R}	0.586	0.740
Mean Life	τ	2.4316	4.5413
Standard Deviation	σ	0.154330	0.120698

VII. Hypothesis on Possible Causes responsible for distinct Reliability behaviour

A. Distribution of Cosmic Radiation over Interplanetary Space

High energetic particles from Cosmic rays and Galactic cosmic rays greatly affect and cause rupture to the electronic components of the spacecraft. Notable incidence is the damage of electronic chips aboard the spacecraft computer of the Fobos-Grunt mission [12]. Galactic cosmic rays, solar cosmic rays, and solar particle events are the natural phenomena of the space environment. High energetic particles from these phenomena can cause damage to the on-board circuitry system of spacecraft thereby rupturing the electronic components and hardware. Notable incidences were the damage of the electrical system of Nozomi and Phobos spacecraft on their interplanetary transit from Earth to Mars [12]. So, the spacecraft operating within the bounds of SE-Extremity have increased vulnerability to the solar particle event and solar flares or eruption that ultimately impairs the circuitry system. Since the SE-Extremity lies in close proximity to the Sun with a distance of 0.4 - 1.0 AU. Comparably the spacecraft functioning within the bounds of EH-Extremity exhibits substantial reliability because the spacecraft has decreased vulnerability to the harmful effects of solar events as well as the intensity of cosmic rays. Observation from the radiation measurement of Pioneer and Voyager spacecraft showed that the intensity of cosmic radiation gradually decreases as we move far from the SE-Extremity [13-16]. Since solar events play a significant role in the distribution of radiation throughout the solar system environment [17-18]. Hence we conclude that the EH-Extremity is found to have a promising environment for the interplanetary spacecraft to operate with extended reliability.

B. Power Source of the Spacecraft

Spacecraft power plays a principal component in spacecraft's reliability. Major interplanetary spacecraft encounters a challenge in power generation at both extremities. Because the solar panels of the spacecraft operating at SE-Extremity get depleted with time due to the extreme temperature and collision of hazardous particles during

solar eruptions or events, resulting in the loss of power and spacecraft function. Therefore, spacecraft malfunction proportionate decreased reliability. In parallel to the mission operation, solar power generation poses a challenging task for the spacecraft operating at EH-Extremity as the intensity of solar irradiance decreases from SE to the EH Extremity and remain unavailable during solar conjunctions [21]. But the potential cause for the increased reliability behaviour at EH-Extremity may be due to the power source, i.e. the magnificent and extended operating probes like Voyager 1 and 2, and New Horizons that embraces nuclear thermoelectric generators as their primary power source which provides uninterrupted power supply throughout the mission life and enhancing reliability [22-24].

C. Space Environment and Temperature

The region of interplanetary space between the Sun and the Heliopause is habituated with a hostile space environment adversely affecting the spacecraft’s operation and reliability. The region at SE-Extremity experiences extreme temperature that ultimately affects the stabilization of the spacecraft’s internal temperature. Further, the probe’s internal temperature assists the spacecraft in the management of on-board fuel storage plighted for attitude control and course-correcting maneuver and determines the efficiency or lifetime of electronic components. Hence this hostile environment at SE-Extremity prompts a potential impact on spacecraft reliability whereas the environment at EH-Extremity experiences curtailed temperature due to the non-availability of adequate solar irradiance [21]. Thus the EH-Extremity affords an auspicious environment for nuclear-powered spacecraft to maintain the probe’s internal thermal stability and improved reliability as compared to the SE-Extremity.

D. Impact of Spacecraft Mass

The gross mass of the spacecraft (which includes the spacecraft’s dry mass + fuel mass) has a significant contribution to their reliability. But here the fuel mass has a direct role in the determination of spacecraft reliability. The spacecraft is fuelled to perform maneuver correction and to stabilize the attitude control system to remain itself in a stabilized orbit around the planetary body. So, fuel depletion results in failure of orientation and attitude control system resulting in the disposal of spacecraft despite the perfect functioning of spacecraft’s sub-system. Notable spacecraft encountered this issue is ESA’s Cassini Spacecraft that finally plunged into Saturn’s atmosphere [25]. Considerably both extremities possess a challenging environment for fuel management and cryogenic storage to maintain zero boil-off, the SE-Extremity may endorse fuel depletion and the EH-Extremity may spawn fuel solidification (Nozomi’s fuel solidification during interplanetary transit [12]). These circumstances may result in a malfunction of attitude thrusters and a drop in reliability. Hence, the spacecraft with a considerable amount of fuel mass within a mass limit of 500-2500 kg is desirable for a reliable mission.

E. Spacecraft Components, Design, Testing, and Integration

The quality of electronic components and hardware, dimension of the spacecraft, its attentive integration and testing affects the reliability of the spacecraft. For example, the standard of electronic components manufactured during the 1970s that are integrated with the series of interplanetary spacecraft’s like Pioneer 10 & 11 (that operated for more than 20 years), Voyager 1 & 2, and New Horizons in 2006 are still functioning and has crossed their estimated mission lifetime [26-27]. But modern electronic components have reduced dimension with uncertainty in their reliability. Further, large spacecraft is associated with complex hardware and wiring configuration that has increased the chances of human error during the integration of spacecraft in ground-based laboratories. Furthermore, lack of adequate shielding and design, testing and validation of spacecraft’s sub-system, and negligent fabrication are the other factors substantially influencing the spacecraft’s reliability.

VIII. Testification of Reliability Effect Interpreted by G.F.Dubos.2010

A. Data Categorization and Censoring

In this section, the spacecraft data were sorted in ascending order concerning the gross mass. Then the overall data were distributed to the mass column of distinct mass category shown in table 5.

Table 5 Spacecraft Categorization

Spacecraft’s Mass Category	Mass Range	Example at SE-Extremity	Example at EH-Extremity
Small	0-500 kg	Helios A & B, Genesis	Mariner 4, New Horizons
Medium	500-2500 kg	Venera 11 & 12, Messenger	Solar Orbiter, Voyager 1 & 2
Large	>2500 kg	Venera 14 and 15	Tianwen-1

There were 50 spacecraft in the small category, 55 spacecraft in the medium-sized category, and 26 spacecraft in the large category. These sorted data were analyzed over powerful Kaplan-Meier estimation and then with Weibull probability fit with random data censoring. Our analysis executed here is to address the question of whether the spacecraft's mass affects reliability. And to assert the reliability effect interpreted by Duboset.al.2010 employing Castet and Saleh spacecraft's reliability model [1, 6].

IX. Non-Parametric and Parametric Results for Mass Category

A. Non-Parametric Results (Kaplan-Meier)

Small Category: Our analysis showed that the spacecraft exhibits $\approx 50\%$ reliability after 2.5 years of operation in interplanetary space, and extends up to 10 years with 20% reliability. Spacecraft of this category can function up to a maximum lifespan of 20-25 years.

Medium Category: The spacecraft under this category exhibited excellent reliability than the other two mass categories. Our analysis showed that the spacecraft operates with 60% reliability after 2.5 years of continuous operation and extends up to 5 years with 55% reliability. It continues its operation with the efficiency of 20% reliability for 13 years in interplanetary space. The maximum estimated lifespan of the spacecraft of this category is 25-30 years.

Large Category: This category spacecraft exhibits $\approx 30\%$ reliability after 2.5 years of operation with a hazard rate of 15% and the reliability readily drops to 10% after 7 years with a hazard rate of 25% at 7.5 years. Space probes having this mass limit is expected to function up to a maximum lifespan of 10-13 years. The reliability and Hazard rate estimated from the parametric analysis is shown in Fig 6.

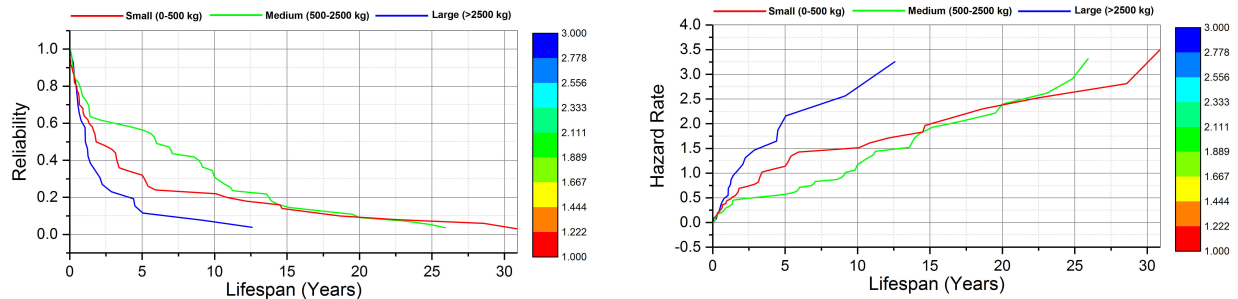


Fig 6 Kaplan-Meier Estimation: Reliability and Hazard Rate Plot for Various Mass Category

B. Parametric Results (Weibull Fit)

Small Category: Weibull analysis showed that the spacecraft exhibits $\approx 30\%$ reliability after 7 years of operation with 95% upper confidence of 40% reliability and lower confidence of 20%. The overall hazard rate of 1%, the probe experiences during their period of operation from 10-20 years.

Medium Category: Medium-sized spacecraft exhibits $\approx 48\%$ reliability after 5 years of functioning with 95% upper confidence of 60% reliability and lower confidence of 30%. The spacecraft of this category is found to have an overall hazard rate of 1% after 10 years of operation that gradually decreases relative to an increase in lifespan.

Large Category: Large-sized spacecraft having mass >2500 kg exhibits $\approx 20\%$ reliability after 5 years of operation with 95% upper confidence of 50% and lower confidence of 10% reliability. Spacecraft having this much mass limit is found to have a maximum hazard rate of 3% after 5 years of operation and a minimum of 2% after 10 years. The reliability behaviour of spacecraft of various mass category and its hazard rate is shown in Fig 7-8.

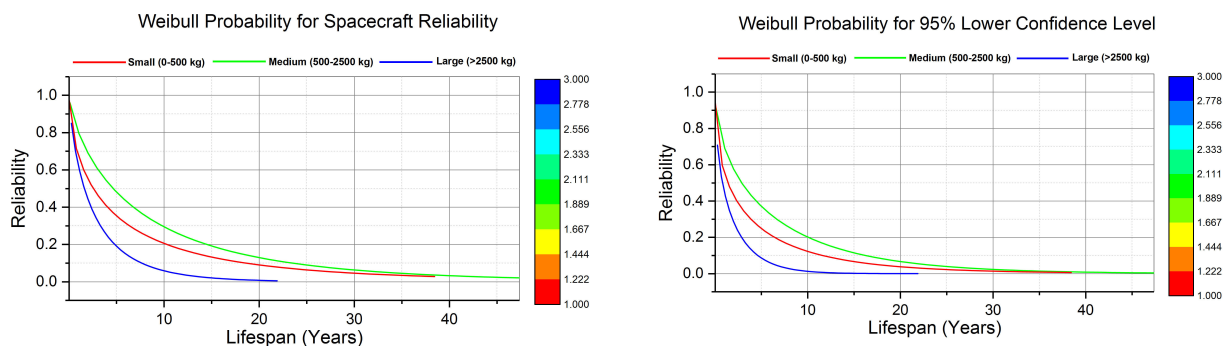


Fig 7 Weibull Analysis: Reliability and 95% LCL Reliability Plot for Various Mass Category

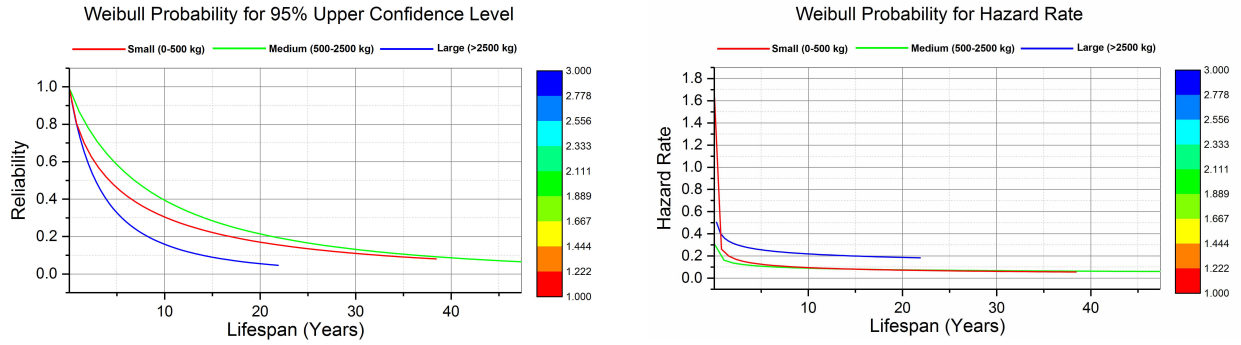


Fig 8 Weibull Analysis: 95% UCL Reliability and Hazard Rate Plot for Various Mass Category

C. Comparison of Results

In contrast to the results, medium-sized spacecraft exhibits superior reliability than the other two mass categories with the least hazard rate of 1%. It can be realized from the expression below

$$\text{Reliability, } R(t)_{\text{Medium}} = e^{-\left(\frac{t}{7.63407}\right)^{0.74117}} \quad (13)$$

$$\text{Hazard Rate, } \lambda(t)_{\text{Medium}} = 0.097 \left(\frac{t}{7.63407}\right)^{0.74118-1} \quad (14)$$

where $\lambda(t)_{\text{Medium}}$ is the hazard function that decreases with an increase in the lifespan of medium-sized spacecraft.

The resultant plot for the Reliability and Hazard rate of the spacecraft from scale and shape parameter of various mass categories is shown in Fig 9. Further, Mean and Quartile estimate from Kaplan-Meier estimation and Weibull probability distribution is shown in table 6-8.

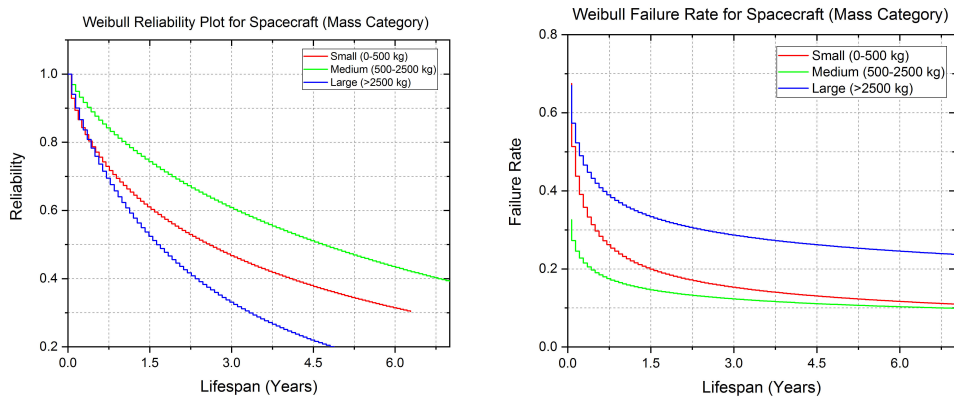


Fig 9 Weibull Probability: Reliability and Hazard Rate Plot for Various Mass Category

Table 6 Mean Estimate from Kaplan-Meier Analysis

Mean Estimate	Small Category	Medium Category	Large Category
Estimate	6.4262	8.5254	2.9407
Standard Error	1.3071	1.2933	0.8692
95% LCL	3.8642	5.9905	1.2371
95% UCL	8.9881	11.0603	4.6444

Table 7 Quartile Estimate from Kaplan-Meier Analysis

Quartile Estimate	Small Category			Medium Category			Large Category		
Percent Failures	25	50	75	25	50	75	25	50	75
Estimate	0.65	1.83	5.93	0.9	6	11.25	0.58	1.08	2.87
95% LCL	0.31	1.25	3.33	0.42	2.08	9.16	0.33	0.66	1.26
95% UCL	1.33	3.41	14.66	2.08	9.16	15.16	1.08	2.08	5.05

Table 8 Estimate from Weibull Probability Distribution

Parameters	Small Category				Medium Category				Large Category			
DF	1	1	1	1	1	1	1	1	1	1	1	1
Estimate	1.5467	1.6517	4.6960	0.6054	2.0326	1.3492	7.6340	0.7411	0.9586	1.2916	2.6082	0.7742
Standard Error	0.2478	0.1885	1.1637	0.0691	0.1924	0.1511	1.4693	0.0830	0.2704	0.1887	0.7054	0.1131
95% LCL	1.0610	1.3206	2.8893	7.6326	1.6553	1.0831	5.2351	0.5950	0.4285	0.9700	1.5350	0.5814
95% UCL	2.0324	2.0658	7.6326	0.7572	2.4098	1.6805	11.1322	0.9232	1.4887	1.7198	4.4315	1.0309

Table 9 Parametric Results of Spacecraft Reliability (Mass Category)

Results	Notation	Small Category	Medium Category	Large Category
Shape Parameter	β	0.6054	0.7411	0.7742
Scale Parameter	η	4.6960	7.6340	2.6082
Variance	Var	0.0180	0.0116	0.0802
Mean Reliability	\bar{R}	0.5538	0.6964	0.6877
Mean Life	τ	2.5614	4.6518	1.6216
Standard Deviation	σ	0.1343	0.1079	0.2833

D. Possible causes accountable for Reliability behaviour of Spacecraft of Various Mass Category

We have not discussed much the possible causes behind the reliability behaviour of spacecraft of distinct mass category, because the significance and possible causes were clearly explained in [6]. However, the role of spacecraft reliability in terms of mass category in interplanetary space was discussed in section 7 “Impact of Spacecraft Mass”.

X. Conclusion

Reliability of the spacecraft is one of the significant parameters to ascertain the extent of mission proficiency and competency. Numerous space environmental factors enhance and recede reliability. To realize whether the spacecraft at distinct interplanetary extremity exhibits different reliability, we performed statistical analysis employing Kaplan-Meier and Weibull Probability distribution over spacecraft data. Our analysis concluded that the expanse of the interplanetary boundary between the Earth and the farthest point of the solar system renders a protecting and favouring environment for sustainable and reliable missions. In addition to this, reliability analysis of interplanetary spacecraft of the different mass categories using the Castet-Saleh model showed that spacecraft of a medium category (with a mass limit of 500-2500 kg) appears to reflect competent reliability than small and large category. Further, we have discussed the potential causes responsible for the difference in the reliability behaviour of spacecraft operating at the distinct interplanetary boundary. Finally, we expect that our work may provide a useful framework for space agencies and spacecraft manufacturers to contemplate adequate spacecraft design and integration along with the perspective of interplanetary boundary selection for future interplanetary missions.

Acknowledgements

I would like to extend my sincere thanks to the General Manager **Mr. Raajesh Ghoyal**, Pulkit Metals Private Limited, Pondicherry, India for the financial aid for the research. Further, I would like to acknowledge my research guide **Dr. A. Ramesh Naidu, Ph.D**, for his kind and wholehearted support throughout this research work.

Dedication

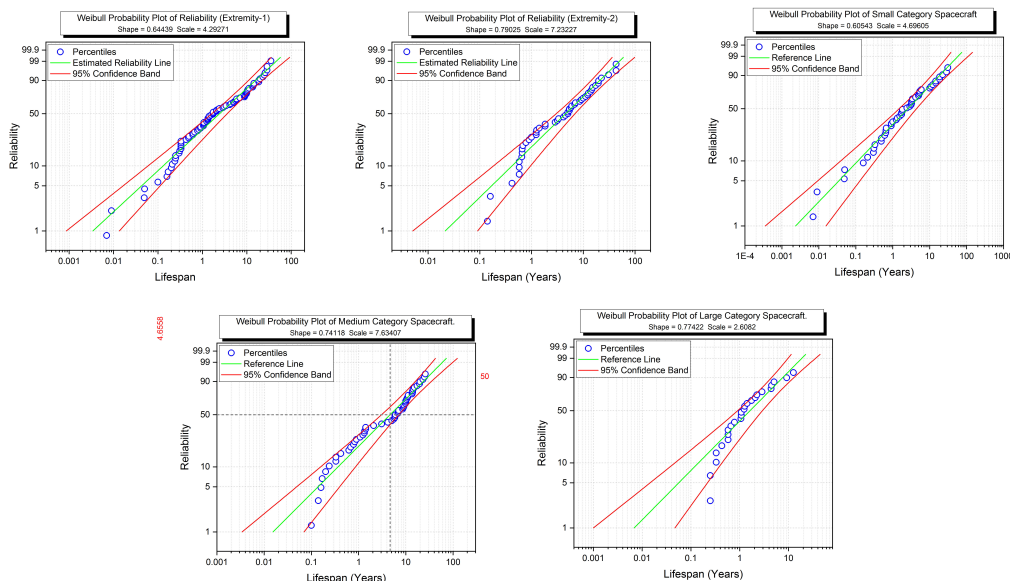
I would like to dedicate my research work to my beloved mother late. **Mrs. Malathi Biswal** for her motivational speech and emotional support throughout my life.

References

- [1] Castet, J. F., & Saleh, J. H. (2009). Satellite reliability: statistical data analysis and modeling. *Journal of Spacecraft and Rockets*, 46(5), 1065-1076.
- [2] Castet, J. F., & Saleh, J. H. (2009). Satellite and satellite subsystems reliability: Statistical data analysis and modeling. *Reliability Engineering & System Safety*, 94(11), 1718-1728.
- [3] Tafazoli, M. (2009). A study of on-orbit spacecraft failures. *Acta Astronautica*, 64(2-3), 195-205.
- [4] Biswal M, M. K., & Naidu Annavarapu, R. (2020). Assessment of Efficiency, Impact Factor, Impact of Probe Mass, Probe Life Expectancy, and Reliability of Mars Missions. arXiv e-prints, arXiv:2009.08534.
- [5] Biswal M, M. K., & Naidu Annavarapu, R. (2021). A Study on Mars Probe Failures. In *AIAA Science and Technology 2021 Forum and Exposition*. (Submitted)
- [6] Dubos, G. F., Castet, J. F., & Saleh, J. H. (2010). Statistical reliability analysis of satellites by mass category: Does spacecraft size matter?. *Acta Astronautica*, 67(5-6), 584-595.

- [7] McDowell, J. (2001). Jonathan's Space Report – Satellite Catalog. Jonathan McDowell.
- [8] Biswal M, Malaya Kumar; Annavarapu, Ramesh Naidu (2020), “Master Catalogue of Lunar and Mars Exploration Missions and their Probe Parameters”, Mendeley Data, V2, doi: 10.17632/mdkzgz23dj.2
- [9] Siddiqi, A. A., & Launius, R. (2002). Deep space chronicle: A chronology of deep space and planetary probes 1958-2000.
- [10] Kaplan, E. L., & Meier, P. (1958). Nonparametric estimation from incomplete observations. Journal of the American statistical association, 53(282), 457-481.
- [11] Rinne, H. (2008). The Weibull distribution: a handbook. CRC press.
- [12] Biswal M, M. K., & Naidu A, R. (2020). Mars Missions Failure Report Assortment: Review and Conspectus. In AIAA Propulsion and Energy 2020 Forum (p.3541). <https://doi.org/10.2514/6.2020-3541>.
- [13] Stassinopoulos, E. G., & Raymond, J. P. (1988). The space radiation environment for electronics. Proceedings of the IEEE, 76(11), 1423-1442.
- [14] Fan, C. Y., Meyer, P., & Simpson, J. A. (1960). Rapid reduction of cosmic-radiation intensity measured in interplanetary space. Physical Review Letters, 5(6), 269.
- [15] Webber, W. R., & Higbie, P. R. (2009). Galactic propagation of cosmic ray nuclei in a model with an increasing diffusion coefficient at low rigidities: A comparison of the new interstellar spectra with Voyager data in the outer heliosphere. Journal of Geophysical Research: Space Physics, 114(A2).
- [16] Stone, E. C., Cummings, A. C., McDonald, F. B., Heikkila, B. C., Lal, N., & Webber, W. R. (2013). Voyager 1 observes low-energy galactic cosmic rays in a region depleted of heliospheric ions. Science, 341(6142), 150-153.
- [17] Echer, E., Gonzalez, W. D., Guarnieri, F. L., Dal Lago, A., & Vieira, L. E. A. (2005). Introduction to space weather. Advances in Space Research, 35(5), 855-865.
- [18] Bourdarie, S., & Xapsos, M. (2008). The near-earth space radiation environment. IEEE transactions on nuclear science, 55(4), 1810-1832.
- [19] Mbarki, M., Sun, G. C., & Bourgoin, J. C. (2004). Prediction of solar cell degradation in space from the electron-proton equivalence. Semiconductor science and technology, 19(9), 1081.
- [20] Yamaguchi, M., Uemura, C., & Yamamoto, A. (1984). Radiation damage in InP single crystals and solar cells. Journal of applied physics, 55(6), 1429-1436.
- [21] Biswal M, M. K., & Naidu A, R. (2021). Human Mars Exploration and Expedition Challenges. In AIAA Science and Technology 2021 Forum. (Submitted)
- [22] de Winter, F., Stapfer, G., & Medina, E. (1999). The Design of a Nuclear Power Supply with a 50 Year Life Expectancy: the JPL Voyager's SiGe MHW RTG (No. 1999-01-2586). SAE Technical Paper.
- [23] Ottman, G., & Hersman, C. (2006, June). The Pluto-new horizons RTG and power system early mission performance. In 4th International Energy Conversion Engineering Conference and Exhibit (IECEC) (p. 4029).
- [24] O'Brien, R. C., Ambrosi, R. M., Bannister, N. P., Howe, S. D., & Atkinson, H. V. (2008). Safe radioisotope thermoelectric generators and heat sources for space applications. Journal of Nuclear Materials, 377(3), 506-521.
- [25] Edgington, S. G., & Spilker, L. J. (2016). Cassini's grand finale. Nature Geoscience, 9(7), 472-473.
- [26] Heacock, R. L. (1980). The Voyager Spacecraft. Proceedings of the Institution of Mechanical Engineers, 194(1), 211-224.
- [27] Hall, C. F. (1983). The Pioneer 10/11 program: from 1969 to 1994. IEEE transactions on reliability, 32(5), 414-416.

Appendices



Weibull Probability Plot for SE & EH- Extremity, and Small-Medium-Large Mass Category

Store Separation Predictions for Weapon Integration on a Fighter-Type Aircraft

Francesco Marco Riboli¹

University “Federico II”, Naples, 80138, Italy

An integrated test and evaluation approach is being developed by the Italian Air Force Flight Test Center in the area of store integration and separation. Furthermore, Computational Fluid Dynamics has gained a vital role in the realization of reliable predictions, thanks to the technological advancements of the past few decades. The present work harnesses state-of-the-art software to develop store separation predictions, which, in turn, will be implemented to mitigate flight test-related risks. Moreover, the obtained predictions will be compared to flight test data to validate the CFD model and to reduce the number of flight test sorties in future test campaigns. As a result, numerical and flight test results will be included in the military certification process for the integration of the new stores.

I. Nomenclature

<i>CFD</i>	=	Computational Fluid Dynamics
<i>M&S</i>	=	Modelling & Simulation
<i>ItAF</i>	=	Italian Air Force
<i>JDAM</i>	=	Joint Direct Attack Munition
<i>STV</i>	=	Separation Test Vehicle
<i>C.G.</i>	=	Center of Gravity
<i>EMACC</i>	=	European Military Airworthiness Certification Criteria
<i>MIL-HDBK</i>	=	Military Handbook
<i>AoA</i>	=	Angle of Attack
<i>Nz</i>	=	Normal Load Factor

II. Introduction

In the first half of the past century whenever a new store had to be integrated on and separated from an aircraft a “hit or miss” approach (known also as “Fly-Fix-Fly”) was used, leading, in some cases, to the loss of the platform itself [1]. Nowadays the advancements in wind tunnel testing and Computational Fluid Dynamics (CFD) have led to a more comprehensive approach to flight test called “Predict-Test-Validate”, which for the specific case of store integration is exposed in the document at reference [2]. The cited approach uses CFD to design wind tunnel tests, which in turn is used to design the flight test matrix to reduce the number of flight test sorties and to assess and mitigate programmatic, technical, and safety risks. The process uses also wind tunnel test results to validate CFD predictions and then, flight test results to both check wind tunnel test data and CFD predictions.

The optimization of this kind of approach has led to numerous benefits in the area of Modelling&Simulation (M&S). A clear and practical example of the impact of CFD simulations on wind tunnel development testing is shown in Fig. 1, [3].

With the advancement of computational fluid dynamics (CFD) and computational resources, numerical methods can safely produce reliable trajectory and carriage data in a shorter time, at a reduced cost, and mitigate risks by lowering the volume of flight testing. The objective of the paper is to demonstrate the efficiency of the overset mesh for this purpose, using an initial wind tunnel test case, and then applying this method to a scenario of interest for the Italian Air Force (ItAF): the certification of a light laser-guided store on a fighter-type aircraft.

¹ 2nd Lieutenant of the Italian Air Force Academy, Aerospace Engineering Master’s Student, AIAA Student Member n° 986750.

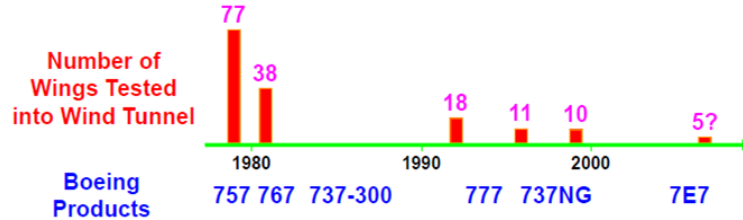


Fig. 1 - Effect of CFD on Wind Tunnel Testing [3]

III. CFD Model Description and Validation

Before applying the selected CFD methodology to a real scenario, a test case of store separation widely diffused in the literature [4] shall be validated. For the analysis of the fluid flow and geometry design, ANSYS Inc. 2019R2 Fluent® Meshing and Solver have been used, as well as the Spaceclaim® 3D CAD Modeler. In the following section, the model characteristics will be discussed, along with the procedure adopted to generate the CFD simulation and its results compared to experimental data.

A. Overview of 6-DOF Solvers and the Overset Meshing Method with Mosaic Meshing

A complete description of the unsteady aerodynamics of a store released from an aircraft depends on the successful integration of the flow solver and a 6-DOF rigid body dynamics solver. The flow solver needs to produce an accurate prediction of the forces and moments acting on the store that can be used to update the configuration of the store via 6-DOF solver (see [5] and [6]).

Together with quasi-steady [7] and dynamic mesh techniques [8], overset meshing, as described in [9], allows the decomposition of the task of meshing to individual components, and potentially simplifies the overall mesh generation. Furthermore, the quality of the mesh is preserved for bodies undergoing general motion.

The overset method comprises of two or more cell zones overlapping each other. Since different cell zones are not required to be aligned with each other, zonal grids can be generated completely independently. Hole-cutting is the process to deactivate multiple cells at overlapping zones and establish an interface to couple cells zones to provide a continuous solution. Where the grids overlap donor and receptor cells are generated, which will share information as their name describes. For further details regarding the overset mesh method please refer to ANSYS Inc. Fluent's documentation ([5] and [6]).

ANSYS Inc. Fluent supports all types of elements such as tetrahedral, hexahedral, polyhedral, or hybrid for overset mesh assembly, in particular, a new technology introduced in version 2019R2 known as *Mosaic Meshing*, further enhances the capability of the overset method.

As depicted in [10], transitioning between varying types of mesh elements in complex geometries and flow regimes has long been a major simulation challenge. ANSYS Inc. Mosaic technology meets this challenge by automatically connecting different types of meshes with general polyhedral elements. Poly-Hexcore, the first application of Mosaic technology, fills the bulk region with octree hexes, keeps a high-quality layered poly-prism mesh in the boundary layer, and conformally connects these two meshes with general polyhedral elements. The resulting simulation is faster with greater solution accuracy while using less RAM. A result of the use of such method is depicted in Fig. 2.

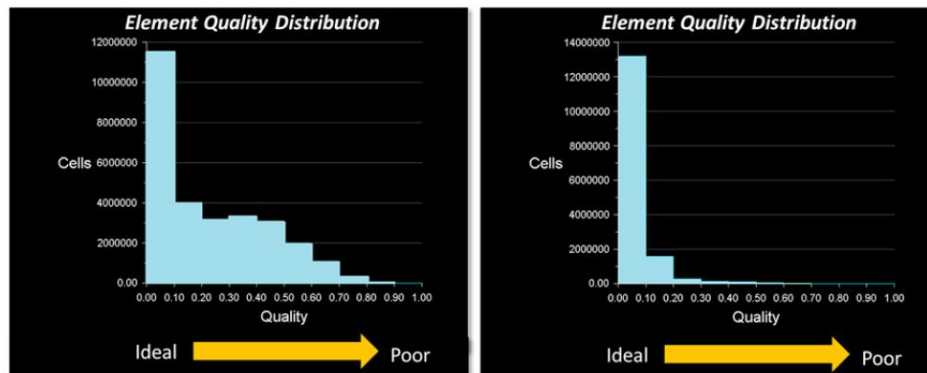


Fig. 2 – ANSYS Inc. analysis of Poly-Hexcore Mosaic (right) technology compared with conventional Tet-Hexcore meshing (left) technology on a generic Formula One wing. Mesh size is reduced by 46% [10]

B. Test Case Description and Geometry

To verify the effectiveness of the application of the overset method with ANSYS Inc. Poly-Hexcore Mosaic meshing a known test case must be evaluated. The experimental data and setup used refers to the EGLIN test, conducted at the Arnold Engineering Development Center in the Aerodynamic Wind Tunnel (4T) in 1990 [4].

The test was carried out through a Captive Trajectory System (CTS) which simulated the motion of the store during separation. The store physical data contained in [4] were generated by considering the model to have been constructed on a 5-percent scale, while a 1:1 scale has been used in the present computation.

Experimental data have then been confronted with the CFD data to determine the error in the trajectory and Euler Angles of the store in transonic flow (Mach Number 0.95) and supersonic flow (Mach Number 1.20).

EGLIN test model consists of three parts, which have been modeled using Spaceclaim 3D. The first is a delta wing of constant NACA 64A010 airfoil section with 45° sweep, the second is a pylon with an ogive-flat plate-ogive cross-section shape, and the third is a finned store body of ogive-cylinder-ogive shape. The trailing edge of the wing has no sweep angle and has a taper ratio of 0.133. There are four identical fins on the store consisting of a clipped delta wing of a constant NACA 0008 airfoil section with a 45° sweep. Leading and trailing edge sweep angles of fins are 60 degrees and 0 degrees, respectively. The gap between the pylon and the finned body is 35.6 mm. Store length and diameter are 3017.5 mm and 508.1 mm, respectively (see [4] for further details). The sting that was used in the CTS test has not been modeled: it has been substituted with a flat surface in the transonic test and with an ogive symmetrical to the nose in the supersonic test, thus to provide additional data regarding this type of approximation.

The store is ejected with a force to commence a safe initial separation until it falls for 100 mm (which is the stroke of the ejector piston), and later, its motion is subjected to gravity and aerodynamic forces. The used reference frame and conventions are shown in Fig. 3. Store mass, center of mass position, inertial properties, and ejector parameters are tabulated in Table 2.

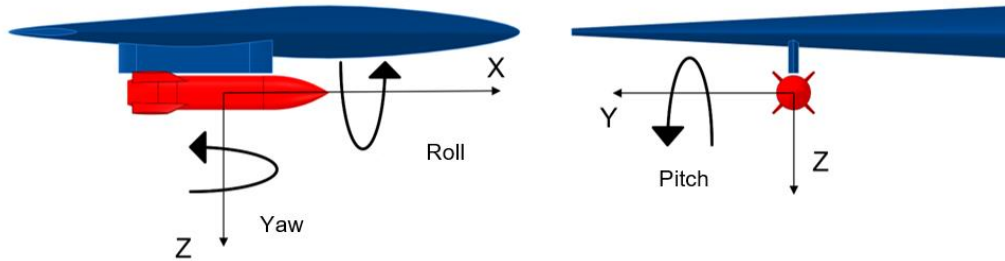


Fig. 3 – EGLIN Test Case Reference Frame

C. Test Case Computational Domain and Mesh

A half symmetry model is used for the delta wing section. Two cell zones have been created considering overset requirements, one is the stationary background including wing and pylon, and the other for the moving store component. The mesh is generated using ANSYS Inc. Fluent Watertight Workflow. Uniform inflation layers of prismatic cells are generated on the wing, pylon, and store surfaces. Refined mesh resolution is used near the surface and grown coarser along the far-field. A Body of Influence region is used around the wing and pylon to enhance the interface interpolation. Using ANSYS Inc. Poly-Hexcore Meshing, near 1.05 million mesh cells are created in component and background together (Table 1), compared to the near 3 million obtained in a previous overset analysis of the same test case [9]. Curvature sizing is applied on store, pylon, and wing surfaces to obtain a good grid resolution for representing the surface geometry. Mesh around the store is shown in Fig. 4, with a close-up of the prismatic layers around the store nose. The mesh for the entire domain and a close-up of the mesh around the wing and pylon is shown in Fig. 5.

Component	Number of Cells	Min. Orthogonal Quality
Store	172'684	0.48
Wing and Background	879'258	0.23

Table 1 - Meshes Characteristics of the components in the validation test case, the total cell count is 1.05 Million

Mass	907.185 kg
Center of Mass	1417.3 mm (aft of STV nose)
Ixx	27.1163 kg-m ²
Iyy	488.0944 kg-m ²
Izz	488.0944 kg-m ²
Forward Ejector Force [F_Z]	10676.0 N
Aft Ejector Force [F_Z]	42703.0 N
Forward Ejector Moment [M_Y]	-1920.0 Nm
Aft Ejector Moment [M_Y]	14057.0 Nm
Ejector Piston stroke length	0.10 m

Table 2 – 6-DOF Properties of the Store Model

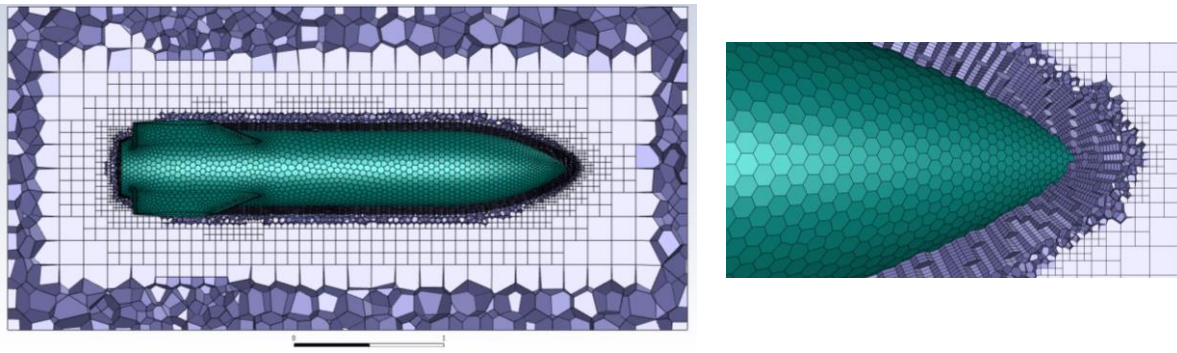


Fig. 4 - Poly-Hexcore Mesh around the Store and a close-up of the prismatic layers near the nose

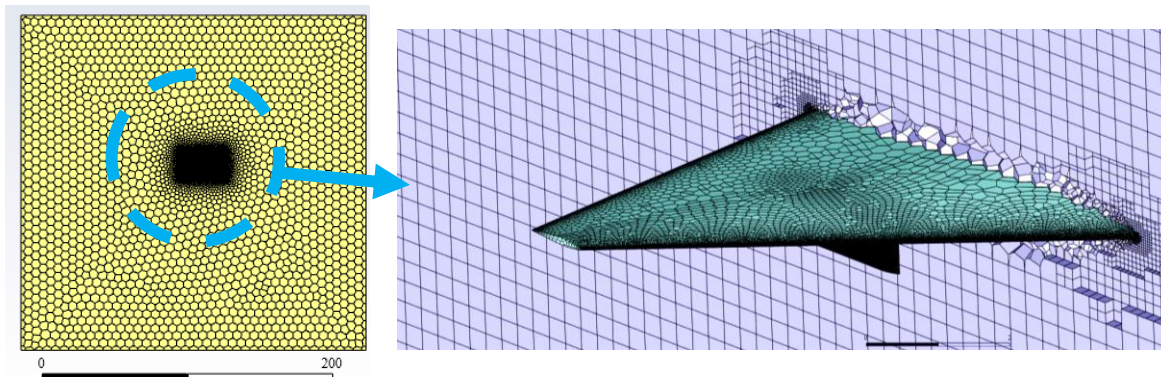


Fig. 5 - Poly-Hexcore Mesh around wing and pylon. Dimensions in meters

D. Solver Settings and Boundary Conditions

A boundary distance-based donor priority method is used to achieve an accurate overset interface for this problem. This method is efficient when there is a small gap between the walls, like the one between the store and the pylon.

Inviscid flow is invoked as viscous effects are not considered critical to the analysis, as shown in multiple studies [8, 9, 11]. Exploiting the symmetry of the geometry only one wing is modeled. A far-field boundary condition is applied on all the remaining surfaces of the background mesh, while an overset boundary condition is used on the surfaces of the component fluid volume, to define the interface between the background and the component.

Rigid body motion settings are defined for store wall. In order to do so, a User Defined Function has to be previously defined, containing the mass and inertial data of the store, as well as the ejection forces and moments. The component zone attached to the store is also given a passive rigid body motion attribute to ensure it follows the store. The ideal gas equation is obeyed for this case. Air properties are described in Table 3.

Density-based coupled solver with implicit formulation is used along with second-order upwind discretization in space and first-order-backward-Euler in time (refer to [5] and [6] for additional details). Least squares method is employed for special gradient calculation as well as for the overset interpolation weights. A fully developed steady-

state solution is used as an initial condition for the transient analysis. The Courant number of 1 is used for the initial few time steps and later increased to 10, as per best practices [5, 6]. A time step size of 0.0005 seconds is used for transient solution for the transonic flow, while a time step size of 0.001 seconds is used for the supersonic flow.

Flow Speed (Mach number)	0.95	1.20
Altitude	7924.8 m	11600 m
Pressure	35988.8 Pa	20589 Pa
Temperature	236.639 K	216.65 K
Gravity Acceleration	9.771 m/s ²	9.7646 m/s ²

Table 3 – Free Stream far-field Boundary Conditions

E. Transonic Flow Analysis

Transient simulation for Mach number 0.95 is performed for 0.45 seconds with a time-step size of 0.0005 seconds. The store C.G location in the global coordinate system as a function of time is shown in Fig. 6. Ejector and gravity forces dominate the aerodynamic forces in the Z (vertical) direction. C.G coordinates display a satisfactory agreement with the experimental data, Table 4 shows a maximum error of 0.11 m in the X-coordinate. The store moves rearward and slightly inward as it falls. The discrepancy in the X-direction is expected since viscous effects are not included in this analysis. Overall, the inviscid assumption and the reduced computational associated with inviscid calculations seem reasonable. Store's angular orientation in the global coordinate system as a function of time is shown in Fig. 7. While the store is separated, the nose pitches up for some time due to the initial ejector forces, later the store pitches down due to the action of aerodynamic and gravity forces. Substantially, the store exhibits rolling and yawing motion outward towards the wingtip. A higher discrepancy can be found in the rolling motion leading to a maximum error of 6.0° in the time frame. All the maximum errors in absolute terms are reported in Table 4. A frame by frame motion of the store is shown in Fig. 8 (next page).

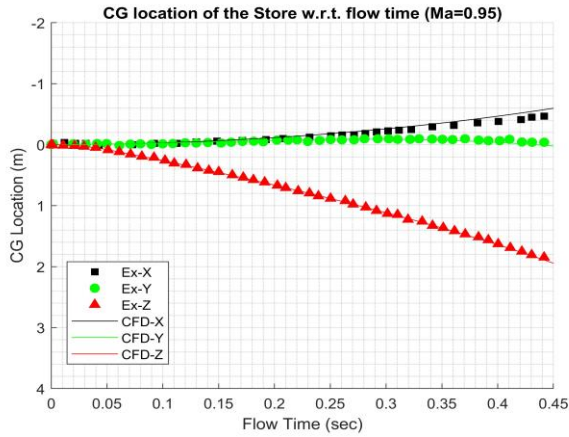


Fig. 6 – C.G. coordinates at M=0.95

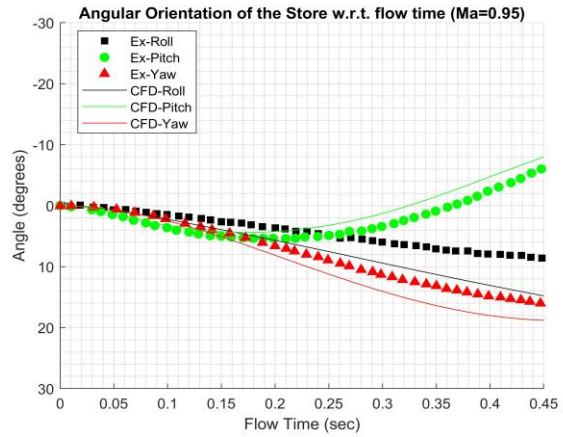


Fig. 7 – Euler's Angles at M=0.95

ΔX [m]	ΔY [m]	ΔZ [m]	$\Delta Roll$ [°]	$\Delta Pitch$ [°]	ΔYaw [°]
0.11	0.06	0.04	6.0	2.5	3.2

Table 4 – Maximum Errors in the Transonic Simulation

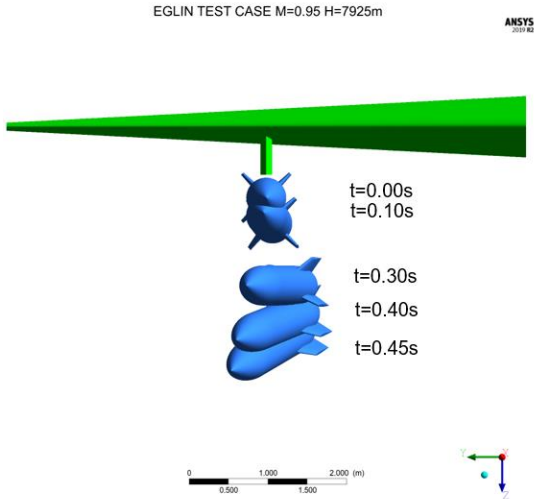


Fig. 8 – Store position and orientation in Transonic Flow

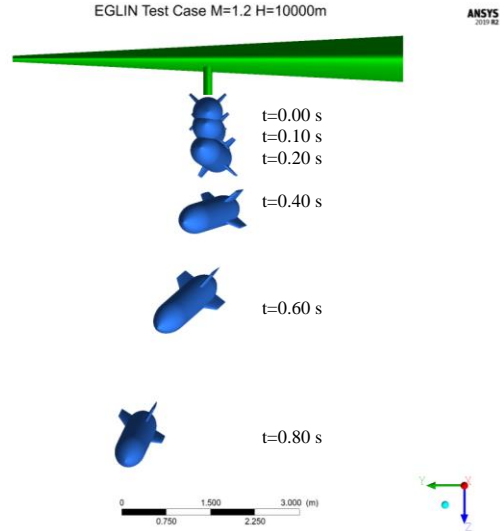


Fig. 9- Store position and orientation in Supersonic Flow

F. Supersonic Flow Analysis

Transient simulation for Mach number 1.20 is performed for 0.80 seconds, with a time-step size of 0.001 seconds. Comparing the results, the C.G. coordinates have a maximum error of 0.1 meters up to $t=0.4$ seconds, then the error starts to increase almost linearly, as shown in Fig. 10. The angular orientation (Fig. 11) displays a similar error up to $t=0.4$ seconds as well, then the errors in yaw and pitch start to decrease, following the experimental trend, while the roll error increases up to 8.7° . These results require further investigation in order to fully understand their peculiar behavior, which cannot be attributed to a single cause: the absence of viscous effects, as well as the use of a twice larger time-step, might be the parameters that should be firstly investigated in a future study regarding the supersonic flow. Despite this, the solution for the first 0.40 seconds can be considered satisfactory. A frame by frame motion of the store can be seen in Fig. 9 (above).

ΔX [m]	ΔY [m]	ΔZ [m]	$\Delta Roll$ [°]	$\Delta Pitch$ [°]	ΔYaw [°]
0.33	0.64	0.48	8.7	3.8	6.7

Table 5 – Maximum Error for Supersonic Flow

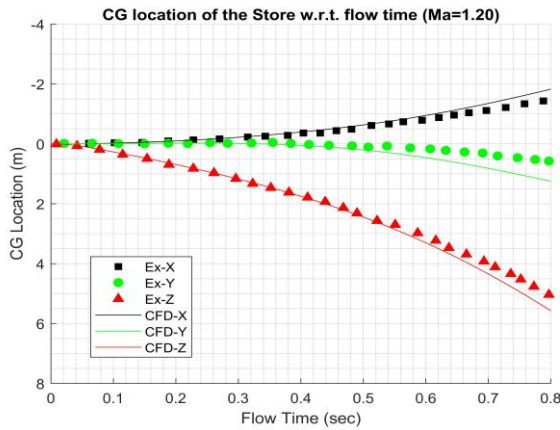


Fig. 10 – C.G. coordinates at M=1.20

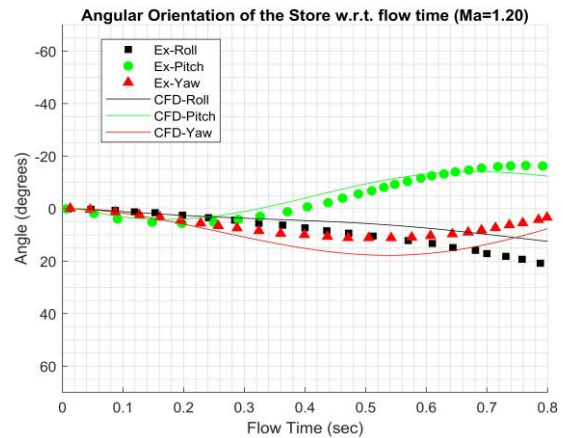


Fig. 11 – Euler's Angles at M=1.20

IV. CFD Study of an STV Safe Separation from a Fighter Aircraft

In the following section, the simulation of the separation procedure of two STVs from a fighter aircraft will be developed. For the sake of synthesis only one release sequence will be analyzed, despite the number of performed runs has been much greater. These calculations will be used by the Flight Test Engineers of the ItAF Flight Test Department (“*Reparto Sperimentale Volo*”), in the preliminary phase of the upcoming flight test campaign to assess and mitigate risks related to the release of the STVs. The data obtained in the flight tests will then be confronted with the CFD data to optimize the model for future analysis.

A. Task Origin Description

The Flight Test Department of the ItAF, in particular the Technical Squadron, has always been responsible for the aeromechanical integration and safe separation testing of new stores onboard of ItAF military aircraft. In the context of cooperation between the Air Force Chiefs of Staff, and some Aerospace Industries, the Flight Test Department was given the task of certifying the safe separation of a laser-guider light weapon from a fighter-type aircraft. To do so, as the MIL-HDBK Test 271 (release test) prescribes in section 271.3.1 [12], the test article individuated is an inert separation test vehicle (STV) of identical shape and mass properties, but without complex mechanisms, as described in the following paragraphs.

B. System Configuration Description and Geometry

The worst separation configuration and test conditions have been used in the present calculation: on the ventral fuselage pylons 3 stores are mounted, 2 STVs in the central and left pylons, and a Pod on the right pylon. The 3D CAD model used can be seen in Fig. 12. The aircraft has not been modeled, making the approximation of considering the pylons attached to an infinite flat plate. The Pod geometry also has been simplified, using the geometry shown on the left of Fig. 12. The STV geometry and reference frame can be seen in Fig. 13. As far as the CFD model is concerned, each STV has been modeled as a component, whereas the pylon and Pod have been modeled together as the background domain.

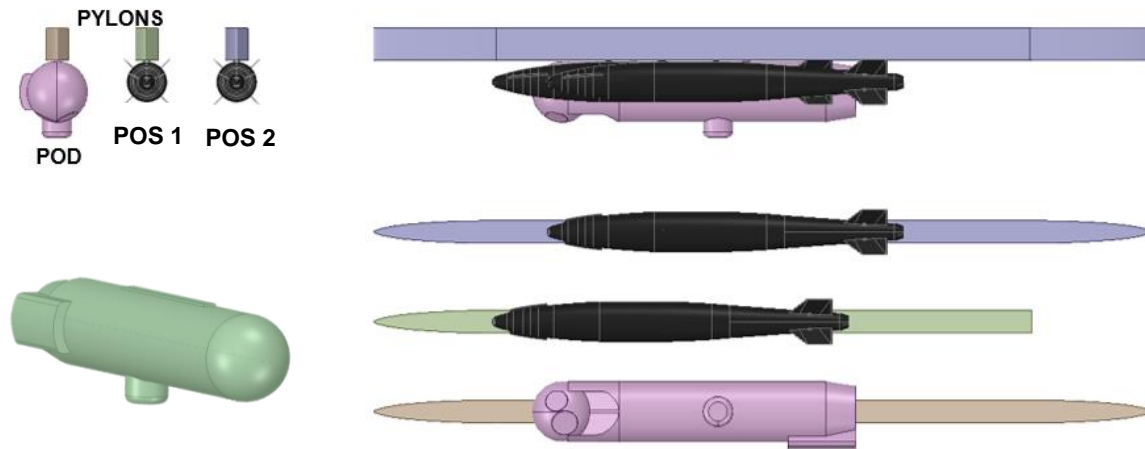


Fig. 12 – 3D CAD Model of pylons, stores, and simplified Pod geometry

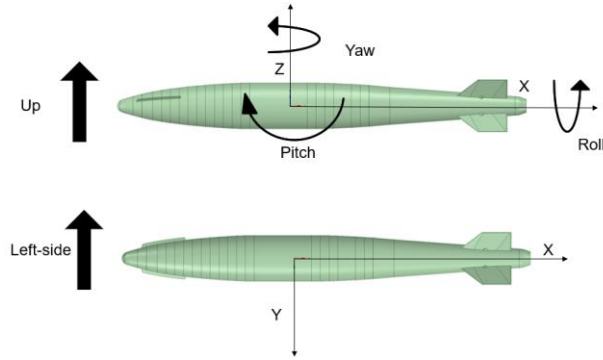


Fig. 13 – STV Reference Frame

Mass	246.754 kg
Center of Mass (aft of STV nose)	1016.84 mm
Ixx	2.4472kg-m ²
Iyy	72.7518kg-m ²
Izz	72.7288 kg-m ²
Forward Ejector Force [F_Z]	-3922.66 N
Aft Ejector Force [F_Z]	-3922.66 N
Forward Ejector Moment [M_Y]	-1208.6 Nm
Aft Ejector Moment [M_Y]	784.1 Nm
Ejector Piston stroke length	0.10 m

Table 6 – STVs Inertial properties and ejection forces

The release sequence consists of two distinguished moments: the first store released is the one from the central position (called Station 1, and in this paper, this STV will be referred to as STV 1), and then, after a period long enough to consider the two separations as independent, the second store is released from the left shoulder (called Station 2, and in this paper, this STV will be referred to as STV 2). The stores are ejected using two pistons positioned at 20 inches between the centerline of the suspension lugs, the latter are not modeled. Store mass, center of mass position, inertial properties, and ejector parameters are tabulated in Table 6.

C. Computational Domain and Mesh

The same methodology illustrated in section III has been applied, using ANSYS Inc. Fluent® Poly-Hexcore Mosaic Meshing and Solver. The computational domain for the background component consists of a parallelepiped (150x100x100) m, generated around the pylons and the Pod, while the component mesh is a parallelepiped (4.4x2.3x2.3) m. The mesh is a Poly-Hexcore mesh with inflation, using a curvature local sizing on the wall surfaces of the pylons and stores, as well as a body of influence region closer to the pylons. Each component mesh (shown in Fig. 14) is then appended to the background mesh, and one release per run is performed using the 6-DOF solver.

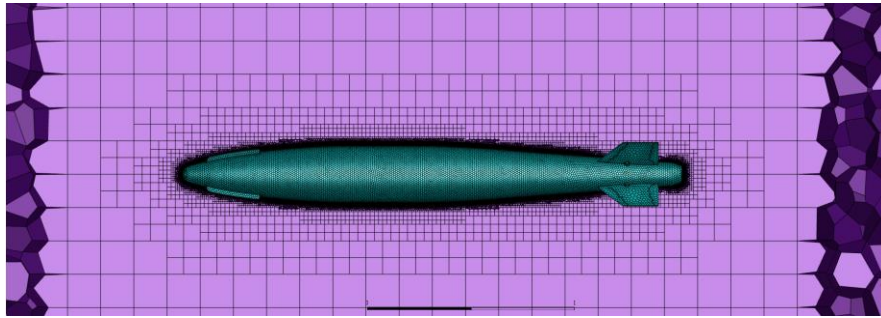


Fig. 14 – Poly-Hexcore mesh of each STV

D. Solver Settings and Boundary Conditions

The same hypothesis invoked in section III will be applied. The background face where the pylons are attached is modeled as a wall surface, and a far-field boundary condition is applied on all the remaining surfaces of the background mesh. Air properties are described in Table 7. The ideal gas equation is obeyed for this case. The overset boundary condition is used on the surfaces of the component fluid volume, to define the interface between the background and the component. Rigid body motion settings are defined for store walls.

Density-based coupled solver with implicit formulation is used along with second-order upwind discretization in space and first-order-backward-Euler in time (refer to [5] and [6] for additional details). Least squares method is employed for special gradient calculation as well as for the overset interpolation weights. A fully developed steady-state solution is used as an initial condition for the transient analysis. The Courant number of 1 is used for the initial few time steps and later increased to 10, as per best practices [5, 6]. A time-step size of 0.001 seconds is used.

Altitude [ft]	Mach	AoA	Pressure [Pa]	Temperature [K]	Nz	CFD method
20'000	0.85	5°	46'563	249	1	Density Based

Table 7 - Free Stream far-field Boundary Conditions

E. STV 1 Release Simulation Results

In the following figures, the simulation results of the STV 1 separation can be seen. The STV presents a nose-down motion up to 0.40 seconds, while it oscillates in yaw and has a constant roll rotation. The roll motion is due mostly to the interference generated by the Pod and the second store. Overhaul the store behavior can be considered safe&acceptable.

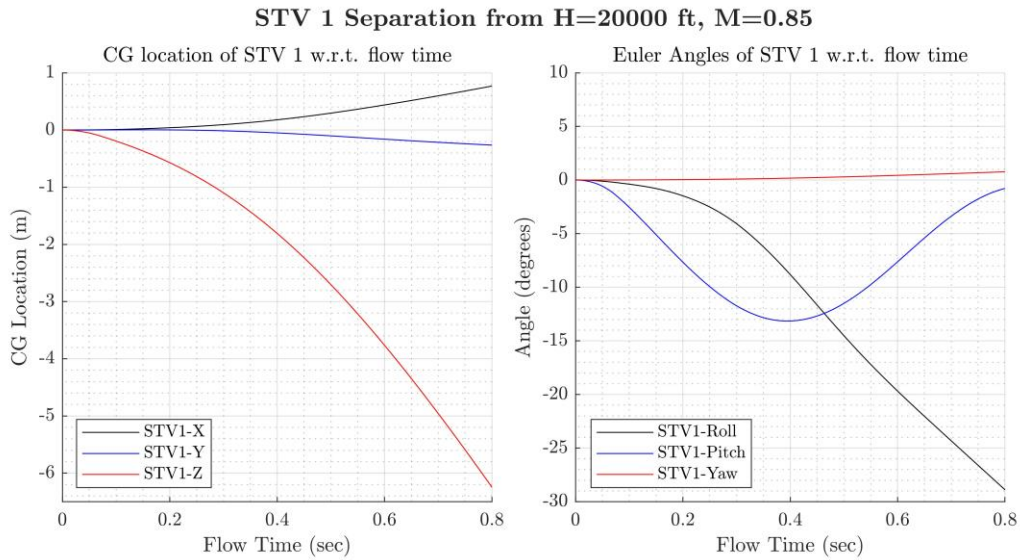


Fig. 15 – C.G. position and Angular Orientation of STV 1 released from 20'000 ft at Mach number 0.85

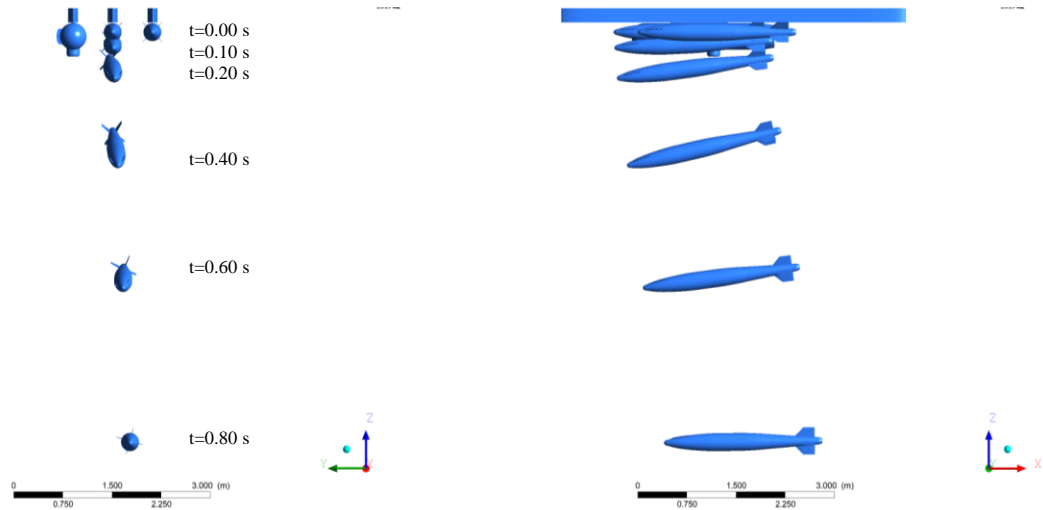


Fig. 16 – STV 1 position and orientation during release from 20'000ft at Mach number 0.85

F. STV 2 Release Simulation Results

In the following figures, the simulation results of the STV 2 separation can be seen. The STV presents a nose-down motion up to 0.35 seconds, while it oscillates in yaw and has a constant roll rotation. The roll motion is due mostly to the interference generated by the Pod. The angular motion has a smaller amplitude compared to STV 1. Overhaul the store behavior can be considered safe&acceptable.

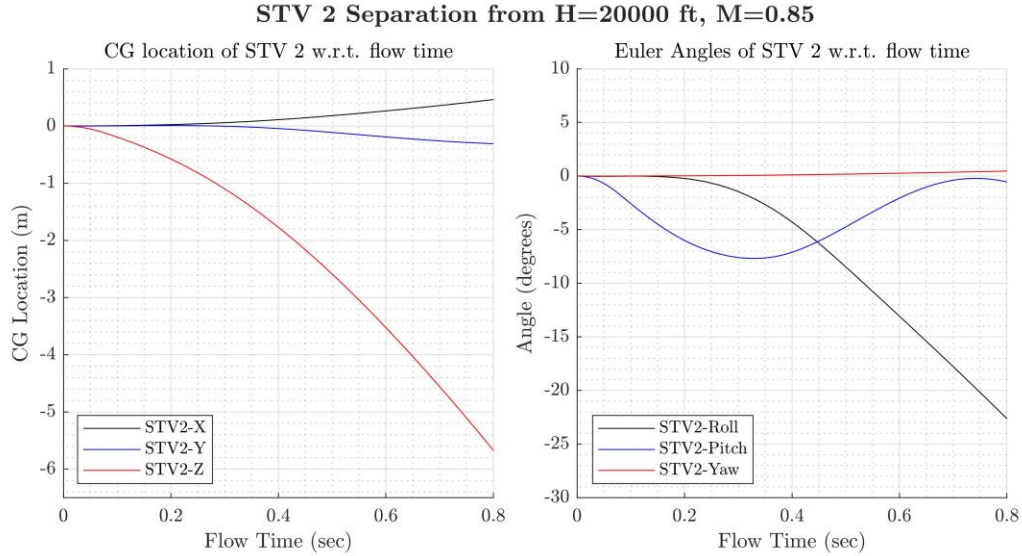


Fig. 17 - C.G. position and Angular Orientation of STV 2 released from 20'000 ft at Mach number 0.85

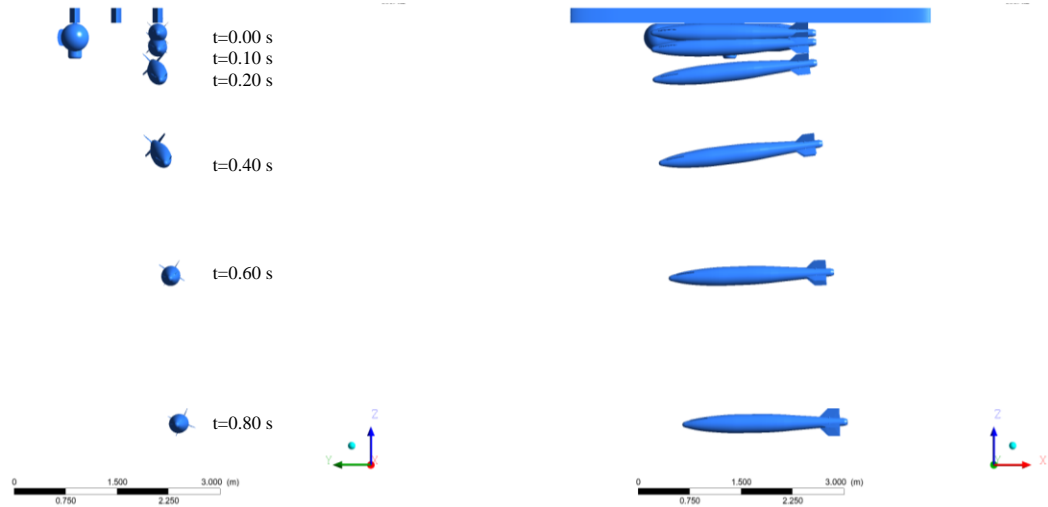


Fig. 18 - STV 2 position and orientation during release from 20'000ft at Mach number 0.85

V. Conclusions

In this paper, the validation of a CFD model based on an innovative overset Mosaic meshing algorithm (patented by ANSYS Inc. Fluent®), was performed. Experimental and CFD results in section III display a good agreement and, therefore, demonstrate good potential for the method applications in support of future test campaigns, as evaluated in section IV. The predicted motion of the STVs separations can be considered safe and acceptable in the selected test conditions and will be used by the ItAF Flight Test Department in the risk assessment and mitigation of an upcoming flight test campaign. In turn, the flight test results are going to be used in future studies to improve the CFD model, using a *Predict-Test-Validate* methodology. Another application that has been studied by the author but not added to

the present paper, is the study of the separation of a conceptual small-satellite multi-stage launcher from an underwing hardpoint of a different fighter aircraft in a steep climb (Fig. 19). The predictions are going to be used by the University “La Sapienza” to improve their design of the launcher, for a future realization of an air-launch-to-orbit capability.

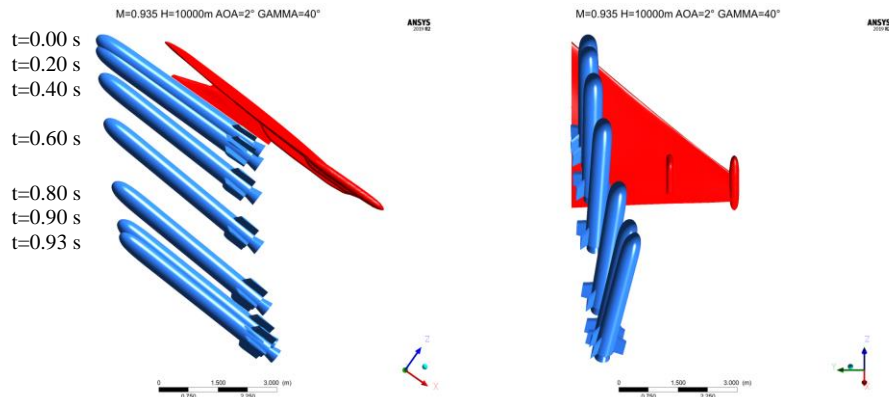


Fig. 19 – Conceptual small-satellites launcher separation from an underwing hardpoint

Acknowledgments

The author would like to thank Professor Carlo de Nicola for his eminent guidance during the course of this work, Captain Alessandro D’Argenio for being a supportive advisor and mentor of the Flight Test environment, CMSgt. Pasquale Di Biase for his important suggestions and constant maintenance of the experimental workstation efficiency, and, finally, all the Flight Test Department personnel for supporting the development of this work.

References

- [1] A. Cenko, "Store Separation Lessons Learned during the last 30 years", 27th International Congress of the Aeronautical Sciences, 2010.
- [2] F. Taverna and A. Cenko, "The United States Navy's Integrated Approach to Store Separation Analysis", RTO-Meeting Proceedings 16, paper 13, Sept. 1998.
- [3] F. T. Johnson, E. N. Johnson and N. Jong Yu, "Thirty Years of Development and application of CFD at Boeing Commercial Airplanes, Seattle", American Institute of Aeronautics and Astronautics.
- [4] E. HEIM, "CFD Wing/Pylon/Finned Store Mutual Interference Wind Tunnel Experiment", Arnold Engineering Development Center, AD-B152 669, September 10-17 1990.
- [5] ANSYS, Inc, Ansys User Manual, Version: release 2019 R2.
- [6] ANSYS, Inc, Ansys Theory Manual, Version: release 2019R2.
- [7] A. Cenko, "Experience in the use of computational aerodynamics to predict store release characteristics", Progress in Aerospace Sciences, 37, 2001, pp. 477-495.
- [8] Y. E. Sunay, "Numerical Simulations of Store Separation Trajectories Using the EGLIN Test", vol. 63, Scientific Technical Review, 2013, pp. 10-16.
- [9] A. Khaware, A. Sivanandham, V. K. Gupta and S. Ramakrishnan, "Numerical Simulation of Store Separation Trajectory for EGLIN Test Case Using Overset Mesh", AIAA, 2018.
- [10] ANSYS Inc., "ANSYS Fluent Mosaic Technology Automatically Combines Disparate Meshes with Polyhedral Elements for Fast, Accurate Flow Resolution", White Paper, 2019.
- [11] G. Demir, M. Can Erdem and N. Alemdaroglu, "Comparison of the EGLIN Test Case with CFD Based Captive Trajectory Simulation and Grid Method", 35th AIAA Applied Aerodynamics Conference, 2017.
- [12] USA Department of Defense, "MIL-HDBK-1763, Aircraft/Stores Compatibility: System Engineering Data Requirements and Test Procedures", 1998.

Aerodynamic Performance Comparison of a Conventional UAV Wing with a FishBAC Morphing Wing

A. Wong¹

Royal Melbourne Institute of Technology, Bundoora, Victoria, 3038, Australia

Morphing wings have been studied for their favourable aerodynamic performance under a wide range of lift coefficients. This paper presents a simple but effective structure and mechanical actuation system for a UAV morphing wing using flexible ribs (Fish Bone Active Camber), a Flexible Matrix Composite skin and a torsion rod for actuation. A standard Precedent T240 R/C model aircraft wing was retrofitted with an equivalent full-span 70% chord morphing wing. The aerodynamic performance of both wings was compared using TORNADO, XFLR5 and wind tunnel test. Because the morphing wing replaced conventional ailerons and flaps, maximum lift and roll performance were also compared. The results show that the morphing wing gives 14% to 89% better performance in L/D ratio for a typical range of C_L . The maximum lift coefficient had an increase in performance by 23%. Whilst the roll rate of the morphing wing was near identical to the conventional T240 wing.

Keywords: Morphing wing, FishBAC, wind tunnel test, XFLR5, TORNADO, Flexible Matrix Composite

I. Nomenclature

α	=	Angle of attack, in <i>deg</i>
α_{stall}	=	Angle of attack at which stall occurs, in <i>deg</i>
L	=	Lift, in N
D	=	Drag, in N
L/D	=	Lift to Drag ratio
C_L	=	Coefficient of Lift
C_D	=	Coefficient of Drag
C_l	=	Coefficient of Rolling Moment
δ	=	Control surface deflection angle, in <i>deg</i>
δ_a	=	Aileron deflection angle, in <i>deg</i>
δ_f	=	Flap deflection angle, in <i>deg</i>
δ_m	=	Morphing wing deflection angle, in <i>deg</i>
\dot{p}	=	Initial roll rate, in <i>deg/s</i>
ρ	=	Density, in <i>kg/m³</i>
V	=	Airspeed, in <i>m/s</i>
S	=	Wing area, in <i>m²</i>
b	=	Wingspan, in <i>m</i>
c	=	Chord, in <i>m</i>
Re	=	Reynolds number
I_{xx}	=	Mass moment of Inertia about <i>x</i> -axis, in <i>kg/m²</i>
Γ	=	Dihedral angle, in <i>deg</i>

II. Introduction

Morphing wings provide various benefits for aircraft depending on the type of morphing wing the aircraft adopts however there are general advantages that all morphing wings can provide. Morphing wings improve the aerodynamic

¹ Masters by Research Student, School of Engineering, and AIAA Student Member #1192974.

performance of the aircraft since they have smooth continuous profile [1,2] (discontinuous profiles cause disrupted airflow) and they are able to increase the lift coefficient for the same altitude through changes in wingspan, chord length, camber and sweep. The improved aerodynamic performance of an aircraft results in less fuel consumption and results in improved range [2]. The lift to drag ratio is improved due to the increase in lift [2]. The take-off distance and landing distance of aircrafts can be reduced through the use of morphing. There can be a reduction in noise due to the lack of control surfaces [3].

Morphing wings also come with disadvantage which is dependent on the type of morphing wing that the aircraft uses however there are general disadvantages that all morphing wings have. Morphing wings have more complex systems than the conventional wings leading to an increase of weight when compared to conventional wings. There is an increase in drag, in the form of induced drag which is due to the increase in lift however the increase in drag is small compared to the increase in lift. And in-order to draw out the maximum potential of morphing wings, they should not be retrofitted to aircraft but instead aircraft should be designed with the use of morphing wings in mind.

The morphing wing concept was first introduced before the first powered flight in 1903 [4]. However due to the technological limitations of the time that is materials available during that time was not strong and flexible enough, the concept was abandoned in favour of powered flight.

Birds have inspired early aviators with their flight. This led to the pursuit of morphing vehicles. The smooth and continuous shape-changing capability that birds possess however was beyond what was technological capable at the time. Aviators turned to variable geometry designs using conventional hinges and pivots both of which were used for many years. Since the recent advances in aerodynamics, controls, materials and structures the interest in morphing vehicles have been reignited and bird-like flight that is smooth and continuous shape change for aircraft is now once again pursued [5].

Morphing wings can be split into three major groups: planform alternation, out-of-plane transformation and camber change. Planform alternation is the when the wing is altered through a change in area or wing sweep adjustment. Out-of-plane transformation is the when the wing is twisted or the chord or the span wise camber are adjusted. Airfoil adjustment is when the thickness of the airfoil is altered. Planform alternation and out-of-plane transformation both have multiple methods of morphing. Planform alternation has three general methods of alteration; wing span adjustment, change in chord length and change in sweep angle. Out-of-plane transformation also has three general methods of alteration; chord-wise bending, span-wise bending and wing twist [1].

In this paper the performance of a medium sized UAV, the Precedent T240 wing will be compared to a morphing wing. The wings were compared on their aerodynamic performance specifically C_L , V_{stall} , L/D at any given C_L and \dot{p} . To be comparable to the conventional wing, the morphing wing was designed to have the same geometry as the precedent T240 wing.

III. Morphing Wing Design

There are three general methods to morph a wing which are: morphing through internal mechanisms, piezoelectric actuation, and shape memory alloy actuation. Internal mechanisms - Morphing is achieved through the alteration of the internal structure of the wing. Where rib deformation (hinge) is the most common [1]. Piezoelectric actuators- Morphing by piezoelectric actuation is achieved through the deformation through electrical current i.e when the piezoelectric material experiences an electrical current the material deflects [6]. Shape memory alloys (SMA), has the property of shape memory as the name implies has the ability to return to the initial shape after being deformed by a weight load that is activated by heat caused by an electrical current [7].

The morphing wing design in this study was based on the FishBone Active Camber better known as FishBAC is a morphing wing concept that provides an alternative to conventional flaps and other morphing camber designs. The FishBAC is biologically inspired from fish skeleton, the FishBAC's purpose is to generate large continuous changes in airfoil camber and section aerodynamic properties. The structure of a FishBAC is generally made up of a rib that consists of thin chordwise bending beam spine with stringers branching off that are connected to a pre-tensioned elastomeric matric composite (EMC) skin surface. The core and skin of the FishBAC are designed to have close to zero Poisson's ratio in the spanwise direction.

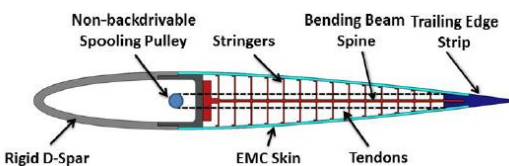


Fig. 1 An example of a FishBAC rib design [8].

The out-of-plane stiffness is increased by pre-tensioning the skin in the chordwise direction this also eliminates lower surface skin buckling when undertaking morphing. The deformation of the FishBAC occurs through compliance, the bending deflections are caused by a high stiffness tendon system.

In Wood's design, shown in Fig. 1, actuators are mounted in the D-spar drive, a tendon spooling pulley through a non-backdrivable mechanism [8]. Therefore, no actuation energy is required to hold the deflection position of the structure. This also allows the stiffness of the tendons to contribute to load carrying (chordwise bending is experienced when under aerodynamic loads), without increasing the energy required to deflect the structure. A torsion rod is used for actuation, this will be covered further in the paper.

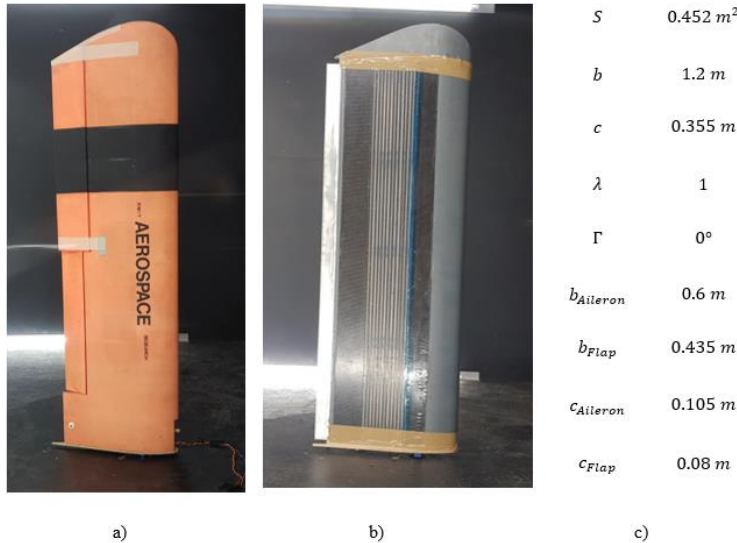


Fig. 2 Comparison of wing geometry a) T240 b) Morphing Wing c) Wing parameters.

morphing skins or compliant skins. These geometrical changes could be extensions and/or contractions depending on the morphing method of the wing. Various compliant morphing skins are available, however using an elastomer sheet on its own and in combination with structural actuation components is common [9-13].

Some examples of compliant morphing skins include: the honeycomb and its variant the accordion a honeycomb [9-11], corrugated skin [14], a SMA actuator skin composite [15], the elastomer skin and corrugated core composite [12], elastomer foam [13], a pneumatic muscle fibre with a silicone matrix [16], and the Saristu, silicone and foam with aluminium [13]. The pneumatic muscle fibre with a silicone matrix skin inspired further reading into the concept, leading to the Flexible matrix composites (FMC) concept.

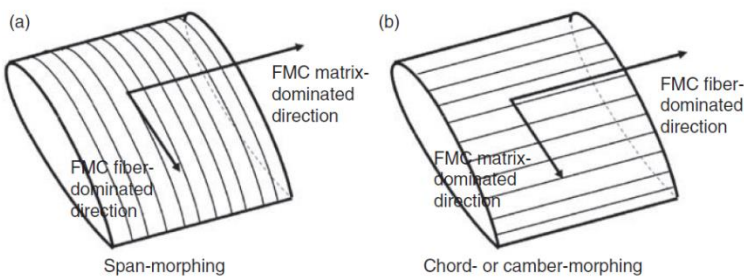


Fig. 3 FMC fibre orientation for a) span morphing and b) for camber morphing [18].

however they use the same formulae for various mechanical properties for example elastic modulus and Poisson's ratio [18]. Matrix materials for FMC tend to typically be silicone, rubber and thermoplastic whilst fibre materials are typically fibreglass, carbon fibre and Kevlar [18,19].

Considering that part of the scope of the research is to have a simple design that can be utilized by a wider aerospace community that may lack resources to implement said design, the FMC skin concept was selected over the other concepts as it the simplest concept of the three yet still effective as there it does not require perfection as there are fewer variables to account for that is the matrix material, fibre material and the fibre orientation.

A. Compliant morphing skin

The skin for the wing will be a dual skin concept consisting of an upper and lower skin, the upper skin being the compliant morphing skin and the lower skin being a thin aluminium plate able to bend without plastic deformation. The morphing skin will need to have low out-of-plane stiffness that is being able to be deformed chordwise and so that it will not require a high actuation force whilst also possessing high in-plane stiffness that is being rigid in the spanwise direction. The morphing skin will also require a zero Poisson's ratio since the skin should not contract in the spanwise direction when the camber morphing occurs.

Morphing wings require skins that are able to facilitate geometrical changes which are better known as

Flexible matrix composites (FMC) like normal composites are constructed from two or more materials; one generally being an elastic material which is called the matrix material and the second being the rigid, strength providing fibre material. An FMC allows for large strains and low in-plane stiffness in the matrix dominated direction whilst the fibre matrix dominated has high stiffness and improves out of plane load carrying capability.

In comparison to regular composites FMC have a higher ratio of fiber/matrix

The initial FMC skin was to have unidirectional carbon fibre to be infused with silicone as proposed by Murray and Kirn [18,19]. Following the advice of Murray and Kirn in their respective papers, various methods were carried out to manufacture a proper working compliant morphing skin. The issue with the initial concepts was that they all prioritized the flexibility of the skin which is why the carbon fibre in the silicone was not hardened by any resin. The final skin used carbon fibre laminate instead of dry carbon fibre fabric. The skin incorporated strips of carbon fibre corresponding to the lengths of the leading edge to the initial rib section of the wing, the width of the spine of the rib and the final rib to the trailing edge section of the wing with spacing in between for silicone. The carbon fibre laminate infused with silicone did show some slack between the ribs however the slack was less than that of what was seen with the initial skin. The slack was then eliminated by adding brackets along the FishBAC spines and by adding two brackets on the underside of the FMC skin where the skin meets the start and end of the trailing edge and leading edge respectively.

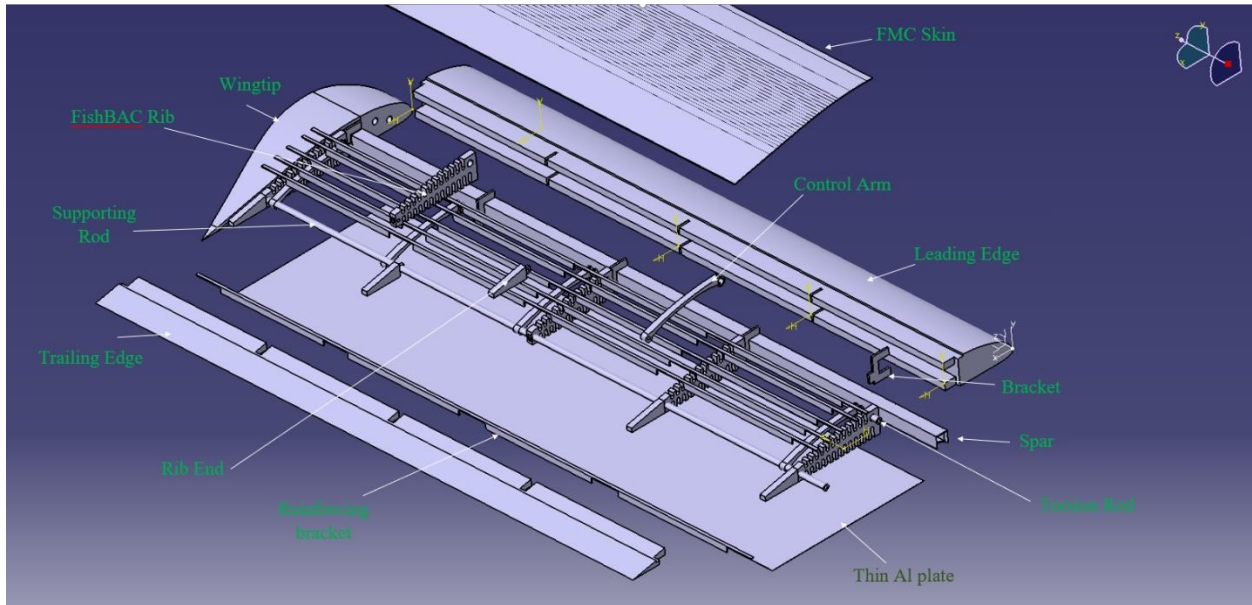


Fig. 4 Isometric view of the Morphing Wing components

B. Morphing Wing Components

The internal structure of the morphing wing is shown in Fig 4. The morphing of the wing is conducted through rotation of the torsion rod. The control arm is also deflected due to the rotation of the torsion rod. The control arm acts as a guide for the deflection for the FishBAC rib. The ribs are made of three components: bracket, FishBAC rib and rib end. Since only the middle section of the rib is deflected i.e. the FishBAC rib the bracket and rib end are rigid components. The supporting rod assists in deflecting each of the ribs across the wingspan uniformly. The bracket and rib end attach the rib to the spar and leading edge and the trailing edge respectively. The reinforcing brackets located along the spines of the FishBAC ribs prevent the FMC skin from slacking into the gaps between each of the spines. The compliant morphing skin and the thin aluminium plate facilitates the extension in the upper surface and the contraction of the lower surface of the wing respectively.

To prevent any separation of the thin aluminium plate from the wing, a thin aluminium sleeve was bonded to the trailing edge to allow for the plate to freely slide in as necessary to prevent any separation from the wing, this is shown in Fig.2 and Fig.5.



Fig. 5 Morphing Wing deflected for the Wind tunnel testing a) Top surface view b) Bottom surface view.

IV. Simulation & Results

Aerodynamic performance was predicted using both XFLR5 and TORNADO. XFLR5 is a performance approximation tool based on the XFOIL airfoil tool [22] whilst TORNADO is a VLM based solver that is an extension of MATLAB [23]. XFLR5 can perform both viscous and non-viscous aerodynamic analyses using any of the three methods; LLT, VLM and 3D panel methods [7]. XFLR5 does have its limitations as it cannot capture flow separation at low Reynolds numbers (less than Re 25000) and it tends to overestimate results however the results are still generally acceptable [24]. XFLR5 does not consider the thickness of the airfoil as it takes a thin body principle i.e it uses the mean camber line as the airfoil. [7,25]. Because XFLR5 does not consider the thickness of the airfoil, XFLR5 is mostly suited and accurate for thin airfoils [26].

XFLR5 is suited for low Re number analyses and for α before stall as it fails to capture separation of the flow [27-29]. XFLR5 performs well for viscid 2D applications and with limitations in 3D [30]. Since XFLR5 is best used for low Re number and low α applications it is best used for small UAVs. XFLR5 tends to underestimate drag because it cannot determine viscous drag and that simulating the aircraft is a detriment [30].

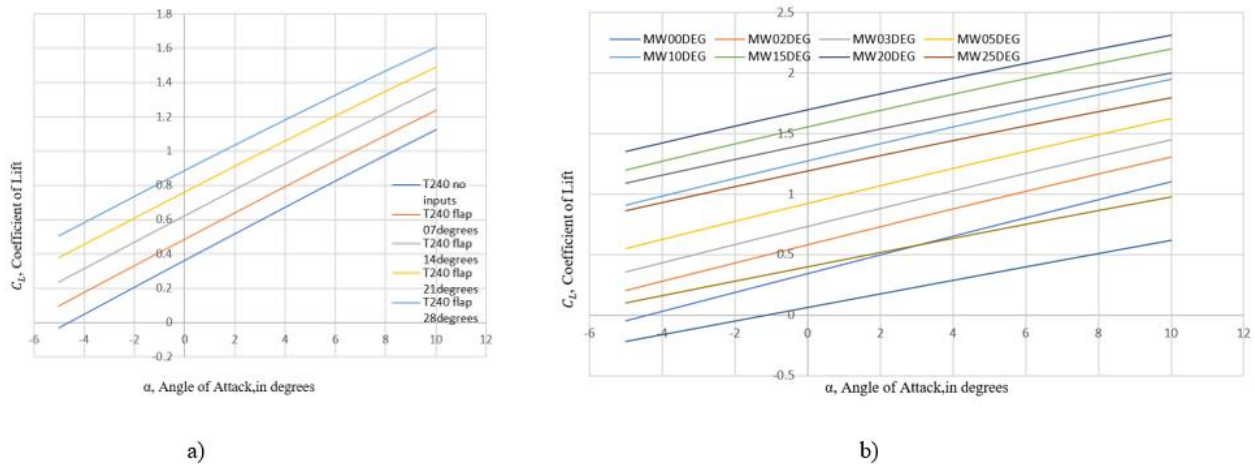


Fig. 6 XFLR5 analysis at Re 337,000 for a) T240 - C_L vs α at Re 337,000 b) Morphing Wing - C_L vs α .

The inviscid VLM method was performed for the 3D results of the morphing wing simulations. TORNADO can solve for aerodynamics coefficients using two methods; regular VLM which is based on fixed wake, or the TORNADO method which has a free stream following the wake [31]. Because one of the methods TORNADO uses is VLM, TORNADO is best suited for pre-stall α [23]. Pereira [31] found that the variation of results in TORNADO tend to decreases as the number of panels assigned to the lifting surface increases. TORNADO does not capture cambered wings performance well, since it treats the cambered wing as a flat thin wing approximation where the boundary conditions are shifted [23]. Melin found that a minimum of eight panels should be used, as it still gives good comparable results when compared to experimental data [23]. Like XFLR5, TORNADO is best suited for larger forces and not suited for viscous forces such as drag [23, 31]. For the roll motion of the morphing wing TORNADO begins to diverge from the experimental results immediately.

This could be due to the fact that TORNADO uses the VLM method which treats the wing as a thin plate where only pressure difference between the top and bottom surfaces is taken into consideration.

From Fig. 6 and Fig.7, the results from XFLR5 and TORNADO could be considered identical for the conventional T240. However, this is not the case for the morphing wing, as seen in Fig. 7, due to TORNADO treating the wing as a thin plate whilst XFLR5 still has the fully cambered 2D results to generate the 3D results.

The difference between the two shows that TORNADO would not be suitable to predict the results of the morphing wing from $\delta_m > 10^\circ$ as C_L continues to increase when reality it would decrease due to separation of flow i.e. where morphing no longer provides a benefit. This is seen again in Fig.8 where \dot{p} generally increases as δ increases while it begins to decrease after $\delta_m > 25^\circ$ in the wind tunnel test results. This difference in accuracy also extends to the conventional wing analysis where results are most accurate for $\delta_a < 10^\circ$. This again shows TORNADO, VLM does not consider separation when conducting analyses as the method is best suited for low α .

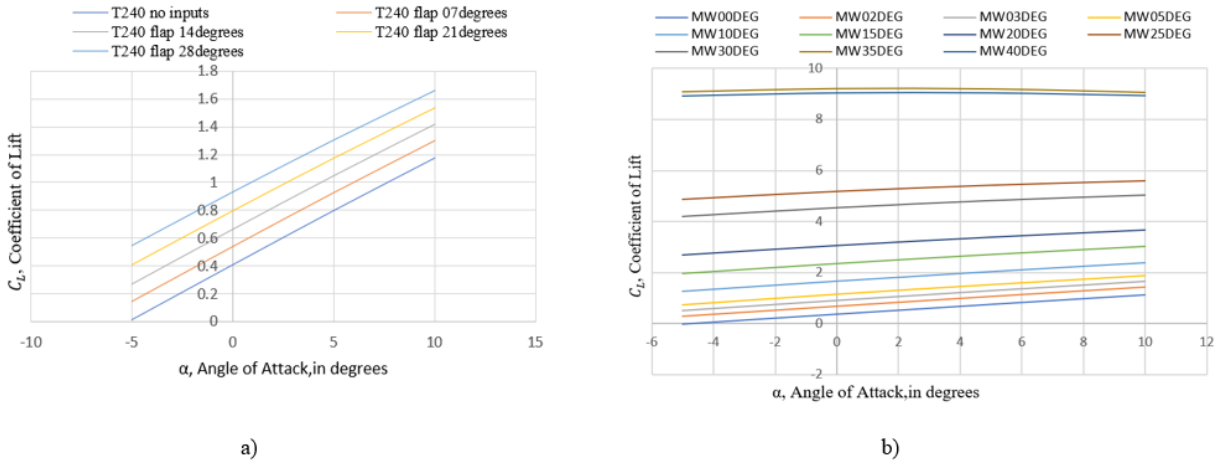


Fig. 7 TORNADO analysis at Re 337,000 for a) T240 - C_L vs α at Re 337,000 b) Morphing Wing - C_L vs α .

However, that being said the accuracy of the results from XFLR5 and TORNADO are considered satisfactory it is in within 10% - 20% of the actual result for low δ_m as the maximum benefit of morphing comes from this range where C_D would still be low. Therefore, for morphing wings XFLR5 and TORNADO should be used as an initial estimate for the aerodynamic performance and a wind tunnel test should be conducted to obtain the actual performance of the wing.

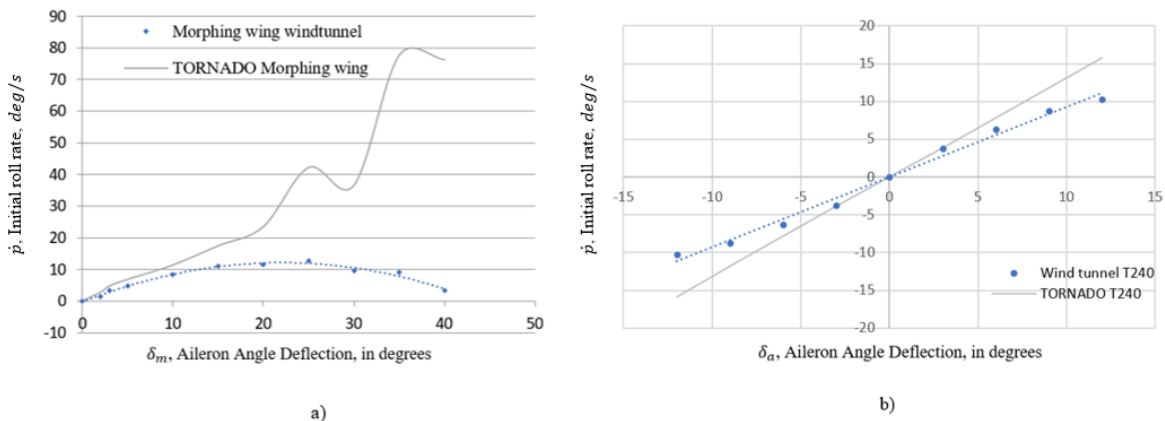


Fig. 8 Difference in TORNADO and wind tunnel testing for \dot{p} vs δ at Re 337,000 for a) Morphing Wing b) Conventional T240.

V. Results & discussion

Post wind tunnel testing Eq. 1 to Eq. 3 and the Lift and Drag equations were used to generate Fig. 8 to Fig. 12. From both Fig. 10 and Fig.11 the C_{Lmax} of the conventional T240 and the morphing wing was approximately 1.2 and 1.4 respectively an increase of 15%. By using Eq. 1, the V_{stall} of the conventional T240 and the Morphing wing was 10.9 m/s and 12.9 m/s respectively given that a difference in V_{stall} is only 2 m/s. If C_L performance during turbulent flow is considered then the morphing wing can increase the C_L 23%.

Considering that the morphing wing is heavier than the conventional T240 and given that it has yet to be optimised for weight. This means that there is room for improvement for example; if the weight of the morphing wing was reduced so that it would be only 75% heavier than the conventional T240 wing then the stall speed would match with the T240 wing.

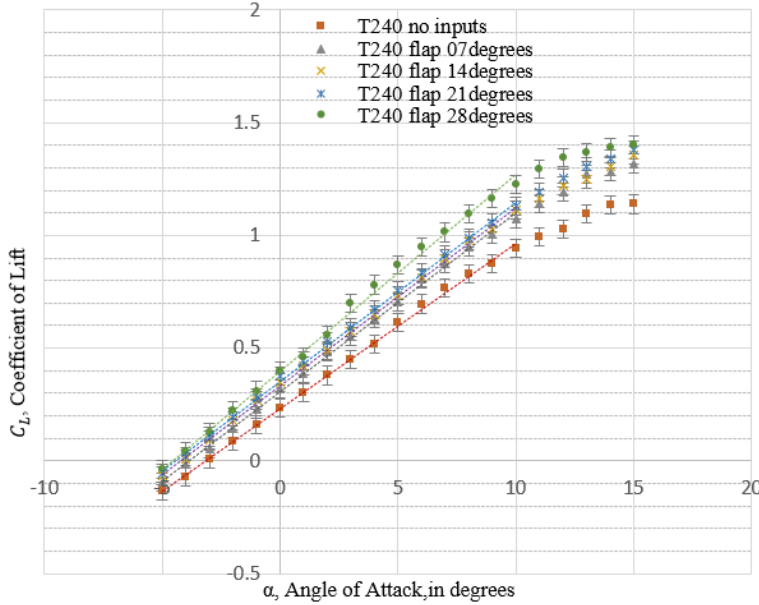


Fig. 9 Wind tunnel test result of the T240 for C_L vs α at Re 337,000

The dotted lines through each of the δ_m in Fig. 10 displays the possible linear conditions of the morphing wing, however the most stable behaviour was taken when C_{Lmax} was determined. From Fig. 12 it can be seen that, as δ_m increases the pool of data points shift towards the right and lower this is due to the increase in C_L due to δ_m and the decrease in L/D due to the increasing D . For conventional wing, L is a function of both V and α . A camber morphing wing, L is a function of both V , α and δ_m .

$$V_{stall} = \sqrt{\frac{m}{\frac{1}{2}\rho S C_{Lmax}}} \quad (1)$$

Therefore if V is kept consistent then for any given C_L there are various possible combinations of α and δ_m to achieve said C_L . From the large pool of L/D for C_L it would be ideal to cruise at the highest L/D for any given C_L . Therefore, during cruise it would be ideal for a camber morphing wing aircraft to alter its α and δ_m to achieve a maximum L/D for a given C_L . From Fig.12 it can be said that, as δ_m increases the pool of data points shift towards the right and lower this is due to the increase in C_L due to δ_m and the decrease in L/D due to the increasing D .

For conventional wing, L is a function of both v and α . A camber morphing wing, L is a function of both v , α and δ_m . Therefore if V is kept consistent then for any given C_L there are various possible combinations of α and δ_m to achieve said C_L . From the large pool of L/D for C_L it would be ideal to cruise at the highest L/D for any given C_L . Therefore, during cruise it would be ideal for a camber morphing wing aircraft to alter its α and δ_m to achieve a maximum L/D for a given C_L .

By observing Fig. 10 it can be seen that in the base morphing wing outperforms the conventional T240. The L/D for a given C_L for the morphing wing at $\delta_m = 0^\circ$ is generally 20% larger than the conventional T240 wing with zero inputs. Since the morphing wing is designed to be identical to the T240 wing it should have identical performance to the T240 wing. The only difference being that the morphing does not have discontinuous control surfaces such as flaps and ailerons as well as components related to their actuation. The difference in performance could be due to a number of factors such as the aforementioned lack of control surfaces, difference in geometry due to manufacturing

and surface finish. Given the T240's range of C_L , the morphing wing has larger L/D for a given C_L than the T240 until $\delta_m = 20^\circ$. Therefore the 20% offset in performance should be ignored. To facilitate this the morphing wing was compared to itself in relation to $\delta_m = 0^\circ$ and is treated as the T240 wing. The median increase in the performance of the morphing wing for each applicable δ_m , considering the range of C_L and in relation to $\delta_m = 0^\circ$;

- $\delta_m = 2^\circ$: 14%
- $\delta_m = 3^\circ$: 30%
- $\delta_m = 5^\circ$: 41%
- $\delta_m = 10^\circ$: 89%

$$C_l = \frac{M}{qSb} \quad (2)$$

$$\dot{p} \approx \frac{M}{I_{xx}} \quad (3)$$

Note that for roll motion of the conventional T240, a roll moment occurs via deflections of both ailerons in opposite directions. Whilst for the morphing wing a roll moment occurs via a single wing being deflected whilst the other wing remains undeflected. From Fig. 11 for roll motions conducted the morphing wing outperformed the conventional T240 wing from a $\delta_m = 3^\circ$, where the difference in performance increase until around $\delta_m = 15^\circ$, at $\delta_m = 20^\circ$ the benefits of morphing wing for begins to taper off.

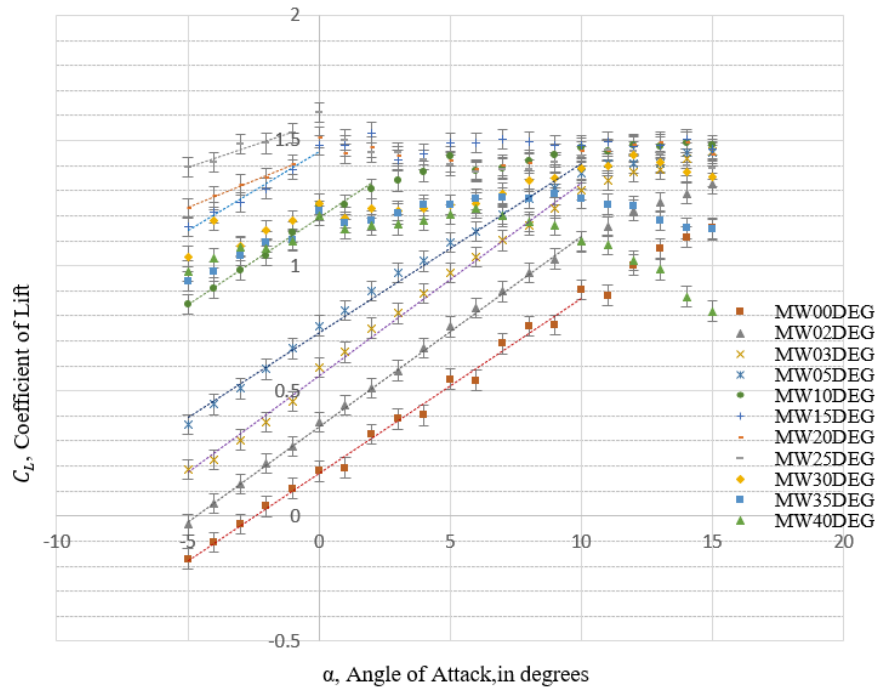


Fig. 10 Wind tunnel testing results for the Morphing Wing - C_L vs α @ Re 340000 (50 km/h).

With this observation it could be said that the morphing wing generally has a larger C_L for most δ than the conventional T240. This is likely due to more chord length of the morphing wing is deflected and the deflection is

continuous whilst the conventional T240 uses less chord length and the deflection is discontinuous and sharp.

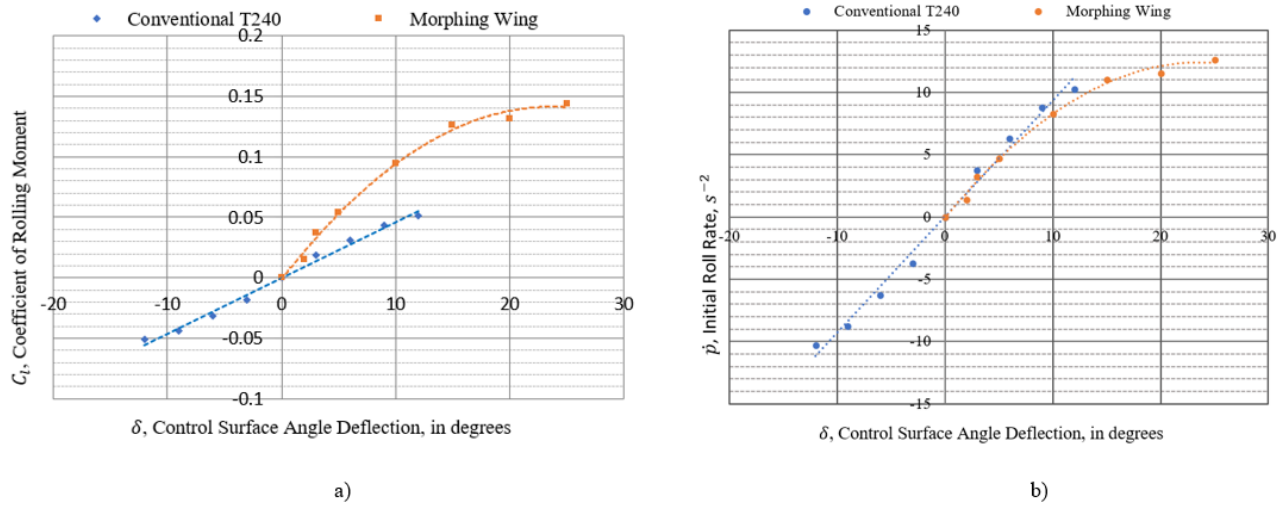


Fig. 11 Wind tunnel test result for both T240 and Morphing Wing: a) C_l vs δ at Re 337,000 b) \dot{p} vs δ at Re 337,000.

It can be concluded that the morphing wing has a better roll performance than that of the conventional T240 wing. This would only be the case if the morphing wing has the same I_{xx} as the conventional wing. Because of the wing is being retrofitted on aircraft, therefore only I_{xx} of the wings was considered since I_{xx} of the rest of the aircraft would be the same as the conventional T240 wing setup. Because of the difference in the I_{xx} , the \dot{p} , initial roll rate must be considered.

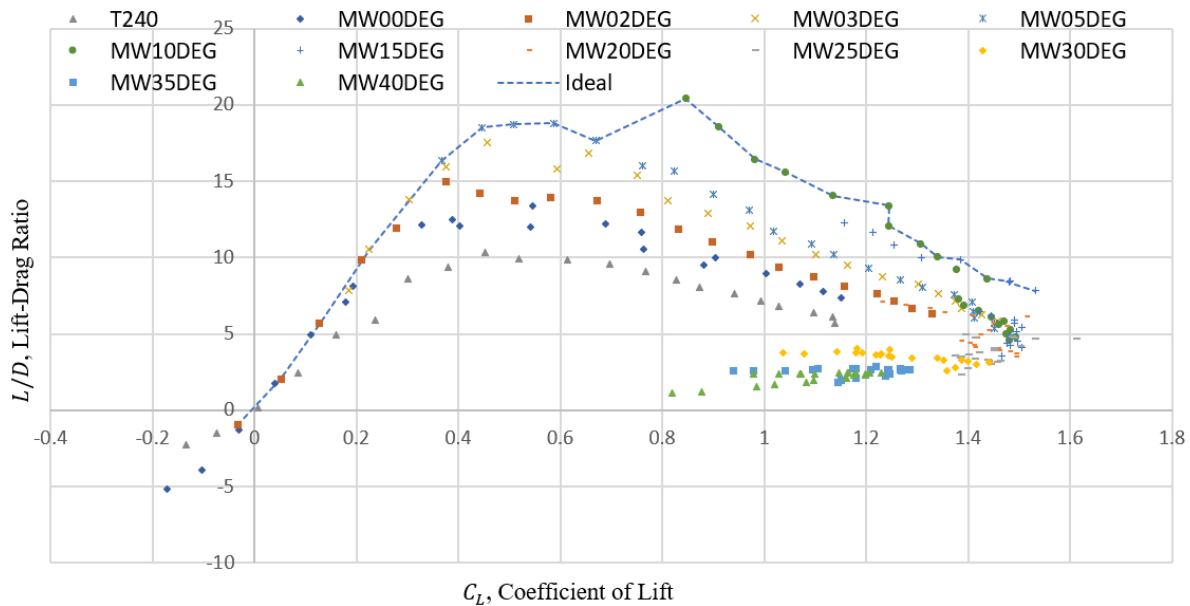


Fig. 12 Wind tunnel test results for both T240 wing and Morphing Wing - L/D vs C_L @ Re 337000.

Since both configurations have identical wingspans and are tested at the same airspeed, the \dot{p} is examined instead of p . By examining the \dot{p} of both wings seen in Fig. 11, the conventional T240 slightly outperforms the morphing wing for all δ . This however does not disprove the notion that morphing wing outperforms conventional T240 wing as the morphing wing has not yet been optimised for weight therefore weight reductions can be made and the internal layout of the morphing wing could be altered which would reduce the I_{xx} of the morphing wing setup. \dot{p} is dependent on moments generated by the wings and the I_{xx} . To increase the \dot{p} one could increase the rolling moments generated by the wing or decreases the I_{xx} of the aircraft. Since the rolling moment has already been increased through morphing

of the wing, the most logical step would be to decrease the I_{xx} of the aircraft or in this case wing. As predicted there is a drop in C_L if δ_m too large, this would in turn lead to a drop in roll (L or M) which in turn would decrease the p (roll rate). Therefore, anymore further morphing beyond $\delta_m = 25^\circ$ is detrimental to C_L , C_l , and \dot{p} .

VI. Conclusion

In this study a comparison between the aerodynamic performance of a Precedent T240 model aircraft and a simple morphing wing of the same geometry was designing, manufactured, and tested using simulation and wind tunnel experiments. The morphing wing has better L/D performance for a given C_L ranging from 14% to 89% depending on the combination α and δ_m . The C_{Lmax} performance of the morphing was also greater than the conventional T240 by 15% at a lower α . The morphing wing is heavier than the conventional wing, but this was offset by a better roll capability using differential morphing which resulted in a near identical initial roll rate to the T240. A compliant morphing skin using the FMC concept with silicone and carbon fibre was designed, manufactured and tested. The FMC skin was able to expand and contract without any damage to the skin during morphing process. The study has shown that a simple design for a morphing wing is a feasible actuation method and effective design as the aerodynamic behaviour of the wing is typical for a camber morphing wing.

References

- [1] Sofla, A.Y.N. et al., 2010. Shape morphing of aircraft wing: Status and challenges. *Materials & Design*, 31(3), pp.1284–1292. Available at: <http://dx.doi.org/10.1016/j.matdes.2009.09.011>.
- [2] Barbarino, S. et al., 2011. A Review of Morphing Aircraft. *Journal of Intelligent Material Systems and Structures*, 22(9), pp.823–877. Available at: <http://dx.doi.org/10.1177/1045389x11414084>.
- [3] Weisshaar, T.A., 2013. Morphing Aircraft Systems: Historical Perspectives and Future Challenges. *Journal of Aircraft*, 50(2), pp.337–353. Available at: <http://dx.doi.org/10.2514/1.c031456>.
- [4] Flammer, P.M. & Gibbs-Smith, C.H., 1972. Aviation: An Historical Survey from Its Origins to the End of World War II. *The American Historical Review*, 77(3), p.747. Available at: <http://dx.doi.org/10.2307/1870370>.
- [5] Valasek, J. ed., 2012. Morphing Aerospace Vehicles and Structures. Available at: <http://dx.doi.org/10.1002/9781119964032>.
- [6] Vasista, S., Tong, L. & Wong, K.C., 2012. Realization of Morphing Wings: A Multidisciplinary Challenge. *Journal of Aircraft*, 49(1), pp.11–28. Available at: <http://dx.doi.org/10.2514/1.c031060>.
- [7] Ko, S.-H., Bae, J.-S. & Rho, J.-H., 2014. Development of a morphing flap using shape memory alloy actuators: the aerodynamic characteristics of a morphing flap. *Smart Materials and Structures*, 23(7), p.074015. Available at: <http://dx.doi.org/10.1088/0964-1726/23/7/074015>.
- [8] Woods, B.K. & Friswell, M.I., 2014. Structural Characterization of the Fish Bone Active Camber Morphing Airfoil. 22nd AIAA/ASME/AHS Adaptive Structures Conference. Available at: <http://dx.doi.org/10.2514/6.2014-1122>.
- [9] Zhang, P. et al., 2015. Conceptual Design and Experimental Demonstration of a Distributedly Actuated Morphing Wing. *Journal of Aircraft*, 52(2), pp.452–461. Available at: <http://dx.doi.org/10.2514/1.c032739>.
- [10] Olympio, K.R. & Gandhi, F., 2009. Zero Poisson's Ratio Cellular Honeycombs for Flex Skins Undergoing One-Dimensional Morphing. *Journal of Intelligent Material Systems and Structures*, 21(17), pp.1737–1753. Available at: <http://dx.doi.org/10.1177/1045389x09355664>.
- [11] Liu, W. et al., 2013. In-plane corrugated cosine honeycomb for 1D morphing skin and its application on variable camber wing. *Chinese Journal of Aeronautics*, 26(4), pp.935–942. Available at: <http://dx.doi.org/10.1016/j.cja.2013.04.015>.
- [12] Dayyani, I., Ziaei-Rad, S. & Friswell, M.I., 2013. The mechanical behavior of composite corrugated core coated with elastomer for morphing skins. *Journal of Composite Materials*, 48(13), pp.1623–1636. Available at: <http://dx.doi.org/10.1177/0021998313488807>.
- [13] Aliabadi, FMH, Ricci, S, Semperlotti, F, & Botez, R (eds) 2017, *Morphing Wings Technologies : Large Commercial Aircraft and Civil Helicopters*, Elsevier Science & Technology, Oxford. Available from: ProQuest Ebook Central. [20 September 2018].
- [14] Navaratne, R. et al., 2015. Development and Testing of a Corrugated Skin for a Camber Morphing Aerofoil. 23rd AIAA/AHS Adaptive Structures Conference. Available at: <http://dx.doi.org/10.2514/6.2015-0792>.
- [15] Leal, P.B. et al., 2018. Skin-based camber morphing utilizing shape memory alloy composite actuators in a wind tunnel environment. 2018 AIAA/AHS Adaptive Structures Conference. Available at: <http://dx.doi.org/10.2514/6.2018-0799>.
- [16] Chen, Y. et al., 2011. Structural design and analysis of morphing skin embedded with pneumatic muscle fibers. *Smart Materials and Structures*, 20(8), p.085033. Available at: <http://dx.doi.org/10.1088/0964-1726/20/8/085033>.
- [17] Dayyani, I. et al., 2015. The mechanics of composite corrugated structures: A review with applications in morphing aircraft. *Composite Structures*, 133, pp.358–380. Available at: <http://dx.doi.org/10.1016/j.compstruct.2015.07.099>.
- [18] Murray, G., Gandhi, F. & Bakis, C., 2010. Flexible Matrix Composite Skins for One-dimensional Wing Morphing. *Journal of Intelligent Material Systems and Structures*, 21(17), pp.1771–1781. Available at: <http://dx.doi.org/10.1177/1045389x10369719>.

- [19] Kim, J., Lorkowski, T. & Baier, H., 2011. Development of flexible matrix composites (FMC) for fluidic actuators in morphing systems S. Pantelakis, ed. *International Journal of Structural Integrity*, 2(4), pp.458–473. Available at: <http://dx.doi.org/10.1108/17579861111183948>.
- [20] Dayyani, I. et al., 2014. The design of a coated composite corrugated skin for the camber morphing airfoil. *Journal of Intelligent Material Systems and Structures*, 26(13), pp.1592–1608. Available at: <http://dx.doi.org/10.1177/1045389x14544151>.
- [21] Xia, Y., Bilgen, O. & Friswell, M.I., 2014. The effect of corrugated skins on aerodynamic performance. *Journal of Intelligent Material Systems and Structures*, 25(7), pp.786–794. Available at: <http://dx.doi.org/10.1177/1045389x14521874>.
- [22] Hieu, N.K. & Loc, H.T., 2016. Airfoil Selection for Fixed Wing of Small Unmanned Aerial Vehicles. *Lecture Notes in Electrical Engineering*, pp.881–890. Available at: http://dx.doi.org/10.1007/978-3-319-27247-4_73.
- [23] Melin, T., 2000. A vortex lattice MATLAB implementation for linear aerodynamic wing applications. Royal Institute of Technology, Sweden.
- [24] Counsil, J.N.N. & Goni Boulama, K., 2013. Low-Reynolds-Number Aerodynamic Performances of the NACA 0012 and Selig–Donovan 7003 Airfoils. *Journal of Aircraft*, 50(1), pp.204–216. Available at: <http://dx.doi.org/10.2514/1.c031856>.
- [25] Koreanschi, A., Sugar-Gabor, O. & Botez, R.M., 2016. Drag optimisation of a wing equipped with a morphing upper surface. *The Aeronautical Journal*, 120(1225), pp.473–493. Available at: <http://dx.doi.org/10.1017/aer.2016.6>.
- [26] Gryte, K. et al., 2018. Aerodynamic modeling of the Skywalker X8 Fixed-Wing Unmanned Aerial Vehicle. 2018 International Conference on Unmanned Aircraft Systems (ICUAS). Available at: <http://dx.doi.org/10.1109/icuas.2018.8453370>.
- [27] Prameswari, C., Simulation Model Development of a Subscale Fighter Demonstrator.
- [28] Communier, D. et al., 2015. Aero structural modeling of a wing using CATIA V5 and XFLR5 software and experimental validation using the Price- Païdoussis wing tunnel. AIAA Atmospheric Flight Mechanics Conference. Available at: <http://dx.doi.org/10.2514/6.2015-2558>.
- [29] Kody, F. & Bramesfeld, G., 2012. Small UAV Design Using an Integrated Design Tool. *International Journal of Micro Air Vehicles*, 4(2), pp.151–163. Available at: <http://dx.doi.org/10.1260/1756-8293.4.2.151>.
- [30] Deperrois, A., 2009. About XFLR5 calculations and experimental measurements. XFLR5 documentation.
- [31] Pereira, R.L., 2010. Validation of software for the calculation of aerodynamic coefficients with a focus on the software package Tornado. Linköping University.